An investigation into the behaviour of prestressed reactive powder concrete girders subject to non-flexural actions

Author:
Voo, Jackie Yen Lei

Publication Date:
2004

DOI:
https://doi.org/10.26190/unsworks/9955

An Investigation into the Behaviour of Prestressed Reactive Powder Concrete Girders Subject to Non-Flexural Actions

by

Yen Lei VOO

A thesis submitted to The University of New South Wales

in partial fulfilment of the requirement for the degree of

Doctor of Philosophy

SCHOOL OF CIVIL AND ENVIRONMENTAL ENGINEERING

THE UNIVERSITY OF NEW SOUTH WALES

26th May, 2004

CERTIFICATE OF ORIGINALITY

I hereby declare that this submission is my own work and to the best of my knowledge it contains no material previously published by another persons, nor material which to a substantial extent has been accepted for award of any other degree or diploma at UNSW or any other educational institution, except where due acknowledgement is made in the thesis. Any contribution made to the research by others, with whom I have worked at UNSW or elsewhere, is explicitly acknowledged in the thesis.

I also declare that the intellectual content of this thesis is the product of my own work, except to the extent that assistance from others in the project's design and conception or in style, presentation and linguistic expression is acknowledge.

This is to dedicated to all mankind.

ACKNOWLEDGEMENTS

First and foremost, I gratefully thank my supervisor Associate Professor Stephen Foster, for his sincere assistance and guidance, encouragement and friendship throughout the past four years. Without his guidance this thesis would not have been possible to complete. I am particularly thankful to him for his patience and critical reading of the draft chapters, and for his efforts at securing financial support.

I am also grateful to Professor Ian Gilbert and Dr. N. Gowripalan for many fruitful discussions on the study. Particular thanks are due also to Mr. Bill Terry for his support and advice with the experimental work and to Mr. Brian Cavill of VSL Prestressing (Aust) in providing guidance toward this project is gratefully acknowledged. The continuation of this project is supported via an Australian Research Council Strategic Partnership with industry Grant 2001-2003. This support is also thankfully acknowledged.

Special thanks are due also to Ms. Zora Vrcelj for her friendship, advice and encouragement throughout the course of my research, which has made my experience at The University of New South Wales such an enjoyable one.

I would like to sincerely thank all the technical staff in the Heavy Structures Research Laboratory. My thanks to Mr. Tony Macken, Mr. Chris Gianopoulos and Mr. Frank Scharfe for their practical advice and assistance in constructing and testing the specimens.

Furthermore, I would like to thank all the computer support staff, namely Robert Hegedus and Jong Perng in the School of Civil and Environmental Engineering for the great help that they have provided.

Lastly, thanks are address to International Postgraduate Student Scholarship (IPRS) for financially supporting me during this project.

ABSTRACT

The commercial use of high performance concrete (HPC) as a building/construction material is well established. In contrast the use of ultra-high performance concrete (UHPC) in structural members is in its infancy and there is a lack of design tools and lack of research on the performance of structural elements constructed with this new generation material. To date, many publications on the material properties of UHPC have been reported whereas publications on the structural behaviour of UHPC are few.

The general objective of this thesis is to study the behaviour of structural members constructed with a steel fibre reinforced ultra high-strength, high-performance, concrete mix known as reactive powder concrete (RPC) and subjected to non-flexural actions. More specifically, this study investigates: (i) the behaviour of fibre reinforced RPC prestressed girders without stirrups, failing in shear and; (ii) the capacity and stability of cracks under load that develop due to bursting forces in anchorage regions of prestressed concrete girders.

This thesis is divided into three main sections: (I) development of a RPC mix using locally available materials; (II) testing of six deep panels designed to simulate bursting in anchorage regions of prestressed RPC girders and; (III) testing of seven prestressed RPC girders to investigate the behaviour of steel fibre RPC failing in shear.

In addition to the experimental investigations, an analytical model is developed to describe the constitutive behaviour of fibre reinforced concrete. The model, named the variable engagement model (VEM), is capable of describing both the pre- and post-peak behaviour of fibre reinforced concrete subjected to Mode I fracture. The model is

verified using the results of 29 direct tension tests undertaken by 10 researchers. The results of the verification show that the VEM correctly models Mode I fracture of fibre reinforced concrete for a wide range of concrete strengths (20 MPa to 200 MPa) and with varying fibre types and quantities.

Following the development of the VEM the model was incorporated into a finite element formulation for the analysis of fibre reinforced concrete, plane stress, members. The numerical verification of the finite element model, which followed, showed that the constitutive law developed for Mode I fracture of fibre reinforced concrete correctly captured the overall behaviour of the specimens tested both in this study and in the wider literature; including the load versus displacement response and the failure mode. The numerical analyses were extended to parametric studies investigating the behaviour of fibre reinforced RPC girders with varying fibre types and quantities, shear-span to depth ratios and varying levels of prestress. From the parametric studies, it was concluded that the shear strength of the specimens increased as the level of prestress and fibre quantities increased. Also, the failure mode is more ductile for specimens with higher quantities of steel fibres. In terms of shear span-to-depth ratios, the shear strength becomes a constant for shear span-to-effective depth ratios of greater than three.

In the final part of the thesis, a design model based on the theory of plasticity, combined with observations from the VEM, is used to calculate the shear capacity of fibre reinforced RPC prestressed girders that are not reinforced with stirrups. The results of the model compared well with the experimental data for the beams tested in this study.

NOMENCLATURE

A_c	area of the concrete section
A_{cf}	area of the top flange
$A_{cf,ef}$	effective area of flange
A_{cw}	area of web
A_f	cross section area of a fibre
A_g	gross cross-section area
A_p	area of prestressing steel
$A_{p,bot}$	area of prestressing steel at bottom flange
$A_{p,top}$	area of prestressing steel at top flange
A_s	longitudinal reinforcement area
a	notched depth
a	shear span
a'	distance from the external load to the starting point of a yield line (in case of T-beams)
a/d_e	shear span to effective depth ratio
a/h	shear span to depth ratio
b	width of specimen
b_f	width of flange
b_{fef}	effective width of flange
b_w	width of web
C_{HF}	capacitance
D_{eff}	effective diffusion coefficient
d	diameter of specimen
d_e	effective depth of specimen
d_f	fibre diameter

d_o	distance of the neutral axis from the plastic centroidal
$d_{p,i}$	distance of *ith* level of prestressing steel from top surface
$\bar{d}$	equals $2d_o/d_f$
E_{corr}	corrosion potential
E_{cp}	secant modulus
E_f	modulus of elasticity of fibre
E_m	modulus of elasticity of matrix
E_o	modulus of elasticity
E_p	modulus of elasticity of prestressing strand
E_s	modulus of elasticity of steel
e	distance from the top surface of a beam to the centre of gravity of the cross section
f_c	compressive strength
f_{cf}	concrete flexural tensile strength
f_{cm}	mean concrete compressive strength
f_{cp}	in-situ compressive strength
f_{ct}	tensile strength of the matrix (excluding fibres)
$f_{ct,c}$	tensile strength of the fibre-matrix composite
f_{cu}	cube concrete compressive strength
f_c^*	in-place concrete effective compressive strength
f_{dp}	double punch concrete tensile strength
f_{sp}	split-cylinder concrete tensile strength
f_t^*	effective plastic tensile strength of concrete
G_c	shear modulus
G_F	fracture energy determined from uniaxial tension tests
G_{Fm}	fracture energy of concrete without fibres

G_f	fracture energy determined from three point flexural tensile test
h	height of cylinder; total depth of specimen
I	abrasion coefficient
I_g	gross second moment of area
K	air permeability
K_d	damage factor
K_f	global orientation factor
k	local orientation factor; decay factor
k_{ave}	average value of the local orientation factor for all engaged fibres
L	total length of prism
L_o	clear span
l_{ch}	characteristic length
l_a	initial fibre embedment length
$l_{a,crit}$	critical fibre embedment length
l_c	critical fibre length
l_f	fibre length
M_{cr}	cracking moment
N_{ua}	axial force at the point of fibre-fracture
P	total load
P_{cf}	failure load of flexural tension test
P_{cr}	shear cracking load
P_{dp}	failure load of double punch tension test
$P_{e,i}$	effective prestressing force at *ith* level
P_f	fibre pullout force
P_{sp}	failure load for split cylinder tension test
P_{tear}	tearing load
P_u	maximum load

R_{Ω}	electrical resistance
r	radius of curvature
t	effective thickness of top flange
V_{cr}	diagonal shear cracking load
V_u	ultimate shear strength
w	crack opening displacement
w_{cr}	critical crack width
w_e	engagement length
w_i	initial water content
w_r	residual water content
x	diameter of steel punch; horizontal projection of yield line
y	distance from the centroidal axis of fibre
y_b	distance from the bottom surface of a beam to the centroidal axis
y_t	distance from the top surface of a beam to the centroidal axis
α	engagement constant
α_f	fibre aspect ratio
$\alpha_1, \alpha_2, \alpha_3$	bilinear softening model parameters
β	fibre fracture-bending coefficient
ε_{au}	axial strain at the extreme tensile fibre at fracture
ε_{bu}	bending strain at the extreme tensile fibre at fracture
ε	strain
ε_c	concrete strain
ε_{cp}	concrete strain at peak stress
ε_{ct}	strain at peak stress of the matrix
ε_f	failure strain
ε_{fu}	fibre failure strain
ε_{fy}	fibre yield strain
ε_{pi}	initial pre-strain of prestressing strand

ε_{py}	yield strain of prestressing strand
ε_r	strain at the guaranteed ultimate tensile strength of prestressing strand
ε_{tp}	tensile strain at cracking
ε_u	tensile strain corresponding to the critical crack opening displacement
ε_y	yield strain
ε_1	major principal strain
ε_2	minor principal strain
κ	curvature, $=1/r$
ν	Poisson's ratio
ν_c	effectiveness factor for concrete in compression
ν_{corr}	reinforcement corrosion rate
ν_m	effectiveness factor for membrane action
ν_t	effectiveness factor for concrete in tension
θ	angle of inclination with respect to the cracking plane
θ_{crit}	critical angle for fibre engagement for a given COD
θ_{lim}	limiting angle for fibre engagement
ρ	resistivity of concrete
ρ_f	volumetric ratio of fibres
ρ_w	tensile reinforcement ratio
σ	stress
σ_0	tensile strength of a fibre-composite at $w = 0$
σ_{fu}	tensile strength of a fibre
σ_{au}	average axial stress at fracture
σ_{bot}	extreme fibre stress at bottom of beam at transfer of prestress
σ_{bu}	bending stress at the extreme tensile fibre at fracture
σ_{ct}	tensile strength of matrix
σ_r	guaranteed ultimate tensile strength (GUTS)

σ_{top}	extreme fibre stress at top of beam at transfer of prestress
σ_t	tensile strength contribution from fibres
σ_{web}	average prestress in the web
σ_y	yield stress
σ_1	major principal stress
σ_2	minor principal stress
τ_b	fibre-matrix interfacial bond stress
τ_u	shear strength

ABBREVIATIONS

CMOD	crack mouth opening displacement
COD	crack opening displacement
CSM	crack sliding model
DM	Demec
ESG	electronic strain gauge
FE	finite element
FPM	fibre pullout model
FPRM	fibre pullout and rupture model
FR	fibre reinforced
FRC	fibre reinforced concrete
FR-RPC	fibre reinforced reactive powder concrete
GUTS	guaranteed ultimate tensile strength
HPC	high performance concrete
HSC	high strength concrete
NLFEA	non-linear finite element analysis
NSC	normal strength concrete
RECAP	Reinforced Concrete Analysis Program
RPC	reactive powder concrete
VEM	variable engagement model
W/B	water binder ratio

TABLE OF CONTENTS

CHAPTER 1 – INTRODUCTION

1.1 Statement of the Problem

Since the beginning of the 20th century, concrete has become the most widely used construction material. According to CEMBUREAU, the world production of cement in 1998 was about 1.6 billion tonnes compared to just 10 million tonnes in 1900 (Aïtchin, 2000). Traditionally, concrete was understood as a mixture of cement, water and aggregate but in modern concrete other constituents may also be present such as mineral components (e.g. fly ash, silica flour and silica fume), chemical admixtures (e.g. air-entrainer, superplasticizer and retarder) and fibres (steel, carbon or synthetic). Figure 1.1 shows the development of concrete throughout the age with normal strength concrete (NSC) and high strength concrete (HSC) developed in the early 1900's and 1950's, respectively. The development of ultra-high-strength high-performance composite known as the reactive powder concrete (RPC) originated in the mid 1990's. Compared with general purpose concrete, research into structures and structural components constructed with RPC as a building material is still in its infant stage.

What is RPC? In brief, RPC is an ultra-high strength cementitious material that contains a high quantity of cement and silica fume, low quantity of water, incorporates large amounts of fibres and exhibits remarkable characteristics such as high fracture energy, low permeability, limited shrinkage and increased corrosion resistance.

Over the last four decades extensive research has been undertaken on the strength and behaviour of non-flexural members cast using both non-fibre reinforced and fibre reinforced normal strength and high strength concrete. Current methodologies for design of non-flexural members include empirically based design methods, strut-and-tie modelling, limit design and finite element modelling.

In contrast, studies on the structural behaviour of fibre reinforced RPC members reported in the public literature is minimal. Most of the reported literature of RPC structural members is on the material properties of RPC and experimental tests of fibre reinforced girders designed to fail in bending. Testing of RPC members under non-flexural action has yet to be reported.

The purpose of this thesis is to explore the mechanical behaviour of steel fibre reinforced RPC in non-flexural actions for structural application. This study includes an analysis of the effect of fibres on the shear behaviour of RPC concrete beams and the development and stability of cracks formed in non-flexural, bursting, regions of RPC prestressed girders.

1.2 Aims and Scope

The aim of this thesis is to investigate the behaviour of non-flexural elements of RPC bridge girders reinforced with steel fibres. These regions include the disturbed zones adjacent to prestressing anchorages and the transfer of shear forces from applied external loads to the supports. The work in this thesis is divided into three main parts:

- (i) experimental programmes,
- (ii) analytical derivations with experimental verifications, and
- (iii) numerical analyses.

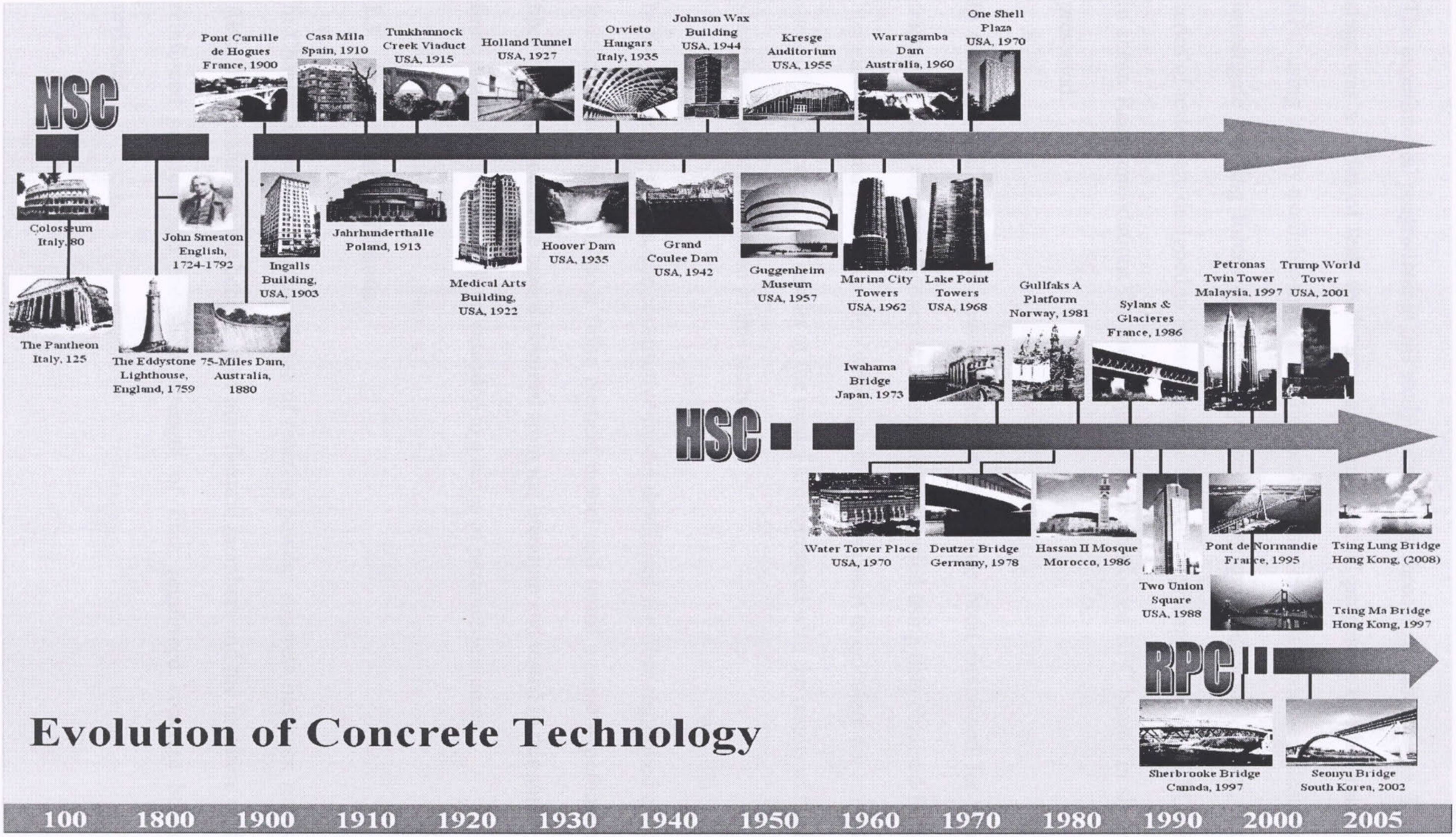

Figure 1.1 – Evolution of concrete technology.

The experimental programme in this study consisted of three distinctive stages. The first stage was a series of tests to determine the mechanical properties of fibre reinforced RPC using locally available materials. The second, a series of the tests were designed to investigate bursting forces developed by prestressed anchorages and, lastly, a third series of tests were designed to investigate the behaviour of fibre reinforced RPC beams in shear. Recommendations for the design of fibre reinforced RPC beams in shear are presented.

In the analytical studies, a new constitutive model has been developed for mode I fracture of fibre reinforced concrete. The model is verified using data obtained from the literature and used in combination with a plasticity approach to calculate the strength in shear of RPC beams. The results of the model are compared with the results of the RPC shear beam tests undertaken in this study.

In the numerical studies, the constitutive model developed for fibre reinforced concrete fracture is incorporated into a finite element model and tested against experiments on fibre reinforced concrete beams obtained from the literature and tested in this study. The finite element analyses are then extended to a series of parametric studies.

1.3 Organisation of Thesis

In Chapter 2, the existing knowledge of reactive powder concrete has been reviewed. Also, the literature on the behaviour of non-flexural members and the literature on fibre reinforced concrete and the shear strength of fibre reinforced concrete beams is reviewed.

In Chapters 3 to 5, the experimental programs of this study are presented. In Chapter 3, the mechanical properties of nineteen different RPC mix designs using locally available materials are reported. This covers the basic principles involved in producing RPC, suggested mix designs and a comparison of results for different standard strength tests.

In Chapter 4, the mechanical behaviour fibre reinforced RPC deep panels with nominal compressive strength of 150 MPa, dimensioned to simulate bursting in anchorage zones of thin webbed prestress I-girders, is reported. Included in this chapter are the selection of variables, specimen fabrication procedures, test configuration, instrumentation and gauging, experimental results and comments on test results.

In Chapter 5, the results of tests of seven fibre reinforced RPC prestressed beams with nominal compressive strength of 150 to 170 MPa without stirrups are reported. Included in this chapter are the selection of variables, specimen fabrication procedures, test configuration, instrumentation and gauging, experimental results and comments on test results.

In Chapter 6, an analytical model named the "Variable Engagement Model" is derived. The model is developed to simulate the behaviour of randomly orientated steel fibre reinforced composites subject to uniaxial tension or mode I fracture. The variable engagement model is a deterministic model and it is capable of describing the peak and post-peak response of fibre-cement-based composites in tension. Included in this chapter is the development and the experimental verification of the model.

In Chapter 7, a finite element model is presented incorporating the variable engagement model as the constitutive law for tension. The model is verified using the experimental results presented in Chapter 5 and using fibre reinforced concrete shallow and deep beams, with various concrete strengths, reported in the literature. The results of parametric studies which include different levels of prestress, fibre quantities, shear span-to-depth ratio and fibre types are also presented in this chapter.

In Chapter 8, a design model for the shear strength of fibre reinforced concrete beams without stirrups is presented and verified against the fibre reinforced RPC beams tested in this study and presented in Chapter 5.

Lastly, in Chapter 9 the major conclusions from the experimental and numerical analysis results of this study are presented with recommendations for future studies given.

CHAPTER 2 – LITERATURE REVIEW

2.1 Evolution of Concrete Technology

In 12 million BC, it is believed that a natural deposit of cement compounds was formed from the reactions between limestone and oil shale during spontaneous combustion (Shaeffer, 1992). In 3,000 BC, the Egyptians used lime and gypsum mortar as a binding agent for building the Pyramids and the Chinese used cementitious materials in the Great Wall of China. It is believed that in about the second century BC, the first use of cementitious binding agent was used in southern Italy. The Romans used volcanic sand called pozzuolana in their cement where it was first found near Pozzuoli in the bay of Naples. One of the most well known masterpieces by the Romans using ancient concrete is the Pantheon. Probably due to the lack of availability of similar pozzuolans throughout the world, this type of concrete was not used elsewhere and stone and brick masonry continued to be the dominant construction materials for many centuries.

The modern use of concrete can be traced back to John Smeaton who, born in 1724, is famous for his work on the Eddystone Lighthouse in Cornwall, England, which he had been commissioned to rebuild in 1756. Smeaton used interlocking courses of masonry bound with a pozzolanic mortar. In his later work, he added aggregate to the mix and built Ramsgate Harbour, Perth and Coldstream Bridges and the Forth and Clyde Ship Canals (Skempton, 1982). In the early 1850's, the use of reinforcing steel was introduced by Jean-Louis Lambot in his boats (Shaeffer, 1992). With the use of reinforcing, a new building form, the thin shell, was developed. In 1889 the first concrete reinforced bridge was built, Alvord Lake Bridge in the USA.

Basic cement tests were standardised in the early 1900's. In 1904, Ingalls building in USA was the first mounted concrete skyscraper. In 1916, the Portland Cement Association was founded. A year later, the US Bureau of Standards and the American Society for Testing Materials established a standard formula for Portland cement. In 1922, the tallest concrete building of the time was built, the Medical Arts Building (70 metres high, Omaha, USA). Eugene Freyssinet successfully developed prestressed concrete in the mid 1930's. In 1935, the first major concrete dams, Hoover Dam and Grand Coulee Dam were built (Shaeffer, 1992, Armstrong, 2001).

Interest in advanced cement-based materials is not solely because of their increased strength but also because of their generally high-performance characteristics. The earliest use of high performance concrete (HPC) can be traced to the 1950's and in the time since there has been numerous projects that have used HPC in their construction. In 1973, Water Tower Place reached 260 metres with concrete strengths as high as 60 MPa (Shaeffer, 1992). In the following two to three decades, high performance concrete has been widely used in bridges and high rise buildings such as Two Union Square (USA), Petronas Twin Tower (Malaysia), Tsing Ma Bridge (Hong Kong) and Trump World Tower (USA) but to list a few.

In the mid-1990's, ultra-high performance cementitious mortar known as reactive powder concrete (RPC) was developed with concrete strengths as high as 200 MPa. In 1997, the worlds first RPC filled steel tube composite foot-bridge was constructed at Sherbrooke in Canada (Adeline et al., 1998) and in 2002 the worlds first fully RPC footbridge spanning 120 metres was constructed in Seoul, South Korea (Deem, 2002). At this time, a project is being developed by VSL (Aust) for the world's first RPC highway traffic bridge to be constructed at Shepherds Gully Creek in Australia (Cavill and Chirgwin, 2003). A schematic drawing showing the development of concrete through to RPC is provided in Figure 1.1.

2.2 Reactive Powder Concrete

Reactive powder concrete is an ultra-high strength, low porosity cementitious material with high cement and silica fume contents, low water-binder ratios and uses a new generation of superplasticizer. Reactive powder concrete may also incorporate large quantities of steel or synthetic fibres giving enhanced ductility and high temperature performance. Unlike conventional concrete, reactive powder concrete contains no coarse aggregate and the fine aggregate is replaced by fine sand and crushed quartz. Richard and Cheyrezy (1994, 1995), Cheyrezy (1999) and Bonneau et al. (1996, 1997) have reported the mechanical properties of RPC and the results showed RPC demonstrated compressive strengths greater than 200 MPa and a modulus of rupture of 25-50 MPa.

2.2.1 Principle of RPC Development

Reactive powder concrete is founded on the principle that a material with a minimum of defects such as micro-cracks and pore spaces will be able to achieve a greater proportion of the potential ultimate load carrying capacity as defined by its constituent materials. Applying these guidelines, Richard and Cheyrezy (1994) proportioned a powder type concrete with particle sizes ranging from a minimum of around 150 μm to less than 600 μm to provide a very dense mixture, thus minimising the concrete void spaces.

Conventional concrete is a highly heterogeneous material, in which the aggregate (i.e. sand and gravel) form the skeleton of contiguous granular elements within the cementitious paste. According to Richard and Cheyrezy (1994), the homogeneity can be improved by:

(i) elimination of the coarse aggregate with replacement by a fine aggregate such as crushed quartz of less than 600 μm;

(ii) improvement of the mechanical properties of the paste; and

(iii) reduction in the aggregate/matrix ratio.

Compared with conventional concrete, the distribution in the size of the particles is reduced by nearly two orders of magnitude. Richard and Cheyrezy (1994) reported that a FR-RPC with the reduction in the size of the aggregate by a factor of about 50 (i.e. from 20 mm to 400 μm) results in a major reduction in the size of micro-cracks from mechanical, chemical and thermo-mechanical sources.

The main factor governing the minimum amount of water needed for fluidising a concrete mix is the compacted density of the dry solids. The density can be increased by optimisation of the grain size distribution or by the application of pressure. The optimal distribution is achieved by addition of approximately 25 percent by weight of cement and silica fume. According to Richard and Cheyrezy (1995), the silica fume has three main functions:

(i) filling the voids between the cement particles;

(ii) enhancement of rheological characteristics by the lubrication effect resulting from the perfect sphericity of the basic particles; and

(iii) production of secondary hydrates by pozzolanic reaction with the lime resulting from the primary hydration.

An application of pressure to the fresh concrete during setting can lead to an increase in density of about 5 to 6 percent and an associated increase in strength (Table 2.1). The increase of density is due to a reduction of entrapped air bubbles, removal of any excess water giving a greater than 2 percent increase in the relative compacted density and partial compensation of chemical shrinkage of concrete during setting.

Richard and Cheyrezy (1995) reported that heat-treating at 90 degrees centigrade for a period of three days substantially accelerates the pozzolanic reaction and modifies the microstructure of the hydrates that have formed. High temperature curing (between 250 and 400 degrees Celsius) on FR-RPC lead to extremely high compressive strength as shown in Table 2.1.

Table 2.1 – Compressive strength of confined and heat treated RPC (Richard and Cheyrezy, 1995).

Casting Method	Curing Temperature (°C)	Compressive Strength (MPa)
No confinement	250	488
	400	524
50 MPa confinement	250	631
	400	673

Zanni et al. (1996) shows that the high temperature heat-treatment leads to the formation of crystalline hydrates called Xonotlite (C_6S_6H). The formation of Xonotlite results in a considerable loss of weight due to intense dehydration but increases the compressive strength as a function of residual water ratio, where the residual water ratio is the ratio of the mass of water remaining (w_r) in the sample at the time of the test to the mass of water initially (w_i) introduced into the matrix. The compressive strength as a function of the residual water ratio is shown in Figure 2.1.

Using the techniques described above enhances the strength of the concrete but with ductility no better than that of conventional mortar (Cheyrezy, 1999). Ductility is greatly improved if high quantities of steel fibres are added to the mix or if the concrete is externally confined such as may occur by placing the concrete within a steel tube. The addition of 190 kg/m^3 of 12 mm long non-deformed straight steel fibres (i.e. approximately 2 percent by volumetric fraction) have been shown to give RPC some ductility in compression.

The flexural behaviour of steel FR-RPC is similar to that of fibre reinforced concrete. Typical mix designs for 200 MPa RPC (known as RPC200) and 500-600 MPa (known as RPC800), as reported by Richard and Cheyrezy (1994), is shown in Table 2.2. Typical mechanical properties for these mixes are given in Table 2.3.

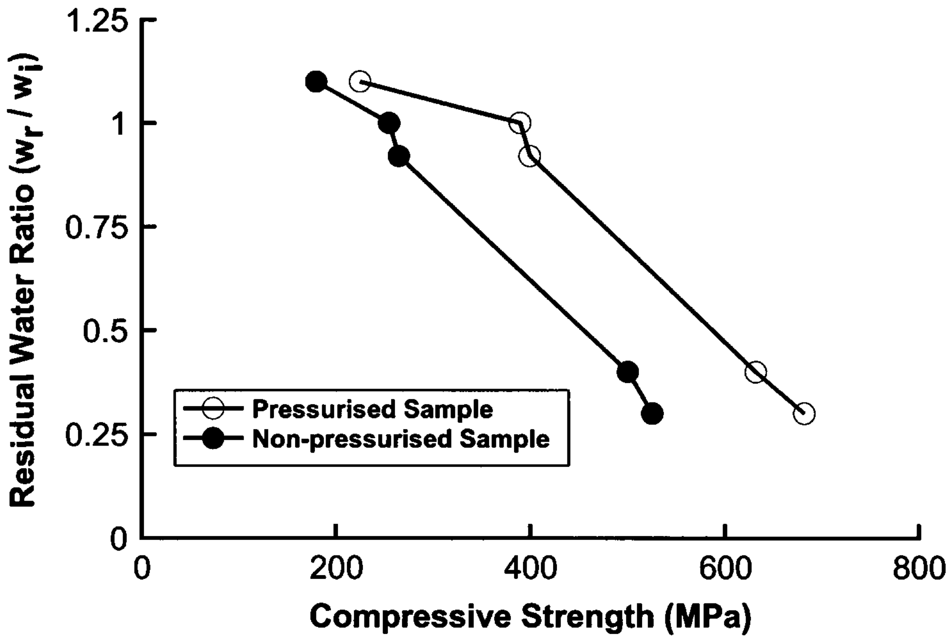

Figure 2.1 – Compressive strength as a function of residual water ratio (Richard and Cheyrezy, 1995).

Table 2.2 – Typical RPC composition by weight relative to cement (Richard and Cheyrezy, 1994).

Constituent Material	**RPC200**	**RPC800**	
	Fibre	**Silica aggregate**	**Steel aggregate**
Portland cement	1	1	1
Silica fume	0.23	0.23	0.23
Fine sand (150-600 μm)	1.1	0.5	-
Crushed quartz (d_{50} = 10 μm)	0.39	0.39	0.39
Superplasticizer (polyacrylate)	0.019	0.019	0.019
Steel fibres (l_f = 12 mm)	0.175	-	-
Steel fibres (l_f = 3 mm)	-	0.63	0.63
Steel aggregate (< 800 μm)	-	-	1.49
Total water	0.19	0.19	0.19

Table 2.3 – Mechanical properties of RPC200 and RPC800 (Richard and Cheyrezy, 1994).

Property	**RPC200**	**RPC800**
Compressive strength of cylinders	170-230 MPa	490-680 MPa† 650-810 MPa‡
Modulus of rupture	30-60 MPa	45-141 MPa
Fracture energy	20-40 N/mm	1.2-20 N/mm
Young's modulus	50-60 GPa	65-75 GPa
Pre-setting pressurization	None	50 MPa
Heat-treating (3 days)	20-90°C	250-400°C

† using quartz sand ‡ using steel aggregate

2.2.2 Durability

Since the development of RPC in the mid 1990's, many experimental investigations have been conducted on the durability of this material (Bonneau et al., 1997, Roux et al., 1996). According to Roux et al. (1996) the durability of RPC can be defined by measuring the porosity, air permeability, water absorption, diffusion and migration of chloride ions, accelerated carbonation, resistance to reinforcement corrosion, resistivity and resistance to mechanical abrasion. Tables 2.4 to 2.6 and Figure 2.2 present some of the durability tests on RPC and the results compared to 30 MPa normal strength concrete (C30) and 80 MPa high performance concrete (C80 MPa). The results of Roux et al. (1996) show that the excellent durability characteristics of RPC make it a revolutionary material with, potentially, a significant increase in the life expectancy of structures constructed using RPC.

Table 2.4 – Air permeability coefficient of non-pressurised RPC200 compared with C30 and C80 (Roux et al., 1996).

Air permeability, K (m^2)	Preconditioning of samples	
	5 days at 50°C	30 days at 80°C
C30	30×10^{-18}	-
C80	0.3×10^{-18}	120×10^{-18}
RPC200	-	2.5×10^{-18}

Table 2.5 – Concrete effective diffusion coefficient for C30, C80 and RPC200 (Roux et al., 1996).

	C30	C80	RPC200	
			Non-pressurised	Pressurised
Effective diffusion coefficient, D_{eff} ($\times 10^{-12}\ m^2/s$)	1.1	0.6	-	0.02
Resistivity, ρ (kΩ·cm)	16	96	1130	-
Abrasion coefficient, I	4.0	2.8	1.3	-

Table 2.6 – Results of corrosion-resistance tests (Roux et al., 1996).

Impedance test	Corrosion threshold	C30	C80	RPC200
Corrosion potential, E_{corr} (in mV)	>- 200	-0.82	+0.28	+0.90
Electrical resistance, R_{Ω} (in kΩ·cm^2)	>500	0.37	12	3.022
Capacitance, C_{HF} (in pF/cm^2)	-	10.793	145	14
Reinforcement corrosion rate v_{corr} (in μm/yr)	<1	1.2	0.25	<0.01

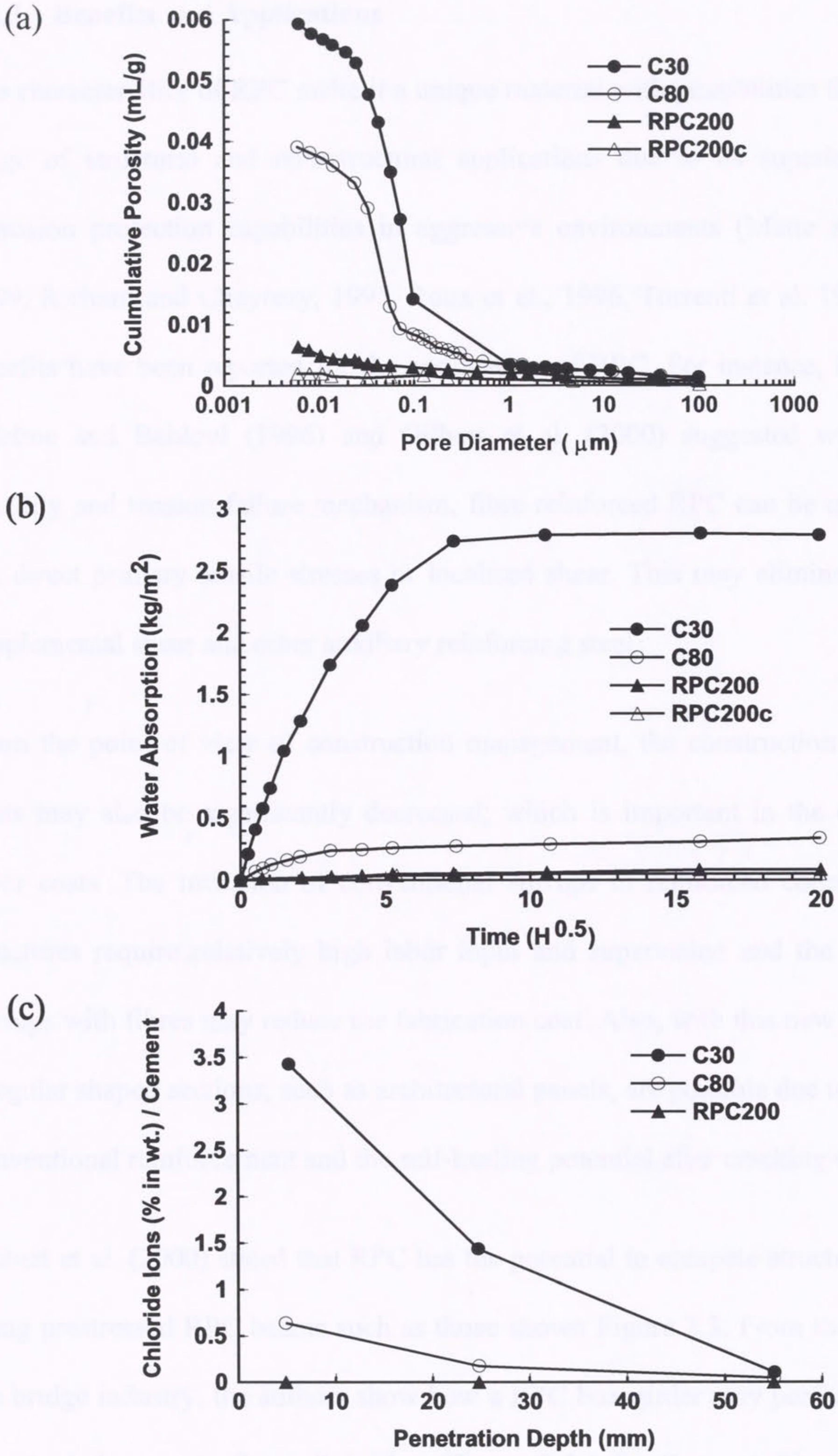

Figure 2.2 – Non-pressurised RPC200 and pressurised RPC200c compared to C30 and C80 for (a) Cumulative porosity; (b) water absorption and; (c) concentration profile of chloride ions of (Roux et al., 1996).

2.2.3 Benefits and Applications

The characteristics of RPC make it a unique material with possibilities for use in a wide range of structural and non-structural applications due to its superior strength and corrosion protection capabilities in aggressive environments (Matte and Moranville, 1999, Richard and Cheyrezy, 1995, Roux et al., 1996, Torrenti et al. 1996). Enormous benefits have been reported for the application of RPC. For instance, Richard (1996), Adeline and Behloul (1996) and Gilbert et al. (2000) suggested with its superior ductility and tension failure mechanism, fibre reinforced RPC can be used to resist all but direct primary tensile stresses or localised shear. This may eliminate the need for supplemental shear and other auxiliary reinforcing steel.

From the point of view of construction management, the construction time and labor costs may also be significantly decreased; which is important in the century of high labor costs. The inclusion of conventional stirrups in reinforced concrete beams and structures require relatively high labor input and supervision and the replacement of stirrups with fibres may reduce the fabrication cost. Also, with this new material thin or irregular shaped sections, such as architectural panels, are possible due to the absence of conventional reinforcement and the self-healing potential after cracking of RPC.

Gilbert et al. (2000) stated that RPC has the potential to compete structurally with steel using prestressed RPC beams such as those shown Figure 2.3. From the perspective of the bridge industry, the authors show how a RPC box girder may perform in place of a constructed concrete Super T bridge (Figure 2.4a) for Georges River Bridge, NSW, Australia. The existing deck consisted of seven simply supported, pretensioned, Super T box girder sections placed side by side and spanning 35 m with a 175 mm thick in-situ reinforced concrete deck placed over the 75 mm thick top flange of the girder. The RPC box girder, shown in Figure 2.4b, has been designed to perform the same task but the RPC girder requires no conventional transverse reinforcement for shear. As the girder is prestressed both longitudinally and transversely, no in-situ deck is required. The longitudinal prestressing requirement for both girders is similar. Furthermore, the weight of the RPC bridge superstructure is approximately 60 percent of the Super T girder and deck slab.

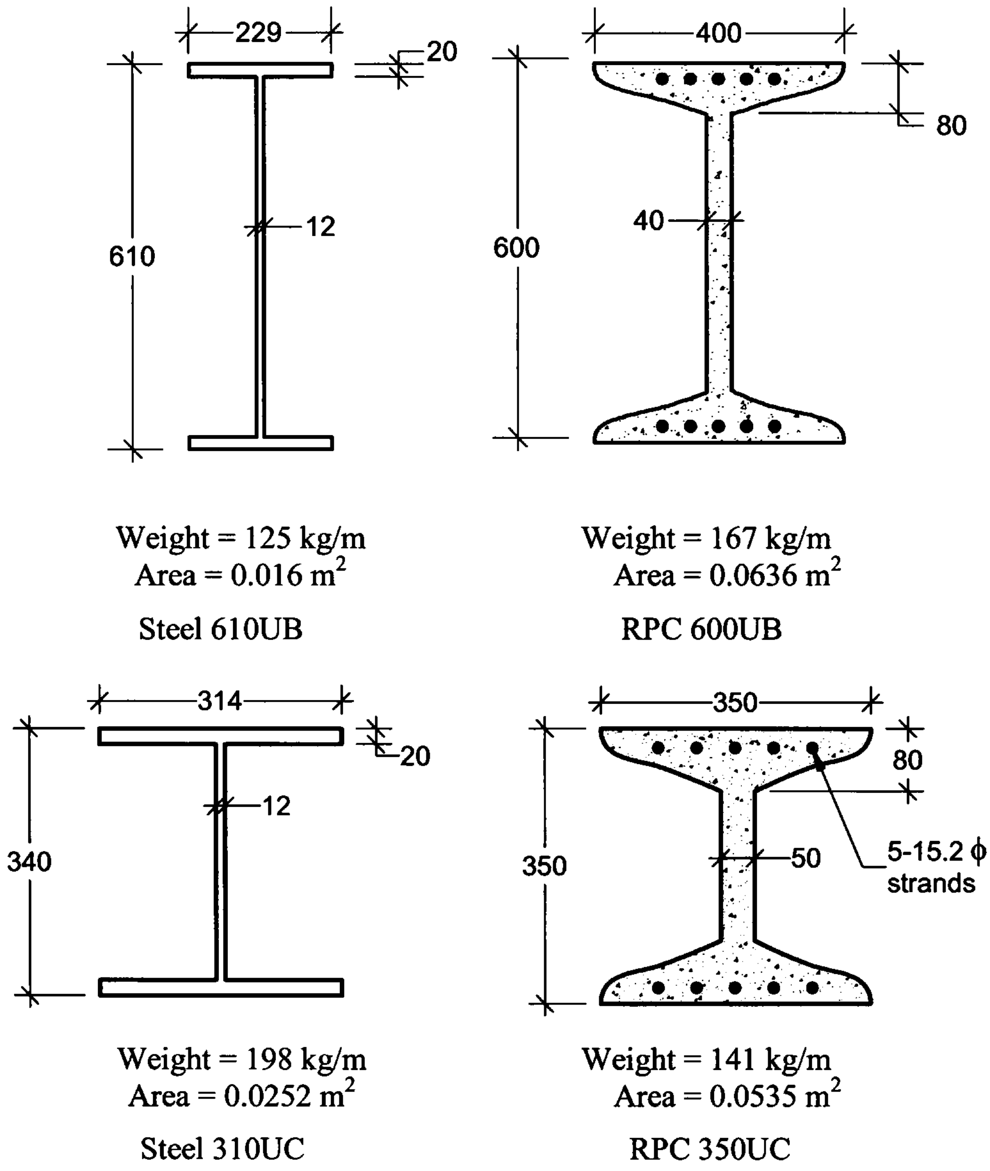

Figure 2.3 – Comparison of equivalent RPC beam and column sections and structural steel (Gilbert et al., 2000), dimension in mm.

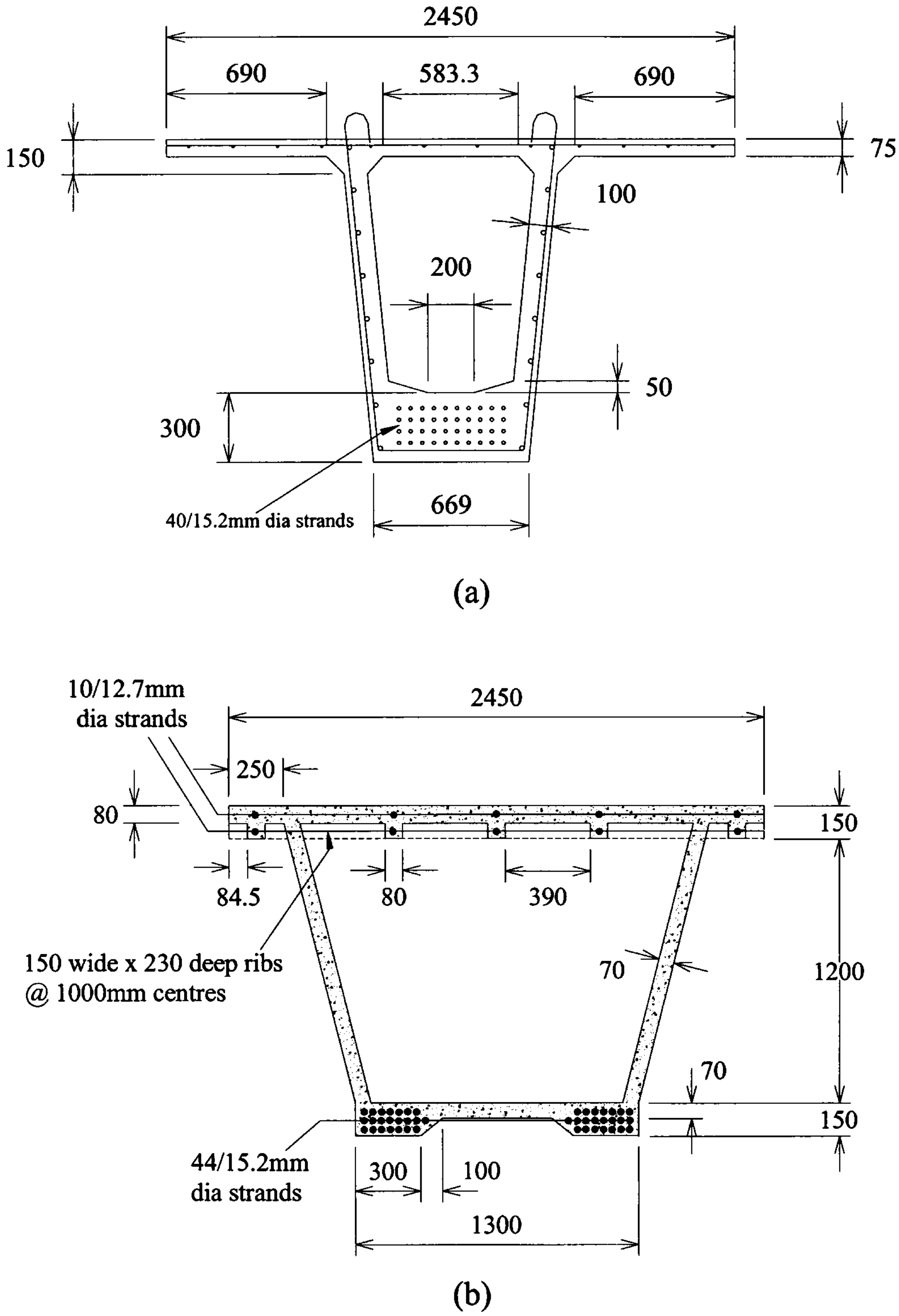

Figure 2.4 – (a) Existing and (b) alternative RPC girder sections for Georges River Bridge, New South Wales, Australia (Gilbert et al., 2000).

Reactive powder concrete is well known as a durable material. Its low and non-interconnected porosity minimises mass transfer making penetration of liquid, gas, or radioactive elements nearly non-existent. This increased durability and abrasion resistance over conventional and high strength concrete makes RPC ideal for the storage of nuclear waste or other hazardous materials (Richard and Cheyrezy, 1995, Torrenti et al., 1996, and Matte and Moranville, 1999).

From the point of view of structural design, regarding long-term behaviour, RPC exhibits low creep and shrinkage properties and has remarkable properties that allow the elimination of most of the design considerations linked to time-dependent strains (Richard and Cheyrezy, 1995, Cheyrezy, 1999).

Three completed projects using RPC, Sherbrooke footbridge (Canada), Seonyu footbridge (South Korea) and Bourg-les-Valence Bridge (France) and an on going project, Shepherds Gully Creek, Australia, highlight the potential use of RPC in the application to civil infrastructure.

The first major structure to use RPC200 was the 60-metre single span Sherbrooke Pedestrian Bridge crossing the river of Magog in Sherbrooke, Province of Quebec, Canada (see Figure 2.5). The walkway deck, which serves as the top chord to the truss, consists of 3.3 metres wide by 30 mm thick RPC slab (see Figure 2.5). The web members, which slope in both directions, are of a composite design involving RPC placed in thin walled stainless steel tubing having compressive strengths up to 350 MPa. The success of this structure dawned a new era in design methodology of concrete structures with no conventional reinforcing steel used for any part of the superstructure (Lachemi et al., 1998).

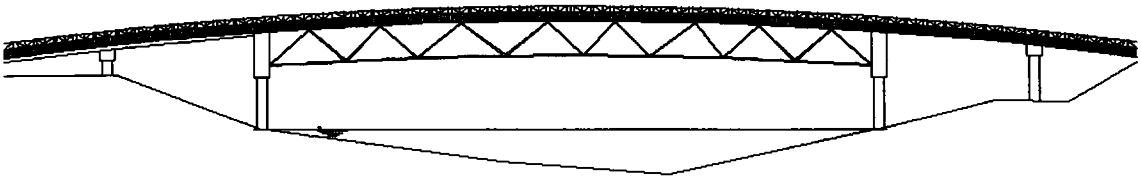

(a)

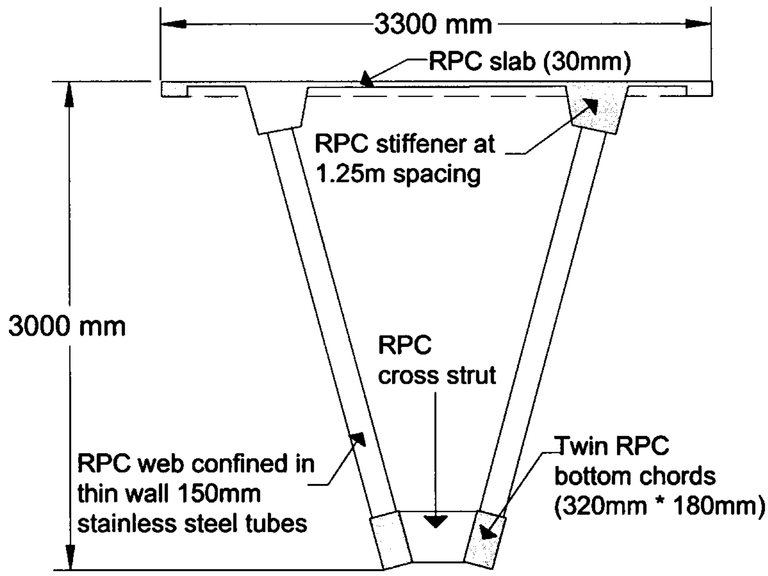

(b)

Figure 2.5 – Sherbrooke RPC bridge, Canada: (a) elevation; (b) cross-section (Lachemi et al., 1998).

Figure 2.6 shows the Seonyu Footbridge (the Footbridge of Peace) in Seoul, South Korea and constructed in April 2002 using RPC. The structure connects the city of Seoul to Seonyu Island on the Han River. Constructed by Bouygues Construction, the bridge consists of an arch with a 120 metre span supporting a 30 mm thick RPC deck. According to Bouygues Construction (Deem, 2002), the structure required only about half of the amount of material that would have been used with traditional concrete construction, yet provides equivalent load-bearing and strength properties.

An on going project on the world's first RPC highway traffic bridge is under construction by VSL at the Shepherd's Gully Greek at NSW, Australia. The road bridge is to comprise of four traffic lanes plus a footway. The superstructure of the bridge will comprise of 16 precast pretensioned RPC beams singly spanning 15 metres (Figure 2.7). The total width of the bridge is 21 metres.

Figure 2.6 – Seonyu Footbridge on the Han River.

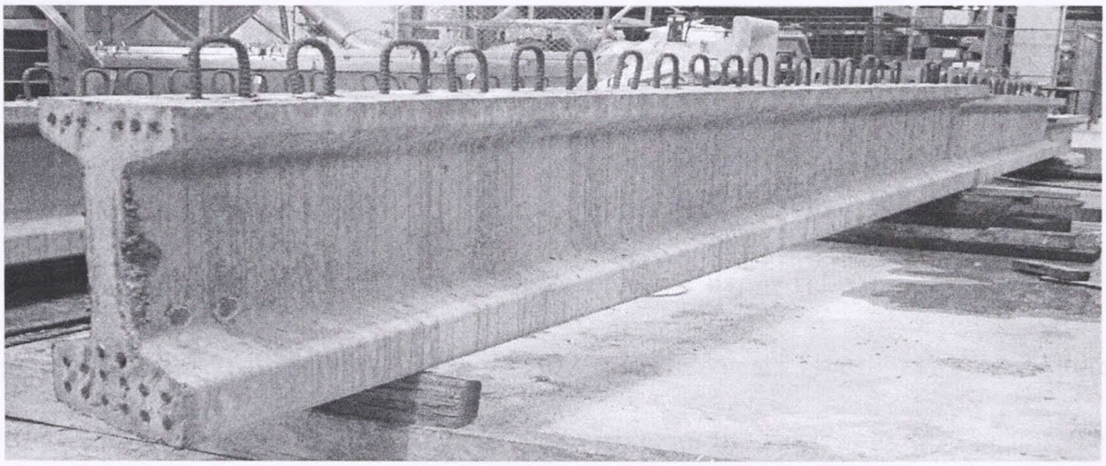

Figure 2.7 – Typical precast pretensioned RPC beam used in Shepherds Gully Creek Bridge.

2.3 Non-Flexural Members

Over the past four decades, extensive experimental programmes have been undertaken to investigate the behaviour of reinforced concrete non-flexural members, such as deep beams, nibs, corbels, beam-column joints, etc. The experimental evidence is that non-flexural members display an increase in shear capacity relative to that of flexural members due to the effect of arching. That is, the process by which load is transferred directly to a support through the development of struts. Early studies concentrated on development of empirical design methodologies, many of which are summarised by Kong (1990) and in the ASCE-ACI Joint Task Committee 426 report (1973). The major limitations of these empirical approaches are a limited range of shear span to depth ratios for which the design equations apply and an inability to explain the mechanics of non-flexural behaviour.

More recently finite element studies incorporating non-linear material models have been developed in combination with experimental programmes to determine the mechanics of non-flexural behaviour. These studies have led to the development of rational design models.

2.3.1 Early Numerical Studies

A large amount of work has been carried out on the behaviour of single span and continuous span deep beams with span-to-effective depth ratio (a/d_e) of 1 to 3 subjected to different loading conditions. In the earlier years investigators used finite-differences and trigonometric series methods to predict the stresses in deep beams. The accuracy for reinforced concrete deep beams was limited as only linear elastic behaviour was considered.

Uhlmann (1952) investigated a simply supported beam by solving the governing differential equations using Richardson's method of successive approximation. He successfully illustrated the fundamental difference between the load carrying action of deep beams and a shallow beam by computing the stress trajectories for a number of load cases.

Chow et al. (1953) used the finite difference method to investigate the stresses of deep beams with various span to effective depth (a/d_e) ratios when subjected to five common load cases. Distributions and magnitudes of bending and shear stresses were provided in graphical and tabular form and are applicable to structures made of homogeneous material such as steel but not reinforced concrete.

Archer and Kitchen (1956) used a direct strain-energy method for the analysis of deep beams and compared their solution to the finite difference and strain energy methods of Chow et al. (1953), simple beam theory and photo-elastic methods were used. Archer and Kitchen's bending stress values agreed fairy well with the results of Chow et al. (1953) but their shear stress results were not in good agreement.

Geer (1960) found a considerable amount of error in the works of Chow et al. (1953) due to the earlier investigators' use of a coarser net and rounding off of peak values. Geer used a finer grid. His study showed that one of the most distinctive features of deep beams, compared to flexural beams, is that the highest tensile stress occurs not at the mid-span of the beam but near the face of the support. The maximum stress intensity is a function of the magnitude of load and is also dependent on the reaction rather than the location of the load which caused it. Geer concluded that a deep beam needs reinforcement in the bottom over the support more than anywhere else in the beam.

Barry and Ainso (1983) used the multiple Fourier series technique to compare the stress fields in single span deep beam due to uniform loading at the top edge and at the bottom edge. The method involved superposition of three stress functions. The first stress function is used to satisfy the boundary conditions on the upper and lower edges of the beam. The second and third stress functions were used to satisfy the boundary condition on the vertical edges of the beam. This approach allowed satisfaction of all the required boundary conditions.

2.3.2 Experimental Investigations

Leonhardt and Walther (1966) had experimentally demonstrated the formation of tie arch action in deep beams in the mid 1960's. An example of one of Leonhardt and Walther's deep beams is presented in Figure 2.8. They became aware that the main flexural reinforcement retained a large proportion of its force close to the support and therefore a full strength anchorage is required. The authors concluded that for deep beams with a clear span-to-depth ratio less than 2, vertical and inclined web reinforcement is of no benefit because the concrete always failed by crushing under the bearing area. This work formed the basis for the CEB-FIP Model Code (1978) design recommendations for deep beams.

During the 1970's, Kong and his collaborators conducted numerous experimental tests on reinforced deep beams. The investigated parameters consisted of the shear span-to-depth ratio (a/h), vertical and horizontal web reinforcement ratio, effect of inclined web reinforcement, weight of concrete and size and position of web openings.

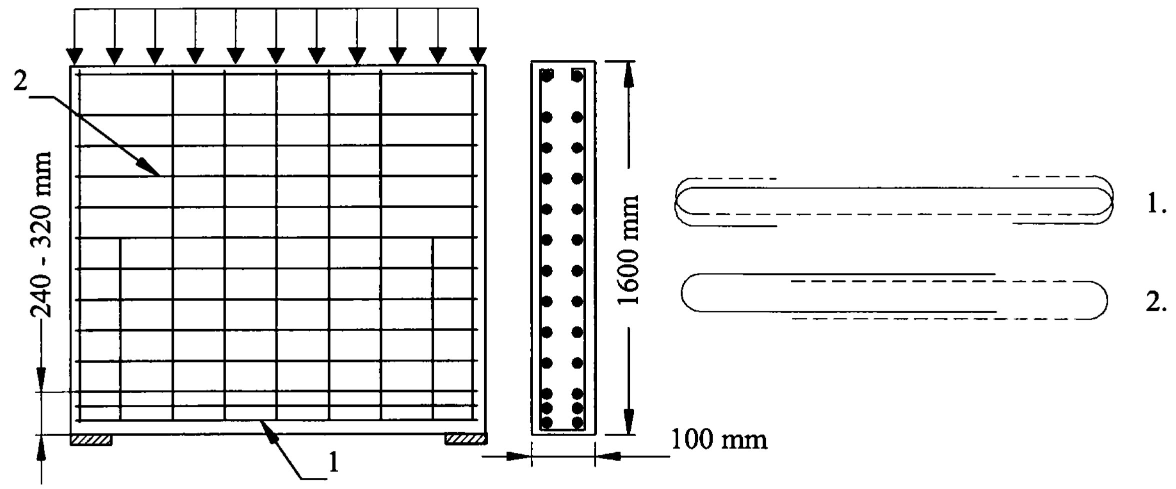

Figure 2.8 – Single span deep beam test of Leonhardt and Walther (1966).

Kong et al. (1970) tested 35 simply supported deep beams of shear span-to- depth ratios (a/h) ranging from 1 to 3. The effects of seven different types of web reinforcement on deflection, crack widths, crack pattern, failure modes and ultimate loads in shear were studied. The authors noted the experimental failure load was in good agreement with formulas proposed by both de Paiva and Siess (1965) and Ramakrishnan & Ananthanarayana (1968) whereas the results were in poor agreement from the British and American codes. Kong and Robbins (1971) performed similar tests on 38 simply lightweight concrete deep beams with the same investigated parameter as mentioned above. The authors concluded that inclined web reinforcement was the most effective type of web reinforcement and the ultimate strength formulas suitable for normal weight concrete deep beams were not necessarily suitable for lightweight concrete deep beams.

Kong and Sharp (1973) tested 24 lightweight concrete deep beams with the objective to study the effects of web openings on strength and cracking. The results of the investigation led to useful empirical design methods for deep beams with web openings. The effect of an opening on the ultimate shear strength of a deep beam depends primarily on the extent to which it intercepts the load path joining the load bearing blocks at the loading points and the support reaction point and on the location at which this interception occurs.

Rogowsky and MacGregor (1983) and Rogowsky et al. (1986) reported on an extensive investigation into the strength behaviour of continuous deep beams. The objective of their tests was to identify the difference in behaviour between simply supported and continuous deep beams. The investigation showed that the ACI predictions for shear strength of deep beams was generally poor and in the case of continuous beams with little or no web reinforcement, were unconservative due to the fact that they were based on an incorrect mechanical model. Rogowsky et al. proposed a model for the shear strength of deep beams using strut and tie modelling similar to that of Marti (1978), Mueller (1979) and Nielsen et al. (1978).

Narayanan and Darwish (1988) conducted an experimental investigation on the shear strength of fibre reinforced concrete deep beams with 11 of 12 beams tested containing steel fibres provided to act as web reinforcement. Their investigated parameters included the volume fraction of fibres, shear span-to-depth ratio and the concrete compressive strength. The study reported that the inclusion of steel fibres in reinforced concrete deep beams resulted in enhancing their deformation characteristics at all stages of loading up to failure. Narayanan and Darwish also reported that fibre reinforced concrete deep beams exhibited substantial increases in their ultimate loads as well as in the load at first cracking. The authors modified the model proposed by Kong et al. (1975) to calculate the ultimate strength of deep beams made of conventionally reinforced concrete to account for the inclusion of steel fibres into the matrix.

Teng et al. (1998a, b) extended the work of Kong et al. (1970-1978) from reinforced concrete deep beams to prestressed concrete deep beams. Thirty-four deep beams were tested. The parameters investigated included deformation, ultimate behaviour, various cracking loads, modes of failures, main tension steel, various types of web reinforcement, prestressing strains and span-to-depth ratio. The experimental results show that the use of prestressing and orthogonal web reinforcement improved the ultimate shear strength and the serviceability performance (crack widths) of deep beams. The use of prestressing introduces a pre-compression in the beam web that eliminates some of the induced tensile stress thus leading to an increase in the diagonal cracking load and flexural cracking load. Teng et al's equation to calculate the ultimate shear strength was rewritten from the Kong-CIRIA (1977) equation in a form for application to both reinforced and prestressed concrete deep beams.

Tan and Tong (1999) reported on six large pretensioned concrete girders of I-shape cross-section. Two parameters were investigated being the shear-span to effective-depth ratio and the partial prestressing ratio. In their tests, it was observed that the shear strength of deep beams increases with the partial prestressing ratio and the level of prestressing delays the occurrence of the initial crack. However, once formed, the crack widths are not affected by the prestressing. The authors developed a strut and tie model and used Mohr-Coulomb's failure criterion and the Kupfer and Gerstle (1973) equations for biaxial stress to explain the results with the model verified against the experimental data. The model was shown to give reasonable agreement with the test data with a mean theoretical to experimental failure load of 0.8 and a coefficient of variation of 0.035.

Similar tests on the behaviour of deep beams were also conducted by numerous other investigators such as de Pavia and Seiss (1965), Ramakrishnan and Ananthanarayana (1968), Manuel et al. (1971), Singh et al. (1980), Smith and Vantsiotis (1982), Vecchio and Collins (1982), Rogowsky and MacGregor (1983), Mansur and Alwis (1984), Besser and Cussens (1984), Selvam and Natarajan (1985), Ricketts and MacGregor (1985), Subedi et al. (1986), Foster (1992b), Tan et al. (1995), Foster et al. (1996), Ashour (1997), Tan et al. (1999), Shin et al. (1999) and others. Their results indicated similar behaviour to that discussed above.

2.3.3 Theoretical Models

Tan and Mansur (1982) adopted a simplified strut-and-tie model approach to determine the shear strength of partially prestressed concrete deep beams. The authors' method is intended for both non-prestressed and prestressed concrete deep beams. However the effect of vertical web reinforcement is not considered in their model.

Mau and Hsu (1987, 1989) introduced a shear design formula based on their softened-truss model for deep beams having a shear span/depth ratio a/d of less than 1.3 and a clear shear span-to-depth ratio L_0/h of less than 3.3. Their formula is based on the equilibrium condition of a shear element in a shear span of a deep beam.

Mau and Hsu compared the results of the model with 64 test results which were available in literature at the time (from Smith & Vantsiotis, 1982, Kong et al., 1970, de Pavia & Seiss, 1965) with the specimens selected on the basis that the predominant mode of failure was by web shear. Their results showed a good agreement for their model with the test results. Mau and Hsu extended this work further deriving a formula for the shear strength of deep beams.

Kotsovos (1988b) proposed a simple design procedure for deep beams which is based on the concept of the compressive force path (Kotsovos, 1988a). In his model, Kotsovos theorises that the shear resistance of a member is provided by a direct compressive force transmitted to the supports by means of a load path. This is in contrast to the traditional treatment which uses concepts of aggregate interlock and dowel action. The author's model was verified against the experimental results of de Pavia and Seiss (1965), Ramakrishnan and Ananthanarayana (1968), Kong et al. (1970) and Smith and Vantsiotis (1982) and also the continuous deep beam test results of Rogowsky and MacGregor (1983) and Rogowsky et al. (1986). The method showed a reasonable correlation with the experimental results, with the calculated values generally on the conservative side.

In 1991, Mansur and Ong proposed modifications to the softened truss model of Mau and Hsu (1987, 1989) incorporating the inclusion of short discrete steel fibres in concrete on the behaviour and strength of deep beams. Experimental tests were carried out on 10 fibre reinforced concrete deep beams in shear. The major parameters of the study were span-depth ratio, volumetric fraction of fibres and the ratio of longitudinal and transverse reinforcement. The authors considered an orthogonally reinforced concrete element subjected to in-plane stresses and concluded a reduction in the shear span to depth ratio increases both the diagonal cracking and ultimate shear strengths of reinforced fibre concrete beams. The experimental program of Mansur and Ong (1991) showed that the addition of discrete steel fibres in the concrete mix provides better crack control and enhances the strength and deformation characteristics of deep beams containing conventional reinforcement.

2.3.4 Finite Element Modelling

With advances in computer technology through the 1980's the application of the finite element method became a feasible method for the design of non-flexural members. The main advantage of numerical methods is that they provide an economical way of analysing complex structures, rather than building and testing prototype models; that is, provided a suitably accurate constitutive model is used. In short, when verified against a wide range of experimental data, the finite element (FE) method is a valuable numerical model for use in design practice.

One of the earliest finite element investigations into deep beams was carried out by Al-Mahaidi et al. (1978). The constitutive relationship utilised by the authors was derived from the work of Liu et al. (1972) in conjunction with the linearised biaxial stress failure envelope proposed by Tasuji et al. (1976). The authors' model used both linear isoparametric quadrilateral element and constant strain triangular elements to represent the concrete. Reinforcement was modelled using discrete bar elements and a linkage element with fictitious orthogonal springs used to model the bond-slip, dowel action and aggregate interlock mechanisms.

Al-Mahaidi used two approaches to model the effects of concrete cracking; the distributed cracking approach and the discrete cracking approach (Figure 2.9). Whilst the discrete crack approach provides for more realistic modelling of the physical condition of crack propagation, including the effects of dowel action and aggregate interlock, it has the disadvantage of requiring greater computational effort.

Al Mahaidi et al. carried out analyses on three experimental deep members reported in the literature with the intention to test the validity of their analytical model. These were a deep beam with web reinforcement, tested by Leonhardt and Walther (1966) and shear wall panels with and without web reinforcement tested by Jimenez (1977). The FE mesh used for the Leonhardt and Walther deep beam is shown in Figure 2.10. From their analyses Al-Mahaidi found that the distributed cracking approach was sufficiently accurate to predict the load carrying capacity and behaviour of Leonhardt and Walthers' deep beam. For the wall panel with web reinforcement, it was found that a combination of the distributed and discrete cracking models produced the best results.

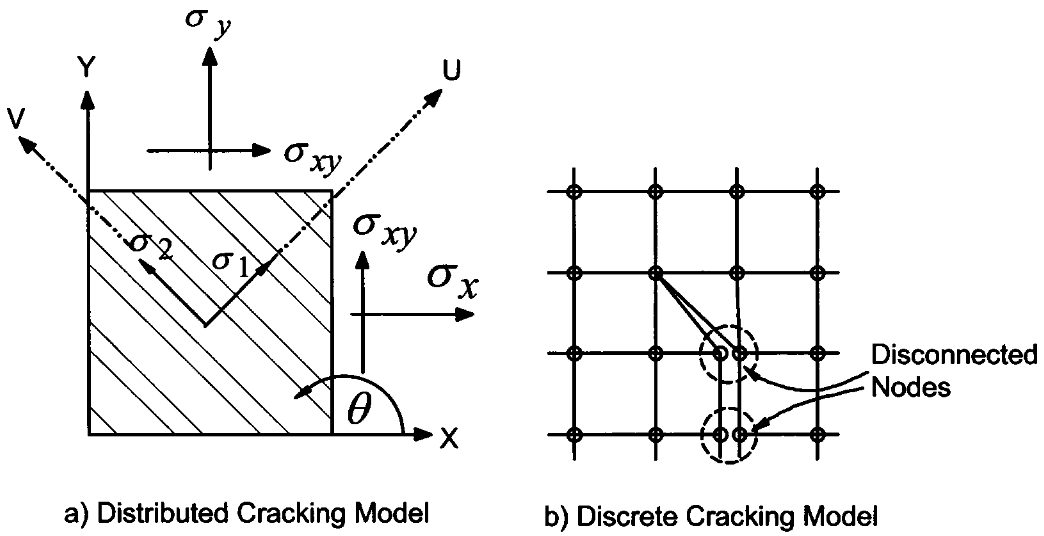

Figure 2.9 – Two types of crack representations in Al-Mahaidi's analytical model (Al-Mahaidi et al., 1978).

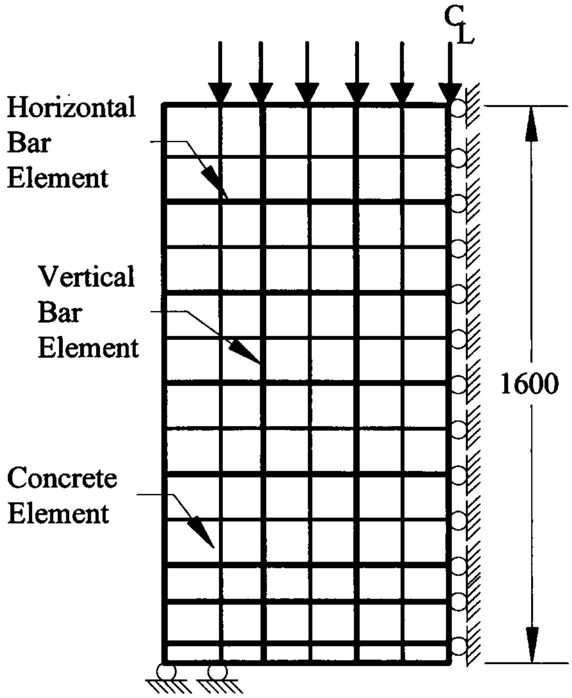

Figure 2.10 – Al-Mahaidi's FE model for Leonhardt and Walther's (1996) deep beam WT3.

Balakrishnan and Murray (1988) reported on a FE model which they applied to analyse a number of deep beams and reinforced concrete panels tested experimentally by Vecchio and Collins (1982) and deep beams tested by Leonhardt and Walther (1966) and Rogowsky and MacGregor (1983). For the reinforced concrete panels, the finite element results showed a good correlation with the experimental results with a mean of experimental/theoretical ratio of 1.04. The Leonhardt and Walther deep beam used for comparison had a single span of 1600 mm, width of 100 mm, and was subjected to a uniformly distributed load on its top edge (Figure 2.8). The reinforcement consisted of 4 layers of 8 mm diameter bars anchorage with hooks at each end and an orthogonal mat of web reinforcement. With symmetry only half of the beam was modelled, using 50 square bi-linear elements.

Vecchio (1989) developed a nonlinear finite element procedure that incorporates the modified compression field theory (MCFT) as described by Vecchio and Collins (1986). The FE modelling used by the author was an analytical model for reinforced concrete membranes based on a smeared crack approach in which the cracked concrete is treated as a new material with unique stress-strain characteristics. Vecchio carried out analyses on two experimental beams reported in the literature with the intention to test the validity of his analytical model. These were a deep beam with web reinforcement, tested by Leonhardt and Walther (1966) and a shallow beam with stirrups tested by Bresler and Scordelis (1963). The FE meshes used are given in Figure 2.11. Vecchio's analysis showed that the FE model correctly captures the overall behaviour of the tested beams and he concluded that nonlinear finite element formulation can be used to calculate the structural behaviour of reinforced concrete membrane elements.

Foster and Gilbert (1990) and Foster (1992a, 1992b) developed a NLFEA program (called RECAP) to provide a non-linear analysis of reinforced concrete elements in plane stress. It combined the constitutive relationships of Darwin and Pecknold (1977), for undamaged concrete, with the modified compression field theory of Vecchio and Collins (1986), for cracked concrete.

One of the most useful applications of NLFE modelling is the ability to analyse complex, indeterminate, structures such as continuous deep beams. One constraint in design of continuous deep beams is that it is difficult to ascertain accurately the proportion of load taken by each of the supports. However the reactions are needed before one can calculate the internal forces, and hence the size of the struts, ties and reinforcement details. Rogowsky and MacGregor (1983) showed linear elastic analyses would provide unsafe designs in some cases. However NLFE programs, using appropriate constitutive relationships are able to assess the support reactions for such structures with relative ease.

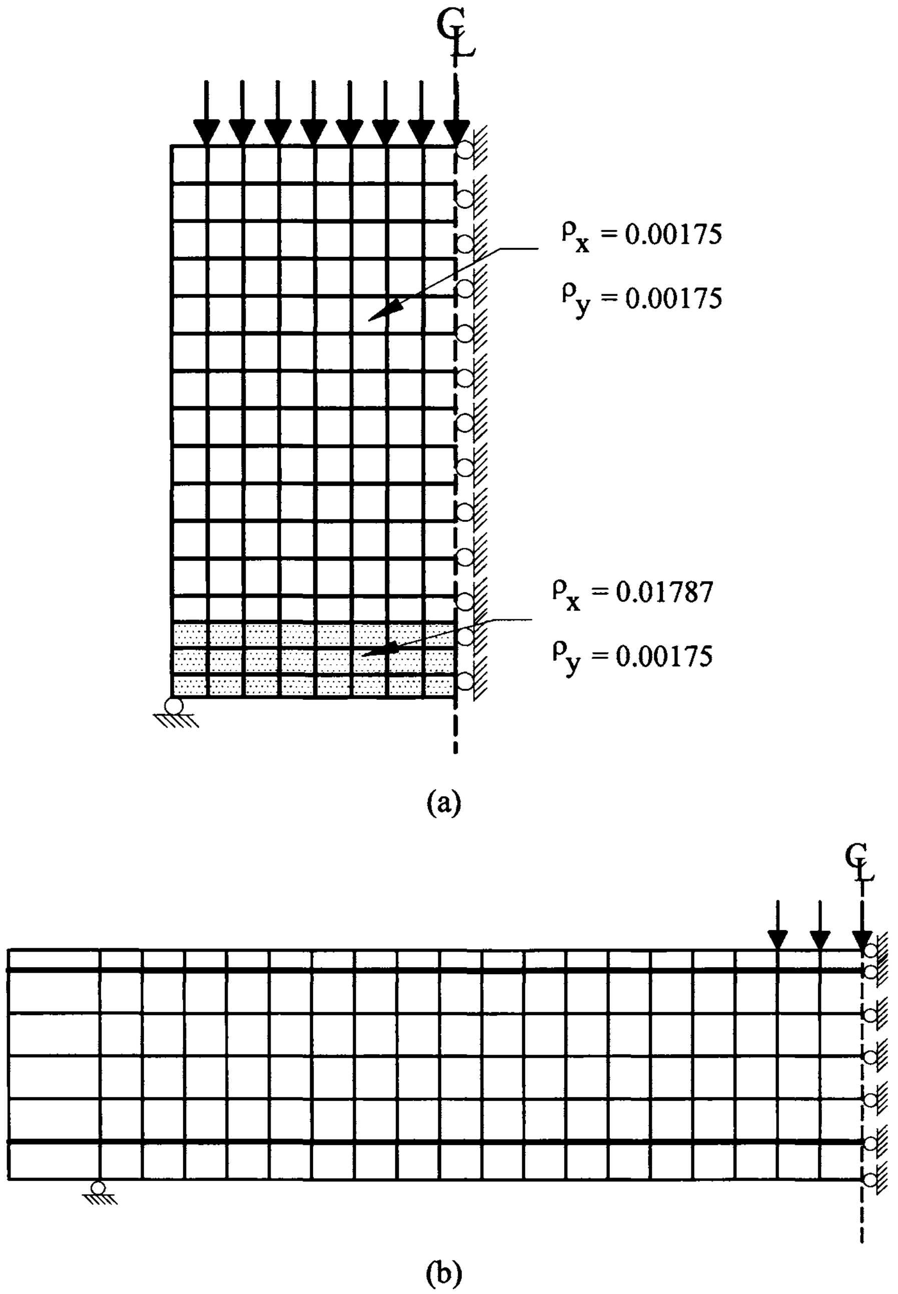

Figure 2.11 – Vecchio's FE model for (a) Leonhardt and Walther's (1996) deep beam and (b) shallow beam (Specimen No. A1) of Bresler and Scordelis (1963).

Foster (1992b) carried out an extensive series of numerical studies on continuous deep beams using NLFEA's and prepared charts for various geometrical configurations. He used the program to assess the effects of various parameters on the support reactions, namely; concrete strength, horizontal and vertical reinforcement, width of load and support plates, location of load within span and shear span to depth (a/d) ratios. Foster found that the three most important parameters were the amount of vertical web reinforcement, a/d ratio and loading geometry. These general observations are consistent with Rogowsky and MacGregor's (1983) experimental results on continuous deep beams.

In conclusion, nonlinear finite element analysis can be used with reasonable confidence to predict the behaviour of non-flexural members since NLFEA has the ability to account for equilibrium, compatibility and boundary conditions. Also, this powerful method can be used directly to calculate the behaviour of complex structures for the entire load range up to and beyond failure.

2.4 Constitutive Laws for Fibre Reinforced Concrete

The idea of using discrete, ductile, fibres to reinforce brittle materials such as concrete is not new with many studies having been undertaken over the past four decades. Early studies by Romualdi and Batson (1963) indicated that the tensile strength of concrete can be improved by providing suitably arranged and closely spaced wire reinforcement. The low tensile strength of concrete matrix is primarily due to the propagation of internal cracks and flaws.

Romualdi and Batson hypothesised that, if these flaws can be locally restrained from extending into the adjacent matrix, the initiation of tension cracking can be retarded and a higher tensile strength of the material achieved. In addition to increasing the tensile strength, the inclusion of fibres may also enhance a number of other material properties such as fatigue resistance (Romualdi et al., 1968), energy absorption and toughness, ductility, durability and improve the service life of the material (Shah and Rangan, 1971). By adding fibres to a concrete mix the objective is to bridge discrete cracks providing for some control to the fracture process and increase the fracture energy.

Since the early work of Romualdi and Batson (1963), the pullout mechanism of discontinuous fibres embedded in a variety of cementitious materials has been studied by a number of researchers. Some of the major studies in the field include those of Gray (1984a, b), Gopalaratnam and Shah (1987a), Mandel et al. (1987), Namur et al. (1987), Naaman et al. (1989), Namur and Naaman (1989), Wang et al. (1990a, b) and many others.

2.4.1 Fibre Pullout or Fibre Fracture

The current understanding of the behaviour of fibre-matrix interfacial mechanics is based on a number of pullout studies using single or multiple fibres where steel fibres are embedded within a cementitious matrix. The experimental parameters investigated including the rate of loading (Banthia and Trottier, 1991, Hughes and Fattuhi, 1975 and Maage, 1977), curing and environmental temperatures (Banthia and Trottier, 1989b and Banthia and Trottier, 1992), the quantity and quality of the matrix (Gray and Johnston, 1984, Banthia and Trottier, 1989a, and Gopalaratnam and Abu-Mathkour, 1987), addition of adhesive agents (Guerrero and Naaman, 2000) and fibre type and fibre orientation (Banthia and Trottier, 1994, Naaman and Shah, 1976, and Soroushian and Bayasi, 1991).

In spite of a belief sometimes expressed (Banthia and Trottier, 1994) that no correlation exists between the behaviour of a single fibre pullout test and the behaviour of bulk fibres in a real composite matrix, the effectiveness of a fibre as a medium of stress transfer is often assessed using fibre pullout tests where slip between the fibres and the matrix is monitored as a function of the applied load.

Despite numerous publications on fibre concrete behaviour, limited research has been undertaken on developing general design models for fibre reinforced composites in tension. Visalvanich and Naaman (1983) derived a semi-empirical model for the tension-softening curve in discontinuous randomly distributed steel fibre-reinforced mortar by assuming a purely frictional fibre-matrix interface and complete fibre pullout. With the same assumptions and taking into account an additional frictional effect called the snubbing effect, Li (1992) derived an analytical model named the fibre pullout model (FPM) that predicts the complete bridging stress-COD relationship for fibre reinforced brittle-matrix composite. One limitation of this model is it does not account for the potential fracture effect of fibres in the composite.

A micromechanical model known as the fibre pullout and rupture model (FPRM) was developed by Maalej et al. (1995). In their model, the FPM model of Li (1992) was extended to account for the possibility of fibre rupture in the composite. The model is able to predict the composite bridging stress-COD relationship, account for fibre pullout, fibre rupture and the local frictional effect or snubbing. A limitation of the FPRM is that it does not account for interaction between neighbouring fibres and the modification of the matrix properties by the addition of fibres, bending rupture and possible effects of matrix spalling at the exit points of fibres inclined to the cracking plane.

Using the "fibre-matrix misfit" theory of Timoshinko (1941), Naaman et al. (1991a) proposed an analytical model for straight, undeformed, circular steel fibres aligned perpendicularly to the cracking plane. The model was shown to capture the pullout-slip relationship between steel fibres and concrete when compared to the experimental data as published by the authors. However this model is limited for use in directionally orientated plain fibre composites.

Gilles (1999) developed a micromechanical model taking into account the different phenomena observed during pullout of a deformed fibre, including the interfacial adhesion between the fibre and the matrix, friction and fibre deformation. The model can be used for predicting pullout behaviour of fibres having various geometries but is limited to the case where the fibres are aligned perpendicular to the cracking plane.

Marti et al. (1999) developed a simple parabolic model to describe the stress-COD relationship of randomly orientated fibre reinforced composites with the tension stress of the fibre composites given by

$$\sigma = \sigma_0 \left(1 - \frac{2w}{l_f}\right)^2 \tag{2-1}$$

where σ_0 is the peak tensile strength, w is the crack opening displacement (COD) and l_f is the length of the fibres. The peak tensile strength is, in turn, given by

$$\sigma_0 = \frac{\rho_f l_f \tau_b}{2d_f} \tag{2-2}$$

where ρ_f is the volumetric fraction of fibres, d_f is the diameter of the fibres and τ_b is the bond stress between the fibres and the concrete. In Eq. 2-1 it is assumed that after cracking of the matrix there is zero contribution to tensile strength from the matrix and that the shear stress (τ_b) is constant along the shorter embedded length.

Many other models have been proposed such as those of Romualdi and Batson (1963), Aveston and Kelly (1973), Naaman et al. (1973), Pakotiprapha et al. (1974), Gray (1984a), Brandt (1985), Lim et al. (1987b) and Easley and Faber (1999) but these models are generally limited in their use as tools for structural designers due to limitations of the models or due to the complexity of the models.

2.4.2 Factors Affecting Fibre-Matrix Bond

Many experimental and analytical investigations on bond between fibres and a concrete matrix have been undertaken but the results are sometimes contradictory. Naaman and Shah (1976) reported that the bond efficiency in a pullout test of steel fibres inclined with respect to the line of stress is at least as good as that of fibres parallel to the direction of stress. They also found that efficiency of the bond is inversely proportional to the number of fibres being pulled out across a plane. In tests on fibre-matrix specimens, Gray and Johnston (1984) reported that the direction of casting has a substantial influence on the bond strength between the fibres and the mortar-matrix. They stated that vertically cast specimens have interfacial bond strengths higher than that of horizontally cast specimens. They also reported that an increase in the sand-cement ratio in the mortar matrix leads to a decrease in interfacial bond for the vertically cast specimens and an increase in bond for the horizontally cast specimens.

Maage (1978) found that the bond properties between steel fibres and cement-based matrixes are mechanical in nature and the anchorage of the fibres in the matrix is more important than the adhesion. He also noted that the mean pullout load per fibre is not affected by the number of fibres crossing the failure surface. Maage stated that

> *"...based on the weakest link theory, it should be reasonable that the pullout per fibre would decrease when the number of fibres across an area is increased..."*

This is in contradiction with the results reported by Naaman and Shah (1976) and an indication of the variability often encountered in fibre bond tests.

Pinchin and Tabor (1978) carried out tests on wire fibres and showed that compaction of the concrete surrounding a fibre gives an increase in the mechanical bond and, thus, the pullout load. They also determined that the pullout load increases linearly with confinement and showed analytically that the pullout load is proportional to the fibre-matrix misfit, which they defined as the difference between the radius of the wire and that of the hole in the matrix when subject to shrinkage.

Burakiewicz (1978) reported that the shape of the pullout load-displacement curve depends on the fibre type and that hooked fibres show smaller scatter in bond strength than the other fibre types tested (plain and indented). He reported that the pullout of hooked and indented fibres requires more energy than that of plain fibres, which implies that deformed fibres have higher bond strengths than straight fibres. Burakiewicz concluded that there is no significant influence on the fibre-matrix bond strength due to the orientation of fibres during setting and hardening of the matrix. This is in contradiction with the findings of Gray and Johnston (1984). Burakiewicz also observed that the bond strength appears to depend on the rate of pullout from the matrix and contradicts the findings of Gokoz and Naaman (1981).

Gopalaratnam and Abu-Mathkour (1987) studied the effect of the fibre embedment length, fibre diameter and matrix quality on fibre pullout characteristics. From their experiments, Gopalaratnam and Abu-Mathkour observed that the average bond strength is inversely related to the embedment length and that the average bond strength of the fibre-matrix interface increases with an increase in fibre diameter. Gopalaratnam and Abu-Mathkour also reported that the strength of the concrete does not significantly influence the fibre pullout load. Their reasoning was that the frictional bond strength may be unrelated to the matrix compressive strength.

2.5 Shear Strength of Fibre Reinforced Concrete Beams

Over the past three decades, a number of experimental studies have been conducted to investigate the shear strength of fibre reinforced (FR) concrete beams without any conventional shear reinforcement. These studies have indicated that the addition of fibres to concrete in beams without stirrups can significantly increase the ultimate shear strength and transform the failure mode from one of brittle-failure to a more ductile one (Swamy et al. 1993). Fibres are effective after the formation of cracks and resist significant tension until the fibres pullout from the cracks or fracture. Cracks in fibre reinforced beams are closely spaced with, typically, several dominant diagonal cracks forming at failure, compared to a single dominant diagonal crack at failure in plain concrete beams without stirrups.

Table 2.7 – Summary of previous tests on FRC beams without stirrups updated from (Adebar et al., 1997)

Authors	Year	No of. Beams	Beam Type	$b_w x d_e$ mm	ρ_w percent	a/d_e	f_{cm} MPa	f_{cu} MPa	Fibre Type	l_f mm	ρ_f percent
Batson et al.	1972	21 72	R	102 x 126	3.1	4.8 1.2-5.0	33-40	-	SS, CS	19-25	0-2.7 0.22-1.8
Williamson and Knab	1975	3	R	305 x 457	2.5	5	30	-	S*	*	0, 1.5
LaFraugh and Moustafa	1975	8 3	R T	102 x 175 125 x 600	3.0 6.5	3.8 4.0	30-50 55	-	SS, ME	25-64	1.0, 1.5 1.0
Muhidin and Regan	1977	21	I	50 x 320 50 x 330	5.0 2.4	4.7 3.2	-	25-75	CW	25, 40, 60	0-3
Roberts and Ho	1982	9	R	50 x 170	2.4	0.8, 1.6, 2.4	-	40, 48	SS	38	0-1.3
Jindal	1984	44	R	102 x 127	2.0	2.0-4.8	20	-	SS, CW	3-28	0, 1.0
Swamy and Bahia	1985	2 7	R T	175 x 210 175 x 210	1.95 1.95-4.0	4.4	-	44, 54 44-52	CS	50	0, 0.8 0-1.2
Sharma	1986	3	R	150 x 276	1.0	1.8	42-49	-	HS	50	0, 1.0
Mansur et al.	1986	24	R	150 x 200	0.8-2.0	2.0-4.4	20-33	-	HS	30	0-1.0
Narayanan and Darwish	1987	39	R	85 x 130	2.0-5.7	2.0-3.0	-	36-75	CS	30, 40	0-2.0
Lim et al.	1987a	16	R	152 221	1.1, 2.2	1.5-3.5	34	-	HS	30	0-1.0
Murty and Venkatacharyulu	1987	9	R	100 x 180	1.3	2, 3	-	23-33	CW	27-54	0-1.5
Kaushik et al.	1987	20	R	102 x 135	1.7	2.5	-	22	CW	28-46	0-1.5
Batson and Alguire	1987	11	T	57 x 254	2.3	3.7	42-60	-	EH	30	0-1.5
Narayanan and Darwish	1988	12	R	100 x 345	3.6	0.5-0.7	-	38-68	CS	30	0-1.25
Ashour et al.	1992	18	R	125 x 215	0.4-4.6	1-6	92-101	-	HS	60	0.5-1.5
Li et al.	1992	51 9	R	63.5 x 102 127 x 204	1.1-2.2 2.2	1-3 3	18-26	-	HS; P	30, 50; 13	0, 1.0
Tan et al.	1993	6	I	60 x 350	3.8	1.5-2.5	35	-	HS	30	0-1.0
Imam et al.	1994	16	R	200 x 300	1.9, 3.1	1.8-4.5	110	-	HS	60	0, 0.75
Shin et al.	1994	22	R	100 x 175	3.6, 7.2	2.0-6.0	80	-	SS	100	0-1.0
Furlan Jr and Hanai	1997	7	R	100 x 86	0.8	3.5	43-55	-	PP; CS	840; 33, 50	0.5-2.0
Kützing and Meister	1998	4	R	300 x 173	4.1	3.0	50, 115	-	*	60	0.5, 1.0
Noghabai	2000	32	R	200 x 180 200 x 235 200 x 410 300 x 570	3.1, 4.5 4.3 3.0 2.9	3.1, 3.3 2.8 2.9 3.0	46-91 60-93 60-77 60-77	-	SS; PO; C	30, 60 25, 50 *	0-1.0
This study	2003	7	I	50 x 600	5.72	3.3	150-170	-	SS, HS	13,30	1.3,2.5

Note: Beam type; R = rectangular; T = T-beam; I = I-beam. * information not given

Fibre type: CW = chopped wires; CS = crimped steel; HS = hooked steel; SS = straight steel; ME = melt-extracted; P = polyethylene; PP = polypropylene; C = carbon straight; PO = polyolefin

Adebar et al. (1997) conducted an extensive review of shear strength tests of fibre concrete beams without stirrups reporting the results of over 400 fibre reinforced (FR) beam tests. More than 80 percent of the testes of FR beams have been on small-scale specimen with effective depths less than 200 mm. Most of the remaining tests have been on beams with depths of the order of 300 mm. A summary of tests is given in Table 2.7.

The first shear tests on fibre reinforced mortar beams were undertaken in the late 1960's by Batson et al. (1972). There experimental parameters were span to depth ratios and fibre types. The authors' results show the replacement of vertical stirrups by round flat and crimped steel fibres provided effective reinforcement against shear failure. Since the first study, numerous tests have been conducted on fibre reinforced concrete beams with varying fibre types and quantities (ρ_f), shear span to effective depth ratio (a / d_e), beam size, concrete strength and reinforcement ratios (ρ_w).

In 1975, Williamson and Knab reported the results of four large scale fibre reinforced concrete beams with a total depth of 546 mm (see Figure 2.12). Among the four beams, one beam was not fibre reinforced and it was treated as a reference specimen whereas another beam contained U stirrups as shear reinforcement and the remaining two beams contained 1.5 percent by volume of steel fibre. It was reported that the fibre reinforced concrete beams increased the shear strength by 40 percent. However, steel fibres are not effective in preventing catastrophic shear failure in full scale beams. In 1977, Muhidin and Regan tested 21 medium size I-beams (i.e. with overall depth of 360 mm) with crimped steel fibres in the concrete mix (see Figure 2.13). The parameters investigated were fibre quantities, fibre geometries, concrete strength, width of web, shear span to effective depth ratios and flange depths. The concrete strength was varied between

25 MPa and 75 MPa. The fibre volumetric ratios were varied from 0 to 3 percent. Two shear span to effective depth ratios were used, being 3.2 and 4.7. In their tests, the authors observed shear strength increases as high as 150 percent. In the experiments, the fibre reinforced concrete beams developed similar crack patterns to plain concrete beams with stirrups.

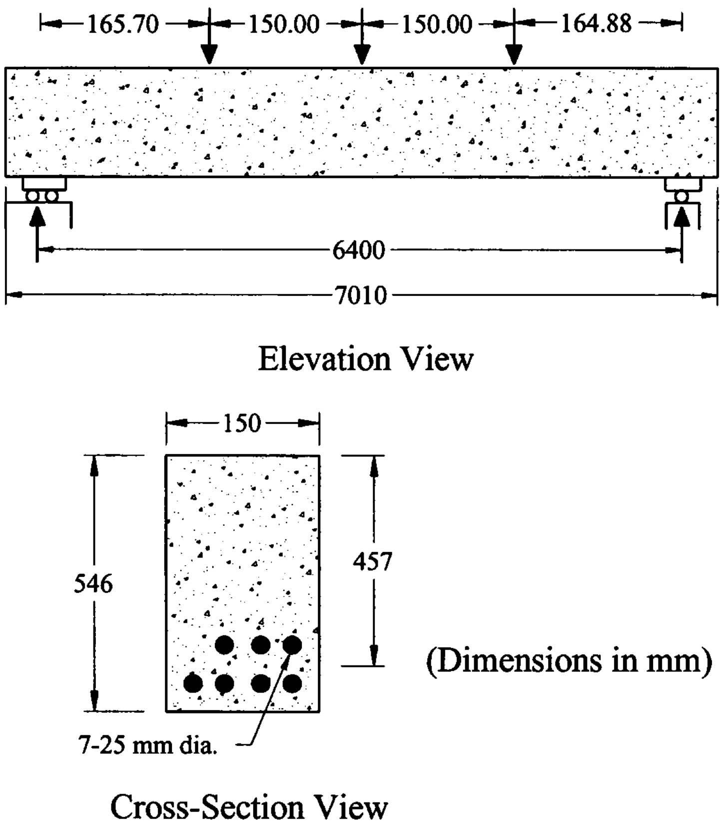

Figure 2.12 – Details of specimens tested by Williamson and Knab (1975).

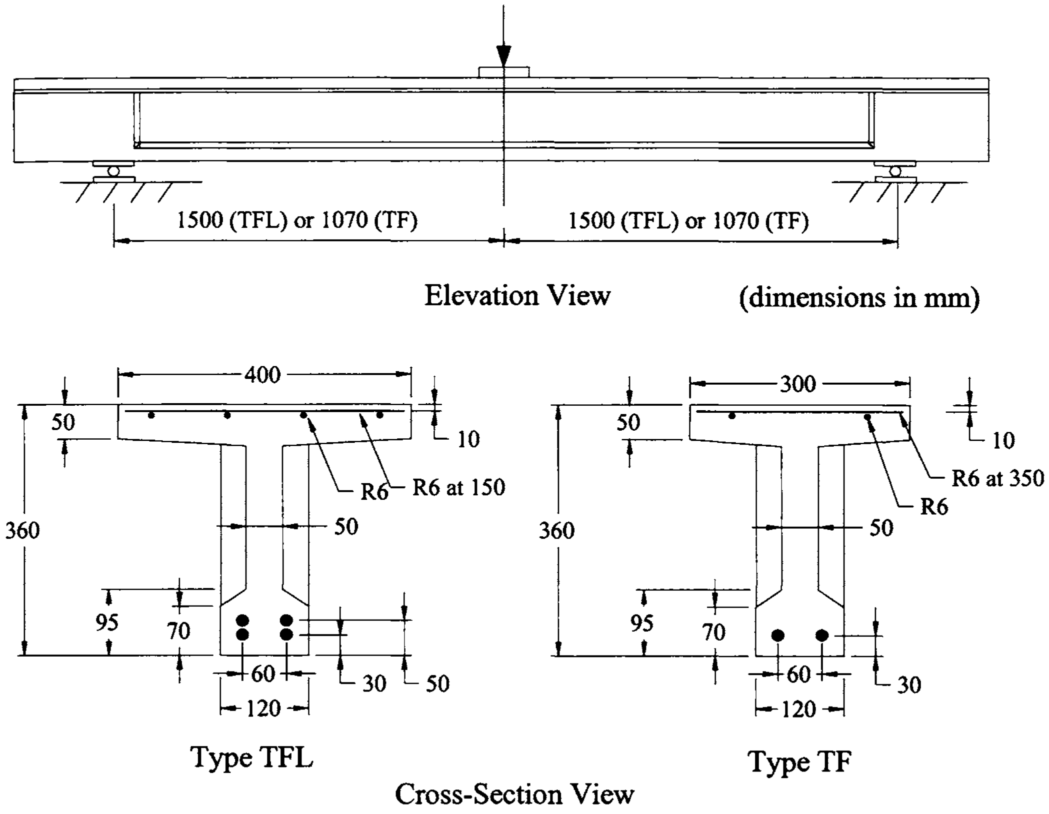

Figure 2.13 – Details of specimens tested by Muhidin and Regan (1977).

In 1985, Swamy and Bahia tested seven T-beams and two rectangular beams without stirrups. All the beams had a shear span to effective depth ratio of 4.4 and the effective depth of the specimens was 210 mm. The steel fibre used in their tests was crimped and was varied to a maximum of 1.2 percent by volume. The authors reported an 80 percent increase in shear strength in the T-beams with 0.8-1.2 percent of 50 mm crimped steel fibre and a 30 percent increase in shear strength of rectangular beams with 0.8 percent of fibre. Swamy and Bahia concluded that the presence of fibres in concrete mixes reduced shear deformations and were particularly significant in preserving the stiffness of the beams allowing for higher failure loads. The use of fibres controlled the cracking and displacement in the dowel zone and acted as shear reinforcement.

In 1988, Narayanan and Darwish tested a series of 345 mm deep beams using short shear spans. The longitudinal reinforcement was artificially anchoraged by external plate to prevent anchorage failure (see Figure 2.14). The investigated parameters were fibre volumetric ratios, shear span to depth ratios and concrete strengths. In the Narayanan and Darwish tests, the authors concluded that the inclusion of fibres in the concrete mix not only increased the stiffness of the beams but also increased the spalling resistance, reduced crack widths and increased the failure loads.

Similar tests on the shear strength of fibre reinforced concrete beams were also conducted by numerous other investigators such as LaFraugh and Maustafa (1975), Jindal (1984), Sharma (1986), Mansur et al. (1986), Li et al. (1992), Imam et al. (1994) and others. Their results indicated similar behaviour to that discussed above.

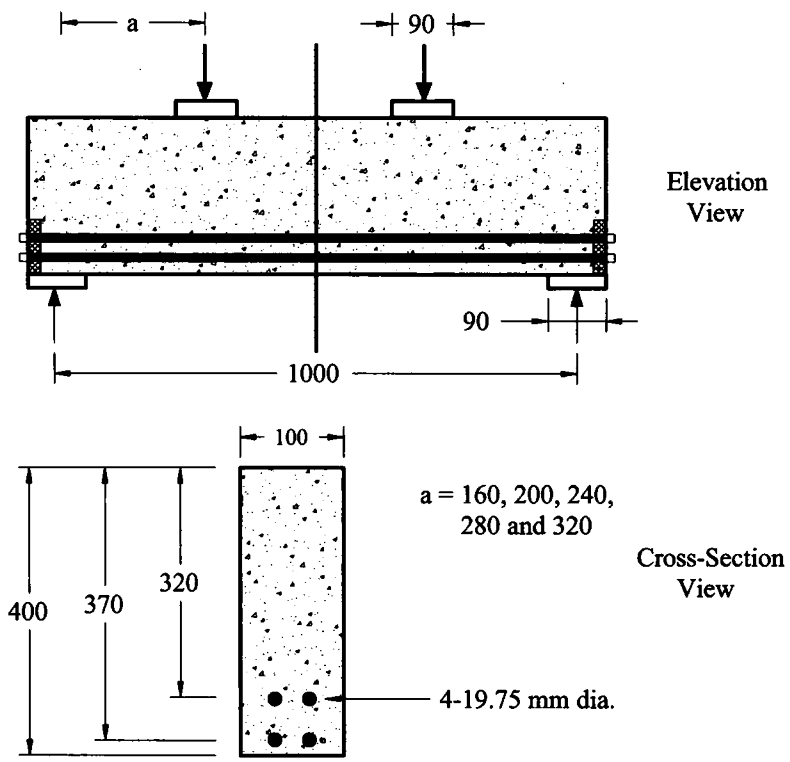

Figure 2.14 – Details of specimens tested by Narayanan and Darwish (1988).

CHAPTER 3 – MECHANICAL PROPERTIES OF REACTIVE POWDER CONCRETE

3.1 Introduction

Prior to the new millennium, mix designs for RPC were reported by Richard and Cheyrezy (1994, 1995), Bonneau et al. (1997) and, using Australian materials, by Gowripalan et al. (2000) and Gilbert et al. (2000). One objective of this study was to determine a highly workable RPC mix, using Australian materials, with a compressive cylinder strength (f_{cm}) of at least 160 MPa and with a split cylinder tensile strength (f_{sp}) and flexural tensile strength (f_{cf}) of the order of 20 and 30 MPa, respectively.

In this chapter, experimental results of the mechanical properties of both fibre reinforced and non-fibre reinforced RPC using Australian materials are reported. The results of cylinder and cube compressive strengths, modulus of elasticity, modulus of rupture, double punch tension, split cylinder tension and flow table tests are reported.

3.2 Mix Designs and Material Selection

In this study, nineteen RPC mixes were prepared as presented in Tables 3.1 and 3.2. The main variables include the volumetric quantity of fibre, type of fibres and water/binder ratio. The components of the reactive powder concrete mix used in this project were: Kandos Type 1 General Portland cement manufactured to AS3972 (1997); undensified silica fume produced in Western Australia; Sydney sand and quartz sand produced with a particle size range between 150 μm and 400 μm; and ground silica flour (Grade 200) with particle size less than 4 μm which was used as filler and manufactured in Granville, NSW. Grading curves for the sand, ground quartz and silica flour are given in Figure 3.1.

Without the use of superplasticizer the production of RPC would not be possible. The superplasticizer used in the mix was Glenium 51, which is a new generation, modified, superplasticizer based on polycarboxylic ether. With these improved superplasticizers water / binder (*W/B*) ratios of 0.10-0.14 are possible. Glenium 27, another type of superplasticizer which contained a retarding admixture was used to delay the onset of setting.

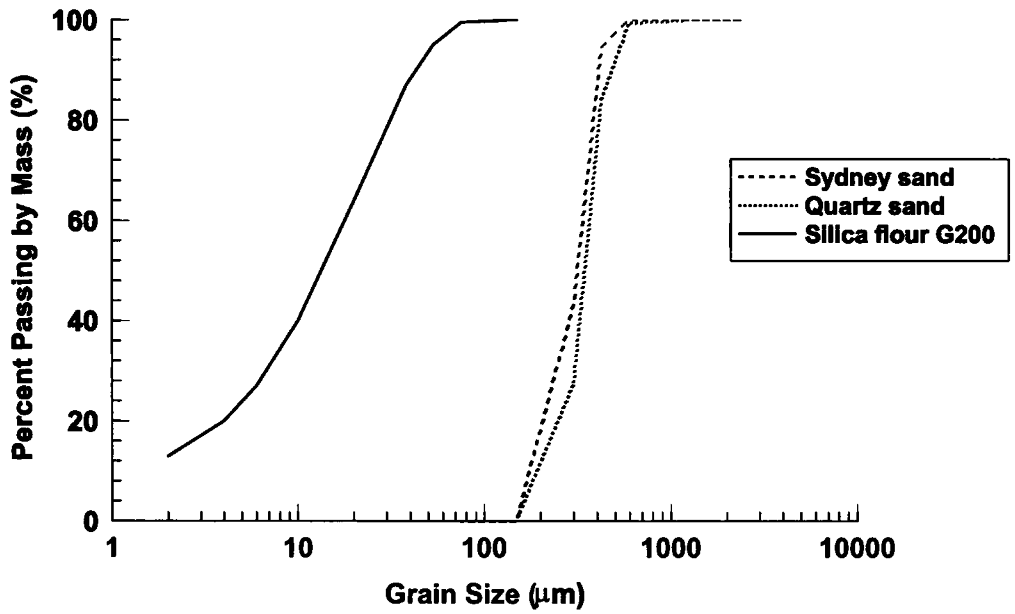

Figure 3.1 – Grading curve of Sydney sand, quartz sand and silica flour.

Table 3.1 – Reactive powder concrete mix designs (proportion by weight relative to weight of cement).

Component	**Mix Designs No.**																		
	1	**2**	**3**	**4**	**5**	**6**	**7**	**8**	**9**	**10**	**11**	**12**	**13**	**14**	**15**	**16**	**17**	**18**	**19**
GP Cement	1	1	1	1	1	1	1	1	1	1	1	1	1	1	1	1	1	1	1
Sydney sand	-	-	-	-	-	-	-	-	-	-	-	-	-	-	1.32	1.32	1.32	1.32	1.32
Quartz sand	1.32	1.32	1.32	1.32	1.32	1.32	1.32	1.32	1.32	1.32	1.32	1.32	1.32	1.32	-	-	-	-	-
Silica fume	0.32	0.32	0.32	0.32	0.32	0.32	0.32	0.32	0.32	0.32	0.32	0.32	0.32	0.32	0.24	0.24	0.24	0.32	0.32
Superplasticizer (Glenium 51)	0.056	0.056	0.056	0.056	0.056	0.056	0.056	0.056	0.056	0.056	0.056	0.056	0.056	0.056	0.063	0.063	0.063	0.056	0.056
Superplasticizer (Glenium 27)	-	-	-	-	-	-	-	-	-	-	-	-	-	-	0.006	0.006	-	-	-
Steel fibres * (Type I)	-	-	-	0.125	0.125	0.125	0.25	0.25	0.25	0.25	0.25	0.38	0.38	0.38	-	-	-	0.15	0.19
Steel fibres * (Type II)	-	-	-	-	-	-	-	-	-	-	-	-	-	-	0.19	0.09	-	-	-
Steel fibres * (Type III)	-	-	-	-	-	-	-	-	-	-	-	-	-	-	-	-	0.25	0.10	0.06
Total water	0.17	0.20	0.22	0.17	0.20	0.24	0.17	0.20	0.21	0.22	0.24	0.17	0.20	0.24	0.13	0.13	0.24	0.20	0.22

Note: * refer Table 3.3

Table 3.2 – Reactive powder concrete mix designs (proportion by kg/m^3 of RPC).

Component	**Mix Designs No.**																		
	1	**2**	**3**	**4**	**5**	**6**	**7**	**8**	**9**	**10**	**11**	**12**	**13**	**14**	**15**	**16**	**17**	**18**	**19**
GP Cement	836	815	802	825	805	780	814	794	788	782	770	803	784	760	864	874	788	794	782
Sydney sand	-	-	-	-	-	-	-	-	-	-	-	-	-	-	1140	1153	1040	1049	1032
Quartz sand	1103	1076	1059	1089	1062	1029	1074	1049	1040	1032	1016	1060	1035	1004	-	-	-	-	-
Silica fume	267	261	257	264	258	249	260	254	252	250	246	257	251	243	207	210	189	254	250
Superplasticizer (Glenium 51)	47	46	45	46	45	44	46	44	44	44	43	45	44	43	54	55	50	44	44
Superplasticizer (Glenium 27)	-	-	-	-	-	-	-	-	-	-	-	-	-	-	5	5	-	-	-
Steel fibres * (Type I)	-	-	-	103	101	97	203	199	197	196	193	305	298	289	-	-	-	119	149
Steel fibres * (Type II)	-	-	-	-	-	-	-	-	-	-	-	-	-	-	164	79	-	-	-
Steel fibres * (Type III)	-	-	-	-	-	-	-	-	-	-	-	-	-	-	-	-	197	79	47
Total water	142	163	176	140	161	187	138	159	166	172	185	137	157	182	112	114	189	159	172
W/B	0.13	0.15	0.18	0.13	0.15	0.18	0.13	0.15	0.16	0.17	0.18	0.13	0.15	0.18	0.10	0.10	0.18	0.15	0.17
Total Fibre Volumetric Ratio (%)	0	0	0	1.3	1.3	1.3	2.5	2.5	2.5	2.5	2.5	3.8	3.8	3.8	2.0	1.0	2.5	2.5	2.5

Note: * refer Table 3.3

Details of the steel fibres used are given in Table 3.3 with l_f being the total length of fibre, d_f the diameter of fibre, α_f is the aspect ratio of fibre ($\alpha_f = l_f / d_f$) and σ_{fu} is the ultimate tensile strength of the fibre. Type I fibres were straight 13 mm long by 0.2 mm diameter and fabricated from very high strength steel with a tensile strength of 1800 MPa. Type II fibres were end hooked fibres 35 mm long by 0.43 mm diameter and made from high strength bright mild steel which has a tensile strength of 1200 MPa. Type III fibres were end-hooked fibres 30 mm long by 0.5 mm diameter with a maximum tensile strength of 1200 MPa.

Table 3.3 – Steel fibre types.

Type	Source	l_f (mm)	d_f (mm)	α_f	σ_{fu} (MPa)	Fibre Shape
I	Bekaert	13	0.20	65	1800	
II	Dramix	35	0.43	80	1200	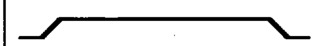
III	Dramix	30	0.5	60	1200	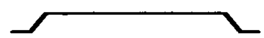

All the constituents were batched by an electronic balance and mixed in a concrete mixer for about 10 minutes. Water, superplasticizer and retarder were added gradually until the materials were uniformly mixed (see Plate 3.1). The fibres were introduced last, dispersed uniformly and mixed for a further 10 minutes. Although fibrous mixes are less workable than plain concrete, the mix procedures proved satisfactory in that the dispersion of fibres were found to be uniform and there was no evidence of fibre balling. Flow table tests as per ASTM C230 were undertaken before casting of the specimens to assure that the fibre reinforced concrete mix had achieved a flow between 160 to 210 mm (see Plate 3.2).

All the stainless steel moulds were cleaned and greased to allow smooth stripping. The fresh FR-RPC was poured and compacted using a vibrating table. Within one hour of casting, all the control specimens were covered under wet hessian and plastic sheet for 24 hours. All specimens were stripped after 24 hours and cured for a further 72 hours at 90 degrees centigrade in a hot water bath. After 3 days the specimens were removed from the hot water bath and air cured until the day of testing.

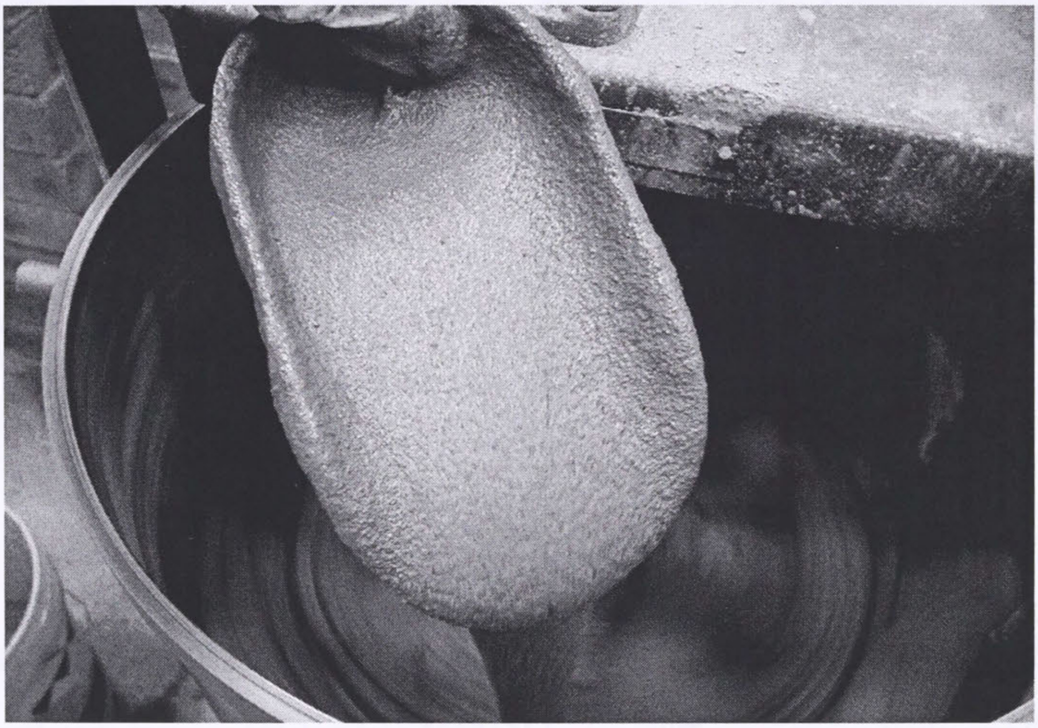

Plate 3.1 – Fresh reactive powder concrete mix prior to addition of steel fibres.

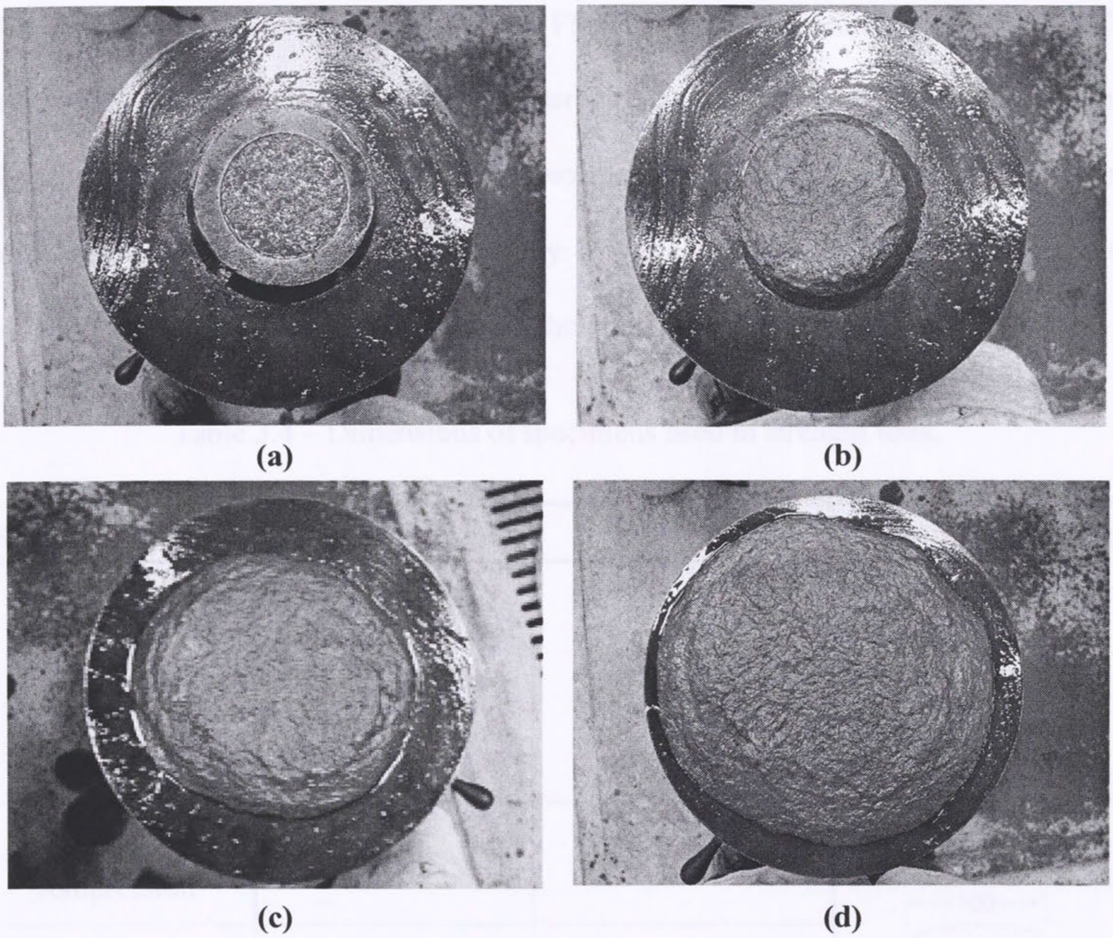

Plate 3.2 – Flow table test as per ASTM C230: (a) before removal of the brass cone, (b) instantaneous after the removal of the brass cone, (c) after 10 drops and (d) after 20 drops.

3.3 Specimens Size, Testing Instrumentation and Test Setup

Table 3.4 summarises the size of the specimens used in the material strength test. The strength tests were undertaken in a 3000 kN Instron stiff compression testing machine with stiff loading platens. Compression strength tests were undertaken on 200 mm high by 100 mm diameter cylinders loaded at 20 MPa/min in accordance with AS1012.9 (1986) with the unformed end of the cylinder ground before testing and on 70 mm cubes at a load rate of 20 MPa/min. A minimum of six specimens were tested in each batch.

The compressive stress-strain curves of the FR-RPC were obtained from a 200 mm high by 100 mm diameter cylinder tested under circumferential displacement control of 50 με/min over an average period of approximately two hours. Split-cylinder tension tests were undertaken on 200 mm high by 100 mm diameter cylinders loaded at 1.0 MPa/min via a 10 mm wide loading strip (shown in Figure 3.2a).

Table 3.4 – Dimensions of specimens used in strength tests.

Strength Test Type	Specimen Type	Load Rate	Specimen Size (mm)
Uniaxial compression	Cube	20 MPa /min	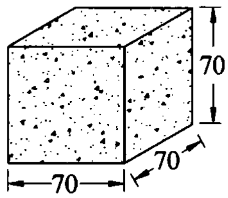
Uniaxial compression	Cylinder	20 MPa /min	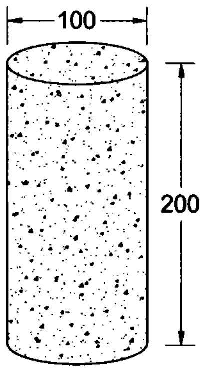
Modulus of elasticity & Poisson's ratio	Cylinder	Circumferential Control : 50 με/min	
Split-cylinder tension	Cylinder	1 MPa /min	
Double punch tension	Cylinder	1 MPa /min	
Flexural tension & fracture energy	Prism (notched)	CMOD Control: 500 με/min	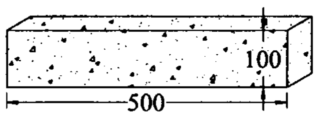
	Prism (unnotched)	Midspan Deflection Control: 1mm/min	

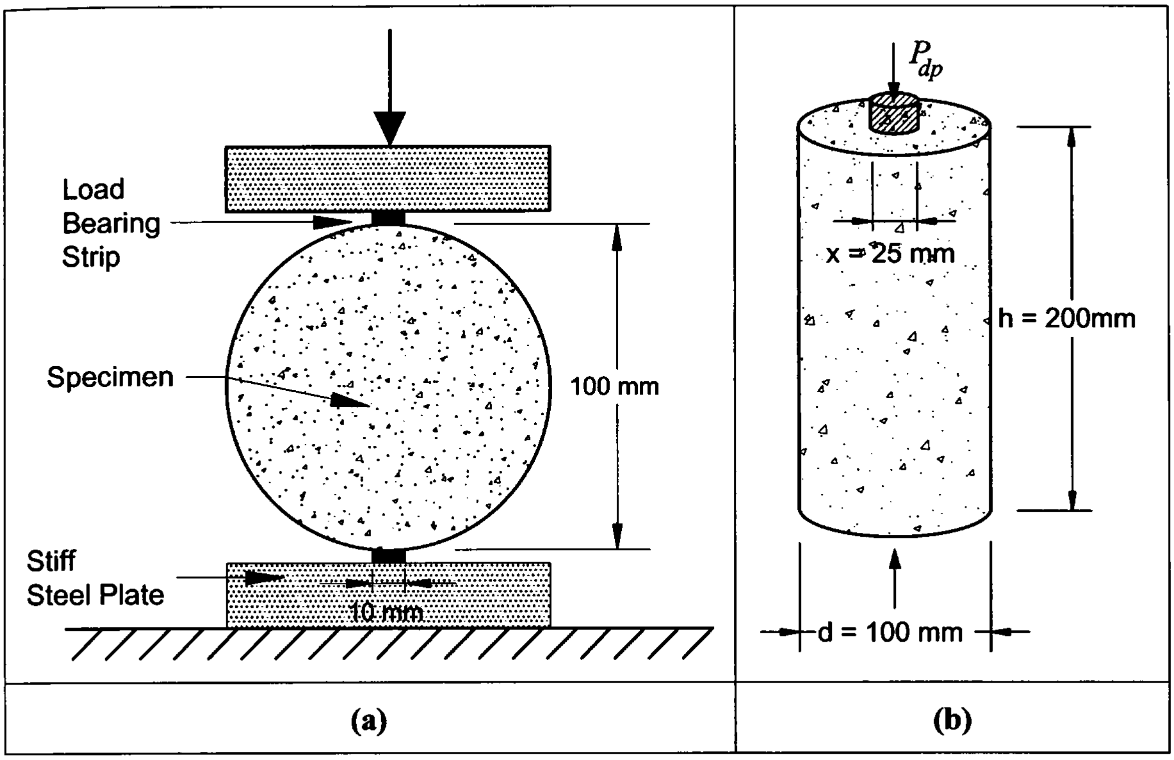

Figure 3.2 – Experimental setup of (a) split-cylinder strength test and (b) double punch tensile strength test.

The flexural tensile strength (f_{cf}) on both fibre reinforced RPC and RPC without fibres were obtained from both notched and unnotched three point bending tests. The specimens used in this test were 100 mm square prisms spanning 400 mm with three different notch depths (a), being $a = 0, 25$ and 50 mm (see Figure 3.3). The notches were formed by a 3 mm wide saw cut across the full width of the specimen. The specimens were counter balanced (Plate 3.3) to eliminate the effect of the self-weight on the fracture measurement. The notched specimens were controlled using the crack mouth opening displacement (CMOD) at a control rate of 500 με/min whereas the unnotched specimen was controlled using the midspan displacement at a control rate of 1 mm/min.

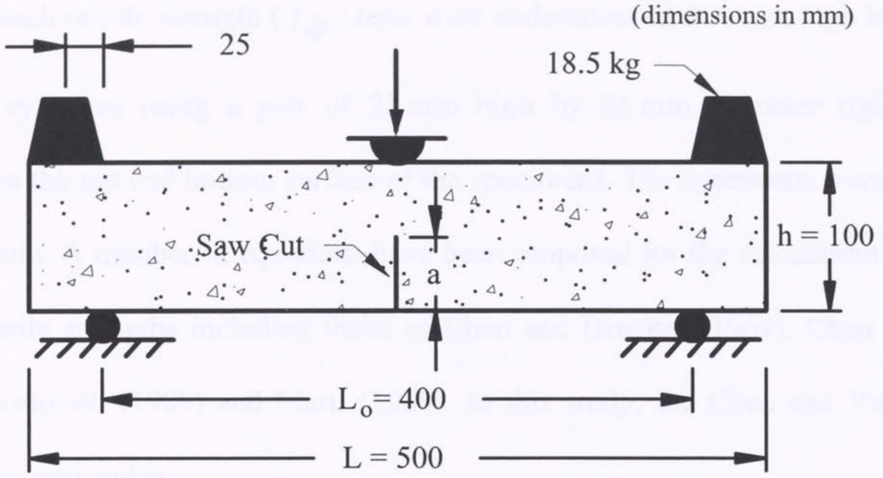

Figure 3.3 – Test setup on flexural tension tests on 100-mm square RPC beams.

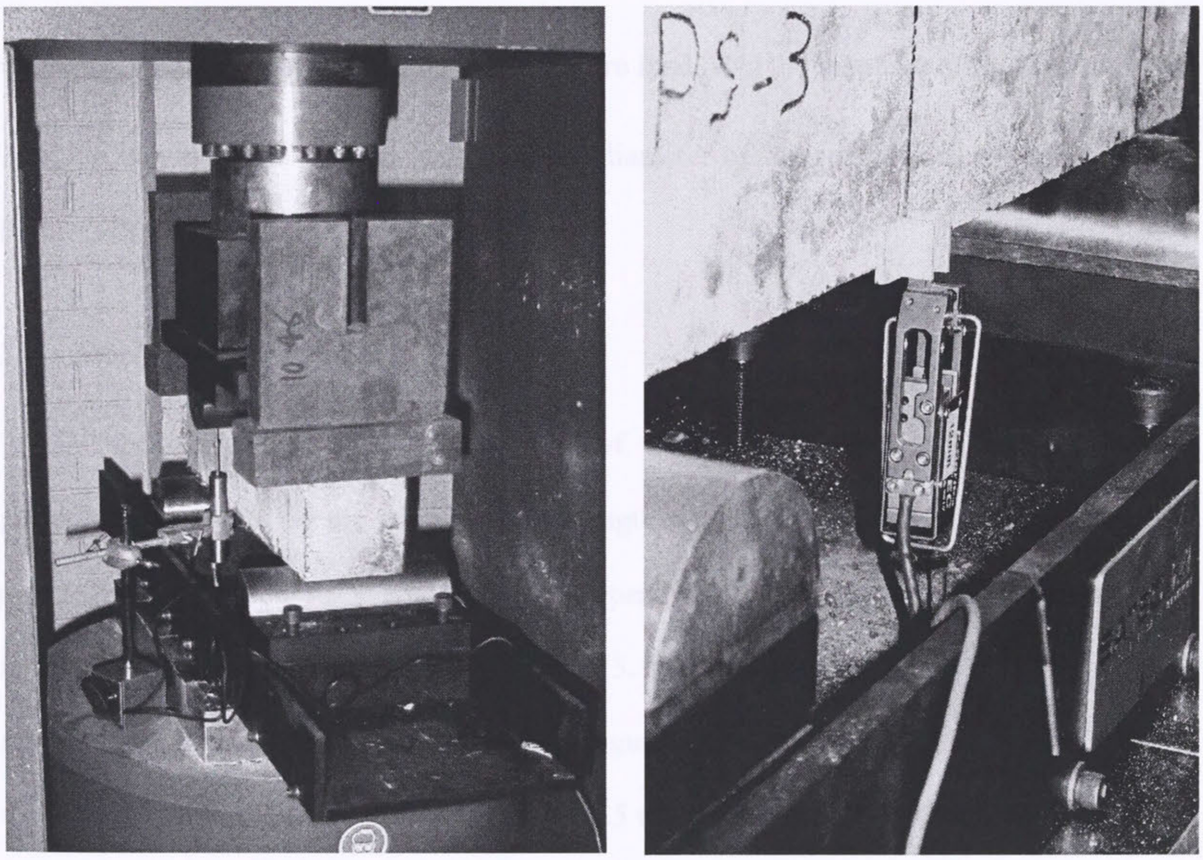

(a) (b)

Plate 3.3 – (a) Experimental setup of three point bending test and (b) CMOD control.

Double punch tensile strength (f_{dp}) tests were undertaken on 200 mm high by 100 mm diameter cylinders using a pair of 25 mm high by 25 mm diameter rigid circular punches on the top and bottom surface of the specimens. The specimens were loaded at 1.0 MPa/min. A number of equations have been proposed for the calculation of double punch tensile strengths including those of Chen and Drucker (1969), Chen and Yuan (1980), Bortolotti (1988) and Marti (1989). In this study, the Chen and Yuan (1980) equation is used and is

$$f_{dp} = \frac{0.75\, P_{dp}}{\pi\left(0.3dh - 0.25x^2\right)} \tag{3.1}$$

where P_{dp} is the maximum double punch failure load, d is the diameter of the cylinder, h is the height of the cylinder and x is the diameter of the steel punch as shown in Figure 3.2b

3.4 Mechanical Properties of RPC

In this section, the mechanical properties of the different RPC mix designs are presented. Raw data on the compressive strength test, split cylinder tension test and double punch tension tests are given in Appendix A. The average values on the mechanical strength are summarised in Table 3.5. The experimental results of the stress-strain curves for FR-RPC mixes are given in Figure 3.4. The experimental results of the three point bending test are given in Figures 3.5 to 3.7 where MID is the displacement at the mid span and CMOD is the crack mouth opening displacement.

Table 3.5 – Mechanical properties on control specimens of mix designs 1 to 19.

Mix No.	E_o (MPa)	v	f_{cm} (MPa)	f_{cu} (MPa)	f_{sp} (MPa)	f_{dp} (MPa)	f_{cf} (MPa)	$G_{f,CMOD}$ (N/m)	$G_{f,mid}$ (N/m)	$\frac{G_{f,CMOD}}{G_{f,mid}}$	Flow (mm)
1	44.6	0.12	161	-	7.9	8.2	11.8	-	-	-	160
2	44.4	0.12	148	-	7.5	7.9	9.9	-	-	-	230
3	44.2	0.13	133	-	7.3	7.6	9.5	-	-	-	>350
4	44.6	0.15	168	194	20.2	11.2	29.7	22.8	24.8	0.92	120
5	43.3	0.15	156	180	18.3	10.1	22.9	22.1	21.7	1.02	160
6	40.0	0.14	137	167	15.2	8.4	28.3	23.2	23.2	1.00	290
7	48.8	0.15	181	214	24.4	12.0	42.5	33.9	34.4	0.99	110
8	46.8	0.15	176	181	23.7	11.9	34.9	26.6	20.2	1.32	150
9	44.0	0.15	163	176	19.2	11.9	29.8	27.7	27.8	1.00	170
10	45.0	0.15	161	178	20.9	11.2	26.4	25.1	24.2	1.04	180
11	43.2	0.14	145	166	20.9	10.0	22.5	20.2	20.0	1.01	220
12	46.1	0.16	185	214	26.9	15.6	51.8	43.9	54.4	0.81	100
13	44.9	0.15	177	202	25.0	13.2	45.7	40.9	-	-	130
14	44.0	0.14	160	184	23.6	12.2	45.2	36.4	36.2	1.01	190
15	48.3	0.13	156	-	21.8	-	22.0	6.0	6.2	0.97	-
16	-	-	155	-	-	-	-	-	-	-	-
17	40.0	0.13	157	188	18.3	11.1	25.2	12.4	12.3	1.01	210
18	49.0	0.14	173	187	22.4	13.6	26.3	15.6	15.3	1.02	150
19	46.0	0.15	169	185	23.5	12.2	23.8	18.5	18.6	0.99	180

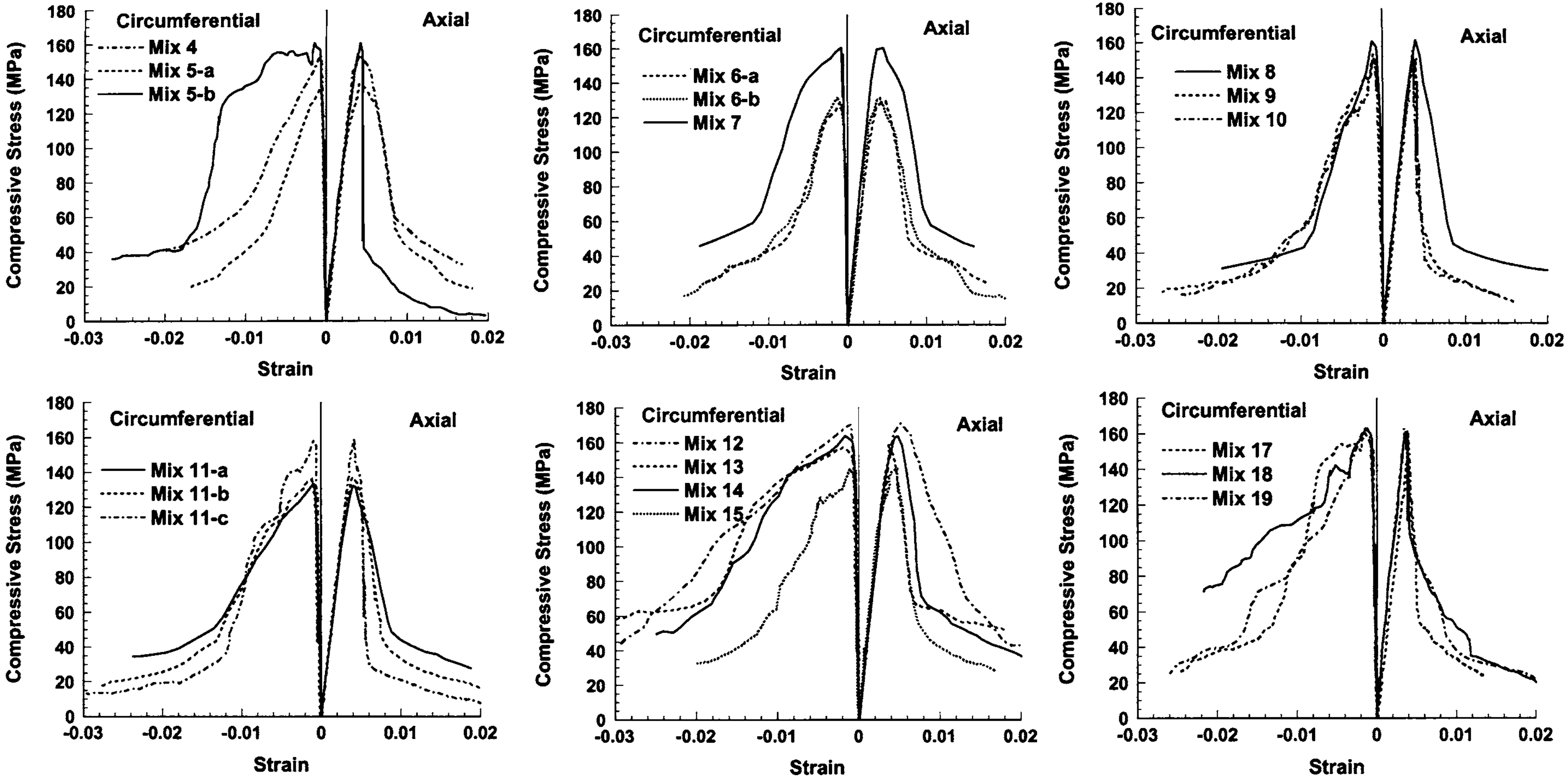

Figure 3.4 – Stress-strain curves.

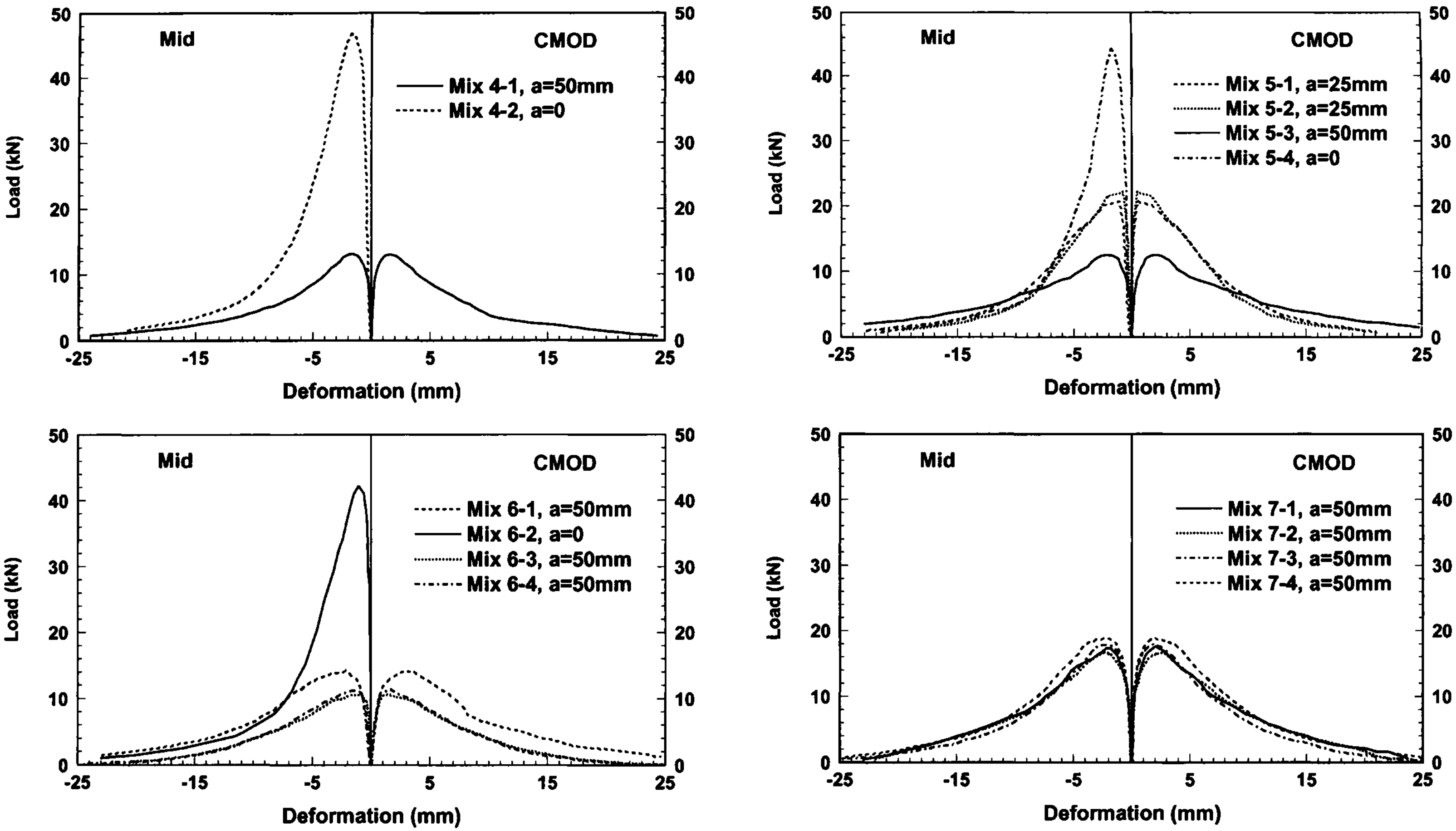

Figure 3.5 – Load versus midspan deflection and load versus CMOD for mix designs 4 to 7.

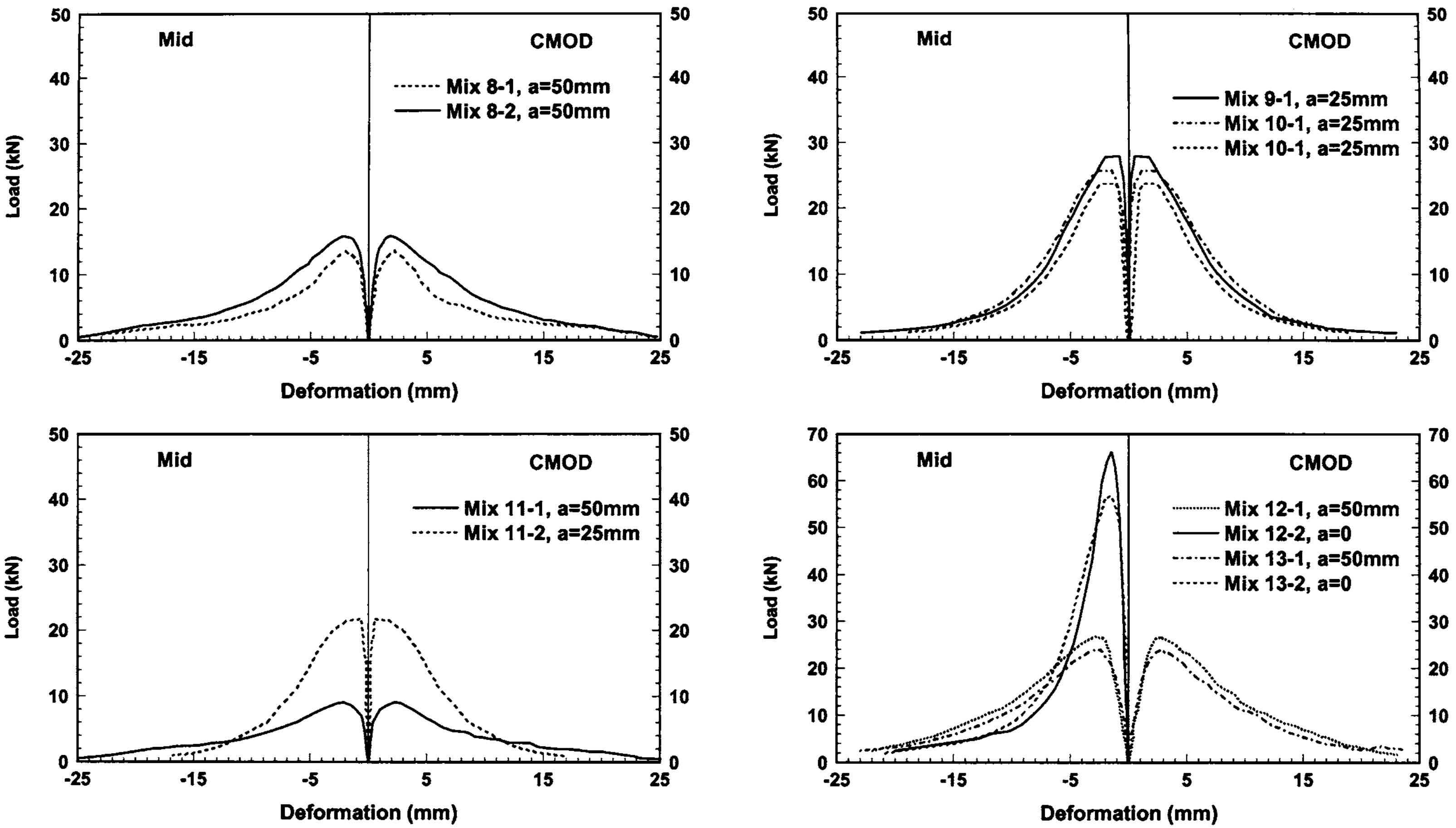

Figure 3.6 – Load versus midspan deflection and load versus CMOD for mix designs 8 to 13.

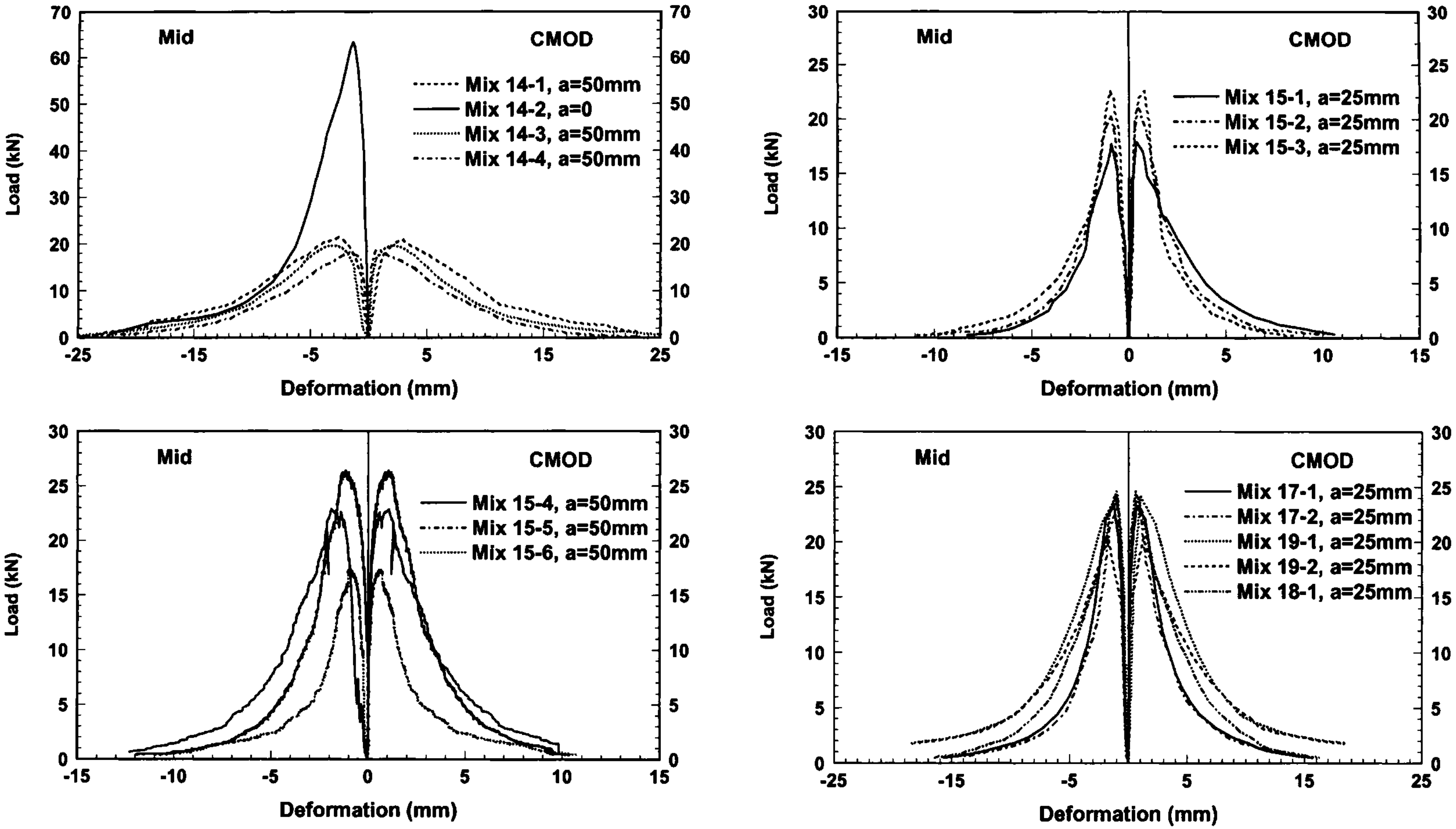

Figure 3.7 – Load versus midspan deflection and load versus CMOD for mix 14 to 19.

3.5 Analysis of Test Results and Discussions

Nineteen RPC mix designs were developed in this study with the major investigating parameters being the fibre type, fibre quantity and water quantity. A summary of the mechanical properties of the reactive powder concrete mixes was presented in Section 3.4. In this section, discussions on the collected data are presented.

Figure 3.8 shows the compressive strength of the RPC mix design 8 (refer Table 3.2) tested in a stiff 3000kN Instron machine at load rate of 20, 60 and 100 MPa/min. The results show the compressive strength is not significantly affected with the increase of load rate from 20 MPa/min to 100 MPa/min.

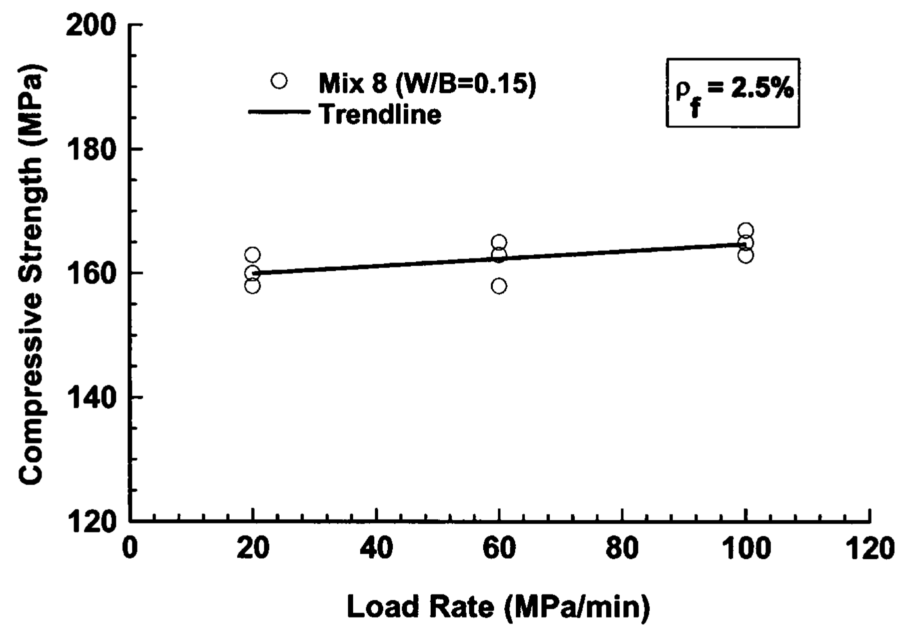

Figure 3.8 – Compressive strength of RPC mix design 8 at load rate of 20, 60 and 100 MPa/min.

Figure 3.9 shows the relationship of the cylinder compressive strength and cube compressive strength (f_{cm}/f_{cu}) corresponding to varying fibre volume and water/binder ratio (W/B). The figure shows the average f_{cm}/f_{cu} ratio for FR-RPC is 0.88 and with a coefficient of variation of 5% and that neither the volume of fibre nor the W/B ratio influenced the result.

In Figure 3.10 the relationship between the double punch tensile strength and fibre volume and the water/binder ratio are plotted. Figure 3.10a shows that for the specimens with greater than 1% of fibre there was a significant and consistent reduction in the punching strength relative to the split cylinder strength. For the specimens without fibres the punching strength to split cylinder strength is approximately unity where for the specimen with one, or more, percent of fibres, $f_{dp} / f_{sp} = 0.55$.

In Figure 3.10b the relationship between the double punch to split cylinder tensile strength ratio is plotted against the water/binder ratio for water/binder ratios from W/B = 0.13 to 0.18. The figure shows that the water binder ratios do not influence the double punch to split cylinder ratio.

Figure 3.11 compares the tensile strengths as measured by the double punch test, split cylinder strength and modulus of rupture tests against the square root of the cylinder strength, that is $f_{dp}/\sqrt{f_{cm}}$, $f_{sp}/\sqrt{f_{cm}}$ and $f_{cf}/\sqrt{f_{cm}}$, for varying fibre quantities. Comparing the two indirect tensile strength results (that is the double punch and split cylinder tests) shows that the results of the split cylinder tests are significantly influenced by the fibre volume relative to compressive strength. Less influence of fibre volume is observed in the double punch test results.

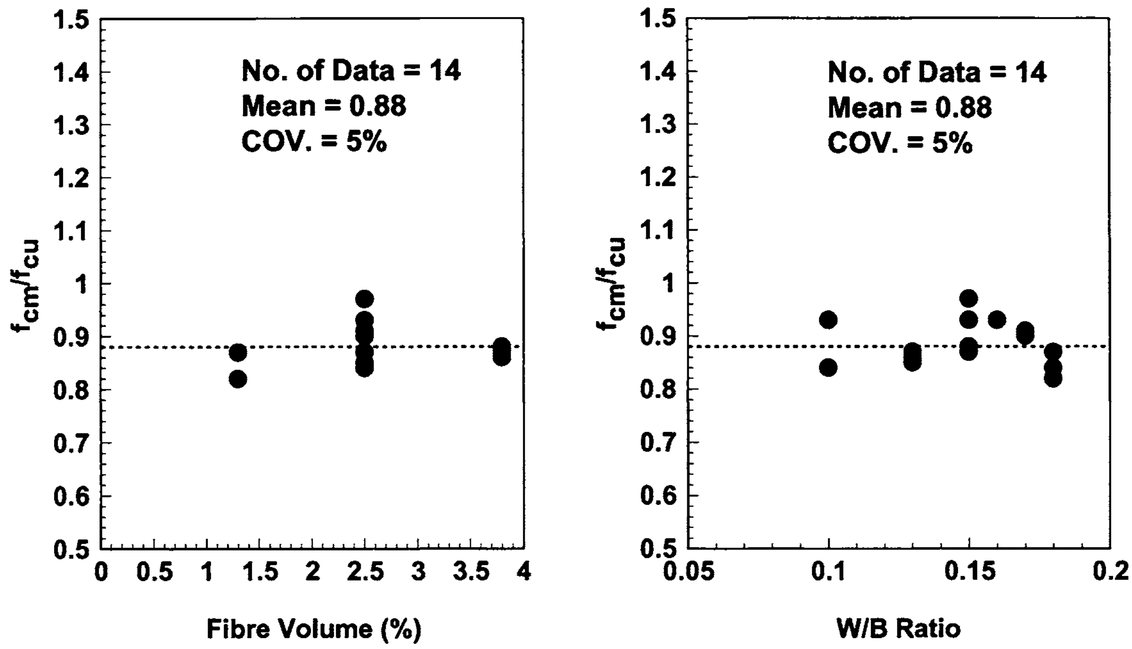

(a) (b)

Figure 3.9 – f_{cm}/f_{cu} ratios versus (a) fibre ratio by volume and (b) water/binder ratio.

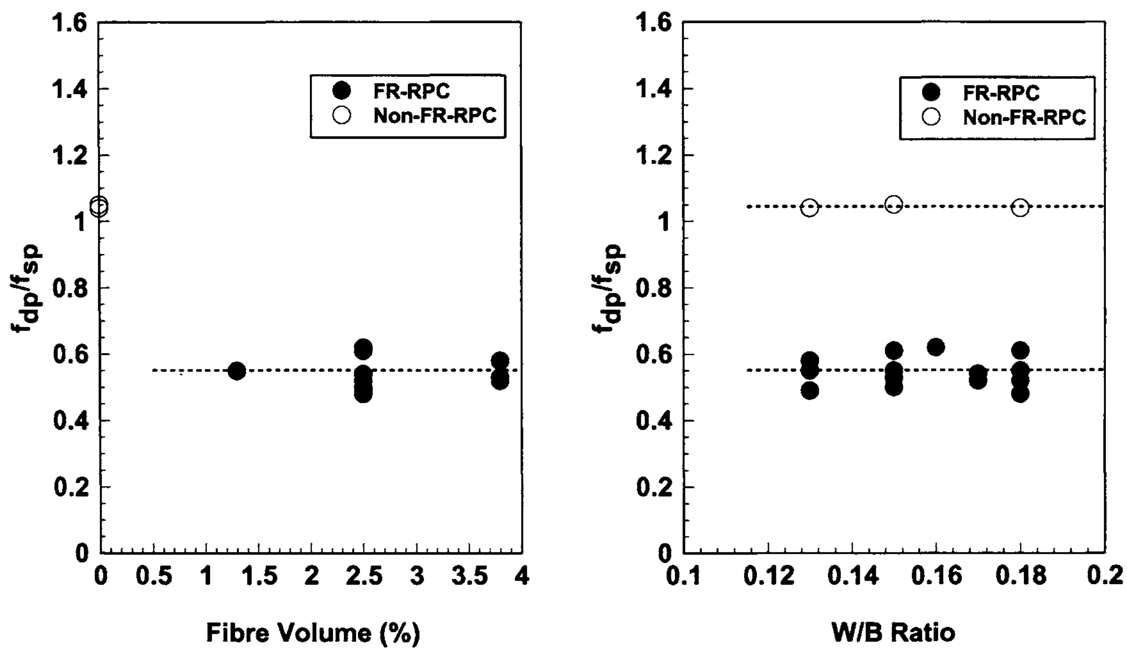

(a) (b)

Figure 3.10 – f_{dp}/f_{sp} ratios versus (a) fibre ratio by volume and (b) water/binder ratio.

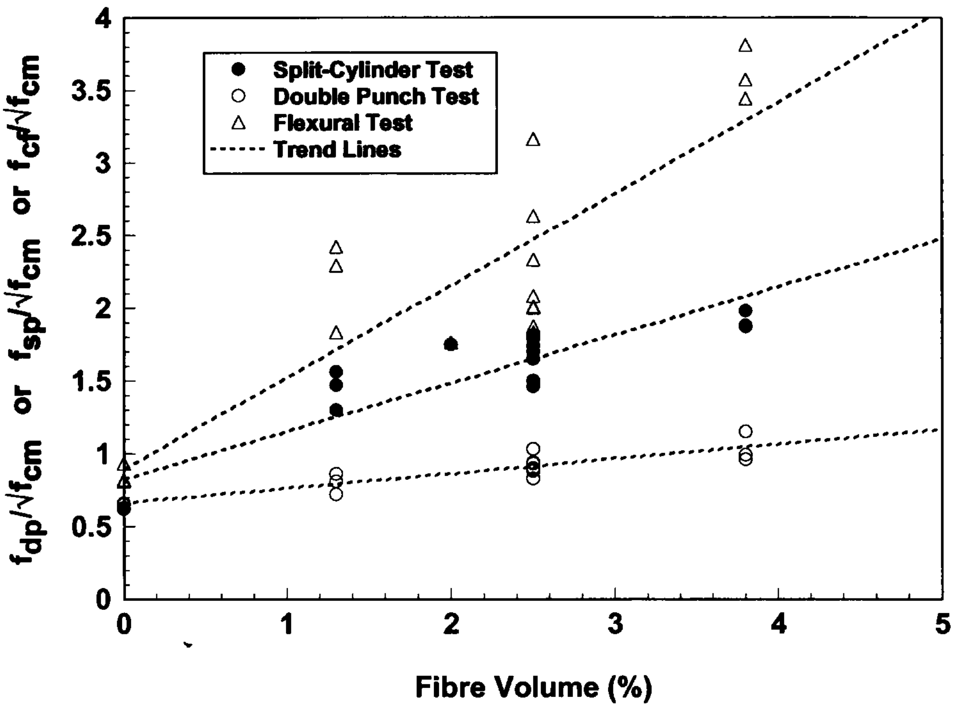

Figure 3.11 – Comparison of $f_{dp}/\sqrt{f_{cm}}$, $f_{sp}/\sqrt{f_{cm}}$ and $f_{cf}/\sqrt{f_{cm}}$ versus fibre volume.

The split cylinder test may not give a good indication of the tensile strength of fibre reinforced concrete. It was observed in the tests that the 10 mm wide Masonite strip placed between the specimen and the loading bearing plate crushed prior to the splitting of the specimens and this crushing was non-uniformly distributed along the length of the specimen. After cracking the presence of fibres can carry tensile splitting forces and, thus, the formation of the splitting crack may not result in failure of the specimen. As the load increases, the load bearing region may crush before complete fracture across the tensile plane, as demonstrated in the strut and tie model shown in Figure 3.12. Further investigation is needed to study the effects of the presence of fibres across the splitting plane on determining the tensile strength of the concrete using the split cylinder test method.

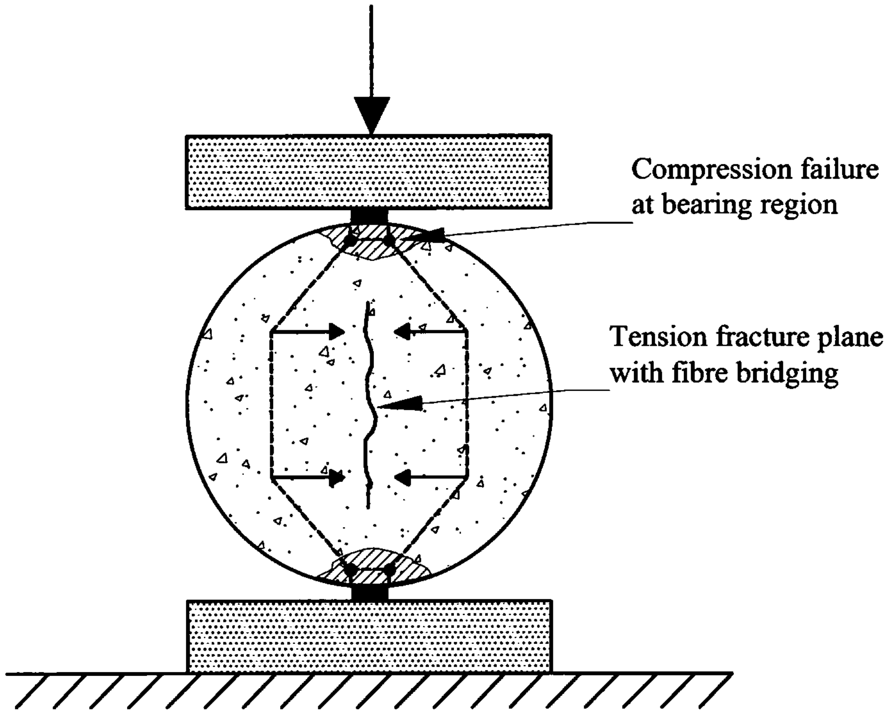

Figure 3.12 – Control of tensile splitting forces in the split cylinder test by fibres crossing the splitting crack.

3.6 Conclusions

Experimental results on the mechanical properties of both nineteen different mix designs fibre reinforced and non-fibre reinforced RPC using Australian materials were reported. The main investigation parameters were fibre types and quantity and water-binder ratios. The tests include cylinder and cube compressive strengths, modulus of elasticity and Poisson's ratio, modulus of rupture, double punch tension, split cylinder tension and flow.

From the strength tests, the following observations were made:

(1) The compressive strength of RPC is not significantly affected by the loading rate for loading rates between 20 MPa/min and 100 MPa/min.

From the strength tests, the following observations were made:

(1) The compressive strength of RPC is not significantly affected by the loading rate for loading rates between 20 MPa/min and 100 MPa/min.

(2) Cylinder compressive strength is approximately 88 percent of the cube compressive strength.

(3) The double punch test is a more reliable measure of tensile strength than that the split cylinder test for the calculation of the indirect tensile strength of fibre reinforced RPC.

(4) A workable RPC mix giving compressive strength of greater than 160 MPa is possible using Australia materials. The favoured mix is mix design 8 (refer Tables 3.1 and 3.2)

CHAPTER 4 – DEEP PANEL STRENGTH TESTS

4.1 Introduction

In the application of steel fibre reinforced reactive powder concrete (FR-RPC) to prestressed concrete girders without stirrups, an important factor that needs to be taken into consideration is the ability of the FR-RPC to resist transverse stresses set up in the prestressed end blocks (refer Figure 4.1). In the end region of a prestressed beam transverse tension is produced by the dispersion of the longitudinal compressive stress trajectories and may lead to longitudinal cracking within the anchorage zone. This chapter studies the mechanical behavior of steel FR-RPC deep panels with the panels designed to simulate tension bursting in anchorage zones of prestressed girders (demonstrated in Figure 4.1). The study includes:

(1) the examination of the effect of fibres on the specimens after cracking,

(2) studying the potential use of fibres to replace shear and bursting reinforcement, and

(3) investigating the effect of adding steel fibres for crack control and stability.

Six tests on steel FR-RPC deep panels were undertaken with the results discussed in this chapter.

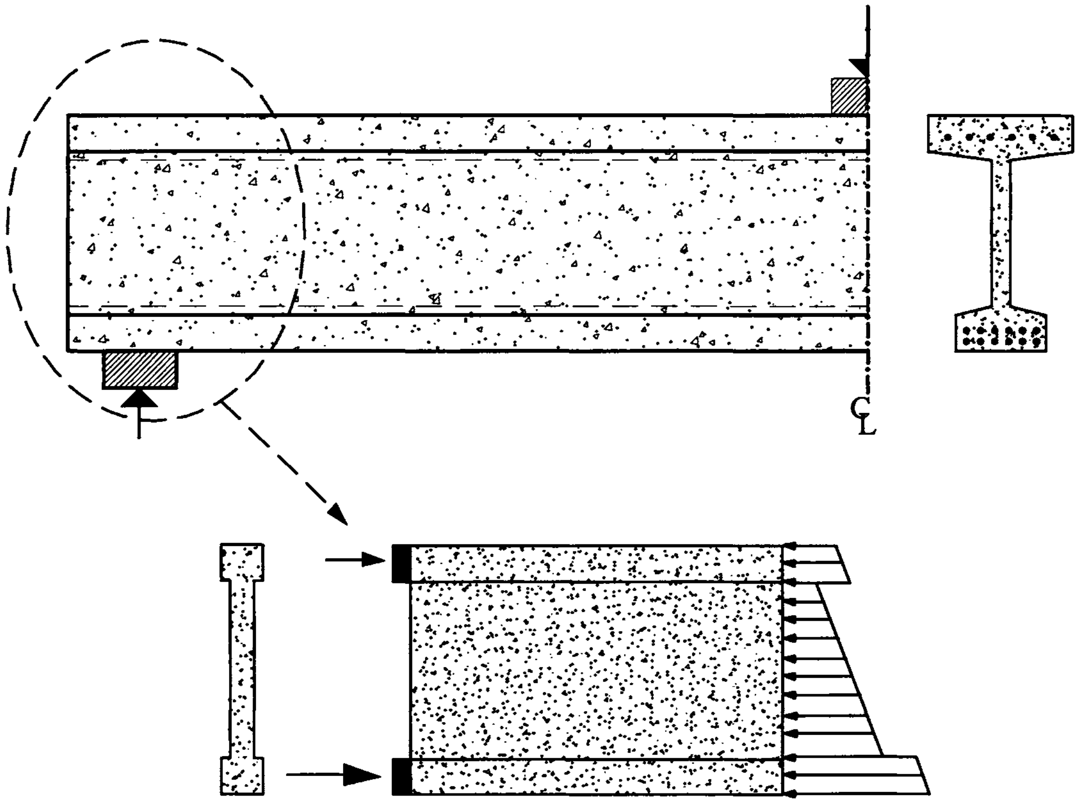

Figure 4.1 – Prestressed I-girder and web section showing simulated boundary forces produced by prestressing.

4.2 Variables and Specimen Dimensions

The variables studied in the experimental program were

- fibre type (fibre aspect ratio and geometry);
- fibre quantity; and
- boundary conditions.

The dimensions of the specimens were designed such that a near uniform stress field was developed away from the disturbed end regions. The panels were 1050 mm high had a clear span of 500 mm and were 70 mm thick in the web and 120 mm thick in the flanges. The deep panel dimensions are shown in Figure 4.2

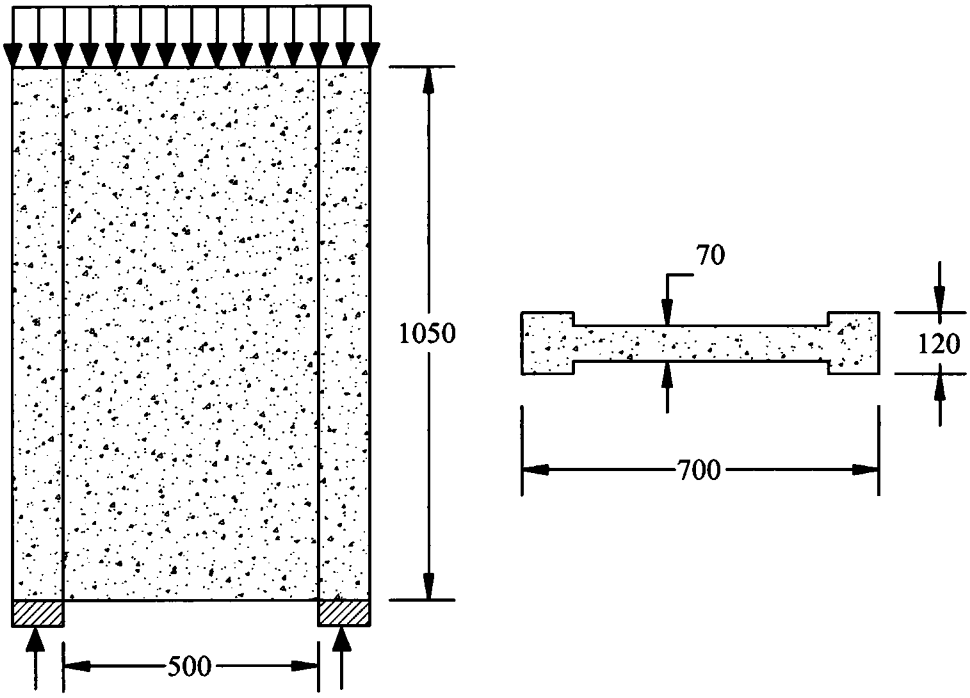

Figure 4.2 – Deep panels dimensions (in mm).

4.3 Materials, Mix Designs and Fabrications

The FR-RPC used in this project was mixed using the facilities available in the Concrete Materials Laboratory in the School of Civil and Environmental Engineering, UNSW. The components of the mix used in this project were Kandos Type 1 General Portland cement manufactured to AS3972 (1997); undensified silica fume produced in Western Australia; Sydney sand and quartz sand produced with a particle size range between 150 μm and 400 μm. Ground silica flour (Grade 200) with particle sizes less than 4 μm was used as a filler and is manufactured at Granville, NSW. Grading curves for the sand, ground quartz and silica flour are given in Figure 3.1. Glenium 51 superplasticizer was used in the mix to increase the workability and Glenium 27 superplasticizer which contained retarder in the admixture was used to delay the onset of setting.

For panels 1 to 3 and 4 to 6 the W/B was 0.10 and 0.18, respectively. Details of the steel fibres used are given in Table 3.3 with l_f being the total length of fibre, d_f the diameter of fibre and σ_{fu} is the ultimate tensile strength of the fibre. Type I fibres were straight 13 mm long by 0.2 mm diameter and are fabricated from very high strength steel with a tensile strength of 1800 MPa. Type II fibres were end hooked fibres 35 mm long by 0.43 mm diameter and are made from high strength bright mild steel with a tensile strength of 1200 MPa. Details of the mix designs are given in Table 4.1.

Table 4.1 – Fibre reinforced RPC mix designs for panels 1 to 6 (proportion by weight relative to weight of cement).

Component	Panel 1	Panel 2	Panel 3	Panel 4	Panel 5	Panel 6
GP Cement	1	1	1	1	1	1
Sydney sand	1	1	1	-	-	-
Quartz sand	-	-	-	1.32	1.32	1.32
Silica fume	0.24	0.24	0.24	0.32	0.32	0.32
Silica flour	0.157	0.157	0.157	-	-	-
Glenium 51	0.063	0.063	0.063	0.056	0.056	0.056
Glenium 27	0.006	0.006	0.006	-	-	-
Steel fibres (Type I)	-	-	-	0.125	0.250	0.375
Steel fibres (Type II)	0.188	0.094	0.188	-	-	-
Total water	0.13	0.13	0.13	0.24	0.24	0.24
W/B	0.10	0.10	0.10	0.18	0.18	0.18
Equivalent Fibre Volumetric ratio (%)	2.0	1.0	2.0	1.25	2.5	3.7

All the constituents were batched by an electronic balance and mixed in a horizontal pan mixer for about 10 minutes. Water and superplasticizer were added gradually until the materials were uniformly mixed (refer Plate 3.1). The fibres were introduced last, dispersed uniformly and mixing continued for a further 10 minutes. Although fibrous mixes are less workable than plain concrete, the mix procedures proved satisfactory in that the dispersion of fibres were found to be uniform and there was no significant fibre balling. Flow table tests were undertaken before casting of the specimens to assure that the fibre reinforced concrete mix had achieved sufficient flow (shown in Plate 3.2).

All specimens were cast vertically in plywood forms. The forms were cleaned and greased to allow smooth stripping. The fresh FR-RPC was poured and compacted using a vibrating table. Within one hour of casting, the specimens and test control samples were covered under wet hessian and plastic sheet for 24 hours. All specimens were stripped after 24 hours and cured for a further 72 hours at 90 degrees centigrade in a hot water bath. After 3 days the specimens were removed from the hot water bath and air cured until the day of testing.

4.4 Test Setup, Testing Procedure and Instrumentation

Details of the panels and the test setup are given in Figure 4.3. For panels 1 and 2 the bounding supports were free to translate horizontally and were fixed for rotation. For panels 3 to 6 the boundaries were modified with pins added to the test arrangement. The pins and rollers were greased to minimize friction to give free rotation and horizontal translation of the supports. Panels 1 to 3 were tested horizontally in a 5000 kN stiff testing frame with 50 mm thick steel plates placed at each loading point. Panels 4 to 6 were tested vertically in a 3000 kN testing frame.

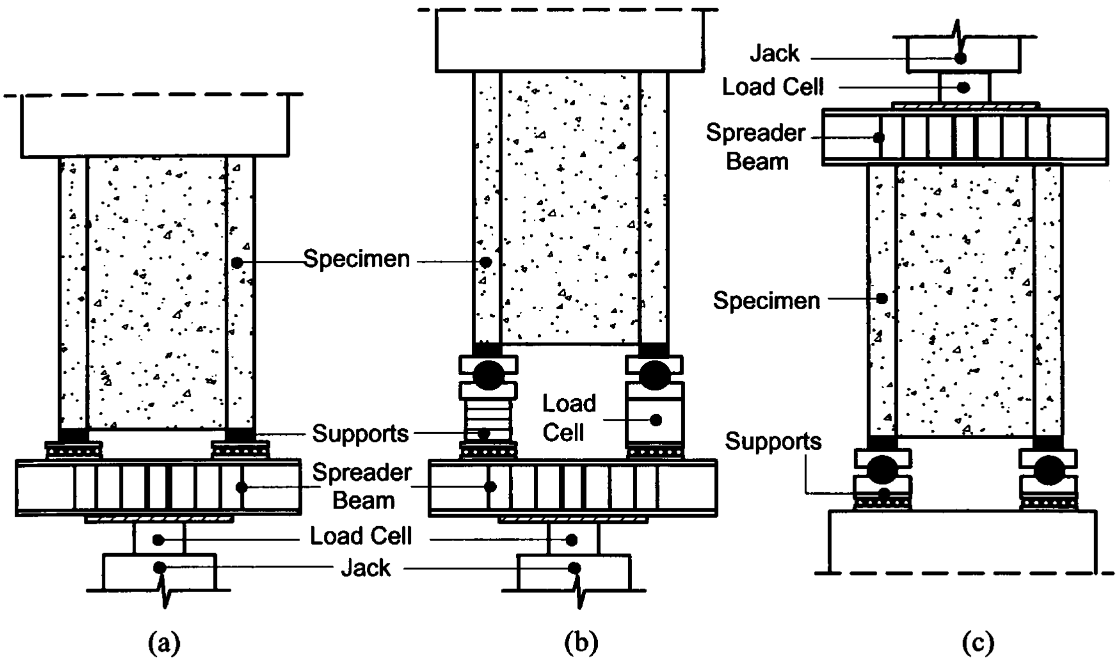

Figure 4.3 - Test specimen dimensions and boundary arrangements: (a) panels 1 and 2; (b) panel 3; (c) panels 4 to 6.

For panel 1, two electronic strain gauges (ESG) and five sets of Demec (DM) strain gauges were used over a gauge length of 60 mm and 250 mm, respectively. For panel 2, four ESG and five sets of DM gauges were used. The locations of the strain gauges used for panels 1 and 2 are shown in Figure 4.4a-b. For panels 3 to 6, twelve sets of DM strain gauges were used to measure strains and crack widths. The location of gauges for panels 3 to 6 are shown in Figure 4.4c. Demec gauges 1 to 12 were located to measure the crack width in the transverse direction of the panels whereas DMs 13 to 17 were used to monitor the far end boundary strains in the longitudinal direction. The loading was applied in 200 kN increments for panels 1 and 2 and 100 kN increments for panels 3 to 6. For each increment of load the DM gauge data were recorded and the crack pattern was traced. This procedure was repeated until failure of the specimen.

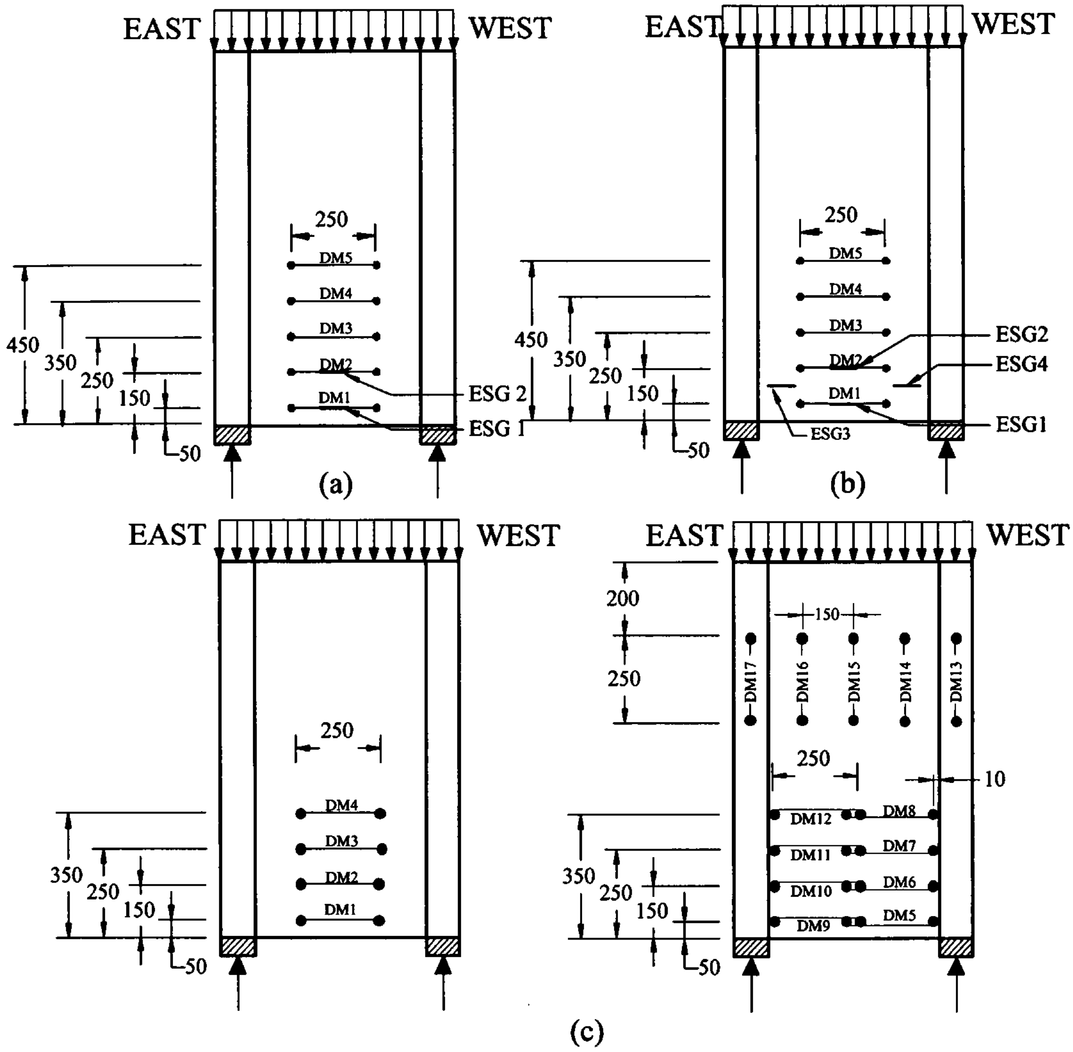

Figure 4.4 – Electronic strain gauge and Demec target locations: (a) panel 1; (b) panel 2 and (c) panels 3 to 6 (dimension in mm).

4.5 Material Properties

Table 4.2 gives the material properties of the steel FR-RPC for the deep panels where ρ_f is the volumetric fibre ratio; E_o is the modulus of elasticity; f_{cm} is the mean compressive strength; f_{sp} is the mean split-cylinder tension strength; f_{cf} is the flexural tension strength; G_f is the fracture energy; f_{dp} is the double punch tension strength and ν is the Poisson's ratio. Details of the strength testing instrumentation, materials test setups and control specimen sizes are given in section 3.3 of Chapter 3.

Table 4.2 – Detail of tested FR-RPC deep panels and strength test results.

Panel No.	1	2	3	4	5	6
Fibre Type †	II	II	II	I	I	I
ρ_f (%)	2.0	1.0	2.0	1.25	2.5	3.72
E_o (GPa)	48	-	50	39	40	44
f_{cm} (MPa)	162	150	162	135	144	158
f_{sp} (MPa)	22	-	22	12.6	16.6	22.3
f_{cf} (MPa)	20	-	20	18	24	30
f_{dp} (MPa)		-	-	10	12	15
G_f (N/mm)	6	-	6	9.3	16.3	19.3
ν	0.13	-	0.13	0.13	0.12	0.13
Flow* (mm)	-	-	-	260	220	160

Notes: * Flow test per ASTM C230; † refer Table 3.3

4.6 Cracking Loads, Peak Loads and Failure Modes

The experimental results of the panel tests are given in Table 4.3 where P_{cr} is the first cracking load determined by visual tracing of cracks on the specimens and P_{tear} is the load at which a large tearing (or splitting) crack occurred in the panel and at which time the experiment was stopped. It is seen that for the panels with rotational and translational freedom (i.e. panels 3 to 6) the tearing load was in the order of two times the cracking load whereas for the panels with only translational freedom the ultimate load to cracking load ratio was in the order of three.

Figures 4.5 and 4.6 present the crack patterns for the six deep panels tested in this study. First cracking occurred in the tension zone by splitting at the bottom surface of the panels. For panels 1 and 2 the major crack was initiated at the junction of the flange and web adjacent to one support. The crack then propagated vertically and laterally in with increasing load and it appeared that the boundary conditions influenced the location of the initial cracks. The boundary conditions were then modified for the following tests to allow for both free translation and free rotation of the ends.

With the boundaries free to rotate (panels 3 to 6) first cracking occurred approximately at the mid-span of the panels, as seen in Figures 4.5c and 4.6. After initial cracking, the crack propagated with increasing load until failure at which time the bursting crack had propagated such that the specimens were divided in two.

Table 4.3 – Experimental results.

Panel	**1**	**2**	**3**	**4**	**5**	**6**
P_{cr} (kN)	800	600	700	500	600	700
P_{tear} (kN)	2800	2000	1600	1010	1160	1530
P_{tear}/P_{cr}	3.5	3.3	2.3	2.0	1.9	2.2

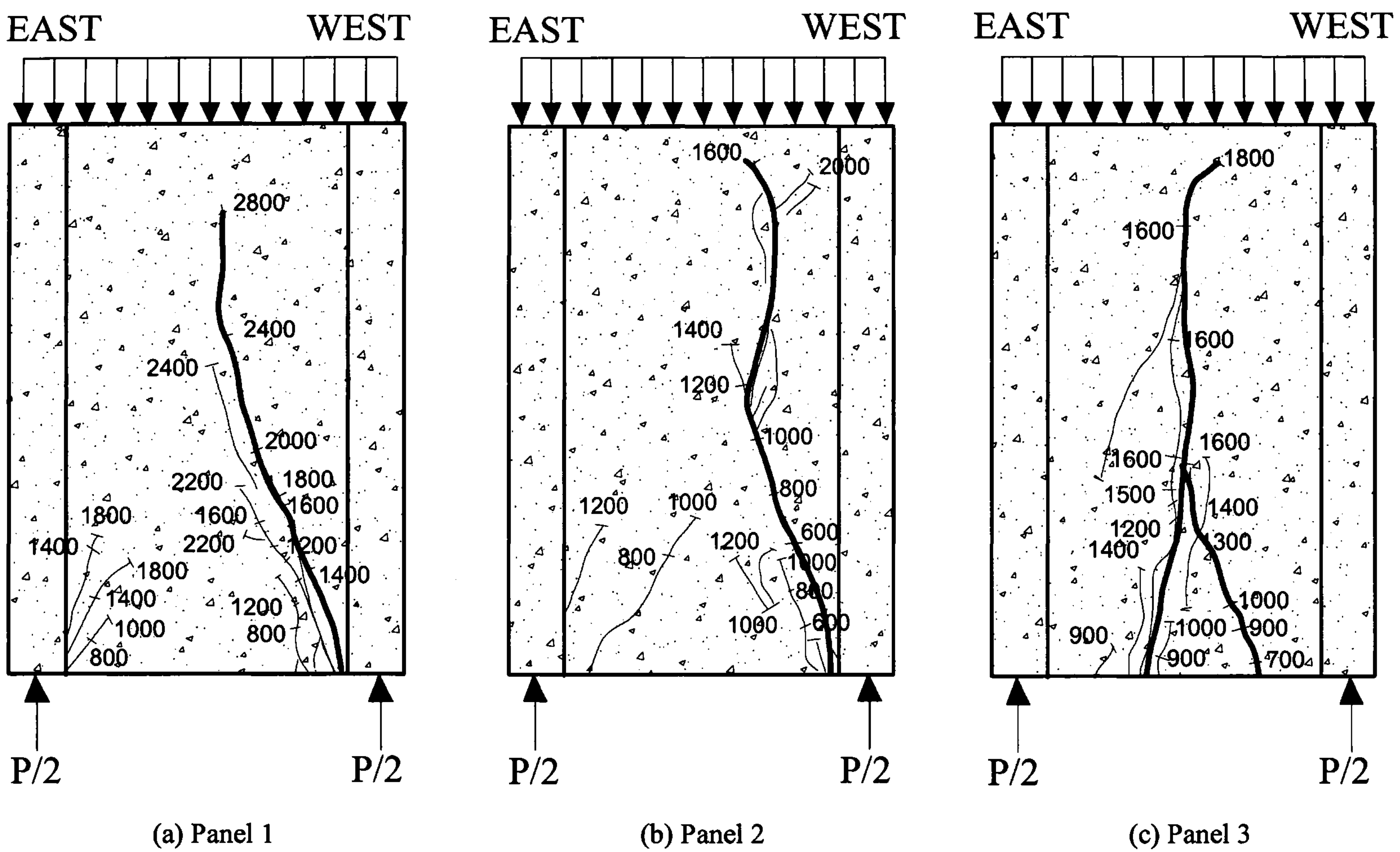

Figure 4.5 – Crack pattern for panels (a) 1, (b) 2 and (c) 3 (load in kN).

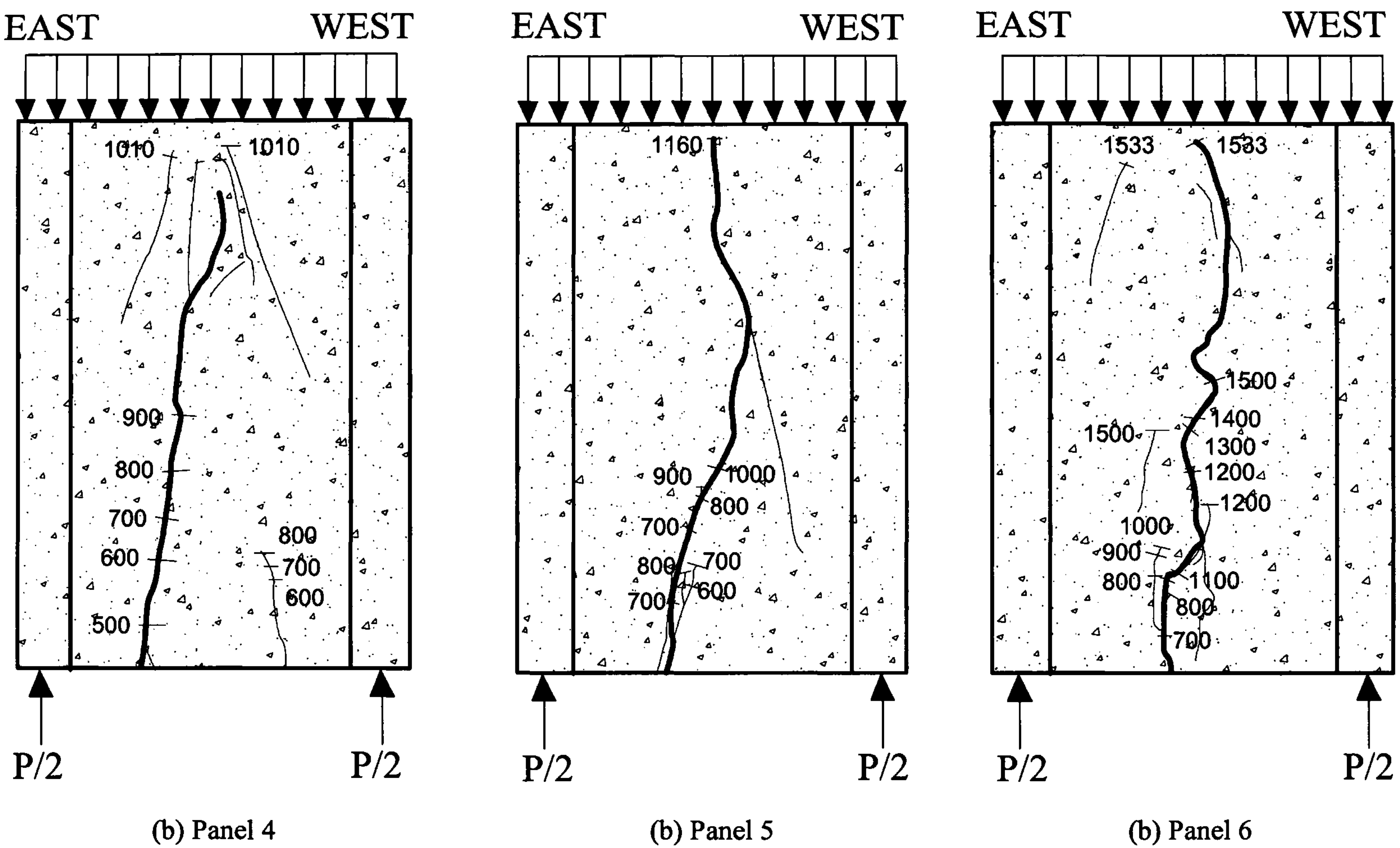

Figure 4.6 – Crack pattern for panels (a) 4, (b) 5 and (c) 6 (loads in kN).

4.7 Individual Panel Test Results

The raw data for the six panel tests is given in Appendix B and the plots of strains measured versus loads of each specimen are presented at the end of this chapter in Figures 4.7 to 4.37. Experimental observations of each specimen is reported below.

4.7.1 Panel 1

In panel 1 the first cracks were observed (by visual inspection) at a load of 800 kN. As the loading was increased the cracks grew gradually until the major inclined cracking initiated at the junction of the flange and web on the west side of the specimen (see Plate 4.1). The cracks then propagated longitudinally and transversely with increasing load. A major tearing crack occurred in the specimen at 2400 kN and testing was concluded at a load of 2800 kN. The strains measured from DM1 to DM5 in the mid-region of the specimens are shown in Figure 4.7. The figure shows that at the level of DM1 and DM2 the crack did not pass through the gauged zone and, hence, low strains were measured. Figure 4.7 shows that strains of approximately 4000 $\mu\varepsilon$ were recorded at DM 3 in the last step of the measurement before failure (i.e. at $P = 2400$ kN). This corresponds to a crack width of 1.0 mm. Strains measured from the electronic strain gauges (ESG1 and ESG2) at the same level as DM1 and DM2 in the mid-region of the specimens are shown in Figure 4.8. Similarly, at the level of ESG1 and ESG2 the crack did not pass through the gauged zone, thus, leading to low strains measured at these levels (see Plate 4.1).

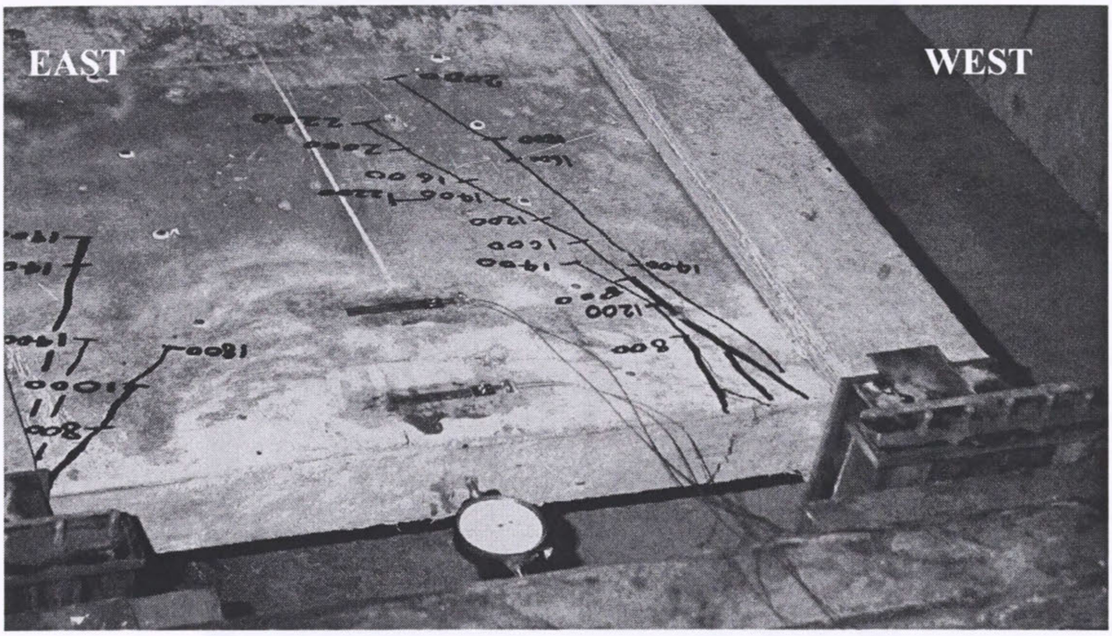

Plate 4.1 – Cracking of panel 1 at P = 2200 kN.

4.7.2 Panel 2

The general behaviour of panel 2 was similar to that of panel 1 with first cracking observed (visually and via strain readings) at a load of 600 kN. As the loading increased the cracks grew gradually until the major inclined cracking initiated on the west side of the specimen at the junction of the flange and the web. The cracks then propagated longitudinally and transversely in with increasing load. A major tearing crack occurred in the specimen at 1400 kN with a crack width of 0.6 mm. At 2000 kN the crack width was 1.0 mm and the test was concluded at this point.

Plate 4.2 shows that the tearing crack did not pass through the gauged region measured by DMs 1 to 5. The strains measured from the electronic strain gauges of the specimens are shown in Figure 4.10. From the electronic strain gauge measurement of ESG4, cracking of the specimen occurred at a load between 400 kN and 600 kN.

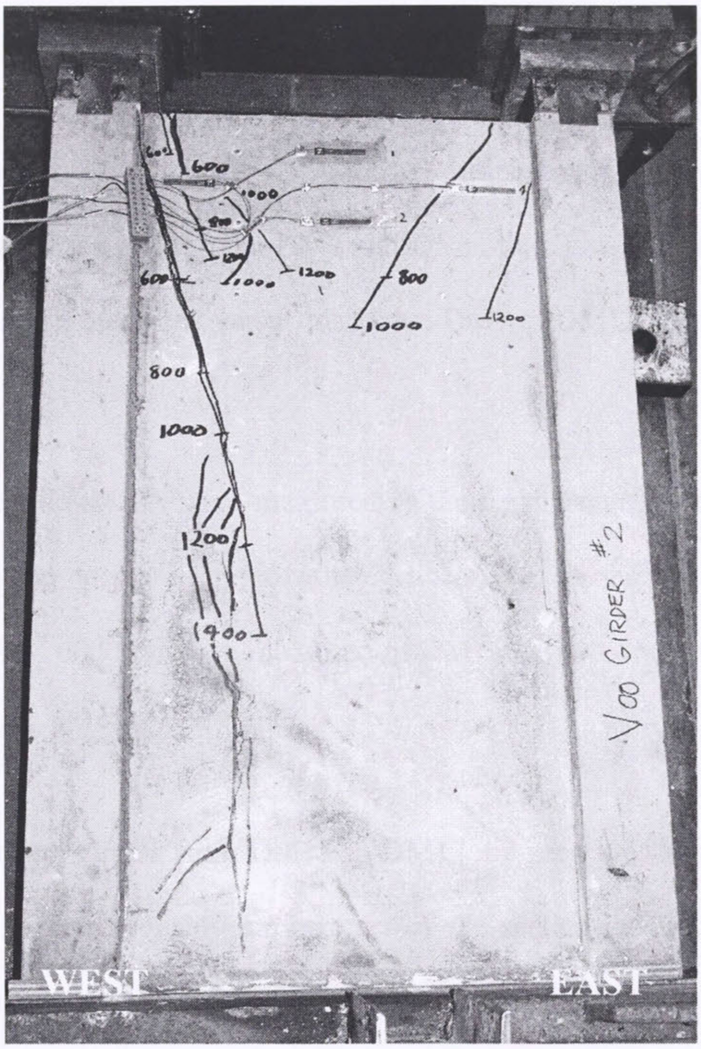

Plate 4.2 – Cracking of panel 2.

4.7.3 Panel 3

The experimental setup for panel 3 is shown in Plate 4.3. In specimen 3 the first crack was observed visually in the mid-region of the web at a load of 700 kN and the bursting cracks grew gradually until a load of 1600 kN (2.3 times the cracking load). As the loading was increased the cracks grew gradually until the major longitudinally crack opened in the mid-region of the specimen. At 1800 kN the crack width was greater than 2.0 mm and the test was stopped. Plate 4.4 shows fibre bridging across the major tearing crack at the completion of the test.

Strains measured versus the depth from the tensile surface of the specimen from DM1 to DM4 in the mid-region, from DM5 to DM8 in the west side and DM9 to DM12 in the east side are shown in Figures 4.11, 4.12 and 4.13, respectively. Figure 4.12 shows the major crack did not pass through the DM5 and DM6, thus low strains were measured. The plots on the strain measured versus load from DM1 to DM12 are shown in Figures 4.14 to 4.16.

The maximum tensile strains were measured at the tensile face of the specimen (i.e. DM1 and DM9) and decreased approximately linearly as the height from the surface increased. Strains of 6000 $\mu\varepsilon$ were measured in DM1 and DM9 at P = 1600 kN which corresponds to a crack width of 1.5 mm.

The far end boundary strains from DM13 to DM17 are presented in Figure 4.17. The measured strains were reasonably uniform across the section indicating uniformity of stress at the boundary.

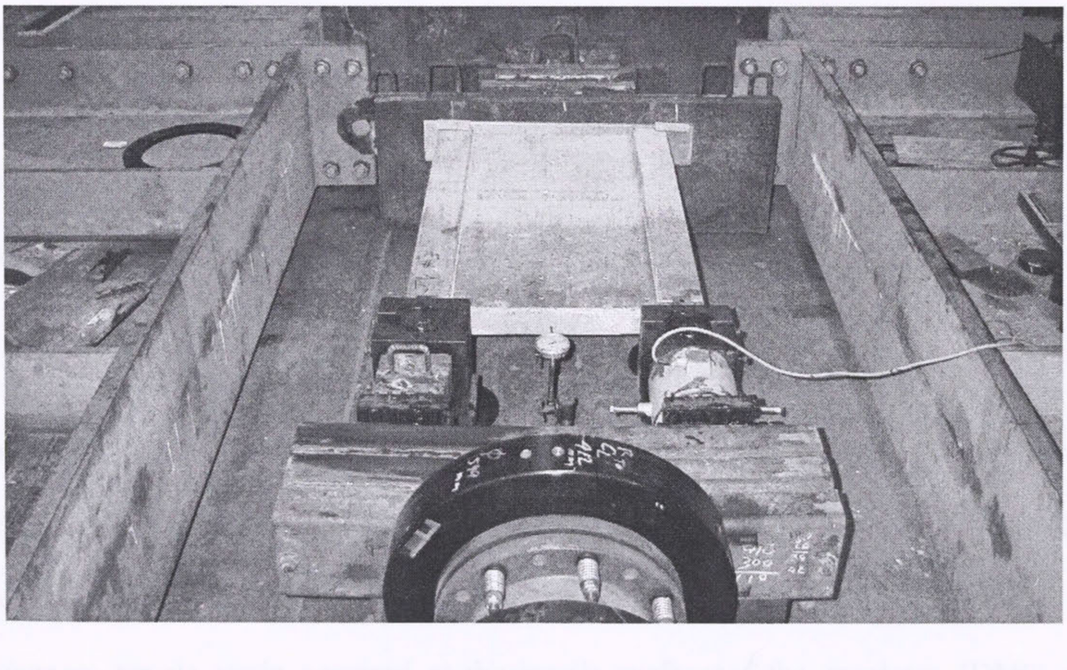

Plate 4.3 – Test set-up for Panel 3.

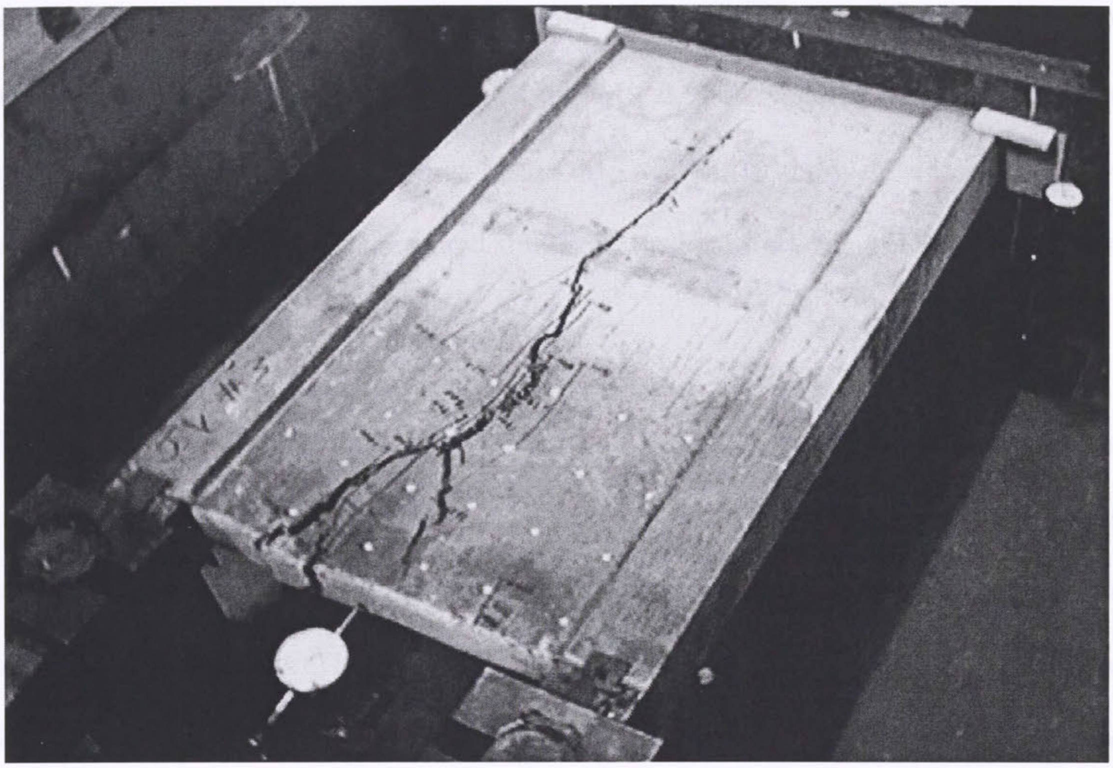

Plate 4.4 – Tearing of panel 3, P = 1600 kN.

4.7.4 Panel 4

The experimental set up of panel 4 is shown in Plate 4.5. The general behaviour of panel 4 was similar to that of panel 3 with the first crack observed at 500 kN in the mid-span of the web. As the loading was increased the cracks grew gradually and consistently until a major tearing crack formed in the mid-region of the specimen. Tearing of the specimen occurred at 1000 kN (twice the cracking load).

With the exception of gauge DM1, the major tearing crack, shown in Plate 4.6, ran through the central and east gauges zones of the panel. The measured strains versus depth from the tensile surface for DM1 to DM4 in the mid-region and DM9 to DM12 in the east side are shown in Figures 4.18 and 4.19, respectively. Figure 4.19 shows the maximum tensile strain occurred at the tensile surface of the specimen (DM9) and decreased approximate linearly as the depth from the tensile surface increased. A maximum strain of 2000 $\mu\varepsilon$ was recorded in DM9 at 900 kN, corresponding to a crack width of 0.5 mm. The strain readings from DM5 to DM8 at the west side are given in Figure 4.20. The plots on the measured strains versus load for DM1 to DM12 are shown in Figures 4.21 to 4.23.

The far end boundary strains from DM13 to DM17 for panel 4 are presented in Figure 4.24. The strain measured at the far end boundary show some variation across the section. In panels 4 the strains in the web are reasonably uniform with lower strains in the flanges observed. This indicates that for these specimens the webs were more highly stressed at the boundary than the flanges. This was most likely due to some unevenness in the finished surface of the far end boundary.

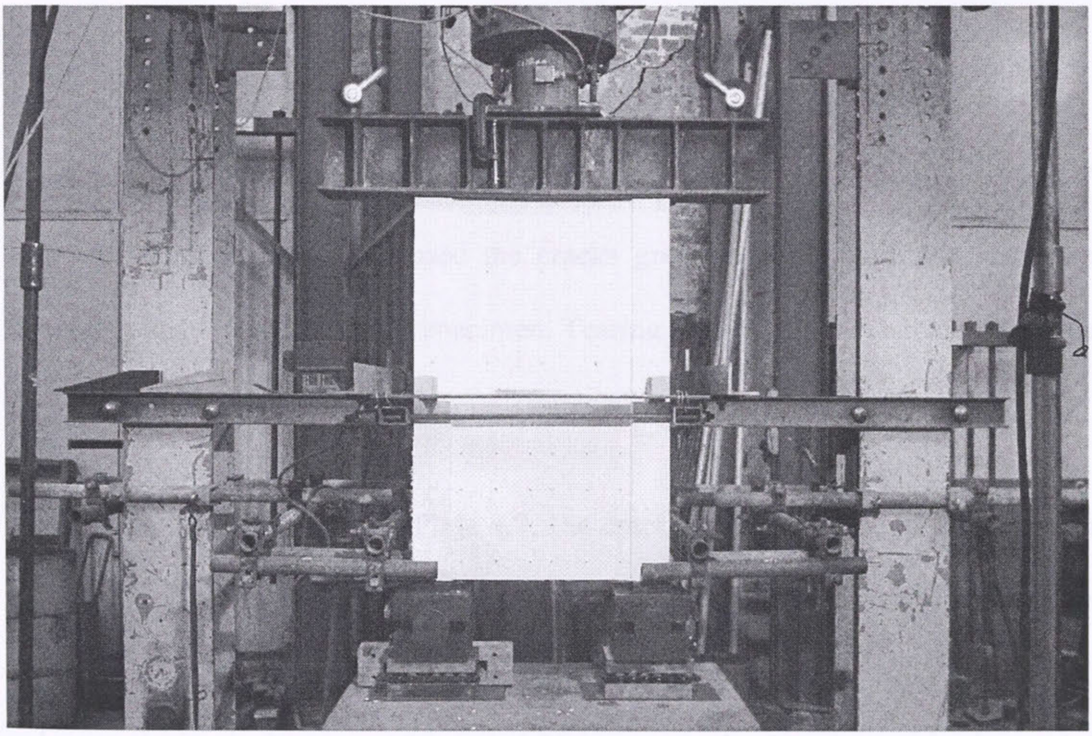

Plate 4.5 – Set-up for panels 4 to 6.

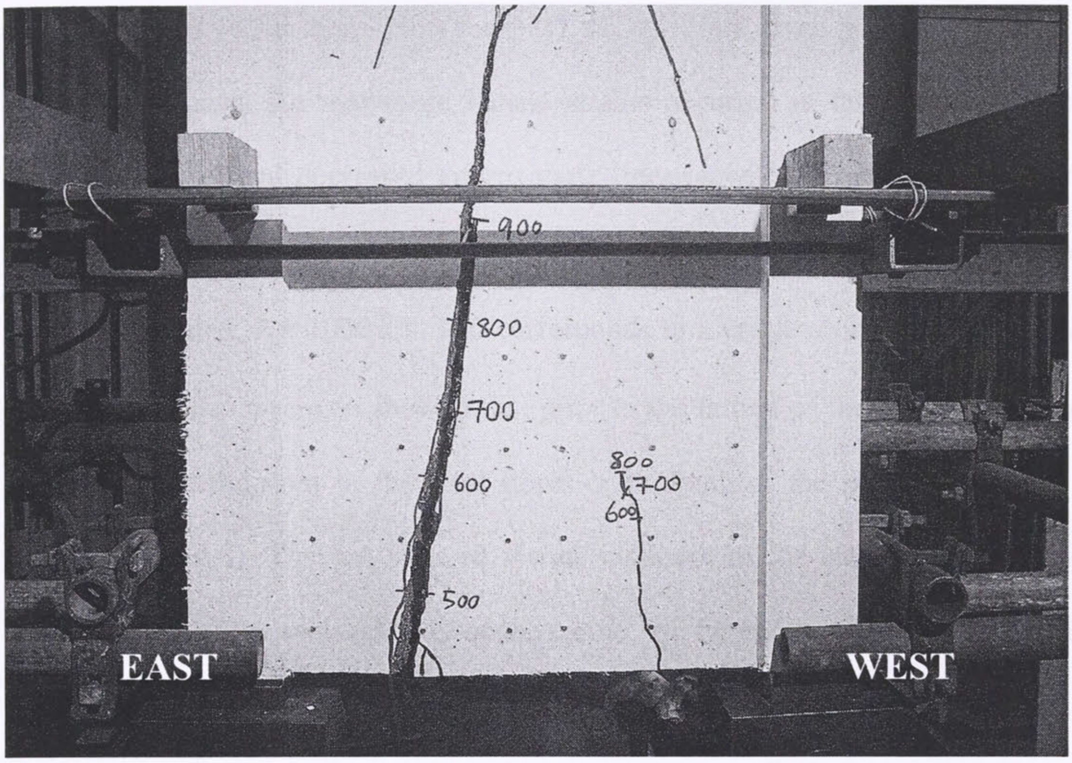

Plate 4.6 – Tearing of panel 4 - the end of the test.

4.7.5 Panel 5

The general behaviour of panel 5 was similar to that of panels 3 and 4 with the first crack observed in the mid-span of the web. The first crack was observed at a load of 600 kN. As the loading was increased the cracks grew gradually until the tearing crack opened in the mid-region of the specimen. Tearing of the specimen occurred at a load of 1100 kN (approximately twice the cracking load).

The tearing crack is shown in Plate 4.7; the crack ran through the gauged zone in the mid-section (DM1 to DM4) and the east side (DM9 to DM12) of the specimen. Average strains measured from DM1 to DM4 in the mid-region and DM9 to DM12 on the east side are shown in Figures 4.25 and 4.26, respectively. No data was obtained from gauges DM6, DM8 or DM9 as the targets were inadvertently located out of gauge range. The load versus strain plots for DM1 to DM12 are given in Figures 4.27 to 4.29. Figure 4.25 shows the maximum tensile strains occurred at the bottom face of the specimen (DM1) and decreased approximate linearly with increasing depth from the tensile surface. A maximum strain of 3000 με was recorded in DM1 for the last measurement step, P = 1000 kN, and corresponds to a crack width of 0.75 mm. Visual assessment of the specimen showed that prior to the failure of the specimen, there was considerable pulling out of the steel fibres or bridging of the fibres across the crack surface (Plate 4.8). The test showed visible evidence of the steel fibres bridging the cracks enhancing the serviceability of the panel. The far end boundary strains measured from DM13 to DM17 are presented in Figure 4.30. Similarly to panel 4, the strain measured at the far end boundary show some variation across the section.

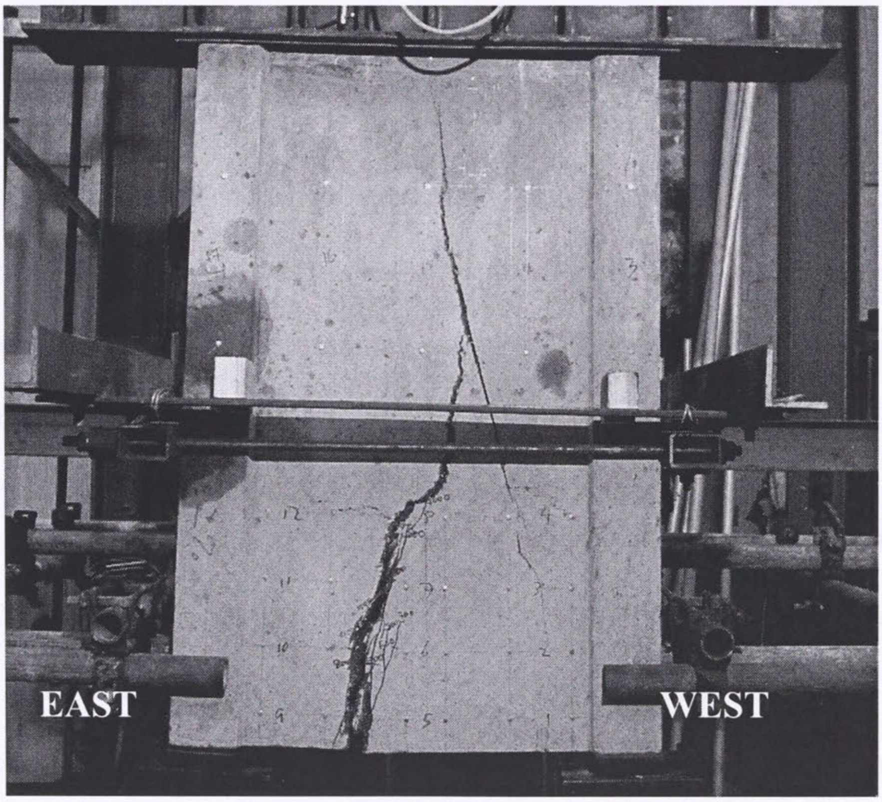

Plate 4.7 – Tearing of panel 5 - the end of the test.

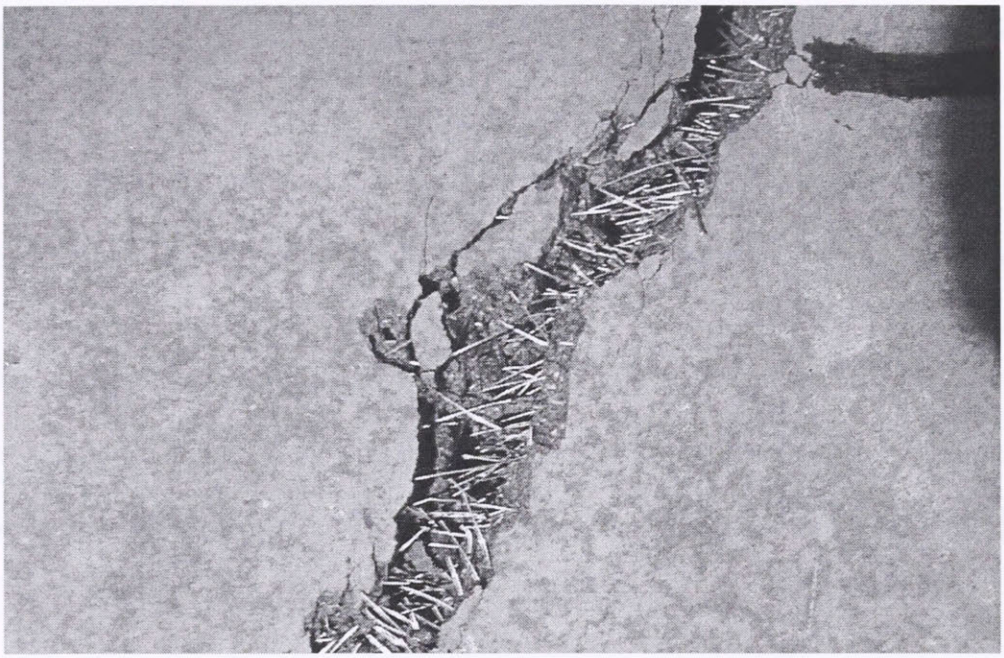

Plate 4.8 – Panel 5: Steel fibres bridging a tearing crack and pulling out of the fibres across the crack surface.

4.7.6 Panel 6

The general behaviour of panel 6 is similar to that of panels 3, 4 and 5 with the first crack observed at 700 kN in the mid-span of the web. As the loading was increased the cracks grew gradually until development of the tearing crack initiated in the mid-region of the specimen. Tearing of the specimen occurred at a load at 1500 kN (approximately twice the cracking load).

Plate 4.9 shows the major tearing crack ran through all the gauge zones of the mid-section (DM1 to DM4) and the east side (DM9 to DM12) of the specimen. Strains measured from DM1 to DM4 and DM9 to DM12 are shown in Figures 4.31 and 4.32, respectively. The strain readings from DM5 to DM8 at the west side are given in Figure 4.33. The load versus strain plots for DM1 to DM12 are given in Figures 4.34 to 4.36.

Figure 4.31 shows the maximum tensile strains were measured at the bottom face of the specimen (DM1) and, as for specimen 3 to 5, decreased approximate linearly with increasing distance from the tensile surface. A strain of 9000 με was recorded in DM1 in the last measurement step P = 1500 kN and corresponds to crack width of 2.25 mm.

The far end boundary strains given by DM13 to DM17 are presented in Figure 4.37. While the far end boundary strains show some variation across the section, it is reasoned that the far end strains were sufficiently uniform and are sufficiently distant from the tension face as not to have affected the bursting forces.

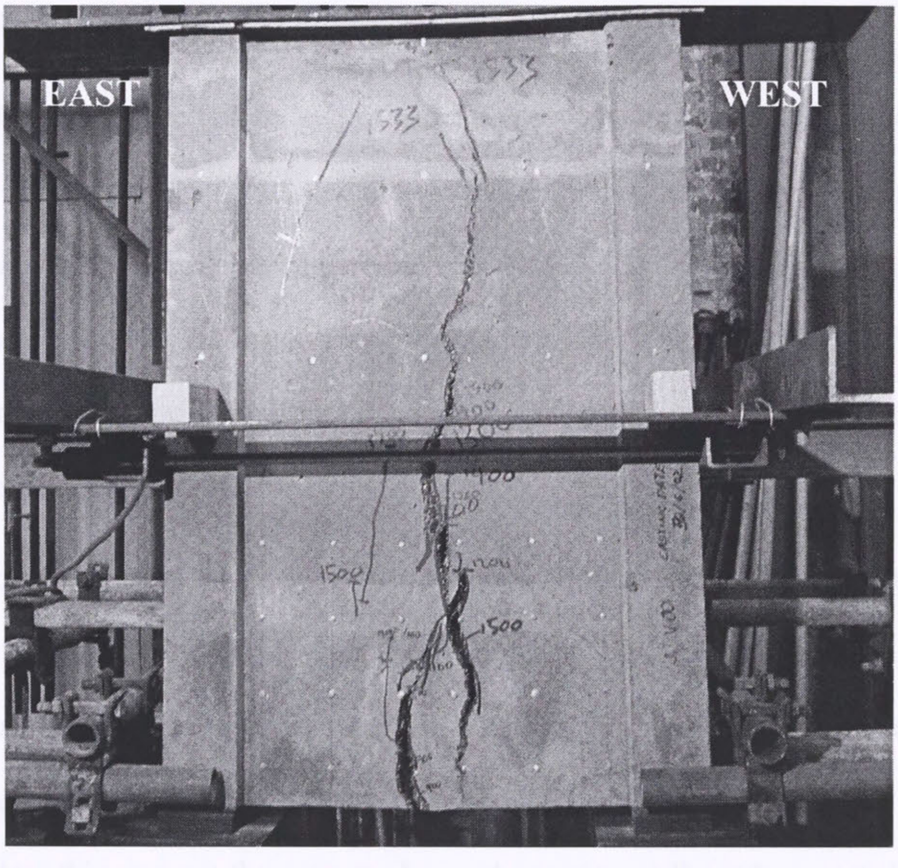

Plate 4.9 – Tearing of panel 6 – P = 1500 kN

4.8 Behaviour under Load and Discussion

Cracking and crack propagation for the panels was monitored throughout each test. Comparison of the crack patterns in the deep panels showed that the quantity of fibres in the concrete mix did not significantly affect the initial cracking load (P_{cr}) but did have an influence on the rate of crack growth and on crack widths. After the initial cracking of the specimens, the cracks propagated at a faster rate in the panel with the lowest quantity of steel fibres. The experimental results indicate that the panels with free translation and free rotational setup fail at approximately twice the cracking load. Panels with free translation and constrained rotations failed at approximately three times the cracking load.

Table 4.4 compares the failure load of panel 3 (i.e. containing only end-hooked fibres) to those of panels 4 to 6 (i.e. containing various quantities of straight fibres). The experimental failure load are compared to that for panel 3 corrected for the variation in compressive strength. Table 4.4 shows the failure load is generally lower for panels reinforced with straight steel fibre. For example, the normalised failure load for panel 5 is 82 percent of the failure load of panel 3.

Comparing the fracture energies given in Table 4.2, for specimens 4 to 6 with 13 mm long straight steel fibres, it is seen that the fracture energies are significantly higher than the fracture energy measured for specimen 3. It would therefore be expected that the normalised failure load of panels 4 to 6 should be higher than that for panel 3. Nevertheless this was not the case as observed experimentally and presented in Table 4.4. One of the possible explanations for this outcome is panel 3 which had the longer fibres (that is 35 mm fibres) had a better control over the stability of the tearing crack than was provided by the short fibres.

Table 4.4 - Normalised failure loads.

Panel	f_{cm} (MPa)	Fibre		P_{tear} (kN)	$\frac{P_{tear}}{P_{tear,panel3}} \bullet \frac{f_{cm,panel3}}{f_{cm}}$
		Type	ρ_f (%)		
3	162	EH	2.0	1600	1
4	135	SS	1.25	1010	0.76
5	144	SS	2.5	1160	0.82
6	158	SS	3.7	1530	1.21

4.9 Conclusions

Six steel FR-RPC deep panels were tested to investigate crack growth and stability in RPC panels for increasing load. The specimens were dimensioned to simulate bursting forces in non-flexural regions of prestressed concrete girders. The test variables were the quantity and type of fibres and the boundary support conditions. The steel fibres used consisted of either 35 mm end hooked fibres or 13 mm straight fibres and the fibre content was varied from 1.0 to 3.7 percent, by volume. The support boundaries investigated were free translation with fixed rotation and free translation with free rotation.

From the experimental study the following observations are drawn:

I. The location of the bursting crack is significantly influenced by the boundary conditions. For the specimens with free translation and fixed rotation supports, the tearing crack formed at the junction of the flange and the web. For the free translation with free rotation boundaries the tearing crack formed in the web generally towards the centre of the specimen.

II. The quantity of fibres and type of fibres used in the concrete mix does not significantly affect the initial cracking load but has a significant influence on the failure load. The support boundary restraints also have a significant effect on the failure load in that the failure load is higher for panels with free translation and fixed rotation boundary conditions than for panels with both free translation and free rotation supports.

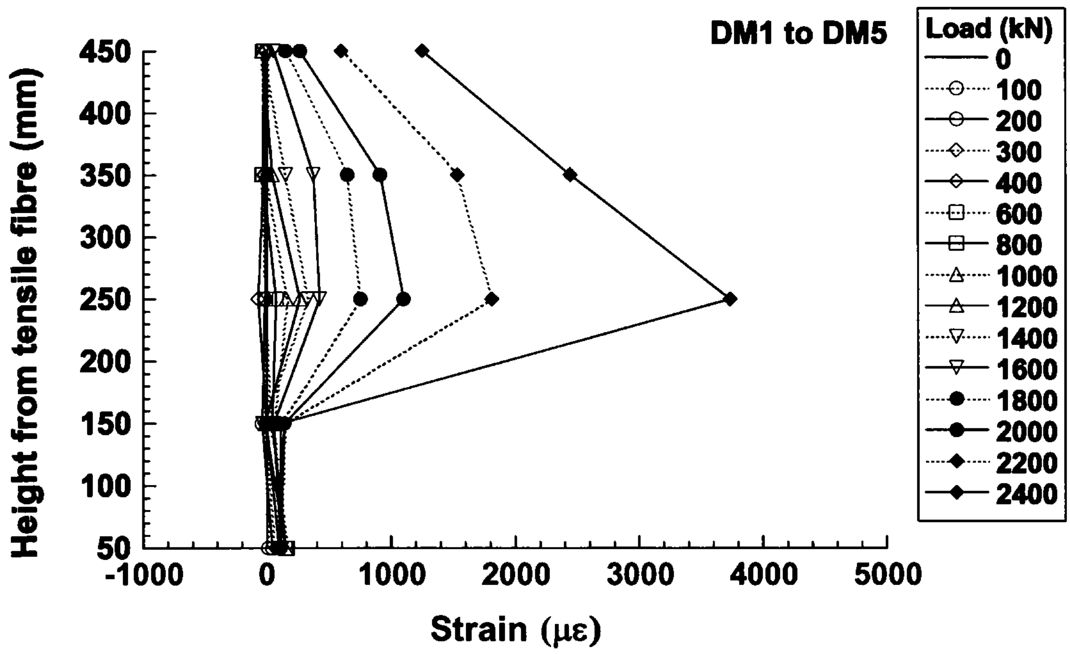

Figure 4.7 – Panel 1: Strain measured in the mid-regions versus height from extreme tensile (DM1 to DM5).

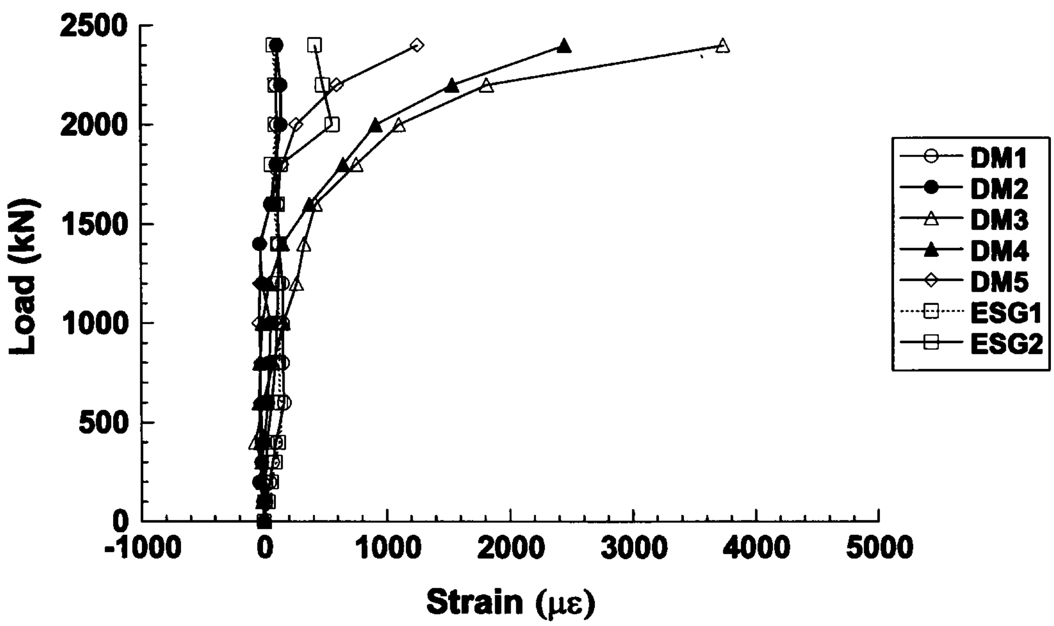

Figure 4.8 – Panel 1: Load versus strain measured.

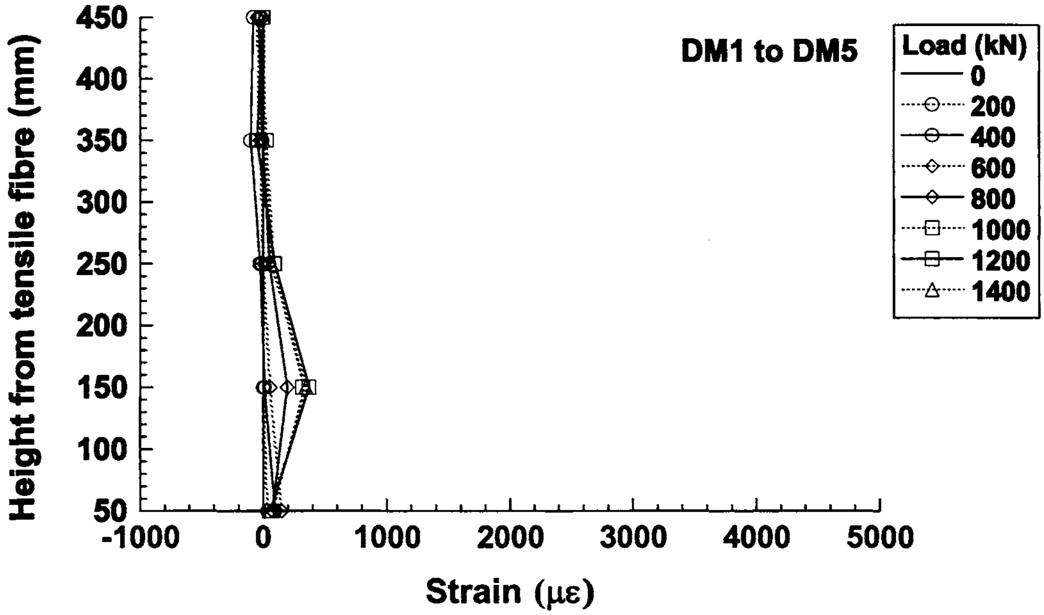

Figure 4.9 – Panel 2: Strain measured in the mid-regions versus height from extreme tensile (DM1 to DM5).

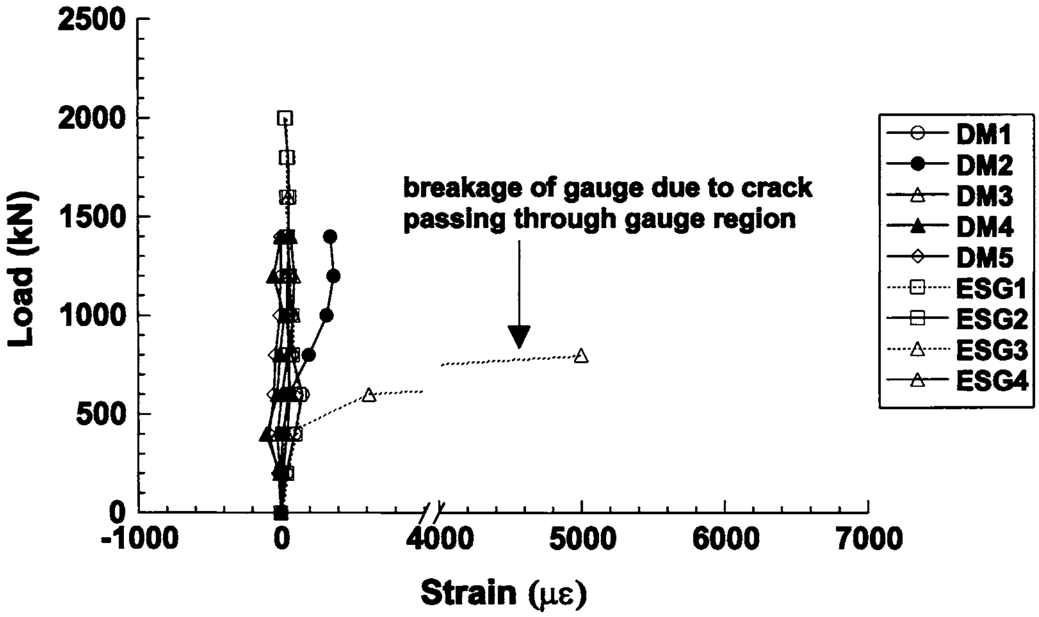

Figure 4.10 – Panel 2: Load versus strain measured.

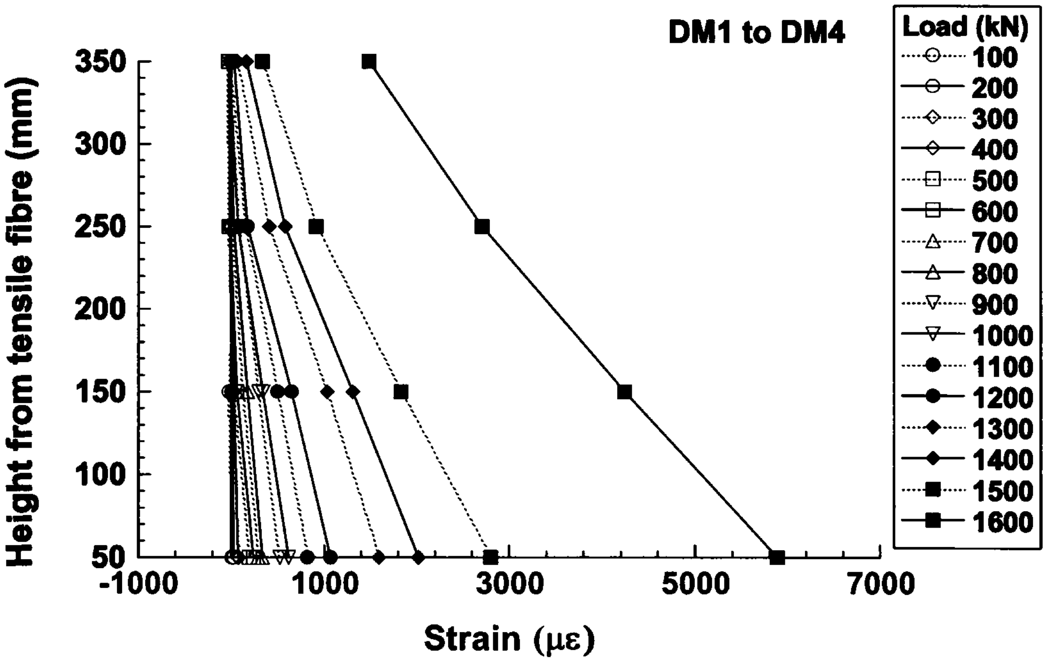

Figure 4.11 – Panel 3: Strain measured in the mid-regions versus height from extreme tensile (DM1 to DM4).

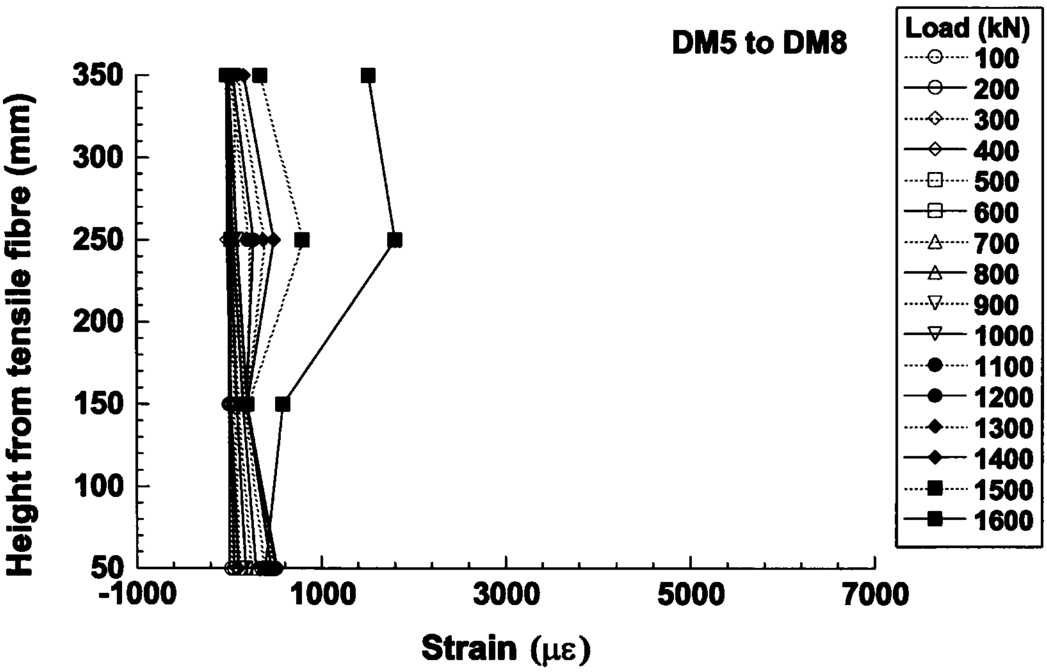

Figure 4.12 – Panel 3: Strain measured in the west side versus height from extreme tensile (DM5 to DM8).

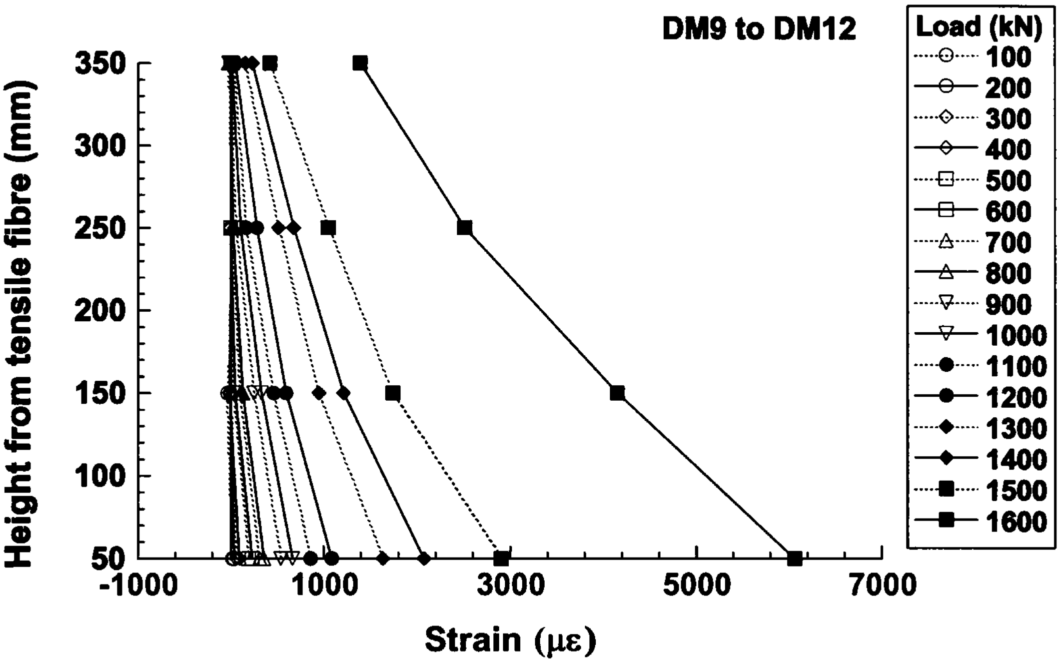

Figure 4.13 – Panel 3: Strain measured in the east side versus height from extreme tensile (DM9 to DM12).

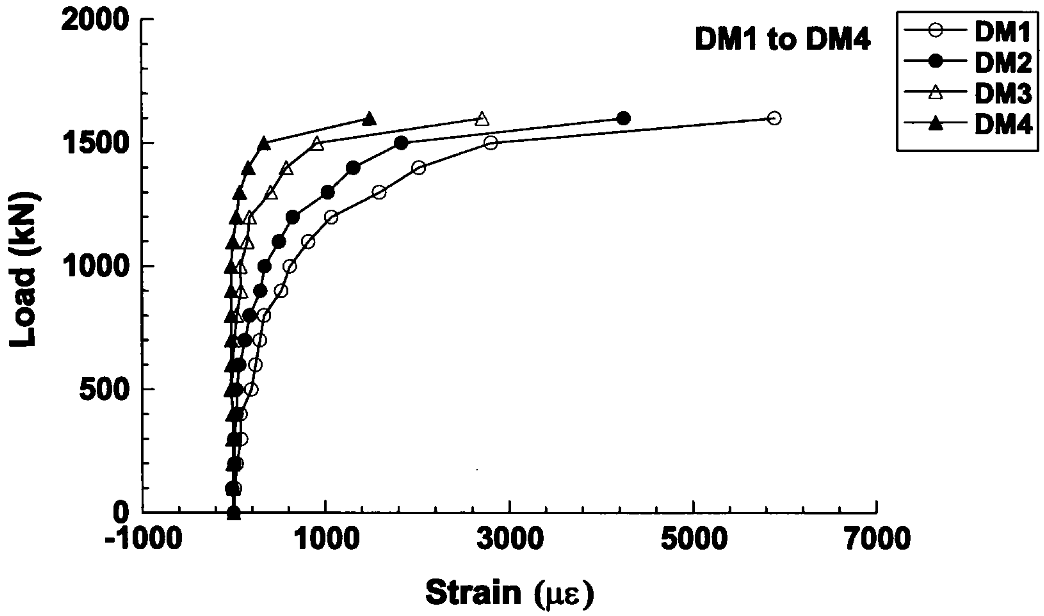

Figure 4.14 – Panel 3: Load versus strain measured (DM1 to DM4).

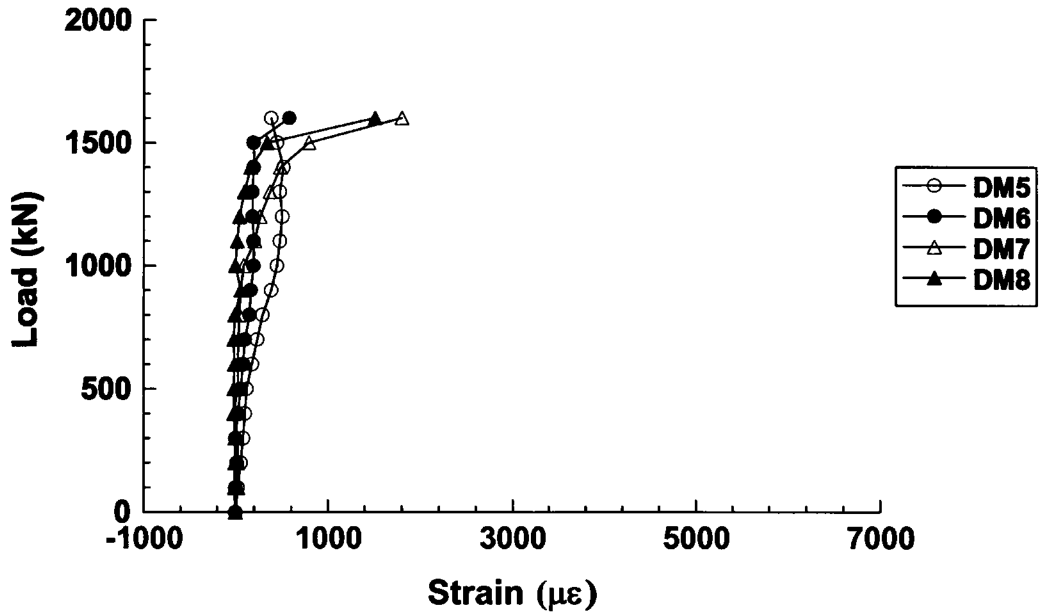

Figure 4.15 – Panel 3: Load versus strain measured (DM5 to DM8).

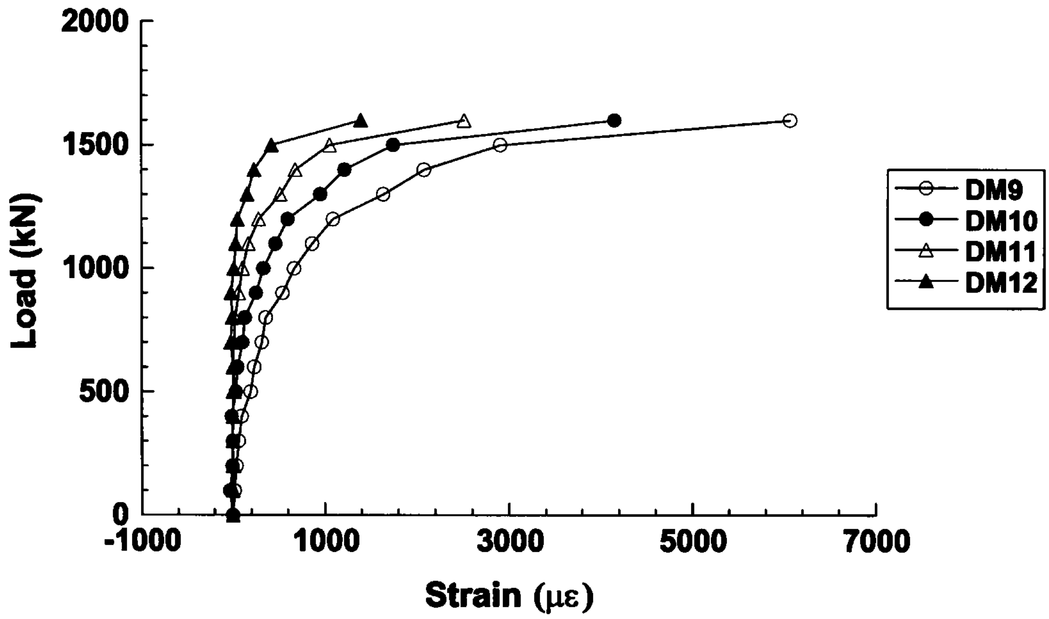

Figure 4.16 – Panel 3: Load versus strain measured (DM9 to DM12).

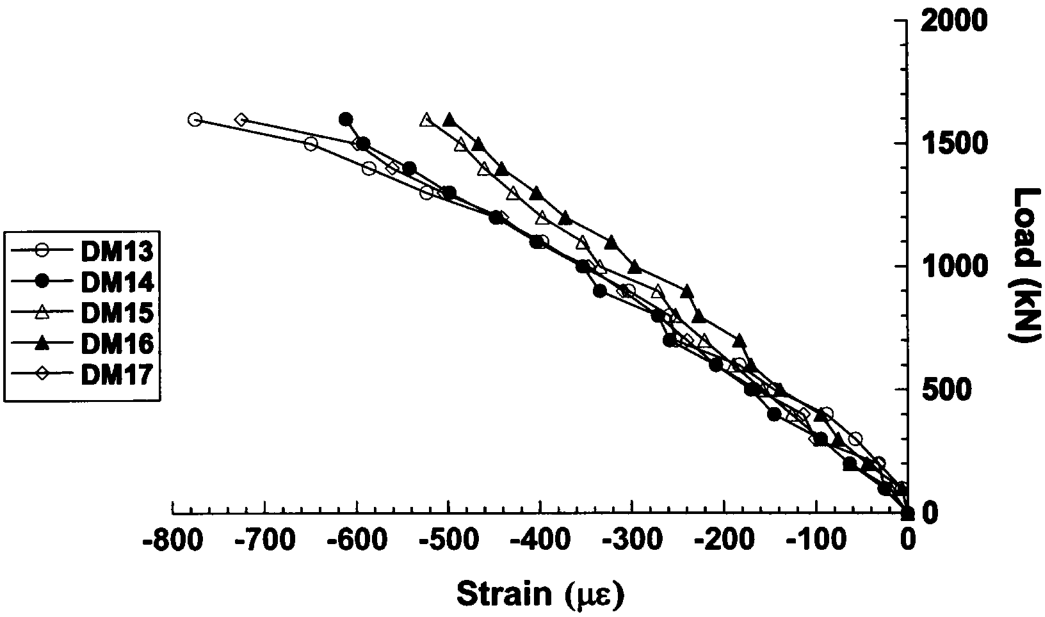

Figure 4.17 – Panel 3: Load versus strain measured (DM13 to DM17).

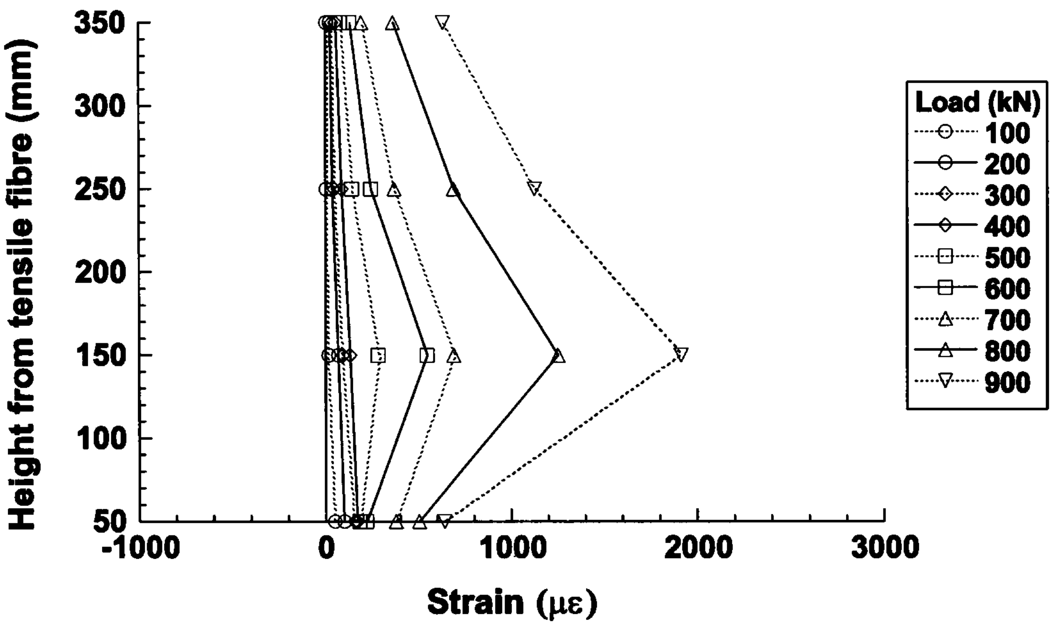

Figure 4.18 – Panel 4: Strain measured in the mid-regions versus height from extreme tensile (DM1 to DM4).

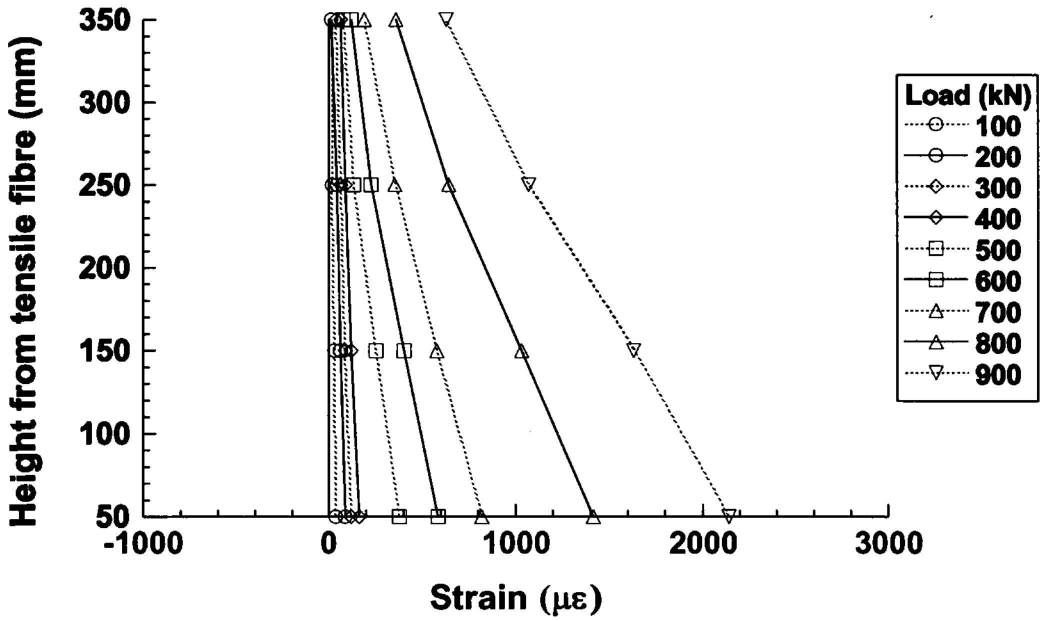

Figure 4.19 – Panel 4: Strain measured in the east side versus depth from the tension surface (DM9 to DM12).

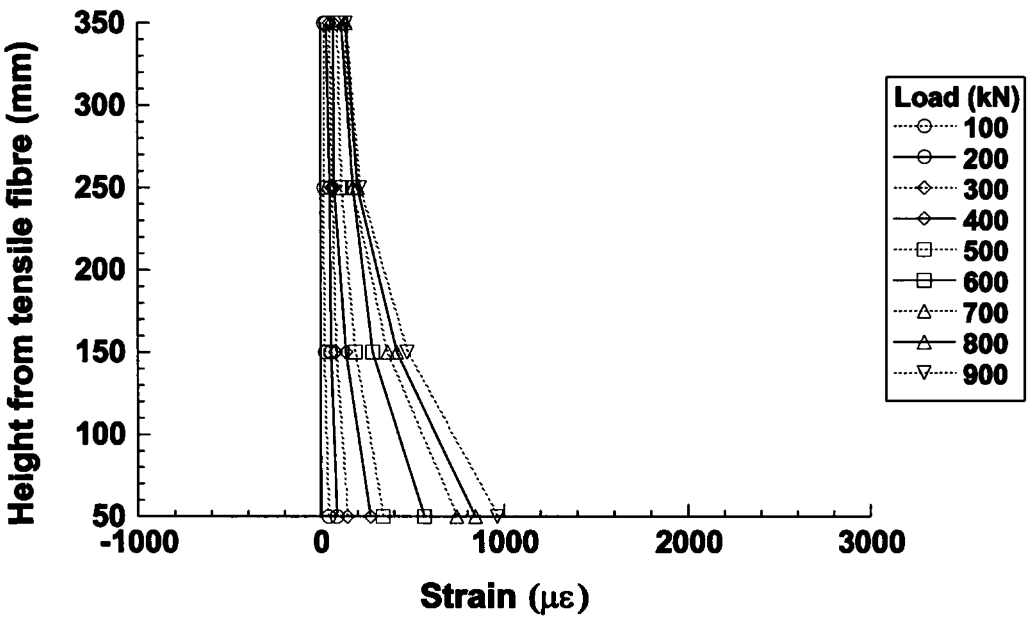

Figure 4.20 – Panel 4: Strain measured in the west side versus depth from the tension surface (DM5 to DM8).

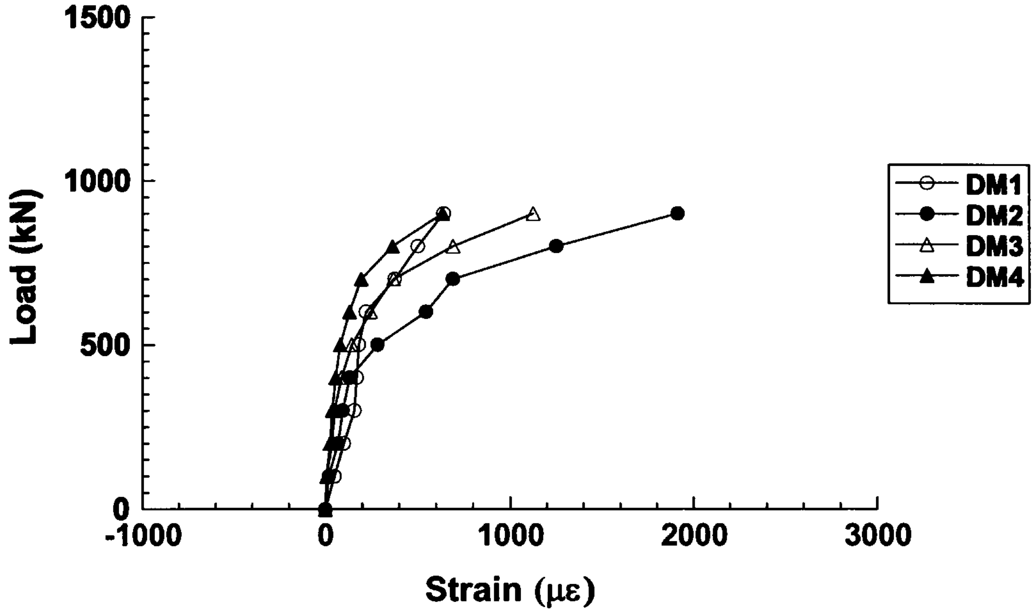

Figure 4.21 – Panel 4: Load versus strain measured (DM1 to DM4).

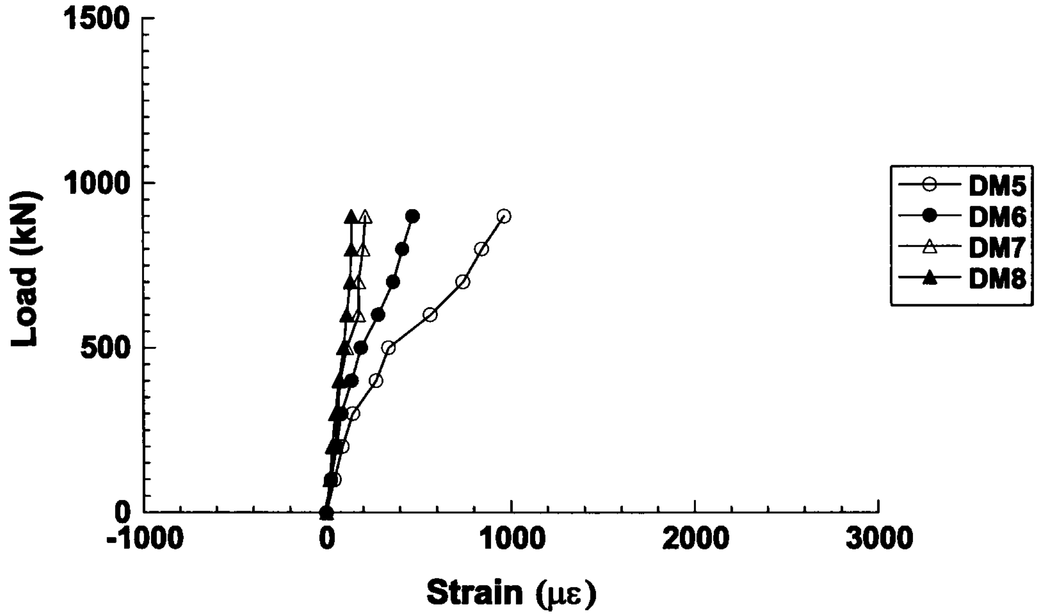

Figure 4.22 – Panel 4: Load versus strain measured (DM5 to DM8).

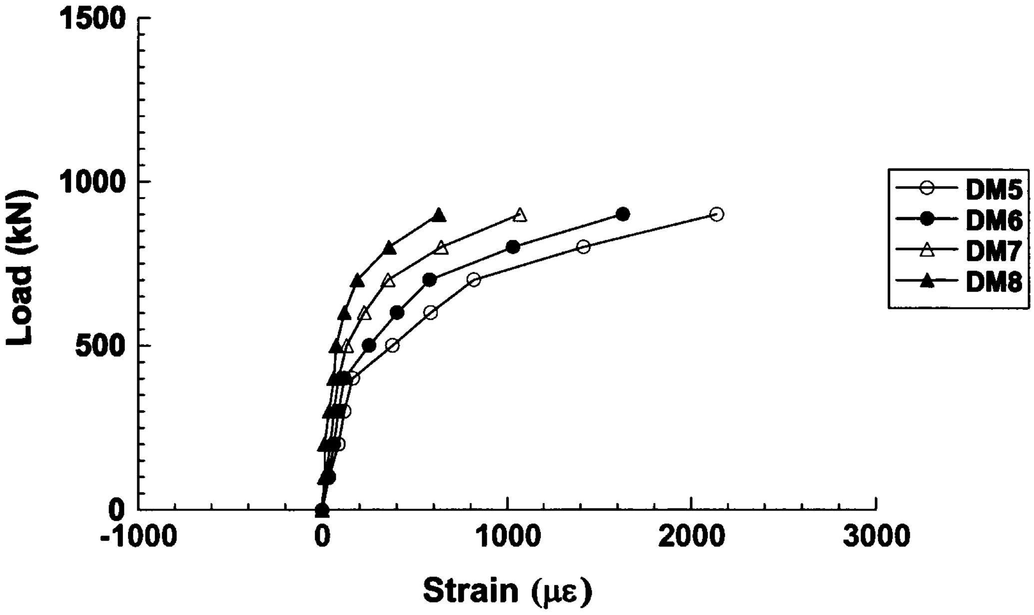

Figure 4.23 – Panel 4: Load versus strain measured (DM9 to DM12).

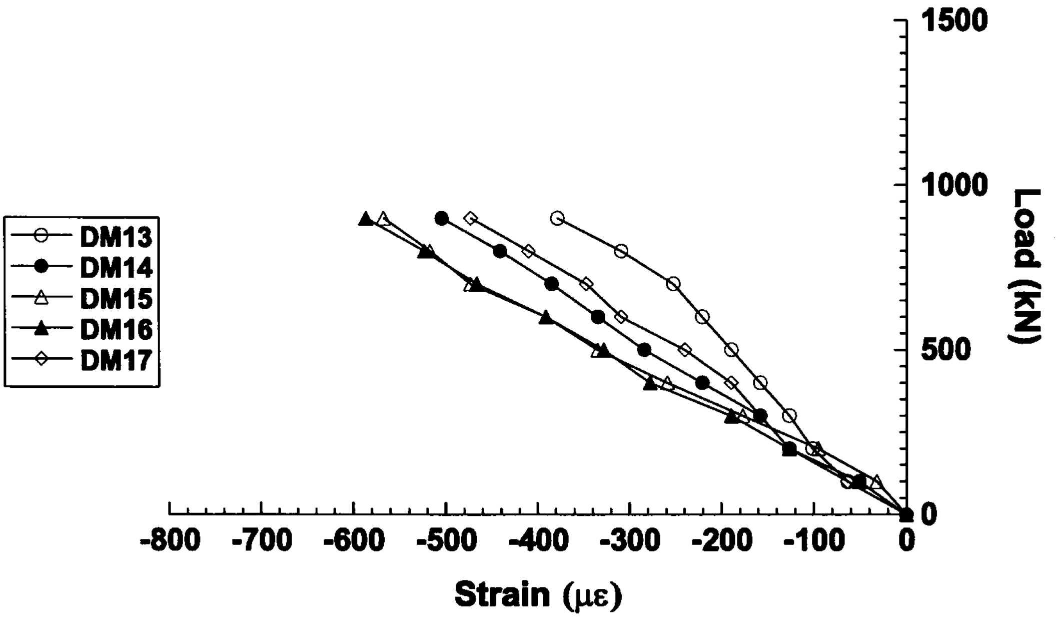

Figure 4.24 – Panel 4: Load versus strain measured (DM13 to DM17).

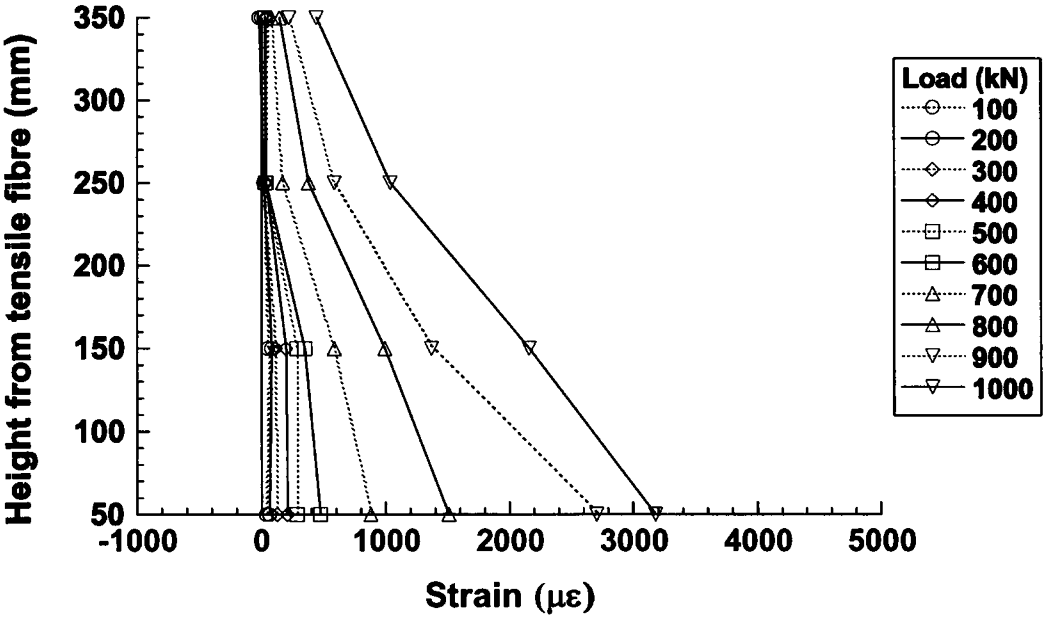

Figure 4.25 – Panel 5: Strain measured in the mid-regions versus depth from the tension surface (DM1 to DM4).

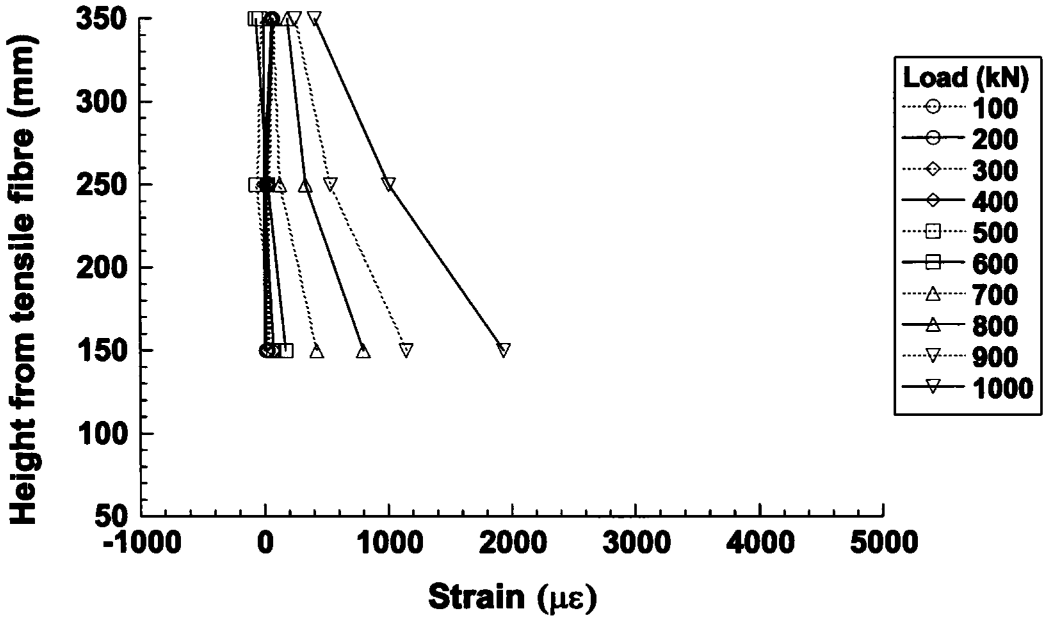

Figure 4.26 – Panel 5: Strain measured in the east side versus depth from the tension surface (DM9 to DM12).

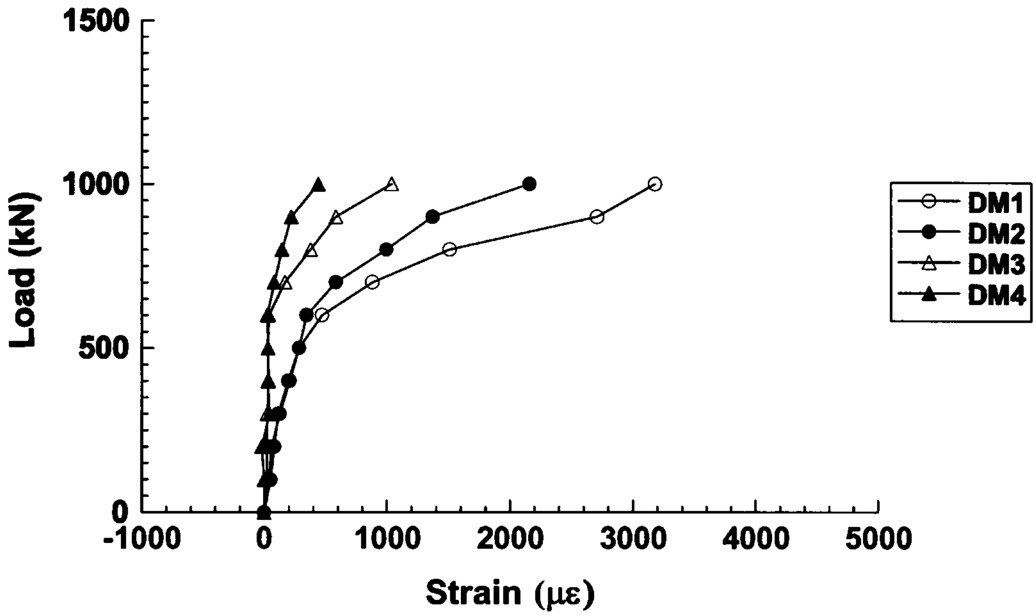

Figure 4.27 – Panel 5: Load versus strain measured (DM1 to DM4).

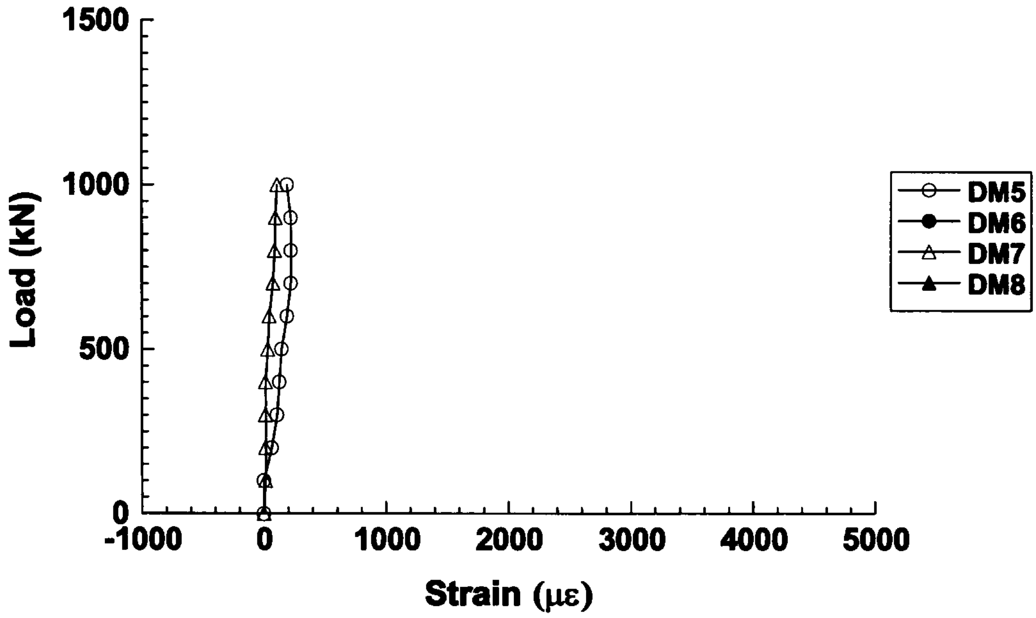

Figure 4.28 – Panel 5: Load versus strain measured (DM5 to DM8).

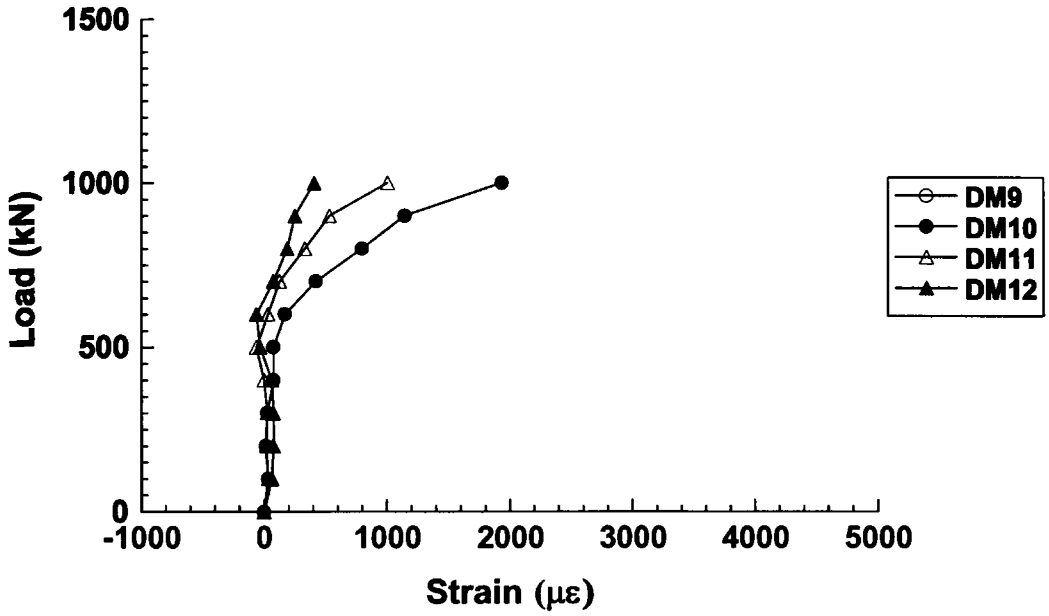

Figure 4.29 – Panel 5: Load versus strain measured (DM9 to DM12).

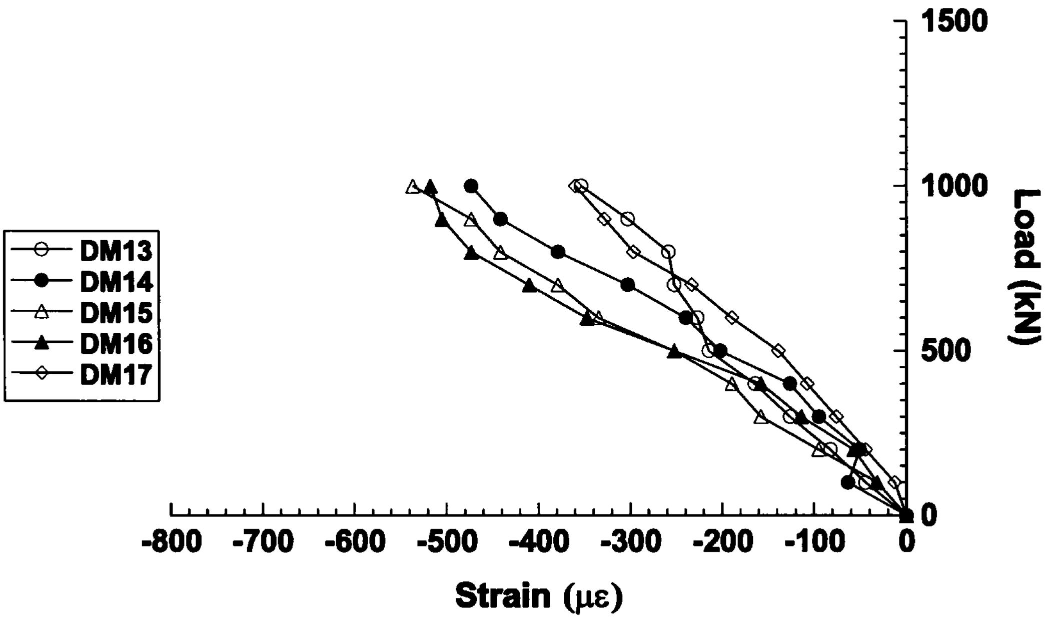

Figure 4.30 – Panel 5: Load versus strain measured (DM13 to DM17).

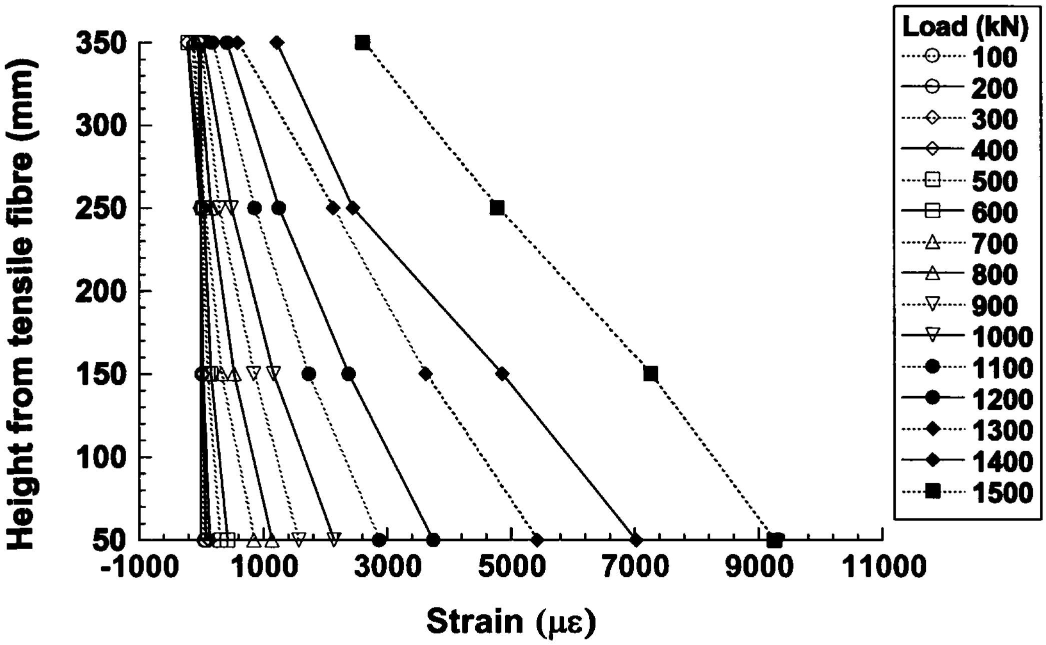

Figure 4.31 – Panel 6: Strain measured in the mid-regions versus depth from the tension surface (DM1 to DM4).

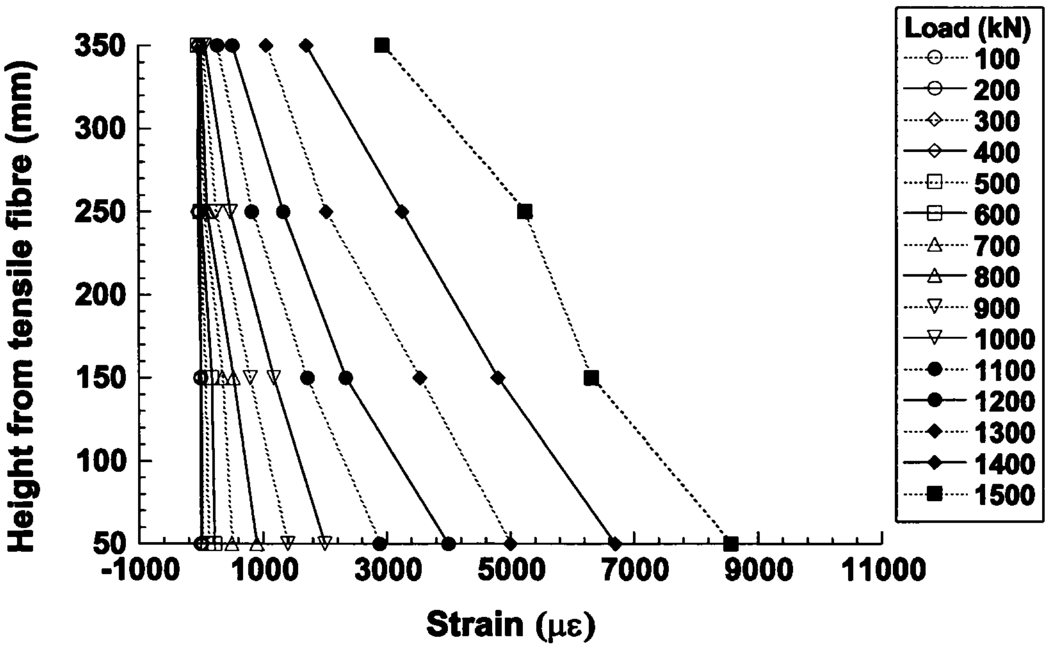

Figure 4.32 – Panel 6: Strain measured in the east side versus depth from the tension surface (DM9 to DM12).

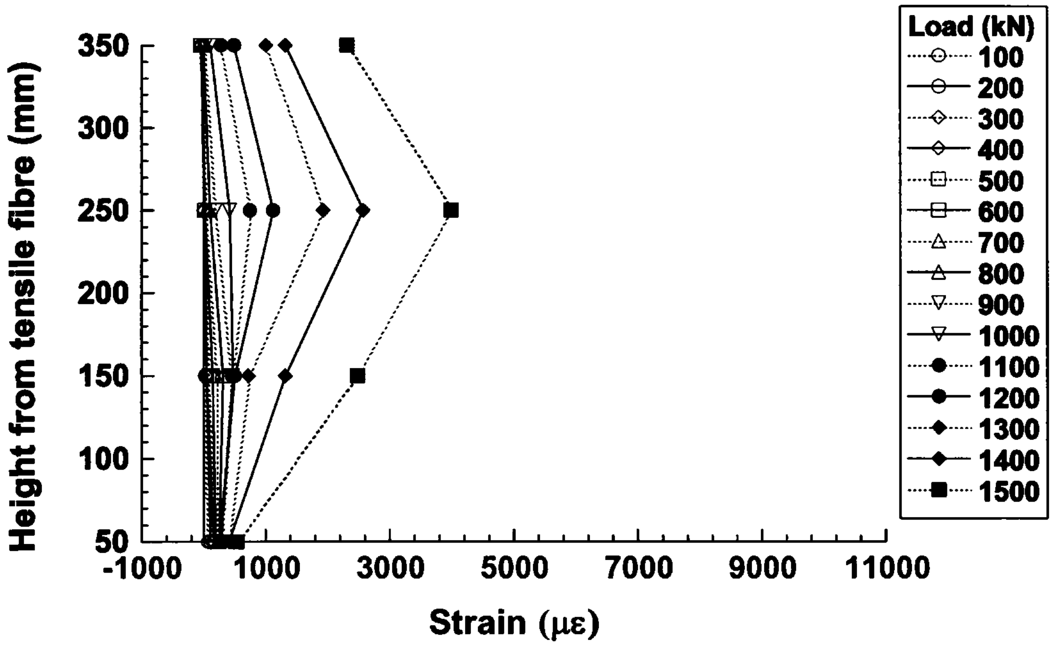

Figure 4.33 – Panel 6: Strain measured in the west side versus depth from the tension surface (DM5 to DM8).

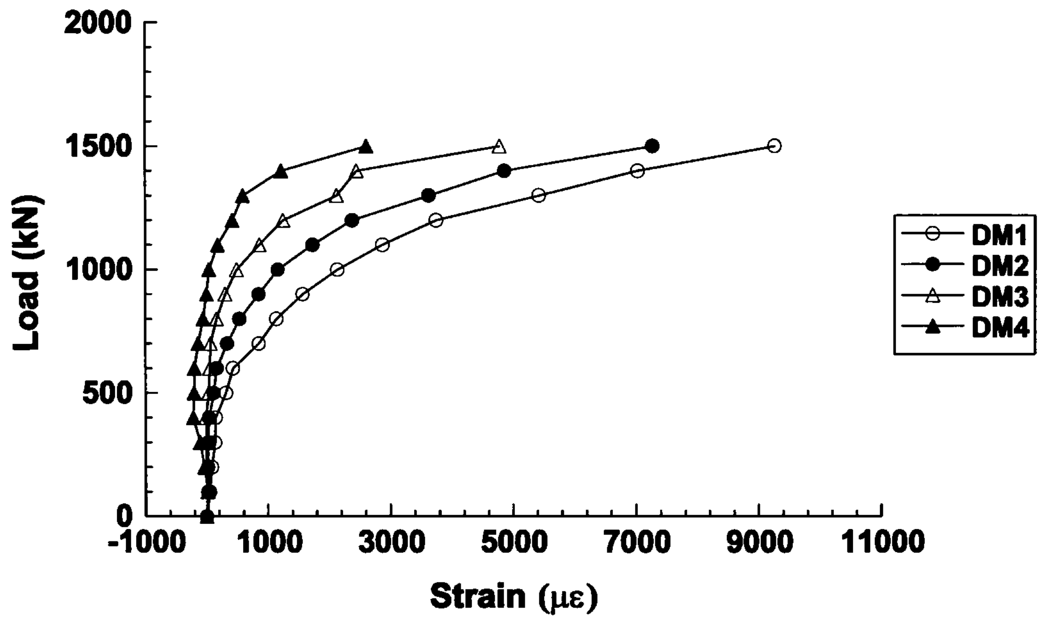

Figure 4.34 – Panel 6: Load versus strain measured (DM1 to DM4).

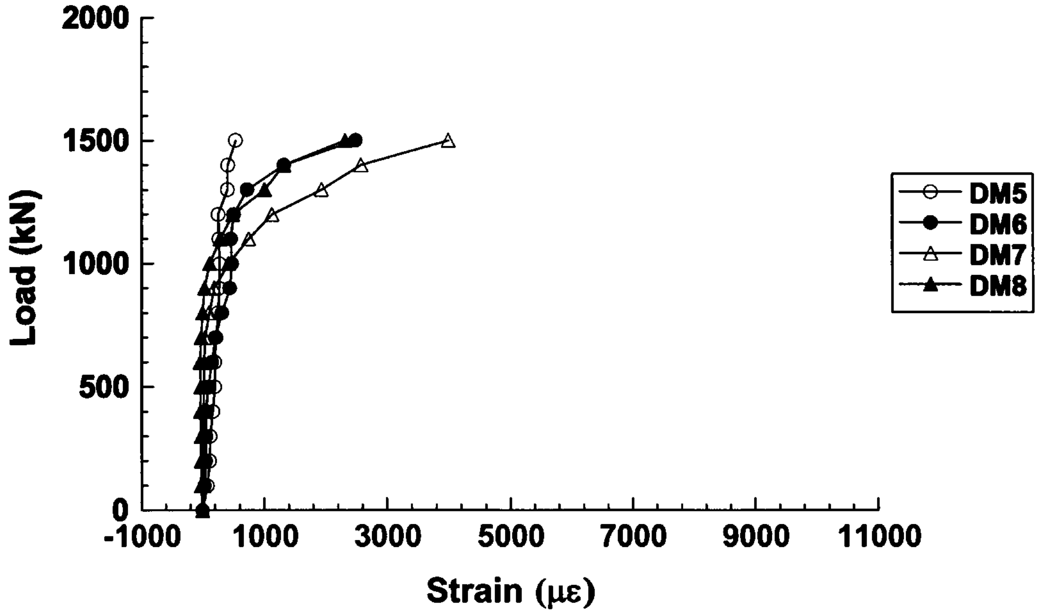

Figure 4.35 – Panel 6: Load versus strain measured (DM5 to DM8).

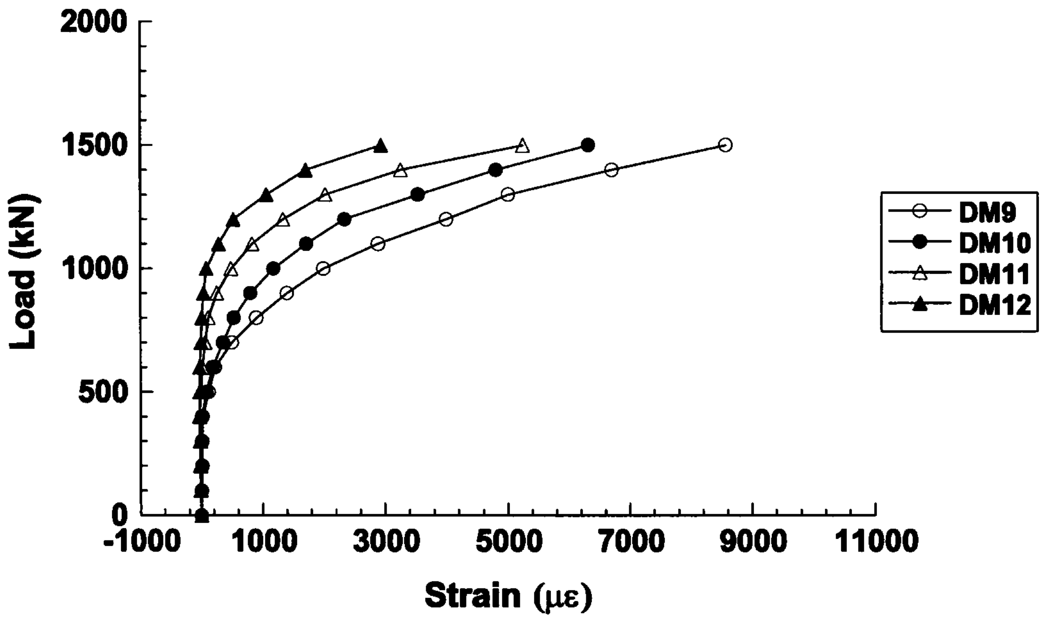

Figure 4.36 – Panel 6: Load versus strain measured (DM9 to DM12).

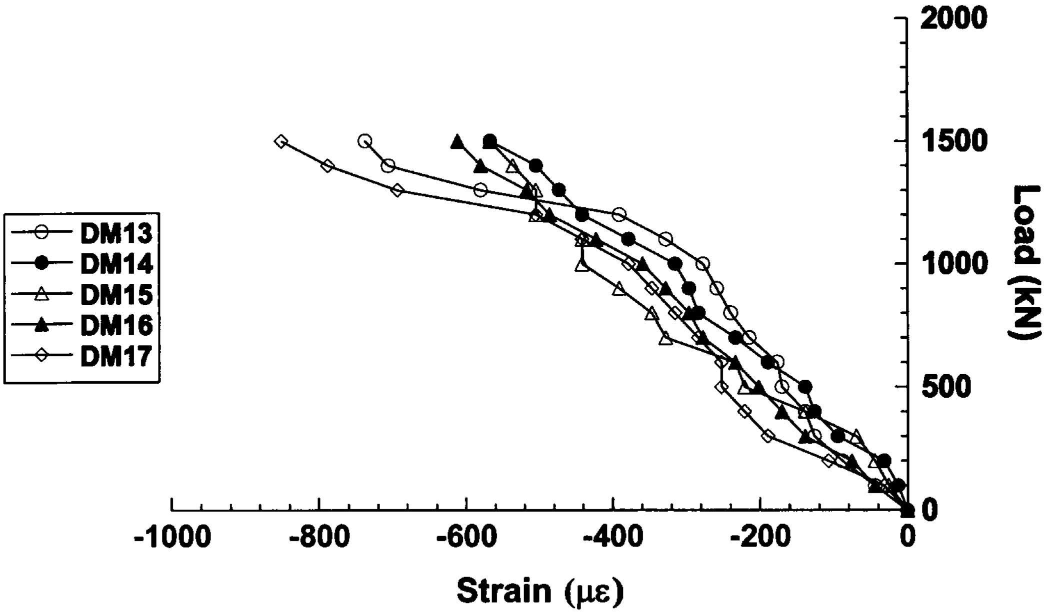

Figure 4.37 – Panel 6: Load versus strain measured (DM13 to DM17).

CHAPTER 5 – SHEAR BEAM STRENGTH TESTS

5.1 Introduction

This series of tests included the testing of seven FR-RPC prestressed beam specimens (SB1 to SB7). In this chapter selection of variables, specimen fabrication procedures, test configuration, instrumentation and gauging, experimental results and comments on test results are reported.

5.2 Variables and Specimen Dimensions

The main variables studied in the experimental program were

- fibre type (i.e. fibre aspect ratio and geometry);
- fibre quantity; and
- prestressing levels

The beams were 4.5 metres in total length having a span of 4.0 metres and a total depth of 650 mm. The webs of the beams were designed as a thin membrane of 50 mm thickness. The top flanges were 400 mm wide and contained six 15.2 mm diameter high strength steel prestressing wires. The bottom flanges were 250 mm wide and contained twelve 15.2 mm diameter strands. The beam dimensions are shown in Figure 5.1. The specimens were designed to fail by diagonal tension (shear) in the web region.

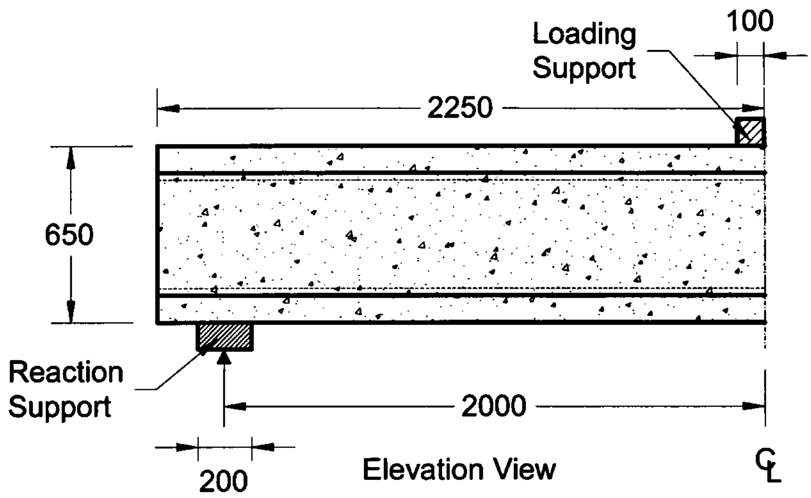

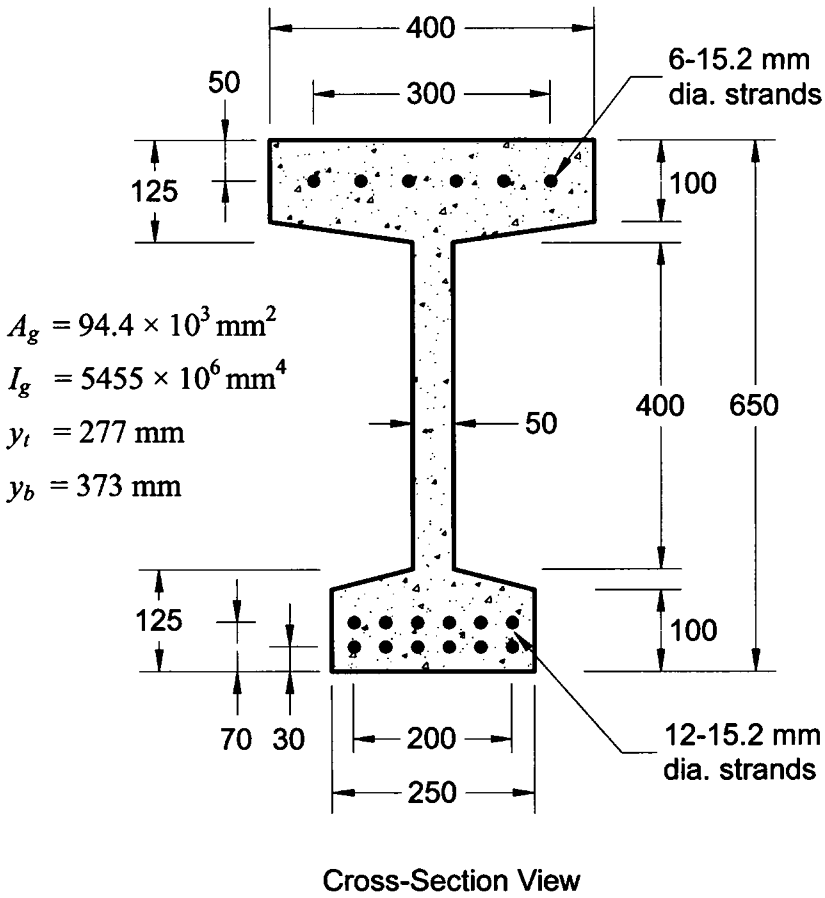

Figure 5.1 – Fibre reinforced RPC prestressed girders dimension (in mm).

5.3 Materials, Mix Designs and Fabrication

Details of the reactive powder concrete (RPC) mix for specimens SB1 to SB7 are given in Tables 5.1 and 5.2. The steel fibre reinforced reactive powder concrete used in this project is produced using a high energy concrete mixer provided by VSL (Aust.) (see Plate 5.1). The cement used in this project was Kandos Type 1 General Portland cement manufactured to AS3972 (1997); the undensified silica fume used was produced in Western Australia and Sydney sand was used with particle size range between 150 μm and 400 μm (refer Figure 3.1 for grading curve). The superplasticizer used in the mix was Glenium 51, which is a polycarboxylic ether based superplasticizer.

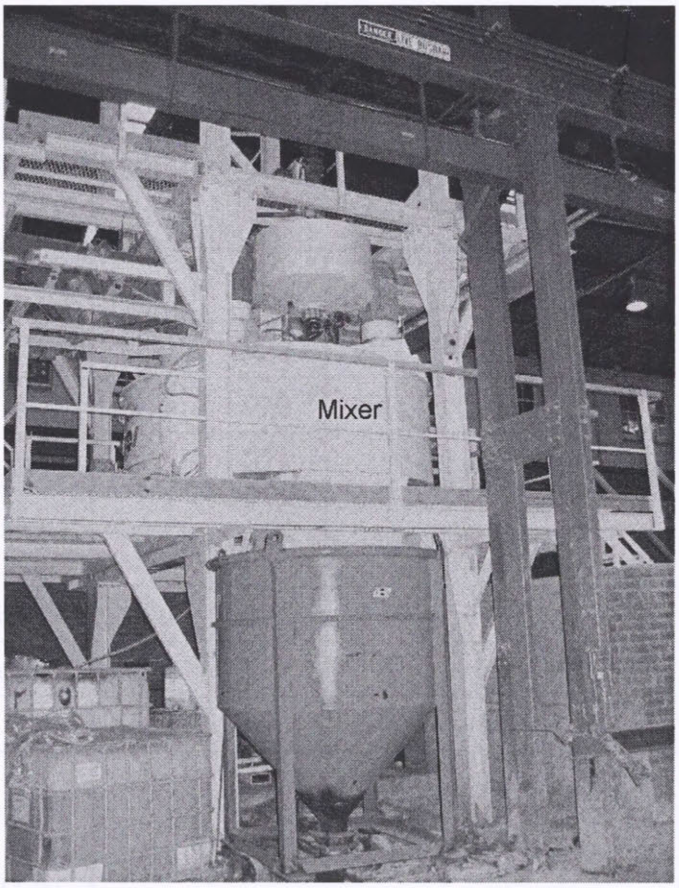

Plate 5.1 – High energy RPC mixer (VSL, Australia).

Table 5.1 – Fibre reinforced RPC mix designs for specimens SB1 to SB7 (proportion by weight relative to weight of cement).

Component	**SB 1**	**SB 2**	**SB 3**	**SB 4**	**SB 5**	**SB 6**	**SB7**
GP Cement	1	1	1	1	1	1	1
Sydney sand	1	1	1	1	1	1	1
Silica fume	0.24	0.24	0.24	0.24	0.24	0.24	0.24
Superplasticizer (Glenium 51)	0.042	0.042	0.042	0.042	0.042	0.042	0.042
Steel fibres (Type I)	0.190	0.190	0.190	0.095	0.114	0	0.143
Steel fibres (Type II)	0	0	0	0	0.076	0.190	0.047
Total water	0.20	0.21	0.22	0.20	0.19	0.22	0.21

Note: SB stands for shear beam.

Table 5.2 – Fibre reinforced RPC mix designs for specimens SB1 to SB7- material quantities (kg per m^3 of RPC).

Component	**SB 1**	**SB 2**	**SB 3**	**SB 4**	**SB 5**	**SB 6**	**SB7**
GP Cement	928	920	911	939	937	911	920
Sydney sand	928	920	911	939	937	911	920
Silica fume	223	221	219	225	225	219	221
Superplasticizer (Glenium 51)	39	39	38	39	39	38	39
Steel fibres (Type I)	176	175	173	89	107	0	131
Steel fibres (Type II)	0	0	0	0	71	173	43
Total water	186	193	200	188	178	200	193
W/B	0.16	0.17	0.18	0.16	0.15	0.18	0.17
Total Fibre Volumetric Ratio (%)	2.5	2.5	2.5	1.25	2.5	2.5	2.5

Note: SB stands for shear beam.

Details of the steel fibres used in the beams are given in Table 5.3 with l_f being the total length of fibre, d_f the diameter of fibre and σ_{fu} is the ultimate tensile strength of the fibre as reported by the manufacturers. Type I fibres were straight 13 mm long by 0.2 mm diameter and are fabricated from very high strength steel with minimum tensile strength of 1800 MPa. Type II fibres were end hooked fibres 30 mm long by 0.5 mm diameter and are made from high strength bright mild steel with a tensile strength of 1200 MPa. Water-binder ratios used varied from 0.15 to 0.18 with the aim to get a minimum flow of 160 mm as measured by ASTM C230. Two fibre volume ratios were used 1.25 and 2.5 percent.

All the dry components (i.e. cement, silica fume and sand) were pre-batched into 0.5 tonne bags. The dry components were then transported to the high energy mixer and mixed for about 10 minutes. Water and superplasticizer were added gradually until the materials were uniformly mixed. The fibres were introduced last, dispersed uniformly and mixing continued for a further 10 minutes. Flow table testing was undertaken before casting of the specimen. All specimens were cast vertically in steel forms as shown in Plate 5.2. The forms were cleaned and greased to allow smooth stripping. The fresh FR-RPC was compacted using external vibrators which were attached to the steel forms. Within one hour of casting, the specimens and test control samples were covered under wet hessian and plastic sheeting until the day of demoulding.

Table 5.3 – Steel fibre types.

No.	Type	l_f (mm)	d_f (mm)	σ_{fu} (MPa)	Fibre Shape
I	Straight	13	0.2	1800	
II	End-hooked	30	0.5	1200	

Plate 5.2 – Pouring of reactive powder concrete in the steel forms.

The time of stripping, curing and testing of the specimens, relative to casting, are summarised in Table 5.4. After stripping, the specimens were cured for 7 days at 80 degrees centigrade in a hot water bath. After 9 days (12 days for specimen SB2) the specimens were removed from the hot water bath and air cured until the day of testing.

Figure 5.2 shows the manufacturers stress-strain curve for the 15.2 mm 7-wire steel strand used in this project. The strand has a guaranteed ultimate tensile strength (GUTS) of 1750 MPa. The nominal cross-sectional area of the strand is 143 mm^2. Table 5.5 shows the results on the 15.2 mm diameter steel strand relaxation over 5 days with initial prestressing forces of 75 kN and 37.5 kN. In conducting the tests the same procedure (and Anchorage length) was used as that for prestressing of the specimens. The relaxation specimens were kept at ambient temperature and humidity with the temperature varying from 15 to 25 degrees Celsius over the period of the test. The test shows the loss of prestress is less than 0.5 percent over a period of 120 hours.

Table 5.4 – Day of event relative to casting.

	Day						
Event	**SB 1**	**SB 2**	**SB 3**	**SB 4**	**SB 5**	**SB 6**	**SB 7**
Casting	0	0	0	0	0	0	0
Stripping	2	5	2	2	2	2	2
Start Curing	2	6	2	2	2	2	2
End Curing	9	12	9	9	9	9	9
Testing	90	85	65	58	49	34	34

Table 5.5 – Strand relaxation test.

Day	**Initial (Day1)**	**2**	**3**	**4**	**5**
Prestressed Force (kN)	75	74.8	74.8	74.7	74.7
	37.5	37.4	37.4	37.4	37.4

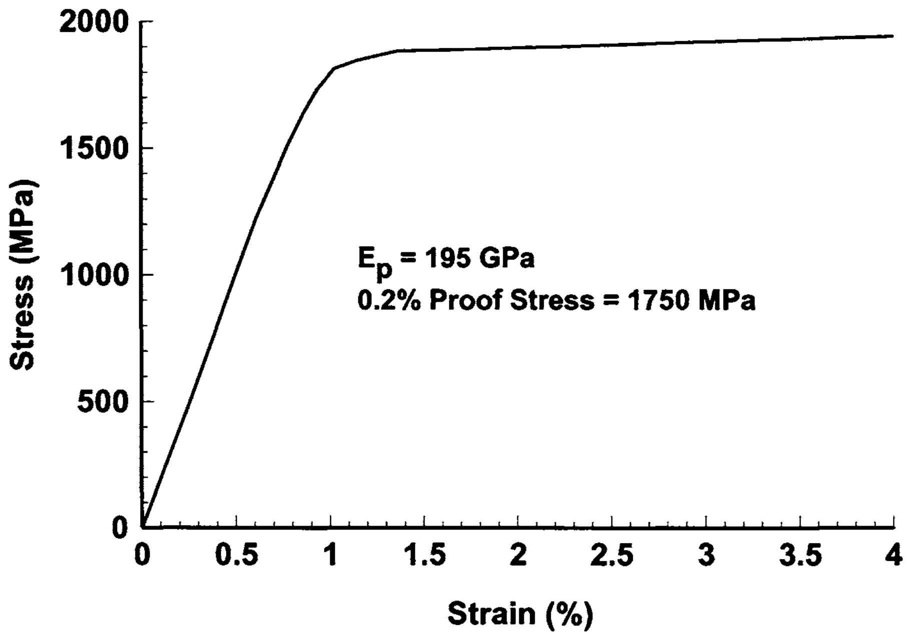

Figure 5.2 – Stress-strain curve of 15.2 mm diameter prestress steel.

5.4 Test Setup, Testing Procedure and Instrumentation

Details of the specimens, experimental variables and the test setup are given in Table 5.6 and Figure 5.3, respectively. Specimen SB3 was set as the reference specimen with 2.5 percent of Type I fibres and with 15 percent prestress (that is, 15 percent of GUTS). Specimens SB3 to SB7 were prestressed to 15% of the guaranteed tensile strength of the strands giving an average prestress in the section of 7.2 MPa. Each strand in specimens SB1 and SB2 was prestressed to 0 and 30 percent of the guaranteed tensile strength, respectively. Specimen SB4 was similar to specimen SB3 except it had half the amount of Type I fibre in its mix. Specimen SB5 and SB7 consisted of fibre cocktail RPC mixes with varying quantities of Type I and II fibres and beam SB6 contained 2.5 percent of Type II fibres.

As the experimental program is designed for the specimens to fail in shear, sufficient residual tensile reinforcing capacity is required, over and above the tension induce in the strands by the prestress, to ensure that a flexural tension failure does not occur. For this reason the prestress was limited to 30 percent of the breaking load of the strands. The total prestress was made consistent with design practice by increasing the total area of prestressing reinforcement.

All the specimens had a similar experimental setup and instrumental gauging (see Figure 5.4). The specimens were simply supported over a 4 metre span (measured between support centrelines) and the applied concentrated load was placed at the centre of the specimens. All specimens were tested in a 5000 kN capacity stiff testing frame and tested under ram displacement control.

Table 5.6 – Details of specimens.

Beam No.	Initial Prestressing Force (kN)		σ_{top} (MPa)	σ_{bot} (MPa)	σ_{ave} (MPa)	Fibre Volume (%)
	Top Flange	Bottom Flange				
SB1	0	0	0	0	0	Type I- 2.5
SB2	450	900	-4.72	-27.2	-14.3	Type I- 2.5
SB3	225	450	-2.36	-13.6	-7.15	Type I- 2.5
SB4	225	450	-2.36	-13.6	-7.15	Type I- 1.25
SB5	225	450	-2.36	-13.6	-7.15	Type I- 1.5 Type II- 1.0
SB6	225	450	-2.36	-13.6	-7.15	Type II- 2.5
SB7	225	450	-2.36	-13.6	-7.15	Type I- 1.88 Type II- 0.62

Note: σ_{top} and σ_{bot} are the extreme fibre stresses of concrete at transfer

σ_{ave} is the average prestress on the section

One end of each specimen was a pinned support and the other end had a pin and roller support, as shown in Figure 5.3. The pins and rollers were greased to minimise friction and to give free rotation and horizontal translation, as required.

The instrumentation used for each specimen is shown in Figure 5.4 with monitoring of 99 sets of Demec (DM) gauges and seven LVDTs. Demec gauges 1 to 16 were located at the top (compression) flange of the specimen with DM gauges 17 to 32 located at the bottom (tension) flange. Demec gauges 33 to 99 were located in the web regions of the specimens to measure longitudinal and shear strains in the web. LVDTs 1 and 6 were used to measure longitudinal strains in the flanges with LVDTs 2 to 5 located to monitor diagonal strains. The displacement transducer LVDT 7 was placed to measure the midspan displacement of the beam. Load was applied in increment until the peak load was attained. For each increment of load the DM gauge data were recorded and the crack pattern was traced.

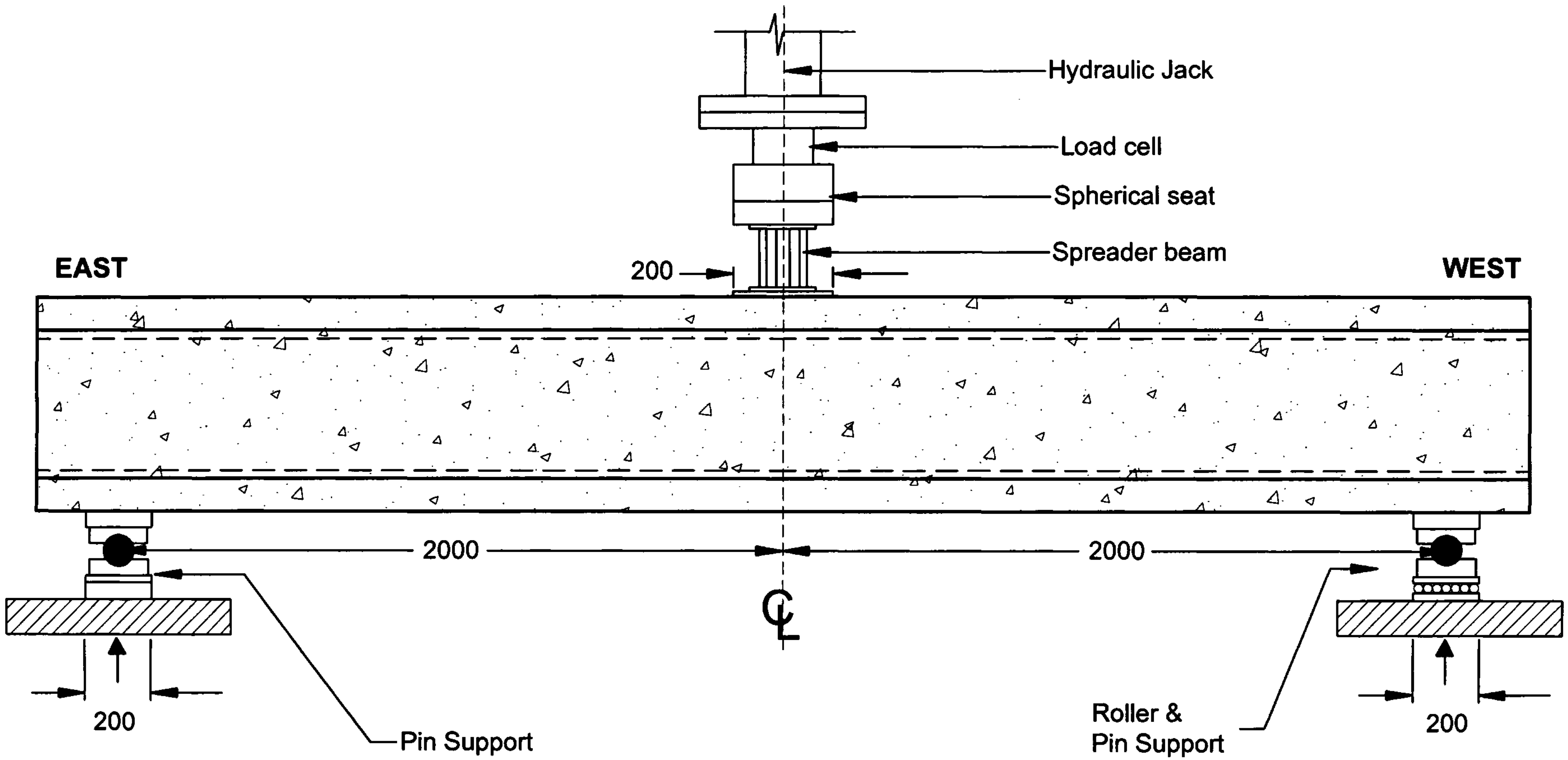

Figure 5.3 - Test specimen dimensions and experimental setup.

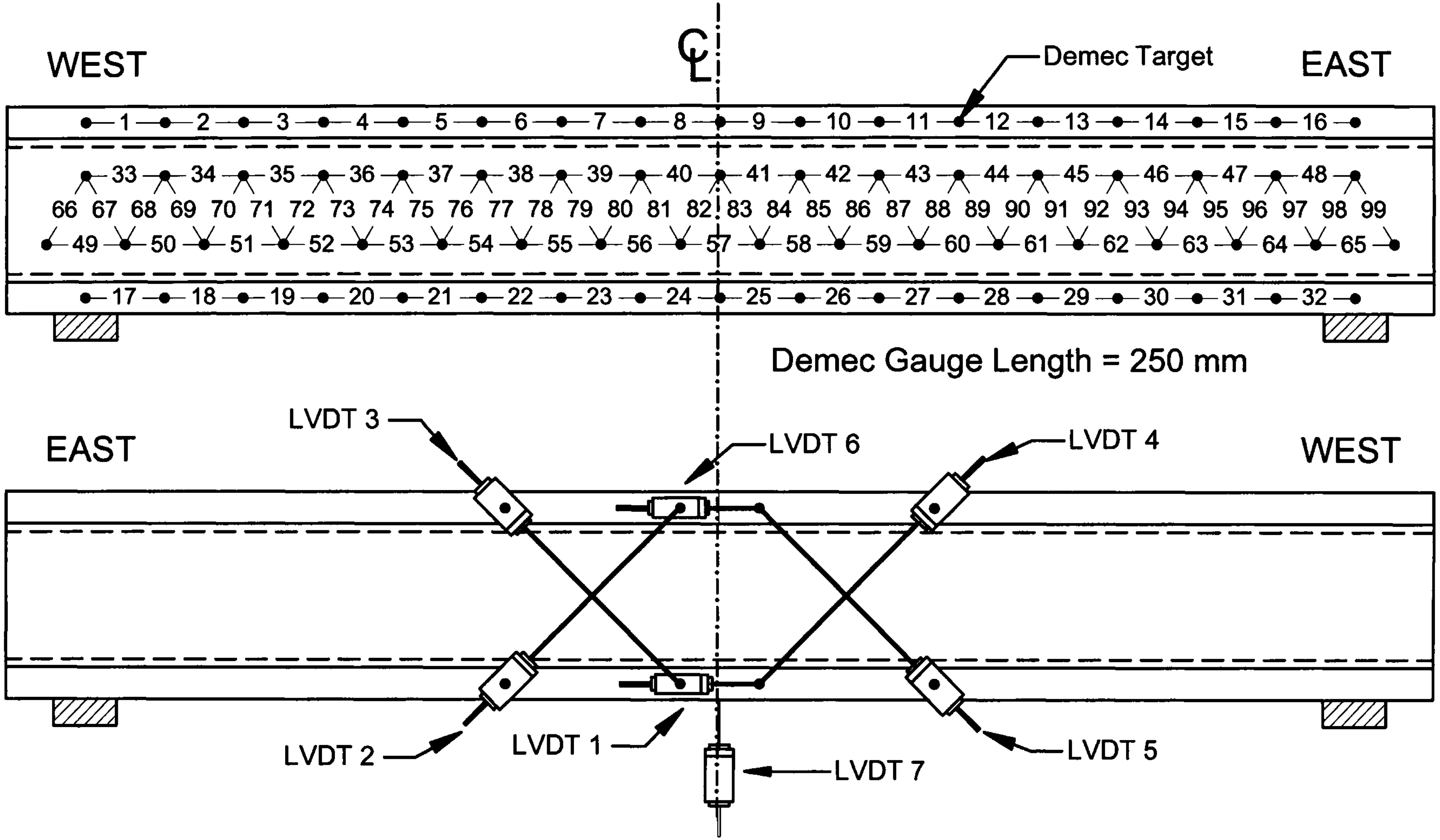

Figure 5.4– Location of Demec gauges and LVDTs.

5.5 Material Properties

The results of the material control tests are summarised in Table 5.7 and presented in Figures 5.5 and 5.6. The complete set of results is given in Appendix C. The mean compressive strength (f_{cm}) was determined from six 200 mm high by 100 mm diameter cylinders stressed under load control at a rate of 20 MPa/min according to AS1012.9 (1986). The ends of the cylinders were ground flat. The cube compressive strength (f_{cu}) was determined from 70 mm cubes stressed under load control at a rate of 20 MPa/min.

The modulus of elasticity (E_o) and the Poisson's ratio (ν) were obtained from stress-strain tests on 200 mm high by 100 mm diameter cylinders tested under circumferential displacement control at a rate if between 25 με/min and 150 με/min over a period of approximately two hours. The full stress-strain curves for the cylinders are given in Figure 5.5 with strains measured between the platen of the testing machine (i.e. over a 200 mm gauge length).

The split cylinder tensile strength (f_{sp}) was obtained from tests on six 200 mm high by 100 mm diameter cylinders loaded at 1.0 MPa/min via a 10 mm wide loading strip (refer Figure 3.2a). The notched three point flexural tension strength (f_{cf}) was obtained from 100 mm square prisms spanning 400 mm with a notch depth of 25 mm. The specimens were counter balanced to eliminate the effect of the self-weight on the fracture measurement and the specimens were controlled under crack mouth opening displacement (CMOD) at a rate of 500 με/min (refer Figure 3.3 and Plate 3.3). The fracture energy (G_f) was obtained from notched three point bending tests with either the total area under the load versus displacement or the load versus CMOD curves divided by the net cross-sectional area of the specimens (that is, $b \times [h - a]$, where b is the width of specimen, h is the total depth and a is the notch depth). The curves of load versus mid-span displacement and load versus CMOD are given in Figure 5.6.

Double punch tensile strength (f_{dp}) tests were undertaken on 200 mm high by 100 mm diameter cylinders using a pair of 25 mm high by 25 mm diameter rigid circular punches on the top and bottom surface of the specimens and were loaded at 1 MPa/min (refer Figure 3.2b). Equation 3.1 as proposed by Chen and Yuan (1980) is used to evaluate the double punch tensile strength.

Table 5.7– Mechanical properties of control specimens.

Specimen No.	E_o (MPa)	ν	ε_{cp}	f_{cm} (MPa)	f_{cu} (MPa)	f_{sp} (MPa)	f_{dp} (MPa)	f_{cf} (MPa)	G_f (N/mm)	Flow (mm)
SB1	44000	0.15	0.004	161	176	19.2	11.9	29.8	27.7	170
SB2	45000	0.15	0.004	160	178	20.9	11.2	26.4	24.7	180
SB3	43000	0.14	0.0045	149	166	21.9	10.6	23.2	21.0	210
SB4	43000	0.14	0.0042	164	180	18.0	10.3	14.8	14.3	170
SB5	49000	0.14	0.004	171	187	22.4	13.6	26.3	15.5	150
SB6	40000	0.13	0.004	157	168	18.3	10.2	25.2	12.4	210
SB7	46000	0.13	0.004	169	185	23.5	11.1	23.8	18.6	180

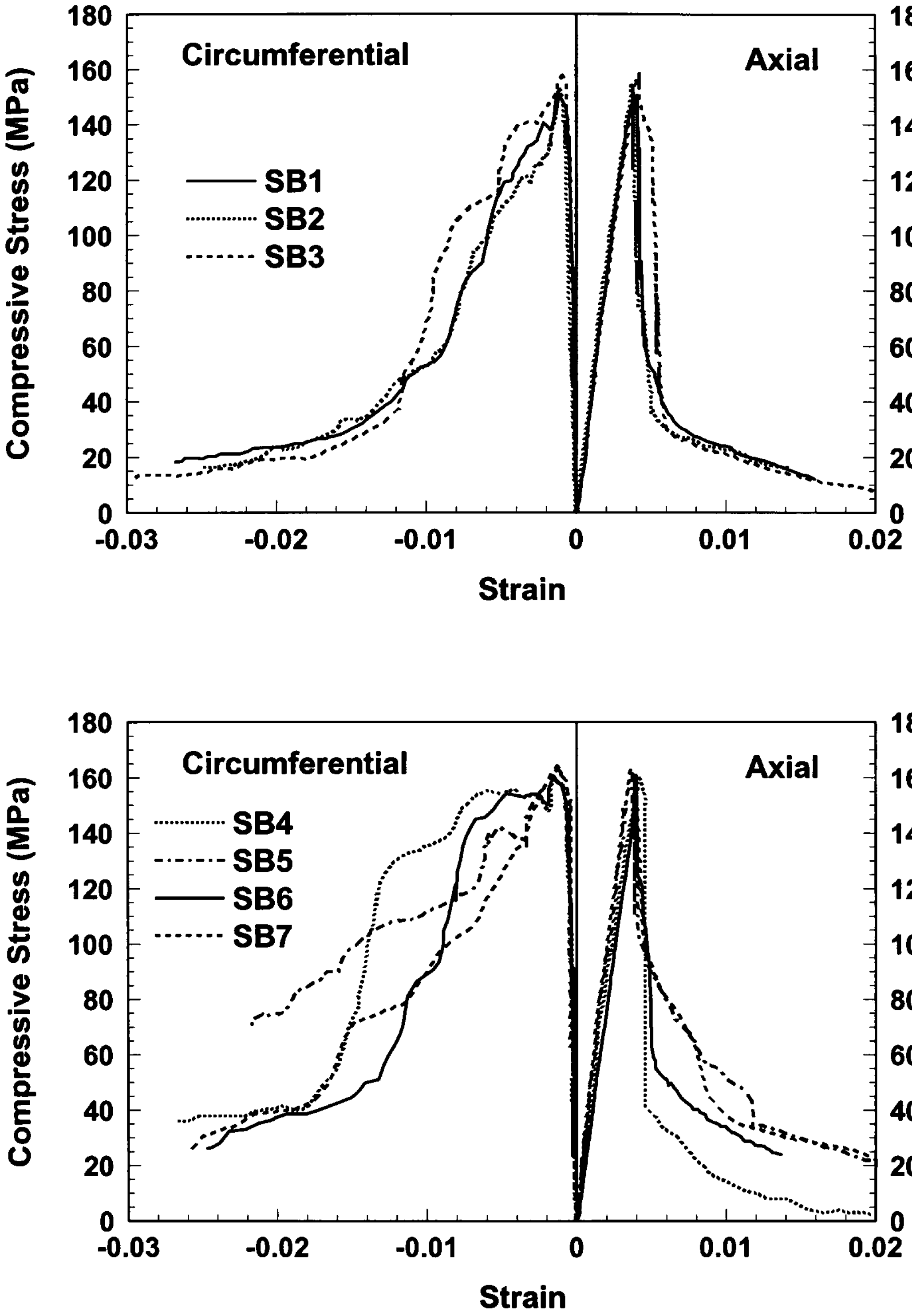

Figure 5.5 – Stress-strain curves.

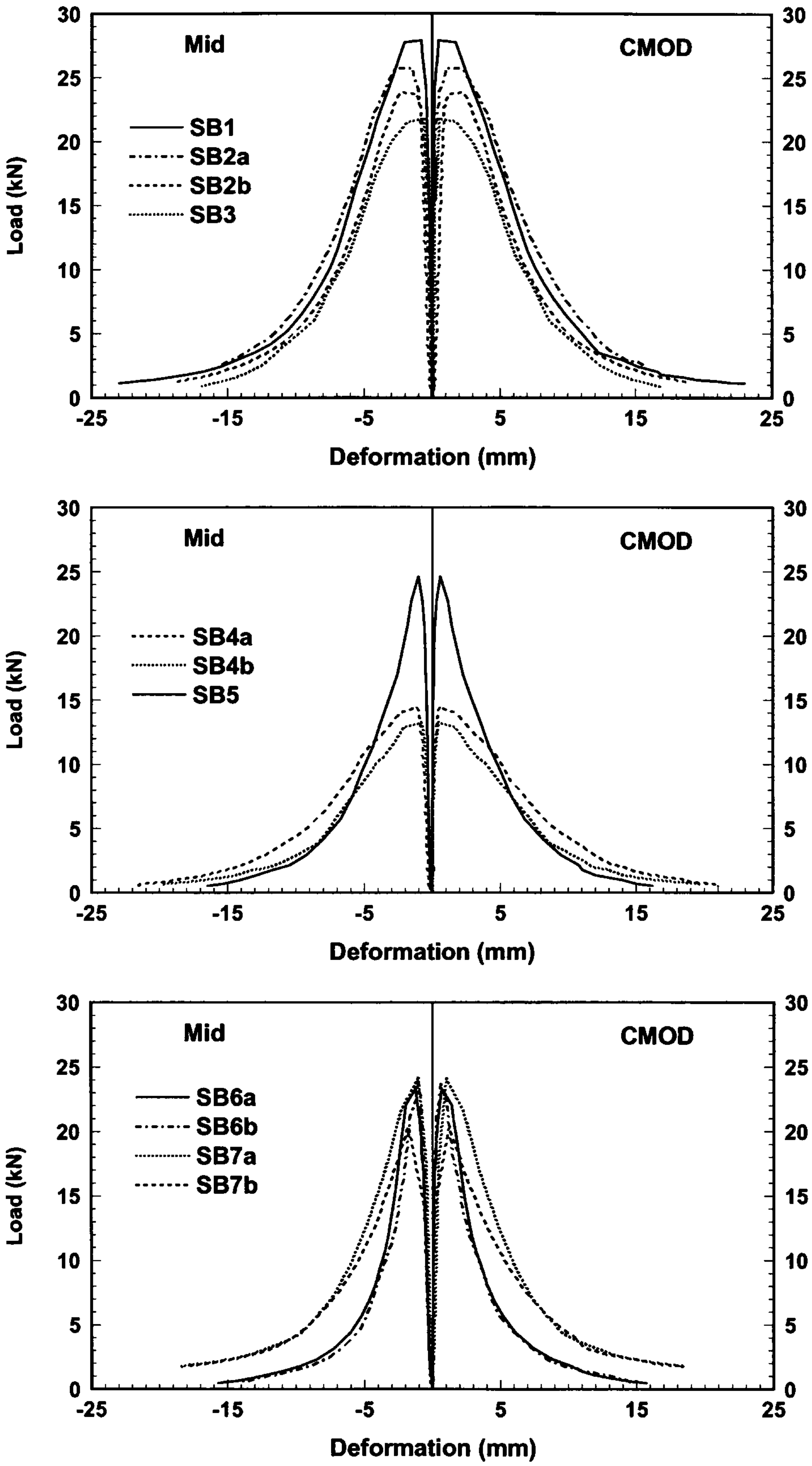

Figure 5.6 – Load versus mid-point deflection and load versus CMOD.

5.6 Individual Shear Beam Test Results

The raw data for the Demec strain readings for the seven shear beams are given in Appendix D. Plots of the LVDT data versus load are given in Appendix E. In this section, experimental observations for each specimen are reported. The load-deflection curves of specimens SB1 to SB7 are given in Figures 5.7 and 5.8.

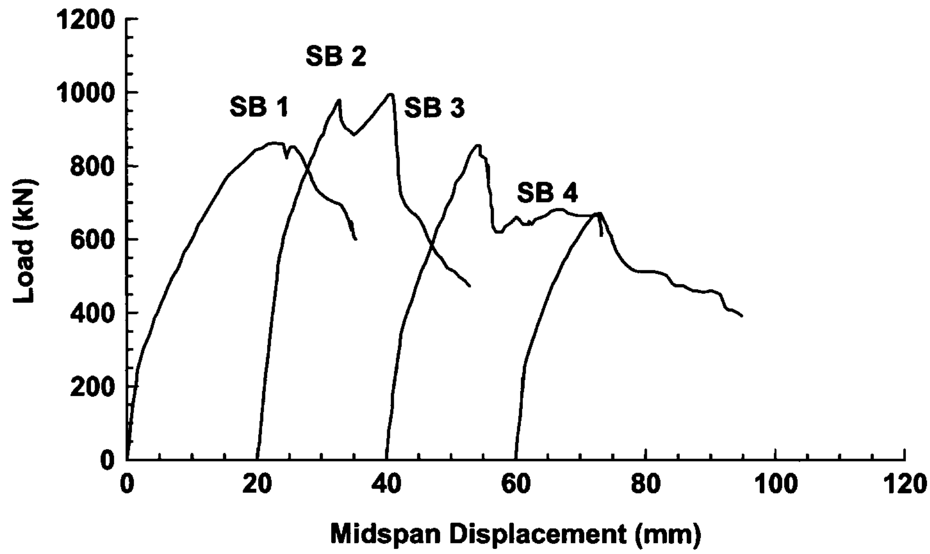

Figure 5.7 – Load versus midspan deflection for specimen SB1 to SB4.

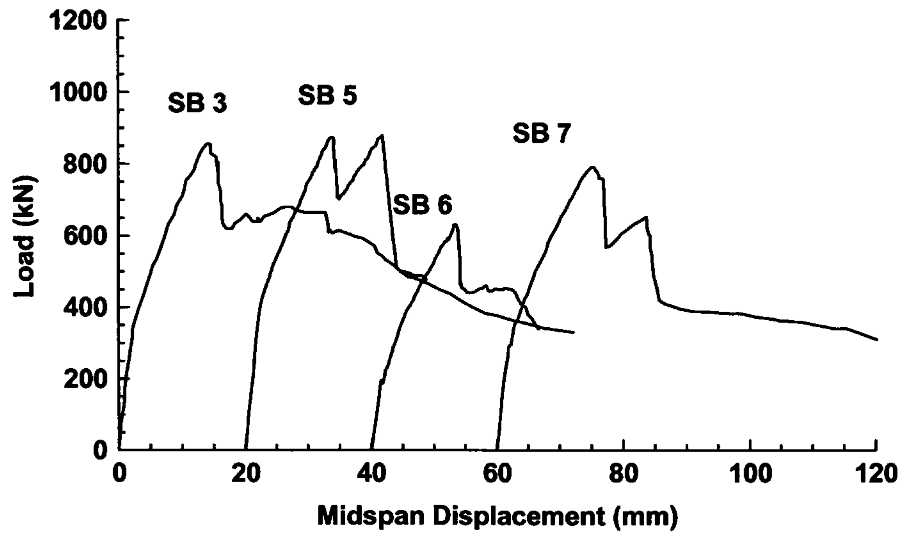

Figure 5.8 – Load versus midspan displacement for specimens SB3 and SB5 to SB7.

5.6.1 Beam SB1

Plate 5.3 shows the experimental setup of specimen SB1 in the stiff steel frame. The first diagonal shear cracks were observed at one of the shear spans (the west shear span) of the girder at a cracking load of $P_{cr} = 300\,\text{kN}$ (see Plate 5.4). As the loading was increased further diagonal shear cracks formed with the cracks distributed across the span. Plate 5.5 shows that the diagonal shear cracks had propagated toward the top flange of the specimen at a load of 700 kN. Eventually, a major inclined crack initiated in the east shear span. Sudden major tearing cracks occurred near the support region in the west shear span of the specimen adjacent to the support at $P_u = 860\,\text{kN}$ (see Plate 5.6). The major diagonal crack in the east shear span ceased to open any further at this point. Testing was concluded when the applied load had reduced to 600 kN and the corresponding recorded maximum deflection at the midspan was 35 mm (refer Figure 5.7).

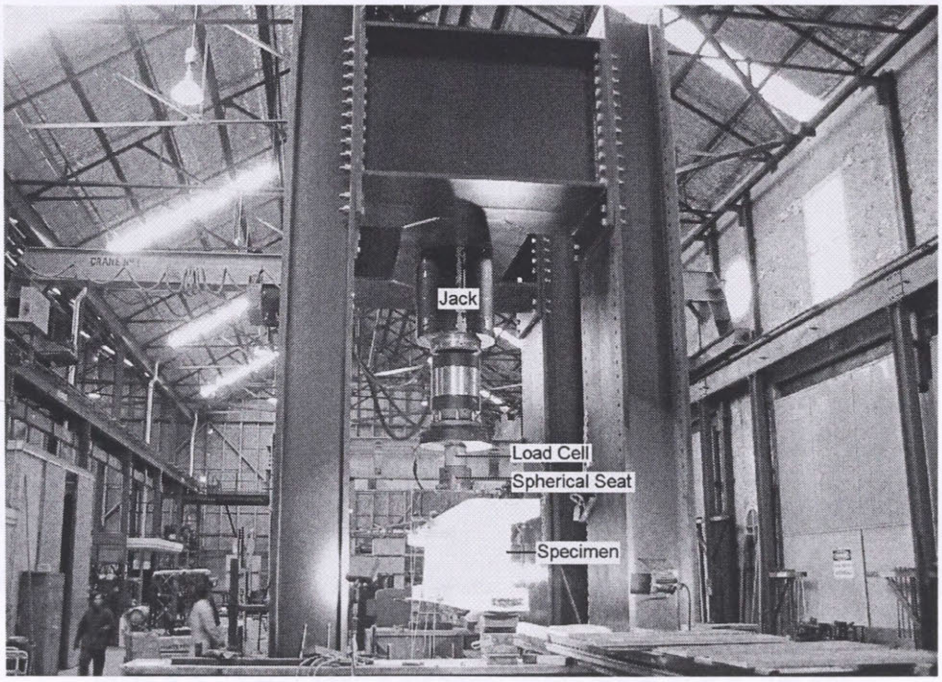

Plate 5.3 – Test specimen setup in the 5000 kN stiff testing frame.

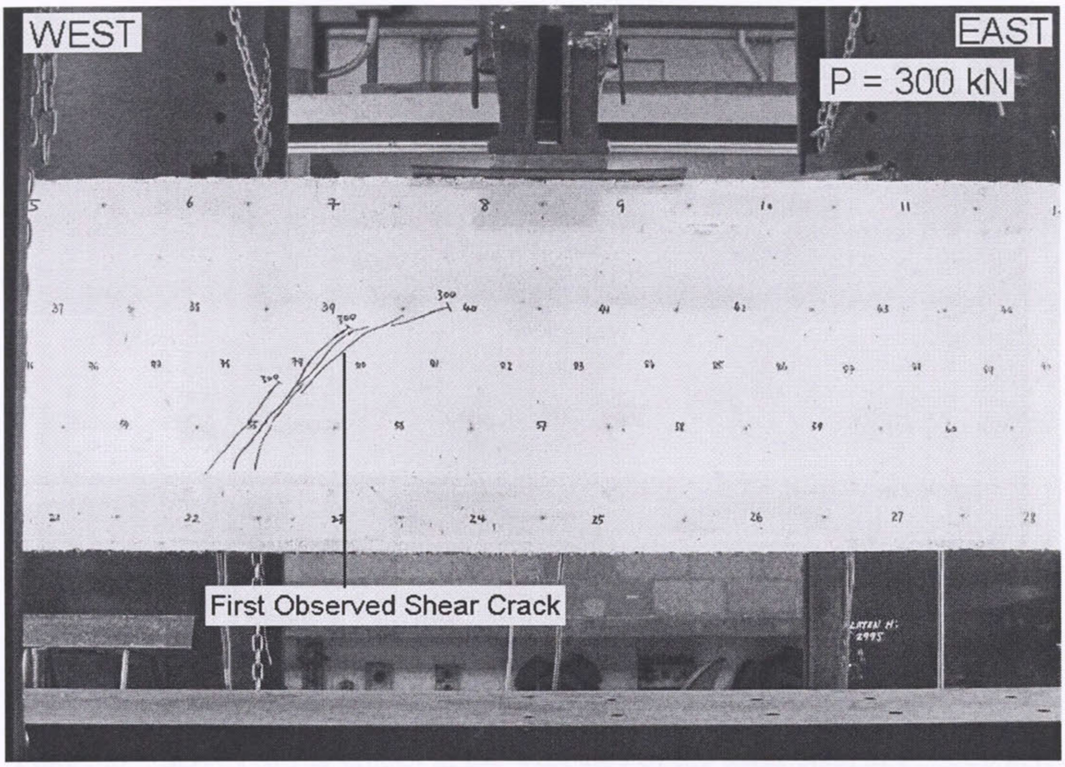

Plate 5.4 – SB1: First observed diagonal shear crack at P = 300 kN.

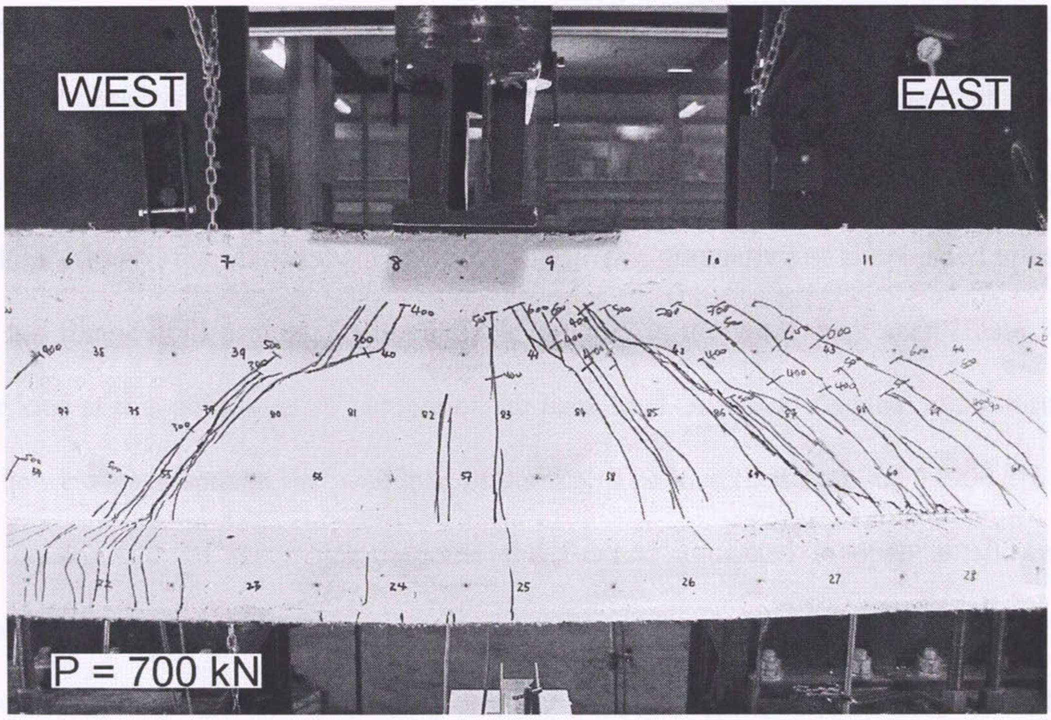

Plate 5.5 – SB1: Major diagonal shear crack at P = 700 kN.

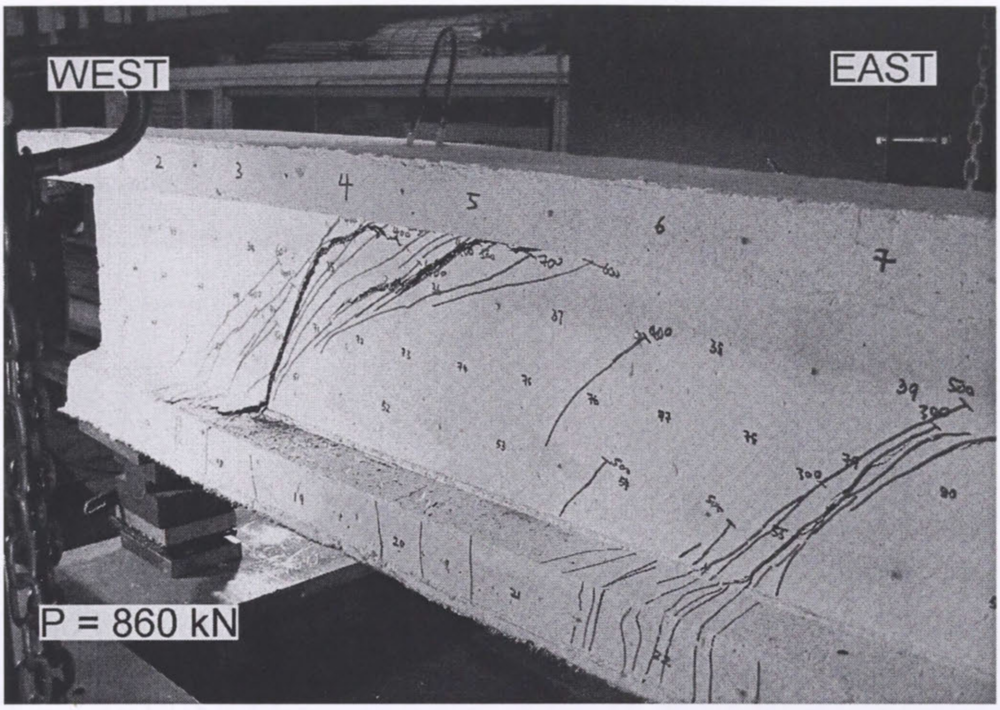

Plate 5.6 – SB1: Tearing cracks in the west side of the shear span at P = 860 kN.

5.6.2 Beam SB2

The general behaviour of specimen SB2 was similar to that of specimen SB1 with first cracking observed at a load of P_{cr} = 400 kN. Plate 5.7 shows that, as the loading was increased, further diagonal shear cracks formed and the cracks smeared cross the span. At load 900 kN, the diagonal shear cracks had grown gradually and propagated towards the top flange until a major inclined crack initiated in the west shear span (Plate 5.8). The load at this point was 96 percent of the peak load. A major diagonal crack formed in the west shear span at the peak load of 966 kN. The load then dropped to 900 kN and the crack width of the major diagonal shear crack continued to open as shown in Plate 5.9. The load then began to increase until a second peak was reached at 994 kN when a second diagonal crack formed near the support region of the west span. Testing was concluded when the load had reduced to 470 kN at a deflection of 30 mm (refer Figure 5.7).

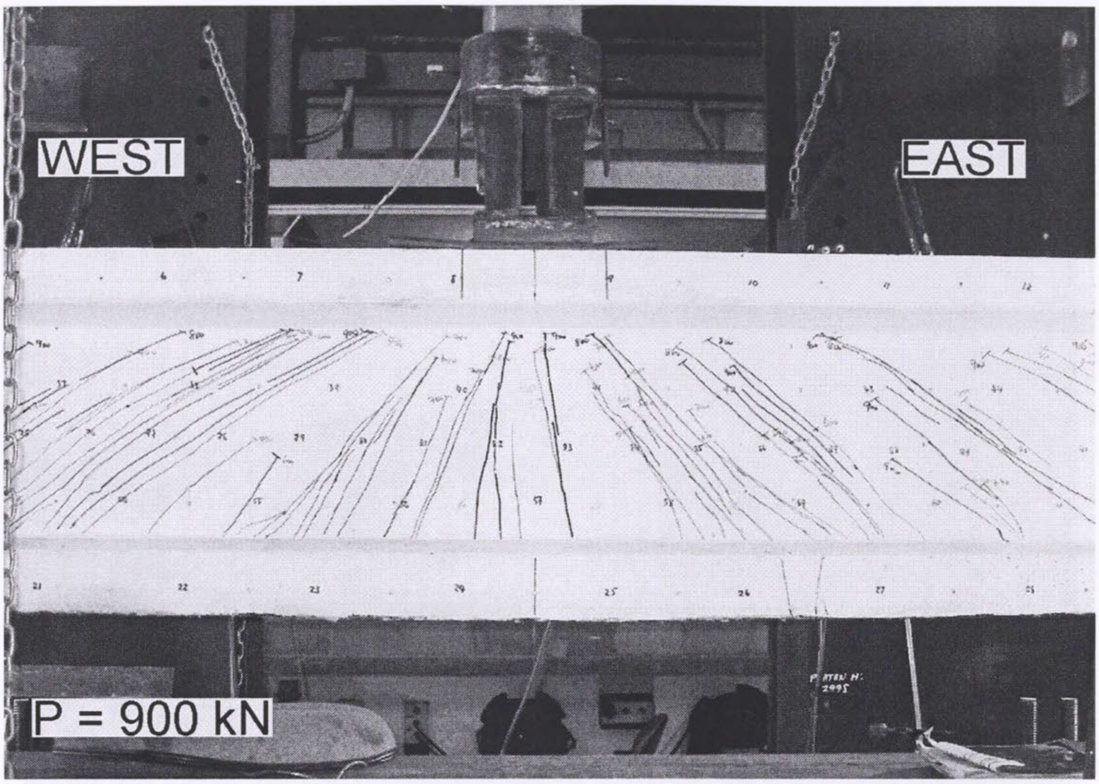

Plate 5.7 – SB2: Diagonal shear at P = 900 kN.

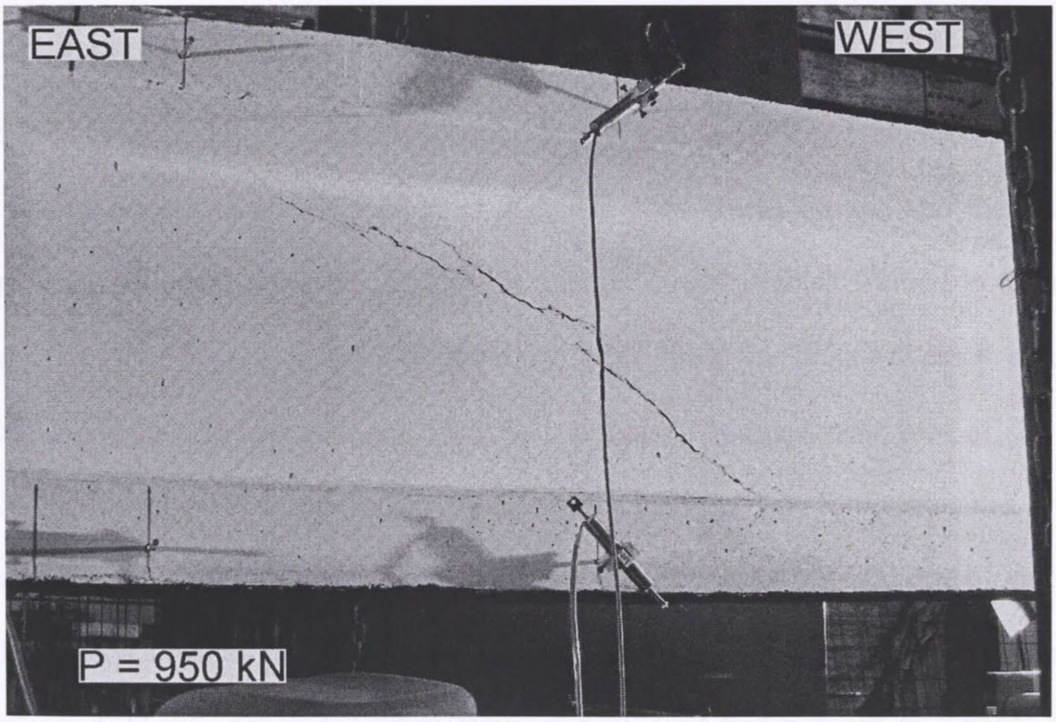

Plate 5.8 – SB2: Formation of first critical diagonal shear crack P = 950 kN.

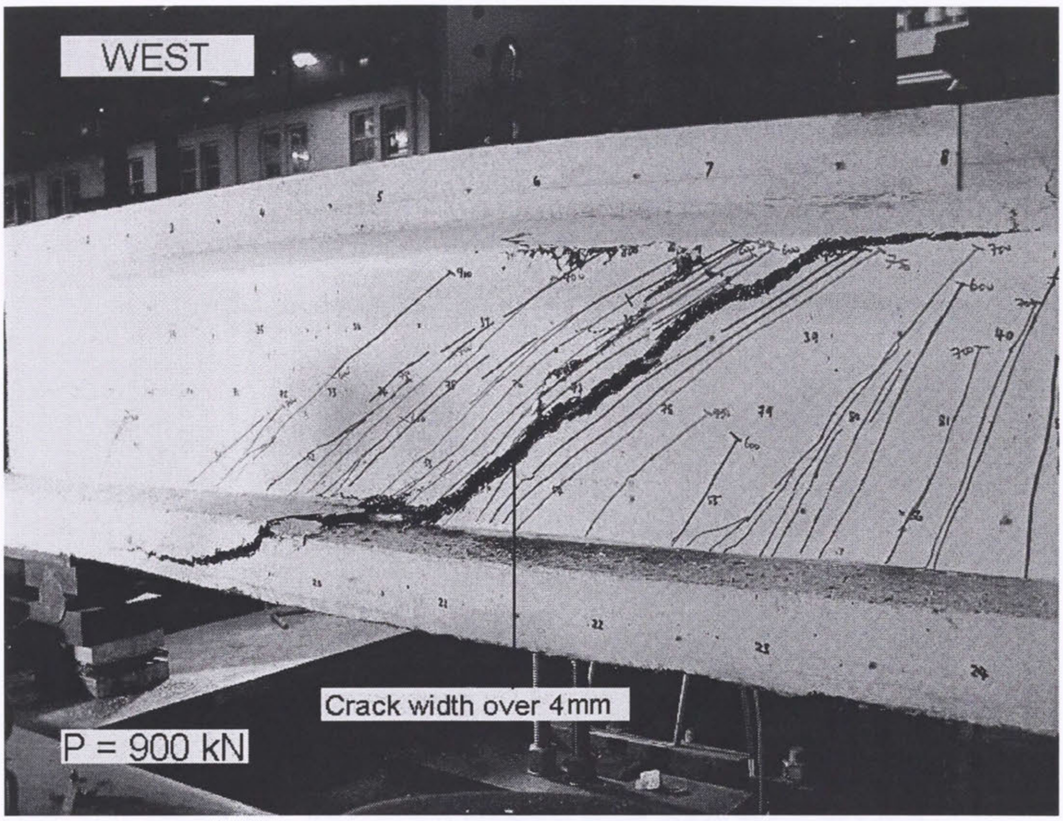

Plate 5.9 – SB2: Crack width over 4 mm at first post peak load of 900 kN.

5.6.3 Beam SB3

The first diagonal shear cracking was observed at a load of 300 kN. Plate 5.10 shows as the loading was increased a number of diagonal shear cracks formed and the cracks were smeared across the span. At 850 kN a major diagonal crack formed in the east span. The peak load was 856 kN. After the peak load, the diagonal crack opened considerably and the load reduced. Plate 5.11 was taken at a post peak load of 700 kN with all fibres having been pulled out along the crack plane. Plate 5.12 shows that at the post peak load of 600 kN, the top flange of the girder is rotated at two distinct locations with the crack width of the major diagonal crack being over 100 mm. Testing of specimen SB3 was concluded when the post peak load had reduced to 320 kN at a midspan deflection of 70 mm (refer Figure 5.7).

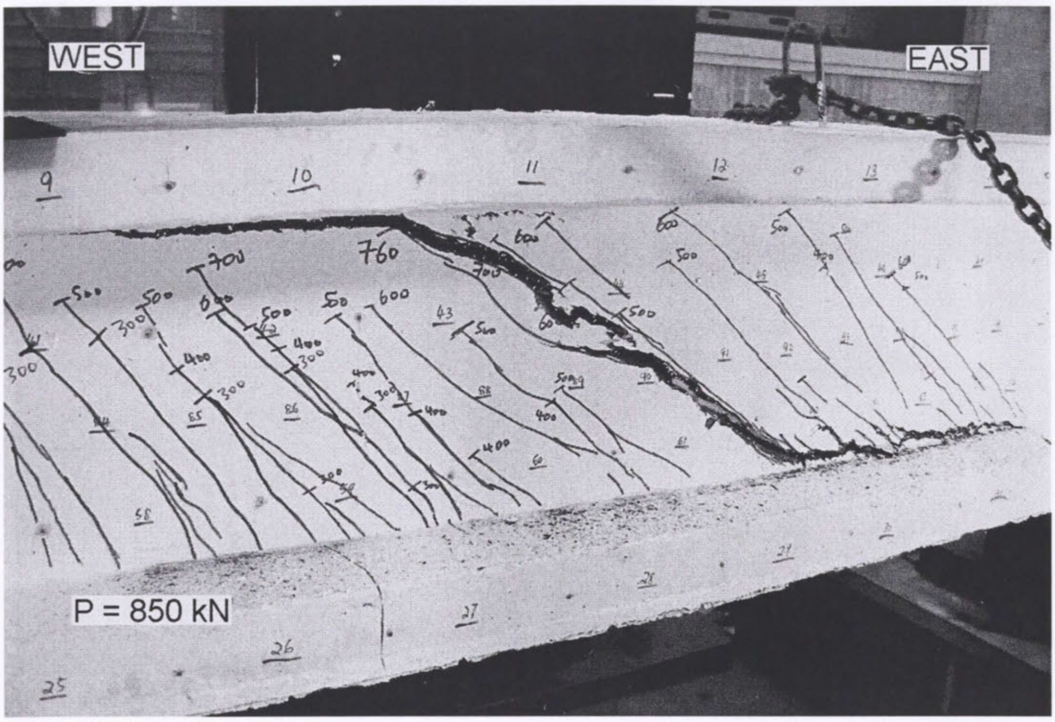

Plate 5.10 – SB3: major diagonal shear crack at P = 850 kN.

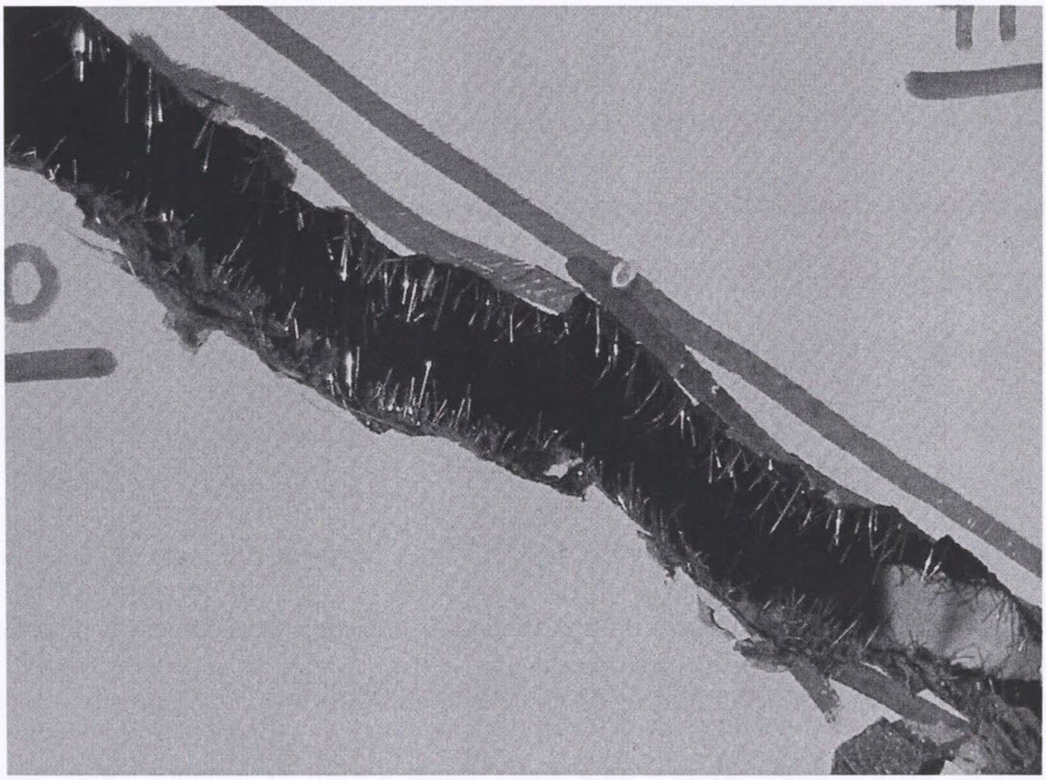

Plate 5.11 – SB3: fibre pullout at the diagonal crack at post peak P = 700 kN.

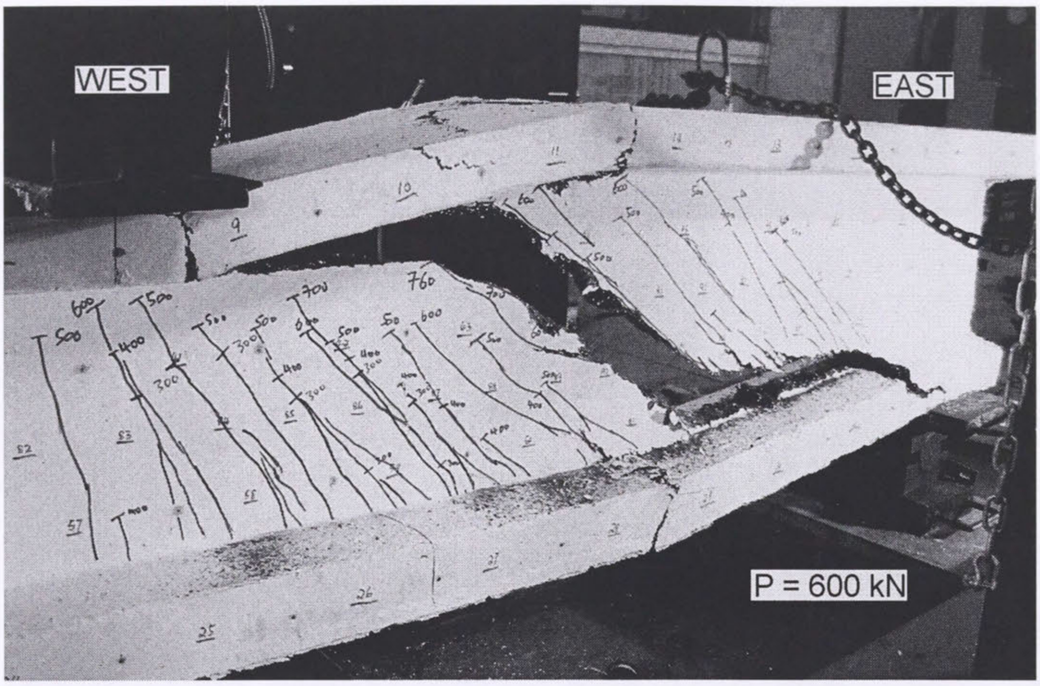

Plate 5.12 – SB3: flange rotation at post peak P = 600 kN.

5.6.4 Beam SB4

First diagonal shear cracking was observed at a load of P_{cr} = 300 kN. The general behaviour of specimen SB4 was similar to specimen SB3 which contained twice the volumetric amount of fibres in the concrete mix. Many minor diagonal shear cracks formed at the pre-peak load and smeared across the span (see Plate 5.13). However, for beam SB4 the peak load was lower at 673 kN (compared to 856 kN for beam SB3).

Plate 5.14 shows at the post peak load of 520 kN, three major diagonal shear cracks had formed in the east shear span and the crack widths measured were over 12 mm. After further deformation, when the load had dropped to 420 kN, the three major diagonal cracks joined together to form a single crack with a crack width of over 30 mm (see Plate 5.15). Testing of specimen SB4 was concluded when the post peak load had dropped to 270 kN at a midspan deflection of 69 mm (refer Figure 5.7).

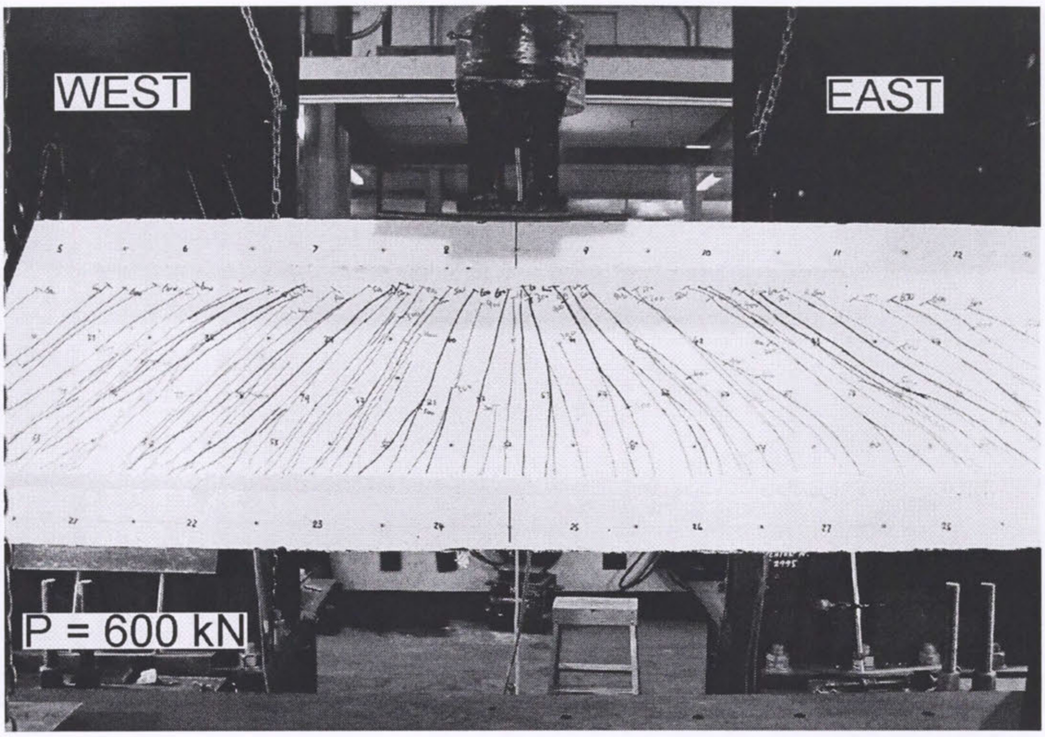

Plate 5.13 – SB4: Shear cracks smeared cross the shear spans at P = 600 kN.

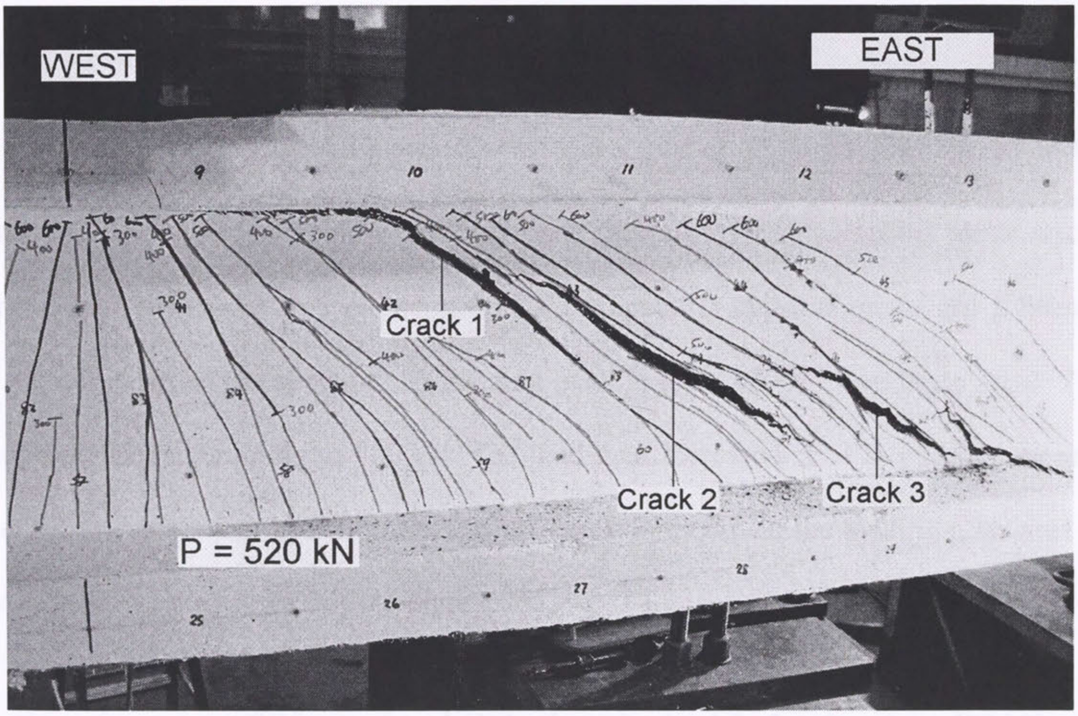

Plate 5.14 – SB4: Major diagonal crack formation from the joining of three cracks at the post peak load of P = 520 kN.

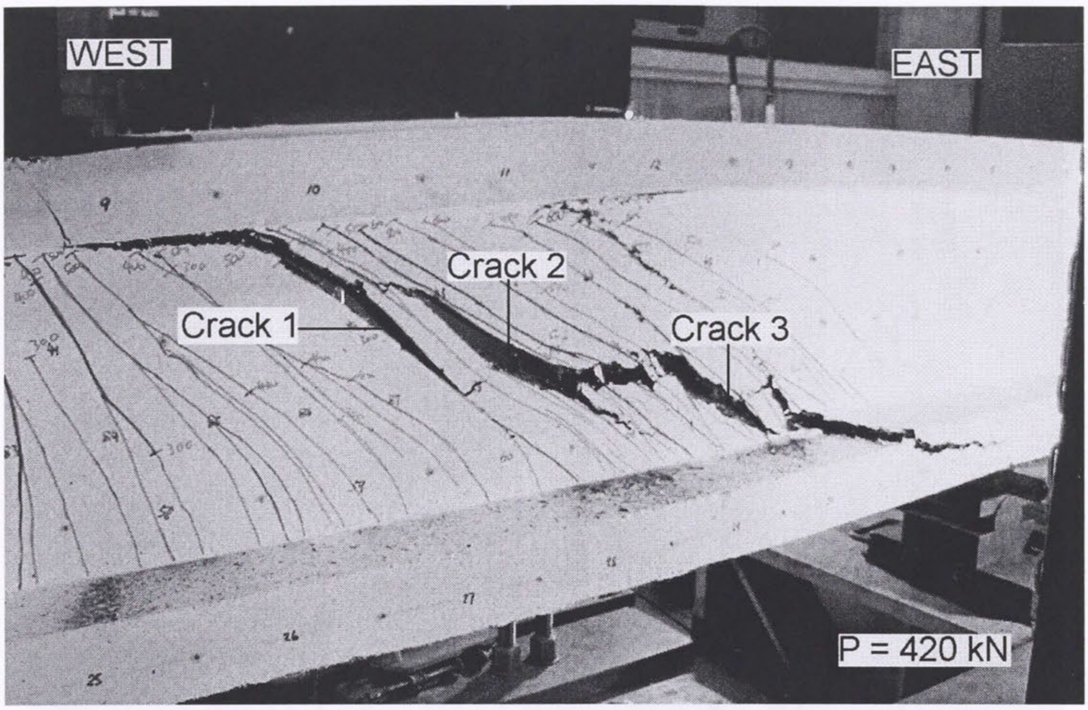

Plate 5.15 – SB4: Coalescence of diagonal cracks to form the failure crack at a post peak load of 420 kN.

5.6.5 Beam SB5

In specimen SB5, first cracking was observed at a load of P_{cr} = 400 kN. Similar to the other specimens, as the loading was increased more distributed diagonal shear cracks formed with the cracks smeared across the shear spans. A major diagonal crack formed in the east span of the specimen at the first peak load of 860 kN (see Plate 5.16). The load then dropped rapidly to 700 kN. The load then increased until a second peak was reached at P = 880 kN and another diagonal crack formed near the loading plate area of the east side of the specimen (see Plate 5.17).

Testing of specimen SB5 was concluded when the load had reduced to 480 kN at a midspan deflection of 30 mm (refer Figure 5.8).

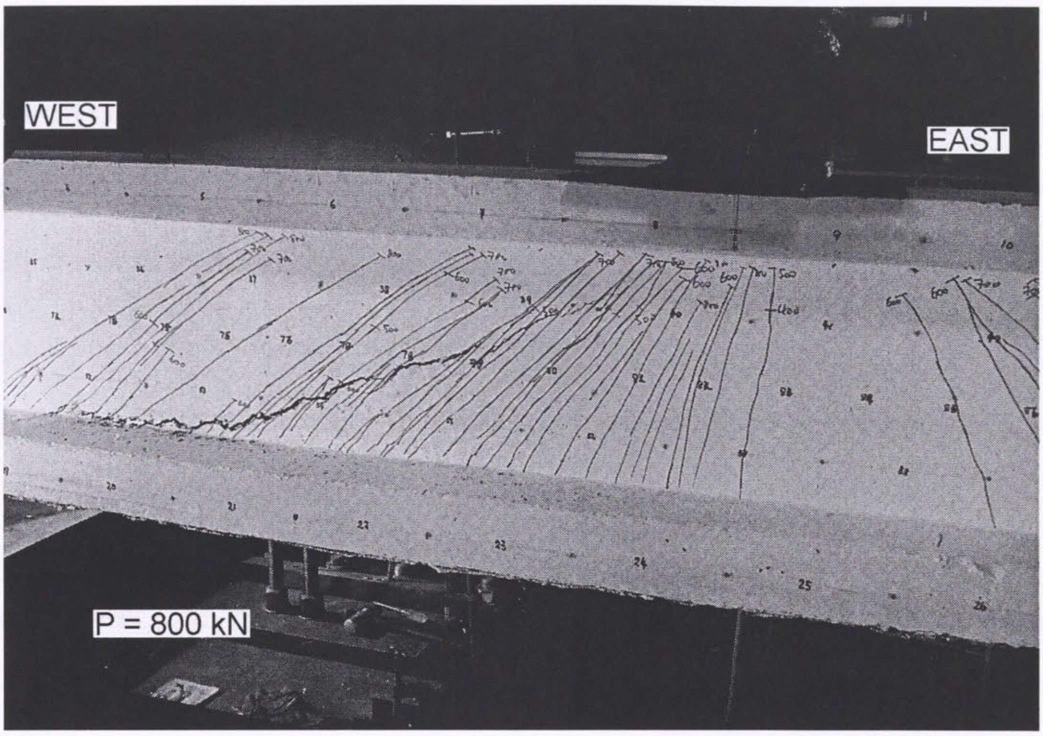

Plate 5.16 – SB5: Crack pattern at P = 800 kN (ascending).

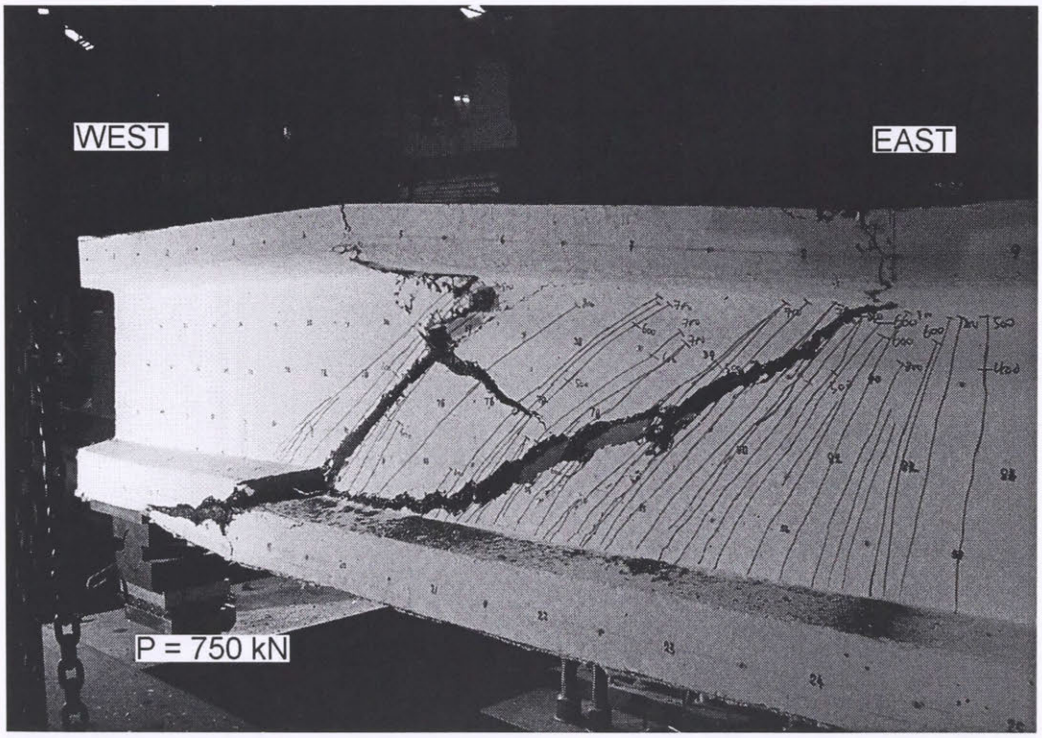

Plate 5.17 – SB5: Failure of specimen post peak load of 750 kN.

5.6.6 Beam SB6

Specimen SB6 containing 2.5 percent by volume of end hooked fibres (0 percent straight fibres) performed similarly to that of the other specimens. First observed cracking was at a load of P_{cr} = 300 kN (see Plate 5.18). As the loading was increased, diagonal shear cracks formed regularly throughout the shear spans, as shown in Plate 5.19. Plate 5.20 shows a major diagonal crack with an average crack width of over 2.5 mm formed at the west end of the specimen at the peak load of 660 kN.

After the peak load, the load steeply dropped away to 450 kN and a constant load of 450 kN was maintained for a further 8 mm of displacement in the mid-span of the specimen. Testing was concluded at the post peak load of 330 kN at a mid-span of 30 mm (refer Figure 5.8).

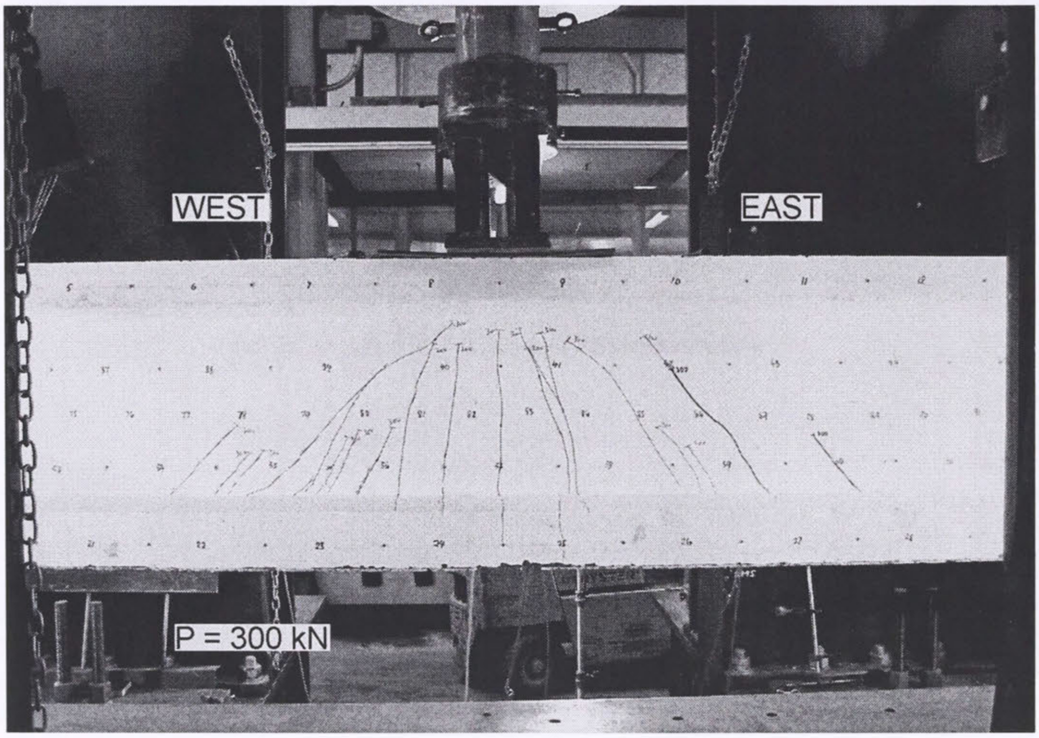

Plate 5.18 – SB6: Shear cracks smeared cross the shear spans at load of 300 kN.

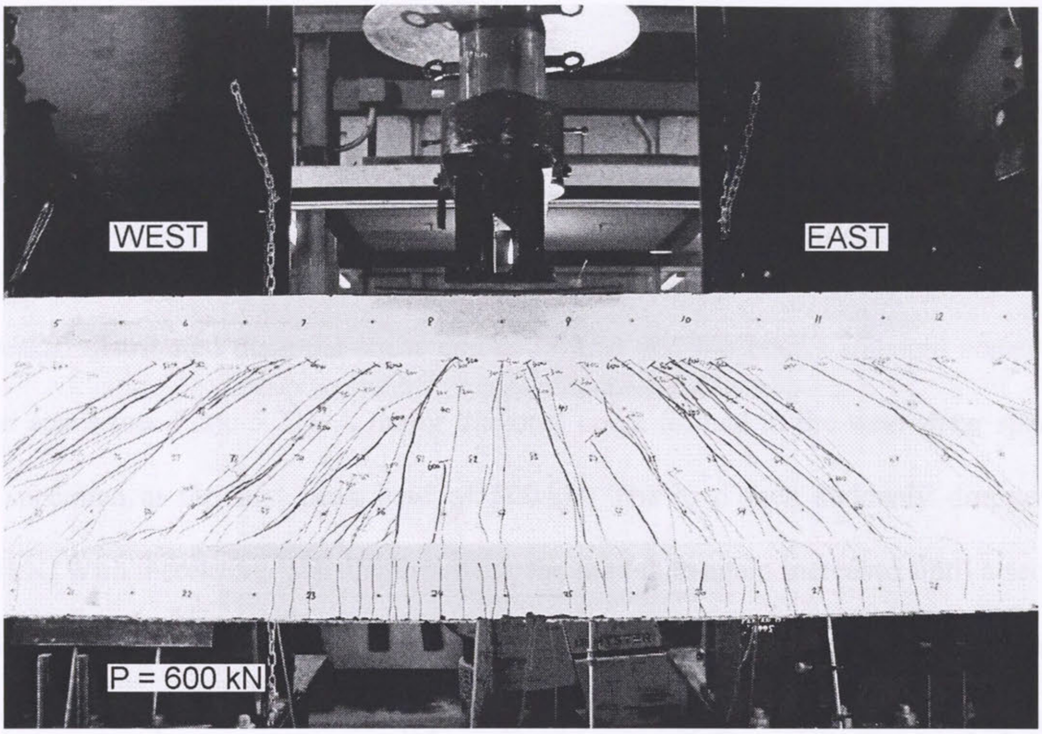

Plate 5.19 – SB6: Shear cracks smeared cross the shear spans at load of 600 kN.

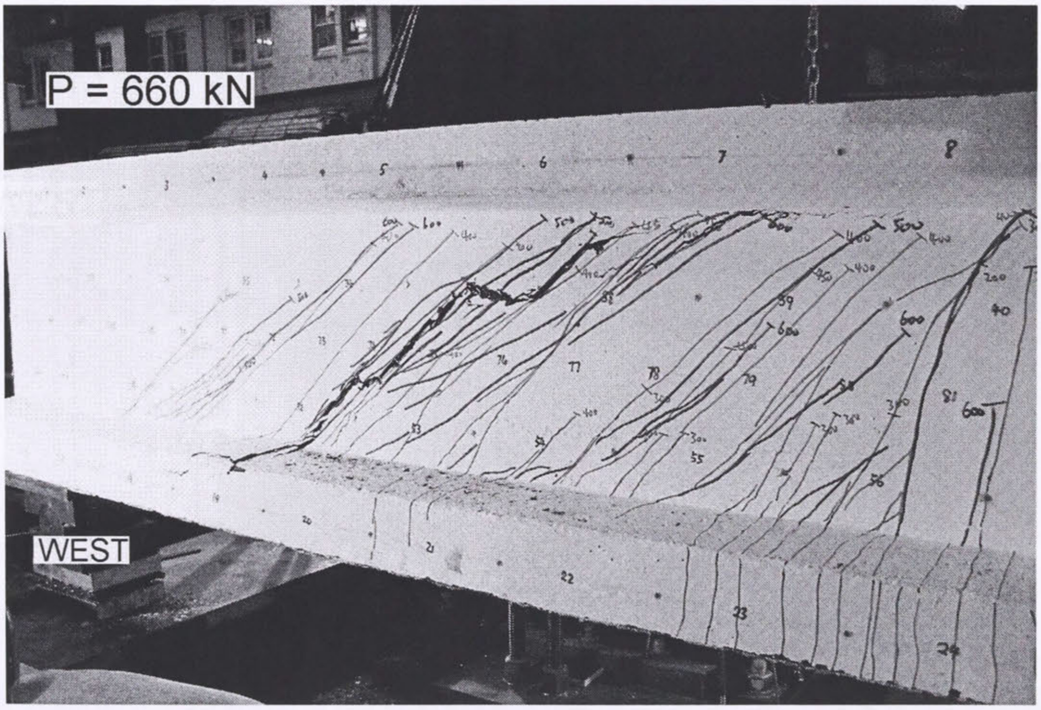

Plate 5.20 – SB6: Major diagonal crack width approximately 2.5 mm at peak load of 660 kN.

5.6.7 Beam SB7

The general behaviour of specimen SB7 was similar to that of specimen SB5 with two peak loads being recorded. In specimen SB7, first cracking was observed at a load of $P_{cr} = 350$ kN (see Plate 5.21). Similar to the other specimens, as the loading was increased distributed diagonal shear cracks formed and the cracks smeared across the shear spans (see Plate 5.22). A major diagonal crack formed in the west shear span of the specimen at the first peak load of 800 kN. The load then suddenly dropped to 570 kN. With increasing jack displacement, the load then again increased until a second peak was recorded at a load of 650 kN. At this point a second diagonal crack formed in the west shear span near the loading plate (see Plate 5.23). Plate 5.24 shows the pullout of straight fibres and fracture of the end-hooked fibre across the failure surface of the major crack. Testing of specimen SB7 was concluded at a displacement of 86 mm, corresponding to a load of 240 kN (refer Figure 5.8).

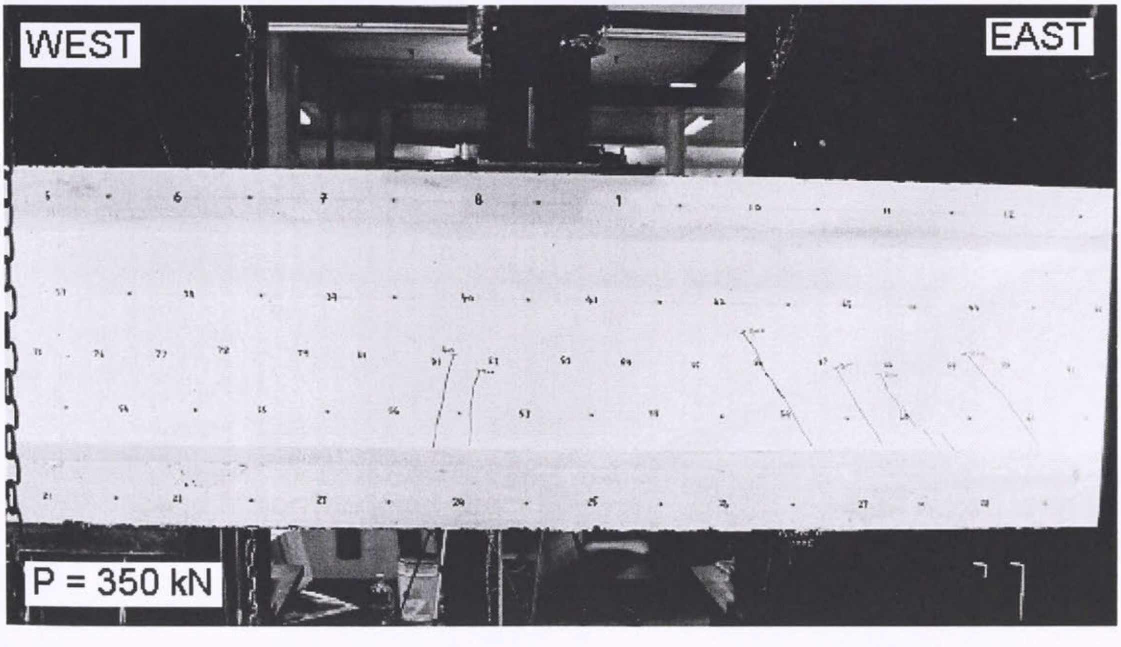

Plate 5.21 – SB7: First observed shear cracking at P = 350 kN.

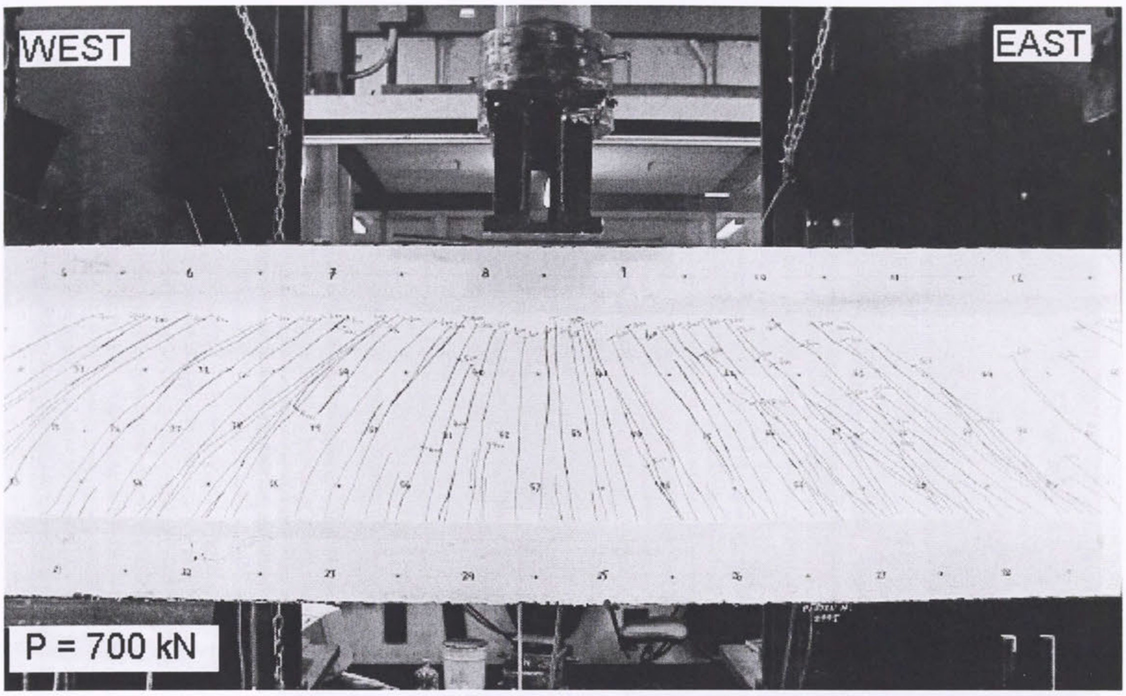

Plate 5.22 – SB7: Multiple shear cracks smeared across the span at P = 700 kN.

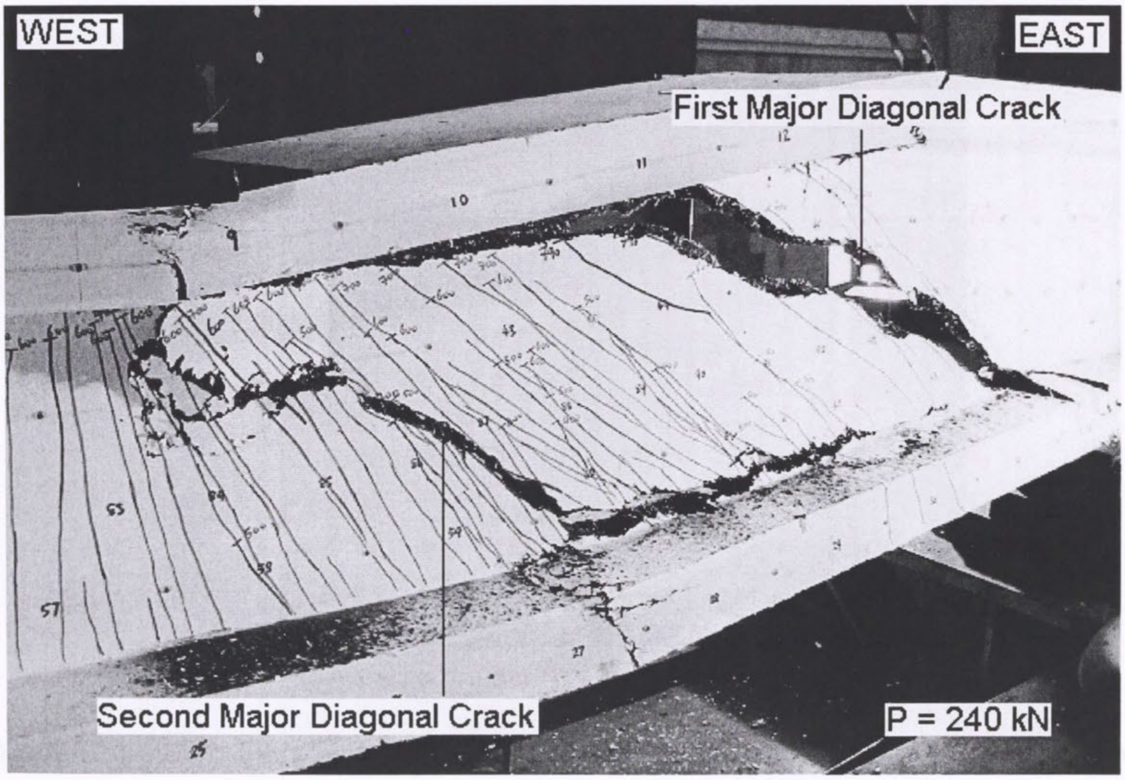

Plate 5.23 – SB7: Major diagonal cracks at the conclusion of the test; P = 240 kN.

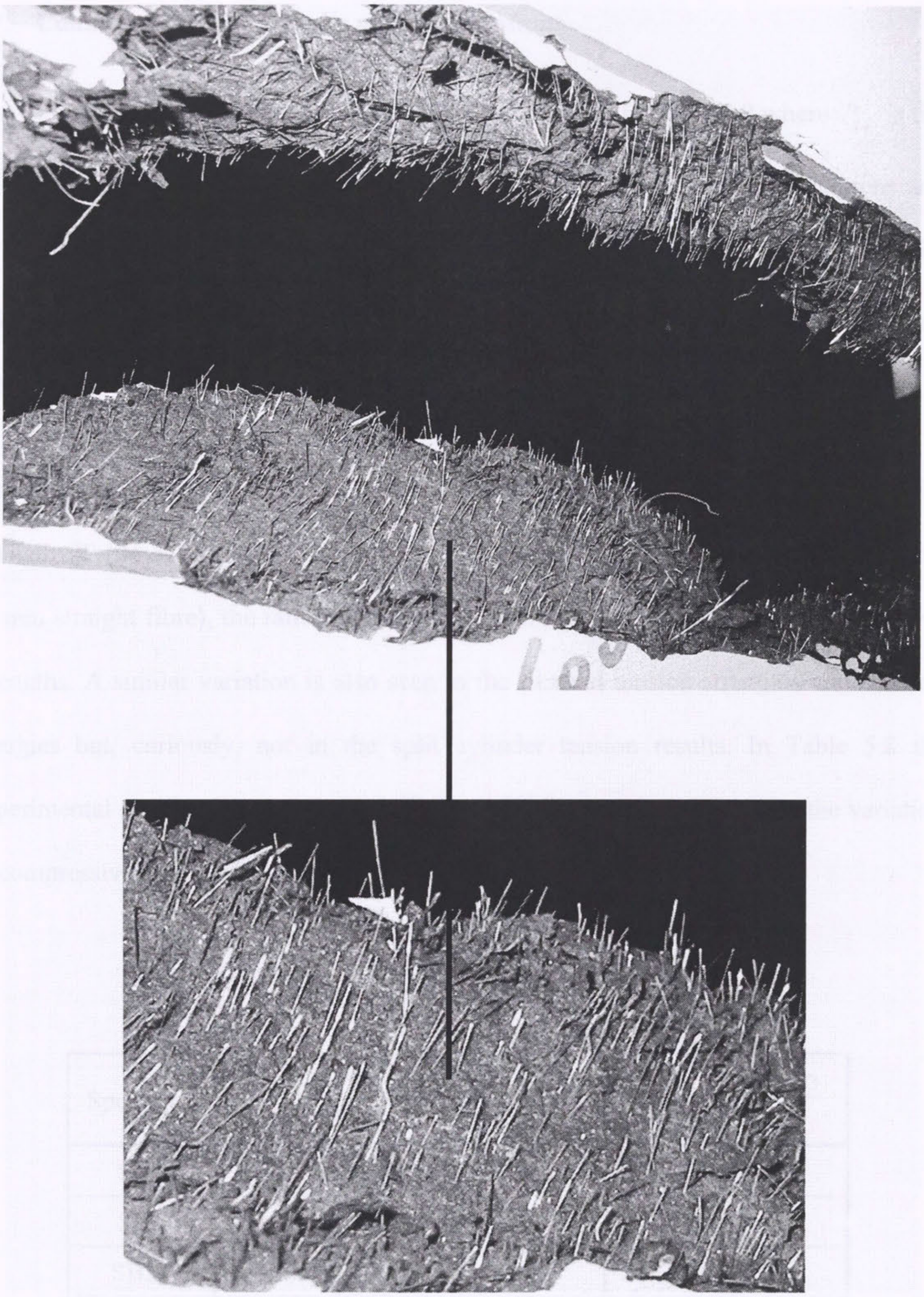

Plate 5.24 – SB7: Fibre pullout of fibre Type I (straight) and fibre pullout and fracture in fibre Type II (end-hooked) fibres.

5.7 Comments on Test Results and Observations

The experimental results of the shear tests are summarised in Table 5.8 where P_{cr} is the first shear cracking load determined by visual tracing of cracks on the specimens and P_u is the maximum or peak load recorded during the experiments. Specimen SB3 is the reference specimen and it is used to compare the ultimate shear strength of the other six specimens.

Comparing the mean cylinder compression strengths with the double punch tensile strength (Table 5.7) for specimens SB1, SB2 and SB3 (the specimens with 2.5% of 13 mm straight fibre), the ratios of tensile strength is similar to that of the compressive strengths. A similar variation is also seen in the flexural tension strengths and fracture energies but, curiously, not in the split cylinder tension results. In Table 5.8 the experimental results are compared to that for specimens SB3 corrected for the variation in compressive strength.

Table 5.8 – Experimental results on shear beams SB1 to SB7.

Specimen	P_{cr} (kN)	P_u (kN)	$\frac{P_u}{P_{cr}}$	$\frac{P_u}{P_{u,SB3}} \bullet \frac{f_{cm,SB3}}{f_{cm}}$
SB1	300	860	2.9	0.93
SB2	400	994	2.5	1.08
SB3*	300	856	2.9	1.00
SB4	300	673	2.2	0.71
SB5	400	880	2.2	0.90
SB6	250	660	2.6	0.73
SB7	350	800	2.3	0.82

Notes: * Reference specimen.

In terms of the prestressing levels, the comparison presented in Table 5.8 indicates a 15 percent variation in strength due to the effect of prestressing. In terms of the quantity of the same type of fibre, Table 5.8 shows the comparative strength of specimen SB4 (with 1.25 percent fibres) was 30 percent lower that specimen SB3 (with 2.5 percent fibres).

For the test using different fibre types, Table 5.8 shows that the failure loads were lower with increasing quantities of the 30 mm end hooked fibres and reducing quantities of 13 mm straight fibres. This indicates that fibre fracture may have had a significantly greater influence for the longer end hooked fibres than for the short straight fibres. This is further evidenced by the lower fracture energies measured in the control specimens for increasing end hooked fibre to straight fibre ratios (refer Table 5.7).

A comparison of the crack patterns (Figures 5.11 to 5.14) show all the girders behaved in a similar manner with the diagonal shear cracking initiated in the web regions of each of the shear spans. The diagonal cracks then multiplied and propagated toward the top flange and smeared across the spans with increasing load. Finally, failure resulted from tensile fracture across a single, dominant, crack or from a coalescence of cracks leading to the formation of a dominant crack.

After the shear failure of the girders, a significant load was carried by the specimen despite wide tearing cracks with all fibres having pulled out or fractured across the failure surface. For example, in Plate 5.12 it is seen that specimen SB3 at 600 kN on the descending path was severely damaged in shear. At this point, it appears that the top and bottom strands remained sufficiently anchored to act as cable structures with the girder maintaining a significant load capacity.

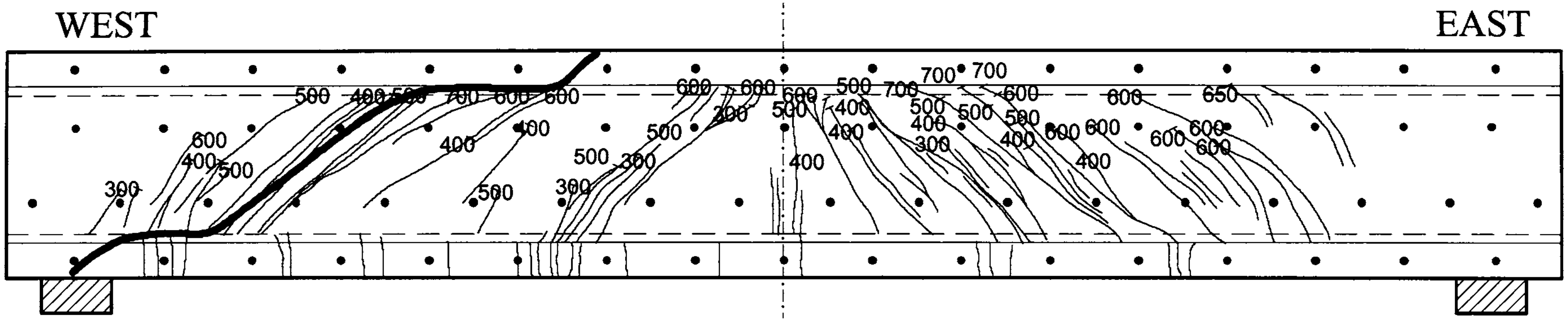

(a) Shear beam SB1

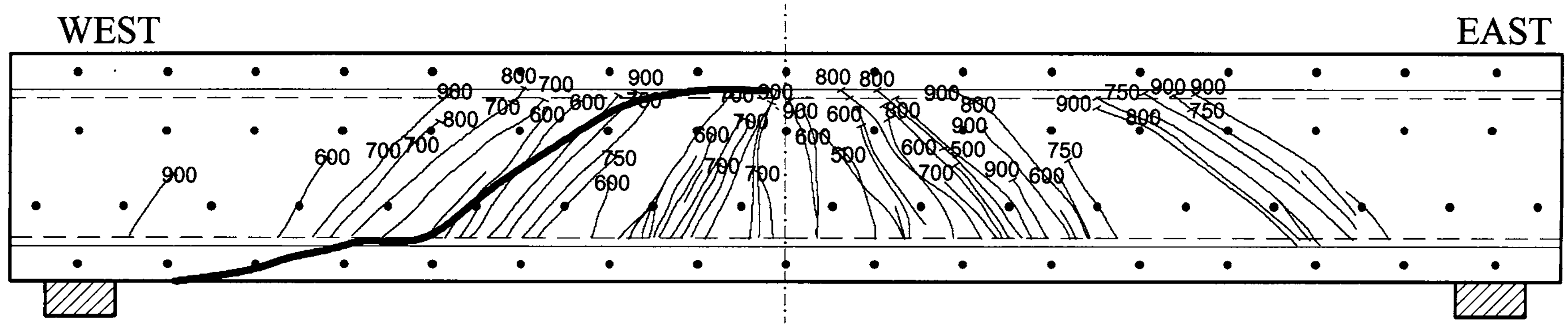

(b) Shear beam SB2

Figure 5.9 – Crack pattern for (a) shear beam SB1 and (b) shear beam SB2.

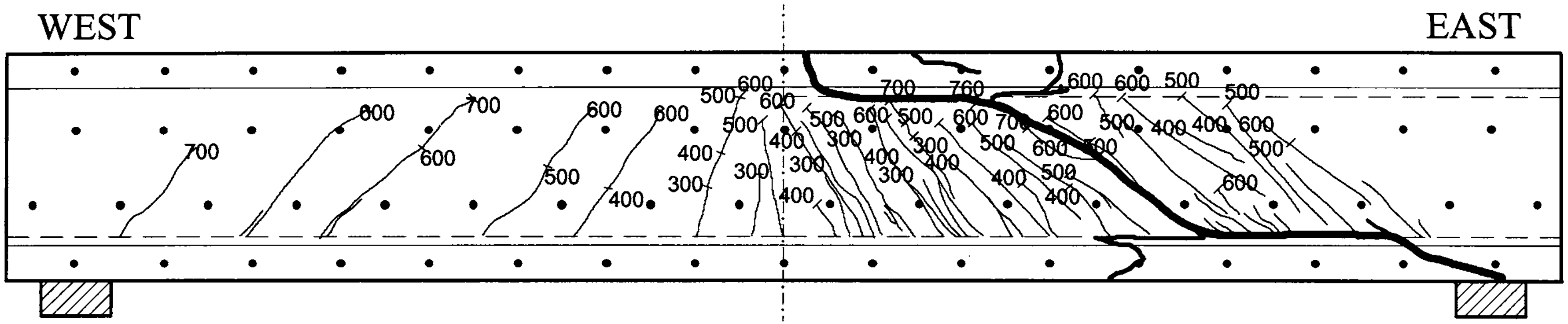

(a) Shear beam SB3

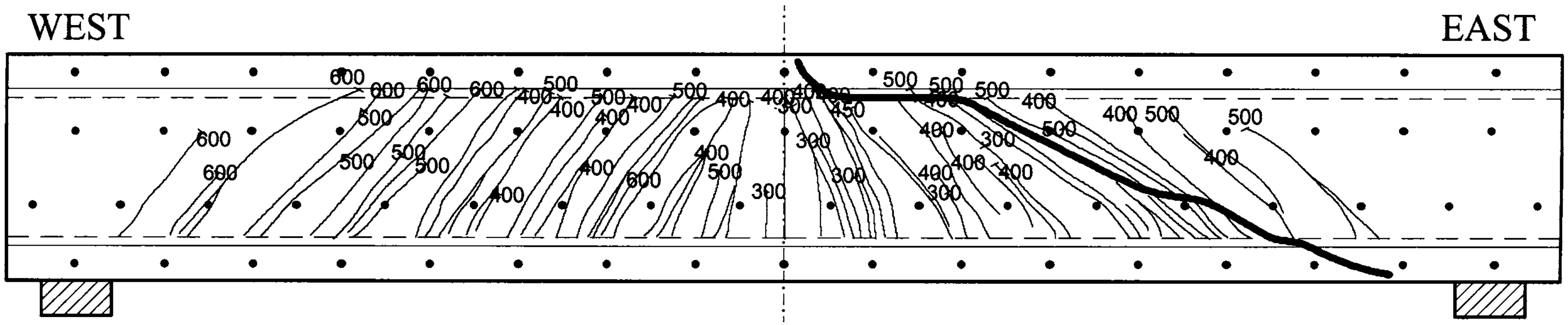

(b) Shear beam SB4

Figure 5.10 – Crack pattern for (a) shear beam SB3 and (b) shear beam SB4.

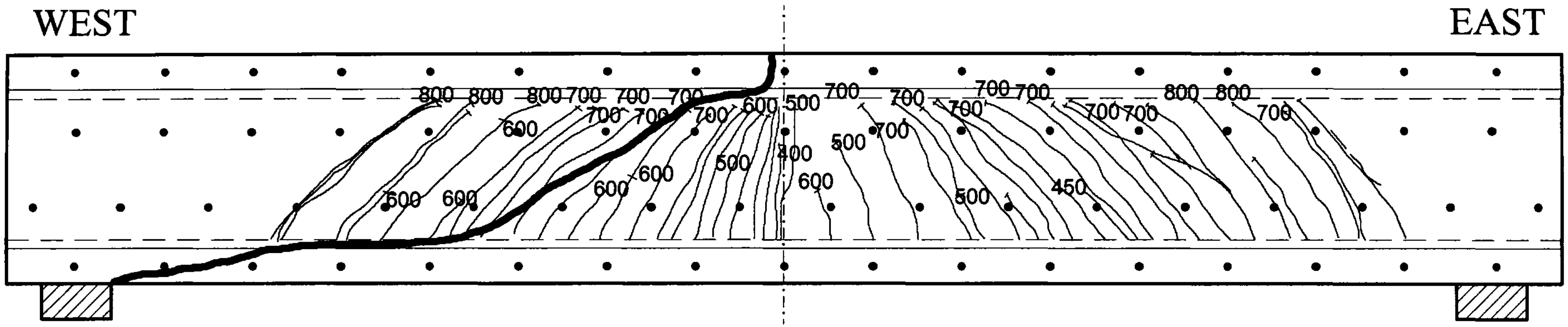

(a) Shear beam SB5

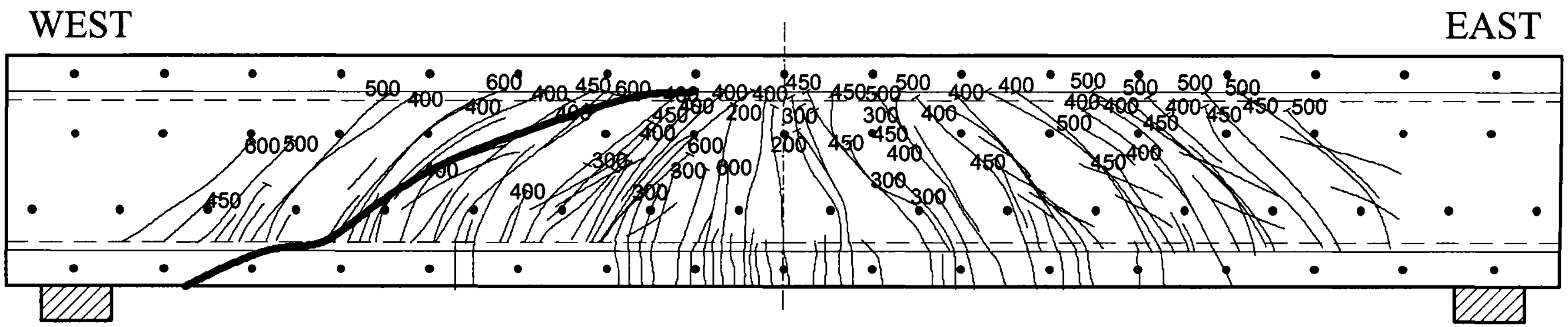

(b) Shear beam SB6

Figure 5.11 – Crack pattern for (a) shear beam SB5 and (b) shear beam SB6.

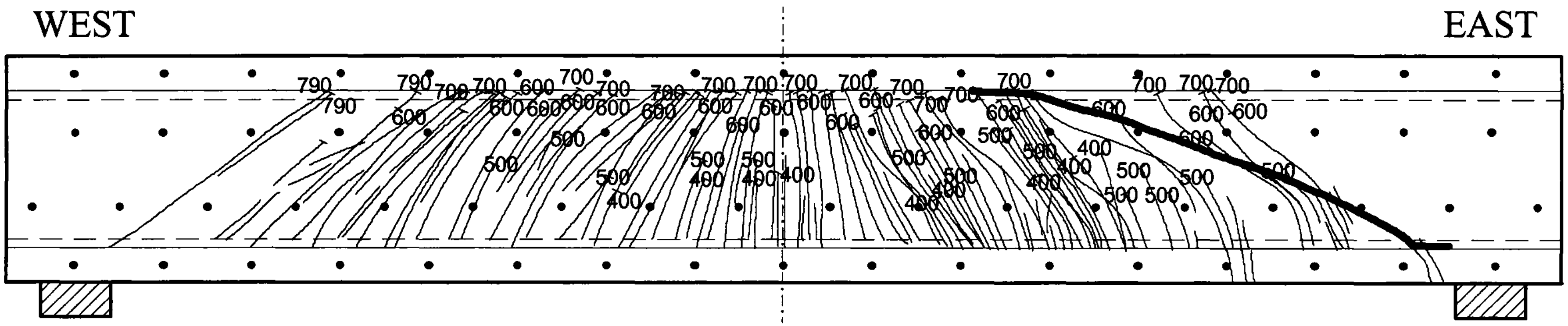

Shear beam SB7

Figure 5.12 – Crack pattern for shear beam SB7.

5.8 Analysis of Results

5.8.1 Assessment of Pre-strain

For the seven specimens, only specimen SB1 was not prestressed. For specimen SB2 to SB7 an assessment of the strain conditions in the specimens at the start of the test is needed in order to evaluate the total strains in the specimen. The change in strain as measured by the gauges may be added to the initial strains to obtain the total strain at each gauge location. The assessment of pre-strain was undertaken using 2D, plane stress linear elastic FE modelling. The material parameters used in the FE model are summarised in Table 5.9 and Figure 5.13. The FE results of the prestrains at the designated location of the Demec gauges are presented in Figure 5.14 and are given for the zero load reading of the raw data section in Appendix D. The prestrains were calculated from the displacements obtained from the nodes of the FE model located as per the Demec targets and measured over the same gauge length as that of the experiment.

Table 5.9 – Material parameters used in pre-strain assessment of beams SB2 to SB7.

Specimen Notation	SB2	SB3 to 7
Concrete		
Top flange Thickness (mm)	400	400
Top flange/web Interface thickness (mm)	225	225
Web thickness (mm)	50	50
Bottom flange/web Interface thickness (mm)	150	150
Bottom flange Thickness (mm)	250	250
E_o (GPa)	45	45
ν	0.15	0.15
Prestressed Steel		
Top steel area (mm^2)	858	858
Bottom steel area (mm^2)	1716	1716
E_p (GPa)	195	195
Strand Prestrain	0.00135	0.00269

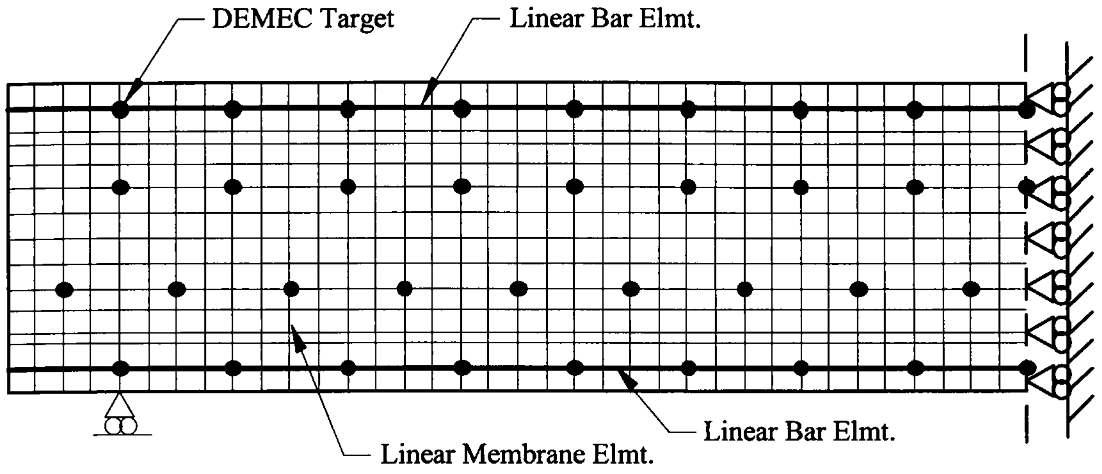

Figure 5.13 – FE mesh.

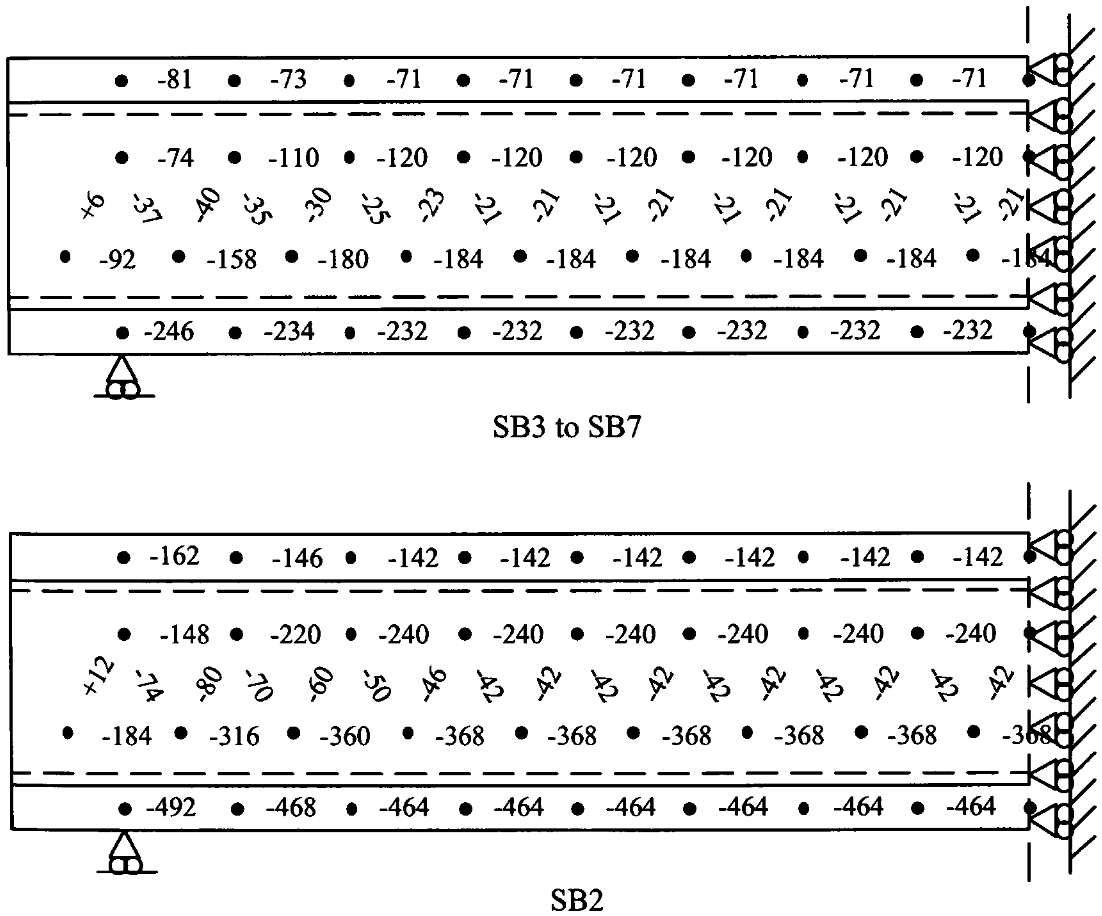

Figure 5.14 – Schematic showing assessment of pre-strain (in microstrain) for each Demec gauge length.

5.8.2 Behaviour under Load

Comparison of the crack patterns in the shear beams show that the quantity of fibres, type of fibre and prestressing level only marginally affected the shear cracking load (P_{cr}) but did have a significant influence on the rate of crack growth. After the initial cracking of the specimens, the cracks propagated at a faster rate in specimens SB2 and SB4, the specimens with the highest prestress and lowest quantity of steel fibres, respectively.

Figure 5.15 compares the load versus mid-span deflection of specimens SB1, SB2 and SB3. The figure shows that at different levels of prestressing, not only did the ultimate shear strength of the specimens increase with increasing prestress but the prestress also influenced the stiffness of the girders. Comparison of specimen SB1 (i.e. with no prestressing) and SB2 (i.e. with average 14.2 MPa prestress in the web) shows the ultimate shear strength increased by approximately 16 percent.

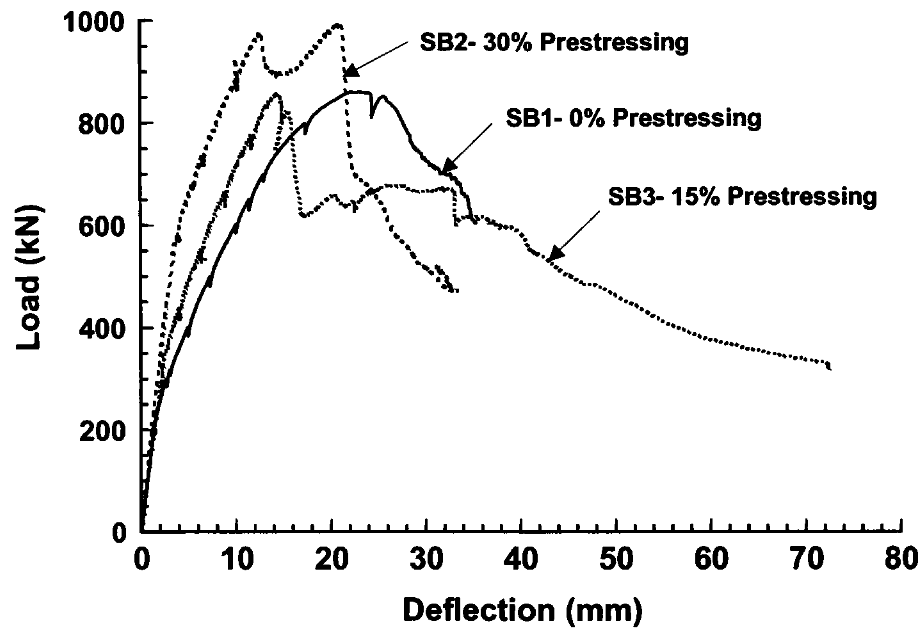

Figure 5.15 – Load versus mid-span displacement of beams SB1, SB2 and SB3.

In terms of varying the ratio of fibre quantities in the cocktail mixes, Figure 5.16 compares the load versus mid-span displacement of specimens SB3, SB5, SB6 and SB7. The ultimate shear strength and the stiffness of the specimens decreased as the quantity of the straight steel fibres was reduced. Apart from SB1 (with no prestress), all other specimens were resilient to the occurrence of second peak phenomenon. This second peak is believed to due to the second order effect due to the arching action of the beam to the supports. In general, modelling of the second order effect is outside of the scope of this thesis and will not discuss in depth.

Figure 5.17 plots the normalised shear strength of specimens SB5 to SB7 against the reference specimen SB3 and shows the replacement of a portion of straight fibres by end-hooked fibres led to a reduction in the ultimate shear strength. Figure 5.18 compares the load versus mid-span displacement of specimens SB3 and SB4 which had 2.5 percent and 1.3 percent of straight fibre, respectively. The ultimate shear strength of specimen SB4 is approximately 30 percent less than the reference specimen SB3.

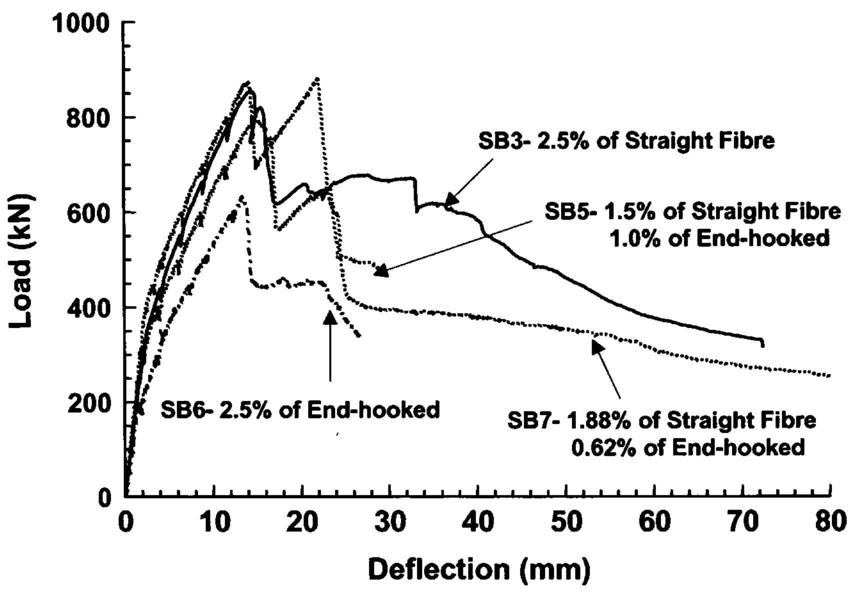

Figure 5.16 – Load versus midspan displacement of beams SB3, SB5, SB6 and SB7.

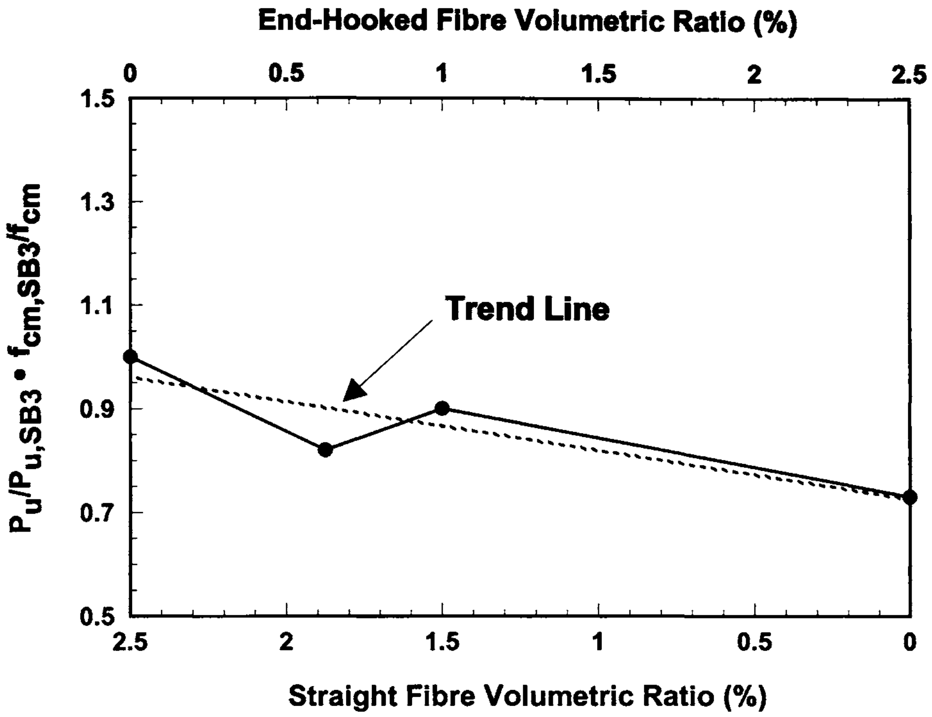

Figure 5.17 – Normalised shear strength of cocktail specimens.

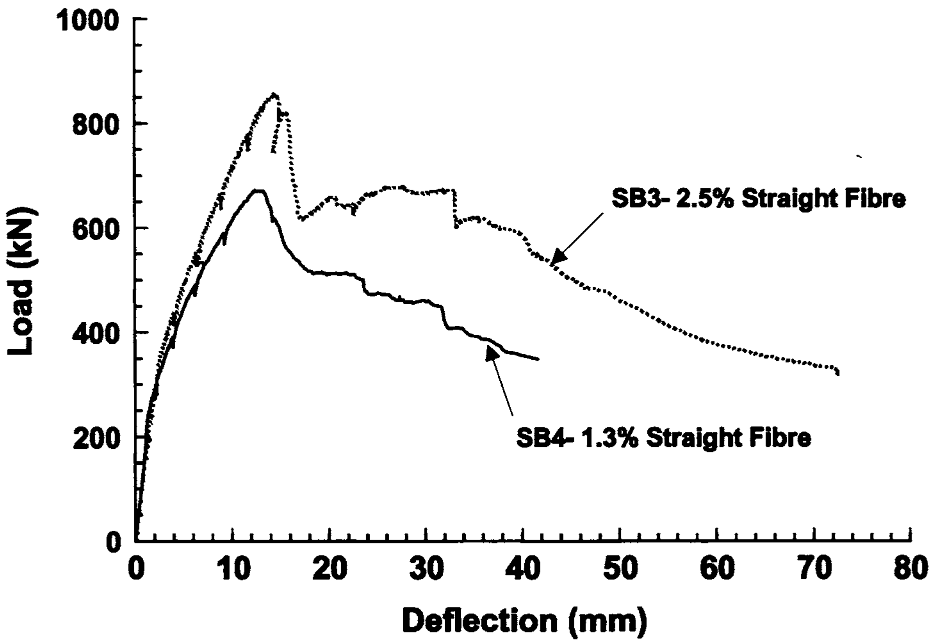

Figure 5.18 – Load versus mid-span displacement of specimens SB3 and SB4.

The horizontal strains measured at the top and bottom flanges of specimens SB1 to SB7 are presented at the end of this chapter in Figures 5.19 to 5.32. The measured compressive strains were of the order of 600 με to 800 με, which are equivalent to compressive stresses of 27 MPa to 36 MPa. This indicates that crushing of the top flanges was not an issue. The maximum tensile strains at the bottom flange were 2500 με to 4500 με. This indicates that the strands remained in the elastic range and yielding of the tensile reinforcement was also not an issue (strand yield strain, ε_{py} = 8970 με).

5.9 Conclusions

Seven reactive powder concrete prestressed girders without stirrups were tested to study the capacity of fibre reinforced RPC beams in shear. The test variables were the quantity and type of fibres and the prestress. The steel fibres used in the tests consisted of either 13 mm straight fibres and/or 30 mm end-hooked fibres. All the tested specimens had the same cross-section and were subjected to mid-point loading over a shear span of 2 metres. The shear span to effective depth ratio for the beams was 3.33.

From the experimental study the following conclusions are drawn:

I. The quantity of fibres and type of fibres used in the concrete mix does not significantly affect the cracking load but has a significant influence on the rate of crack propagation and on the failure loads.

II. At the peak load, many fine cracks had formed in the web, with the cracks well distributed through the shears spans. The failure loads were more than twice the cracking loads.

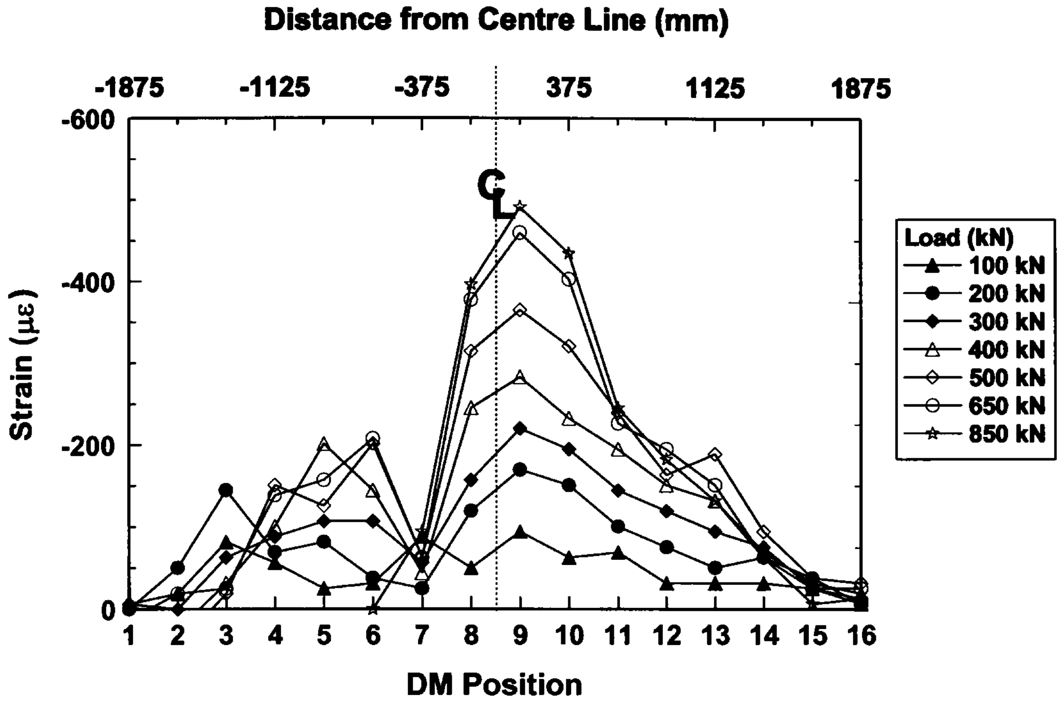

Figure 5.19 – SB1: Strains in top flange (DMs 1 to 16).

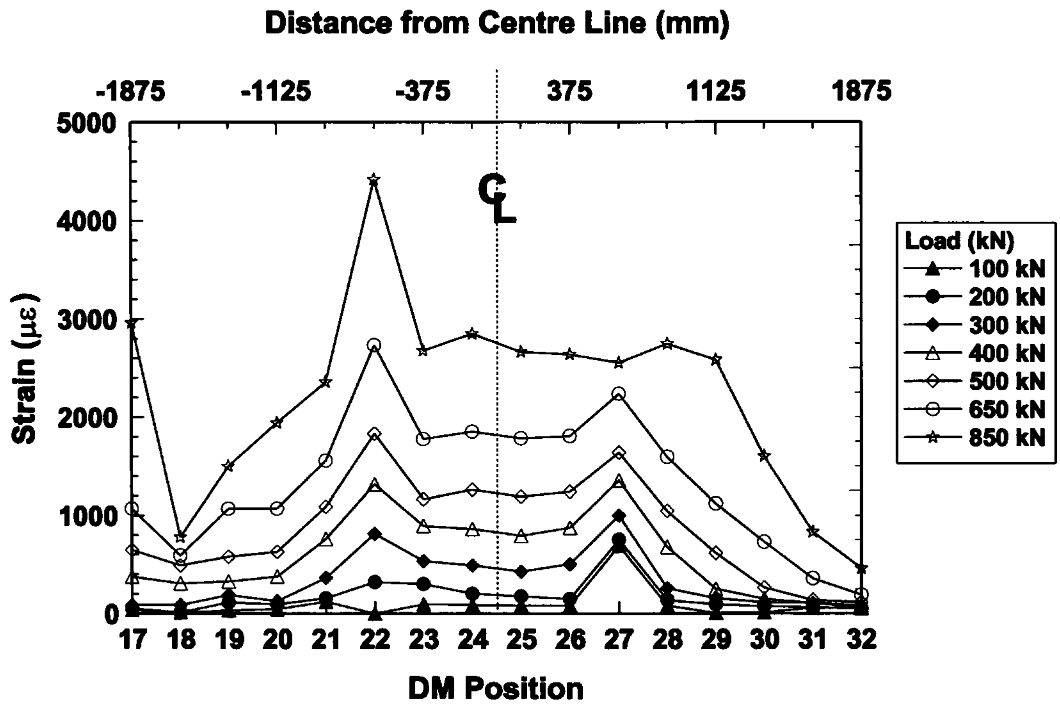

Figure 5.20 – SB1: Strains in bottom flange (DMs 17 to 32).

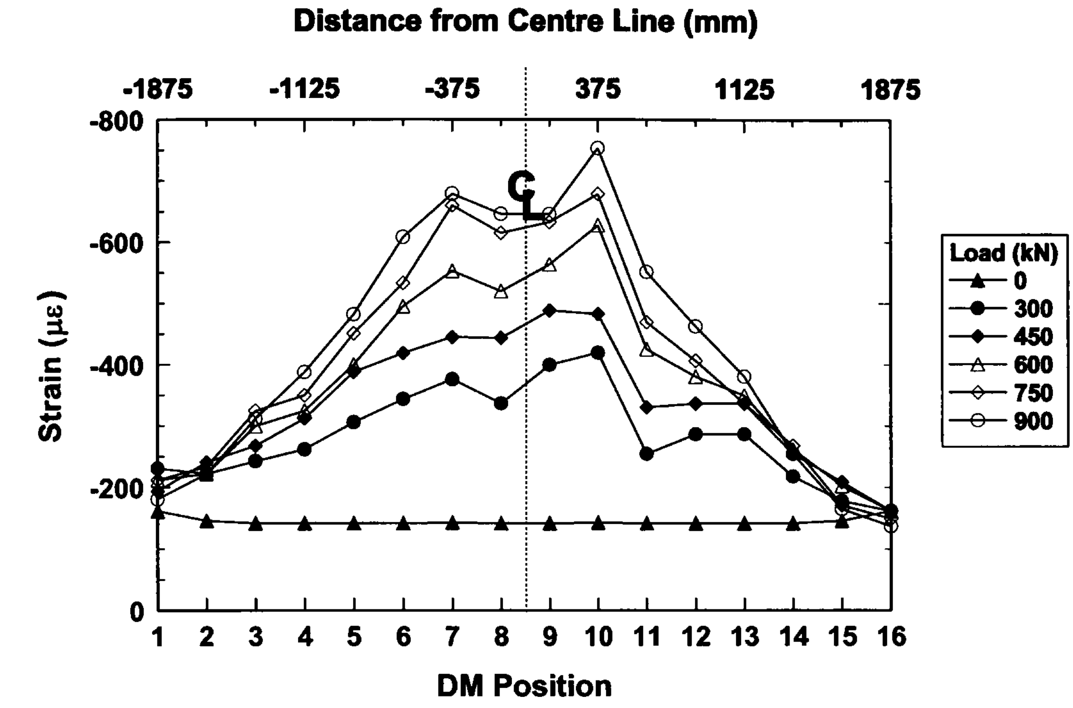

Figure 5.21 – SB2: Strains in top flange (DMs 1 to 16), includes prestrain.

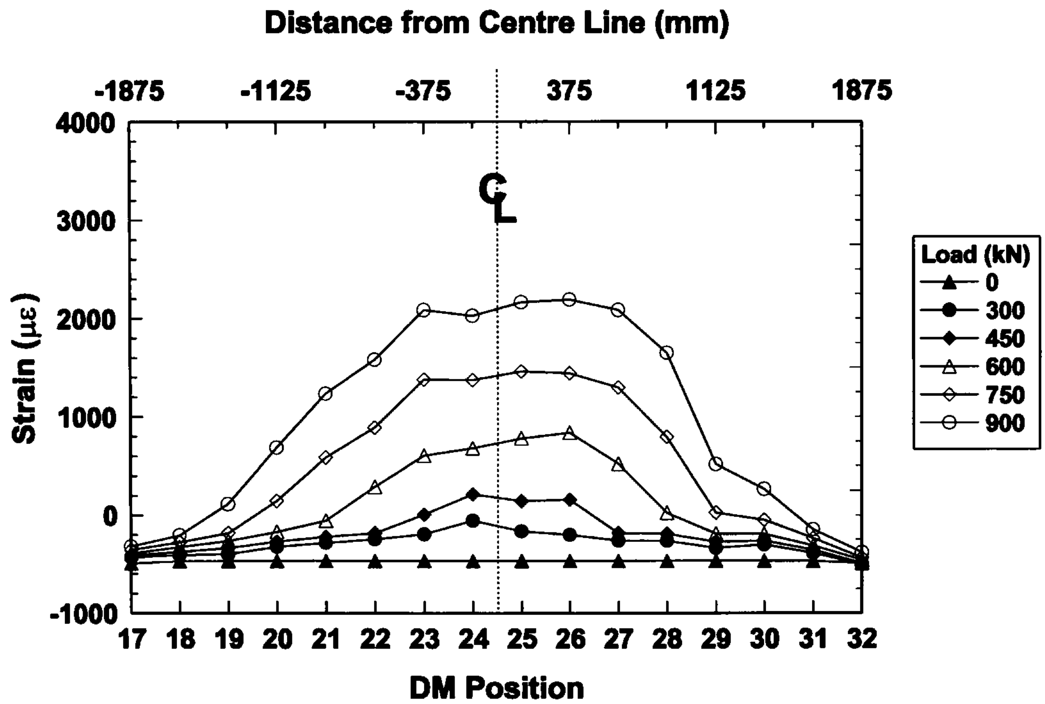

Figure 5.22 – SB2: Strains in bottom flange (DMs 17 to 32), includes prestrain.

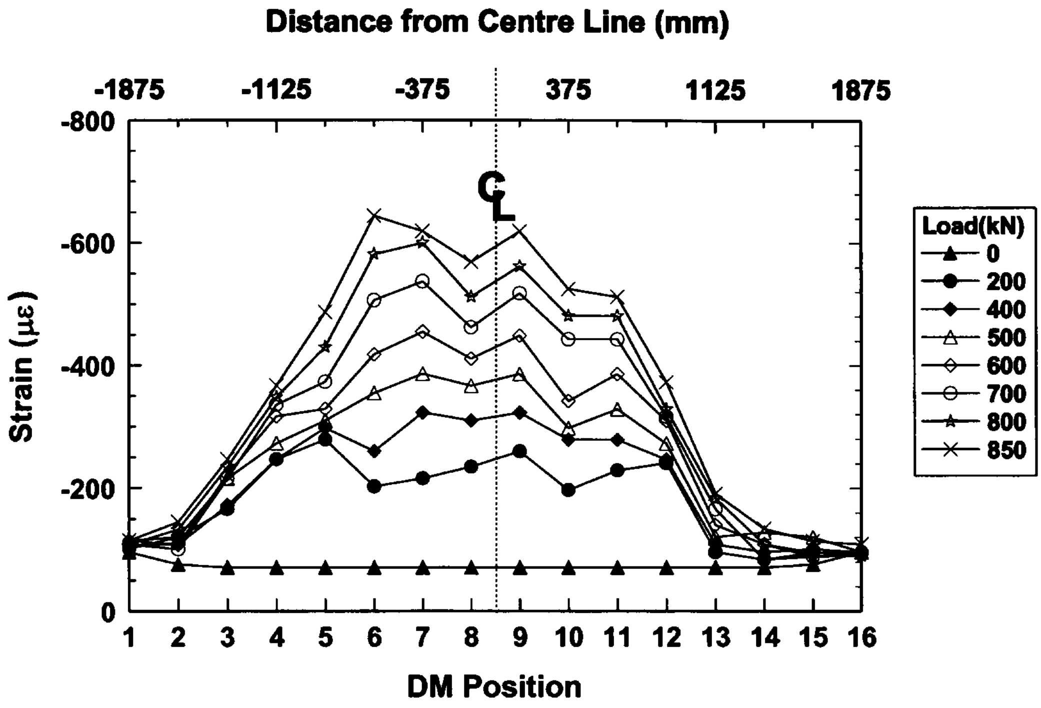

Figure 5.23 – SB3: Strains in top flange (DMs 1 to 16), includes prestrain.

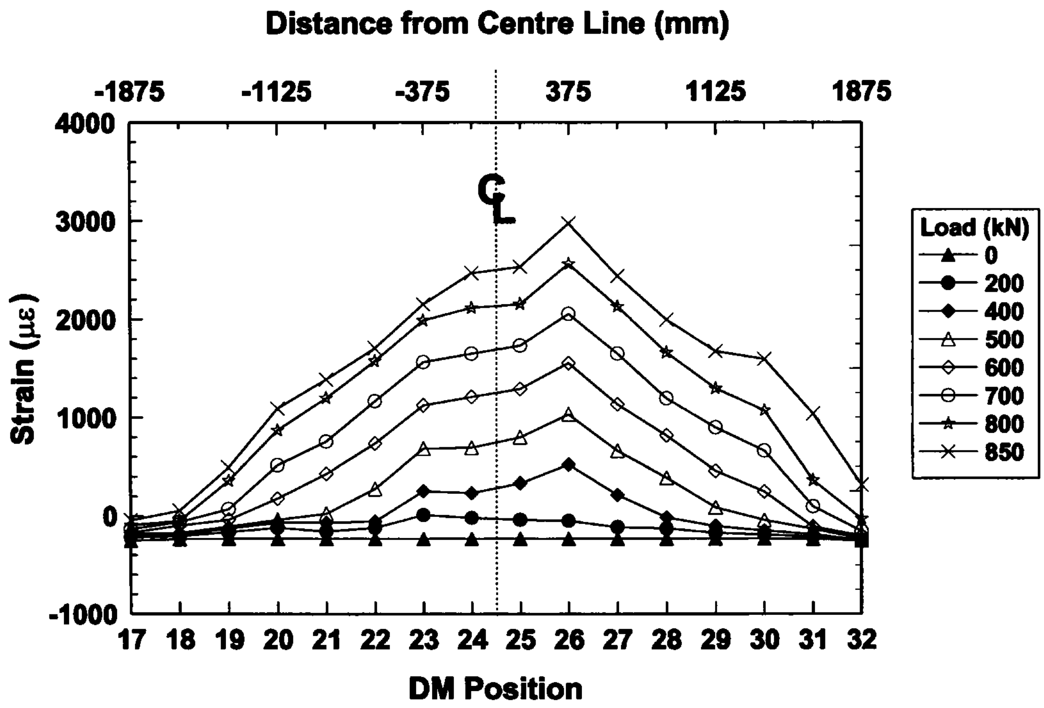

Figure 5.24 – SB3: Strains in bottom flange (DMs 17 to 32), includes prestrain.

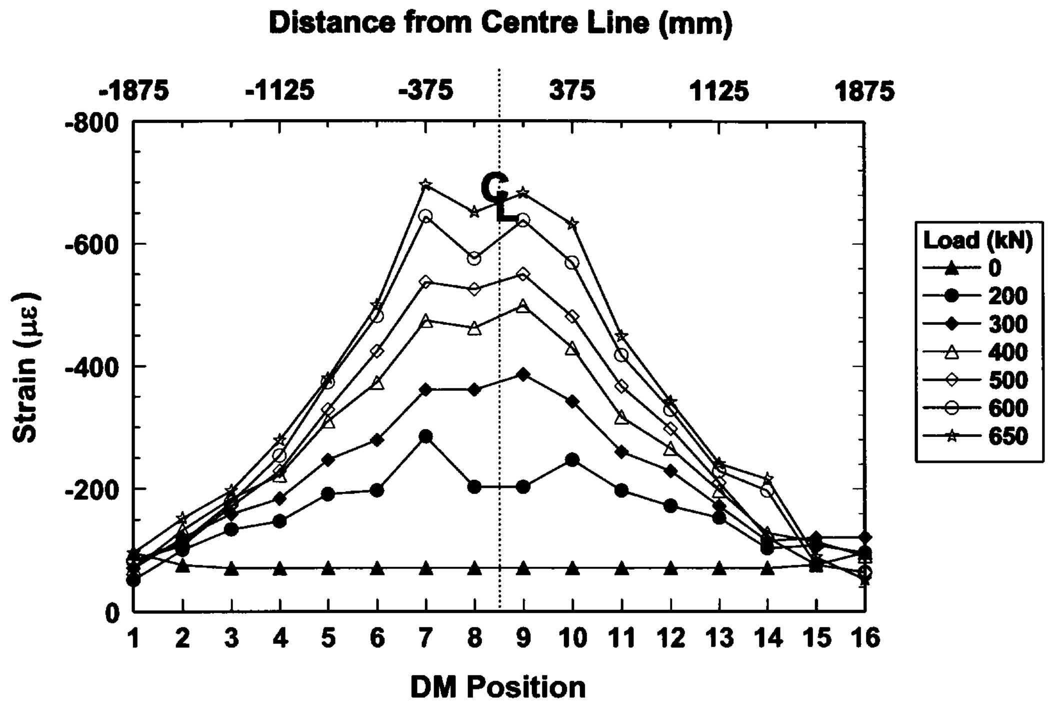

Figure 5.25 – SB4: Strains in top flange (DMs 1 to 16), includes prestrain.

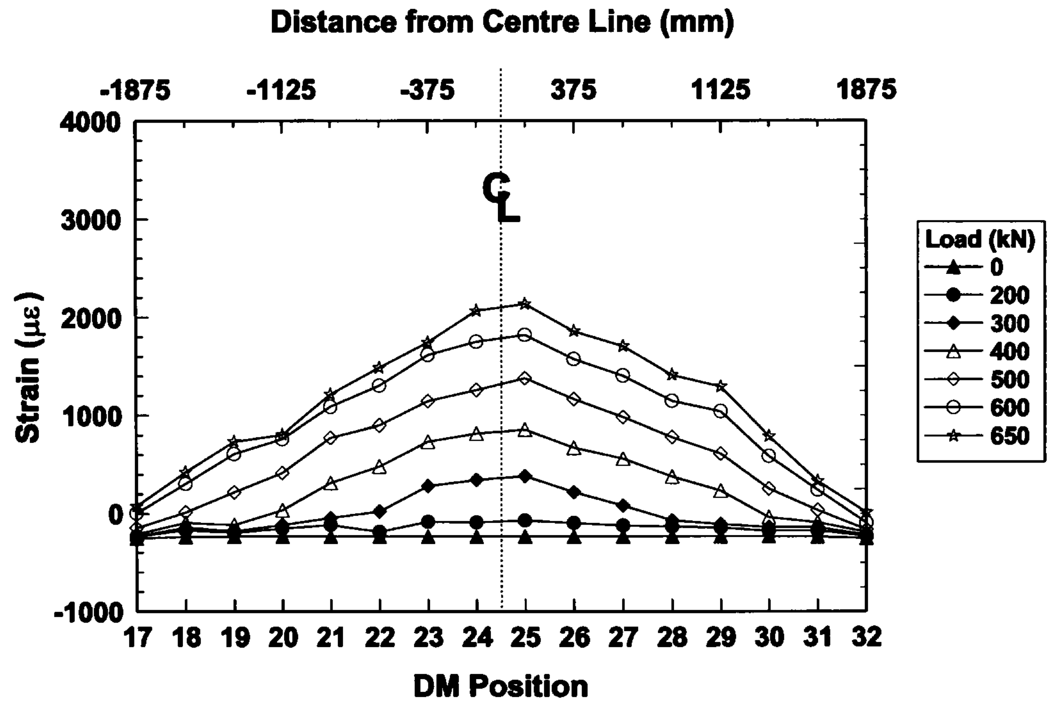

Figure 5.26 – SB4: Strains in bottom flange (DMs 17 to 32), includes prestrain.

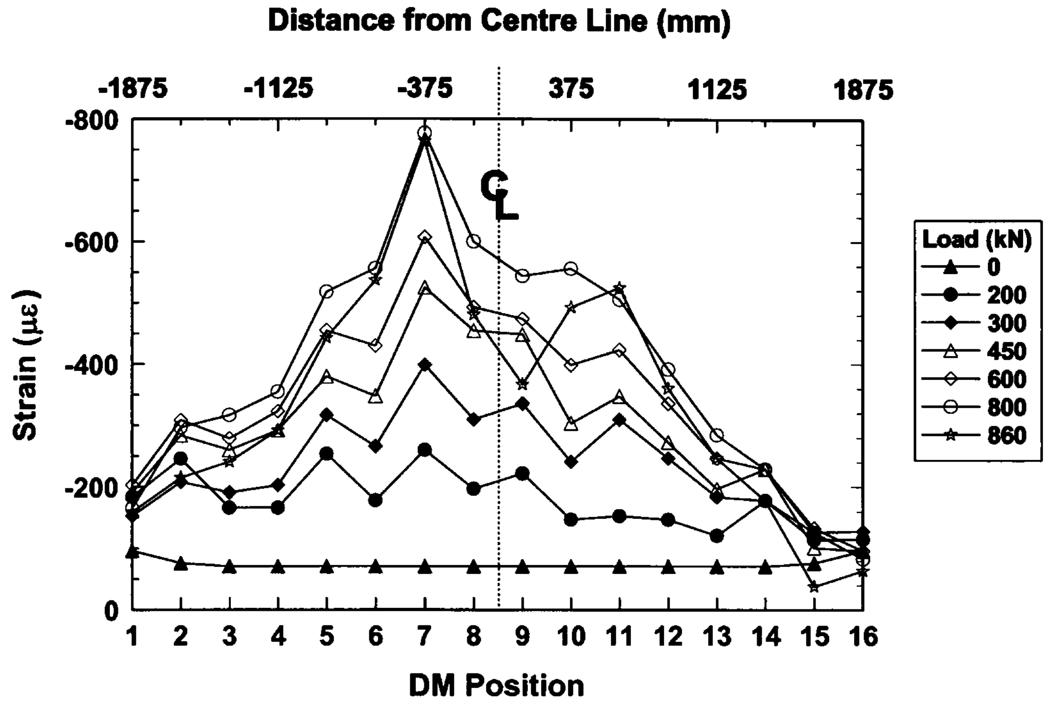

Figure 5.27 – SB5: Strains in top flange (DMs 1 to 16), includes prestrain.

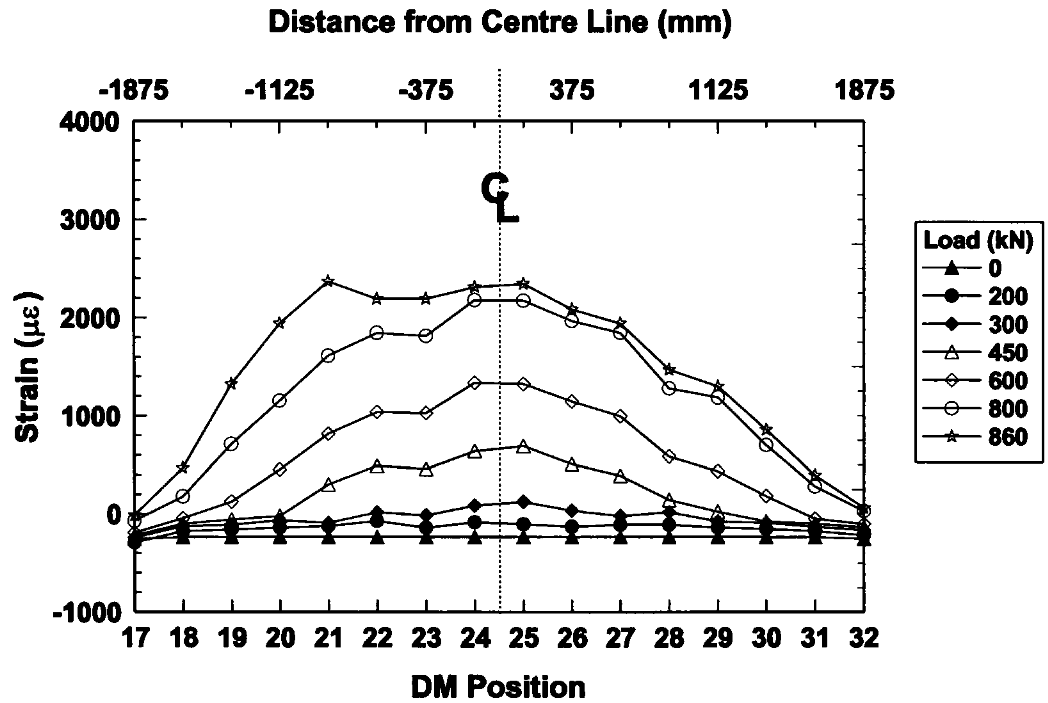

Figure 5.28 – SB5: Strains in bottom flange (DMs 17 to 32), includes prestrain.

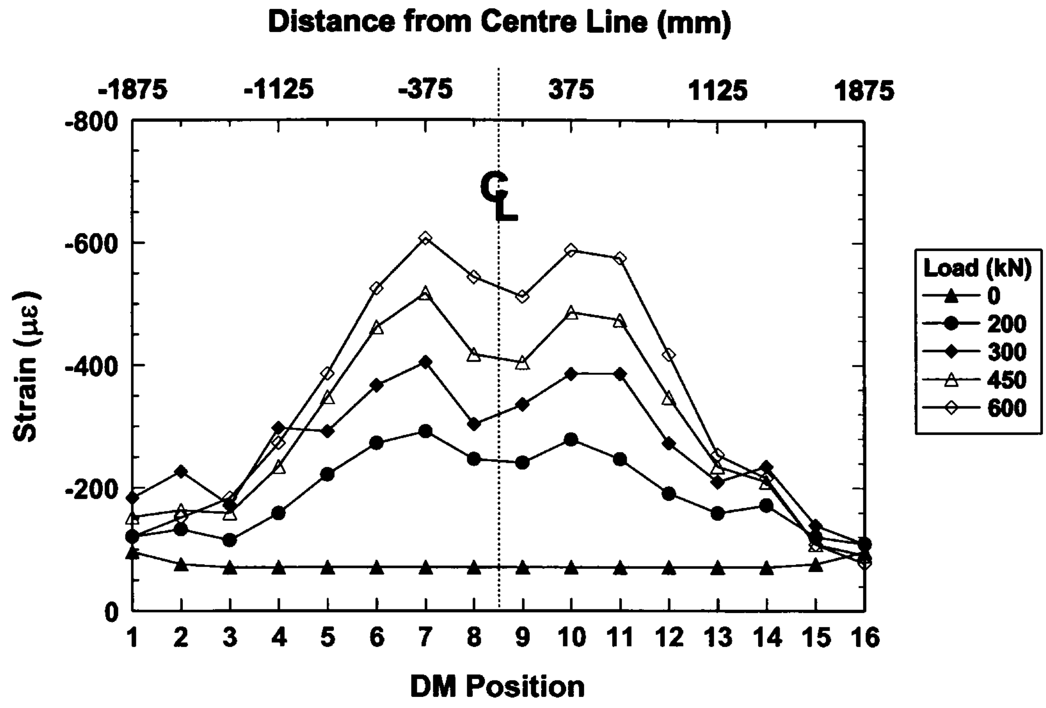

Figure 5.29 – SB6: Strains in top flange (DMs 1 to 16), includes prestrain.

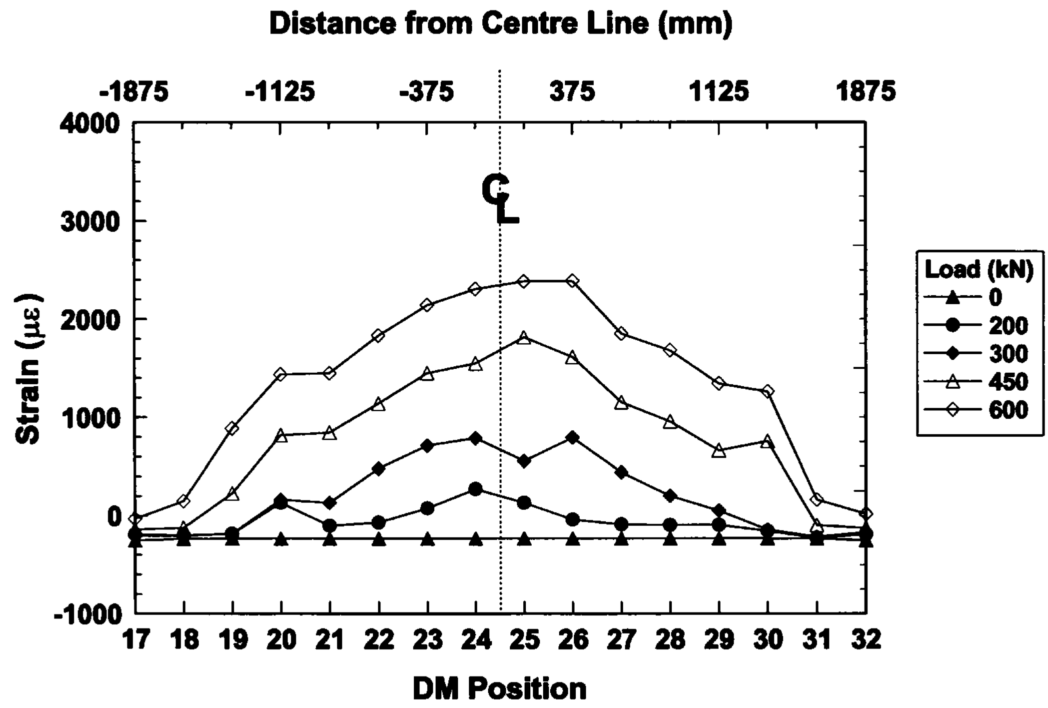

Figure 5.30 – SB6: Strains in bottom flange (DMs 17 to 32), includes prestrain.

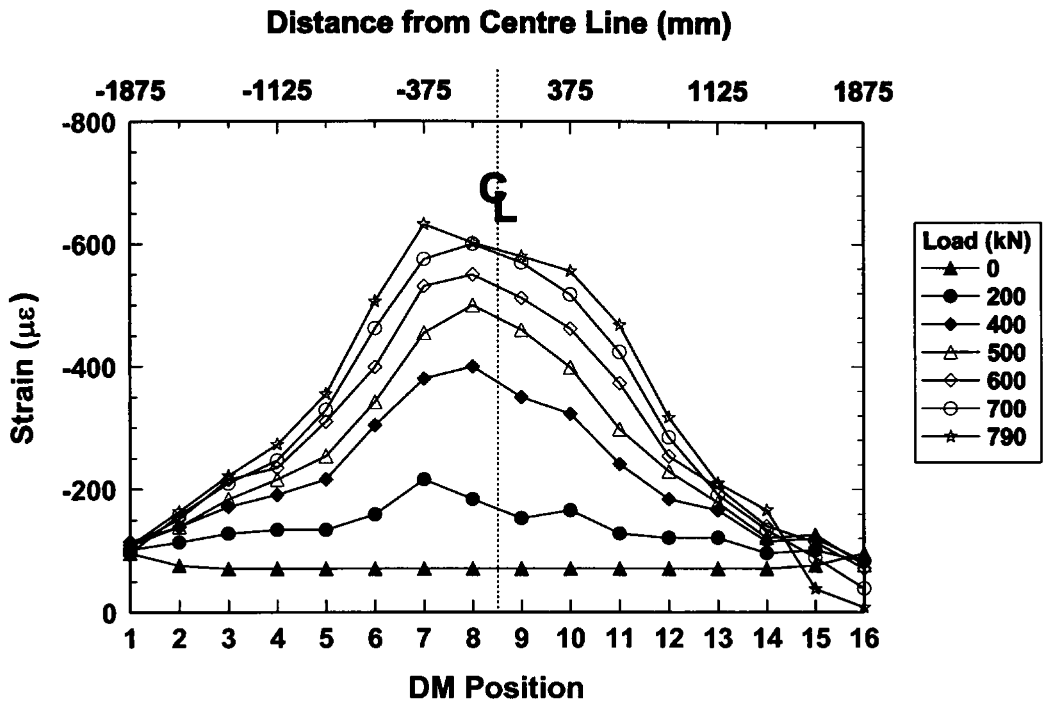

Figure 5.31 – SB7: Strains in top flange (DMs 1 to 16), includes prestrain.

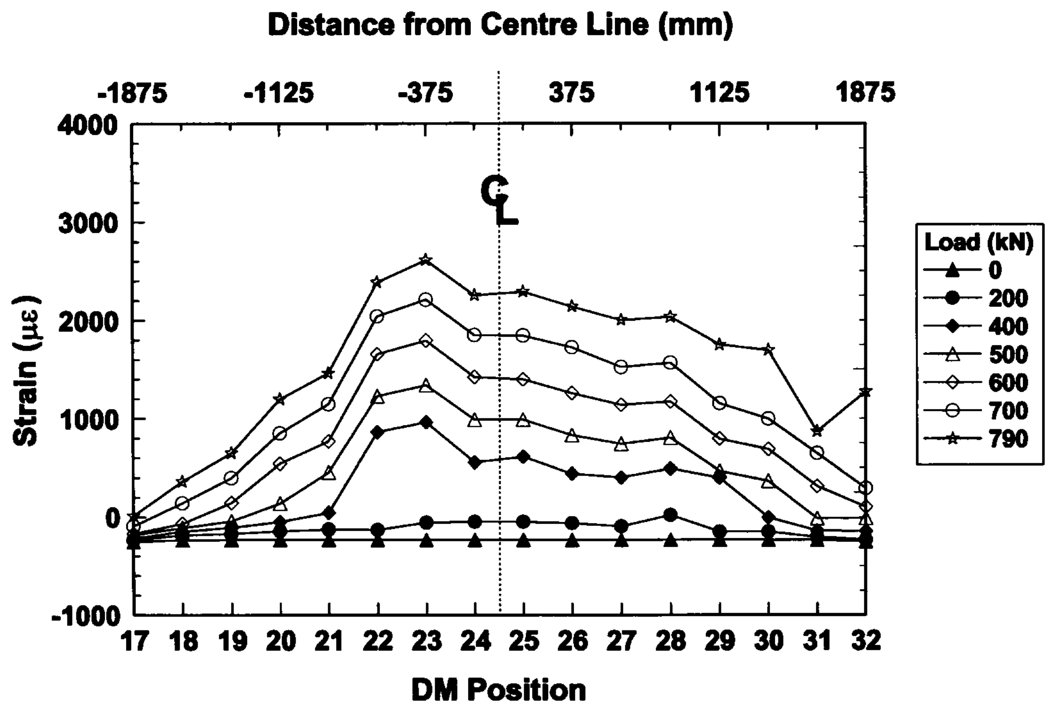

Figure 5.32 – SB7: Strains in bottom flange (DMs 17 to 32), includes prestrain.

CHAPTER 6 – VARIABLE ENGAGEMENT MODEL FOR FIBRE REINFORCED CONCRETE IN TENSION

6.1 Introduction

It is well established that for quasi-brittle materials, such as concrete, loaded in tension that localisation dominates the behaviour beyond the peak load and that this behaviour can be described by the load versus crack opening displacement (w) as shown in Figure 6.1. For plain concrete the critical crack opening displacement that is the crack opening displacement (COD) for which the stress is zero, occurs at the point where the last of the mortar-aggregate matrix bridges the macro-crack. At this point typical CODs are of the order of 0.4-0.5 mm (Petersson, 1981). In the case of fibre reinforced concrete, assuming pullout of the fibre from the matrix and that the fibre pulls out from the side with the shortest embedment, the critical COD is half the length of the fibre. This is typically one to two orders of magnitude greater than that for plain concrete.

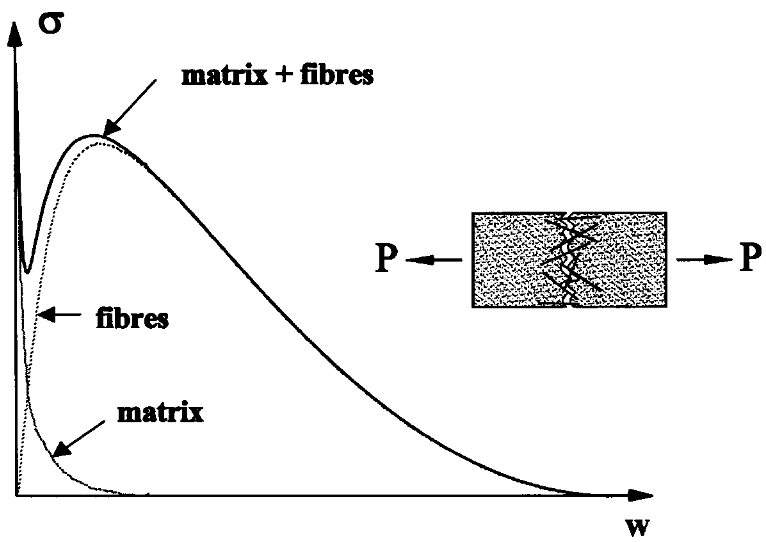

Figure 6.1 – Stress versus crack opening displacement for the matrix, fibres and the fibre matrix composite.

In addition, when a matrix crack is bridged by discontinuous, weakly bonded, fibres, further extension of the crack is inhibited as energy has to be supplied for fibre debonding, fibre pullout against interfacial tractions and deformation of any fibres lying at oblique angles to the crack surface. Figure 6.2a shows a fibre embedded at a flaw line when $w = 0$. The fibre has negligible reaction force as the bond-slip of the fibre-matrix has yet to be developed. As w increases, fibres in the fracture zone become active and deformation of fibre occurs.

Ideally, the pulley approach (Aveston and Kelly, 1973) can be used to describe the bridging phenomena of a fibre crossing a cracked surface, as depicted in Figure 6.2b, with the assumption that the matrix at the exit point of the fibre is infinitely rigid. In this case the bond-slip from the fibre on the side of the shorter embedment equals the crack opening displacement (that is w = fibre slip). According to Morton and Groves (1974), as the fibre-matrix interface has a negligible tensile strength, the fibre is able to "cut through" a part of the matrix a distance of $d_f \tan\theta$, where d_f is the fibre diameter and θ is the fibre inclination angle (refer Figure 6.2a).

Thus the description of the bridging phenomena of a fibre crossing a cracked surface may be better described using a modified pulley approach (Figure 6.2c) where the pulley is attached to the matrix via a spring. From geometrical compatibility, the COD will be larger than the bond-slip ($w >$ slip).

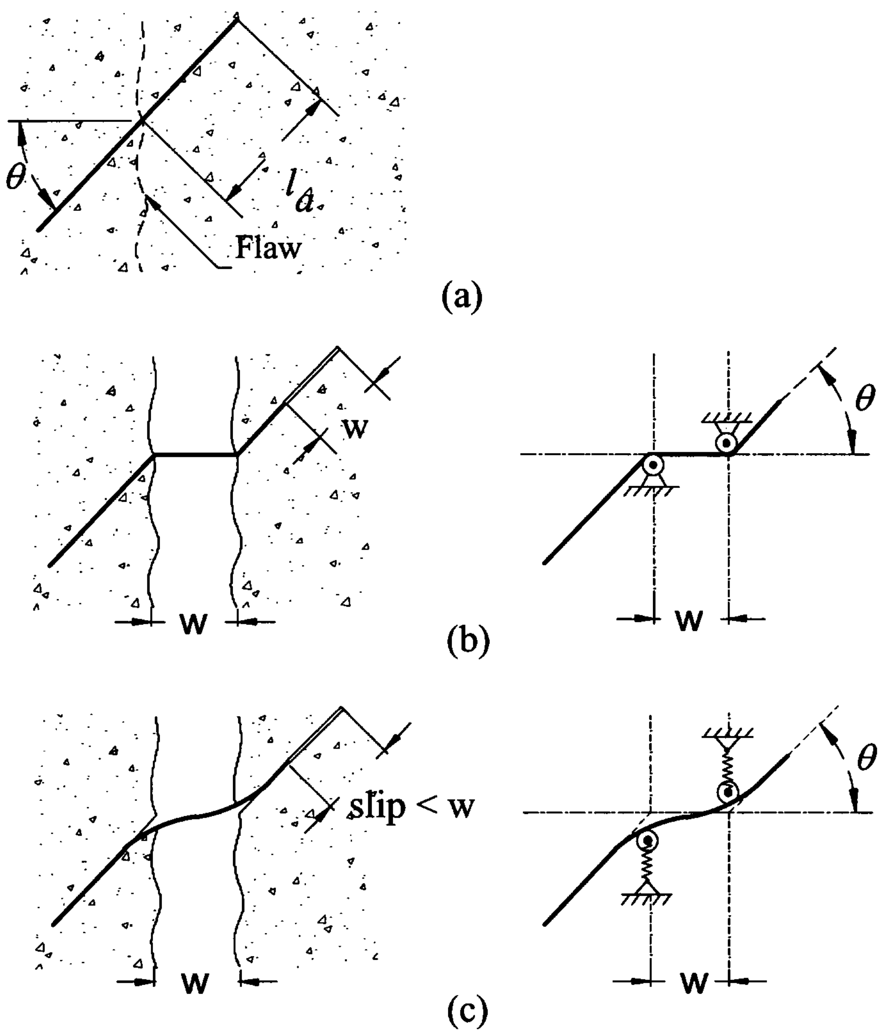

Figure 6.2 – Fibre crossing in a flaw: (a) before cracking; (b) pulley theory; (c) modified pulley theory.

In the development of the deterministic design model that follows, the following assumptions are made:

i. behaviour of a fibre reinforced composite may be obtained by a summation of the individual components. That is, the effects of each individual fibre can be summed over the failure surface to yield the overall behaviour of the composite;

ii. the geometric centres of the fibres are uniformly distributed in space and all fibres have an equal probability of being oriented in any direction;

iii. all fibres pullout from the side of the crack with the shorter embedded length while the longer side of the fibre remains rigidly embedded in the matrix;

iv. displacements due to elastic strains in the fibres are small relative to displacements resulting from slip between the fibres and the matrix;

v. the bending stiffness of a fibre is small and energy expended by bending of fibres can be neglected.

6.2 Fibre Engagement

For mechanically anchored fibres, after the adhesion between the fibres and the matrix is broken, some slip between the matrix and the fibres must occur before the anchorage is engaged. In addition, in the modified pulley theory (Figure 6.2c) the COD is greater than the slip between the fibre and the matrix albeit the difference is small. The COD for which the fibre becomes effectively engaged in the tension carrying mechanism is termed the engagement length and denoted as w_e. Assuming the engagement-length versus fibre-slip relationship can be described using a continuous function then the boundary criteria dictates that for a fibre angle of $\theta = 0$, $w_e = 0$ and the function is to be asymptotic to $\theta = \pi/2$. One such a function is

$$w_e = \alpha \tan\theta \tag{6.1}$$

where w_e is the COD at the point of engagement of the fibre and α is a material parameter obtained from fibre pullout tests for varying θ. To avoid variations along the plateau of the load versus COD curves in the determination of w_e, the fibre is taken to be effectively engaged at the point corresponding to 50 percent of the peak load. With this condition, the data of the single fibre tests of Banthia and Trottier (1994) for end-hooked and for crimped fibres are given in Figure 6.3a and 3b, respectively. For the Banthia and Trottier data, Eq. 6.1 with $\alpha = 1.24$ for the end-hooked fibres and $\alpha = 2.31$ for the crimped fibres correlates well. The model resulting from the engagement equation (Eq. 6.1) is termed the variable engagement model (VEM).

For the VEM, the force in a single fibre is

$$\begin{aligned} &w < w_e \text{ and } w > l_a: && P_f = 0 \\ &w_e < w \le l_a: && P_f = \pi\, d_f\, \tau_b\, (l_a - w) \end{aligned} \tag{6.2}$$

where d_f is the fibre diameter, l_a is the initial length of embedment of the fibre and τ_b is the mean shear stress between the fibre and the matrix measured along the remaining portion of embedded fibre $(l_a - w)$. In the analyses that follow, τ_b is taken as constant for a given fibre-matrix structure. The pullout force as determined from Eqs. 6.1 and 6.2 for the 60 mm long by 0.8 mm diameter end-hooked fibres of Banthia and Trottier (for their medium strength concrete tests, $f_{cm} = 52$ MPa) are compared to the experimental data in Figure 6.4 for various fibre angles θ. The interfacial bond shear stress is calculated from the test of $\theta = 0$ degree giving $\tau_b = 4.4$ MPa. The figure shows for fibres orientated at a high angle to the matrix, while some adhesion exists for low CODs, significant slip is needed before mechanical locking occurs.

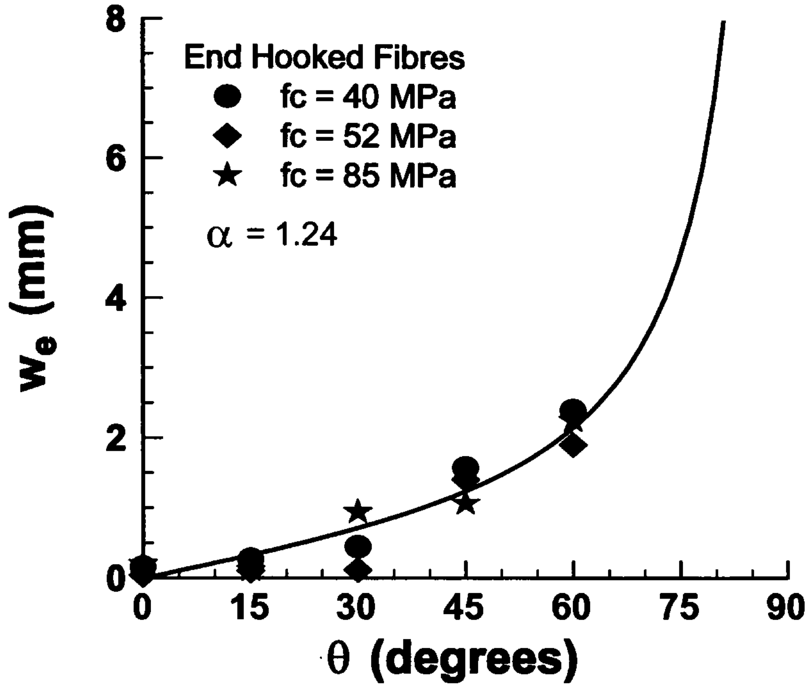

(a)

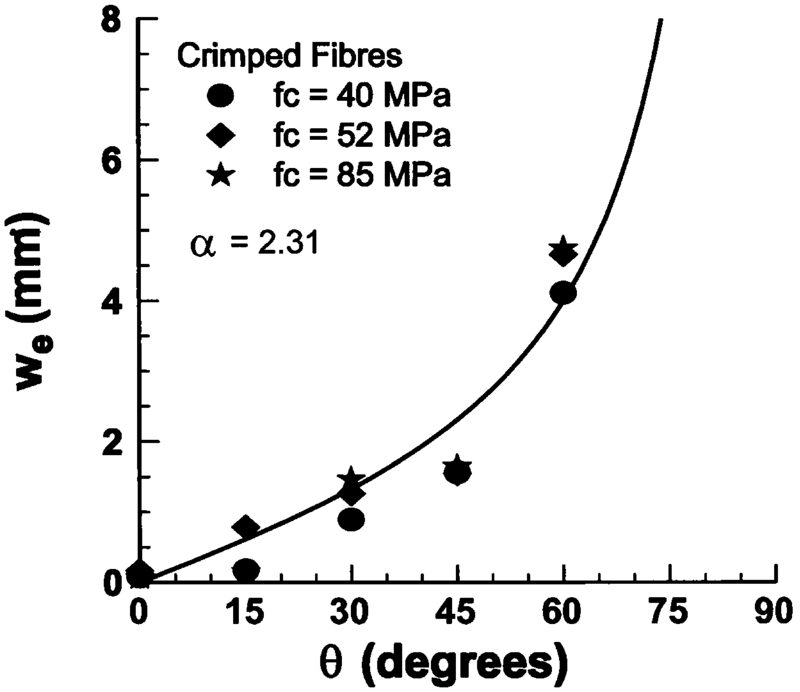

(b)

Figure 6.3 – Engagement COD versus fibre angle for Banthia and Trottier (1994) data: (a) end-hooked fibres; (b) crimped fibres.

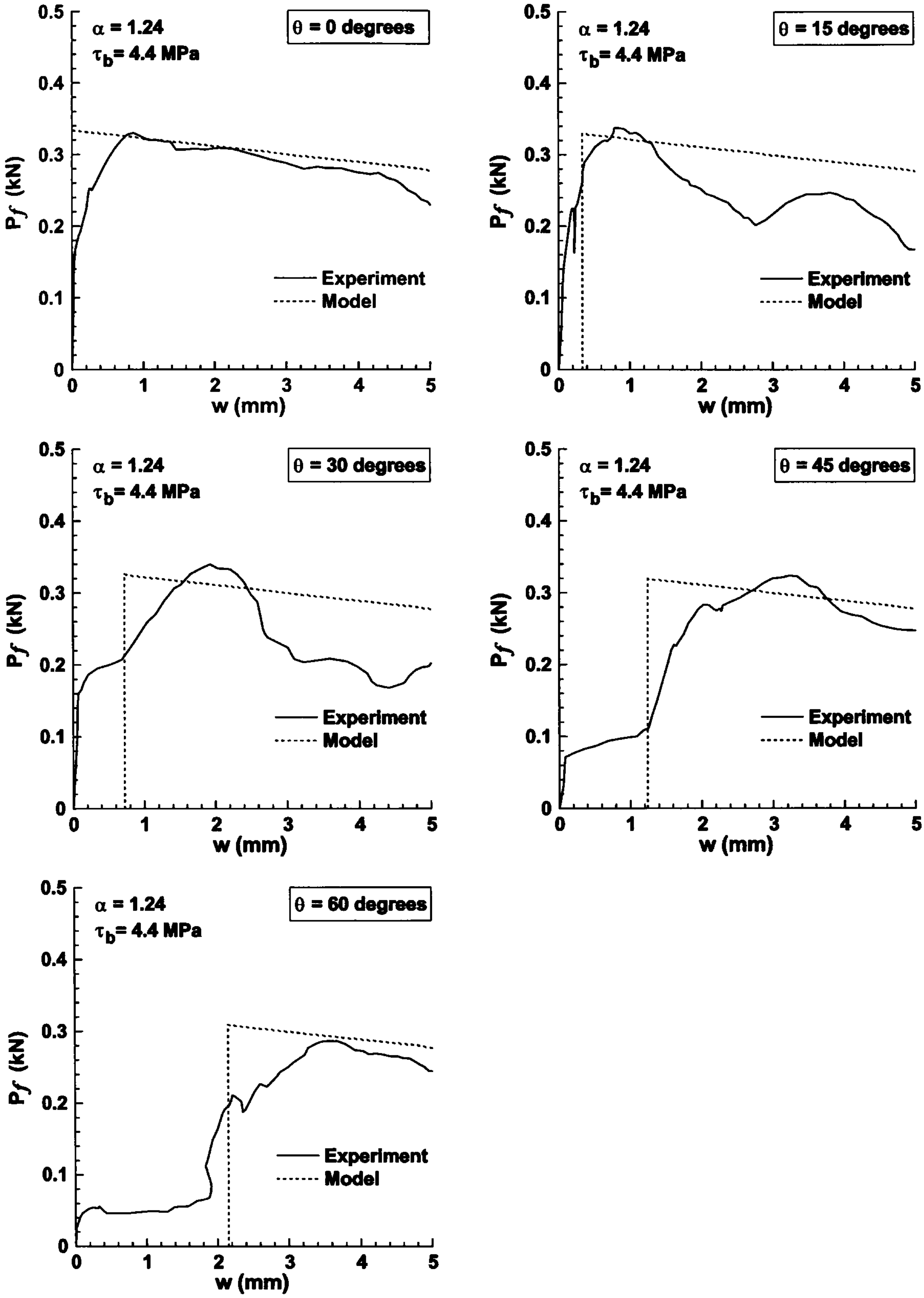

Figure 6.4 – Comparison of experimental data with base model for the data of Banthia and Trottier (1994).

6.3 Engagement Angle

Using the concept of a fibre engagement length, discussed above, we can infer that for a randomly orientated fibre composite material, cracked in tension, at any point in the load-COD path there can be defined a critical angle for which fibres are becoming active. We term θ_{crit} as the point where fibres orientated at $\theta \leq \theta_{crit}$ carry load while for fibres at $\theta > \theta_{crit}$ are yet to be engaged. From Eq. 6.1 we write

$$\theta_{crit} = \tan^{-1}(w/\alpha) \tag{6.3}$$

The model represented by Eqs. 6.1 and 6.3 shows that, for a given COD, as α increases θ_{crit} decreases and, hence, α is a material measure of the resistance to slip between the fibre and the matrix.

From Eq. 6.3 it is seen that θ_{crit} is a function of the current COD. Substituting the maximum possible fibre slip before engagement $w = l_f/2$ into Eq. 6.3 gives the limiting angle

$$\theta_{lim} = \tan^{-1}(l_f/2\alpha) \tag{6.4}$$

Whilst not all fibres at $\theta < \theta_{lim}$ may be engaged (depending on the initial embedded length, l_a), no fibres at $\theta \geq \theta_{lim}$ can ever be engaged.

6.4 Stress-COD Model Excluding Fibre Fracture

For fibres randomly orientated in three dimensions, Aveston and Kelly (1973) show that the number of fibres crossing a plane of unit area is $\rho_f/2$ where ρ_f is the volumetric ratio of fibres. For fibres of length l_f and diameter d_f passing through a cracking plane with the fibre pulling out from the side with the smaller embedded length, Marti et al. (1999) noted that for $w=0$ the average length of embedment is $l_f/4$ and that the number of bonded fibres decreases linearly with increasing COD. Rewriting Eq. 6.2 in the form

$$P_f = k\pi d_f \tau_b l_f/2 \tag{6.5}$$

gives

$$k = 0 \qquad \text{for ....} \; w < w_e \text{ and } w \geq l_a \tag{6.6a}$$

$$k = 2(l_a - w)/l_f \qquad \text{for ....} \; w_e \leq w < l_a \tag{6.6b}$$

where k is denoted as the local orientation factor.

Integrating Eq. 6.5 over a plane of unit area one obtains the tension stress

$$\sigma = K_f K_d \alpha_f \rho_f \tau_b \tag{6.7}$$

where $\alpha_f = l_f/d_f$ is the aspect ratio of the fibre, K_f is the global orientation factor and K_d is a damage factor or fibre efficiency factor.

The damage factor (K_d) in Eq. 6.7 accounts for a loss of efficiency in bond of the fibres when the region around an individual fibre is affected by the pullout of adjacent fibres. As the relative volume of fibres increases the local damage in the region bounded by $l_f/2$ from the crack (Figure 6.5) increases as the crack opens. Thus, as the volume of fibres increases the damage factor decreases. Also, for the case where fibre balling occurs the efficiency of the fibre is reduced. It can be reasonably inferred that the damage factor is a function of the quantity of fibres, fibre type, strength of the adjacent concrete-matrix and the COD. For conventional volumes of fibres used in practice and where no fibre balling occurs, K_d may be taken as unity.

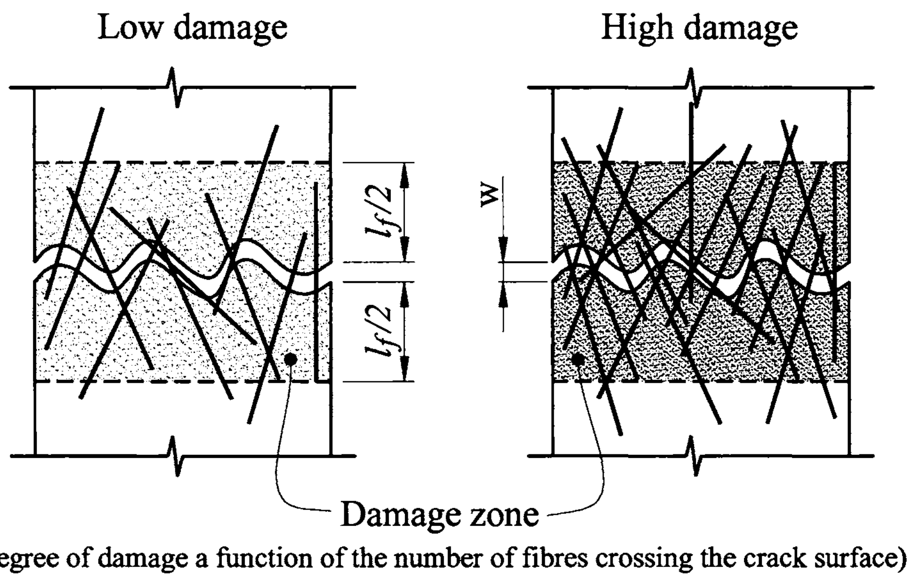

Figure 6.5 – Damage in concrete-matrix due to fibre pullout in the vicinity of a crack.

Various values of K_f have been proposed in the literature. The orientation factor can be determined by probability and is affected by the shape of the domain over which the orientation is considered. In Table 6.1 various values of K_f as defined by different researchers are listed. Taking all fibres as effectively engaged upon cracking of the matrix, Marti et al. (1999) showed that, in general, $K_f = 0.5\left(1 - 2w/l_f\right)^2$ while at the point of initial cracking $K_f = 1/2$. In the model adopted by Foster (2001) where only fibres at $0 \le \theta \le \pi/3$ were considered effective at the point of matrix cracking, $K_f = 3/8$. Using the fibre engagement model described by Eqs. 6.1 and 6.2 one obtains

$$K_f = \frac{1}{N}\sum_{i=1}^{N} k_i \tag{6.8}$$

where N is the number of fibres crossing a plane of unit area and k_i is the local orientation factor for the *i-th* fibre. Alternatively, by Eq. 6.3 we write

$$K_f = \lim_{N \to \infty} \frac{1}{N}\left\{\sum_{0}^{\theta_{crit}} k(w) + \sum_{\theta_{crit}}^{\pi/2} k(w)\right\} = \lim_{N \to \infty} \frac{1}{N}\left\{\sum_{0}^{\theta_{crit}} k(w)\right\} \tag{6.9}$$

Given a random distribution of fibres with equal probability that any given fibre crossing a crack has a shorter embedded length of between zero and $l_f/2$, the average value of the local orientation factor for all engaged fibres is

$$k_{ave} = \frac{1}{2} - \frac{w}{l_f} \tag{6.10}$$

Table 6.1 – Orientation factors (updated from Ganeshalingam et al., 1981).

Authors	K_f *	For 3D randomly orientated fibres
Romualdi and Mandel (1964)	$K_f = \dfrac{\int_0^{\pi/2}\int_0^{\pi/2} \cos\varphi \cos\psi \, d\varphi \, d\psi}{\int_0^{\pi/2}\int_0^{\pi/2} d\varphi \, d\psi}$	0.405
Parimi et al. (1973)	$K_f = \dfrac{\int_0^{\pi/2} \cos\theta \, d\theta}{\int_0^{\pi/2} d\theta}$	0.637
Aveston and Kelly (1973)	$K_f = \int_0^{\pi/2} \sin\theta \cos\theta \, d\theta$	0.5
Pakotiprapha (1976)	$K_f = \dfrac{\int_0^{\psi}\int_0^{\varphi} \cos^2\varphi \cos^2\psi \, d\varphi \, d\psi}{\int_0^{\psi}\int_0^{\varphi} d\varphi \, d\psi}$	0.25
Foster (2001)	$K_f = \int_0^{\pi/3} \sin\theta \cos\theta \, d\theta$	0.375
This study	Given by Eq. 6.12	Variable ≤ 0.5

* Note: see Figure 6.6 for fibre orientation definitions.

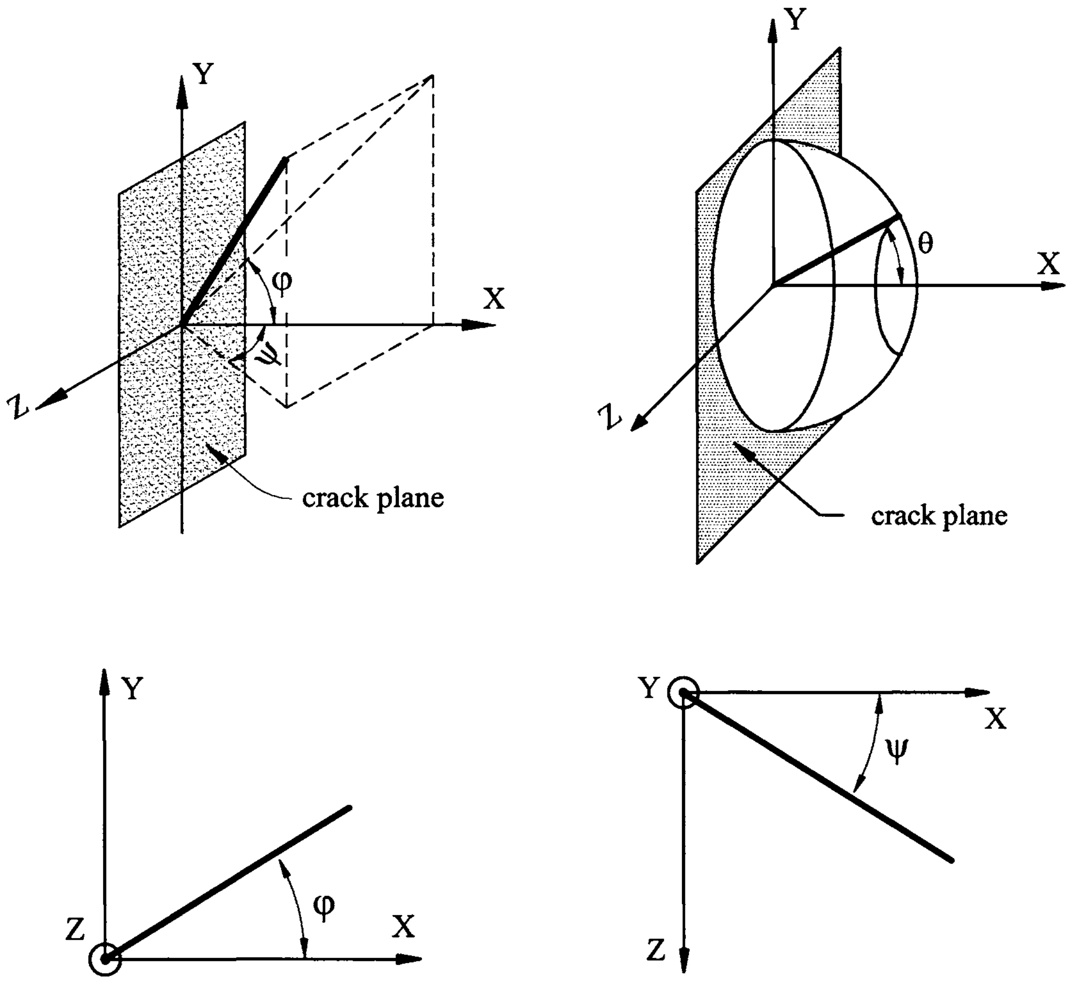

Figure 6.6 – Fibre orientation definitions (ref. Table 6.1).

Further, if all fibre orientations have equal probability and noting that the proportion of bonded fibres decreases linearly with increasing w, then from Eq. 6.9 we write

$$K_f = \frac{2\theta_{crit}\, k_{ave}}{\pi} \bullet \left(1 - \frac{2w}{l_f}\right) \tag{6.11}$$

where the term in parenthesis in Eq. 6.11 is the proportion of fibres that have not pulled out from the matrix for a given COD. Substituting Eqs. 6.3 and 6.10 into 6.11 we find

$$K_f = \frac{\tan^{-1}(w/\alpha)}{\pi}\left(1 - \frac{2w}{l_f}\right)^2 \tag{6.12}$$

Comparing Eq. 6.12 with that of Marti et al. (1999) it is seen that the proposed relationship for K_f approaches that of Marti et al. for $\alpha \to 0$. In Figure 6.7, Eq. 6.12 is plotted for varying α for a fibre length of $l_f = 60\,\text{mm}$. For $\alpha = 0.5$ the peak stress obtained from the fibres is 74 percent of that when all the fibres are assumed engaged at first cracking and occurs at $2w/l_f = 0.074$.

The fracture energy provided by the fibre contribution is calculated by integrating Eq. 6.7 over the domain $w = 0$ to $w = l_f/2$ and gives

$$G_F = \int_0^{l_f/2} \sigma \, dw = K_d \frac{\rho_f \tau_b \alpha_f}{6\pi}[A + B] \tag{6.13a}$$

with

$$A = \theta_{\lim} l_f - 3\,\theta_{\lim} l_f \cot^2(\theta_{\lim}) \tag{6.13b}$$

$$B = 5\,\alpha + 2\,\alpha\,\ln(\cos\theta_{\lim})\left(3 - \cot^2\theta_{\lim}\right) \tag{6.13c}$$

The total fracture energy is the sum of the fibre contribution (given by Eq. 6.13) and that of the matrix. For typical volumes of steel fibres the matrix fracture energy contribution is small relative to that of the fibre and can be neglected. This may not be the case for smaller, finer, glass fibres.

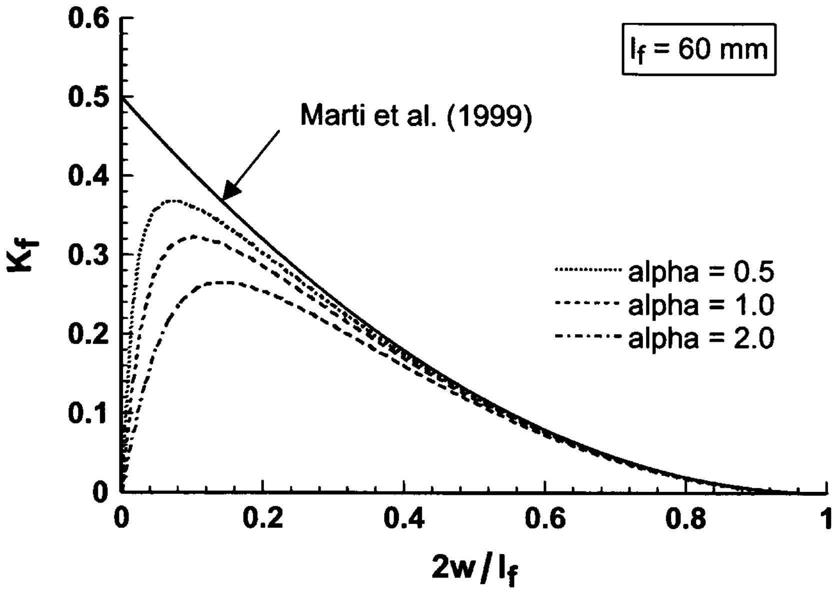

Figure 6.7 – Global fibre embedment parameter (K_f) versus crack opening displacement for $l_f = 60$ mm.

In the formulation of Eq. 6.12 it was assumed that all fibres are pulled out from the matrix and there is no fibre fracture. Thus, Eq. 6.12 applies provided that

$$l_f < l_c = \frac{d_f}{2}\frac{\sigma_{fu}}{\tau_b} \tag{6.14}$$

where l_c is a critical fibre length and σ_{fu} is the ultimate tensile strength of the fibre. If the inequality of Eq. 6.14 is violated then a portion of the fibres will fracture and Eq. 6.12 does not apply.

6.5 Stress-COD Model Including Fibre Fracture (excluding bending)

Assuming a constant bond shear stress along the fibre length then, by force equilibrium, any arbitrarily orientated fibre will fracture if

$$l_a \geq \frac{d_f}{4}\frac{\sigma_{fu}}{\tau_b} + w_e \tag{6.15}$$

For a given COD (w) the global orientation factor is given by

$$K_f = \left[\frac{2}{\pi}\cdot\frac{1}{l_f/2-w}\int_0^{\theta_{crit}}\int_w^{l_{a,crit}} k(l_a,\theta)\,dl_a\,d\theta\right]\cdot\left(1-\frac{2w}{l_f}\right) \tag{6.16}$$

where $l_{a,crit}$ is the critical fibre embedment length for fracture and is given by

$$l_{a,crit} = \min\left(l_c/2 + w_e\ ,\ l_f/2\right) \tag{6.17}$$

Substituting Eq. 6.6 into Eq. 6.16 gives

$$K_f = \frac{4}{\pi\, l_f^{\,2}}\cdot\int_0^{\theta_{crit}}\{\max(l_{a,crit} - w\ ,\ 0)\}^2\,d\theta \tag{6.18}$$

where θ_{crit} is given by Eq. 6.3. Equation 6.18 may be solved by numerical integration. For the case of $l_c < l_f$ no fibres fracture and Eq. 6.18 reduces to Eq. 6.12.

In Eqs. 6.14 and 6.15 the ultimate tensile strength of the fibres σ_{fu} is evaluated excluding the effect of bending stresses on the performance of the fibres. Whilst the effect of bending is commonly ignored in the calculation of the critical length (Eq. 6.14), strains induced by bending of the fibres can reduce the axial capacity of the fibre, particularly for fibres having limited ductility such as glass and carbon fibres. The issue of fibre bending and fracture is discussed in more detail in Section 6.8 of this thesis.

6.6 Experimental Verification

In the experimental verification of the variable engagement model that follows, it was observed that a relationship exists between the type of fibre used, the bond shear resistance, τ_b, and the uniaxial tensile strength of the concrete-matrix without fibres, f_{ct}. Where the bond shear strength was measured directly by the investigators, using fibre pullout tests, the measured data is used in the model verification. Where no bond shear data was available the relationships between the matrix cracking strength and the bond shear data given in Table 6.2 were used. Where f_{ct} was not measured the tensile strength was taken as $f_{ct} = \sqrt{f_{cm}}/3$ where f_{cm} is the mean cylinder strength in MPa (ACI Code, 1999).

Table 6.2 – Relationship between bond strength and tensile strength of the fibre concrete matrix.

Fibre Type	**Matrix**	**Bond Strength, τ_b**
End-Hooked and Crimped	Concrete	$2.5f_{ct}$
	Mortar	$2.0f_{ct}$
Straight	Concrete	$1.2f_{ct}$
	Mortar	$1.0f_{ct}$

In the application of the model the stress-COD relationship of the concrete matrix is required but this data is rarely available and, in general, difficult to obtain. Where the stress-COD relationship of the concrete matrix without fibres was measured by the investigators, using direct uniaxial tension tests, the data is used in the model verification. In the absence of this data, the tensile stress-COD model for the non-fibre matrix was taken as

$$\sigma_t = \sigma_{ct}\, e^{-cw} \tag{6.19}$$

where σ_{ct} is the tensile stress, w is the COD and c is an attenuation factor and is taken as $c = 15$ for both concrete and mortar specimens.

For fibres used in conventional quantities the fracture energy provided by the fibres far exceeds that of the matrix and the VEM is insensitive to the particular stress-COD model adopted for the matrix.

6.6.1 Banthia and Trottier (1994)

Banthia and Trottier (1994) undertook a series of single fibre tension tests for end-hooked, crimped and twin cone steel fibres embedded in conventional, medium and high strength concrete. The VEM is compared against Banthia and Trottier experimental data for their end-hooked and crimped fibre tests and for their conventional and medium strength concrete tests. In the high strength concrete tests for the end-hooked and crimped fibres and in all tests using twin cone fibres the fibres fractured before pullout. The testing arrangements used by Banthia and Trottier are shown in Figure 6.8.

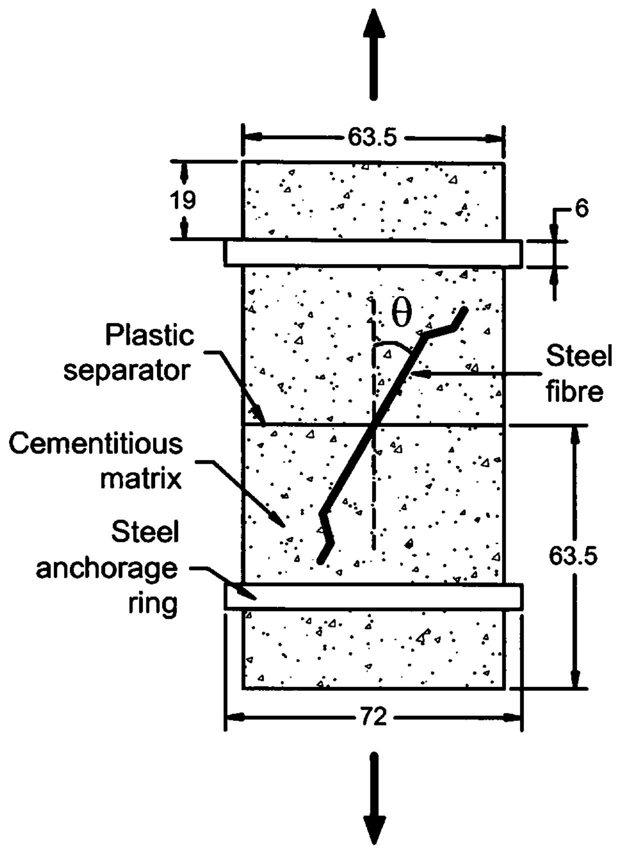

Figure 6.8 – Schematic of Banthia and Trottier (1994) pullout tests (in mm).

The end-hooked fibre tests consisted of 60 mm long by 0.8 mm diameter fibres with a tensile strength of the fibre of 1120 MPa. Taking the point of fibre engagement as 50 percent of the peak load, the fibre engagement parameter was assessed to be $\alpha = 1.24$ (refer Figure 6.3a). The bond strength was taken as the mean of six specimens measured for the $\theta = 0$ degrees tests and was $\tau_b = 3.7$ MPa and $\tau_b = 3.9$ MPa for the $f_{cm} = 40$ MPa and $f_{cm} = 52$ MPa tests, respectively.

The results of the VEM are compared in Figure 6.9 for the pullout load and in Figure 6.10 for the pullout energy. Banthia and Trottier reported energies at slips of 1 mm, 3 mm and at total pullout. It is seen that the VEM compares well against the collected data for the peak loads and the pullout energies reported.

In the crimped fibre tests, Banthia and Trottier used 40 mm long by 1.0 mm diameter fibres with a tensile strength of 1040 MPa. The bond shear strength for the $\theta = 0$ degrees tests (average of six specimens) was $\tau_b =$ 11.0 MPa for the $f_{cm} = 40$ MPa tests and $\tau_b = 11.1$ MPa for the $f_{cm} =$ 52 MPa tests. Again taking engagement at 50 percent of the peak load, the fibre engagement parameter was assessed as $\alpha = 2.31$ (refer Figure 6.3b). The results of the VEM are compared with Banthia and Trottier crimped fibre test data in Figure 6.11 for pullout loads and in Figure 6.12 for the total pullout energy and for the energies measured at slips of 1 mm and 3 mm. Again, the figures show that the VEM results compare well with the measured data.

In Figure 6.13 the results of the verification tests of the Banthia and Trottier data are summarised for the peak pullout force and for the total pullout energy. The figure shows that the bulk of data are within ± 20 percent of the equality lines. The mean theoretical to experimental ratios are 1.05 and 1.16 with coefficient of variations of 0.19 and 0.20 for the pullout load and pullout energies, respectively (excluding the outlier).

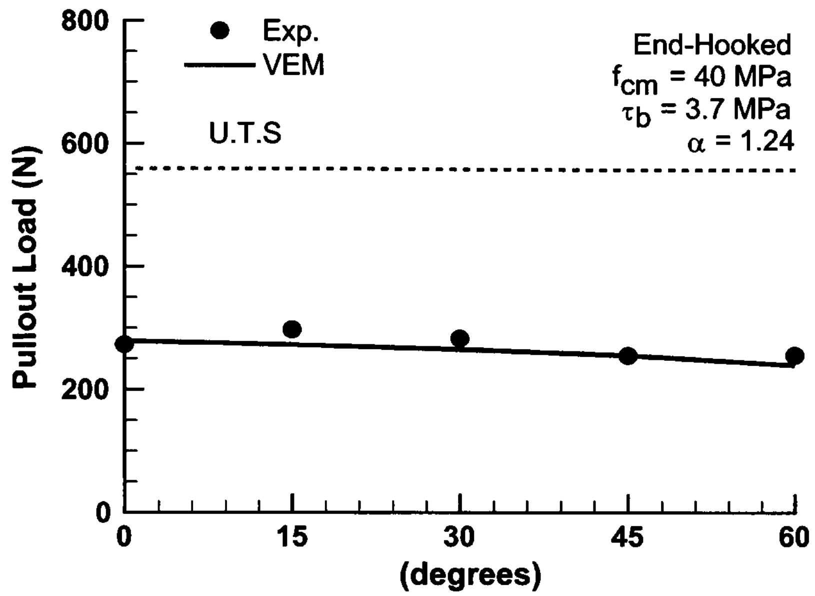

(a)

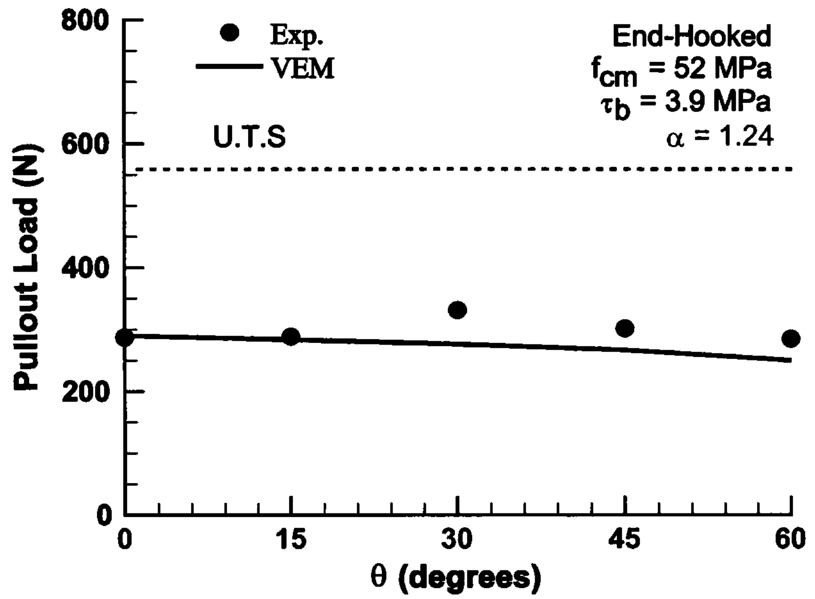

(b)

Figure 6.9 – Comparison of VEM with experimental pullout load on end-hooked fibres (Banthia and Trottier, 1994): (a) f_{cm} = 40 MPa and (b) f_{cm} = 52 MPa.

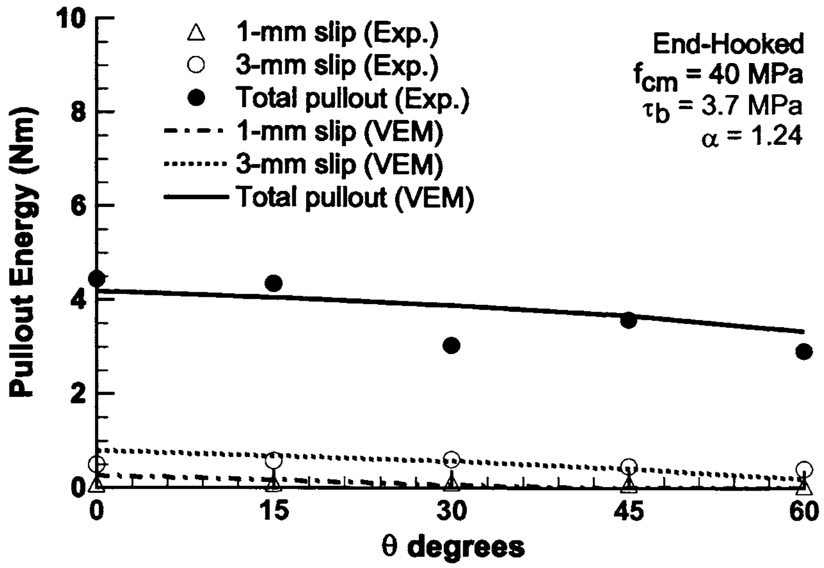

(a)

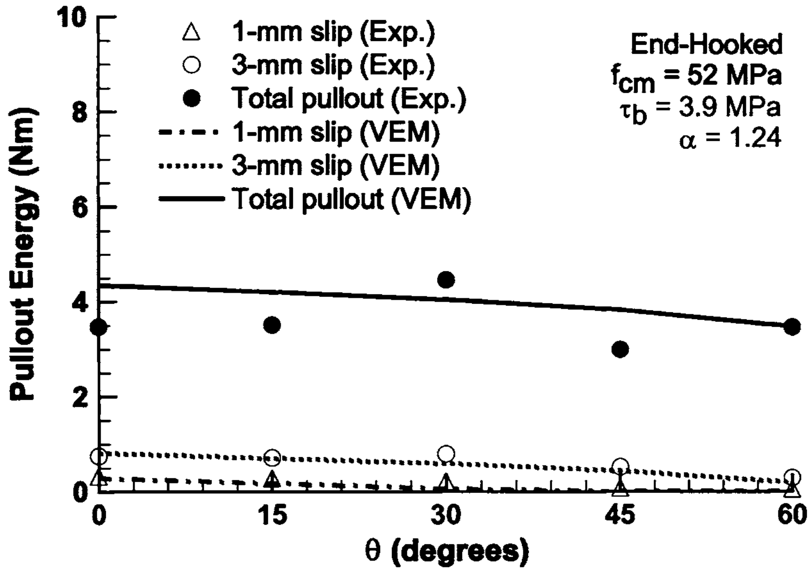

(b)

Figure 6.10 – Comparison of VEM model with experimental pullout energy on end-hooked steel fibres (Banthia and Trottier, 1994): (a) f_{cm} = 40 MPa and (b) f_{cm} = 52 MPa.

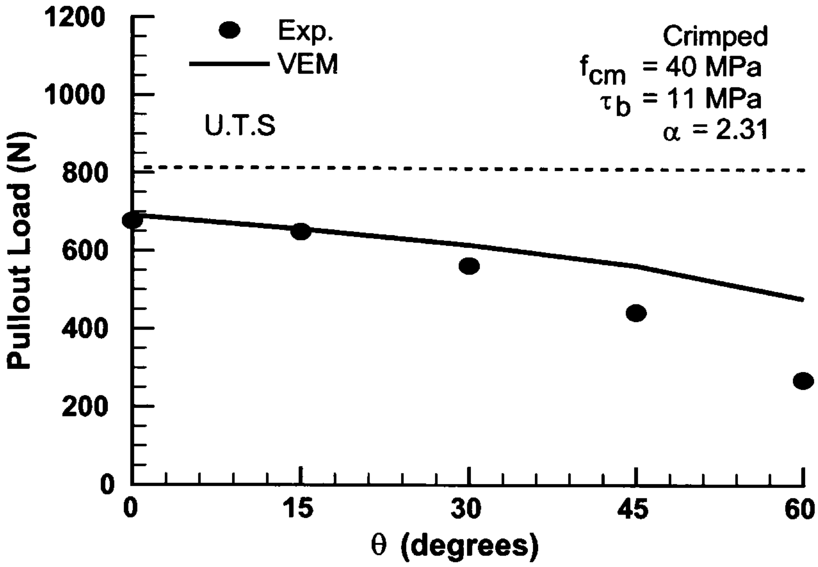

(a)

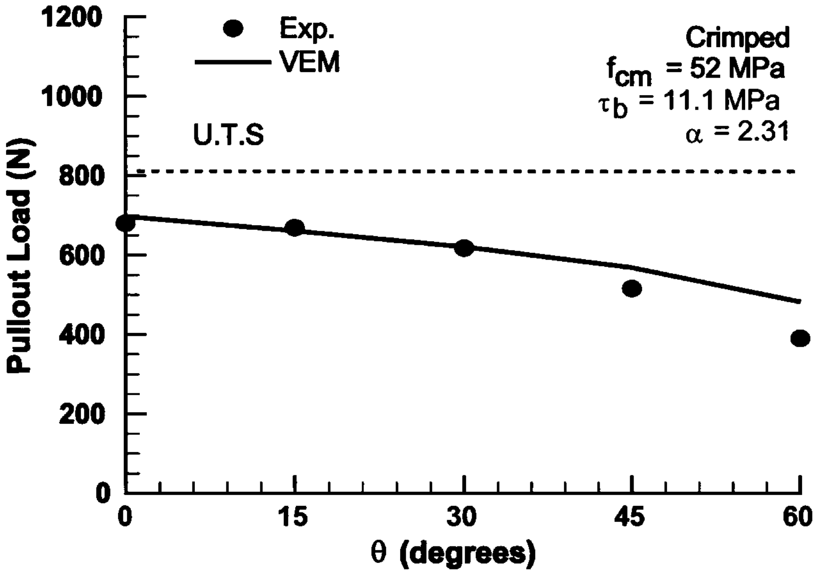

(b)

Figure 6.11 – Comparison of VEM with experimental pullout load on crimped steel fibres (Banthia and Trottier, 1994): (a) f_{cm} = 40 MPa and (b) f_{cm} = 52 MPa.

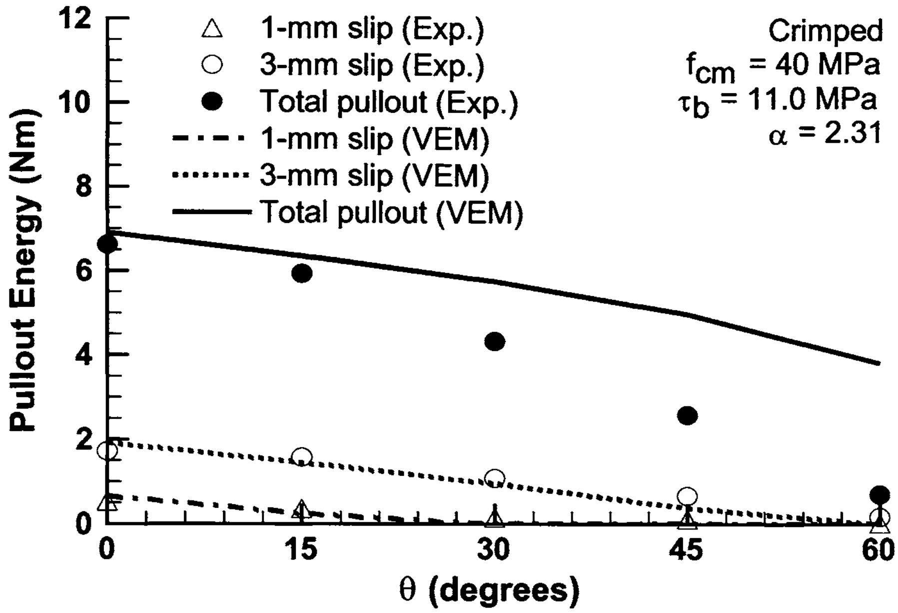

(a)

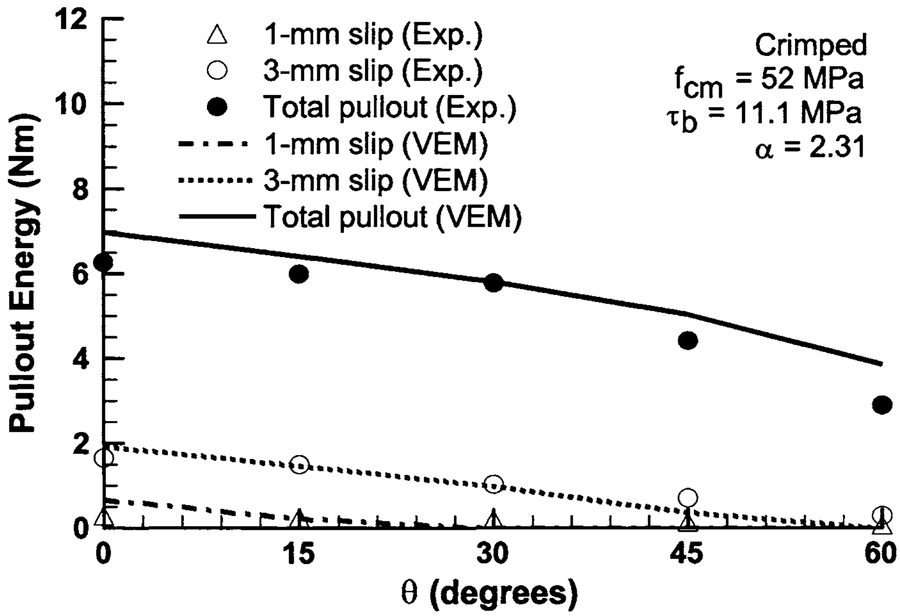

(b)

Figure 6.12 – Comparison of VEM with experimental pullout energy on crimped steel fibres (Banthia and Trottier, 1994): (a) f_{cm} = 40 MPa and (b) f_{cm} = 52 MPa.

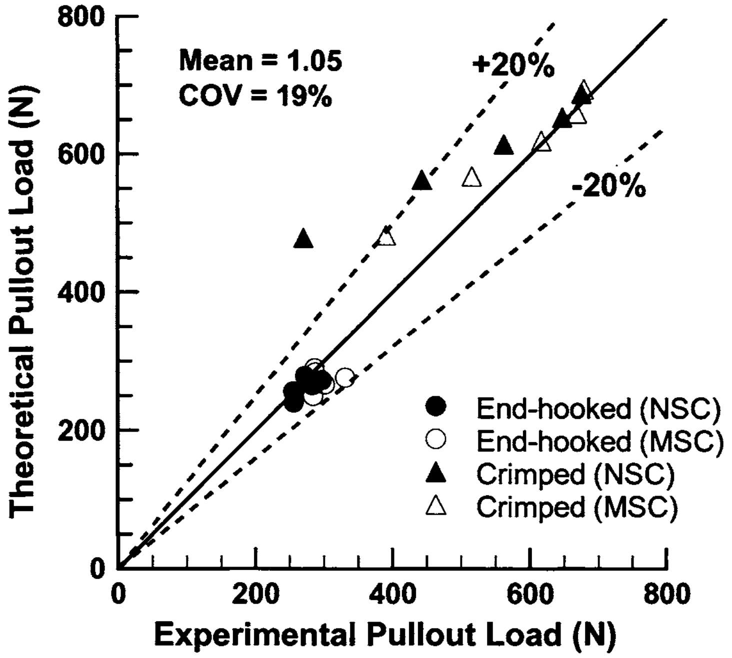

(a)

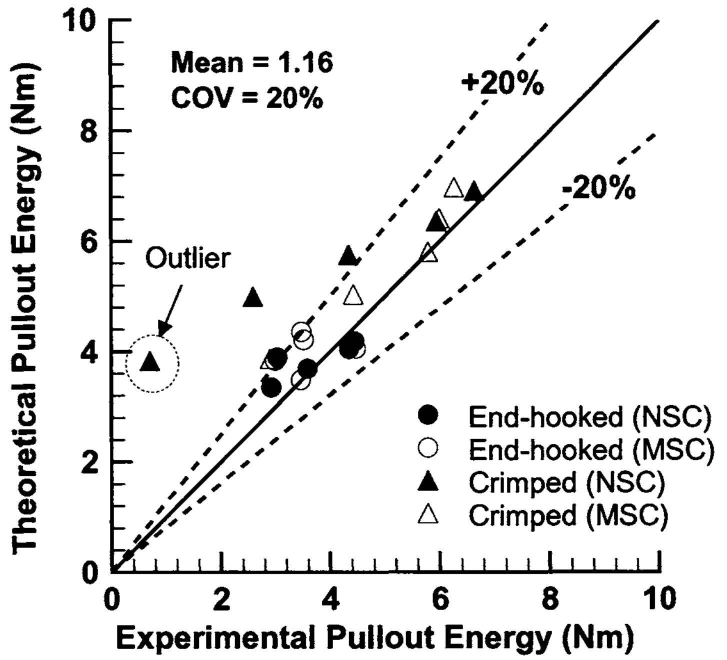

(b)

Figure 6.13 – Comparison of experimental and theoretical results for Banthia and Trottier (1994) fibre pullout tests: (a) peak load and (b) total pullout energy.

6.6.2 Lim et al. (1987b)

Lim et al. (1987b) undertook a series of uniaxial tension strength tests for end-hooked and straight steel fibres in various volumetric ratios in conventional strength concrete. The results of the VEM compared with the Lim et al. tests are discussed below.

In the specimens using straight steel fibres, the fibres were 30 mm or 50 mm long by 0.57 mm diameter and had a tensile strength of σ_{fu} = 340 MPa and modulus of elasticity of E_f = 210 GPa. Fibre volumes were 0.5, 1.0 and 1.5 percent and each specimen had a cross section of 70 mm by 100 mm. The test setup used by Lim et al. is shown in Figure 6.14. The uniaxial specimens were fabricated from normal strength concrete with cement : sand : coarse aggregate : water ratios of 1:1.8:2.8:0.5 and a maximum particle size of 10 mm. The unnotched specimens were tested in direct tension by a pair of specially designed grips using a servo-controlled testing machine at an extension rate of 0.25 mm/min over a gauge length of 200 mm. The final experimental load-extension plots were taken from the average of four displacement transducers distributed uniformly around the specimens. Details of the properties of the material used by Lim et al. for their straight fibre tests are given in, Appendix F, Table F1.

The bond strength (τ_b) was measured directly for each test using single fibre pullout tests and the data collected is used in the VEM verification. The tensile strength of the non-fibre reinforced concrete was measured directly and the concrete matrix strength was taken as f_{ct} = 2.2 MPa. The engagement parameter was taken as α = 0.15. The results of the VEM are compared in Figures 6.15 and 6.16 for the uniaxial strength for their FR composites. It is seen that the VEM compares well against their data.

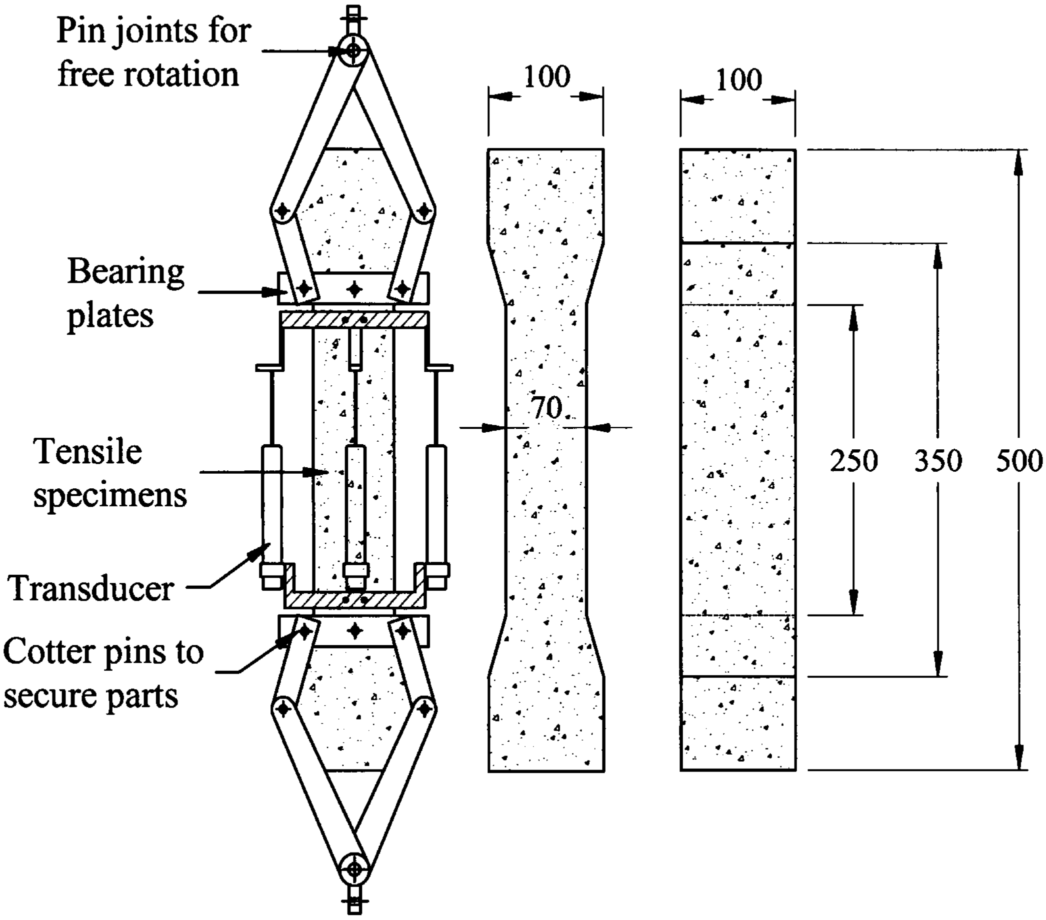

Figure 6.14 – Setup for direct tension test and dimension of test specimens- dimensions in mm (Lim et al., 1987b).

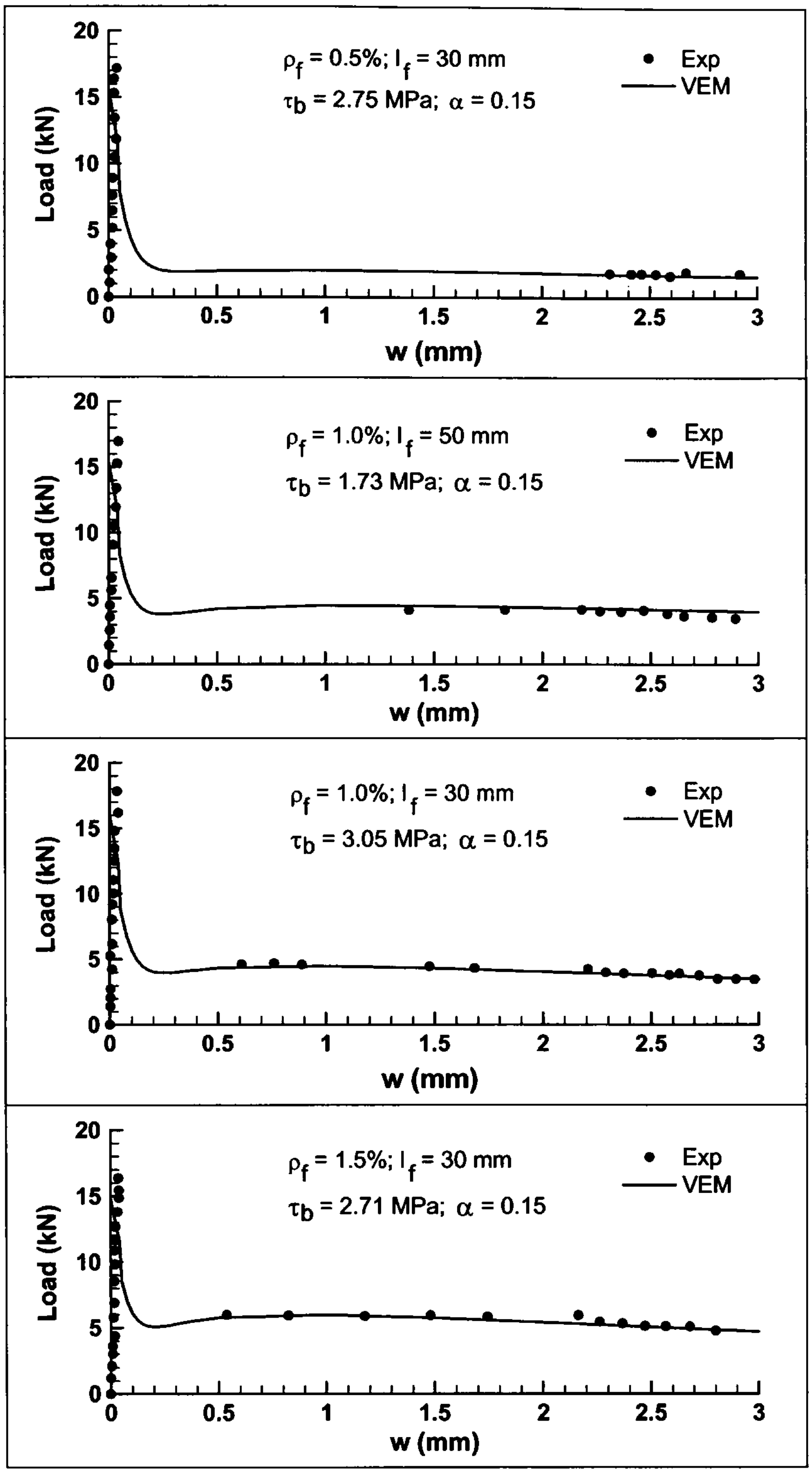

Figure 6.15 - Comparison of Lim et al. (1987b) data and VEM for straight fibres (w = 0 to 3 mm).

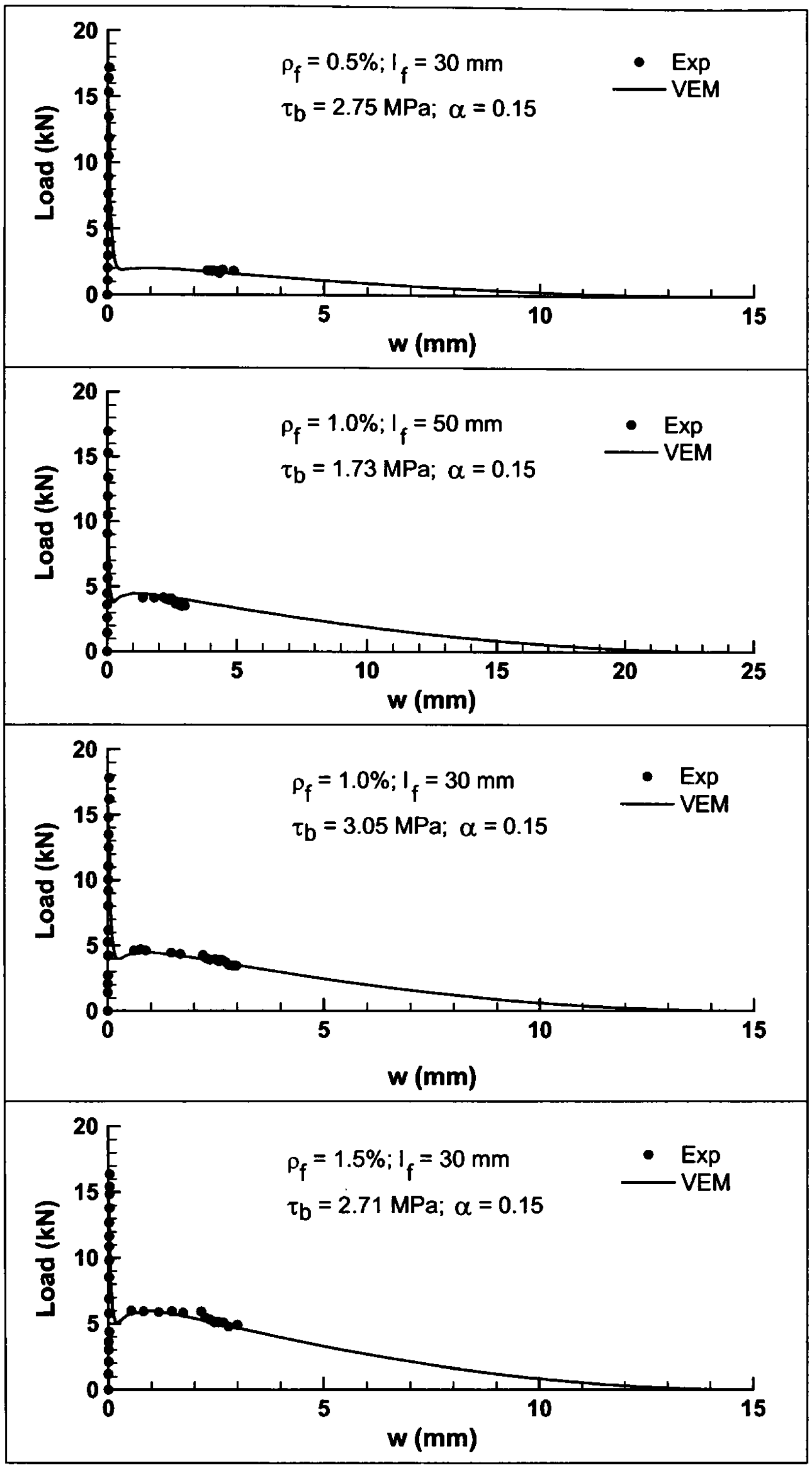

Figure 6.16 - Comparison of Lim et al. (1987b) data and VEM for straight fibres (full curve).

In their end-hooked fibre tests, Lim et al. (1987b) used 30 mm or 50 mm long by 0.5 mm diameter fibres with a tensile strength of 1130 MPa. The uniaxial specimen dimensions and testing procedure was similar to that for the straight fibre specimens with the exception that the normal strength concrete had a cement:sand:coarse aggregate:water ratio of 1:1.5:2.5:0.5. The bond strength was measured directly by the investigators using single fibre pullout tests and the data collected used for the τ_b's in the VEM verification. The tensile strength of the non-fibre reinforced concrete was measured directly and was f_{ct} = 2.7 MPa. The engagement parameter was taken as $\alpha = 0.15$. By Equation 6.14, for the 50 mm long end-hooked steel fibres used by the Lim et al. the critical embedded length is 48 mm and is less than the fibre length. As the critical length is only slightly smaller than the fibre length, the small effect of fibre fracture has not been considered. Details of the material properties for the Lim et al. end-hooked fibre tests are given in Appendix F, Table F2.

The results of the VEM are compared with Lim et als' data in Figures 6.17 and 6.18. It is seen that the VEM compares well against the experimental data. In comparing the engagement parameter, α, adopted for the Lim et al. tests with that measured in the single fibre tests of Banthia and Trottier (1994), discussed in Section 6.6.1, it is observed that for the randomly orientated fibre tension tests, α is significantly lower than for the single fibre pullout tests. This lower α value indicates that fibres have been engaged much earlier in the composite than when embedded singly and pulled out directly from the matrix. It is hypothesised that this phenomena occurs due to the straining of the fibres pre cracking and due to interference effects of adjacent fibres.

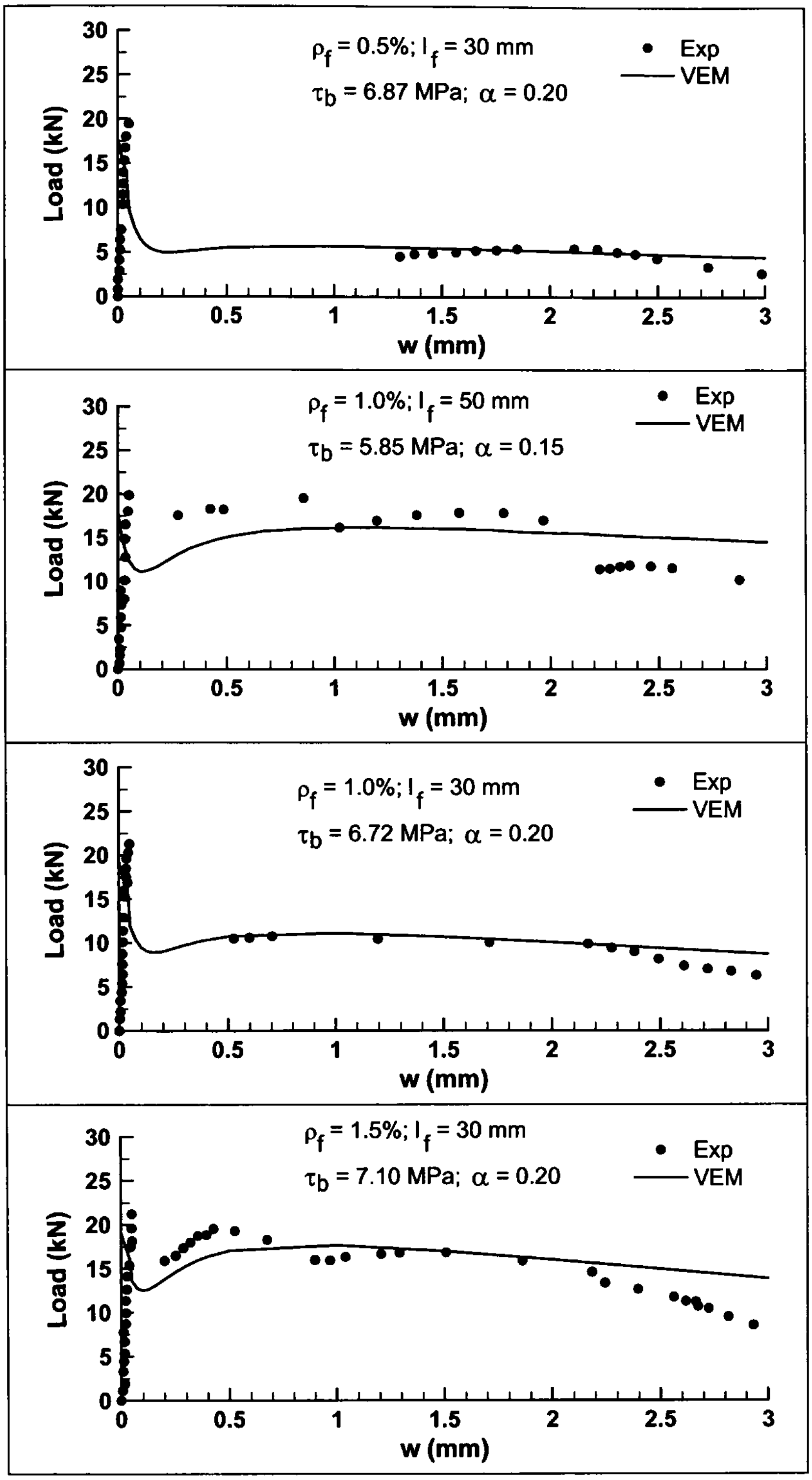

Figure 6.17 - Comparison of Lim et al. (1987b) data and VEM for end-hooked fibres (w = 0 to 3 mm).

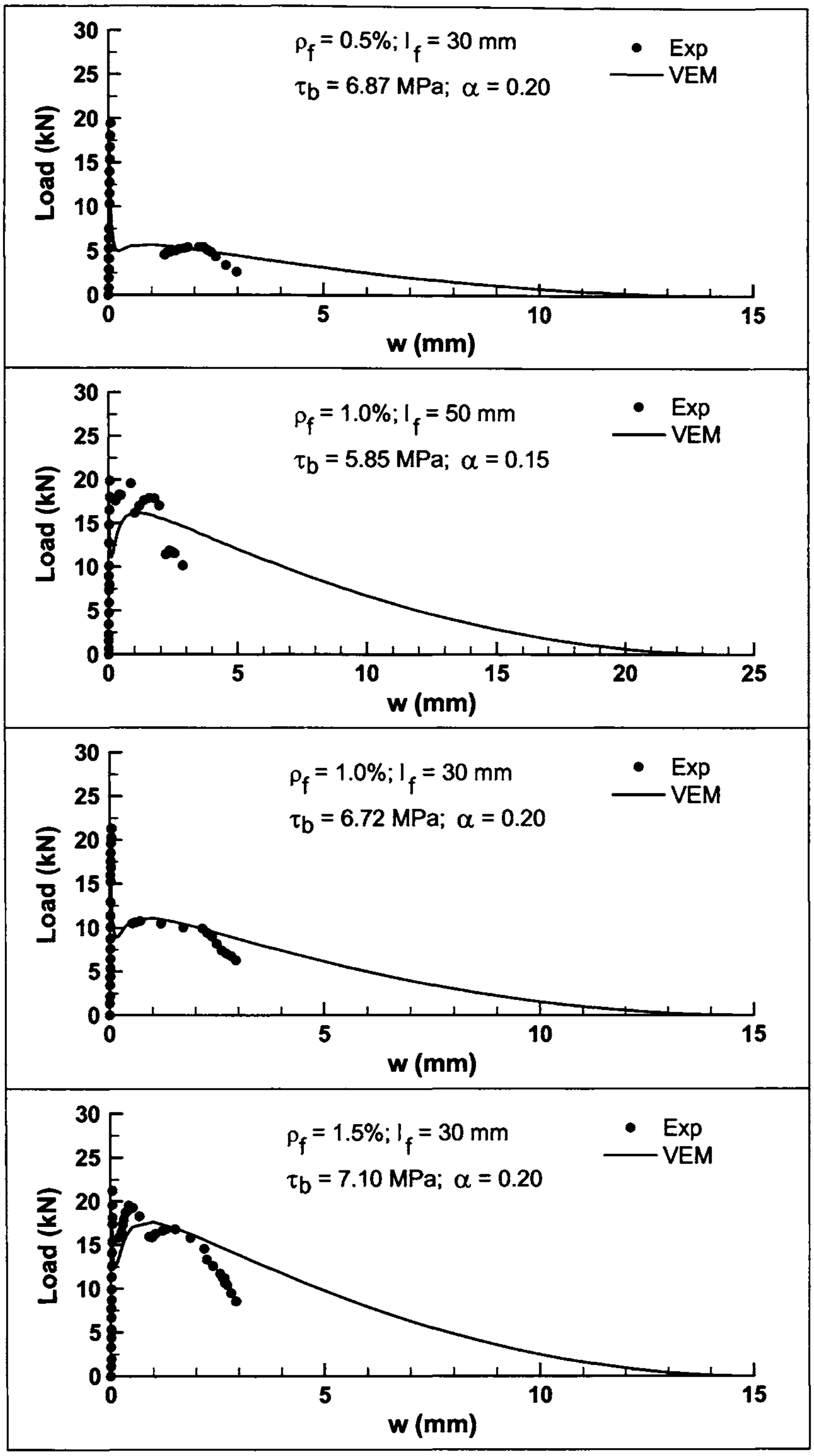

Figure 6.18 - Comparison of Lim et al. (1987b) data and VEM for end-hooked fibres (full curve).

6.6.3 Petersson (1980)

Petersson (1980) undertook a series of uniaxial tension strength tests for indented and straight steel fibres with various volumetric ratios in conventional strength mortars. The VEM is compared against Petersson's experimental data for his straight fibre tests.

The straight steel fibres used were 30 mm long and 0.3 mm diameter. A mortar was used with water/cement ratio of 0.6, cement/sand ratio of 0.31 and the maximum particle size of 4 mm. Specimens with fibre quantities of 0.25, 0.5 and 1 percent were tested with specimen dimension of 30 mm by 50 mm by 200 mm high and with two 15 mm deep notches (see Figure 6.19). The stress-COD for the non-reinforced mortar matrix was measured by Petersson using uniaxial tension tests and this data is used for the σ-COD of the mortar matrix in the verification that follows. The uniaxial tension strength of the non-reinforced mortar was measured as $f_{ct} = 3.0$ MPa and, thus, as per Table 6.2 the bond strength was taken as $\tau_b = 3.0$ MPa. The engagement parameter is taken as $\alpha = 0.08$. The material data for Petersson's specimens are given in Appendix F, Table F3.

The results of the VEM are compared in Figure 6.20 for the tensile stress versus COD. It is seen that the VEM compares well against the experimental data for both the peak load and the reported fracture energies.

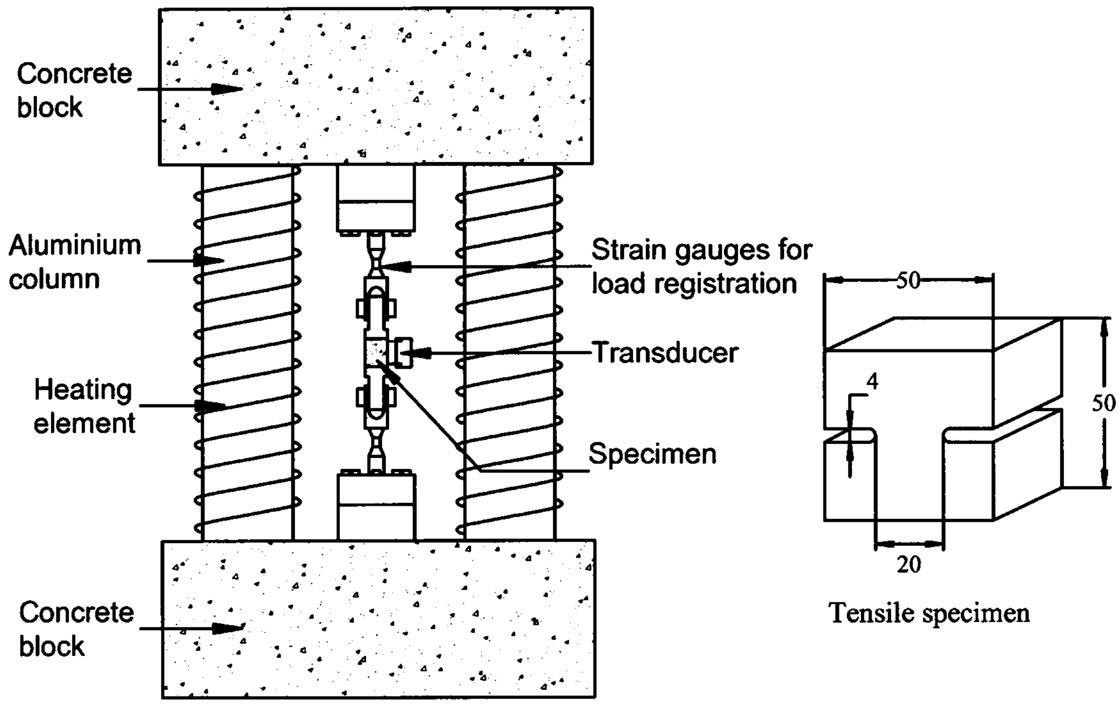

Figure 6.19 – Uniaxial strength test setup of Petersson (1980).

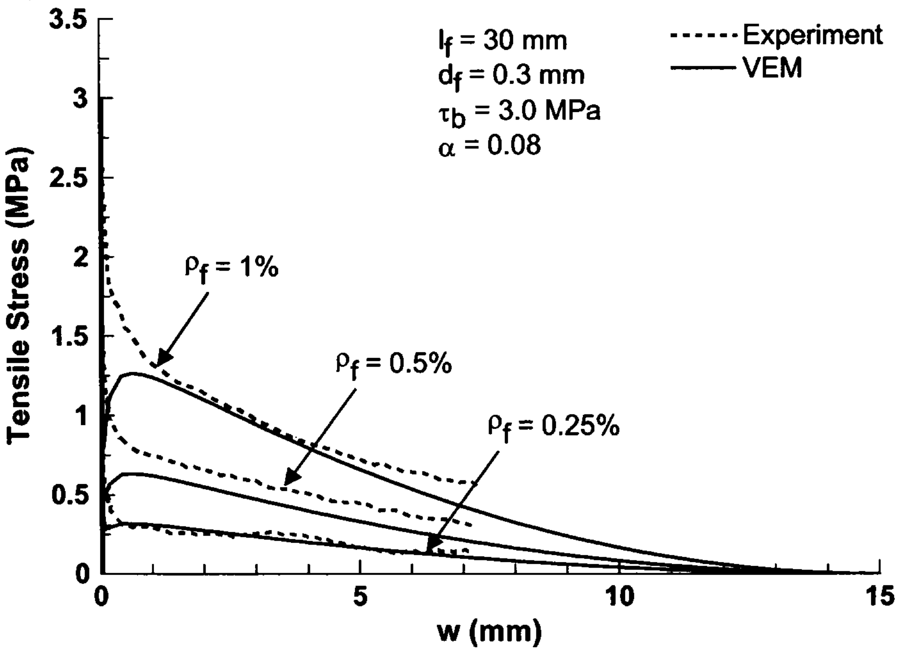

Figure 6.20 – Comparison of VEM with experiments of Petersson (1980) for 30 mm straight fibres in mortar.

6.6.4 Barragán et al. (2003)

Barragán et al. (2003) tested five identical uniaxial tension strength specimens with 40 kg/m^3 of 60 mm long by 0.75 mm diameter end- hooked steel fibres in concrete with a 70 day strength of f_{cm} = 41 MPa. The fibre volume ratio was ρ_f = 0.45 percent and the fibres had a tensile strength of 1000 MPa. Cylindrical test specimens were used with a gross diameter of 150 mm and 15 mm deep notches. The testing arrangements are given in Figure 6.21. The concrete used has a maximum aggregate size of 12 mm, an aggregate/cement ratio of 5.3 and water/cement ratio of 0.57. Further details of the material properties of the Barragán et al. tests are given in Table F3.

In the VEM the tensile strength of the concrete was taken as $f_{ct} = \sqrt{f_{cm}}/3$ = 2.1 MPa. The bond strength was taken as τ_b = 5.3 MPa (refer Table 6.2) and α = 0.2. The results of the VEM are compared with the test data in Figure 6.22 for the tension strength versus COD. The shaded area represents the experimental data range of the five specimens tested by the investigators. The figure shows that although the five specimens were identical in material composition and testing procedure, the variability after cracking in strength, for a given COD, was ± 30 percent from the mean. It is seen in Figure 6.22 that the VEM compares well against the average of Barragán et al's data. The fracture energy of the partial curve (i.e. up to w = 2.0 mm) was 1.62 N/mm for the VEM and compares favourably with the average measured energy of 1.84 N/mm for the five specimens.

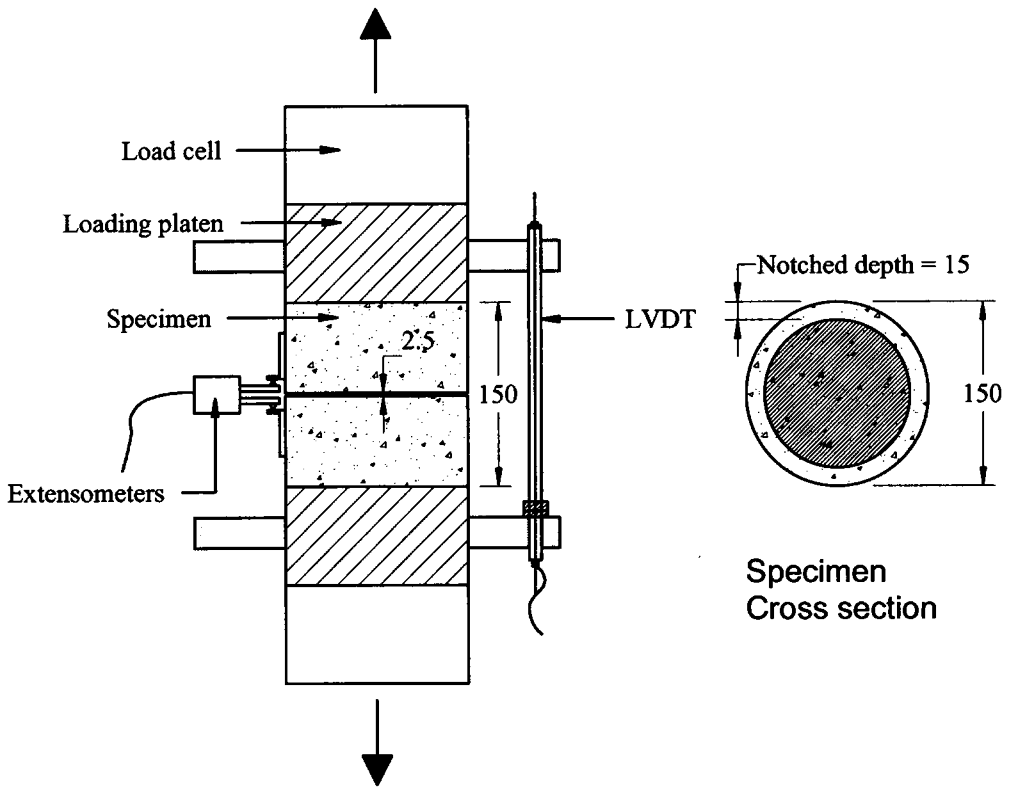

Figure 6.21 – Test setup and dimensions (in mm) of Barragán et al.'s (2003) test specimens.

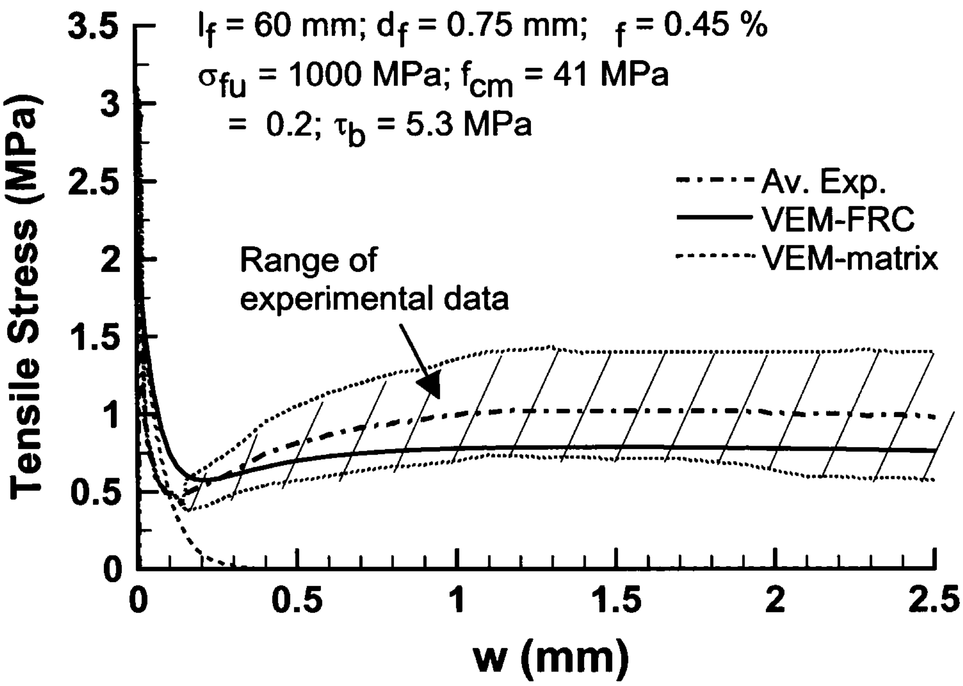

Figure 6.22 – Comparison of VEM with experiments from Barragán et al. (2003).

6.6.5 Li et al. (1998)

Li et al. (1998) undertook a study on uniaxial tension strength tests for end-hooked steel fibres in a medium strength concrete matrix (f_{cm}= 52 MPa) containing 6 percent by volume of 30 mm long by 0.5 mm diameter fibres with a minimum tensile strength and modulus of elasticity of 1000 MPa and 200 GPa, respectively. The constituents making up the concrete-matrix were Type I OPC, coarse aggregate with a maximum size of 10 mm and silica fume. The water/cement ratio was 0.45. The test was conducted on unnotched rectangular uniaxial tension specimen with cross section dimensions of 100 mm by 20 mm. Details of the specimens and the testing arrangement are given in Figure 6.23 and the material properties are summarised in Table F3. The specimens were loaded at a displacement rate of 0.004 mm/min over a gauge length of 120 mm.

The stress-COD relationship of for the unreinforced concrete matrix was measured using uniaxial strength tests and it is used for matrix curve in the modelling analysis. The matrix cracking strength was measured to be 4.2 MPa and the bond strength was taken as 10.5 MPa (as per the formulas given in Table 6.2). By Eq. 6.15 the critical length of the fibres is ℓ_c= 23.8 mm and, being less than the fibre length, will result in a portion of the fibres breaking. The global fibre orientation factor (K_f) was calculated using Eq. 6.18 and the engagement parameter was taken as α = 0.13.

The results of the VEM are compared against the experimental data in Figure 6.24. The figure shows that the VEM compares well with the Li et al. data for the stress versus COD.

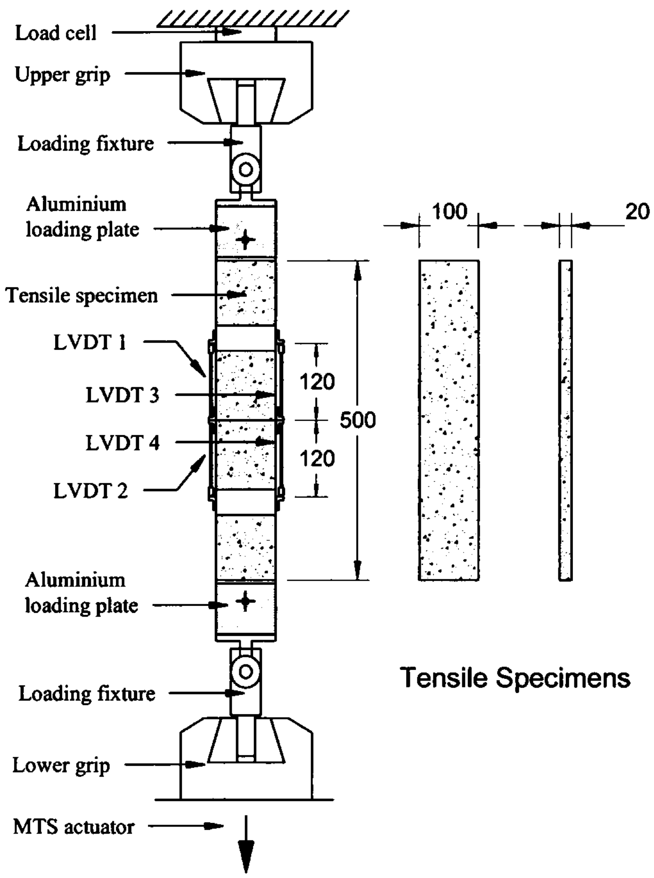

Figure 6.23 – Tensile strength test setup and dimensions of specimen, in mm (Li et al., 1998).

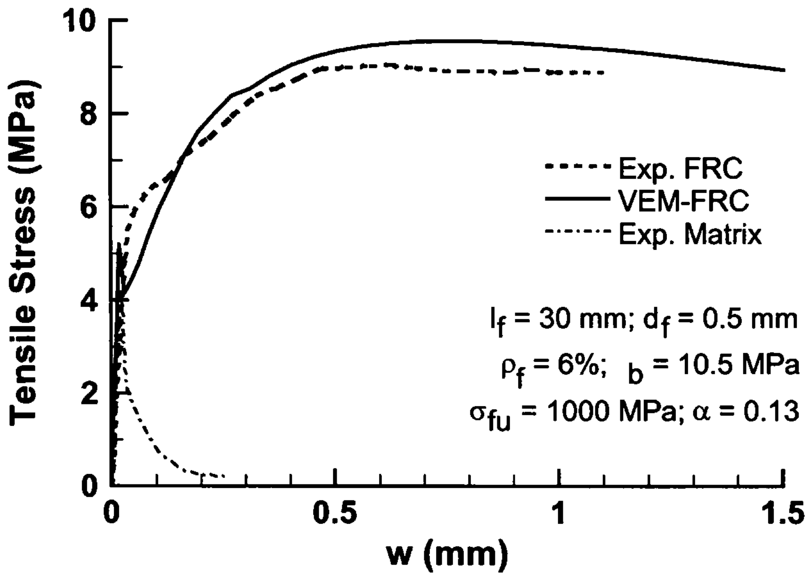

Figure 6.24 – Comparison of VEM with the data of Li et al. (1998).

6.6.6 Groth (2000)

Groth (2000) tested a series of fibre reinforced cement mortar specimens with 0.7 percent by volume of steel fibres. The fibres used were high strength straight DRAMIX fibres 20 mm long by 0.13 mm diameter. The minimum tensile strength and modulus of elasticity of the fibres used were 1000 MPa and 200 GPa, respectively. Four types of cement based matrices were used with varying quantities of ordinary Portland cement, silica fume, quartz sand and blast furnace slag. The binder to sand ratio for each mix was 1:3 and water to binder ratio 1:2. The four mixes used are denoted as ordinary Portland cement (OPC), 50 percent of OPC and 50 percent of blast furnace slag (S50), 50 percent OPC mixed with 50 percent of quartz sand (Q50), and 95 percent OPC and 5 percent of silica fume EMC500). The mechanical properties of the matrix are given in Appendix F, Table F4.

Uniaxial tension tests were performed on notched cylindrical cast specimen with a net diameter of 90 mm (Figure 6.25). The tests were done under closed loop displacement-control using for displacement transducers uniformly spaced around the circumference of the specimens. The tension stress-COD behaviour of the non-reinforced mortar was measured by Groth using uniaxial tension tests and this data was used for the matrix curves used in the verification.

The bond strength of each mix was determined using the relationships presented in Table 6.2 and the engagement parameter was taken as α = 0.04. The VEM results are compared with the experimental data of Groth (2000) in Figure 6.26. The figure shows that the numerical results obtained from the VEM compares well with Groth's experimental data.

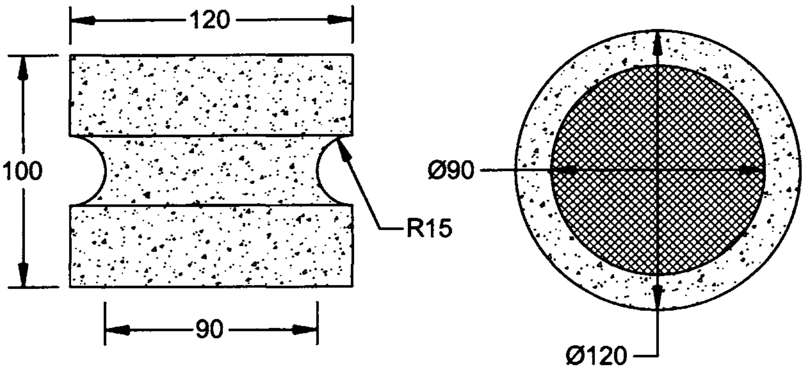

Figure 6.25 – Tensile specimens of Groth (2000).

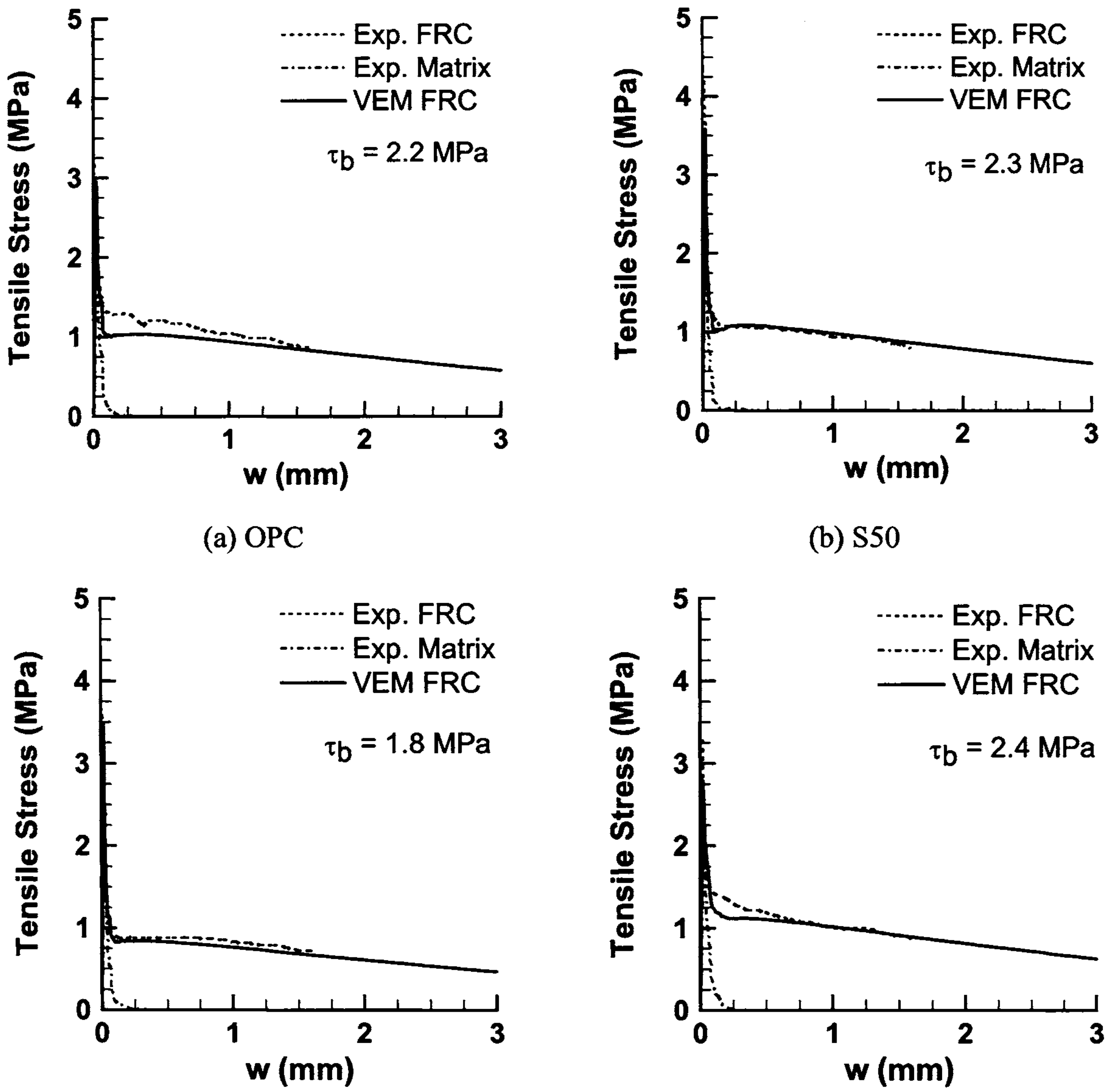

(a) OPC

(b) S50

(c) Q50

(d) EMC500

Figure 6.26 – Comparison of VEM with straight steel fibre reinforced mortar (Groth, 2002): a) OPC, b) S50, c) Q50 and d) EMC500.

6.6.7 Wang (1989) and Wang et al. (1990a,b).

Wang (1989) and Wang et al. (1990a, b) undertook a series of uniaxial tension strength tests on various types of synthetic fibres with various volumetric ratios in normal strength mortar (NSM) and high strength concrete (HSC). The fibres used included aramid, high-strength high-modulus polyethylene and polypropylene micro-fibres with fibre fractions of between 0.6 percent and 3 percent, by volume. For their tests with high-strength, high-modulus, polyethylene (Spectra 900) fibres, Wang et al. tested two specimens with 12.7 mm long by 0.038 mm diameter fibres in NSM and one specimen in HSC with 6.35 mm long by 0.038 mm diameter fibres. The strength and modulus of elasticity of the fibres were 1200 MPa and 120 GPa, respectively. Details of the test specimens are given in Appendix F, Table F5

Wang et al. tested notched specimens in uniaxial tension having net cross section dimensions of 51 mm square (shown in Figure 6.27) and were tested at an extension rate of 0.3 mm/min for the first 1 mm of displacement and at (approximately) 1.5 mm/min for the remainder of the test (Wang, 1989).

For the VEM verification using the polyethylene fibre tests of Wang et al., the engagement parameter was taken as $\alpha = 0.10$, the tensile strength of the normal strength mortar and high strength concrete ware taken as $f_{ct} = 1.8\ \text{MPa}$ and $f_{ct} = 4.2\ \text{MPa}$, respectively and the interfacial bond strengths were taken as $\tau_b = 1.02\ \text{MPa}$ for the NSM and $\tau_b = 1.5\ \text{MPa}$ for the HSC specimens[1].

---

[1] Details of the interfacial bond shear strengths were obtained from similar tests using the same constitutive materials reported by the same cohort group in Li and Wu (1992).

The results of the VEM are compared with the Wang et al. data in Figure 6.28 with a good correlation observed between the model and the test data for the 2 percent NSM and 0.6 percent HSC specimens. The model under predicts the post cracking strength and fracture energies for the 1 percent NSM specimen.

The tests by Wang et al. using aramid (Kevlar and Technora) fibres were subject to fibre fracture and bending. Verification of the model using this data is discussed in Section 6.8.

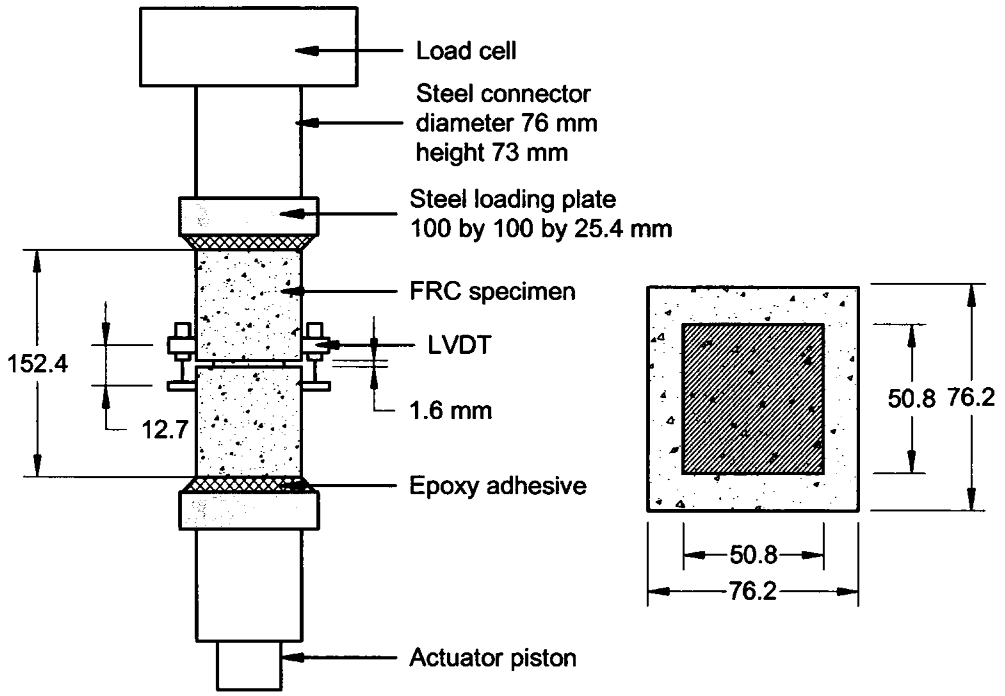

Figure 6.27 – Loading fixture for the direct tensile test and dimension (mm) of direct tensile test specimens.

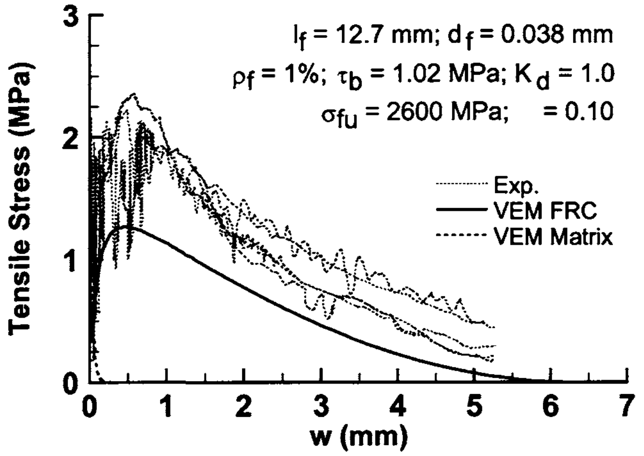

(a)

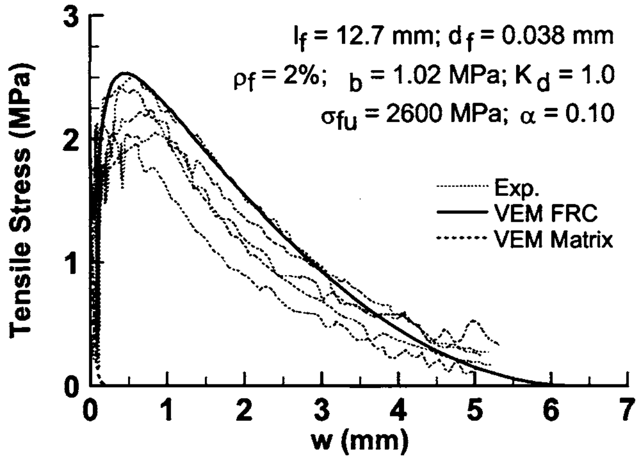

(b)

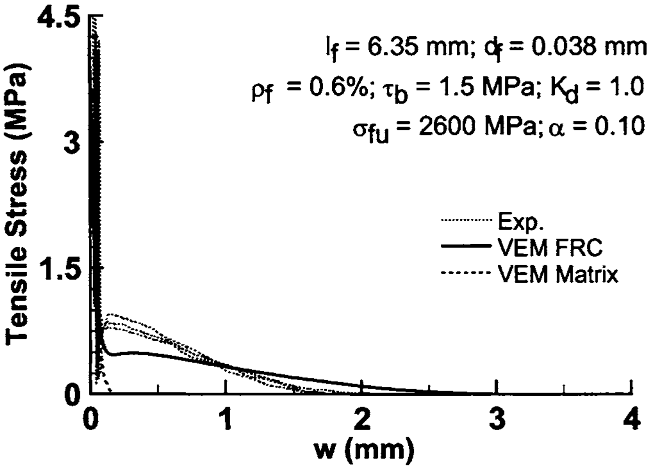

(c)

Figure 6.28 – Comparison of VEM with experiments from Wang (1989) on Spectra 900 fibre reinforced normal strength mortar with a) 1 percent and b) 2 percent of fibre and (c) 0.6 percent of fibres in high strength concrete.

6.6.8 Noghabai (2000)

Noghabai (2000) undertook a series of uniaxial tension strength tests for 1 percent by volume of straight steel fibres in high strength concrete with a standard cube compressive strength of 110-130 MPa. The VEM is compared against Noghabai's experimental data.

The straight steel fibres used were 6 mm long and 0.15 mm diameter and with fracture strength of 2600 MPa. The tension specimens were tested with net cross-section of 55 mm diameter. The matrix tensile strength (f_{ct}) was measured experimentally and it is reported as f_{ct} = 4.15 and 3.77 MPa for specimen denoted as $HSC^{I}_{S6/0.15}$ and $HSC^{III}_{S6/0.15}$, respectively. The bond strength of the fibre-matrix interface is taken as $\tau_b = 1.2 f_{ct}$ as per Table 6.2. The material data for Noghabai's specimens are given in Table F7. The results of the VEM are compared in Figure 6.29 for the tensile stress versus COD. It is seen that the VEM compares well against the experimental data for both the peak load and the descending curves.

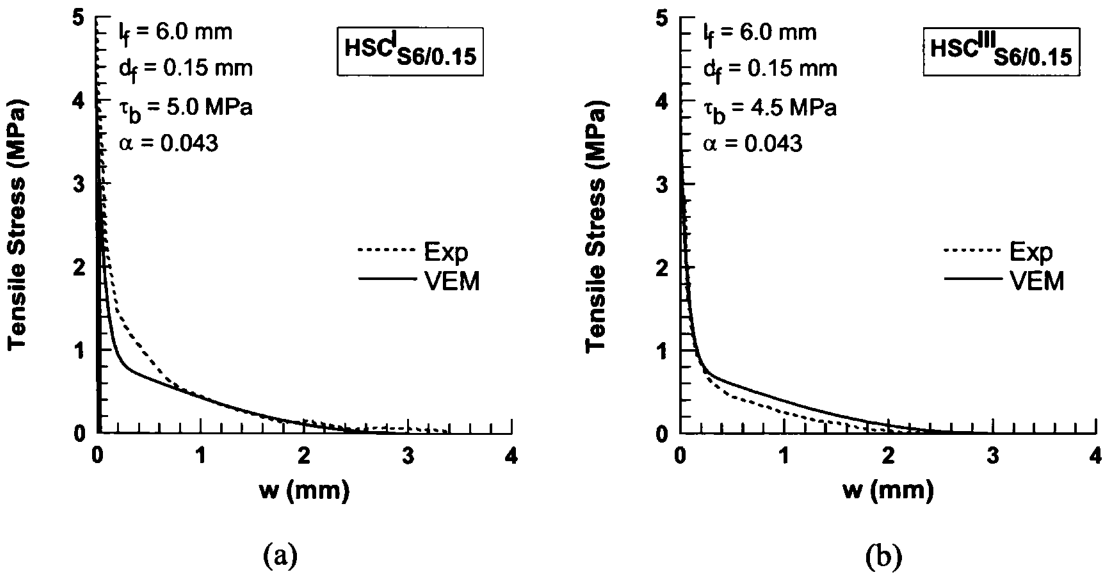

Figure 6.29 – Comparison of VEM with experiments of Noghabai (2000).

6.6.9 Behloul (1995)

Behloul (1995) reported the results of a uniaxial tension strength test on 170 MPa fibre reinforced reactive powder concrete. A matrix was used with water/binder ratio of 0.18, cement/sand ratio of 0.91 and 2.6 percent by volume of 12 mm long by 0.20 mm diameter fibres. Details of the specimens are shown in Figure 6.30. The matrix tensile strength for the non-reinforced RPC matrix (f_{ct}) was measured by Behloul using uniaxial tension tests and this data is used in the verification that follows. In their tests, the average value of the matrix tension strength of the non-reinforced mortar was measured as f_{ct} = 5.1 MPa, and, from tests by Orange et al. (1999) on similar concrete-fibre mix, τ_b = 10 MPa. The engagement parameter is taken as α = 0.043. The material data for Behloul et al.'s specimens are given in Appendix F, Table F7.

The results of the VEM are compared in Figure 6.31 for the tensile stress versus COD. It is seen that the VEM compares well against the experimental data for both the peak load and post peak response.

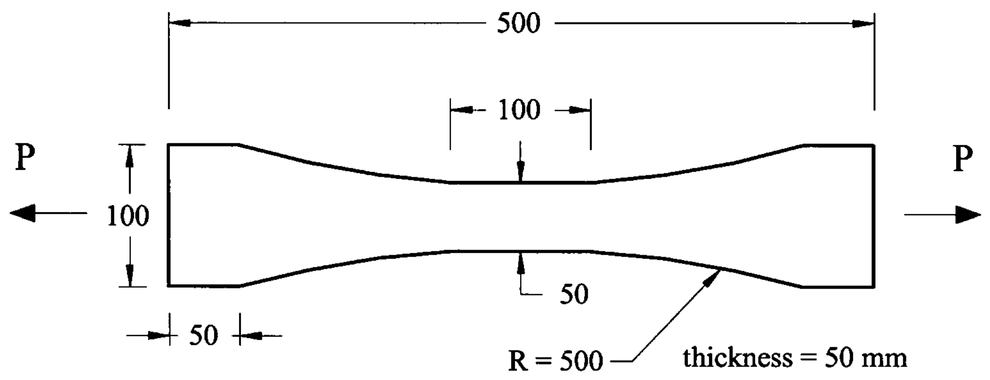

Figure 6.30 – Direct tension specimens of Behloul (1995), (dimension in mm).

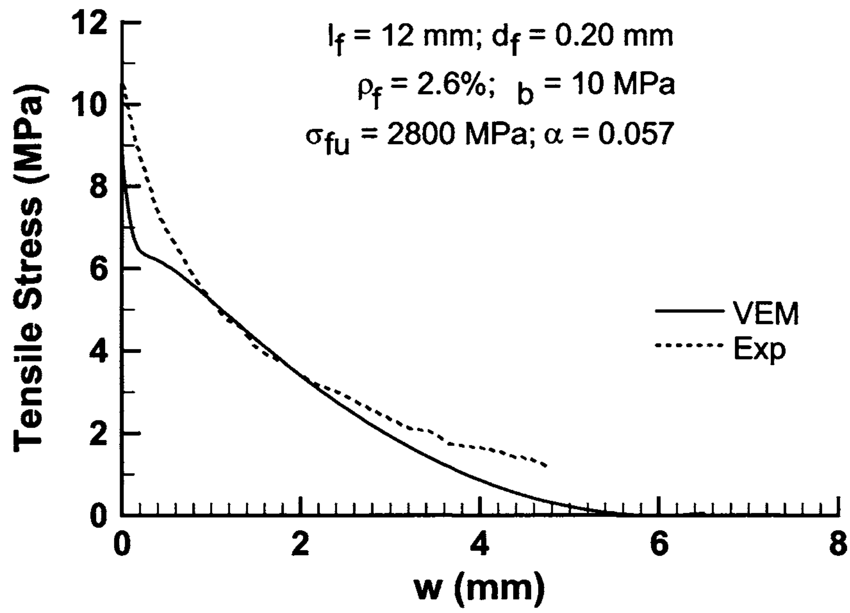

Figure 6.31 – Comparison of VEM with experiments from Behloul (1995).

6.6.10 Denarié et al. (2003)

Denarié et al. (2003) reported two uniaxial tension strength tests for straight steel fibres with 2 percent by volume in reactive powder concrete with a standard cylinder compressive strength of 171 MPa and modulus of elasticity of 57 GPa. Straight steel fibres of 13 mm long and 0.15 mm were used and the water/binder ratio was 0.14. The tensile strength tests were carried out using closed loop servo hydraulic 1000 kN universal testing machine under displacement control. Details of the test specimens and experimental setup are given in Figure 6.32.

The matrix tensile strength for the non-reinforced RPC matrix, f_{ct} was not measured experimentally and, thus, was taken as $f_{ct} = 0.33\sqrt{f_{cm}}$ = 4.36 MPa as per Table 6.2. In the verification that follows, a bond strength of τ_b = 10 MPa was adopted as per the tests of Orange et al. (1999). The engagement parameter is taken as α = 0.043. The material data for Denarié et al.'s specimens are given in Appendix F, Table F7. The results of the VEM are compared in Figure 6.33 for the tensile stress versus COD. Again it is seen that the VEM compares well against the experimental data for both the peak load and post peak response.

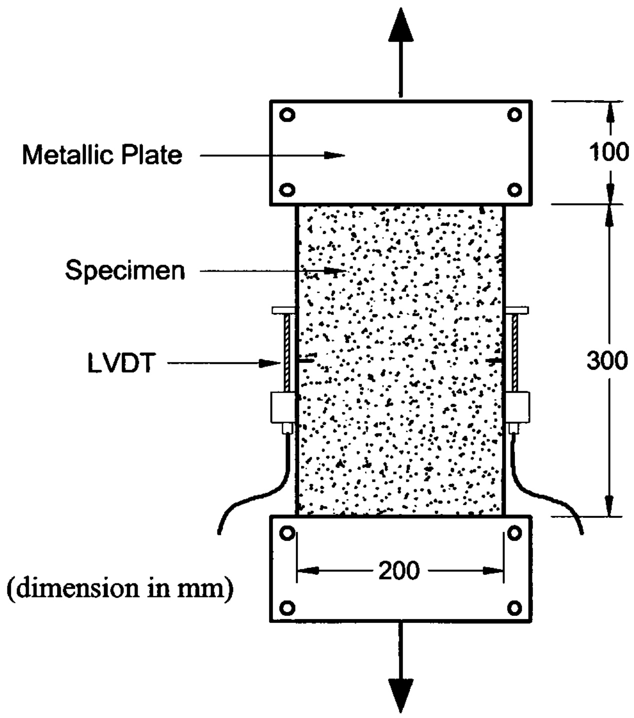

Figure 6.32 – Uniaxial tension test setup (Denarié et al., 2003).

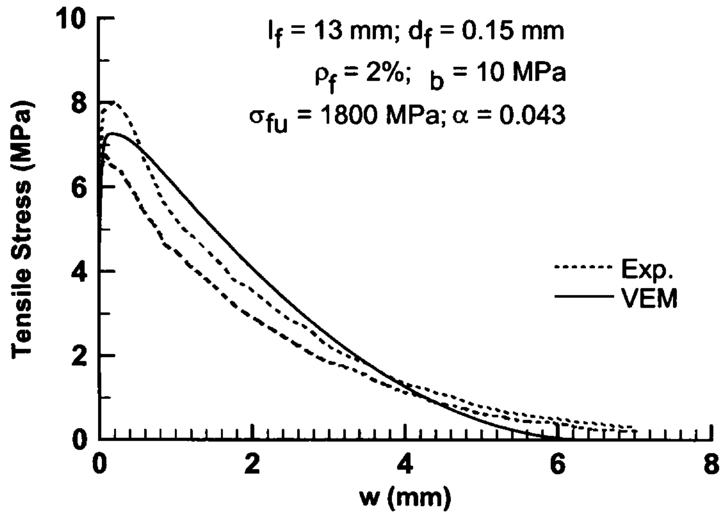

Figure 6.33 – Direct tension specimens of Denarié et al. (2003).

6.7 Comments on the Fibre Engagement Parameter, α

In evaluation of the fibre engagement it may reasonably be assumed that elements such as the constitution of the concrete matrix, the fibre type and fibre diameter maybe important parameters in the determination of α. From the proceeding verification the following observations are made:

1. Banthia and Trottier (1994) undertook a series of tests on different type of fibres embedded in three different concretes. The results for their tests for end-hooked fibres in 40, 52 and 85 MPa concretes were presented in Figure 6.3a. Here it is observed that the concrete strength was not a significant effect in the determination of α. For the Banthia and Trottier tests on crimped fibres a similar observation is made (Figure 6.3b). Thus, while the constitution of the matrix in terms of particle size and density may prove to be a fundamental parameter, the strength of the matrix shows little influence on α.
2. In comparing the Banthia and Trottier data presented in Figure 6.3a and b, it is seen that the type of fibres is an important factor in the determination of α. In the verification above, α was chosen to best match the experimental data. In the verification process, the VEM was compared with 17 sets of experimental data for end-hooked and straight steel fibres and the α's used for these analyses are plotted in Figure 6.34 against the fibres diameter. The figure shows that for steel fibres $\alpha = d_f / 3.5$. The COV for the data presented is 6.2 percent. There is insufficient data available to draw a conclusion on any relationship between the engagement parameter, α, and the fibre diameter for other (non-metallic) fibres and this is a topic for further research.

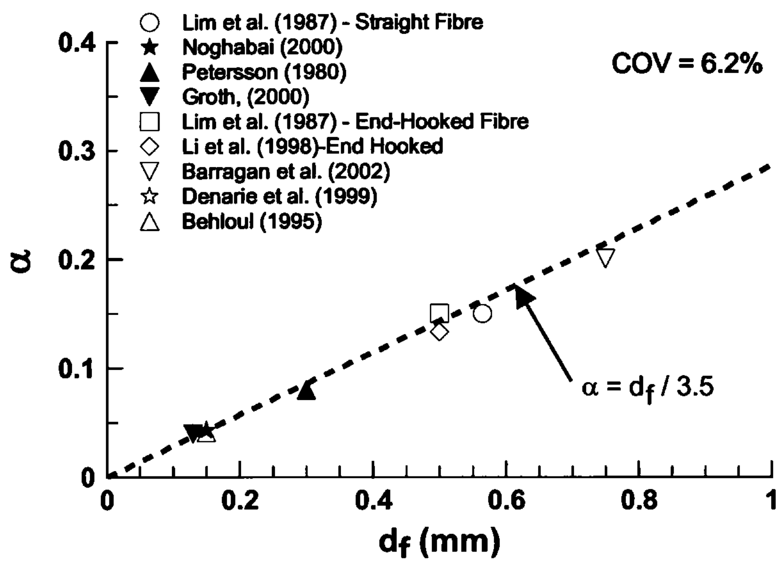

Figure 6.34 – Fibre engagement parameter versus fibre diameter for end-hooked and straight steel fibres.

6.8 Bending of Fibres and Fibre Fracture

In the formulation of FRC in tension, developed above, where fibre fracture is included it was assumed that bending of the fibres has only a small effect on the overall behaviour when using ductile fibres. However, where brittle fibres are used or where a large portion of fibres that cross the cracking plane fracture, the stresses induced through fibre bending can not be ignored. In Figure 6.35, the data of Banthia and Trottier (1994) for their twin cone fibres are plotted comparing the average axial stress in the fibres, normalised for the fracture stress for fibres at $\theta = 0$ degrees, versus fibre angle. In these tests the strength was limited by fibre fracture. The figure shows that as the fibre angle increases the average stress in the fibres, at fracture, decreases. Also plotted in Figure 6.35 is the data of Kanda and Li (1998) for their PVA fibre tests where the fibres fractured. In this chapter a general model is developed that includes fibre bending effects on the influence of fibre fracture for the determination of the $\sigma - \omega$ curve for FRC.

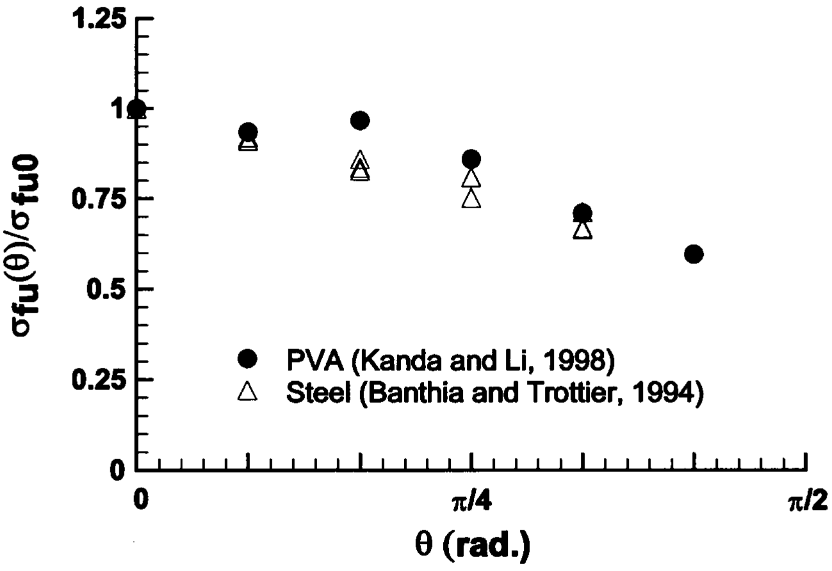

Figure 6.35 – Normalised rupture strength of fibres versus angle of inclination.

6.8.1 Model for Fibre Fracture with Bending

Two cases are considered in the derivation of the limiting axial fracture strength (σ_{au}) for fibre fracture with bending. The first model is based on linear elastic-brittle behaviour (Figure 6.36a) and the second case being of material behaviour for a rigid-plastic material (Figure 6.36b).

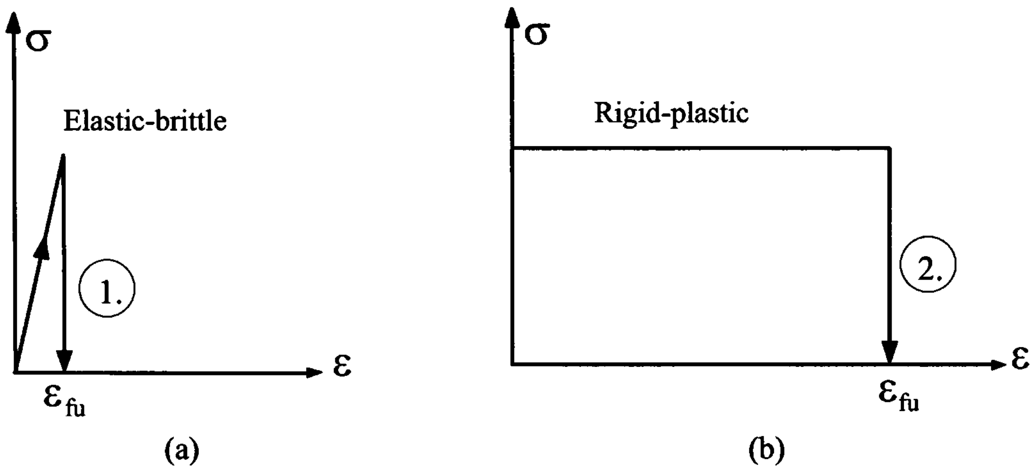

Figure 6.36 – Stress-strain curve for fibre: (a) elastic-brittle and (b) rigid-plastic.

Taking plane sections to remain plane, the axial strain on the fibre and the bending strains can be superimposed to give the total strain as shown in Figure 6.37a. A fibre will fracture when the extreme tensile fibre strain reaches its limiting fracture strain, ε_{fu}. The limiting axial strain of the fibre at any angle of inclination, ε_{au}, can therefore be written as

$$\varepsilon_{au} = \varepsilon_{fu} - \varepsilon_{bu} \tag{6.19}$$

where ε_{bu} is the bending strain at the point of fibre fracture for a fibre orientated at an angle θ to the crack plane. For a perfectly elastic-brittle fibre the limiting average axial fracture strength (σ_{au}) is

$$\sigma_{au} = \sigma_{fu} - \varepsilon_{bu} E_f \qquad \text{for} \qquad 0 \le \varepsilon_{bu} < \varepsilon_{fu} \tag{6.20a}$$

$$\sigma_{au} = 0 \qquad \text{for} \qquad \varepsilon_{bu} \ge \varepsilon_{fu} \tag{6.20b}$$

where σ_{fu} is the fracture stress of the fibre and E_f the elastic modulus of the fibre. For the case of a rigid-plastic material, the limiting average axial fracture strength (σ_{au}) of a fibre of circular cross-section subject to bending is derived in Appendix G and is given by

$$\sigma_{au} = \sigma_{fu} \qquad \text{for} \qquad 0 \le \varepsilon_{bu} < \varepsilon_{fu} / 2 \tag{6.21a}$$

$$\sigma_{au} = \frac{\sigma_{fu}}{\pi} \bullet \left[2\bar{d}\sqrt{1-\left(\bar{d}\right)^2} + 2\sin^{-1}\left(\bar{d}\right) \right] \qquad \text{for} \qquad \varepsilon_{fu} / 2 \le \varepsilon_{bu} < \varepsilon_{fu} \tag{6.21b}$$

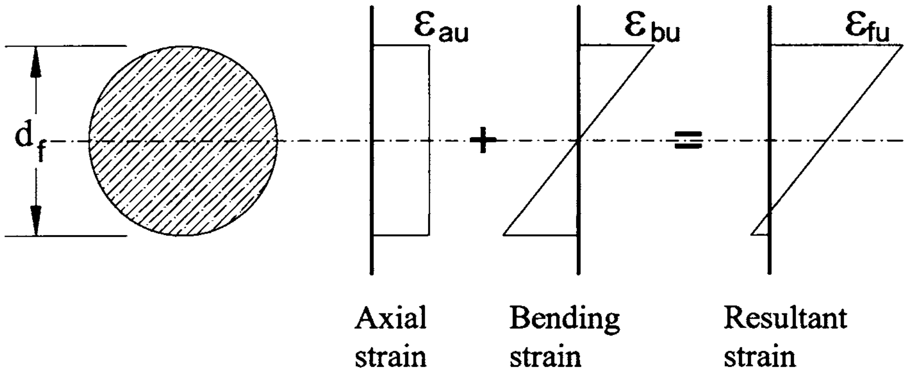

(a) Strains

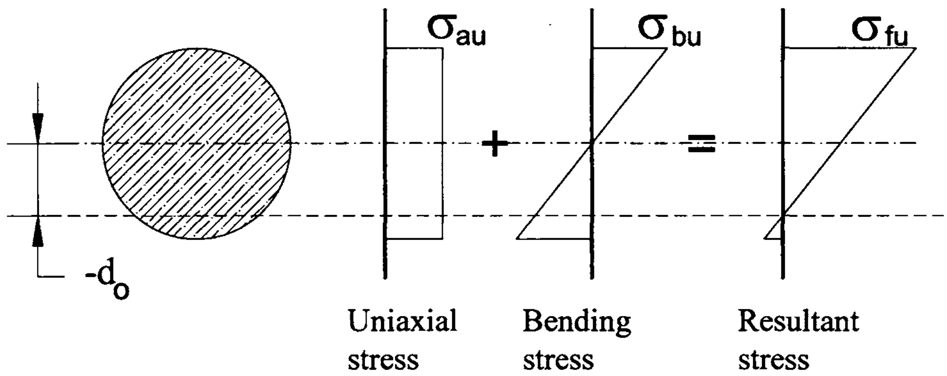

(b) Stresses for elastic-brittle material

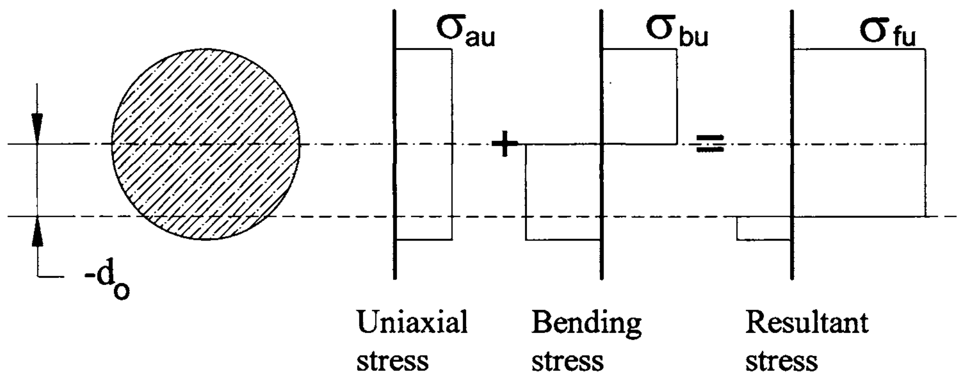

(c) Stresses for rigid-plastic material

Figure 6.37 – Stresses and strains in fibre subject to axial force and bending: (a) strains; (b) stresses for elastic brittle material; and (c) stresses for rigid-plastic material.

where $\bar{d} = 2d_o/d_f$ and d_o is the distance from the plastic centroid of the section to the neutral axis and is given by

$$d_o = \frac{d_f}{2}\left(\frac{\varepsilon_{fu}}{\varepsilon_{bu}} - 1\right) \tag{6.22}$$

Assuming the part of the fibre for which bending occurs has constant moment over an arc of constant radius of curvature (r), shown in Figure 6.38, the relationship between the bending strain ε_{bu} and the diameter of the fibre d_f is written as

$$y'' = \kappa = \frac{2\varepsilon_{bu}}{d_f} \tag{6.23}$$

where κ is the curvature ($\kappa = 1/r$). The boundary conditions dictate that any function describing the radius of the curvature (r) must be asymptotic to the $\theta = 0$ axis as for $\theta = 0$ for $\sigma_{au} = \dot{\sigma}_{fu}$. One function meeting this criteria is $r \propto \cot(\theta)$.

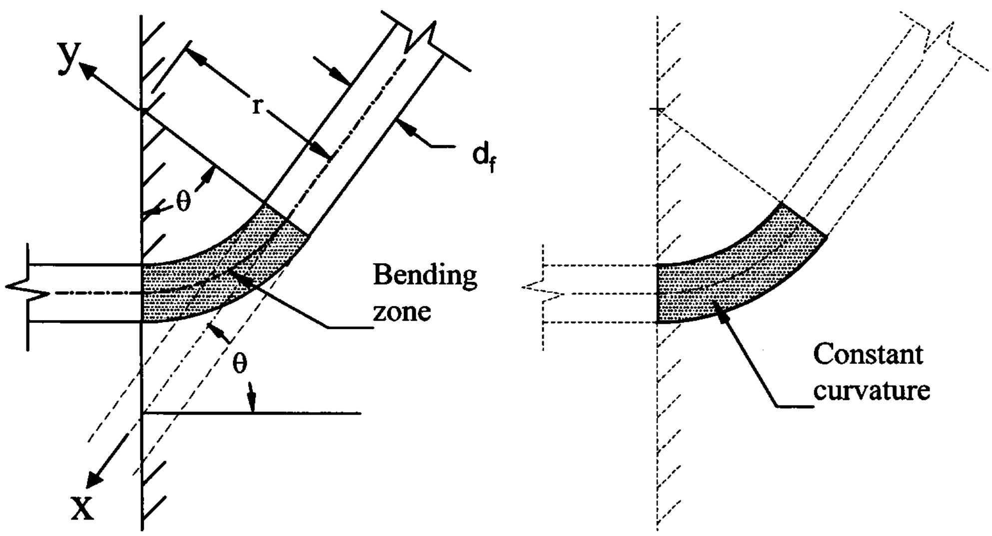

Figure 6.38 – Schematic of bending of fibre in FRC.

For the analyses that follow, we adopt the function

$$r = \frac{\beta\, d_f \cot\theta}{2} \qquad \text{or} \qquad \kappa = \frac{2\tan\theta}{\beta\, d_f} \tag{6.24}$$

where β is an empirical constant. With Eqs. 6.23 and 6.24 we write

$$\varepsilon_{bu} = \frac{1}{\beta}\tan\theta \tag{6.25}$$

The strength interaction diagram for the PVA fibres used by Kanda and Li (1998) are plotted in Figure 6.39 together with the theory for elastic-brittle fibres described by Eqs. 6.20 and 6.25. The fibres used have a diameter of 0.014 mm and an ultimate tensile strength and the modulus of elasticity of 2250 MPa and 60 GPa, respectively. It is shown that with $\beta = 200$ the model correlates well with the experimental data.

Both the elastic-brittle theory given by Eq. 6.20 and the rigid-plastic theory given in Eq. 6.21 are plotted in Figure 6.40 with the results of the twin cone steel fibre of Banthia and Trottier (1994). The fibre used had a diameter of 1.0 mm and an ultimate tensile strength and modulus of elasticity of 1200 MPa and 200 GPa, respectively. The limiting fracture strain of the fibre is taken as 0.04. Comparing the test data with the two models shows that the rigid-plastic theory does not capture well the strength interaction of the more ductile, steel fibre. On the other hand, the elastic theory compares well with the collected data. In the elastic curve shown in Figure 6.40 a value of $E_f / \beta = 300$ MPa is used as was the case for the PVA fibres plotted in Figure 6.39.

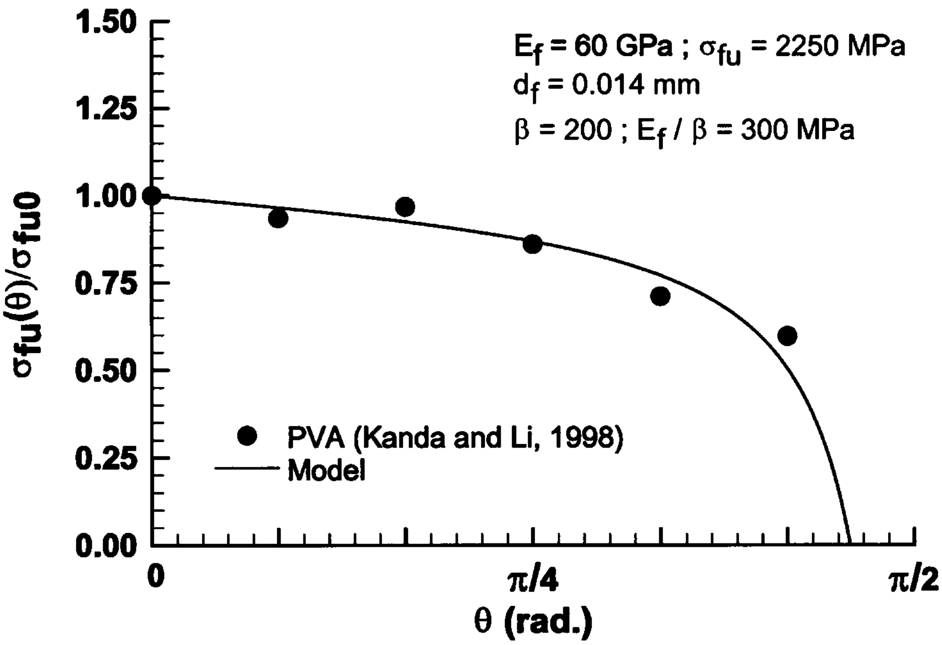

Figure 6.39 – Comparison of VEM with the experimental data of Kanda and Li (1998).

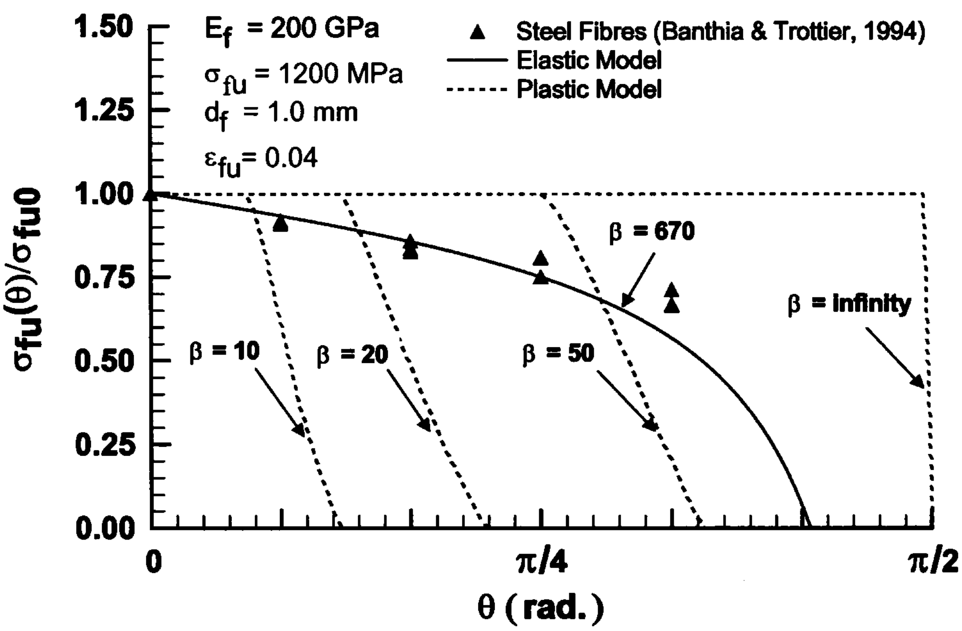

Figure 6.40 – Comparison of proposed models with the twin cone fibre data of Banthia and Trottier (1994).

6.8.2 Wang (1989) and Wang et al. (1990a, b)

As discussed in Section 6.6.7, Wang (1989) and Wang et al. (1990a, b) undertook a series of uniaxial tension strength tests on various types of synthetic fibres with various volumetric ratios in conventional strength mortars and high strength concrete. For the experimental verification of the VEM with fibre bending and fracture, the aramid fibre tests and the polyethylene tests are analysed. Two types of high strength aramid fibres were used, that is Kevlar 49 and Technora. The Kevlar 49 fibres used were 6.35 mm long by 0.012 mm in diameter with an ultimate tensile strength of 3310 MPa and elasticity modulus of 70 GPa. The Technora fibres were 6.35 mm long by 0.012 mm in diameter, had, an ultimate tensile strength of 3940 MPa and elasticity modulus of 60 GPa. Normal strength mortar was used for all specimens with cement / sand / water ratios, by weight, of 1/1/0.5. Notched specimens for the direct tensile strength test had a net cross section dimension of 51 mm square (see Figure 6.27) and were tested as described in Section 6.6.7 of this thesis. The interfacial bond strength is taken as 4.5 MPa for the Kevlar fibre as measured by Wang (1989). The interfacial bond strength of Technora fibre was not reported and is also taken to be 4.5 MPa.

Figure 6.41 compares the $\sigma - \omega$ curve obtained using the VEM with the experimental data for Wang for their tests on Technora FR mortars with one, two and three percent of fibres. It was reported that the measured average composite strength and fracture energy for the 1 percent composite were 3.31 MPa and 1.42 N/mm, respectively; and the composite strength and fracture energy for 2 percent of the composite were 3.11 MPa and 1.28 N/mm, respectively, whereas the average composite strength and fracture energy for 3 percent of the composite were 3.65 MPa and 1.87 N/mm, respectively (see Appendix F, Table F6).

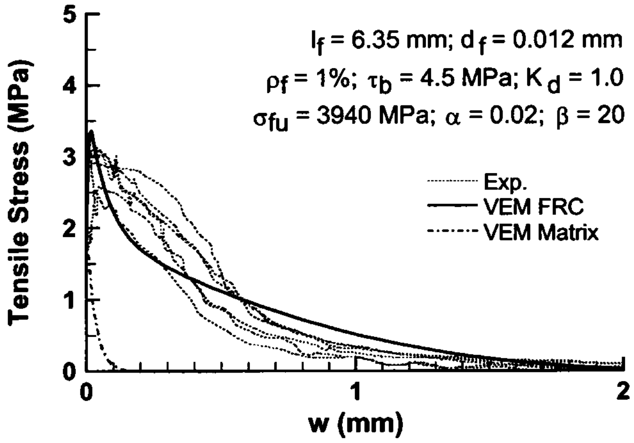

(a)

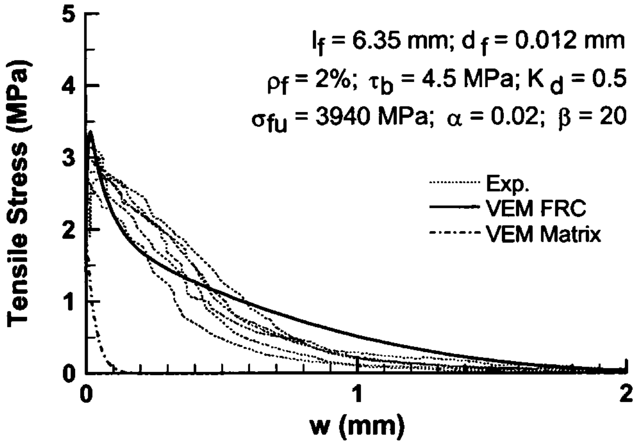

(b)

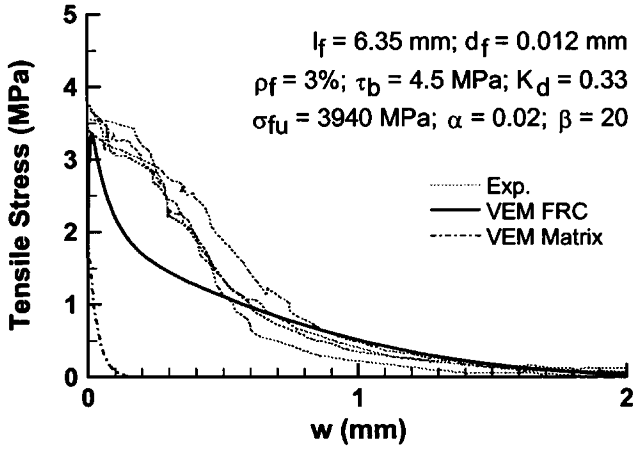

(c)

Figure 6.41 – Comparison of VEM including fibre-fracture with bending with data from Wang (1989) on Technora fibre reinforced normal strength mortar: a) ρ_f = 1 percent; b) ρ_f = 2 percent; and (c) ρ_f = 3 percent.

It was observed that the peak strength and fracture energy of the composite did not increase significantly for increasing fibre volumes. According to Wang et al. (1991), the insignificant increase in strength of higher volume of FRC was due to balling (or clumping) of the fibres as observed in scanning electron micrographs. Also, it was observed that a major failure mechanism for aramid FRC were crack deflection around fibre bundles, bundle splitting and bundle shearing. The authors stated

> "*...it appears from these observations that the maximum fibre volume fractions which can be included in this matrix without causing sever fibre bundling and clumping is around or slightly more than 1% ...*"

Assuming that a fibre volume of 1 percent was the optimum quantity of fibre that is able to be uniformly distributed in the matrix, a fibre efficiency factor (K_d) is used to account for the observed fibre bundling or clumping in the Technora fibre matrix. Thus for 2 percent and 3 percent by volume of fibres $K_d = 0.5$ and $K_d = 0.33$, respectively. The matrix strength was taken as 1.85 MPa. An engagement parameter $\alpha = 0.20$ was taken for the aramid fibre and $\beta = 20$ was used to account for the brittle nature of the fibres. The peak composite strength and fracture energy calculated by the VEM are summarised in Appendix F, Table F6. The table shows that VEM calculates the cracking strength and fracture energies within 20 percent of measured values.

Figure 6.42 and Appendix F (Table F6) compare the uniaxial tensile $\sigma - \omega$ of fibre reinforced cement as determined from the VEM for a 2 percent Kevlar 49 fibre reinforced mortar. The measured average composite strength and fracture energy were 4.0 MPa and 1.3 N/mm, respectively. In the model the matrix cracking strength was taken as 1.85 MPa (as measured from split cylinder tests). As for the Technora fibres, $\alpha = 0.20$ was used for the Kevlar 49 fibres with $\beta = 20$. The model gives a peak composite strength of 3.3 MPa and a fracture energy of 1.3 N/mm and compares favourably with the test data.

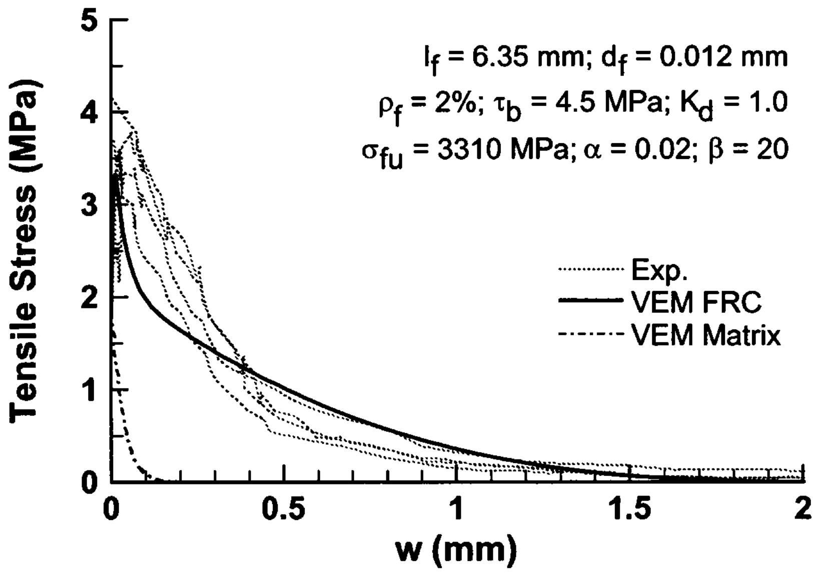

Figure 6.42 – Comparison of VEM including fibre fracture and bending with data from Wang et al. (1990a and b) on 2 percent by volume of Kevlar 49 FR mortar.

6.8.3 Maalej et al. (1995)

Maalej et al. (1995) undertook uniaxial tension tests on aramid fibre reinforced mortar. The fibres used were 12.7 mm long by 0.012 mm diameter Kevlar 49 having an ultimate tensile strength of 3310 MPa and modulus of elasticity of 70 GPa. The matrix consisted of Type 1 Portland cement, silica fume and superplasticizer with ratios of 1:0.1:0.02 and a water to cement ratio of 0.27. The measured elastic modulus of the matrix was 13 GPa. The fibre/matrix interfacial bond strength was taken to be 4.5 MPa (as measured by Wang (1989) for an identical mortar-matrix mix). The uniaxial tension test is conducted on notched rectangular uniaxial tension specimens with a net cross section dimension of 50 mm by 13 mm. The matrix strength is taken as 4.0 MPa and the full $\sigma - \omega$ for the non-reinforced mortar is determined from Eq. 6.19. A constant $\alpha = 0.02$ was used for the aramid (Kevlar) and the fibre fracture-bending constant is taken as $\beta = 20$. The results of the VEM are compared with the Maalej et al. data in Figure 6.43 and Appendix F, Table F8.

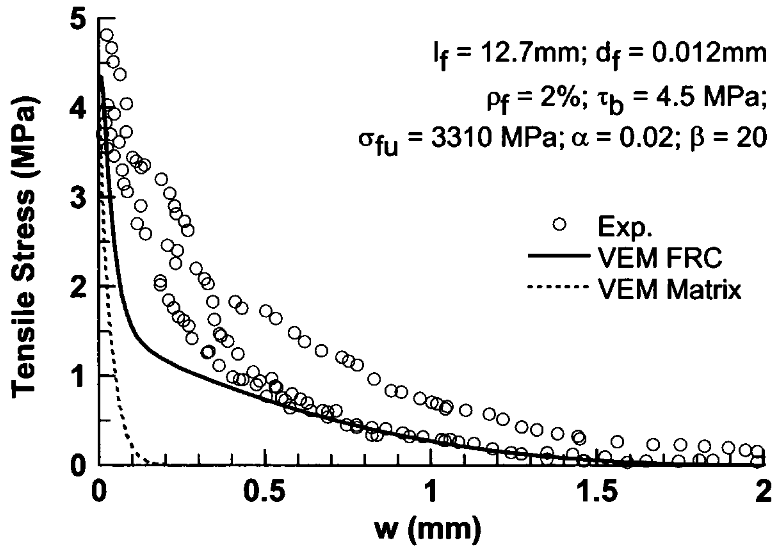

Figure 6.43 – Comparison of VEM with experimental data of Maalej et al. (1995).

6.9 General Comments on the Fibre Fracture-Bending Model Parameter, β

In this section, the influence of bending induced stress on the weakening of fibres in axial tension is discussed. Two models were proposed, the first based on elastic theory and the second based on plastic theory. Of the two models, the elastic model shows significant promise for the modelling of fibre reinforced composites in uniaxial tension where a significant proportion of fibres fracture after cracking of the matrix and at, or before, engagement. Whilst based on a rational concept for elastic fibres, in the extension of the model to include elastic-plastic fibres, the fibre fracture-bending parameter, β, is taken as an empirically derived constant.

While a more general model for elastic-plastic fibres could be developed for bending of circular fibres combined with axial tension, the model becomes complex due to issues such as the order of load application (eg. bending followed by axial loading at the point of engagement), yielding and unloading. To this extent the use of elastic theory provides an attractive semi-rational approach and, in the authors' opinion, explains adequately the concepts of the behaviour while maintaining the simplicity of the model.

6.10 Summary of Verified Fracture Energies

In calibration studies it was found that for end-hooked and straight steel fibers the engagement parameter can be taken as $\alpha = d_f/3.5$. With this relationship and the material properties given in Appendix F, the partial fracture energies were calculated using the VEM and compared with the measured data. The energies compared are those measured at the conclusion of the experimental test. The results, given in Table 6.3, give a mean experimental to theoretical ratio of 0.92 and a standard deviation of 0.19. Two studies used in the verification include multiple, identical, specimens from Barragán et al., (2003) and Toutlemonde and Torrenti, (1999). The standard deviation in measured fracture energies for the test data on the identical tests are 0.26 and 0.19, respectively. Thus, it is concluded that the VEM compares well with the test data with the standard deviation of the test to model within the variation of the experiments.

Table 6.3 – Comparison of partial fractures energies calculated by the VEM with measured data.

Reference	Specimen	Failure Mode	$G_{F,\exp}$ (N/mm)	COD for $G_{F,\exp}$ (mm)	$G_{F,VEM}$ (N/mm)	$\frac{G_{F,VEM}}{G_{F,\exp}}$
Barragán et al. (2003)	Specimen 1	P	2.08	2.0	1.61	0.77
	Specimen 2	P	1.32	2.0	1.61	1.22
	Specimen 3	P	2.02	2.0	1.61	0.80
	Specimen 4	P	1.36	2.0	1.61	1.18
	Specimen 5	P	2.46	2.0	1.61	0.65
Behloul (1995)	2.6% Fibres	P	17.28	4.8	15.80	0.91
Behloul (1996)	1% Fibres	P	11.95	5.0	4.84	0.41
	2.4% Fibres	P	12.20	5.5	11.59	0.95
	4% Fibres	P	17.85	5.5	19.04	1.07
Groth (2000)	OPC	P	1.82	1.5	1.51	0.83
	S50	P	1.61	1.5	1.58	0.98
	Q50	P	1.39	1.5	1.24	0.89
	EMC500	P	1.78	1.5	1.65	0.93
Noghabai (2000)	S-6/015	P	1.63	full curve	1.17	0.72
	M-6/015-2	P	0.78	full curve	1.05	1.34
Li et al. (1987)	Specimen 1	PF	9.04	1.0	8.77	0.97
Lim et al. (1987b)	S22	P	0.163	3.50	1.83	0.867
	S3	P	0.163	3.50	2.38	0.904
	H21	P	0.143	3.50	6.91	1.055
	H22	P	0.143	3.50	4.42	0.994
	H3	PF	0.143	3.50	6.90	1.075
Petersson (1980)	R 0.25%	P	1.69	7.0	1.55	0.92
	R 0.50%	P	4.10	7.0	3.04	0.74
	R 1.00%	P	7.10	7.0	6.04	0.85
Toutlemonde & Torrenti (1999)	Specimen 1	P	9.67	2.0	6.35	0.66
	Specimen 2	P	6.48	2.0	6.35	0.98
	Specimen 3	P	5.49	2.0	6.35	1.16
	Specimen 4	P	7.69	2.0	6.35	0.83
	Specimen 5	P	7.13	2.0	6.35	0.89
Average						**0.92**
Std. Dev.						**0.19**

* Note: P = Fibre pullout; PF = Fibre pullout and fracture.

6.11 Conclusions

Many models have been proposed for the design of fibre reinforced concrete under uniaxial tension, but the models are generally limited in their use as a tool for structural designers due to limitations of the model or due to the complexity of the model. For design, engineers require a simple yet reliable approach that explains and models with sufficient accuracy the behaviour under load of fibre reinforced concrete in tension. In this thesis, a simple deterministic model, the Variable Engagement Model (VEM), is developed to describe the behaviour of randomly orientated steel fibre reinforced composites subject to uniaxial tension. The model is developed by integrating the behaviour of single, randomly oriented, fibres over 3D space and is capable of describing the peak and post-peak response of fibre-cement-based composites in tension.

In the verification studies of the VEM, the proposed model is compared against a wide range of experimental data and includes 29 uniaxial tension tests on fibre reinforced concretes and mortars by 10 researchers. Overall the model showed a good correlation with both the uniaxial tensile strength of the specimens and with the fracture energies. The loads versus crack opening displacements are plotted and again good agreement is seen for the model compared with the experimental data. Finally, a model was proposed for the inclusion of bending effects on the weakening of fibres in axial tension. Two methodologies were pursued, an elastic model and a plastic model. The results of the investigation showed that the elastic approach can capture observed behaviour of fibres subject to combined tension and bending across a cracked medium. Further research is required to confirm the general applicability of the proposed fibre fracture-bending model.

CHAPTER 7 – FINITE ELEMENT MODELLING OF FIBRE REINFORCED CONCRETE BEAMS

7.1 Introduction

In this chapter, the variable engagement model (VEM) is incorporated as a constitutive model for non-linear finite element modelling. The model is verified against a number of experimental tests on fibre reinforced concrete beams with concrete strengths from 30 to 170 MPa. In the numerical analysis, the FE program RECAP (Foster, 1992a) was modified for the incorporation of the VEM as per Chapter 6 for the modelling of Mode I fracture of fibre reinforced concrete. A total of 45 FR-concrete beams are numerically modelled and the results are presented.

7.2 Constitutive Relationship for Orthotropic Membranes

In the FE modelling, the concrete element is modelled as two dimensional orthotropic membrane elements. Details of the material law can be found from the earlier work of Foster (1992a, 1992b), Foster et al. (1996) and more currently, Foster and Marti (2003). In this section, the formulation of the material law on the orthotropic membrane element used in the FE program is briefly presented.

Utilizing the concept of equivalent uniaxial strains, as developed by Darwin and Pecknold (1977), Foster (1992a, 1992b) developed a finite element program (RECAP) for the analysis of reinforced concrete membranes subjected to biaxial stresses. The equivalent uniaxial strain can be thought of as the strain that would exist in one direction when the stress in the other direction is zero. This can be written as

$$\begin{Bmatrix} \varepsilon_1 \\ \varepsilon_2 \end{Bmatrix} = \begin{bmatrix} 1 & -\nu_{12} \\ -\nu_{21} & 1 \end{bmatrix} \begin{Bmatrix} \varepsilon_{1u} \\ \varepsilon_{2u} \end{Bmatrix} \tag{7.1}$$

where ε_1 and ε_2 are the strains in the principal directions, ε_{1u} and ε_{2u} are the equivalent uniaxial strains in the principal directions and ν_{12} and ν_{21} are Poisson's ratios (Foster and Rangan, 1999, Foster and Marti, 2003).

By inverting the coefficient matrix of Eq. 7.1 the equivalent uniaxial strains are obtained such that

$$\begin{Bmatrix} \varepsilon_{1u} \\ \varepsilon_{2u} \end{Bmatrix} = \frac{1}{1-\nu_{12}\nu_{21}} \begin{bmatrix} 1 & \nu_{12} \\ \nu_{21} & 1 \end{bmatrix} \begin{Bmatrix} \varepsilon_1 \\ \varepsilon_2 \end{Bmatrix} \tag{7.2}$$

The stress is then obtained from uniaxial base material models and given by

$$\begin{Bmatrix} \sigma_{c1} \\ \sigma_{c2} \end{Bmatrix} = \begin{bmatrix} E_{c1} & 0 \\ 0 & E_{c2} \end{bmatrix} \begin{Bmatrix} \varepsilon_{1u} \\ \varepsilon_{2u} \end{Bmatrix} \quad \ldots\ldots \; (i = 1, 2) \tag{7.3}$$

where E_{c1} and E_{c2} are the secant moduli in the principal (1, 2) stress directions and are determined from the appropriate uniaxial stress-strain curve.

After cracking, it is taken that there is no transmission of lateral tension strains across the cracks and thus for cracking in the major principal direction $\nu_{21} = 0$. When cracking occurs in the minor principal direction $\nu_{12} = \nu_{21} = 0$.

Relating the stresses and strains in the familiar manner of $\{\sigma\} = [D]\{\varepsilon\}$, the material elasticity matrix in the material 1-2 coordinate system is taken as that suggested by Darwin and Pecknold (1977)

$$[D]_{c12} = \frac{1}{(1-\nu_{12}\nu_{21})}\begin{bmatrix} E_{c1} & \sqrt{\nu_{12}E_{c1} \cdot \nu_{21}E_{c2}} & 0 \\ & E_{c2} & 0 \\ sym. & & (1-\nu_{12}\nu_{21})G_{c12} \end{bmatrix} \quad (7.4)$$

with the shear modulus G_{c12} derived by Attard et al. (1996) and is

$$(1-\nu_{12}\nu_{21})G_{c12} = \frac{1}{4}[E_{c1}(1-\nu_{12}) + E_{c2}(1-\nu_{21})] \quad (7.5)$$

The material elasticity matrix is transformed into the global XY coordinates by

$$[D]_{cxy} = [T]_{\varepsilon}^{T}\,[D]_{c12}\,[T]_{\varepsilon} \quad (7.6)$$

where $[T]_{\varepsilon}$ is the strain transformation matrix.

Finally, the element stiffness matrix is obtained in the usual manner

$$[k] = t\,\int_{A}[B]^{T}\,[D]_{xy}\,[B]\;dA \quad (7.7)$$

where t is the element thickness and $[B]$ is the strain displacement matrix.

7.3 Constitutive Relationship for Reinforcing and Prestressing Steel

The trilinear curve shown in Figure 7.1 is used to model the steel reinforcement used in the FR-beams, where E_p is the modulus of elasticity of prestressing wires, E_s is the modulus of elasticity, σ_y is the yield strength of the reinforcement corresponding to the yield strain of ε_y, σ_r is the tensile strength corresponding to strain of ε_r; and ε_u is the ultimate strain at the point of fracture. In the FE modelling, this trilinear curve is used to model all steel bars. This includes longitudinal tension and compression bars and transverse reinforcement (if any).

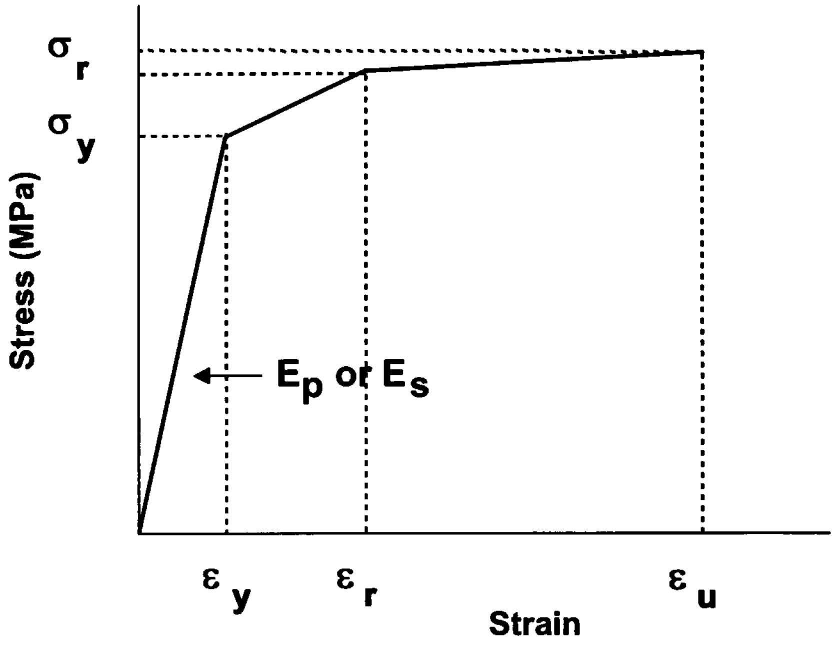

Figure 7.1 – Tri-linear model for reinforcing and prestressing steel.

7.4 Constitutive Relationship for Fibre-Reinforced Concrete

The stress-strain law of the concrete in compression is modelled using Thorenfeldt et al.'s (1987) model

$$f_c = f_{cp} \frac{n\eta}{n-1+\eta^{nk}} \tag{7.8}$$

where $\eta = \varepsilon_c / \varepsilon_{cp}$; ε_c is the concrete strain; ε_{cp} is the strain corresponding to the peak in-situ stress, f_{cp}; n is a curve fitting factor given by $n = E_o / (E_o - E_{cp})$; E_o is the initial modulus of elasticity of the concrete; $E_{cp} = f_{cp} / \varepsilon_{cp}$ is the secant modulus; and k is a decay factor for the post peak response and increases with the concrete strength. The decay factor used in this study is that proposed by Collins and Mitchell (1991) and is taken as $k=1$ before the peak stress and taken as $k = 0.67 + f_{cp}/62 \geq 1.0$ after the peak stress.

Figure 7.2 shows the stress-strain relationship of FR composite in uniaxial tension. The constitutive law of the FR-composite is composed of the superposition of two distinctive components; the first being the tension softening law of the matrix (without inclusion of fibres) and the second being the contribution of the fibres after cracking of the matrix.

For the non-fibre reinforced matrix, the bilinear stress-strain model of Petersson (1981) is used as shown in Figure 7.2a with the tension softening parameters

$$\alpha_1 = 1/3; \quad \alpha_2 = \frac{2}{9}\alpha_3 + \alpha_1; \quad \alpha_3 = \frac{18}{5}\frac{E_o G_{Fm}}{l_{ch}\, f_{ct}^2} \tag{7.9}$$

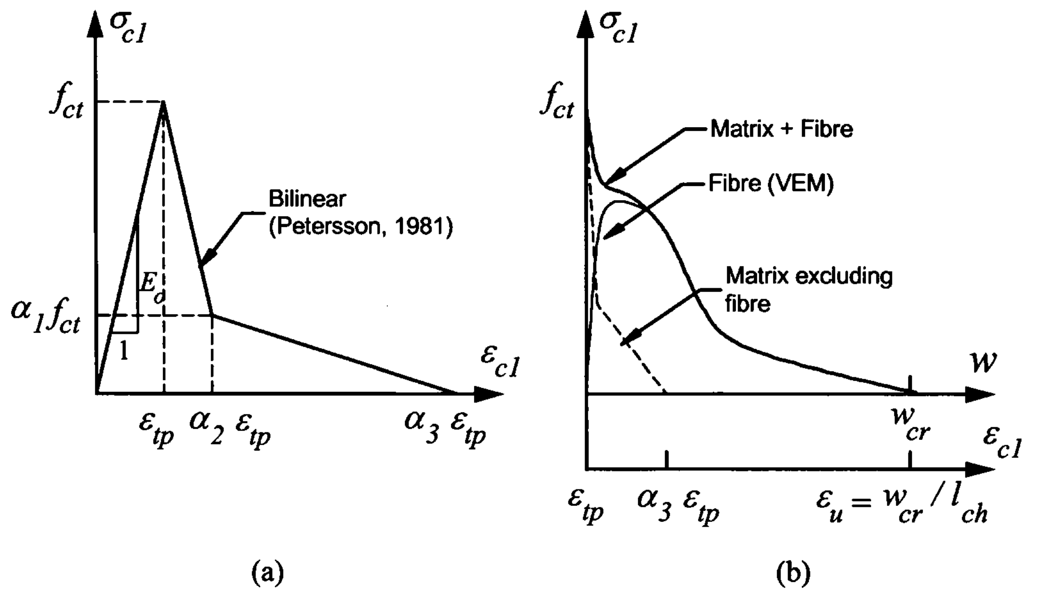

Figure 7.2 – Fibre reinforced concrete in tension: (a) bilinear stress-strain model for RPC matrix and (b) variable engagement model.

where f_{ct} is the tensile strength of the matrix (excluding fibres); ε_{tp} is the cracking strain of the matrix; E_o is the initial elastic modulus of the concrete; G_{Fm} is the fracture energy of the matrix; and l_{ch} is the characteristic length of the finite element. For the strength contribution of the fibres, the stress-COD of the VEM is given by Eqs. 6.7, 6.12 and 6.18.

In the FE modelling, the matrix cracking strength is taken as the experimental results measured by the investigators based on their uniaxial tension strength tests. Where f_{ct} was not measured experimentally the tensile strength was taken as $f_{ct} = 0.33\sqrt{f_{cm}}$. This reduced tensile strength takes into consideration residual stresses due to shrinkage of the specimens and is consistent with models for normal strength and high strength concrete and with the experimentally observed cracking loads compared with that obtained from the FE modelling.

The matrix fracture energy (G_{Fm}) of the concrete is taken as that given by the trend line as given in Figure 7.3 which plots the experimental data for fracture energies of normal and high strength concretes tested in uniaxial tension.

For normal strength and high strength concrete, the bond shear strength is taken as per Table 6.2, that is

$$\tau_b = 2.5 f_{ct} \qquad \text{for deformed fibres} \qquad (7.10a)$$

$$\tau_b = 1.2 f_{ct} \qquad \text{for straight fibres} \qquad (7.10b)$$

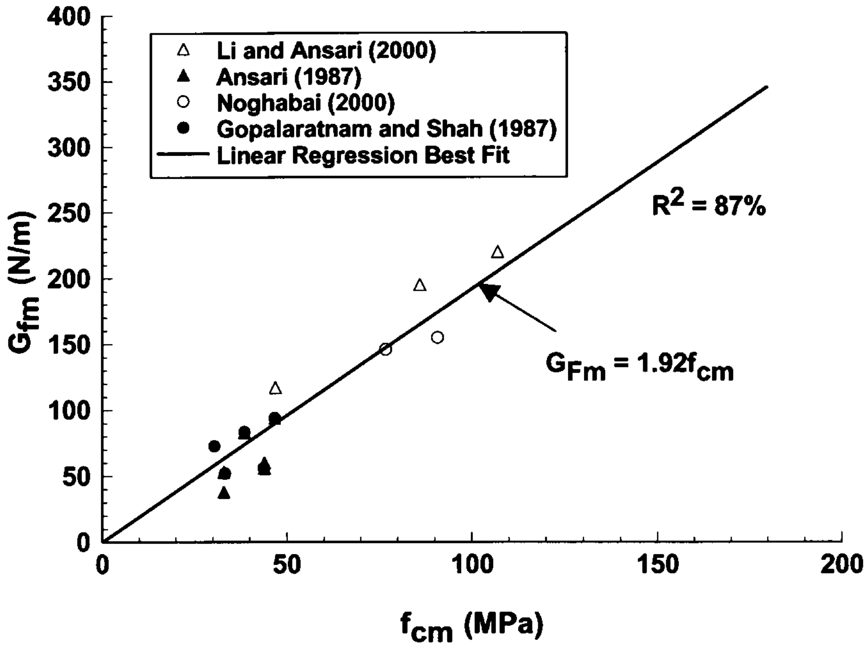

Figure 7.3 – Fracture energy of non-fibre reinforced concrete versus concrete strength.

For reactive powder concrete, the bond strength for straight steel (SS) fibre is taken as 10 MPa as reported by Orange et al. (1999). Since no information is available for the bond strength of end-hooked (EH) fibres in RPC, a value of τ_b = 15 MPa is used in the analyses that follow. The engagement parameter is taken as $\alpha = d_f/3.5$ for all analyses.

7.5 Experimental Verification

In the verification, a total of 45 FR-concrete beams are examined. Among the 45 specimens, the investigating parameters consist of the cross-sectional geometry, specimen size, shear span-to-depth ratio, fibre types and fibre quantities, concrete strengths and steel reinforcement ratios. A summary of the tests used in the verification is given in Table 7.1.

Table 7.1 – Summary of FRC beams without stirrups for FE verification.

Reference	No. of Beams	Beam Type*	$b_w x d_e$ mm	ρ_w %	a/d	f_{cm} MPa	f_{cu} MPa	Fibre Type	l_f mm	ρ_f %
This study (Chapter 5)	7	I	50x600	5.72	3.33	150-170	-	SS, HS	13 30	1.3,2.5
Adeline and Behloul (1996)	2	X	40x350	8, 2	-	150	-	SS	13	2, 2.5
Noghabai (2000)	16	R	200x180 200x410 300x570	3.1, 4.5 3.0 2.9	3.1, 3.3 2.9 3.0	46-91 60-77 60-77	-	SS	6, 30 60	0-1.0
Swamy et al. (1993)	9	I	55x265	1.55 2.76 4.31	2, 3.43 4.91	32-41	-	CS	50	1.0
Narayanan and Darwish (1998)	11	R	100x345	3.6	0.5-0.7	-	38-68	CS	30	0-1.25

Notes: * Beam type; R = rectangular; T = T-beam; I = I-beam; X = X-section
Fibre type: CS = crimped steel; HS = hooked steel; SS = straight steel

7.5.1 FR-RPC Beams Tested in this Study (Chapter 5)

The experimental results of seven FR-RPC I-section beams with concrete standard cylinder compressive strengths of 150 to 170 MPa were reported in Chapter 5 of this thesis. The test variables included fibre type, fibre quantities and prestress.

Details of the FE mesh used are given in Figure 7.4. The FE mesh consists of 630 by 4-node isoparametric concrete elements for the flanges and web and 6 by 4-node stiff elements for the steel plates. The prestressing steel in the specimens are model as 2-node bar elements prestrained as appropriate to simulate the prestressing force. Perfect bond was assumed between the steel and the concrete. One half of the specimen is modelled accounting for symmetry. The material parameters used to develop the constitutive law of the FR-concrete in the FE modelling are given in Table 7.2.

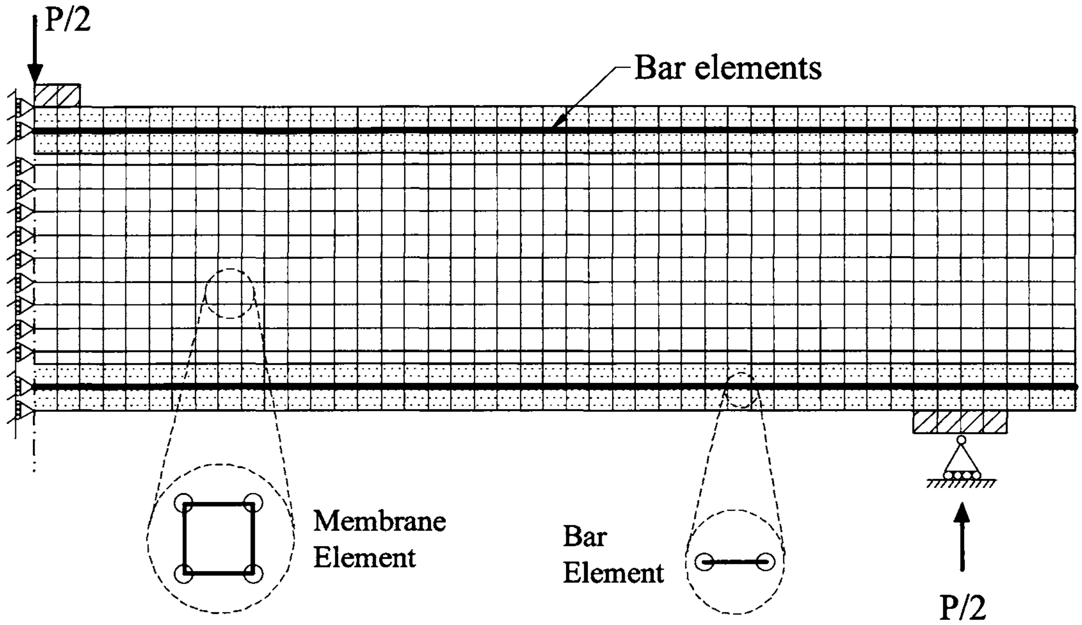

Element Type	Number of Elements	Area (mm^2)	Thickness (mm)
Top flange	90	-	400
Top flange/web interface	45	-	225
Web	360	-	50
Bottom flange/web interface	45	-	150
Bottom flange	90	-	250
Bottom steel plate	4	-	250
Top steel plate	2	-	400
Top prestress steel	45	858	-
Bottom prestress steel	45	1716	-

Figure 7.4 – Finite element mesh for RPC beams tested in this study.

Table 7.2– Material parameters used for modelling the prestress FR-RPC girders tested in this study.

Specimen Notation	SB1	SB2	SB3	SB4	SB5	SB6	SB7
ncrete							
f_{cp} (MPa)	161	160	150	164	171	157	169
f_{ct} (MPa)	4.19	4.17	4.04	4.23	4.32	4.14	4.29
E_o (GPa)	44	45	43	43	49	40	46
G_{Fm} (N/m)	330	330	310	340	350	320	350
l_{ch} (mm)	50	50	50	50	50	50	50
ε_{cp}	0.004	0.004	0.004	0.004	0.004	0.004	0.004
ν	0.15	0.15	0.15	0.15	0.15	0.15	0.15
α_1	0.33	0.33	0.33	0.33	0.33	0.33	0.33
α_2	13.6	13.9	13.4	13.4	15.1	12.3	14.3
α_3	60	61	59	59	66	54	63
estressing Steel #							
Initial Prestress Strain, ε_{pi}	0	0.0027	0.00135	0.00135	0.00135	0.00135	0.00135
E_p (GPa)	195	195	195	195	195	195	195
ε_y	0.00769	0.00769	0.00769	0.00769	0.00769	0.00769	0.00769
ε_r	0.02	0.02	0.02	0.02	0.02	0.02	0.02
ε_f	0.05	0.05	0.05	0.05	0.05	0.05	0.05
σ_y (MPa)	1500	1500	1500	1500	1500	1500	1500
σ_r (MPa)	1750	1750	1750	1750	1750	1750	1750
bre							
Fibre Type	SS	SS	SS	SS	SS / EH	EH	SS / EH
ρ_f (%)	2.5	2.5	2.5	1.25	1.5 / 1.0	2.5	1.88 / 0.62
l_f (mm)	13	13	13	13	13 / 30	30	13 / 30
d_f (mm)	0.2	0.2	0.2	0.2	0.2 / 0.5	0.5	0.2 / 0.5
σ_{fu} (MPa)	1800	1800	1800	1800	1800 / 1200	1200	1800 / 1200
τ_b (MPa)	10	10	10	10	10 / 15	10	10 / 15
α	0.057	0.057	0.057	0.057	0.057 / 0.143	0.143	0.057 / 0.143

Notes: SS = straight steel fibre; EH = end hooked fibre

see Figure 7.1 for stress-strain definitions

Table 7.3 shows the comparison of the shear strengths obtained from the FE modelling ($\tau_{u,FEM}$) with the results from the experimental testing ($\tau_{u,\exp}$) for beams SB1 to SB7. The mean theoretical to experimental ratio for the peak load was 0.91 with a coefficient of variation of 7.6 percent. Figure 7.5 shows that, with the exception of SB1, the FE results compared well with the experimental data for the midspan deflection of the girders.

The FE results for beams SB3 and SB7 are compared to the experimental results in the following (with the results typical of the seven beams tested). In Figures 7.6 to 7.9 the flexural tensile and flexural compressive strains measured in the flanges of beams SB3 and SB7 are plotted. The FE results compare well with the measured data.

Of particular interest in the FE analyses are the behaviour of the shear spans given the absence of conventional shear reinforcement. In Figure 7.10a, the principal tension strains are plotted for the shear span of beam SB3 for a load approximately equal to the FE ultimate load. At the FE ultimate load of 810 kN, the maximum tensile strain in the web of the prestressed beam is 0.055 which is equivalent to a crack width of 2.75 mm. In Figure 7.10b, the principal stress vectors are plotted showing the major critical crack angle of approximately 28 degrees to the horizontal. This compares with the observed failure crack angle of 32 degrees in the test beam.

In Figure 7.11a, the principal tension strains are plotted for beam SB7 for a load equal to the failure load. At the predicted peak load of 794 kN, the maximum tension strain for the prestressed beam is 0.050 which is equivalent to a crack width of 2.5 mm. Comparing the FE results with the experimental crack pattern and Figure 7.11b shows the FE analyses correctly captures the location and angle of the major diagonal shear crack at failure. In Figure 7.11b, the principal strain vectors show that the major critical crack angle is approximately 23 degrees and this compares with an angle measured in the experimental beam of 21 degrees.

In general, the results of the FE model compare well with the experimental data for the overall response of the beams with the FE model able to correctly capture the overall behaviour including the failure mode. The one exception is beam SB1 which gave a significantly lower calculated capacity than that observed in the experiment. The general behaviour and failure mode of SB1, however, is similar to that of the test beam.

Table 7.3 – Comparison of experimental shear strength and FE model for specimens SB1 to SB7.

Specimen No.	$V_{u,\exp}$ (kN)	$\tau_{u,\exp}$ (MPa)	$V_{u,FEM}$ (kN)	$\tau_{u,FEM}$ (MPa)	$\frac{\tau_{u,FEM}}{\tau_{u,\exp}}$
SB1	430	14.33	340	11.33	0.79
SB2	497	16.57	442	14.73	0.89
SB3	428	14.27	405	13.50	0.95
SB4	337	11.23	304	10.14	0.90
SB5	440	14.67	384	11.83	0.87
SB6	330	11.00	324	9.08	0.98
SB7	397	13.23	394	12.67	0.99
Average					0.91
COV.					0.076

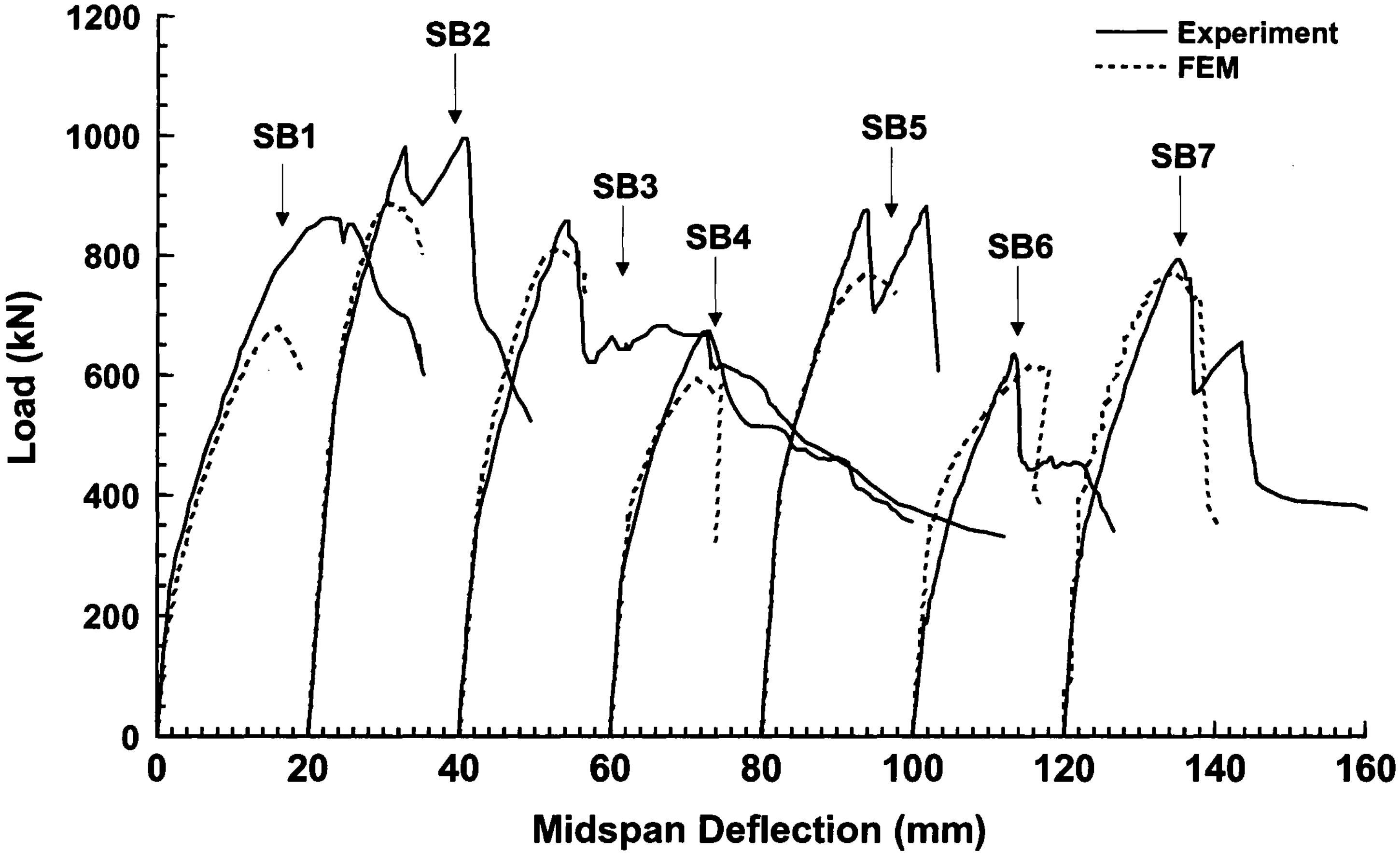

Figure 7.5–Load versus mid-span displacement of specimens SB1 to SB7.

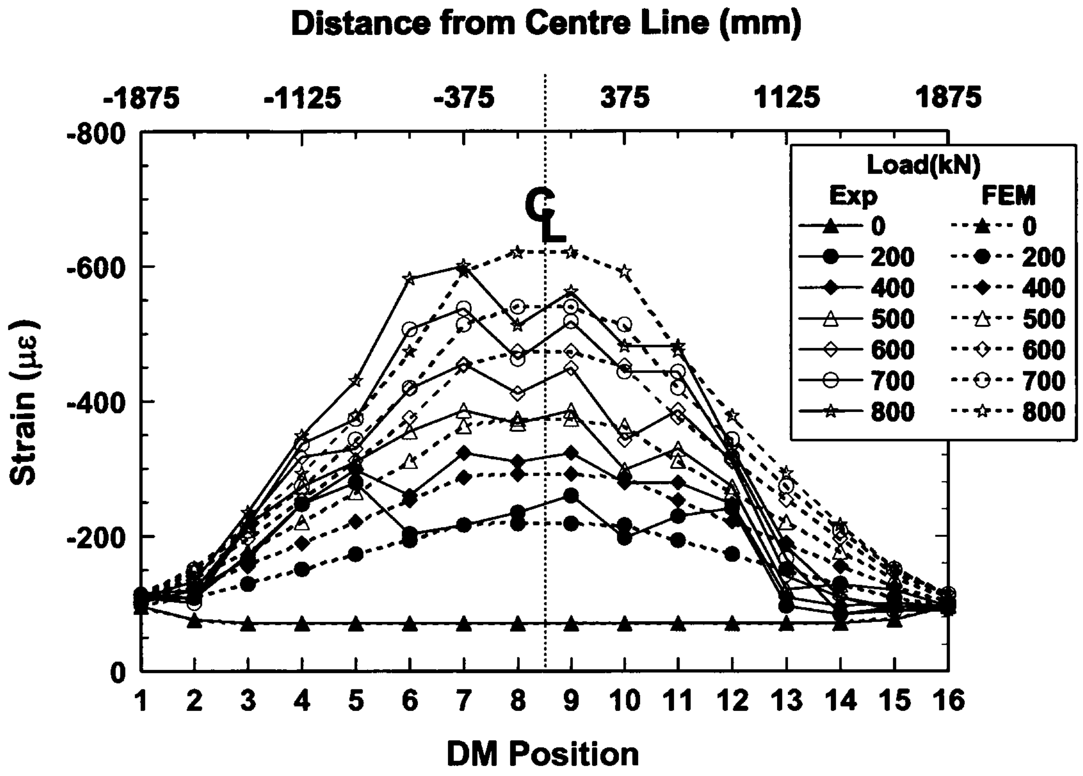

Figure 7.6 – SB3: horizontal strain in top (compressive) flange (DM 1 to DM16).

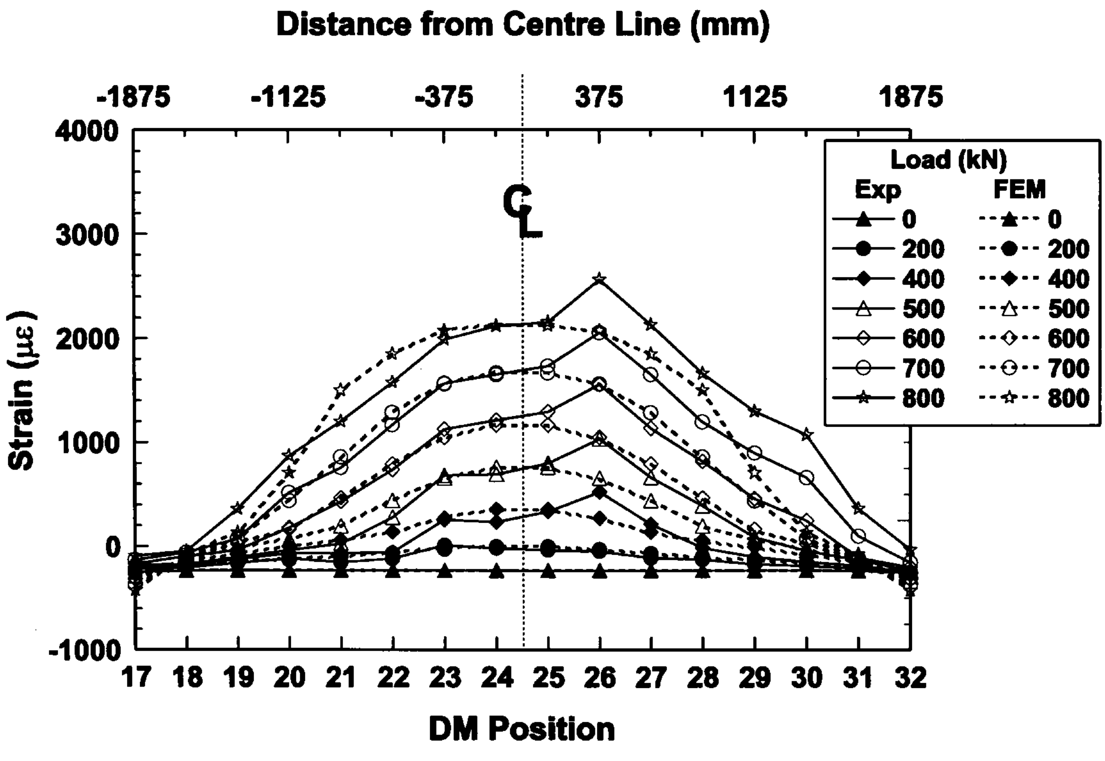

Figure 7.7 – SB3: horizontal strain in bottom (tensile) flange (DM 17 to DM32).

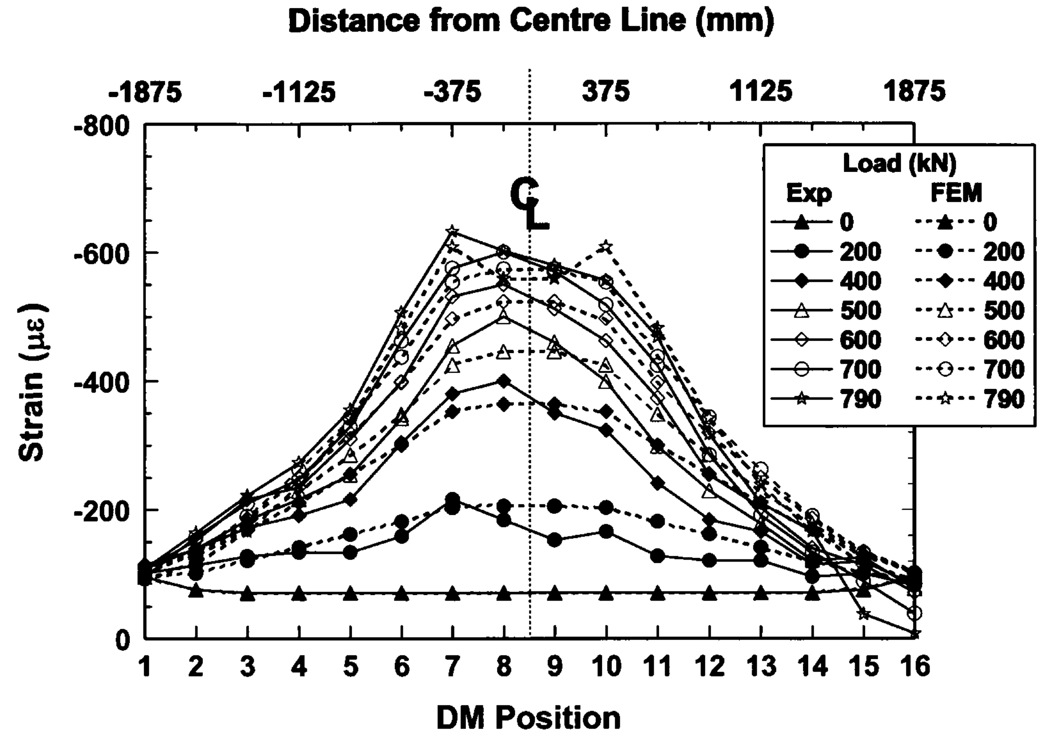

Figure 7.8 – SB7: horizontal strain in top (compressive) flange (DM 1 to DM16).

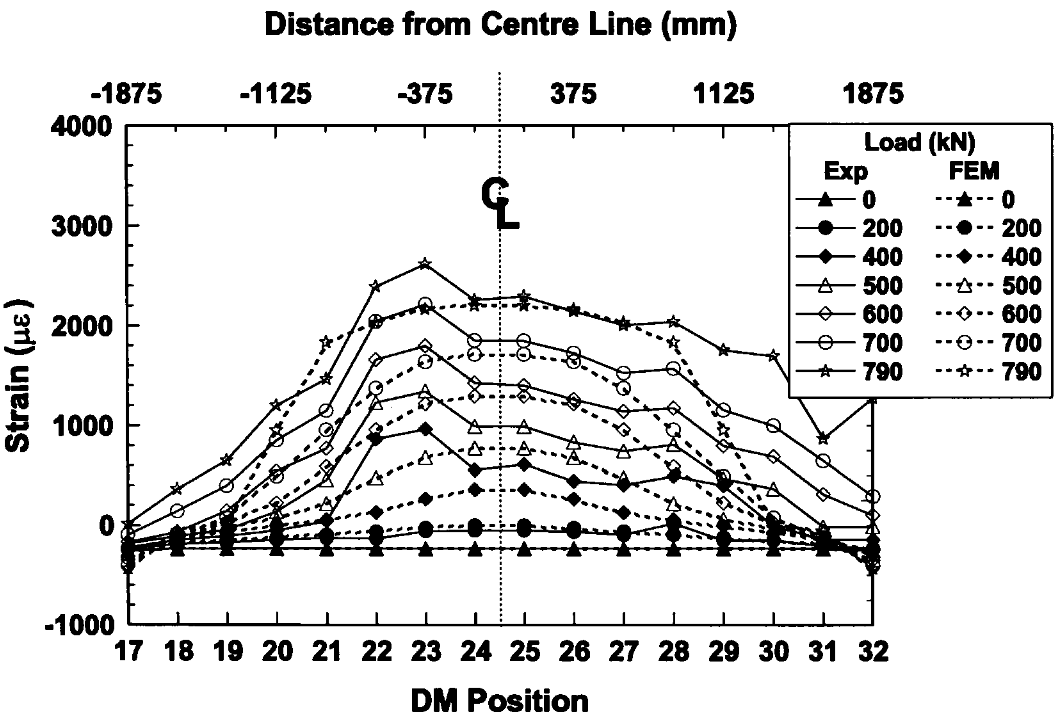

Figure 7.9 – SB7: horizontal strain in bottom (tensile) flange (DM 17 to DM32).

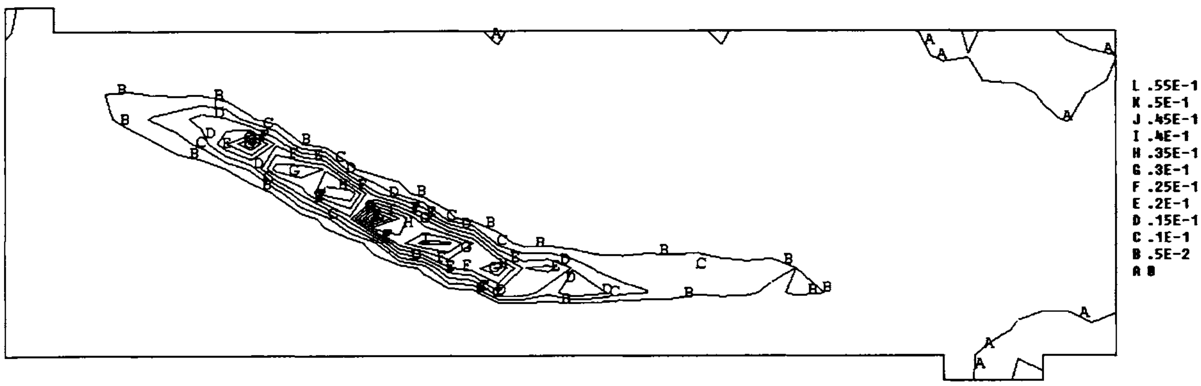

(a)

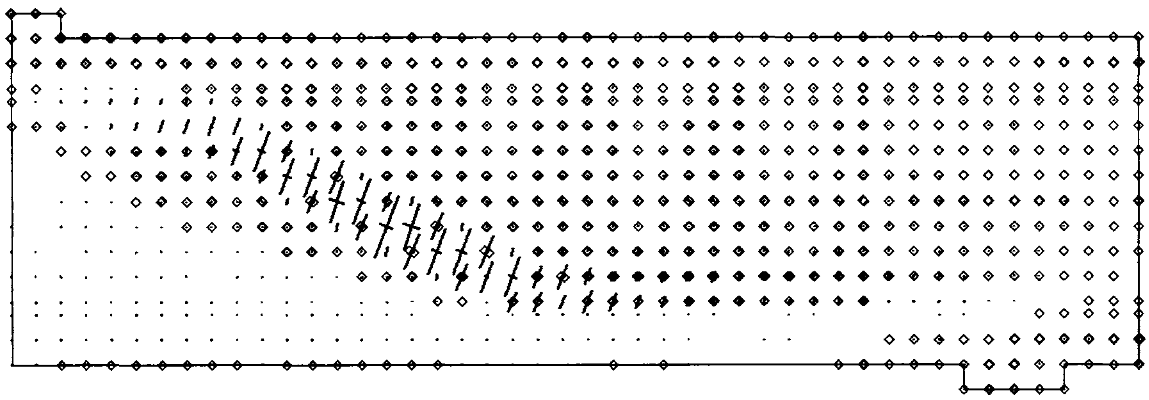

(b)

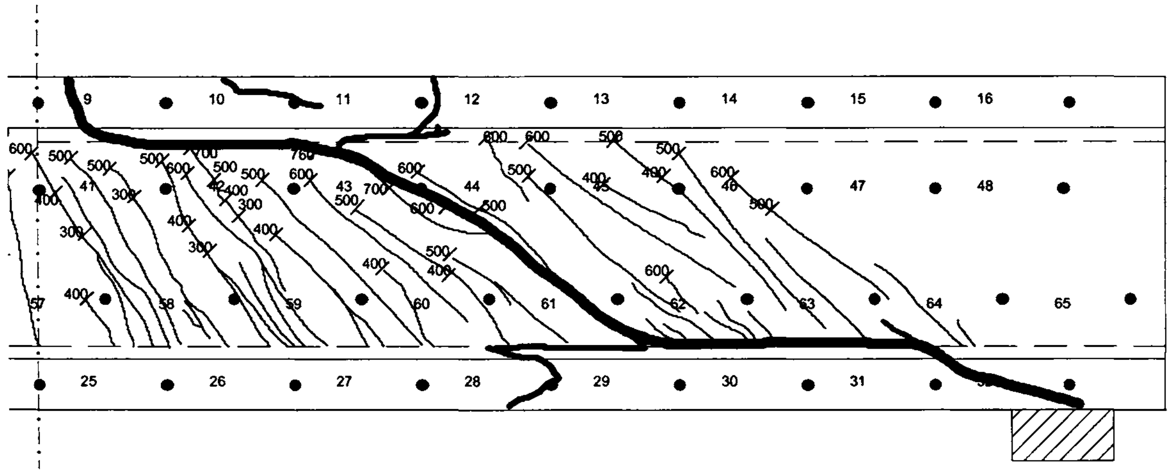

(c)

Figure 7.10 – FE analyses on (a) principal tensile strain contours; (b) principal strain vectors and (c) experimental crack pattern of SB3 at P = 810 kN.

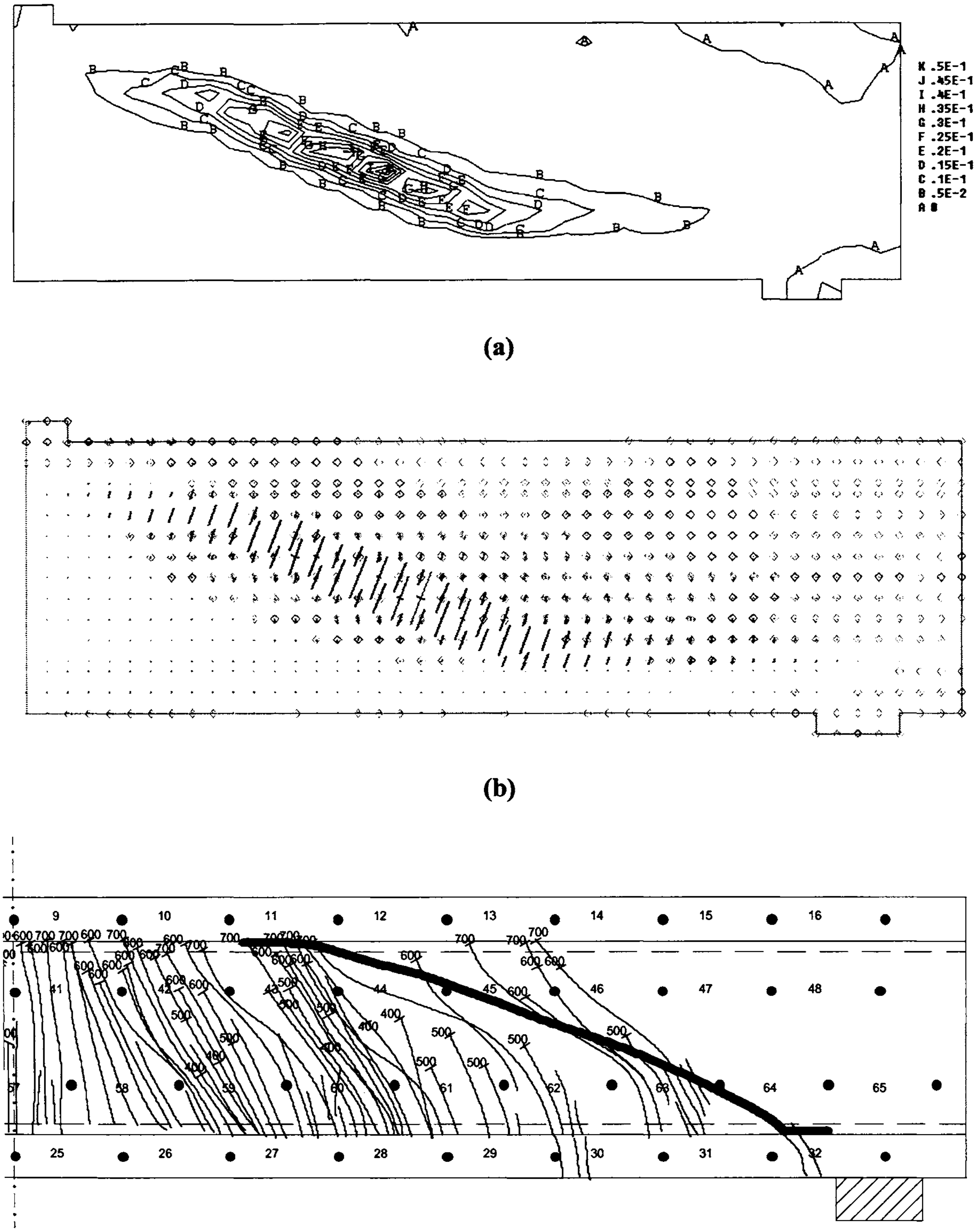

Figure 7.11 – FE analyses on (a) principal tension strain contour; (b) principal strain vectors and (c) experimental crack pattern of SB7 at P = 790 kN.

7.5.2 Mesh Sensitivity

The tension model adopted for the concrete in this study is the crack band model of Bazant and Oh (1983). This model was developed to avoid mesh sensitive results for problems involving concrete fracture.

In section 7.5.1, it is shown that FE modelling can capture the overall behaviour of the beams tested in this study with a good theoretical to experimental correlation being obtained. In this section, the sensitivity of the results to the size of the mesh is reviewed. Beams SB3 and SB7 are analysed for three element sizes in the web (the location of the fracture). The mesh sizes analysed are 25, 50 and 100 mm square within the web region. The material properties used were kept constant as per Table 7.2 with the exception of the characteristic length of the element which was taken as 25, 50 and 100 mm as appropriate.

The results of the load versus midspan deflection for the various FE models are shown in Figure 7.12 and are compared with the test data. The comparison shows the peak load is not sensitive to the mesh and while there is some variation in the load-displacement response, this variation is relatively small and well within any variation that maybe expected from repeating the laboratory tests. Thus, it is concluded that the 50 mm square meshes adopted for the FE models were appropriate and that the results are not sensitive to the FE mesh adopted. In Figures 7.13 and 7.14, the displaced meshes for specimens SB3 and SB7, respectively, are compared and the comparison shows the diagonal crack location is not sensitive to the mesh sizes.

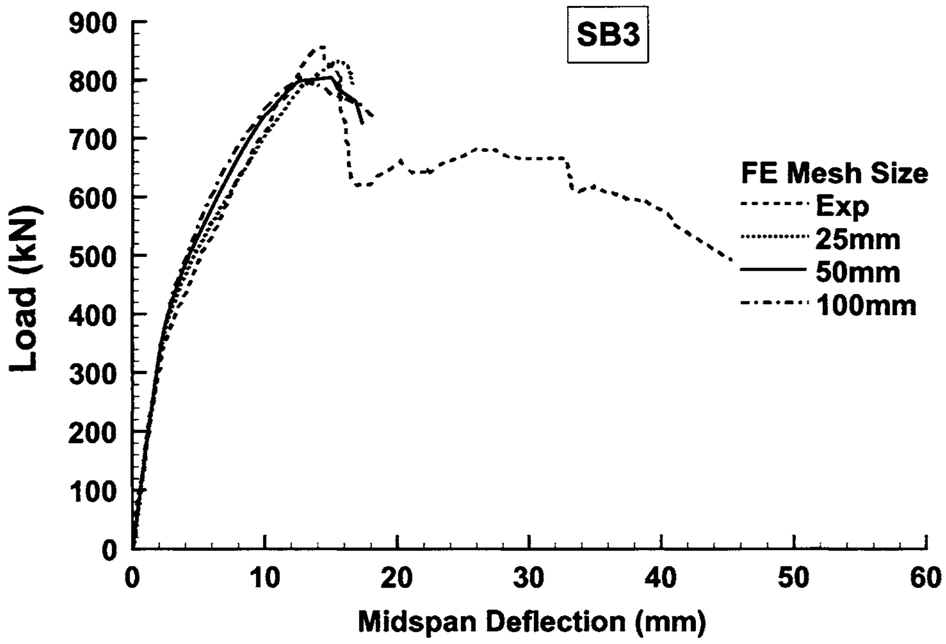

(a)

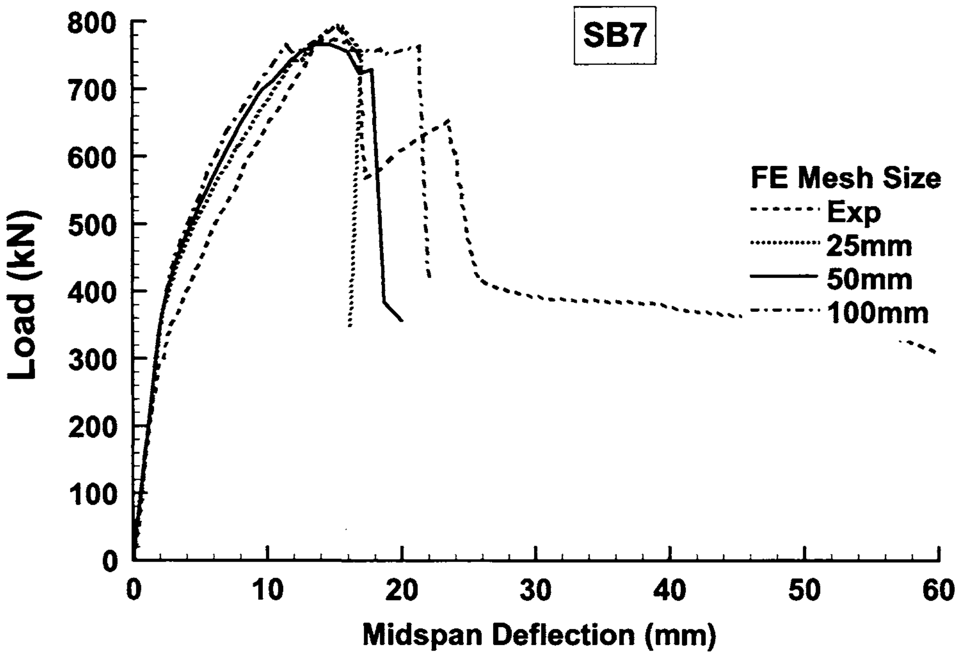

(b)

Figure 7.12 – Load versus midspan displacement for specimens (a) SB3 and (b) SB7 for mesh sizes of 25 mm, 50 mm and 100 mm square in the web.

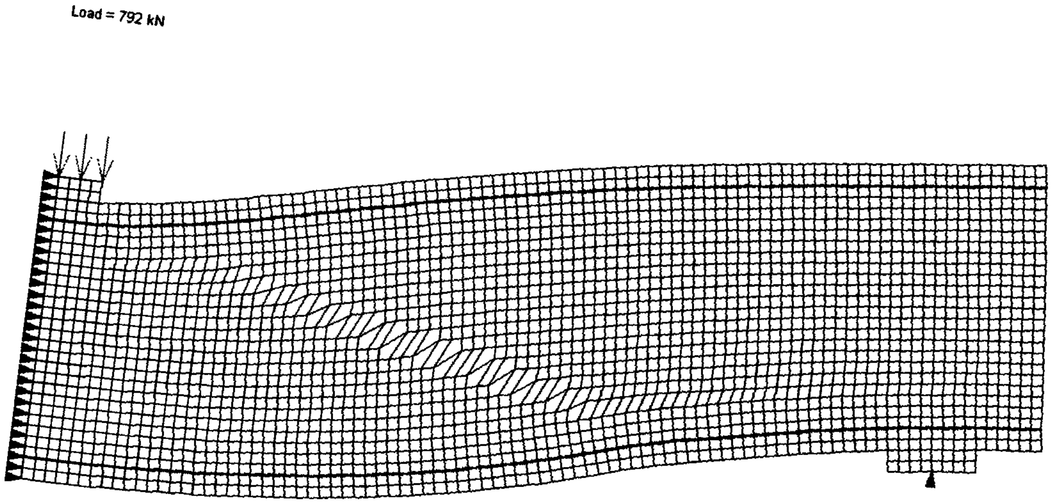

(a)

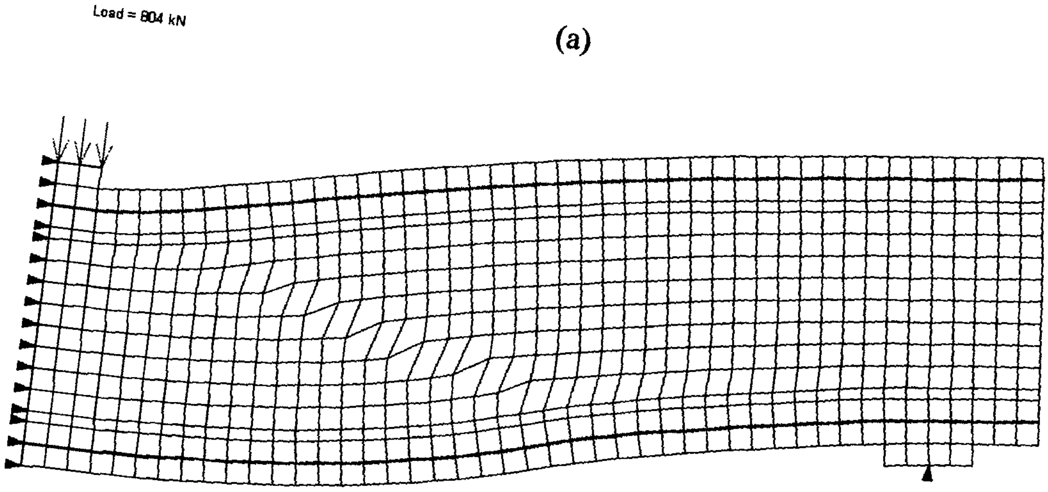

(b)

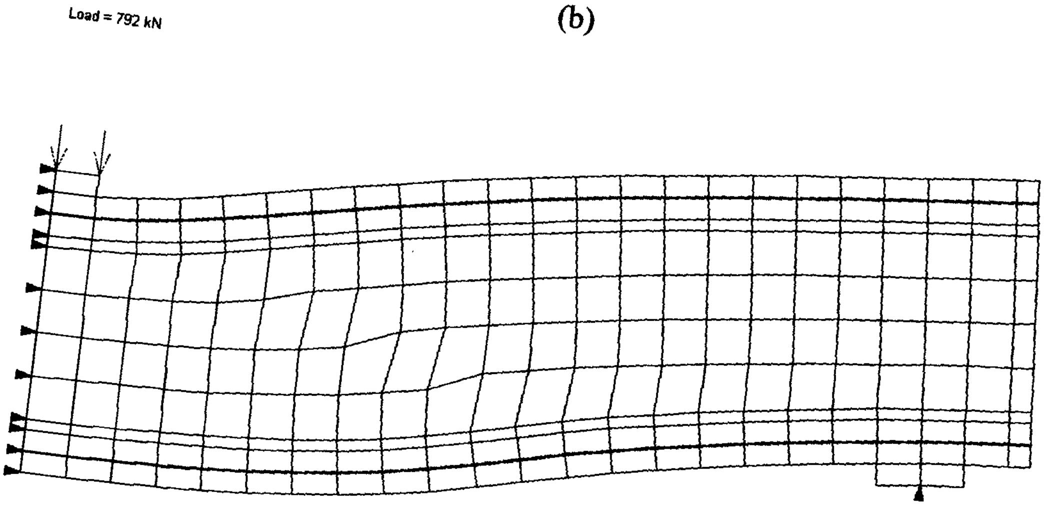

(c)

Figure 7.13 – Comparison of displaced meshes for specimen SB3 (x20): (a) 25 mm, (b) 50 mm and (c) 100 mm square mesh (web).

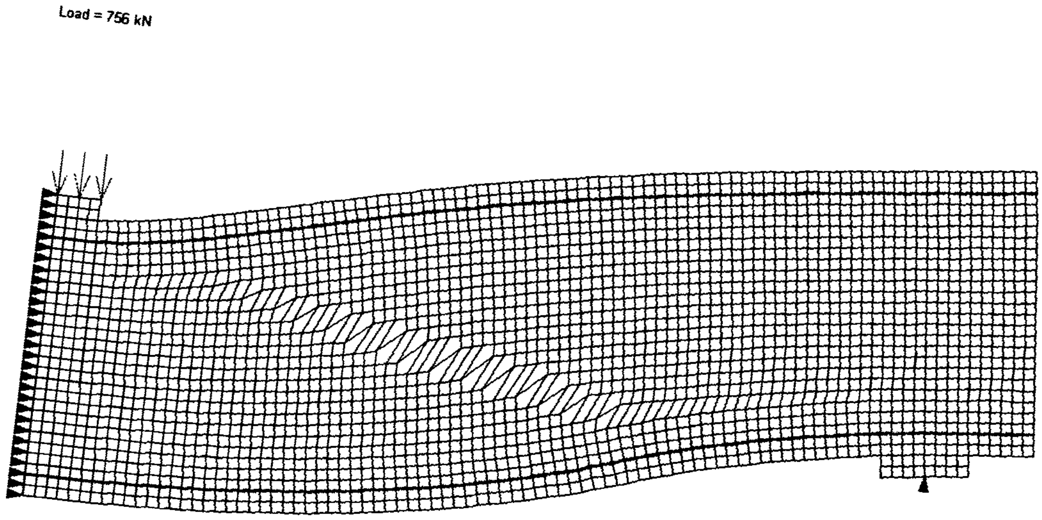

(a)

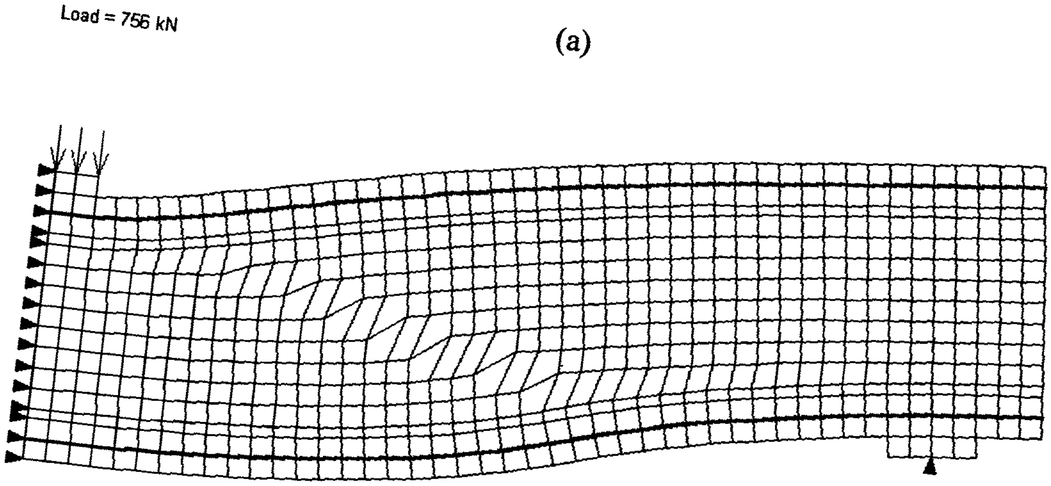

(b)

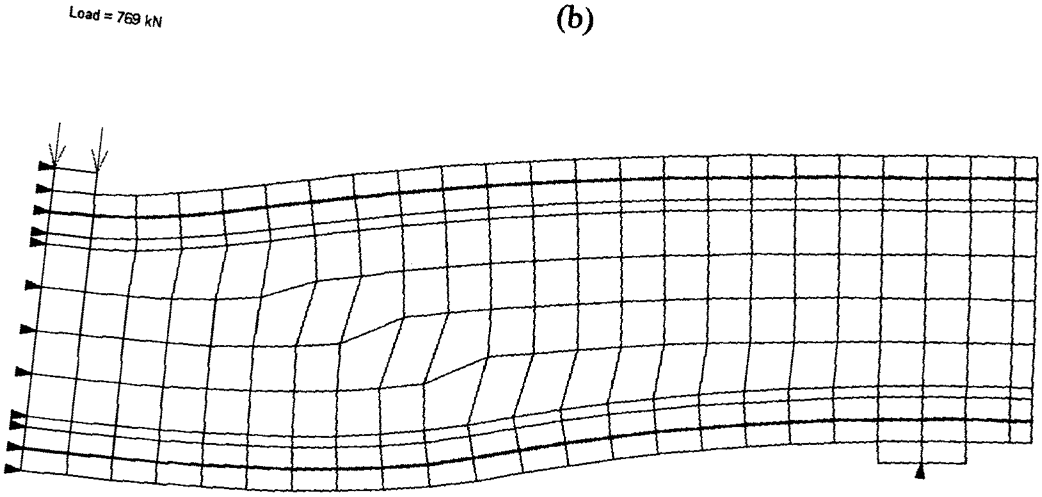

(c)

Figure 7.14 – Comparison of displaced meshes for specimen SB7 (x20): (a) 25 mm, (b) 50 mm and (c) 100 mm square mesh (web).

7.5.3 Sensitivity Tests on the Parameters α and τ_b

There are two independent parameters that are used to calibrate the VEM (Chapter 6), namely the engagement parameter α and the fibre-matrix bond strength τ_b. In this section the sensitivity of the results to these parameters is investigated. Again, specimens SB3 and SB7 are chosen for further analysis.

Firstly, the fibre-matrix strengths are held constant at 10 MPa for the straight fibre and 15 MPa for the end-hooked fibre, respectively, where the engagement parameter is varied by ± 25 percent from the calibrated value of $\alpha = d_f / 3.5$. The load versus midspan displacement of specimens SB3 and SB7 are plotted in Figure 7.15 and show that the results are not sensitive to α.

Next, the fibre engagement parameters are held constant at $\alpha = d_f / 3.5$ and the fibre-matrix bond strengths are varied by ± 25 percent. In Figure 7.16a the results are plotted for the case of holding the bond strength of the straight fibres as constant at τ_b = 10 MPa (as reported by Orange et al., 1999) and varying the bond strength of the end-hooked fibres. The bond strength of the end-hooked fibres was taken as 11.25, 15.0 and 18.75 MPa. The results show that the strength and response of specimen SB7 are not significantly changed for the different bond-strengths modelled for the end-hooked fibres. This is because for all cases of τ_b analysed, the length of fibres dictates that some fibres will fracture at the point of engagement. By reducing the fibre-matrix bond strength each fibre that does not fracture carries a lower load but there are more non-fractured fibres as a proportion of the total fibre volume. The opposite is true for the case of increasing the bond strength of the end-hooked fibres. Thus, the decrease (increase) in bond strength and, hence, load per fibre, is almost equally offset by an increase (decrease) in the proportion of non-fractured fibres crossing the crack.

In Figure 7.16b, the results are plotted for the case of holding the bond strength of the end-hooked fibres as constant at τ_b = 15 MPa and varying the bond strength of the straight fibres. In this case the length of the fibres is less than the critical length for fibre fracture and decreasing (increasing) fibre-matrix bond strength leads directly to a decrease (increase) in the tensile capacity across the cracks. Thus, it can be concluded that an accurate assessment of the fibre-matrix bond strength is required when the length of the fibres is less than then critical fibre length for an accurate analysis of the structure.

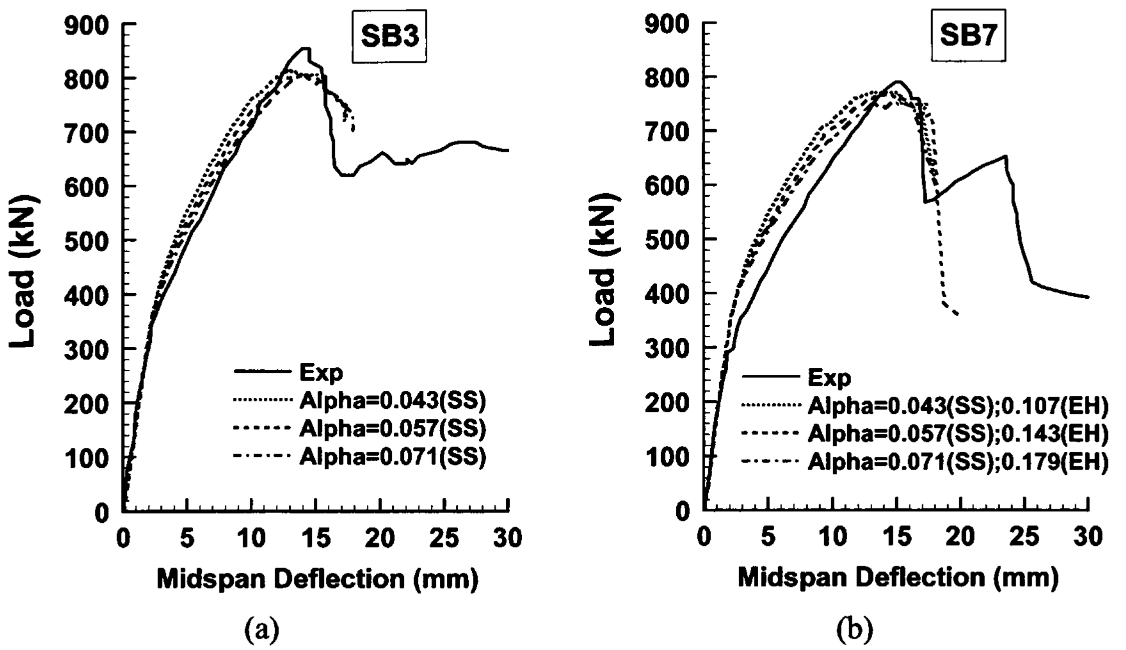

Figure 7.15 - Load versus midspan displacement for specimens (a) SB3 and (b) SB7 for constant bond strength but engagement parameter varied by ± 25 percent.

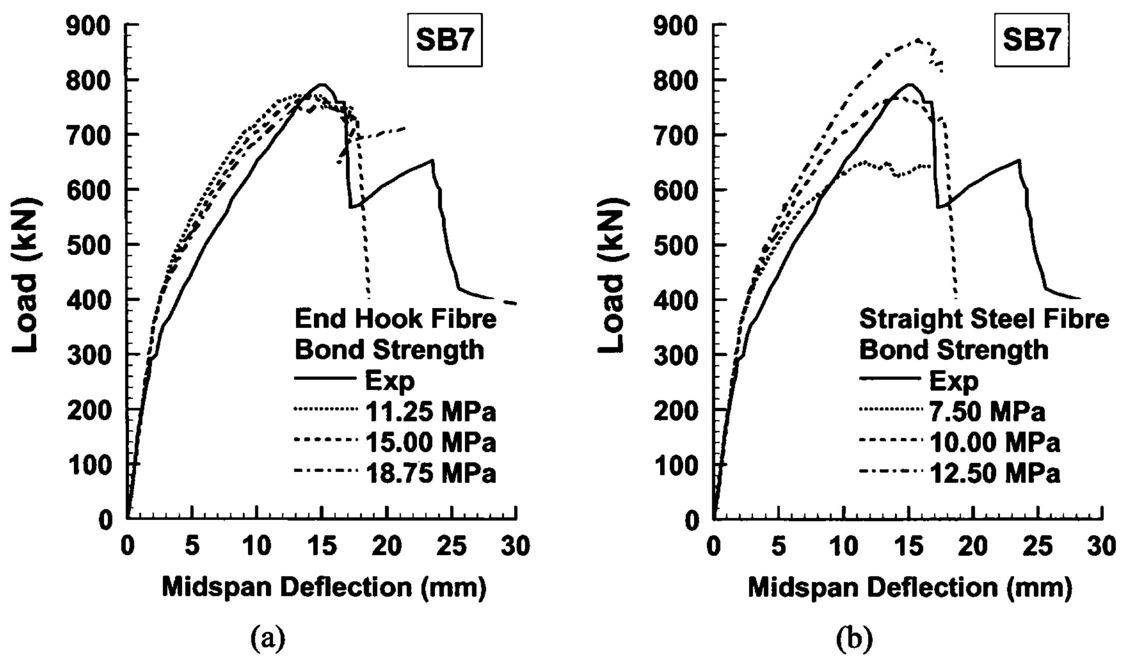

Figure 7.16 – Load versus midspan displacement for specimen SB7 for constant engagement parameter and varying the fibre-matrix bond strength of the (a) end-hook fibres and (b) straight steel fibres.

7.5.4 UHP-FRC Girders (Adeline and Behloul, 1996)

Adeline and Behloul (1996) tested two 15-metre long 150 MPa FR-RPC X-shaped beams. Beam 1 was prestressed by eight T15 tendons and Beam 2 was prestressed with two T15 tendons. For both specimens, the tendons used had a nominal area of 140 mm^2 and a guaranteed ultimate tensile strength of 1770 MPa. The tendons were prestressed to a stress level of 1420 MPa before casting. All the tested beams were without stirrups. Details of the material parameters used for FE modelling and details of the tested beams are given in Table 7.4 and Figure 7.17, respectively.

The details of the FE mesh are given in Figure 7.18. The FE mesh for Beams 1 and 2 consisted of 500 by 4-node isoparametric concrete elements for the flanges and web. The prestressing steel in the specimens are modelled as 2-node bar elements prestrained to simulate the prestressing force. The prestressing stands in Beams 1 and 2 were assumed to have 9 percent and 3 percent of ultimate losses relative to the initial jacking forces, respectively. One half of the specimens are modelled accounting for symmetry.

Figure 7.19 shows that for Beam 1 the FE model gave a lower load at yielding of the specimen but, this aside, the general behaviour was well represented by the model. For Beam 2 the results of the FE model compare well with the test data. Both the experiments and the FE specimens fail in flexure with no indication of shear failure in the non-reinforced web region (see Figure 7.20).

Table 7.4– Material parameters used for modelling the FR-RPC girders of Adeline and Behloul (1996).

	Adeline and Behloul (1996)	
Specimen Notation	Beam 1	Beam 2
Concrete		
f_{cp} (MPa)	150	144
f_{ct} (MPa)	4.1	4.0
E_o (GPa)	43.3	34.8
G_{Fm} (N/m)	290	280
l_{ch} (mm)	148.5	148.5
ε_{cp}	0.005	0.005
ν	0.15	0.15
α_1	0.33	0.33
α_2	4.5	3.6
α_3	18.7	14.8
Prestressing Steel#		
Total Relaxation	**9%**	**3%**
ε_{pi}	0.00663	0.00706
E_p (GPa)	195	195
ε_y	0.00769	0.00769
ε_r	0.02	0.02
ε_f	0.05	0.05
σ_y (MPa)	1500	1500
σ_r (MPa)	1750	1750
Steel Fibre – Straight		
Fibre Type	SS	SS
l_f (mm)	13	13
d_f (mm)	0.16	0.16
ρ_f (%)	2.5	2
σ_{fu} (MPa)	2200	2200
τ_b (MPa)	10	10
α -parameter	0.046	0.046

Notes: SS = straight steel fibre; # see Figure 7.1 for stress-strain definitions

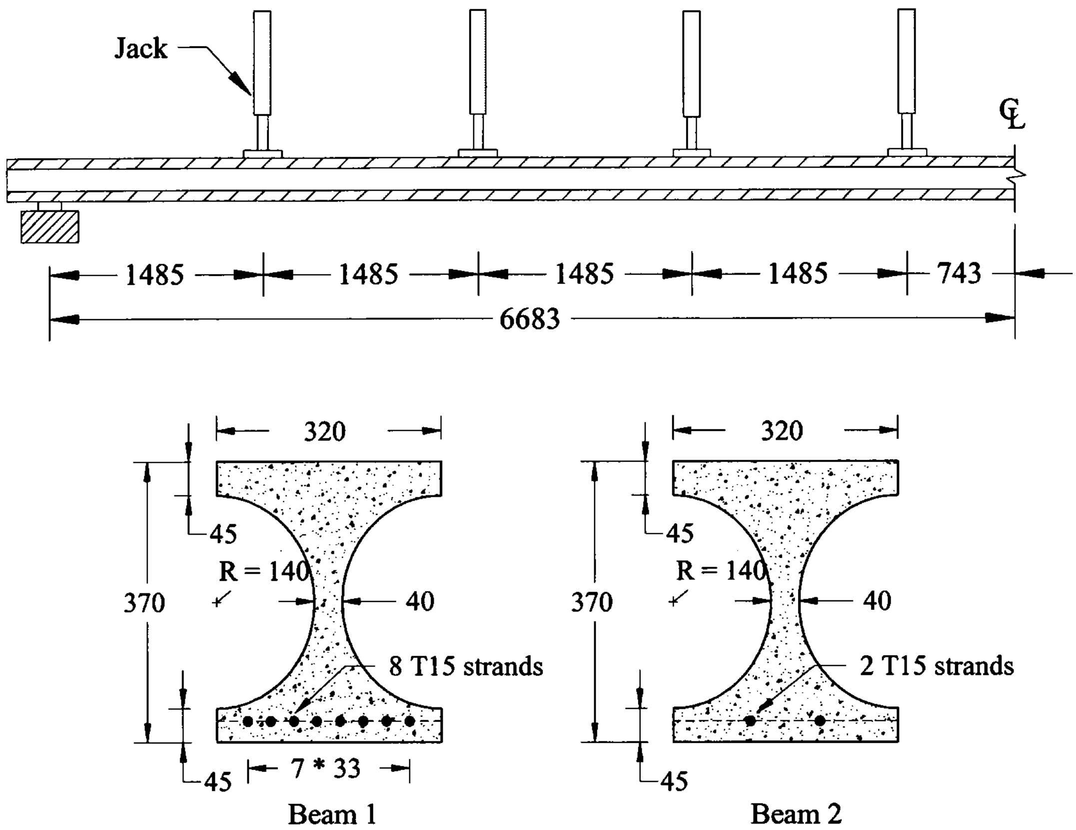

Figure 7.17 – Adeline and Behloul (1996) beams: Experimental setup and details of tested beams.

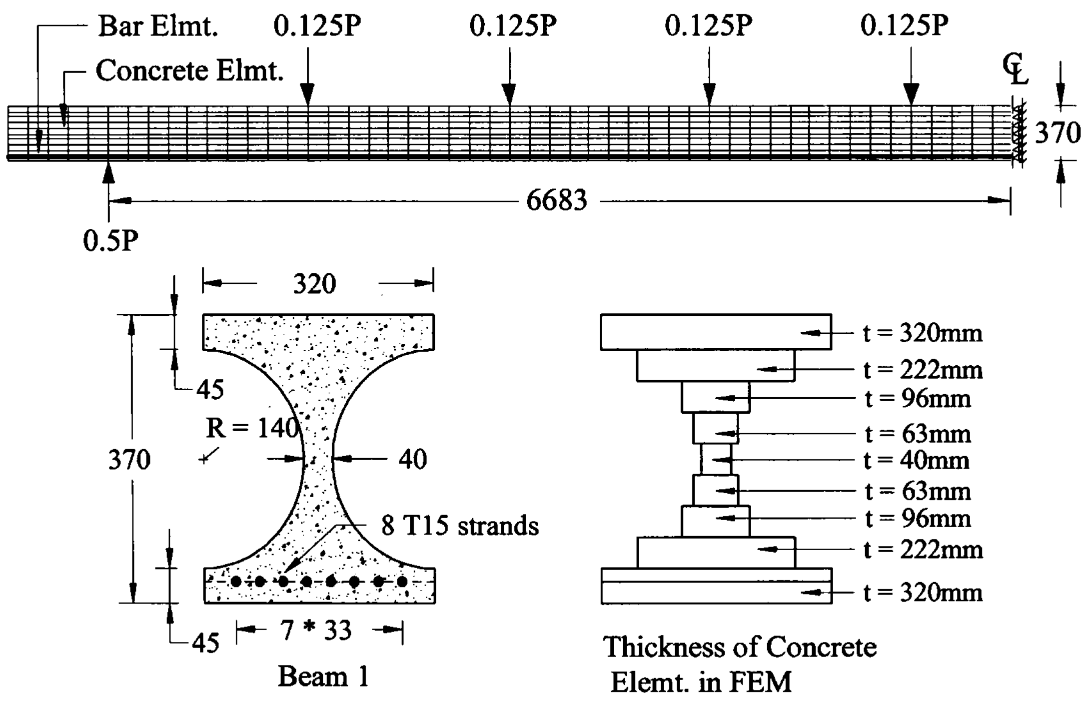

Figure 7.18 – FE mesh for Adeline and Behloul (1996) beams.

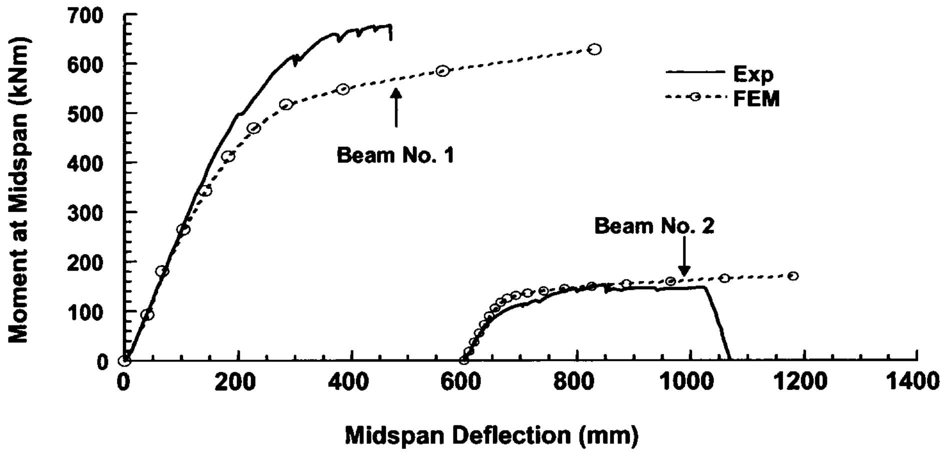

Figure 7.19 - Load versus midspan deflection.

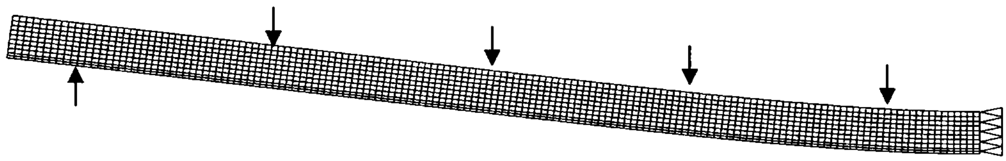

Figure 7.20 – Beam 1 displaced shape at moment equal to 626 kNm.

7.5.5 FR-HSC Beams (Noghabai, 2000)

Noghabai (2000) tested four series of high-strength concrete (up to f_{cu} = 130 MPa) beams designed to fail in shear. The primary experimental variables examined were various types of fibre and fibre volume and various beam depths (from 250 mm to 700 mm). The shear span-to-effective depth ratios were varied from 2.9 to 3.3.

From Noghabai's tests, 16 FR-concrete beams without stirrups were selected to conduct numerical analysis. The material parameters used for the FE modelling are given in Table 7.5 and details of the tested beams and FE mesh as are summarised in Figures 7.21 to 7.23. The uniaxial tension strengths of the matrix (excluding fibre), f_{ct}, were measured experimentally by the researchers and these values were used for the modelling herein.

Table 7.5 – Material parameters used for modelling the FRC beams of Noghabai (2000).

	M-series				L-series		
Specimen Notation	HSC^{III} S6/0.15	HSC^{III} S60.0.7/0.5	HSC^{III} S60/0.7/0.75	HSC^{III} Smix	HSC^{III} S6/0.15	HSC^{III} S60/0.7/0.75	HSC^{IV} Smix
Concrete							
f_{cp} (MPa)	87.3	78.7	68.4	81.8	79.0	68.4	81.8
f_{ct} (MPa)	3.77	3.77	3.77	3.77	3.77	3.77	3.77
E_o (GPa)	24.8	24.2	26.0	24.4	27.2	26	24.4
G_{fm} (N/m)	170	150	130	160	150	130	160
l_{ch} (mm)	50	50	50	50	50	50	50
ε_{cp}	0.0035	0.0035	0.0035	0.0035	0.0035	0.0035	0.0035
ν	0.2	0.2	0.2	0.2	0.2	0.2	0.2
α_1	0.33	0.33	0.33	0.33	0.33	0.33	0.33
α_2	5.1	4.4	4.14	4.73	4.93	4.14	4.73
α_3	21.4	18.4	17.0	19.8	22.7	17.1	19.8
Tension Reinforcing Steel #							
E_s (GPa)	200	200	200	200	200	200	200
ε_y	0.00295	0.00295	0.00295	0.00295	0.00295	0.00295	0.00295
ε_r	0.005	0.005	0.005	0.005	0.005	0.005	0.005
ε_f	0.05	0.05	0.05	0.05	0.05	0.05	0.05
σ_y (MPa)	590	590	590	590	590	590	590
σ_r (MPa)	680	680	680	680	680	680	680
Fibre							
Fibre Type	SS	EH	EH	SS / EH	SS	EH	SS / EH
l_f (mm)	6.0	60	60	6.0 / 30	6.0	60	6.0 / 30
d_f (mm)	0.15	0.7	0.7	0.15 / 0.6	0.15	0.7	0.15 / 0.6
ρ_f (%)	1.0	0.5	0.75	0.5 / 0.5	1.0	0.75	0.5 / 0.5
σ_{fu} (MPa)	2600	2200	2200	2600 / 1100	2600	2200	2600 / 1100
τ_b (MPa)	4.52	9.43	9.43	4.52 / 9.43	4.52	9.43	4.52 / 9.43
α	0.043	0.2	0.2	0.043 / 0.17	0.043	0.2	0.043 / 0.17

Notes: SS = straight steel; EH = end hooked;

see Figure 7.1 for stress-strain definitions

Table 7.5 – continued, material parameters used for modelling the FRC beams of Noghabai (2000).

	S-Series				
Specimen Notation	HSC[I] S6/0.15	HSC[I] S60.0.7/0.5	HSC[I] S60/0.7/0.75	HSC[I] Smix	NSC[II] Smix
Concrete					
f_{cp} (MPa)	103	91.5	91.5	94.5	44.8
f_{ct} (MPa)	4.15	4.15	4.15	4.15	3.75
E_o (GPa)	35.3	33.3	31.9	39.5	32.2
G_{fm} (N/m)	200	180	180	180	85
l_{ch} (mm)	25	25	25	25	25
ε_{cp}	0.0040	0.0035	0.0035	0.0035	0.003
v	0.2	0.2	0.2	0.2	0.2
α_1	0.33	0.33	0.33	0.33	0.33
α_2	13.5	11.5	11.0	13.5	6.56
α_3	59.0	50.1	48.0	59.5	28.0
Tension Reinforcing Steel #					
E_s (GPa)	**200**	**200**	**200**	**200**	**200**
ε_y	0.00295	0.00295	0.00295	0.00295	0.00295
ε_r	0.005	0.005	0.005	0.005	0.005
ε_f	0.05	0.05	0.05	0.05	0.05
σ_y (MPa)	590	590	590	590	590
σ_r (MPa)	680	680	680	680	680
Fibre					
Fibre Type	SS	EH	EH	SS / EH	SS / EH
l_f (mm)	6.0	60	60	6.0 / 30	6.0 / 30
d_f (mm)	0.15	0.7	0.7	0.15 / 0.6	0.15 / 0.6
ρ_f (%)	1.0	0.5	0.75	0.5 / 0.5	0.5 / 0.5
σ_{fu} (MPa)	2600	2200	2200	2600 / 1100	2600 / 1100
τ_b (MPa)	5.0	10.38	10.38	5.0 / 10.38	4.50 / 9.38
α	0.043	0.2	0.2	0.043 / 0.17	0.043 / 0.17

Note: SS = straight steel; EH = end hooked;

see Figure 7.1 for stress-strain definitions

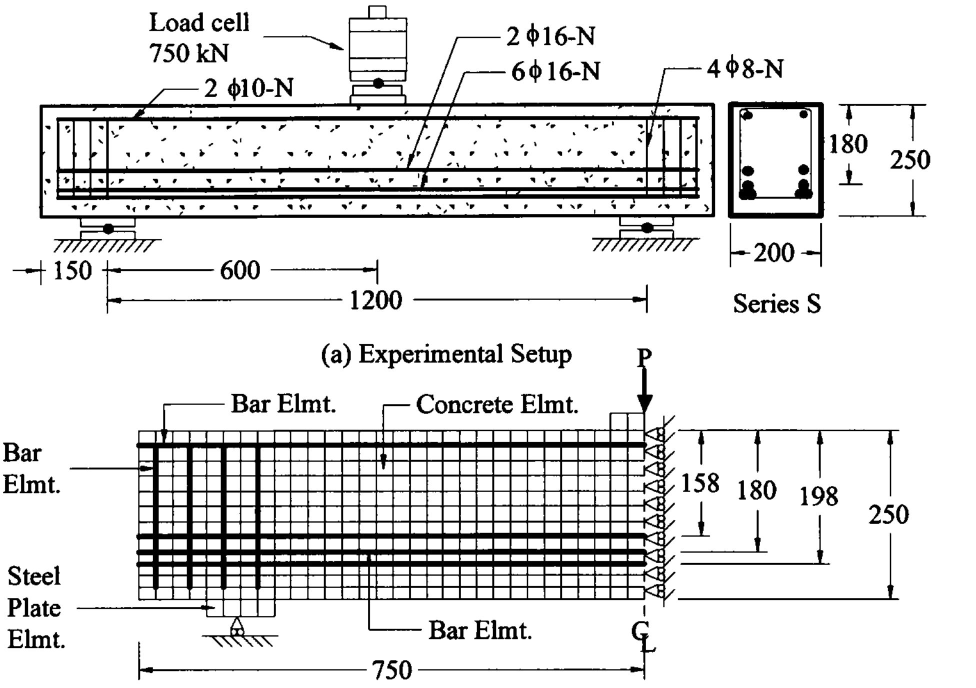

(b) Finite Element Mesh

Figure 7.21 – Noghabai (2000) beams: (a) Test setup; and (b) FE mesh of S-series.

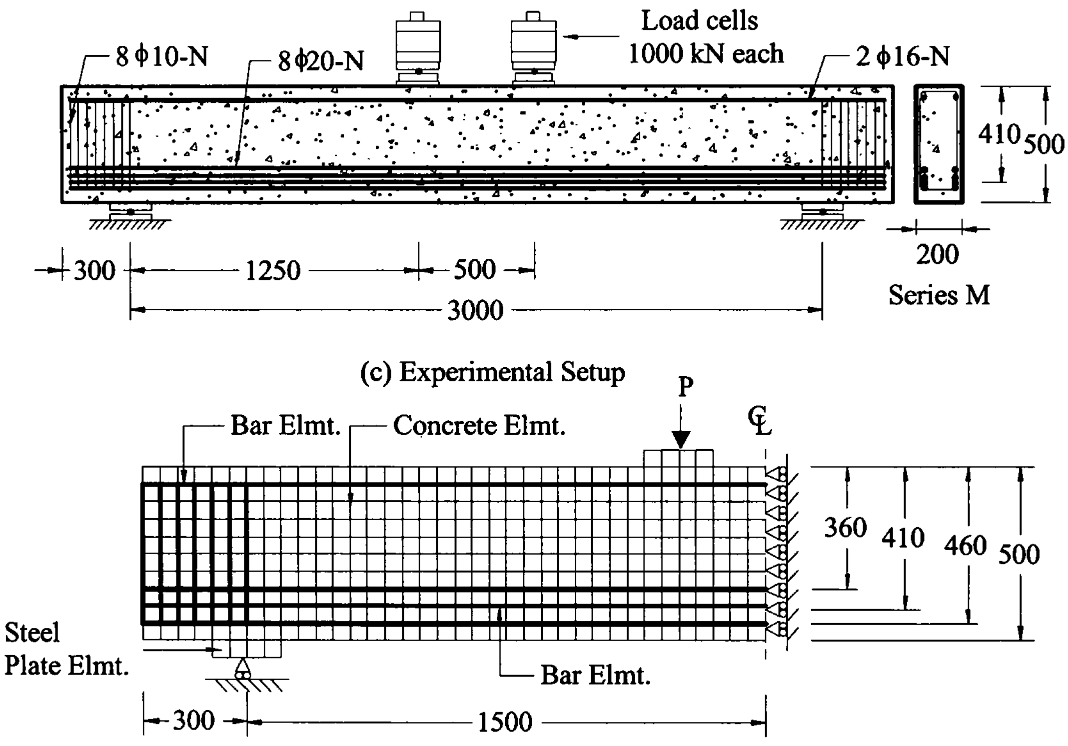

d) Finite Element Mesh

Figure 7.22 – Noghabai (2000) beams: (a) Test setup; and (b) FE mesh of M-series.

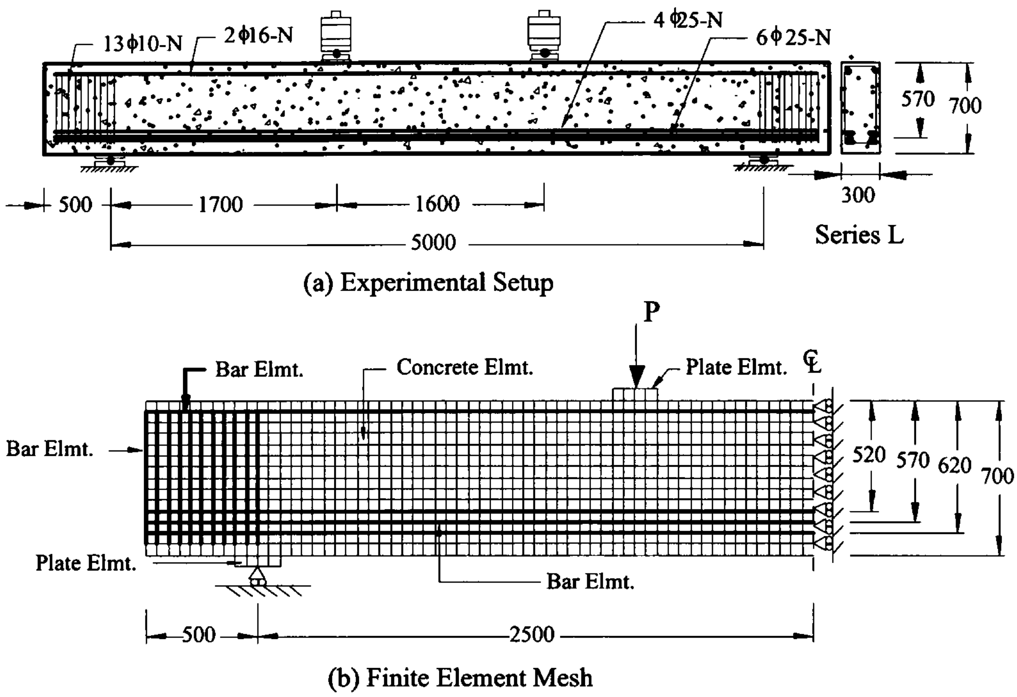

Figure 7.23 – Noghabai (2000) beams: (a) Test setup; and (b) FE mesh of L-series.

Table 7.6 – Noghabai (2000) beams: summary of FE mesh details.

Element Type	No. of Elements	Area (mm^2)	Thickness (mm)
S-series			
Concrete Elements	360	-	200
Steel Plate	6	-	200
Tension Steel	90	536	-
Compression Steel	30	157	-
Anchorage Steel	40	100	-
M-series			
Concrete Elements	360	-	200
Steel Plate	8	-	200
Tension Steel	108	838	-
Compression Steel	36	402	-
Anchorage Steel	32	314	-
L-series			
Concrete Elements	840	-	300
Steel Plate	8	-	300
Tension Steel	180	1636	-
Compression Steel	60	402	-
Anchorage Steel	132	170	-

The ultimate shear strengths obtained from the FE modelling are compared with the test results in Table 7.7. Good prediction of shear strengths are observed with the average FE shear strength to experimental shear strength ratio being 0.97 with a coefficient of variation of 0.10.

Figure 7.24 shows the load versus midspan deflection of Noghabai's test and the FE plots. The comparison shows the FE results generally compare well with the experimental measurements.

Figure 7.25 shows the principal strain vectors of the FE results for the M-series beam HSC^{III}_{Smix} at the point of failure and shows failure was by the diagonal shear splitting in the web.

Table 7.7 –Comparison calculated and experimental shear strength for the Noghabai (2000) specimens.

Series	Specimen Notation	$V_{u,\exp}$ (kN)	$V_{u,FEM}$ (kN)	$\tau_{u,\exp}$ (MPa)	$\tau_{u,FEM}$ (MPa)	$\frac{\tau_{u,FEM}}{\tau_{u,\exp}}$
S	$HSC^{I}_{S6/0.15}$	299	278	8.31	7.72	0.93
	$HSC^{I}_{S60.0.7/0.5}$	252	236	7.00	6.56	0.94
	$HSC^{I}_{S60/0.7/0.75}$	262	277	7.28	7.69	1.06
	HSC^{I}_{Smix}	295	299	8.19	8.31	1.01
	NSC^{II}_{Smix}	189	191	4.85	4.90	1.01
M	$HSC^{III}_{S6/0.15}$ (1)	289	262	3.52	3.2	0.91
	$HSC^{III}_{S6/0.15}$ (2)	336	262	4.10	3.2	0.78
	$HSC^{III}_{S60.0.7/0.5}$ (1)	264	282	3.21	3.41	1.07
	$HSC^{III}_{S60.0.7/0.5}$ (2)	312	282	3.80	3.44	0.91
	$HSC^{III}_{S60/0.7/0.75}$ (1)	339	338	4.13	4.12	1.00
	$HSC^{III}_{S60/0.7/0.75}$ (2)	292	338	3.56	4.12	1.16
	HSC^{III}_{Smix} (1)	367	343	4.48	4.18	0.93
	HSC^{III}_{Smix} (2)	327	343	3.99	4.18	1.05
L	$HSC^{III}_{S6/0.15}$	445	414	2.60	2.42	0.93
	$HSC^{III}_{S60/0.7/0.75}$	509	527	2.98	3.08	1.04
	HSC^{IV}_{Smix}	596	484	3.33	2.83	0.81
Average						0.97
COV.						0.01

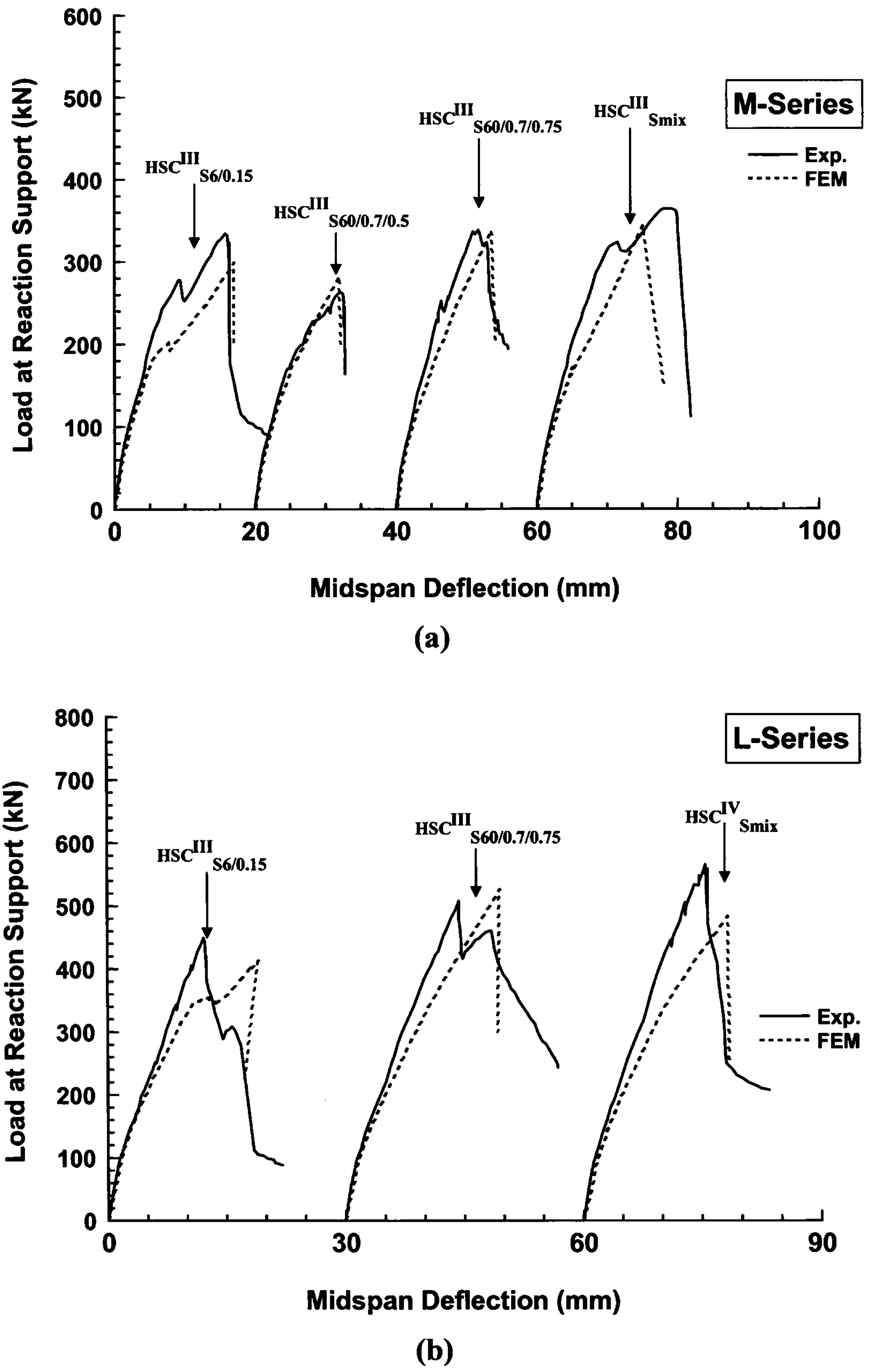

Figure 7.24 – Load versus midspan deflection of Noghabai (2000) beams: (a) M-series and (b) L-series tests.

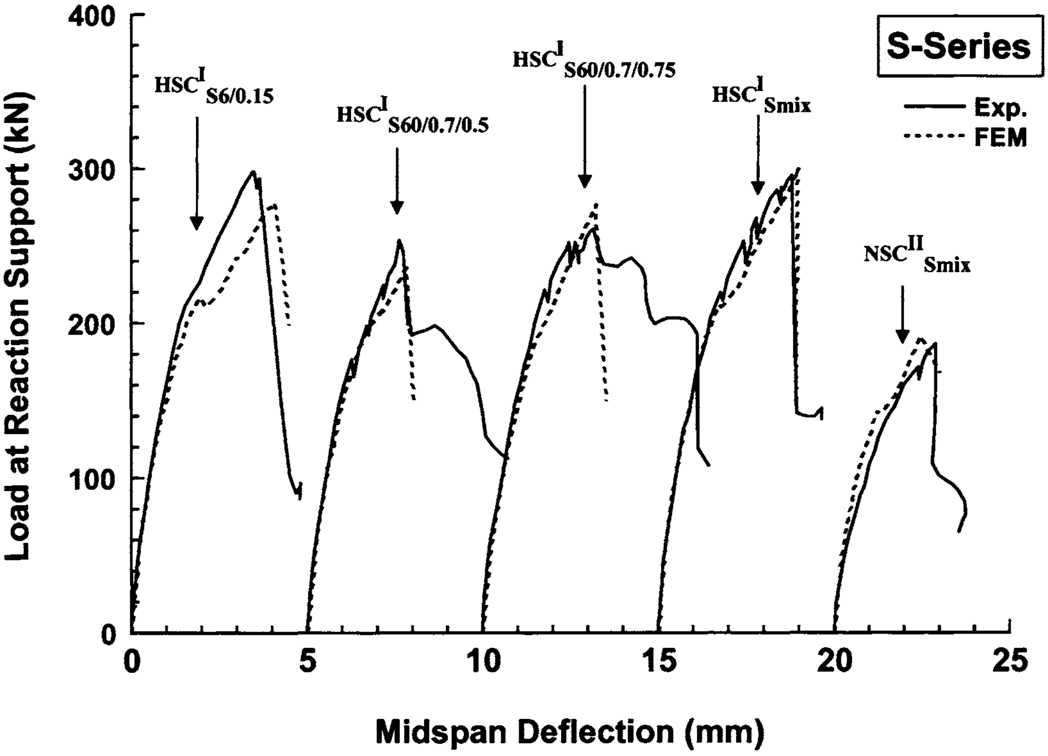

(c)

Figure 7.24 (Continued) – (c) S-series tests.

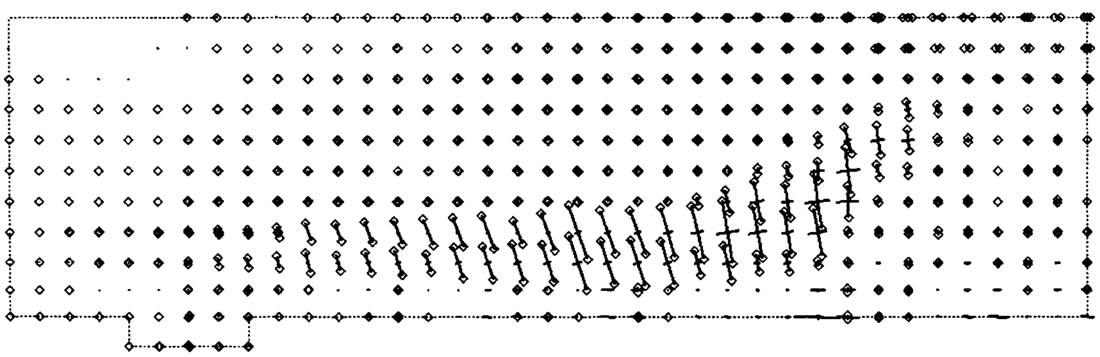

Figure 7.25 – FE analyses showing the principal strain vectors of Noghabai (2000) M-series beam HSC^{III}_{Smix} at the load of 343 kN.

7.5.6 FR-Light-Weight Concrete I-Beams (Swamy et al., 1993)

Swamy et al. (1993) tested nine FR-NSC I-beams with concrete cube compressive strengths of 40 to 51 MPa. The fibres used were 1 percent by volume crimped steel fibre. The test variables included shear span-to-depth ratios and steel reinforcement ratios.

Details of experimental setup and FE mesh are given in Figure 7.26. The FE mesh consisted of 770 by 4-node isoparametric concrete elements for the flanges and web and 107 by 2-node bar elements for the reinforcing steel. One half of the specimen is modelled accounting for symmetry.

The material parameters used for the constitutive laws of the FR-concrete in the FE modelled are given in Table 7.8.

The shear strengths obtained from the FE analysis ($\tau_{u,FEM}$) are compared in Table 7.9 with the experimental ultimate shear strength ($\tau_{u,\exp}$) for nine tested FR specimens. Comparison of the analyses show that the FEM correctly calculates the failure loads and failure modes for the specimens with a mean numerical to experimental ultimate shear stress ratio of 1.0 and a coefficient of variation of 8.4 percent.

Figure 7.27 compares the load versus midspan deflection for specimen 3TLF1, 2 and 3 for the FE and experimental results. The comparison shows that the FE results correlate well with the experimental data. Also, the tensile steel strains and the concrete strain at the top flange region at the midspan are compared in Figure 7.28. Again the figure shows that a good correlation was achieved.

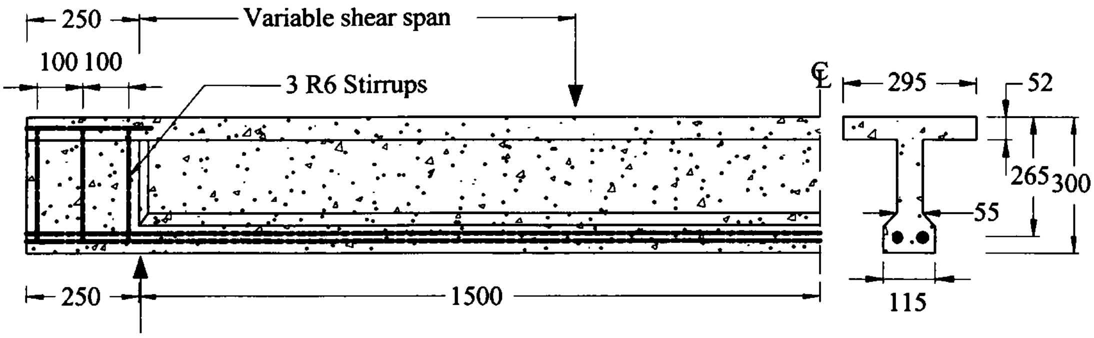

(a)

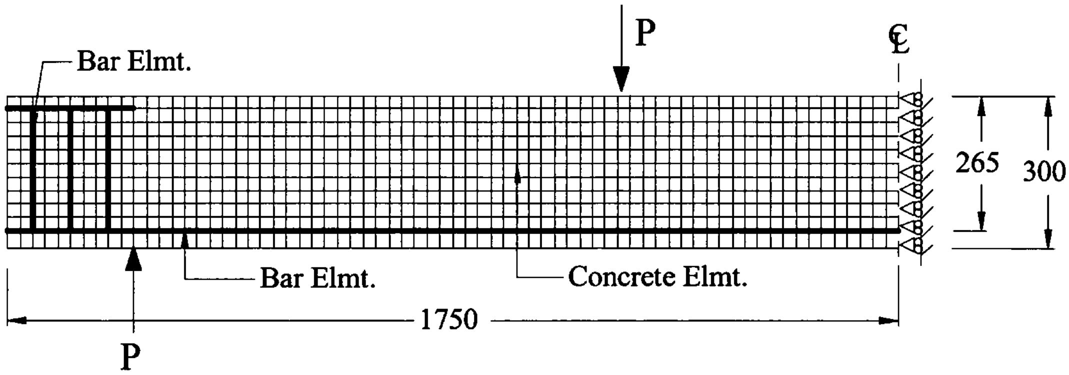

(b)

Element Type	Number of Elements	Area (mm^2)	Thickness (mm)
Top flange	140	-	295
Web	420	-	55
Bottom flange/web interface	70	-	85
Bottom flange	140	-	115
Tension Steel	70	226, 403, 628	-
Top Supporting Steel	10	200	-
Anchorage Steel	27	30	-

(c)

Figure 7.26 – Swamy et al., (1993) I-beams: (a) Experimental setup; (b) FE mesh and (c) summary of FE mesh details.

Table 7.8 – Material parameters used for modelling the FRC beams of Swamy et al. (1993).

Specimen	1 TLF -1	1 TLF -2	1 TLF -3	2 TLF -1	2 TLF -2
Concrete					
f_{cp} (MPa)	35.6	38	34.5	32.5	40.9
f_{ct}* (MPa)	1.97	2.03	1.94	1.88	2.11
E_o (GPa)	20.8	21.6	20	20	22
G_{Fm} (N/m)	70	75	70	60	80
l_{ch} (mm)	25	25	25	25	25
ε_{cp}	0.003	0.003	0.003	0.003	0.003
ν	0.2	0.2	0.2	0.2	0.2
α_1	0.33	0.33	0.33	0.33	0.33
α_2	12.3	12.9	12.2	11.2	13.0
α_3	54.0	56.6	53.6	48.9	56.9
Tension Reinforcing Steel #					
E_s (GPa)	200	200	200	200	200
ε_y	0.0023	0.0023	0.0023	0.0023	0.0023
ε_r	0.005	0.005	0.005	0.005	0.005
ε_f	0.05	0.05	0.05	0.05	0.05
σ_y (MPa)	460	460	460	460	460
σ_r (MPa)	580	580	580	580	580
Fibre – crimped steel					
ρ_f (%)	1.0	1.0	1.0	1.0	1.0
l_f (mm)	50	50	50	50	50
d_f (mm)	0.5	0.5	0.5	0.5	0.5
σ_{fu} (MPa)	1570	1570	1570	1570	1570
τ_b (MPa)	5	5.13	4.9	4.75	5.33
α	0.143	0.143	0.143	0.143	0.143

Notes: * taken as $0.33\sqrt{f_{cp}}$; # see Figure 7.1 for stress-strain definitions

Table 7.8 (continued) - material parameters used for modelling the FRC beams of Swamy et al. (1993).

Specimen Notation	2 TLF -3	3 TLF -1	3 TLF -2	3 TLF -3
Concrete				
f_{cp} (MPa)	36	35.7	33.1	35.9
f_{ct} * (MPa)	1.98	1.97	1.90	1.98
E_o (GPa)	21.5	20	21	21.4
G_{Fm} (N/m)	70	70	65	70
l_{ch} (mm)	25	25	25	25
ε_{cp}	0.003	0.003	0.003	0.003
ν	0.2	0.2	0.2	0.2
α_1	0.33	0.33	0.33	0.33
α_2	12.6	11.9	12.4	12.6
α_3	55.3	52.0	54.5	55.0
Tension Reinforcing Steel #				
E_s (GPa)	200	200	200	200
ε_y	0.0023	0.0023	0.0023	0.0023
ε_r	0.005	0.005	0.005	0.005
ε_f	0.05	0.05	0.05	0.05
σ_y (MPa)	460	460	460	460
σ_r (MPa)	580	580	580	580
Fibre – crimped steel				
ρ_f (%)	1.0	1.0	1.0	1.0
l_f (mm)	50	50	50	50
d_f (mm)	0.5	0.5	0.5	0.5
σ_{fu} (MPa)	1570	1570	1570	1570
τ_b (MPa)	5	5	4.8	5
α	0.143	0.143	0.143	0.143

Notes: * taken as $0.33\sqrt{f_{cp}}$; # see Figure 7.1 for stress-strain definitions

Table 7.9 – Comparison of calculated and experimental shear strengths for Swamy et al. beams.

Specimen	Experiment Failure Mode	FEM Failure Mode	$\tau_{u,\exp}$ (MPa)	$\tau_{u,FEM}$ (MPa)	$\frac{\tau_{u,FEM}}{\tau_{u,\exp}}$
1 TLF -1	Shear	Shear	5.51	5.23	0.95
1 TLF -2	Shear	Shear	4.05	3.79	0.94
1 TLF -3	Shear	Shear	2.92	3.42	1.17
2 TLF -1	Shear	Shear	4.93	5.21	1.06
2 TLF -2	Shear	Shear	3.13	3.41	1.09
2 TLF -3	Shear-flexure	Shear-flexure	2.94	2.8	0.95
3 TLF -1	Shear-flexure	Flexure	4.65	4.51	0.97
3 TLF -2	Flexure	Flexure	2.85	2.67	0.94
3 TLF -3	Flexure	Flexure	2.02	1.92	0.95
Average					1.00
COV					0.084

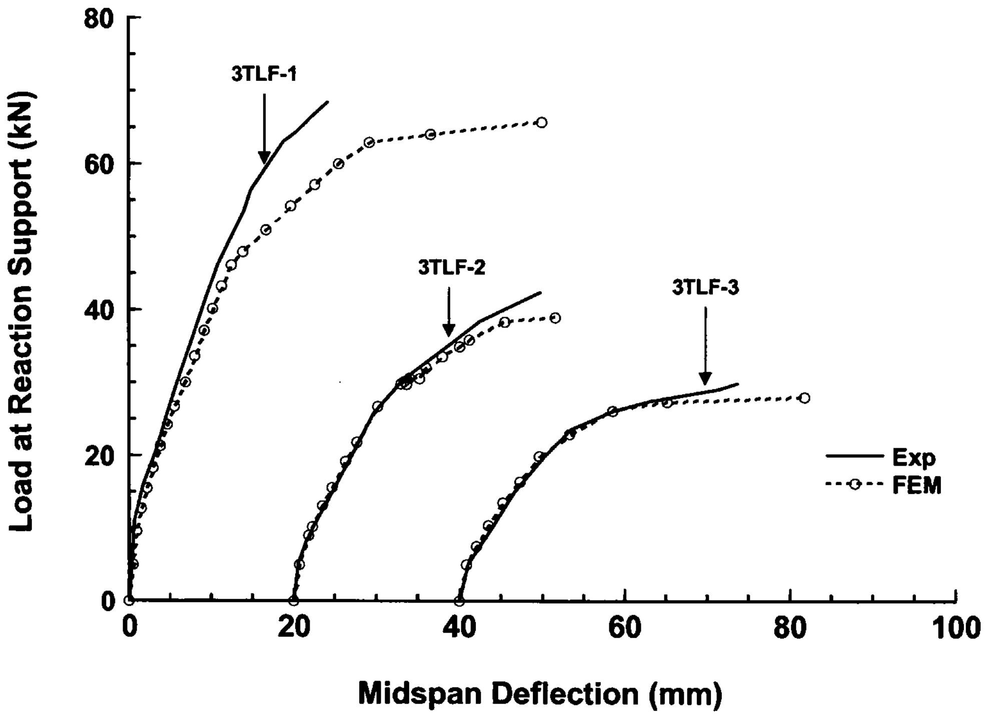

Figure 7.27 – Load versus midspan deflection for Swamy et al. beams 3TLF-1, 3TLF-2 and 3TLF-3.

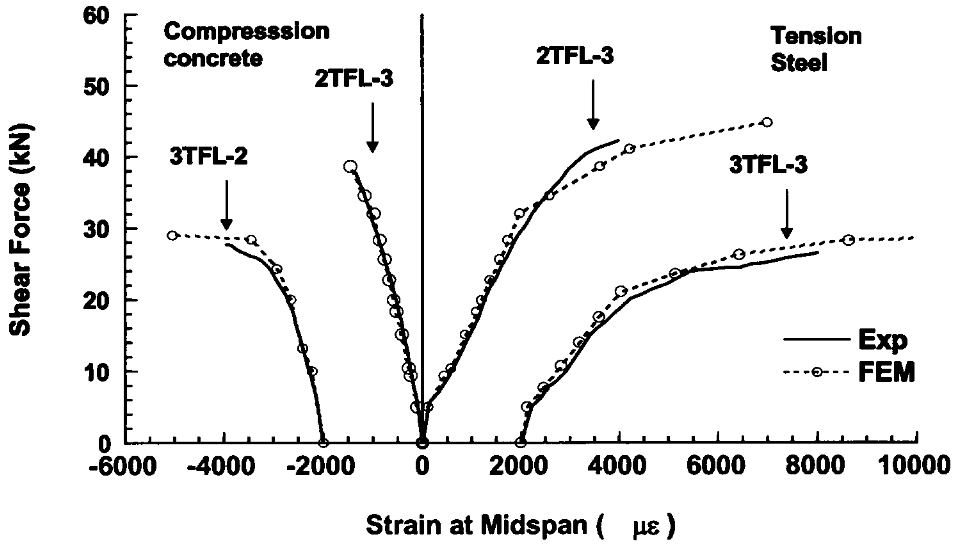

Figure 7.28 – Swamy et al. beams 3TLF-2 and 3TLF-3: tension steel strains and concrete compressive strains at the midspan.

7.5.7 FR-NSC Deep Beams (Narayanan and Darwish, 1988)

Narayanan and Darwish (1988) tested 11 FR deep beams with conventional concrete with cube compressive strengths of 32 to 68 MPa. Three parameters were investigated; the volume fraction of fibres, shear span-to-depth ratio and the concrete strength.

Details of the experimental setup of the test are shown in Figure 7.29 and the FE mesh used is given in Figure 7.30. The FE mesh consisted of 192 by 4-node isoparametric concrete elements for the web and 8 by 4-node stiff elements for the steel plates. The tensile reinforcement in the specimens is modelled as 2-node bar elements with perfect bond between the steel and the concrete. One half of the specimen was modelled accounting for symmetry.

The material parameters used to develop the constitutive law of the FR-concrete in the FE model are given in Table 7.10. Table 7.11 compares the numerical failure loads to the experimental failure loads. Comparison shows a theoretical to experimental shear capacity ratio of 0.99 with coefficient of variation of 8.9 percent.

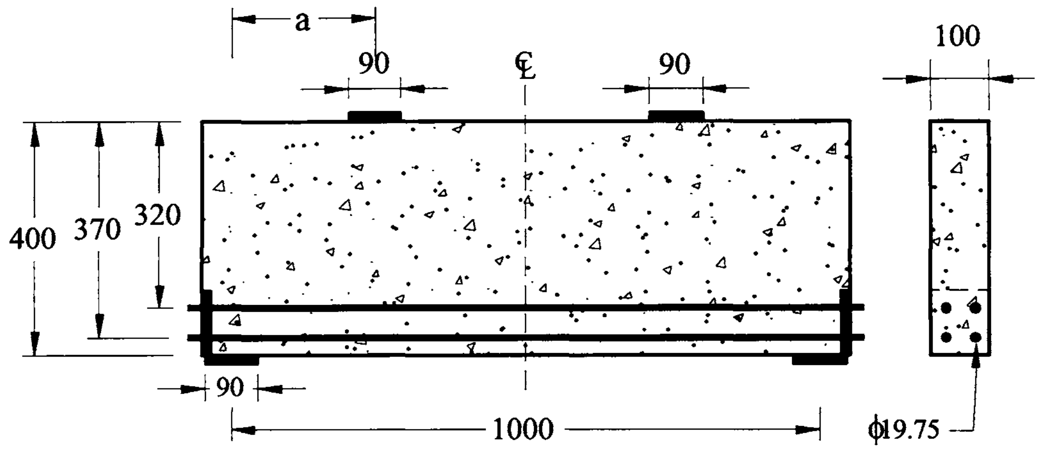

Figure 7.29 – Details of Narayanan and Darwish (1998) beams.

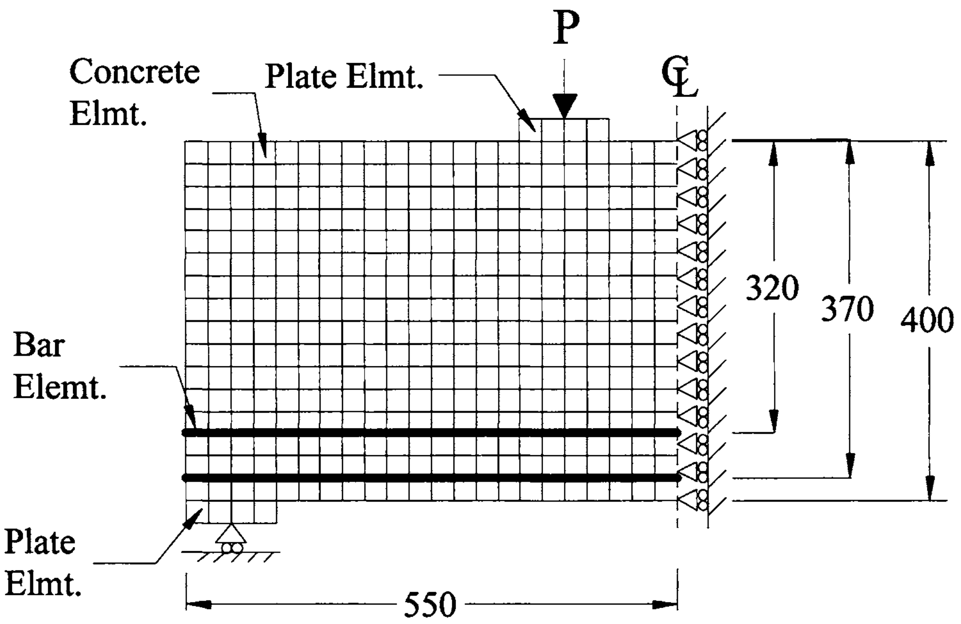

Element Type	Number of Elements	Area (mm^2)	Thickness (mm)
Concrete	352	-	100
Steel Plate	8	-	100
Tension Steel	44	1225	-

Figure 7.30 – FE mesh for Narayanan and Darwish (1998) beams..

Table 7.10 – Material parameters used for modelling the FRC deep beams of Narayanan and Darwish (1988).

Specimen	D2	D3	D4	D5	D6	D7
Concrete						
f_{cp} (MPa)	51.6	49.8	46.4	54.6	53.6	49.3
f_{ct}* (MPa)	2.37	2.33	2.25	2.44	2.42	2.32
E_o (GPa)	36.3	35.6	34.4	37.3	36.9	35.5
G_{Fm} (N/m)	100	90	85	100	100	90
l_{ch} (mm)	25	25	25	25	25	25
ε_{cp}	0.003	0.003	0.003	0.003	0.003	0.003
ν	0.2	0.2	0.2	0.2	0.2	0.2
α_1	0.33	0.33	0.33	0.33	0.33	0.33
α_2	21.0	19.2	18.9	20.4	20.6	19.4
α_3	93.0	85.1	83.3	90.3	91.0	85.7
Tension Reinforcing Steel #						
E_s (GPa)	200	200	200	200	200	200
ε_y	0.00275	0.00275	0.00275	0.00275	0.00275	0.00275
ε_r	0.005	0.005	0.005	0.005	0.005	0.005
ε_f	0.05	0.05	0.05	0.05	0.05	0.05
σ_y (MPa)	550	550	550	550	550	550
σ_r (MPa)	650	650	650	650	650	650
Fibre						
ρ_f (%)	0.25	0.5	0.75	1	1.25	1
l_f (mm)	30	30	30	30	30	30
d_f (mm)	0.3	0.3	0.3	0.3	0.3	0.3
σ_{fu} (MPa)	2000	2000	2000	2000	2000	2000
τ_b (MPa)	6	5.88	5.68	6.16	6.1	5.85
α	0.086	0.086	0.086	0.086	0.086	0.086

Notes: * taken as $0.33\sqrt{f_{cp}}$; # see Figure 7.1 for stress-strain definitions

Table 7.10 – Material parameters used for modelling the FRC deep beams of Narayanan and Darwish (1988).

Specimen	D8	D9	D10	D11	D12
Concrete					
f_{cp} (MPa)	46.6	44.5	47.9	30.2	33.8
f_{ct}* (MPa)	2.25	2.20	2.28	1.81	1.92
E_o (GPa)	34.5	33.7	35	27.8	29.4
G_{fm} (N/m)	85	80	90	50	60
l_{ch} (mm)	25	25	25	25	25
ε_{cp}	0.003	0.003	0.003	0.003	0.003
ν	0.2	0.2	0.2	0.2	0.2
α_1	0.33	0.33	0.33	0.33	0.33
α_2	18.8	18.1	19.7	13.9	15.7
α_3	83.2	80.1	87.0	60.9	69.0
Tension Reinforcing Steel #					
E_s (GPa)	200	200	200	200	200
ε_y	0.00275	0.00275	0.00275	0.00275	0.00275
ε_r	0.005	0.005	0.005	0.005	0.005
ε_f	0.05	0.05	0.05	0.05	0.05
σ_y (MPa)	450	450	450	450	450
σ_r (MPa)	580	580	580	580	580
Fibre					
ρ_f (%)	1	1	0.25	0.5	0.75
l_f (mm)	0.3	0.3	0.3	0.3	0.3
d_f (mm)	30	30	30	30	30
σ_{fu} (MPa)	2000	2000	2000	2000	2000
τ_b (MPa)	5.7	5.6	6	5.88	5.68
α	0.086	0.086	0.086	0.086	0.086

Notes: * taken as $0.33\sqrt{f_{cp}}$; # see Figure 7.1 for stress-strain definitions

Table 7.11 – Comparison of shear strengths calculated for the Narayanan and Darwish deep beams compared to the test data.

Specimen	$V_{u,\exp}$ (MPa)	$V_{u,FEM}$ (MPa)	$\tau_{u,\exp}$ (MPa)	$\tau_{u,FEM}$ (MPa)	$\frac{\tau_{u,\exp}}{\tau_{u,FEM}}$
D2	350	376	10.14	10.90	1.07
D3	325	335	9.42	9.71	1.03
D4	361	335	10.46	9.71	0.93
D5	396	416	11.42	12.06	1.06
D6	393	428	10.99	12.41	1.13
D7	454	441	12.14	12.78	1.05
D8	404	401	11.45	11.62	1.02
D9	342	335	10.20	9.71	0.95
D10	344	316	9.74	9.16	0.94
D11	294	282	9.74	8.17	0.84
D12	333	304	10.00	8.81	0.88
Average					0.99
COV.					0.089

7.5.8 Summary

A constitutive law for FRC elements was developed in Chapter 6 and this material law was incorporated into a FE element subroutine linked into the reinforced concrete analysis program RECAP (Foster, 1992). A total of 45 fibre reinforced concrete beams from five studies with strengths from 30 to 170 MPa were numerically modelled and the results compared with the experimental data. The ultimate load results are compared in Table 7.12 and it is seen that, overall, a good correlation was achieved with a FEM to ultimate load ratio of 0.97 and coefficient of variation of 8.5 percent. The failure modes and overall behaviour of the model results were similar to those reported for the test beams. It is concluded that the FE model has a good accuracy with consistent and reliable results being obtained.

Table 7.12 – Summary of ultimate load results.

Investigator	Designation	Exp. Failure Load (kN)	FEM Failure Load (kN)	FEM / Exp.
This Study	SB1	430	340	0.79
	SB2	497	442	0.89
	SB3	428	405	0.95
	SB4	337	304	0.90
	SB5	440	384	0.87
	SB6	330	324	0.98
	SB7	397	394	0.99
Adeline and Behloul (1996)	Beam 1	676	645	0.95
	Beam 2	153	148	0.97
Noghabai (2000)	$HSC^{I}_{S6/0.15}$ (S)	299	278.2	0.93
	$HSC^{I}_{S60.0.7/0.5}$ (S)	252	236	0.94
	$HSC^{I}_{S60/0.7/0.75}$ (S)	262	377	1.06
	HSC^{I}_{Smix} (S)	295	299	1.01
	NSC^{II}_{Smix} (S)	189	191	1.01
	$HSC^{III}_{S6/0.15}$ (M)-1	289	262	0.91
	$HSC^{III}_{S6/0.15}$ (M)-2	336	262	0.78
	$HSC^{III}_{S60.0.7/0.5}$ (M)-1	264	282	1.07
	$HSC^{III}_{S60.0.7/0.5}$ (M)-2	312	282	0.91
	$HSC^{III}_{S60/0.7/0.75}$ (M)-1	339	338	1.00
	$HSC^{III}_{S60/0.7/0.75}$ (M)-2	292	338	1.16
	HSC^{III}_{Smix} (M)-1	367	343	0.93
	HSC^{III}_{Smix} (M)-2	327	343	1.05
	$HSC^{III}_{S6/0.15}$ (L)	445	414	0.93
	$HSC^{III}_{S60/0.7/0.75}$ (L)	509	527	1.04
	HSC^{IV}_{Smix} (L)	596	484	0.81
Swamy et al. (1993)	1 TLF-1	80	76	0.95
	1 TLF-2	59	55	0.93
	1 TLF-3	43	50	1.16
	2 TLF-1	72	76	1.06
	2 TLF-2	46	50	1.09
	2 TLF-3	43	41	0.95
	3 TLF-1	68	66	0.97
	3 TLF-2	42	39	0.93
	3 TLF-3	29	28	0.97
Narayanan and Darwish (1988)	D2	350	376	1.07
	D3	325	335	1.03
	D4	361	335	0.93
	D5	396	416	1.05
	D6	393	428	1.09
	D7	454	441	0.97
	D8	404	401	0.99
	D9	342	335	0.98
	D10	344	316	0.92
	D11	294	282	0.96
	D12	333	304	0.91
Average				0.97
COV.				0.085

7.6 Parametric Studies

In Section 7.5, extensive experimental verification of the FE model was undertaken with good and consistent results being obtained. In this section, parametric studies are performed to further study the behaviour of FRC beams in shear. In these studies, shear specimens with a cross-section as per the experimental programme presented in Chapter 5 were used with the investigating variables being: (i) level of prestress, (ii) fibre quantities, (iii) shear span-to-depth ratio, (iv) fibre types, (v) flange width to web thickness ratio and (vi) web thickness.

The FE mesh used for the parametric study is shown in Figure 7.4. The FE elements used were 4-node isoparametric concrete elements, 4-node steel plate elements and 2-node bar elements for the prestressing and conventional steel reinforcement (prestrained as appropriate). Perfect bond was assumed between the steel and the concrete. The concrete, steel plate and bar elements are, generally, 50 mm square and the elements in the tapered flange regions were 25 mm by 50 mm. One half of the specimen is modelled accounting for symmetry.

7.6.1 Prestressing Level

The prestressed I-girder was modelled with the variable being the level of prestress. The material parameters kept constant were the concrete strength (f_{cp} = 160 MPa), Poisson's ratio (ν = 0.15), modulus of elasticity (E_o = 45 GPa), matrix cracking strength (f_{ct} = 4.22 MPa), matrix fracture energy (G_{Fm} = 330 N/m), fibre volumetric ratio (ρ_f = 2 %), fibre-matrix bond strength (τ_b = 10 MPa), shear span-to-effective depth ratio (a/d =3.33), top prestressing steel area ($A_{p,top}$ = 858 mm^2) and bottom prestressing steel area ($A_{p,bot}$ = 1716 mm^2). The fibres used are straight steel fibre (shown in Table 5.1) with a fibre length of 13 mm by 0.2 mm in diameter. With a prestressing force between 0 to 90 percent of the tensile strength (1750 MPa) of each strand, the resultant average prestress on the cross-section is between 0 and 43 MPa.

Figure 7.31 shows the load versus midspan deflection curves of a web prestress of 0, 7.2, 14.3, 21.5, 28.6, 35.6 and 43 MPa (equivalent to 0, 15, 30, 45, 60, 75 and 90 percent of the tensile strength of the prestressing steel). The FE results show the stiffness of the girder and the ultimate shear strength increases as the prestressing level increases. At failure, all specimens show a critical diagonal shear crack in the web regions, similar to that observed in Figures 7.10 and 7.11.

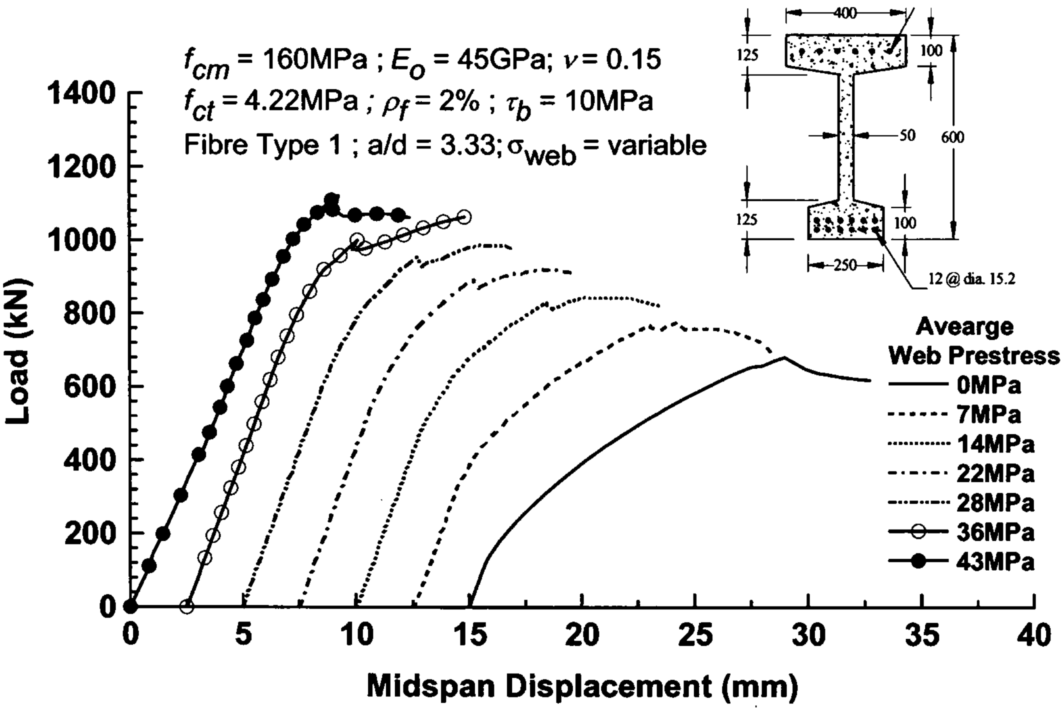

Figure 7.31 – Load versus midspan displacement of FR-RPC beam with varying prestress.

7.6.2 Fibre Quantity

In this section, the varying parameter is the quantity of Type I straight steel fibre as shown in Table 5.1. The fibre quantities were varied from 0 to 5% by volume. The material parameters that are kept constant are the concrete strength (f_{cp} = 160 MPa), Poisson's ratio (ν = 0.15), modulus of elasticity (E_o = 45 GPa), matrix cracking strength (f_{ct} = 4.22 MPa), matrix fracture energy (G_{Fm} = 330 N/m), average web prestress (σ_{web} = 21.5 MPa), fibre-matrix bond strength (τ_b = 10 MPa), shear span-to-effective depth ratio (a/d = 3.33), top steel area ($A_{p,top}$ = 858 mm^2) and bottom steel area ($A_{p,bot}$ = 1716 mm^2). Figure 7.32 shows the load versus midspan deflection curves for girders with fibre volumes of 0, 0.5, 1, 1.5, 2, 2.5, 3 and 5 percent. The analyses show that ultimate strength increases as the fibre volumetric ratio increases.

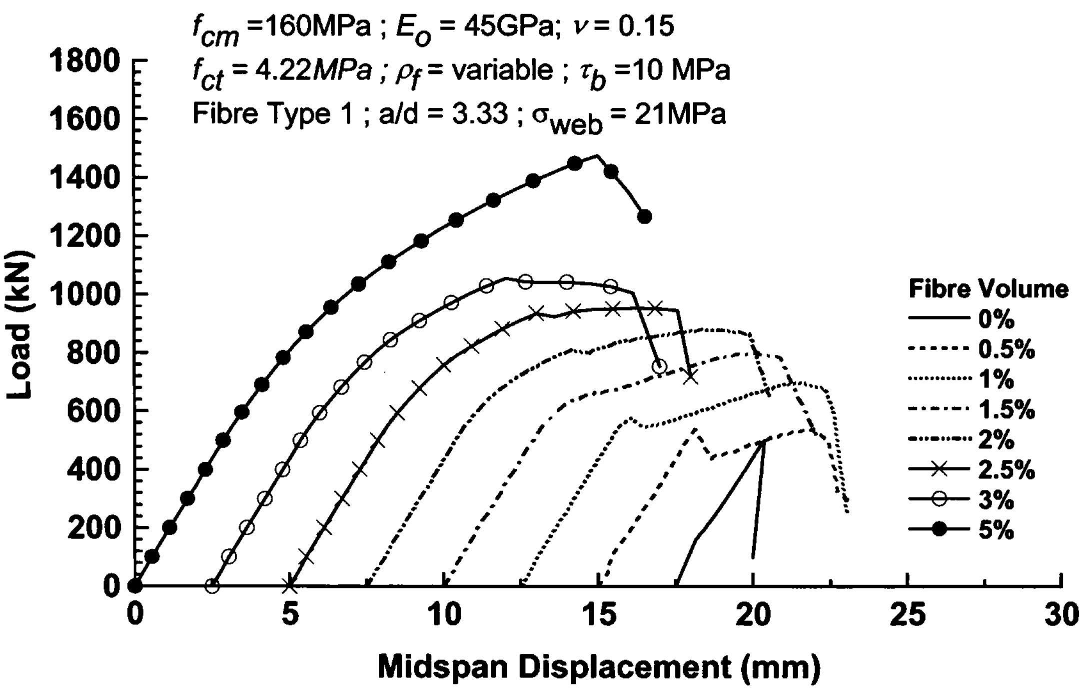

Figure 7.32 – Load versus midspan displacement of FR-RPC beams with varying fibre volumetric ratios.

7.6.3 Shear Span-to-Depth Ratio

In this section, the varying parameter is the shear span-to-effective depth ratio (a/d). The material parameters that are kept constant are the concrete strength (f_{cp}= 160 MPa), Poisson's ratio (ν = 0.15), modulus of elasticity (E_o= 45 GPa), matrix cracking strength (f_{ct}= 4.22 MPa), matrix fracture energy (G_{Fm} = 330 N/m), fibre volumetric ratio (ρ_f = 2%), fibre-matrix bond strength (τ_b = 10 MPa), top steel area ($A_{p,top}$ = 858 mm^2) and bottom steel area ($A_{p,bot}$ = 1716 mm^2).

Figure 7.33 shows the load versus midspan deflection curves of non-prestressed 160 MPa FR-RPC beams with varying shear span-to-effective depth ratios. The FE analyses show as the shear span-to-effective depth (a/d) increases the shear strength of the FR girders becomes constant. For $a/d < 3$, the shear strength increases gradually as the arching action on a deep section becomes dominant.

Figure 7.34 shows the load versus midspan deflection curves of 21.5 MPa prestressed FR-RPC girders with varying a/d. Similar to Figure 7.33, the shear strength becomes constant as the $a/d > 3$. This parametric study shows that the shear span-to-effective ratio used in the shear beam tests undertaken in Chapter 5 (that is experimental programme $a/d = 3.33$) was sufficiently large so that the results were not significantly influenced by arch action before the peak loads were obtained. As discussed in Chapter 5, arching was observed in the post peak response due to second order effects.

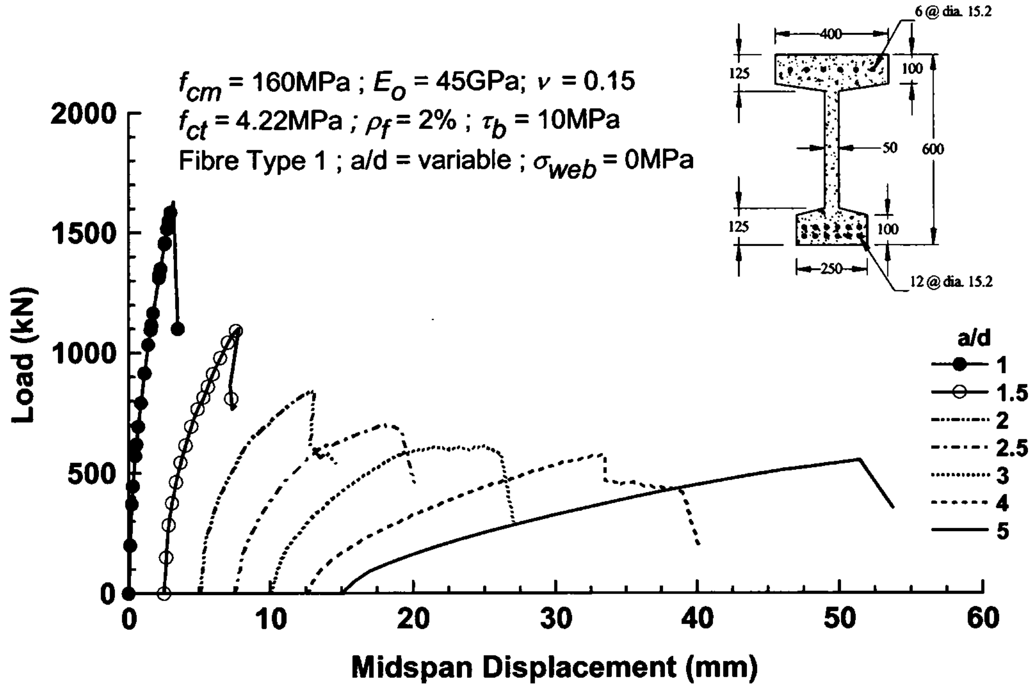

Figure 7.33 – Load versus midspan displacement of non-prestressed FR-RPC beam with varying shears span to effective depth ratio.

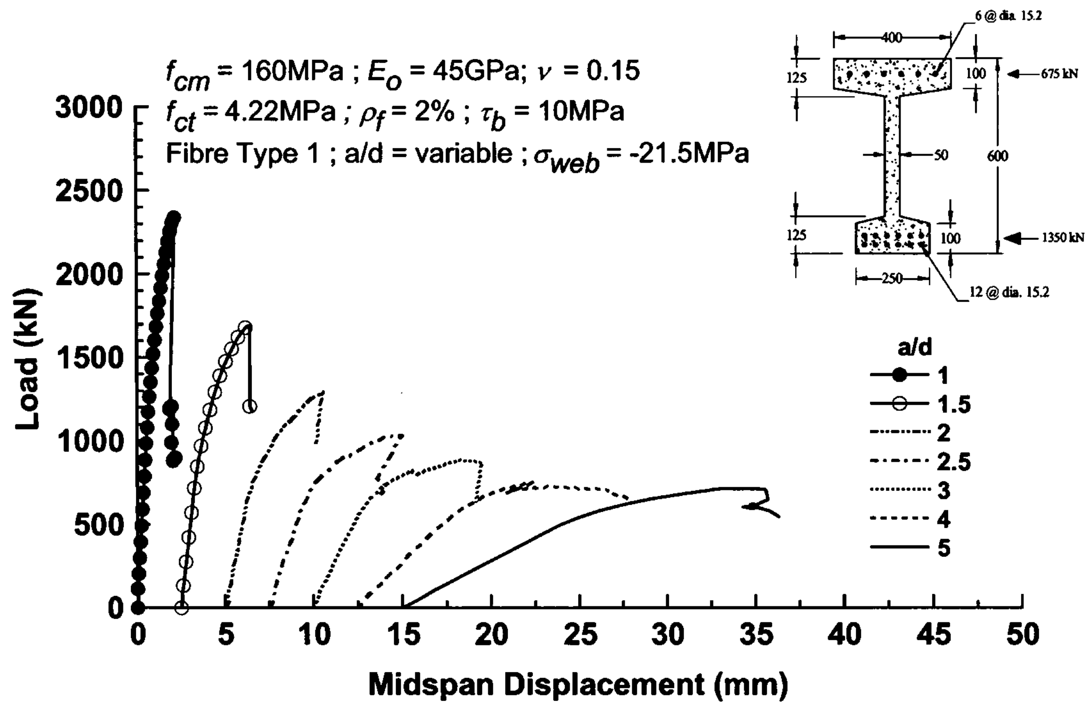

Figure 7.34 – Load versus midspan displacement of prestressed FR-RPC beam with varying shears span to effective depth ratio.

7.6.4 Fibre Types

In this section, the varying parameter was the fibre type. The material parameters keep constant were the concrete strength (f_{cp} = 160 MPa), Poisson's ratio (ν = 0.15), modulus of elasticity (E_o = 45 GPa), matrix cracking strength (f_{ct} = 4.22 MPa), matrix fracture energy (G_{Fm} = 330 N/m), average web prestress (σ_{web} = 21.5 MPa), fibre volumetric ratio (ρ_f = 2%), top steel area ($A_{p,top}$ = 858 mm^2), and bottom steel area ($A_{p,bot}$ = 1716 mm^2), and shear span-to-effective depth ratio (a/d =3.33).

Figures 7.33 and 7.34 show the load versus midspan displacement of beams with varying fibre lengths. Straight steel fibres are analysed with a diameter of 0.2 mm and an ultimate tensile strength of 1800 MPa. The bond strength is taken as 10 MPa. Equation 6.14 calculates the critical fibre length as l_c = 18 mm. Figure 7.35 shows that for fibres with $l_f \le l_c$ the failure load decreases as the fibre length is decreased. In contrast, Figure 7.36 shows for the case of fibre fracture (that is $l_f > l_c$), the ultimate failure load decreases as the fibre length is increased. This shows the optimum response is obtained by using fibre lengths close to the critical fibre length.

Figure 7.37 shows the load versus midspan displacement of beams reinforced with end-hooked fibres. The steel fibres used in the analyses had a diameter of 0.5 mm and an ultimate tensile strength of 1000 MPa. The bond strength was taken as τ_b = 15 MPa, giving a critical length of 16.7 mm as per Eq. 6.14. Similar to that for the straight steel fibres, Figure 7.37 shows the shear strength increases with increasing fibre length until the critical fibre length is reached. Increasing the length of the fibres beyond the critical length reduces the shear capacity of the beams.

In Figure 7.38 the normalised failure load is plotted against the fibre length to critical length ratio. If it is desired to obtain within a 10 percent range of the optimum value then $0.85 \leq l_f / l_c \leq 1.3$ for straight fibres and $0.83 \leq l_f / l_c \leq 1.5$ for end-hooked steel fibres. To get within 20 percent of optimum $0.75 \leq l_f / l_c \leq 1.8$ for straight steel fibres and $0.67 \leq l_f / l_c \leq 2$ for end-hooked steel fibres.

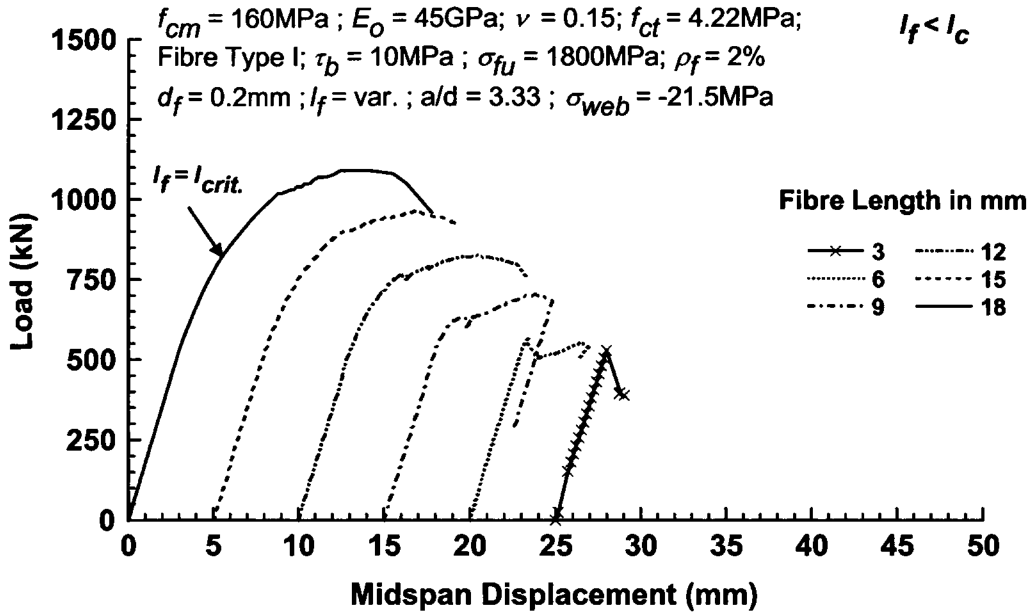

Figure 7.35 – Load versus midspan displacement of FR-RPC beam with varying straight steel fibre length for $l_f \leq l_c$.

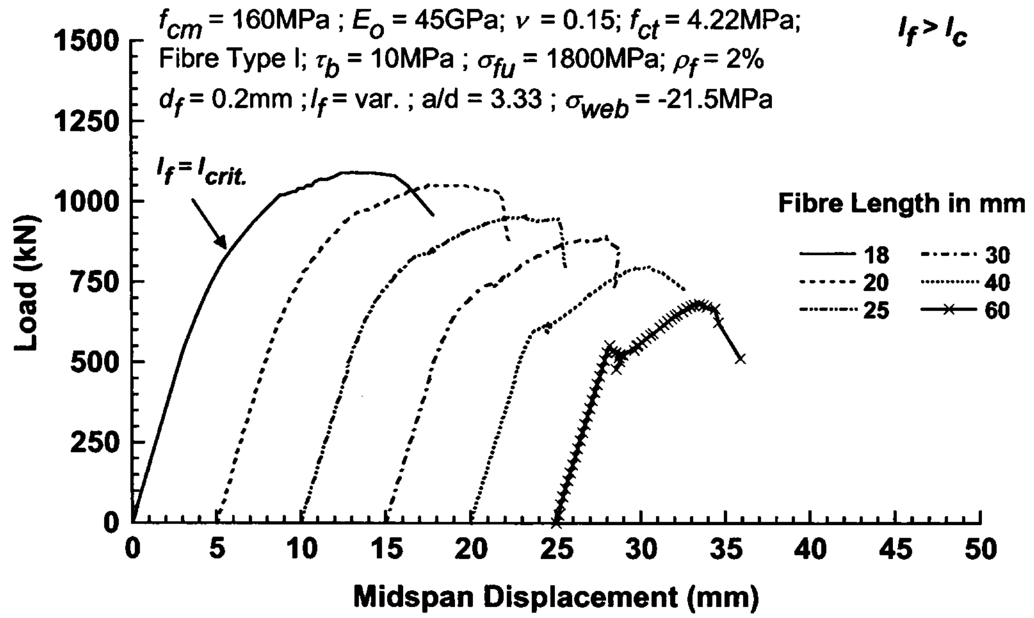

Figure 7.36 – Load versus midspan displacement of FR-RPC beam with varying straight steel fibre length for $l_f > l_c$.

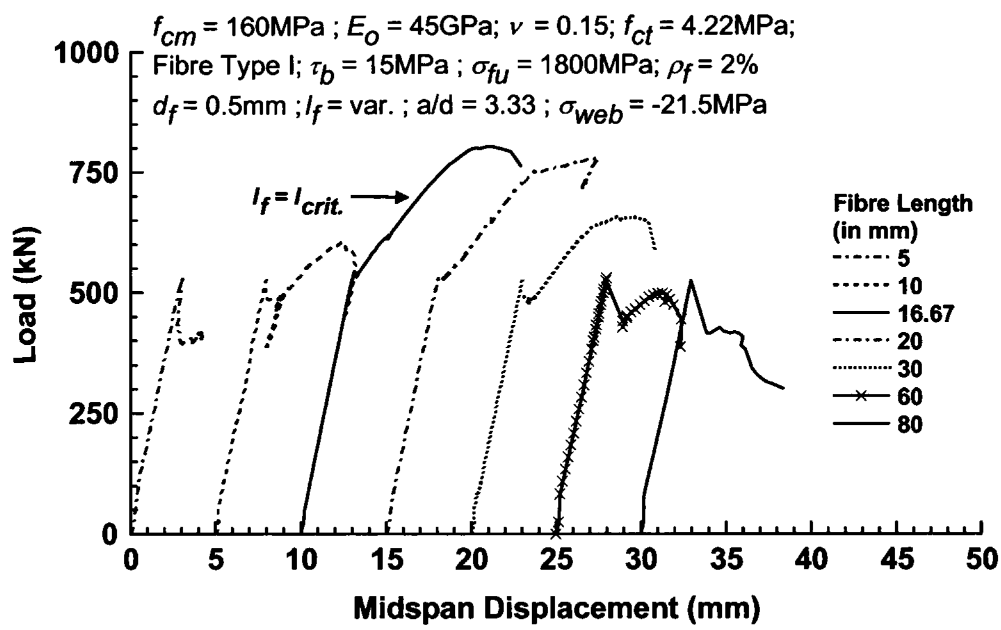

Figure 7.37 – Load versus midspan displacement of FR-RPC beam with varying end-hooked steel fibre length.

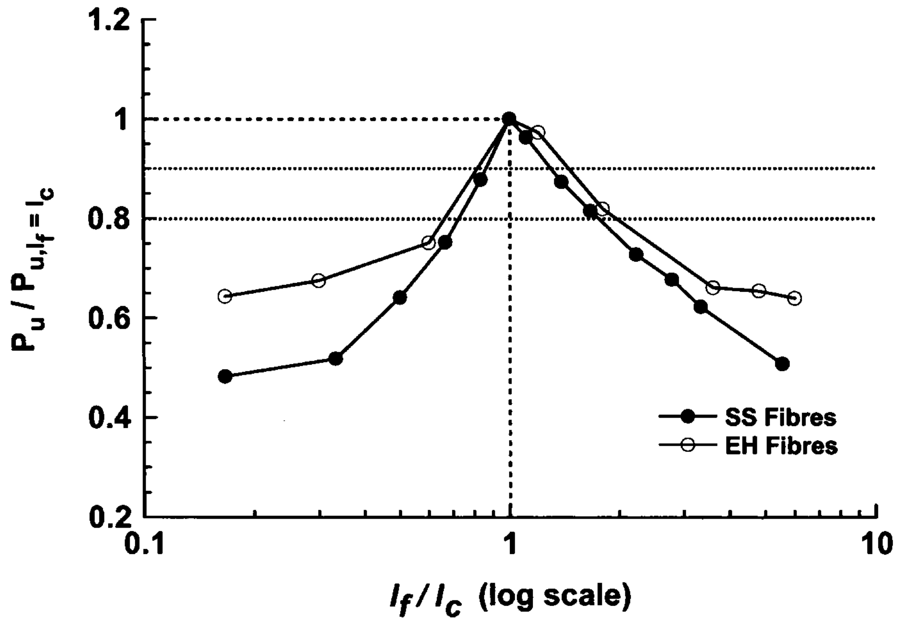

Figure 7.38 – Normalised failure load versus l_f / l_c for straight steel fibres and end-hooked fibres.

7.7 Conclusions

The experimental shear beams presented in Chapter 5 and other fibre reinforced concrete beams from the literature were analysed using finite element modelling with the variable engagement constitutive model used for tensile fracture of fibre reinforced concrete. A total of 45 beams were modelled and the FE results showed a good correlation with the experimental data. The overall mean model to experimental ultimate load ratio was 0.97 and coefficient of variation of 8.5 percent. Comparison of the load versus midspan deflection, strains in the top and bottom flanges and the failure modes shows that the FE model is capable of capturing the overall response of the experimental beams.

Extensive parametric studies were performed to further understand the behaviour of FRC beams in shear. In the parametric studies, shear specimens with a cross-section as per the experimental beams reported in Chapter 5 were used with the investigating variables being: (i) level of prestress, (ii) fibre quantities, (iii) shear span-to-depth ratios and (iv) fibre type. The following conclusions are drawn:

- The shear strength and stiffness of the specimens increase as the level of prestress increases.
- The shear strength increases as the quantity of fibres increases in the mix. The failure mode is more ductile for specimen with higher quantity of fibres.
- The shear strength becomes constant as the shear span-to-effective depth ratio, $a / d_e \geq 3$.

- Shear strength increases with increasing fibre length until the critical fibre length is reached. With increasing the fibre length beyond the critical length, for, a constant volume of fibres, the shear strength of the beam is reduced.

CHAPTER 8 – PLASTICITY MODEL OF FRC BEAMS

In this section, the upper bound plasticity approach for calculating the strength of reinforced concrete beams in shear is used to calculate the shear capacity (V_u) of the experimental beams. Plasticity approaches came to the fore front of reinforced concrete design with work published by Nielsen (1963, 1967). In the following years, extensive research has been undertaken using plasticity approaches by many researchers on various types of concrete structural elements such as beams, joints, slabs and so on.

In this section, two plasticity models are used to calculate the shear strength of the test FR-RPC beams tested in this study. The first approach is based on the work of Zhang (1994) which is used to calculate the shear strength of overly flexurally reinforced rectangular beams without shear reinforcement. In the calculations that follows the flange outstands of the I-girders are ignored for the purpose of assessing the shear capacity. The second approach is more complicated and less user friendly and comes from the work of Hoang (1997). In Hoang's work the shear strength of non-shear reinforced but longitudinally over reinforced simply supported T-beams under concentrated loading were modelled. In this study, Hoang's model for a T-beam is modified to incorporate I-sections. A comparison of the two approaches is presented.

8.1 Plasticity Model for Rectangular Beams

Zhang developed a crack sliding model to determine the shear capacity of rectangular concrete beams without shear reinforcement. A detailed description of this model may be found in Zhang (1994) and Hoang (1997).

The crack sliding model (CSM) is based on the upper bound theorem of plasticity, that is concrete is treated as a Mohr-Coulomb material with a zero tension cut-off. A more comprehensive description of the theory can be found in Johansen (1958), Sandbye (1965) and Nielsen (1967). According to the crack sliding model, the cracking of concrete introduces a potential yield-slip line which, due to a reduced sliding resistance, forms the critical failure mechanism.

For both non-prestressed and prestressed simply supported beams with rectangular cross-sections and loaded with two symmetrically located point loads, the ultimate load of the section can be determined by

$$V_u = \frac{1}{2} f_c^* b\, h \left(\sqrt{1 + \left(\frac{x}{h} \right)^2} - \frac{x}{h} \right) \tag{8.1}$$

where f_c^* is, the effective concrete strength, b and h are the width and depth of the section, respectively, a is the shear span and x is the horizontal projection of the yield line as shown in Figure 8.1.

To determine the starting position of the critical crack, the ultimate load (V_u) is taken as equal to the diagonal cracking load (V_{cr}). For definition purpose, the diagonal cracking load (V_{cr}) is defined as the load capacity of the beam when the diagonal crack is fully developed with a uniform effective tension stress bridging the crack. For a simply supported beam under point loading, the diagonal cracking load is determined by taking the moment about the crack tip (marked A in Figure 8.1b) and is written as

$$V_{cr} = \frac{1}{2} f_t^* \, b \, \frac{h^2 + x^2}{a} + \frac{\sum P_e \, d_{p_i}}{a} \tag{8.2}$$

where b is the width of the section, d_{pi} is the distance of the effective prestressing force (P_e) at the ith level from the top surface of the beam, f_t^* is the effective tensile strength for a beam with a depth of h, a is the length of the shear span.

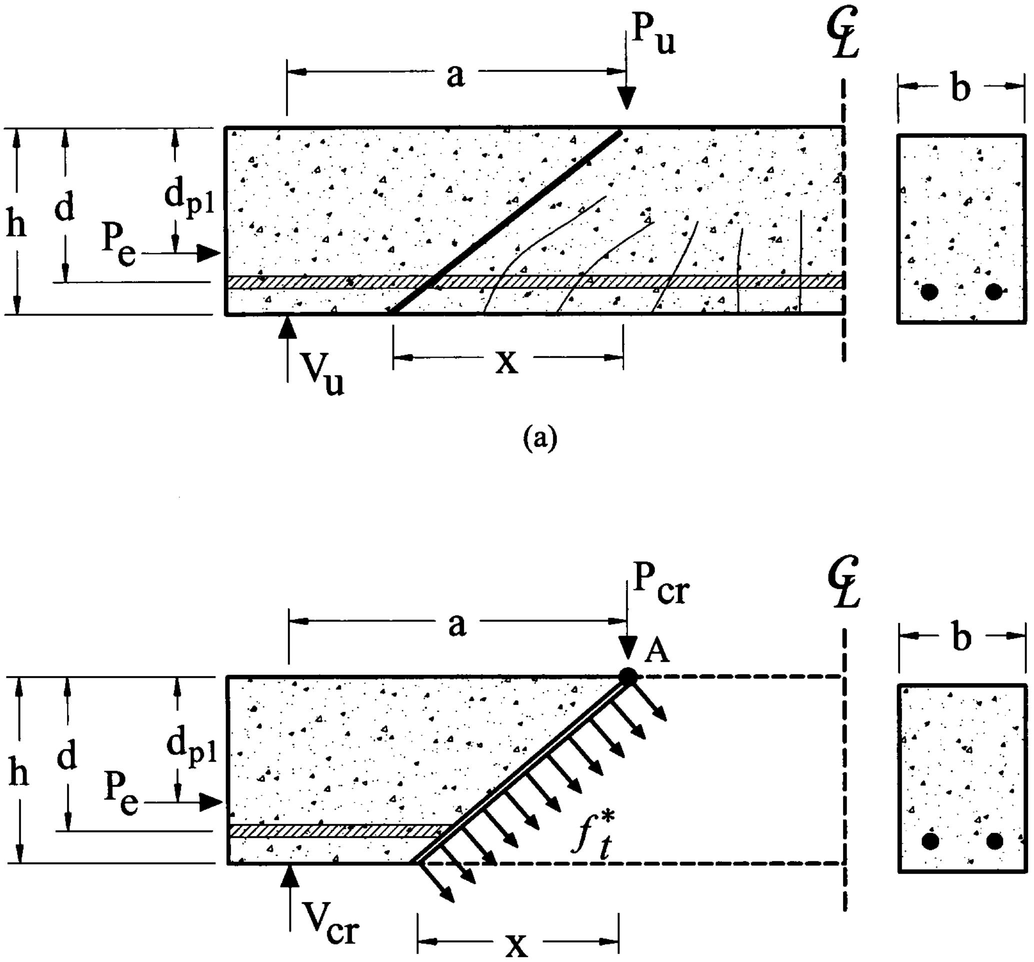

Figure 8.1 – Simply supported beam with critical diagonal crack (a) yield line and (b) cracking load.

The methodology to obtain the solution of x is presented in Figure 8.2 and is obtained by equating V_u by Eq. 8.1 to V_{cr} by Eq. 8.2. Thus, the solution of x is the intersection of Eqs. 8.1 and 8.2, giving

$$f_c^*\left(\sqrt{1+\left(\frac{x}{h}\right)^2}-\frac{x}{h}\right)=f_t^*\frac{\left(x^2+h^2\right)}{ah}+\frac{2\sum P_i d_{pi}}{abh} \quad ; \; for \;\; 0\le x\le a \tag{8.3}$$

From the experimental data it is observed that at the peak load the crack widths for the FR-RPC experimental girders tested in this study were in the range of 0.5 to 1.5 mm. From the VEM (Chapter 6) the effective tensile strengths (f_t^*) in this range for the 13 mm long by 0.2 mm fibres used were in the range of 70 to 90 percent of the peak fibre contribution to the tensile strength (Figure 8.3). In the analyses that follow, the effective tensile strength of the FR composite is

$$f_t^* = \upsilon_t f_{tf} \tag{8.4}$$

with the tensile effectiveness factor taken as $\upsilon_t = 0.8$, where f_{tf} is the maximum stress of the fibre component according to the VEM. The effective compressive strength (f_c^*) is taken as

$$f_c^* = \upsilon_c f_{cm} \tag{8.5}$$

In this study, the compression effectiveness factor is taken as $\upsilon_c = 0.8$. This assumption is discussed later in Section 8.4 of this thesis.

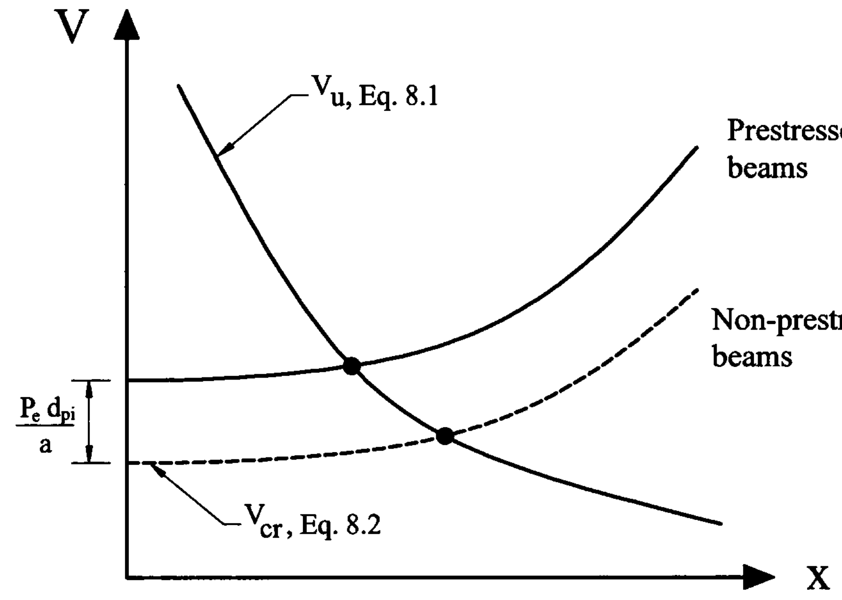

Figure 8.2 – Relationship between V_u and V_{cr} with x.

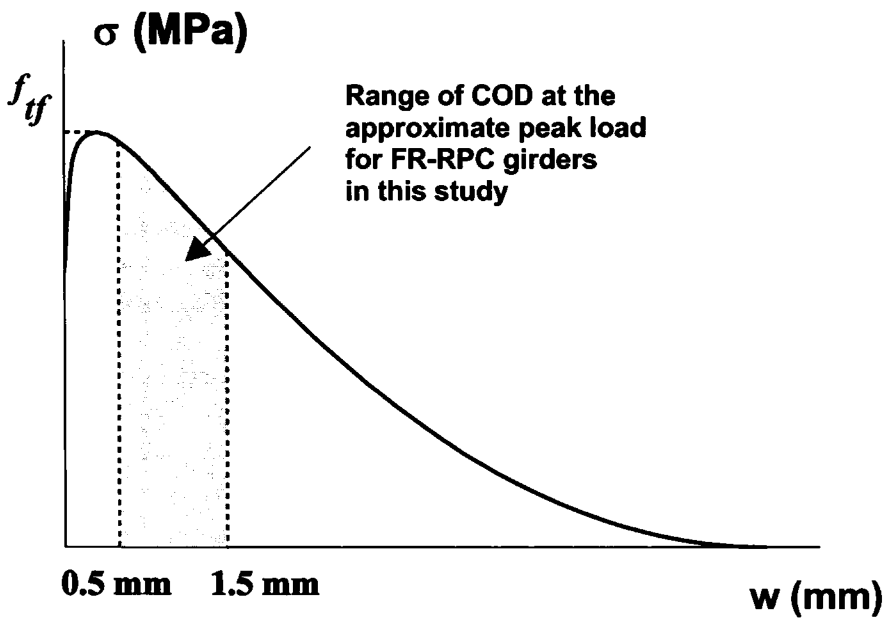

Figure 8.3 – Range of tensile stress across failure surface for SB1 to SB3.

In the calculation of x the limits are $0 \leq x \leq a$. An analytical solution to Eq. 8.3 is not easily obtained. Instead, a numerical method is used to find the critical value of x/h. In this way the starting position of the critical diagonal crack for a given a/h is found and, consequently, the ultimate load and the shear capacity can be determined from Eq. 8.1. Finally, the ultimate shear strength is written as

$$\tau_u = \frac{V_u}{bh} \tag{8.6}$$

8.2 Shear Capacity of T-Beams

Hoang claimed that if the plastic model as outlined in section 8.1 is used without modification for T- beams, the model leads to an overestimation of the shear capacity. The overestimation is especially high for cases with relatively high ratios of flange thickness to beam depth (t/h), the ratio of the width of flange to width of web (b_f / b_w) and in cases where the concentrated loading is not distributed across the entire flange. Similarly to that for rectangular sections, the derivation of the model to account for T-sections was based on the assumptions that concrete is a modified Coulomb material with a zero tension cut-off. The full derivation of the model applied on T-beams is given in Hoang (1997).

Experimental observation shows that the general failure mechanics of the I-girders tested in this study is similar to the failure mechanism of a T-beam without stirrups. That is, the failure mechanism consists of a sliding failure along a crack in the web and rotation in hinges in the top, compression, flange (see Figure 8.4). For T-beams Hoang computed the shear force V_u at failure as

$$V_u = \frac{A_{cw}\, f_c^*}{\frac{a'}{h}} \left[\frac{0.118}{\frac{x}{a'}} + \frac{0.25\,\xi\,\beta_{ef}\,\frac{t}{h}}{1 - \frac{x}{a'}\left(1 - \frac{t}{h}\right)} \right] \tag{8.7}$$

where (refer Figure 8.5) $A_{cw} = b_w(h-t)$ is the effective area of the web, t is the effective thickness of the compression flange, a' is the distance from the applied load to the starting point of a yield line at the external compression fibre and the other terms are as given above. The ratios ξ and β_{ef} are given by $\xi = v_m / v_c$ and $\beta_{ef} = A_{cf,ef} / A_{cw}$, respectively, where v_m is the effectiveness factor for membrane action and is taken as $v_m = 2/\sqrt{f_{cm}}$. The term $A_{cf,ef} = t\, b_{fef}$ is the effective area of the compressive flange and b_{fef} is the effective width of the flange and can be approximated as

$$b_{fef} = b_w + h\frac{a'}{h}\left[1 - \frac{x}{a'}\left(1 - \frac{t}{h}\right)\right] \;\le\; b_f \tag{8.8}$$

By differentiating and minimizing Eq. 8.7 with respect to x/a', Hoang showed that the value of x/a' rendering the minimum shear capacity is

$$\frac{x}{a'} = \frac{\sqrt{C_2{}^2 + 4C_1} - C_2}{2C_1} \tag{8.9}$$

where the constants C_1 and C_2 are

$$\left.\begin{aligned} C_1 &= 2.119\,\xi\,\beta_{ef}\,\frac{t}{h}\left(1 - \frac{t}{h}\right) - \left(1 - \frac{t}{h}\right)^2 \\ C_2 &= 2\left(1 - \frac{t}{h}\right) \end{aligned}\right\} \tag{8.10}$$

For any assumed value of a' the shear capacity may be found by inserting Eq. 8.9 into Eq. 8.7. Any effective flange width b_{fef} used in the calculation must fulfill the requirement given by Eq. 8.8. Since x/a' depends upon b_{fef}, an iterative numerical procedure is required.

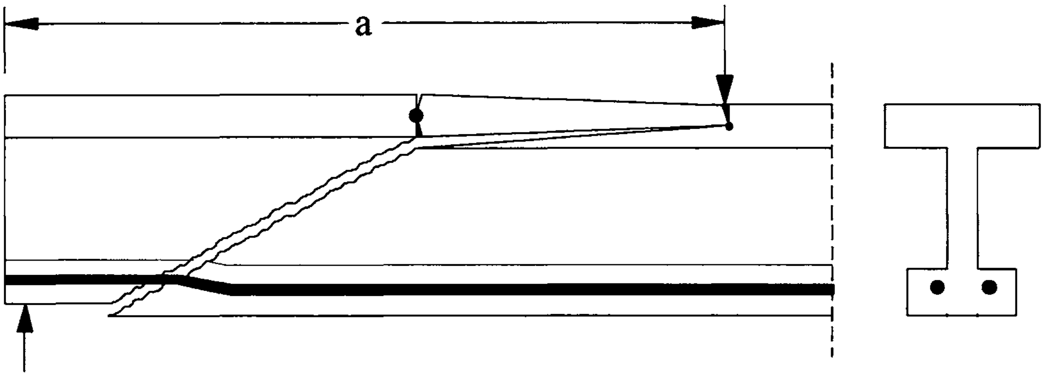

Figure 8.4 – Failure mechanics of simply supported T-beam (Hoang, 1997)

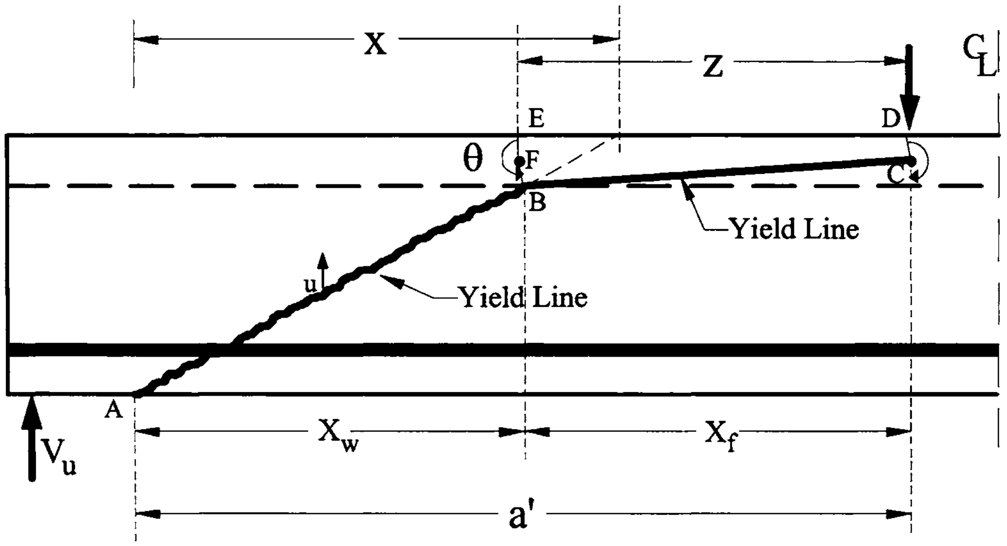

Figure 8.5 – Failure mechanism of simply supported I-beam.

The cracking load for an I-beam is found by taking moments about the upper tip of the crack (see Figure 8.6) and it is written as

$$V_{cr} \cdot (a - a' + x) - \sum P_{e,i}\, d_{pi} = M_{cr} \tag{8.11}$$

where M_{cr} is the moment at cracking about upper tip of the crack (marked as A in Figure 8.6). For any shape of cross-section the cracking moment, M_{cr} can be determined by

$$M_{cr} = f_t^{*}\, A_c\, e \left[\left(\frac{x}{h} \right)^2 + 1 \right] \tag{8.12}$$

where f_t^{*} is the effective plastic tensile strength of the concrete, A_c is the area of the cross section and e is the distance from the top face to the centre of gravity of the concrete section.

Substituting Eq. 8.12 into Eq. 8.11, the cracking load after the formation of the diagonal shear crack with an assumed uniform effective tensile strength bridging the cracking plane is

$$V_{cr} = \frac{f_t^{*} A_c \dfrac{e}{h} \left[\left(\dfrac{a'}{h} \right)^2 \left(\dfrac{x}{a'} \right)^2 + 1 \right] + \dfrac{1}{h} \sum P_{e,i}\, d_{pi}}{\dfrac{a}{h} + \dfrac{a'}{h} \left(\dfrac{x}{a'} - 1 \right)} \tag{8.13}$$

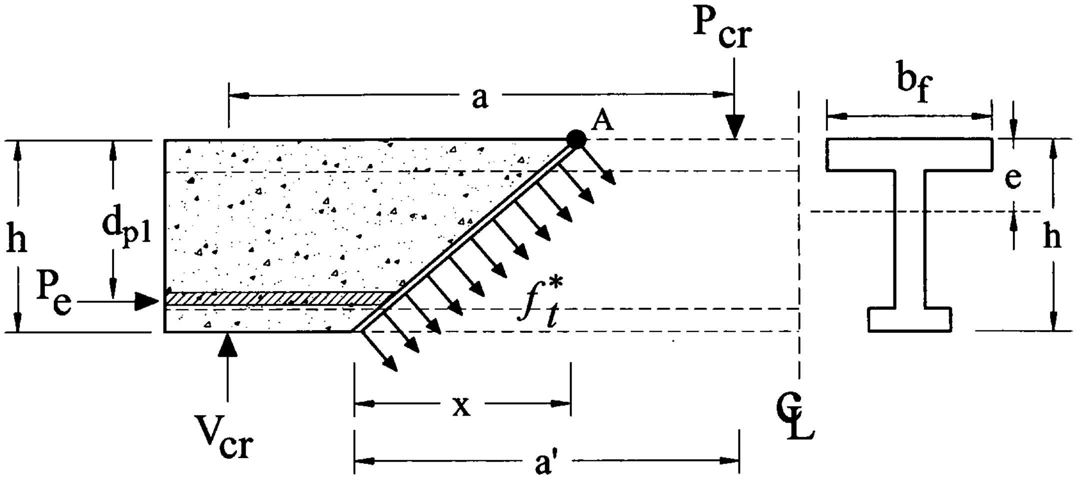

Figure 8.6 – Stress distribution along the critical diagonal crack for I beams.

Finally equating Eqs. 8.7 and 8.13, gives

$$\frac{f_c^*}{f_t^*}\left[\frac{0.118}{\frac{x}{a'}}+\frac{0.25\,\xi\,\beta_{ef}\,\frac{t}{h}}{1-\frac{x}{a'}\left(1-\frac{t}{h}\right)}\right]=\frac{\left(\frac{A_c}{A_{cw}}\right)\frac{e}{h}\left[\left(\frac{a'}{h}\right)^3\left(\frac{x}{a'}\right)^2+\frac{a'}{h}\right]+\left(\frac{a'}{h}\right)\left(\frac{1}{h}\right)\bullet\sum P_{e,i}d_i}{\left[\frac{a}{h}+\frac{a'}{h}\left(\frac{x}{a'}-1\right)\right]} \tag{8.14}$$

which is solved iteratively for a'/h.

In solving for the shear capacity an initial estimate of b_{fef} is selected. Equation 8.14 is then solved with respect to a'/h. Hereafter x/a' is found by Eq. 8.9 and a' revised to give a new estimate of b_{fef} calculated by Eq. 8.8. The solution process continues until convergence is attained. The shear capacity is then determined by Eq. 8.7 and the shear strength by Eq. 8.6.

8.3 Shear Strength Calculation on FR-RPC Prestressed Girders

The shear strengths calculated using the plasticity model described above for the FR-RPC shear beams tested in this study are compared with the experimental data and the results presented in Table 8.1. Details of the calculations are given in Appendix H.

Comparing the results of the plastic design model with the experimental data shows that both the plastic models presented provide reasonable correlation with the ultimate shear strengths with mean theoretical to experimental ratios of 0.89 and 0.85 and with coefficients of variation of 10 percent and 8 precent, respectively.

Comparison of the location of the major diagonal crack for the model and the experiment are given in Figures 8.7 and 8.8 for the rectangular beam model and I-beam model, respectively. Table 8.1 indicates that both models are capable of capturing the shear capacity of the FR-RPC prestressed girders tested in this study, however, comparison of the crack location and crack angle (θ) shows that the I-beam model compares better than the rectangular section model for the failure mechanism. The additional complexity of the I-beam model over that of the rectangular section model, however, makes it less suitable as a general design tool.

Table 8.1 – Comparison of experimental shear strength and plasticity models.

						Rectangular Beam Model			I-Beam Model		
SB No.	f_{tf} MPa	f_t^* MPa	f_c^* MPa	$V_{u,\exp}$ kN	θ deg.	$V_{u,theo}$ kN	θ deg.	$\frac{V_{u,theo}}{V_{u,\exp}}$	$V_{u,theo}$ kN	θ deg.	$\frac{V_{u,theo}}{V_{u,\exp}}$
1	6.5	5.2	129	430	37	332	18	0.77	338	30	0.79
2	6.5	5.2	128	497	34	445	24	0.90	430	43	0.86
3	6.5	5.2	119	428	32	357	21	0.83	336	38	0.79
4	3.4	2.7	131	337	26	338	18	1.00	312	33	0.93
5	5.4	4.3	137	440	29	364	19	0.83	340	35	0.77
6	3.9	3.1	126	330	24	323	18	0.98	299	33	0.93
7	5.8	4.7	135	400	21	370	19	0.92	345	35	0.86
Average								0.89			0.85
COV.								0.095			0.079

Notes: θ is the angle of the failure crack relative to the horizontal axis of the beam

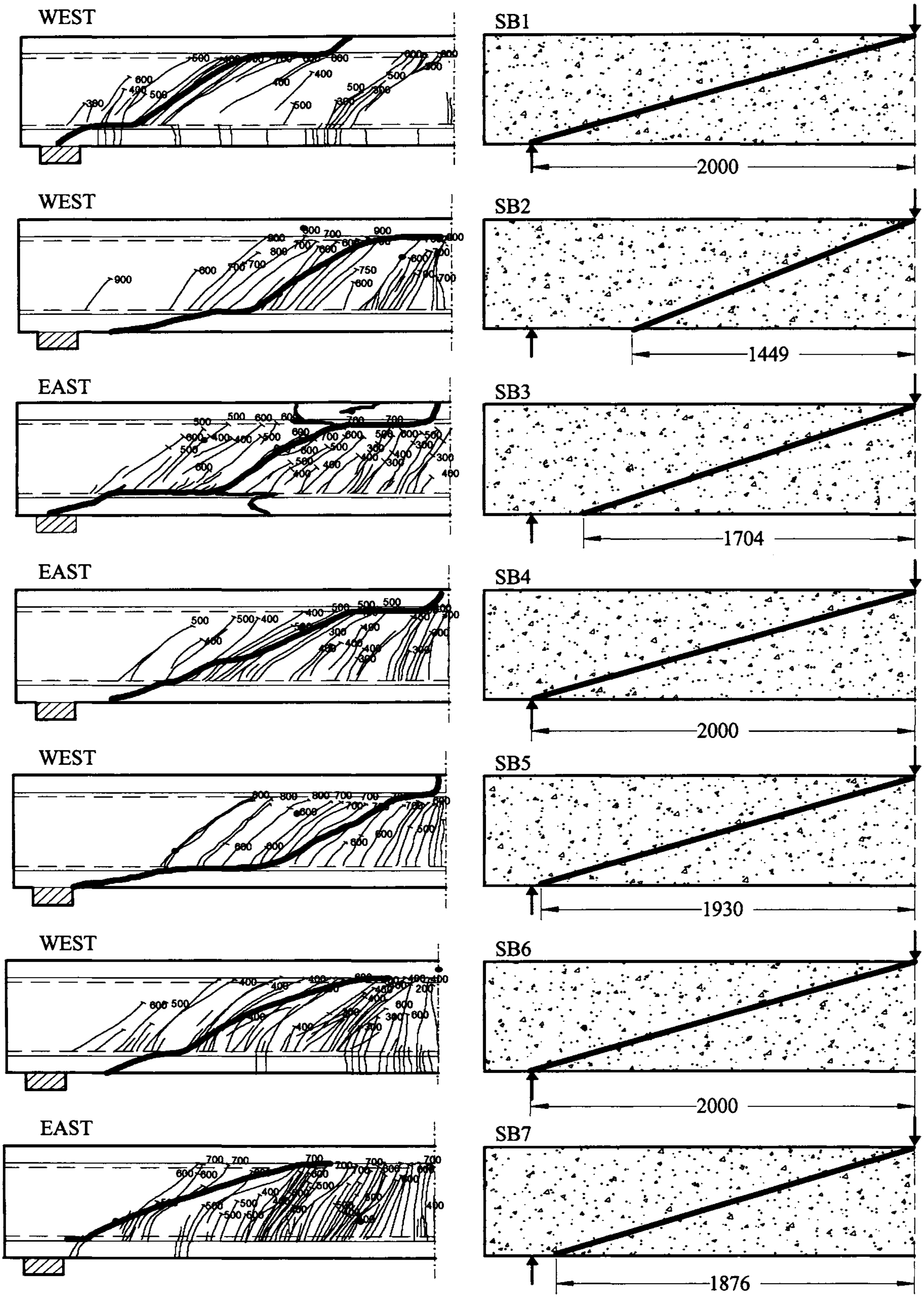

Figure 8.7 – Comparison of experimental crack location and plastic model prediction for rectangular section

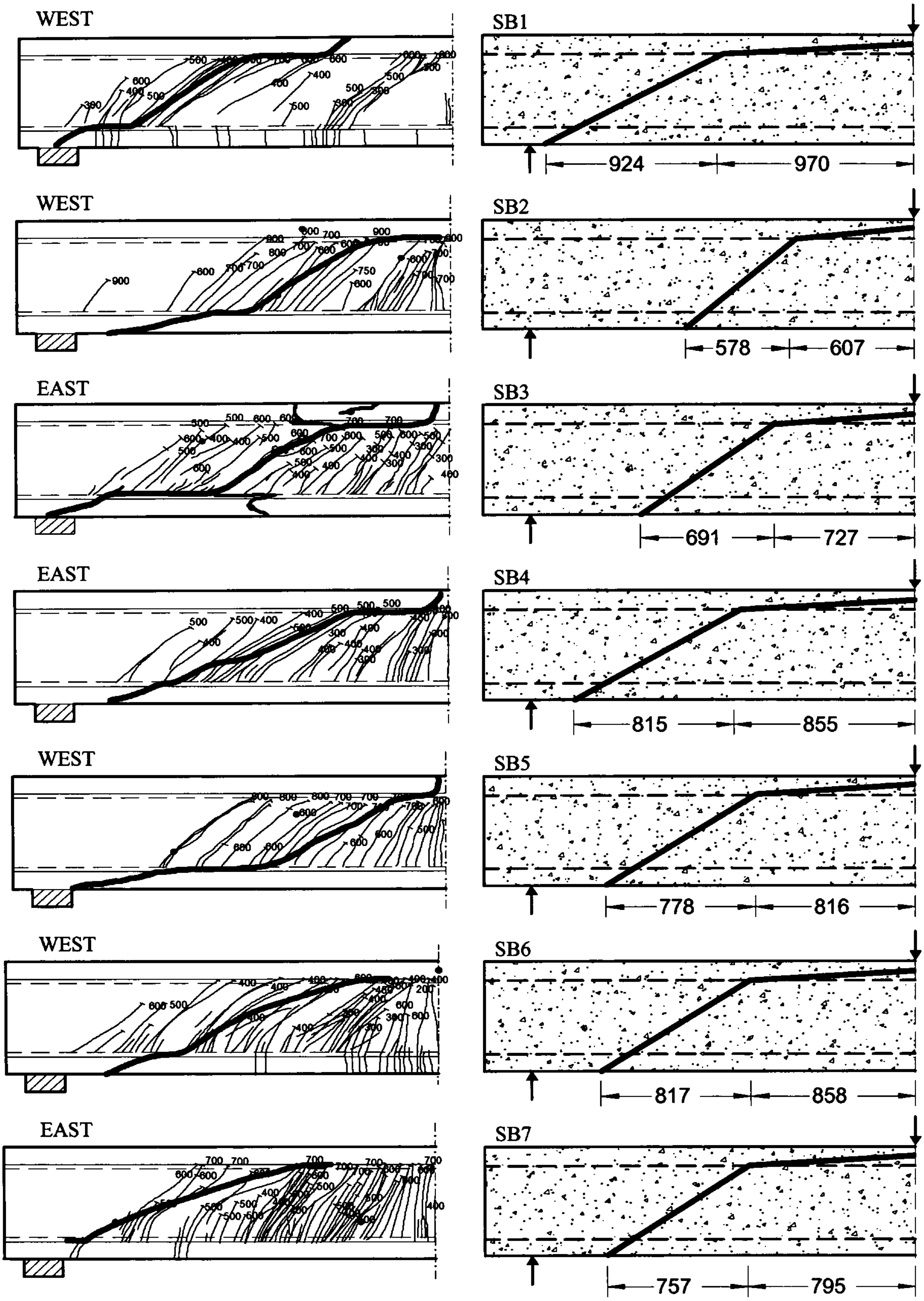

Figure 8.8 – Comparison of experimental crack location and plastic model prediction for I-section.

8.4 Comments on the Efficiency Factors υ_t and υ_c

While it appears from the results above that the model correlates well with the test data, the values of υ_t and υ_c have been, somewhat, arbitrary selected, particularly υ_c. While the values may be justified based on the high quantity of fibres in the mix, further calibration and verification studies are required before any firm conclusions are drawn. Given the limited test data available for shear beams with two percent, or greater, of fibres by volume a healthy skepticism in the general application of the design model should be maintained.

8.5 Conclusions

In this chapter, two upper bound plasticity approaches for calculating the shear strength of reinforced concrete beams in shear are used to calculate the shear capacity of the experimental beams. The first approach is based on the work of Zhang (1994) to calculate the shear strength of a rectangular section and the second approach comes from the work of Hoang (1997) to calculate the shear strength of an I-section beam.

In calculating the shear strength both the models provide reasonable correlation with the ultimate measured shear strengths. For Zhang's model, the mean model to experimental shear capacity ratio is 0.89 and with a coefficient of variation of 0.095. On the other hand, for Hoang's model, the mean model to experimental shear capacity ratio is 0.85 with a coefficient of variation of 0.079.

CHAPTER 9 – CONCLUSIONS

9.1 Concluding Remarks

In Chapter 3, the results of mechanical strength tests for nineteen different RPC mix designs using Australian materials are reported. The test variables were type and quantity of fibres and the water/binder ratio. The reported mechanical strengths consisted of compressive strength on cylinders and cubes, modulus of rupture, split-cylinder tensile strength, double punch tensile strength, modulus of elasticity, Poisson's ratio and workability. From these tests, a highly workable RPC mix was developed with a compressive cylinder strength of 160 MPa and with a split cylinder tensile strength and flexural tensile strength of the order of 15 and 25 MPa, respectively (for two percent by volume of fibres).

Tests on cylinders at stress rates from 20 MPa/min to 100 MPa/min showed no significant variation in the measured compressive strength of RPC. Comparison of the cylinder strength to cube strength showed that the cylinder compressive strength is approximately 88 percent of the cube compressive strength. In the indirect tensile strength tests the double punch test gave consistently lower strengths and lower strength gain with increasing fibre volumes than the split cylinder test and it is concluded that the double punch test is a more reliable method for determining the tensile strength. Further work is, however, required to establish the relationship between the direct tensile strength of RPC and the results obtained from indirect tension tests. Specifically, a testing programme with well designed and controlled tests on RPC in direct tension is needed in combination with indirect measurement from double punch, wedge splitting or other such indirect measures of tensile strength.

In Chapter 4, the mechanical behaviour of six 150 MPa steel fibre reinforced RPC deep panels dimensioned to simulate bursting in anchorage zones of thin webbed prestress girders was reported. The deep panels were tested to investigate crack growth and stability in RPC panels for increasing load. The test variables were the quantity and type of fibres and boundary support conditions. The fibres used consisted of either 35 mm end-hooked steel fibres or 13 mm straight steel fibres. The fibre content was varied from 1.0 percent to 3.7 percent, by volume. The support boundaries investigated were free translation with fixed rotation and free translation with free rotation.

From the experimental study it was observed that the location of the bursting crack is significantly influenced by the boundary conditions. For the specimens with free translation and fixed rotation supports, the tearing crack formed at the junction of the flange and the web. For the free translation with free rotation boundaries the tearing crack formed in the web generally toward the centre of the specimen. The quantity of fibre and type of fibre used in the concrete mix does not significantly affect the initial cracking load but has a significant effect on the failure load and on crack stability and growth. The support boundary restraints also have a significant effect on the failure load in that the failure load is higher for panels with free translation and fixed rotation boundary condition than for panels with both free translation and free rotation supports.

In Chapter 5, the mechanical behaviour of seven 150 MPa–170 MPa steel FR-RPC prestress I-section girders without stirrups were tested to study the capacity of fibre reinforced RPC beams in shear. The test variables were the quantity and type of fibres and amount of prestress. The steel fibres used in the tests consisted of either 13 mm straight fibres and/or 30 mm end-hooked fibres. All the tested specimens had the same cross-section and were subjected to mid-point loading over a shear span of 2 metres. The shear span to effective depth ratio for the beams was 3.33.

From the experimental study it was concluded that the quantity of fibres and type of fibres used in the concrete mix do not significantly affect the cracking load but have a significant influence on the rate of crack propagation and on the failure loads. At the peak load, many fine cracks had formed in the web, with the cracks well distributed through the shear spans. For all tests, the failure loads were more than twice the cracking loads.

In Chapter 6, a simple deterministic model termed the Variable Engagement Model (VEM), was developed to describe the behaviour of randomly orientated steel fibre reinforced composites subject to uniaxial tension. The model was developed by integrating the behaviour of single, randomly oriented, fibres over 3D space and is capable of describing the peak and post-peak response of fibre-cement-based composites in tension.

In the verification studies of the VEM, the proposed model is compared against a wide range of experimental data consisting of 29 uniaxial tension tests on fibre reinforced concretes and mortars by 10 researchers. Overall the model showed a good correlation with both the uniaxial tensile strength of the specimens and with the fracture energies. The load versus crack opening displacements are plotted and again good agreement is seen for the model compared with the experimental data.

Finally, a model was proposed for the inclusion of bending effects on the weakening of fibres in axial tension. Two methodologies were pursued, an elastic model and a plastic model. The results of the investigation showed that the elastic approach can capture the observed behaviour of fibres subject to combined tension and bending across a cracked medium. Further research is required to confirm the general applicability of the proposed fibre fracture-bending model.

In Chapter 7, the experimental shear beams reported in Chapter 5 together with other fibre reinforced concrete beams from the literature were analysed through finite element modelling with the variable engagement model, developed in Chapter 6, adopted for tensile constitutive law for the fibre reinforced concrete. A total of 45 beams were modelled and the FE results showed a good correlation with the experimental data. The overall mean model to experimental ultimate load ratio was 0.97 with a coefficient of variation of 8.5 percent. Comparison of the load versus midspan deflection, strains in the top and bottom flanges and the failure modes showed that the FE model is capable of capturing the overall response of the experimental beams.

Parametric studies were performed to further understand the behaviour of FRC beams in shear. In the parametric studies, shear specimens with a cross-section as per the experimental test beams (reported in Chapter 5) were used with the investigating variables being:

(i) the amount of prestress;

(ii) the quantity of fibre;

(iii) the shear span-to-depth ratios; and

(iv) the fibre type.

From the parametric studies, it was concluded that the shear strength of the specimens increases as the level of prestress and fibre quantities are increased. Also, the failure mode is more ductile for specimens having higher quantities of steel fibres. In terms of shear span-to-depth ratios, the shear strength becomes a constant for shear span-to-effective depth ratios of $a/d \geq 3$. Shear strength increases with increasing fibre length until the critical length fibre length is reached. The most efficient fibre length for shear strength is the critical fibre length. Increasing the length of the fibres beyond the critical length, while maintaining a constant volume of fibres, reduces the shear strength of a beam.

In Chapter 8, two upper bound plasticity approaches for calculating the shear strength of reinforced concrete beams in shear were used to calculate the shear capacity of the experimental beams. The first approach is based on the work of Zhang (1994) to calculate the shear strength of a rectangular section and the second approach comes from the work of Hoang (1997) to calculate the shear strength of a T-section beam and modified for I-sections. The tensile strength of the fibre-matrix was based on the Variable Engagement Model developed in this thesis. In calculating the shear strength, both the models provide reasonable correlation with the experimental results. It was concluded that the more simpler rectangular section model is the most appropriate for design practice. It was also recognised that further work is needed to verify the model for general application to RPC beams.

9.2 Further Studies

In Chapter 3, it was noted that the split cylinder test may not give a good indication of the tensile strength of fibre reinforced RPC. Further investigation is needed to study the effect of fibre crossing the cracking plane on controlling the splitting crack leading to a compression failure below the loading strip. The validity of the results as a function of fibre volume is also questioned and requires further study.

In Chapter 6, in the development of the Variable Engagement Model, the parameter α was introduced to define the point at which a fibre becomes effectively engaged in the matrix. That is, the point where the fibre carries load. The relationship for α obtained from single-fibre pullout tests in a pre-cracked matrix and that for multiple fibres crossing a cracking plane in a composite matrix requires further study. Investigations should focus on the type and size of fibres and on the concrete matrix properties (that is, strength, aggregate type and size, etc.). It was also taken that the bond-stress is constant over the length of the fibre. This assumption needs further investigation for different fibre types.

Further studies can be undertaken on extension of the VEM to describe mode II and mode III fracture. Sliding shear (mode II) may be a critical factor governing the strength of fibre-reinforced beams, in general, and RPC beams, in particular, for the transfer of longitudinal shear stresses in beams, or regions of beams, with high moment gradients; particularly where such regions are pre-cracked or damaged in the longitudinal direction.

REFERENCES

Adebar, P., Mindess, S., Pierre, D.S., and Olund, B., 1997. "Shear Tests of Fiber Concrete Beams without Stirrups", *ACI Structural Journal*, Vol. 94, No. 1, pp: 68-76.

Adeline, R., and Behloul, M., 1996. "High Ductile Beams without Passive Reinforcement", *4th International Symposium on Utilization of High Strength/High Performance Concrete*, Paris, Editors: F. de Larrard and R. Lacroix, Press de l'Ecole Naturale des Ponts et Chaussées, Vol. 3, pp: 1383-1390.

Adeline, R., Lachemi, M., and Blais, P., 1998. "Design of Behaviour of the Sherbrooke Bridge", *International Symposium on High-Performance and Reactive Powder Concretes*, 16-20 August, Sherbrooke, Quebec, Canada, pp: 89-98.

Al-Mahaidi, R.S.H., 1978. "Non-Linear Finite Element Analysis of Reinforced Concrete Deep Beam Members", *PhD Dissertation*, Cornel University, Ithaca, New York, May, 374 pp.

Ansari, F., 1987. "Stress-Strain Response of Microcracked Concrete in Direct Tension", *ACI Materials Journal*, Vol. 84, No. 6, November-December, pp: 481-490.

Archer, F.E., and Kitchen, E.M., 1956. "Stresses in Single Span Deep Beams", *Australian Journal of Applied Science*, Vol. 7, No. 4, pp: 314-326.

Armstrong, P.J., 2001. "Architectural Issues for Concrete Design and Construction", *CTBUH Review*, School of Architecture, University of Illinois, USA, Vol. 1, No. 3, 11 pp.

AS1012.9, 1986. "Determination of the Compressive Strength of Concrete Specimens", *Standards Australia*.

AS3972, 1997. "Portland and Blended Cements", *Standards Australia*.

ASCE-ACI Joint Task Committee 426, 1973. "Shear Strength of Reinforced Concrete Members", *Journal of Structural Engineering,* ASCE, Vol. 99, No. 6, pp: 1091-1187.

Ashour, A.F., 1997. "Tests of Reinforced Concrete Continuous Deep Beams", *ACI Structural Journal,* Vol. 94, No.1, Jan-Feb, pp: 3-12.

Ashour, S.A., Hasanain, G.S., and Wafa, F.F., 1992. "Shear Behavior of High-Strength Fiber Reinforced Concrete Beams", *ACI Structural Journal,* Vol. 89, No. 2, March-April, pp: 176-184.

ASTM C230, Standard Specification for Flow Table for use in Tests of Hydraulic Cement, *ASTM International.*

Attard, M.M., Nguyen, D.M., and Foster, S.J., 1996. "Finite Element Analysis of Out of Plane Buckling of Reinforced Concrete Walls", *International Journal of Computers & Structures,* Vol. 61, No. 6, pp: 1037-1042.

Aveston, J., and Kelly, A., 1973. "Theory of Multiple Fracture of Fibrous Composites", *Journal of Materials Science,* Vol. 8, pp: 352-362.

Aïtchin, P.C., 2000. "Cement of Yesterday and Today Concrete of Tomorrow", *Cement and Concrete Research,* Vol. 30, No. 9, Sept., pp: 1349-1359.

Balakrishnan, S., and Murray, D.W., 1988. "Prediction of Reinforced Concrete Panel and Deep Beam Behaviour by NLFEM", *Journal of Structural Engineering,* ASCE Vol. 114, No. 10, Oct, pp: 2323-2342.

Banthia, N., and Trottier, J.F., 1989a. "Effects of Curing Temperature and Early Freezing on Pull-Out Resistance of Steel Fibers from a Cementitious Matrix", *Cement and Concrete Research,* Vol. 19, No. 5, pp: 727-736.

Banthia, N., and Trottier, J.F., 1989b. "Effects of Curing Temperature and Early Freezing on Pull-Out Behaviour of Steel Fibres", *Cement and Concrete Research,* Vol. 19, No. 3, pp: 400-410.

Banthia, N., and Trottier, J.F., 1991. "Deformed Steel Fiber-Cementitious Matrix Bond Under Impact", *Cement and Concrete Research*, Vol. 21, No. 1, pp: 158-161.

Banthia, N., and Trottier, J.F., 1992. "Micromechanics of Steel Fiber Pullout, Rate Sensitivity at very Low Temperatures", *Cement and Concrete Composites*, Vol. 14, No. 2, pp: 119-130.

Banthia, N., and Trottier, J.F., 1994. "Concrete Reinforced with Deformed Steel Fibers, Part 1: Bond-Slip Mechanisms", *ACI Materials Journal*, Vol. 91, No. 5, Sept-Oct, pp: 435-446.

Barragán, B.E., Gettu, R., Martín, M.A., and Zerbino, R.L., 2003. "Uniaxial Tension Test for Steel Fibre Reinforced Concrete – A Parametric Study", *Cement and Concrete Composites*, Vol. 25, No. 7, pp: 767-777.

Barry, J.E., and Ainso, H., 1983. "Single-Span Deep Beams", *Journal of Structural Engineering*, ASCE, Vol. 109, No. 3, March, pp: 646-663.

Batson, G., Jenkins, E., and Spatney, R., 1972. "Steel Fibers as Shear Reinforcement in Beams", *ACI Journal,* Vol. 69, No. 10, October, pp: 640-644.

Batson, G.B., and Alguire, C., 1987. "Steel Fibers as Shear Reinforcement in Reinforced Concrete T-Beams", *Proceedings of the International Symposium on Fibre Reinforced Concrete,* Madras, India, December, pp: 1.113-1.123.

Bazant, Z.P., and Oh, B.H., 1983. "Crack band Theory for Fracture of Concrete", *Material and Structures*, RILEM, Vol. 16, No. 93, pp: 155-177.

Behloul, M., 1995. "Définition d'une Loi de Comportement du BPR", *Annales de l'ITBTP*, No. 532, pp: 122-127.

Behloul, M., 1996. "Analyse et Modelisation du Comportement d'un Materiau a Matrice Cimentaire Fibree A Ultra Hautes Performance (Bétons de Poudres Réactives)", *PhD Thesis*, Laboratoire de Mécanique et Technologie, Université Paris, Cachan, France, 180 pp.

Besser, I.I., and Cussens, A.R., 1984. "Reinforced Concrete Deep Beam Panels with High Depth over Span Ratios", *Proceedings of the Institution of Civil Engineers*, June, pp: 265-278.

Bonneau, O., Lachemi, M., Dallaire, E., Dugat, J., and Aïtchin, P.C., 1997. "Mechanical Properties and Durability of Two Industrial Reactive Powder Concretes", *ACI Journal of Material Division*, Vol. 94, No. 4, pp: 286-290.

Bonneau, O., Poulin, C., Dugat, J., Richard, P., and Aïtchin, P.C., 1996. "Reactive Powder Concretes: From Theory to Practice", *Concrete International*, Vol. 18, No. 4, pp: 47-49.

Bortolotti, L., 1988. "Double-Punch Test for Tensile and Compressive Strengths in Concrete", *ACI Materials Journal*, Vol. 85, No. 1, pp: 26-32.

Brandt, A.M., 1985. "On the Optimal Direction of Short Metal Fibres in Brittle Matrix Composites", *Journal of Materials Science*, Vol. 20, pp: 3831-3841.

Bresler, B., and Scordelis, A.C., 1963. "Shear Strength of Reinforced Concrete Beams", *ACI Journal, Proceedings*, Vol. 60, No.1, Jan, pp: 51-74.

Burakiewicz, A., 1978. "Testing of Fibre Bond Strength in Cement Matrix", *Testing and Test Methods of Fibre Cement Composites*, RILEM Symposium, The Construction Press, Lancaster, pp: 355-365.

Cavill, B., and Chirgwin, G., 2003. "The Worlds First RPC Road Bridge at Shepherds Gully Creek, NSW", *21st Biennial Conference of the Concrete Institute of Australia (CIA)*, July, pp: 89-98.

CEB-FIP, 1978. Comite Euro-International du Beton/Federation Internationale de la Precontrainte, Paris.

Chen, W.F., and Drucker, D.C., 1969. "Bearing Capacity of Concrete Blocks or Rock", *Journal of the Engineering Mechanics Division*, ASCE, Vol. 95, No. EM4, pp: 955-978.

Chen, W.F., and Yuan, R.L., 1980. "Tensile Strength of Concrete: Double-Punch Test", *Journal of the Structural Division*, ASCE, Vol. 106, No. 8, pp: 1673-1693.

Cheyrezy, M., 1999. "Structural Application of RPC", *Concrete*, London, Vol. 33, No.1, pp: 20-23.

Chow, L., Conway, H.D., and Winter, G., 1953. "Stresses in Deep Beams", *American Society of Civil Engineers*, Transactions, Vol. 118, pp: 686-708.

CIRIA, 1977. "CIRIA Guide 2: The Design of Deep Beams in Reinforced Concrete", *Ove Arup and Partners,* Construction Industry Research and Information Association, London.

Collins, M., and Mitchell, D., 1991. "Prestressed Concrete Structures", Prentice Hall, 1991, 766pp.

Darwin, D., and Pecknold, D.A., 1977. "Nonlinear Biaxial Stress-Strain Law for Concrete", *Journal of Engineering Mech.,* ASCE, Vol. 103, No. EM2, April, pp: 229-241.

de Pavia, H.A.R., and Siess, C.P., 1965. "Strength & Behaviour of Deep Beams in Shear", *ASCE Proceedings*, Vol. 65, No. 2, Feb, pp: 87-97.

Deem, S., 2002. "Concrete Attraction-Something New on the French Menu-Concrete", source at www.popularmechanics.com/science/research/2002/6/concrete/print.phtml.

Denarié, E., Habel, K., and Brühwiler, E., 2003. "Structural Behavior of Hybrid Elements with Advanced Cementitious Materials (HPFRCC)", *High Performance Fiber Reinforced Cement Composite (HPFRCC4)*, Ann Arbor, USA, pp: 301-312.

Easley, T.C., and Faber, K.T., 1999. "Use a Crack-Bridging Single-Fiber Pullout Test to Study Steel Fiber/Cementitious Matrix Composite", *Journal of American Ceramic Society*, Vol. 82, No. 12, pp: 3513-3520.

Foster, S.J., 1992a. "An Application of the Arc Length Method Involving Concrete Cracking", *International Journal for Numerical Methods in Engineering,* Vol. 33, No. 2, pp: 269-285.

Foster, S.J., 1992b. " The Structural Behaviour of Reinforced Concrete Deep Beams", *PhD Dissertation,* University of New South Wales, Kensington, Sydney, Australia, August.

Foster, S.J., 2001. "On the Behaviour of HSC Columns: Cover Spalling, Steel Fibres and Ductility", *ACI Structural Journal,* Vol. 98, No.4, July-August, pp: 583-589.

Foster, S.J., and Gilbert, R.I., 1990. "Non-Linear Finite Element Model for Reinforced Concrete Deep Beams", *UNICIV Report No. R-275,* School of Civil Engineering, UNSW, Kensington, Sydney, Australia, Dec, 110 pp.

Foster, S.J., and Marti, P., 2003. "Cracked Membrane Model: FE Implementation", *Journal of Structural Engineering,* ASCE, Vol. 129, No. 9, pp: 1155-1163.

Foster, S.J., and Rangan, B.V., 1999. "Finite Element Modelling of HSC Squat Walls in Shear", *Mechanics of Structures and Materials,* Proceedings of the 16th Australasian Conference on the Mechanics of Structure and Materials, Sydney, Australia, 8 – 10 December, pp: 115-120.

Foster, S.J., Budiono, B., and Gilbert, R.I., 1996. "Rotating Crack Finite Element Model for Reinforced Concrete Structures", *Computers and Structures,* Vol. 58, No. 1, pp: 43-50.

Furlan Jr. S., and Hanai, J.B., 1997. "Shear Behaviour of Fiber Reinforced Concrete Beams", *Cement and Concrete Composites,* Vol. 19, No. 4, pp: 359-366.

Ganeshalingam, R., Paramasivan, P., and Nathan, G.K., 1981. "An Evaluation of Theories and a Design Method of Fibre Cement Composites", *The International Journal of Cement Composites and Lightweight Concrete,* Vol. 3, No. 2, pp: 103-114.

Geer, E., 1960. "Stresses in Deep Beam", *Journal of the American Concrete Institute*, Vol. 31, No. 7, pp: 651-661.

Gilbert, R.I., Gowripalan, N., and Cavill, B., 2000. "On the Design of Precast, Prestressed Reactive Powder Concrete (Ductal) Girders", *Proceedings of 4th Austroads Bridge Engineering Conference,* Adelaide, Australia, Nov 30 - Dec 1, Vol. 3, pp: 313-324.

Gilles, C., 1999. "Modelling the Pullout of Wire-Drawn Steel Fibers", *Cement and Concrete Research*, Vol. 29, pp: 1027-1037.

Gokoz, U.N., and Naaman, A.E., 1981. "Effect of Strain-Rate on the Behaviour of Fibres in Mortar", *International Journal of Cement Composites*, Vol. 3, No. 3, August, pp: 187-202.

Gopalaratnam, V.S., and Abu-Mathkour, H.J., 1987. "Investigation of the Pull-Out Characteristics of Steel Fibers from Mortar Matrices", *Proceedings*, *International Symposium on Fiber Reinforced Concrete*, Madras, India, pp: 201-211.

Gopalaratnam, V.S., and Shah, S.P., 1987a. "Tensile Failure of Steel Fiber-Reinforced Mortar", *Journal of Engineering Mechanics.*, ASCE, Vol. 113, No. 5, pp: 635-652.

Gopalaratnam, V.S., and Shah, S.P., 1987b. "Softening Response of Plain Concrete in Direct Tension", *ACI Journal*, Vol. 82, No. 3, May-June, pp: 310-323.

Gowripalan, N., Dumitru, I., Smorchevsky, G., Marks, R., and D'Souza, B., 2000. "Development of Modified RPC for Precast Concrete Applications in Australia", *Proceedings of the 19th Biennial Conference of the Concrete Institute of Australia*, Sydney, Australia, 5-7 May, pp: 105-112.

Gray, R.J., 1984a. "Analysis of Effect of Embedded Fibre Length on Fibre Debonding and Pull-Out from an Elastic Matrix; Part 1, Review of Theories", *Journal of Materials Science*, Vol. 19, No. 3, pp: 861-870.

Gray, R.J., 1984b. "Analysis of Effect of Embedded Fibre Length on Fibre Debonding and Pull-Out from an Elastic Matrix; Part 2, Application to Steel Fibre-Cementitious Matrix Composite System", *Journal of Materials Science*, Vol. 19, No. 5, pp: 1680-1691.

Gray, R.J., and Johnston, C.D., 1984. "Effect of Matrix Composition of Fiber/Matrix Interfacial Bond Shear Strength in Fiber Reinforced Mortar", *Cement and Concrete Research*, Vol. 14, No. 2, pp: 285-296.

Groth, P., 2000. "Fibre Reinforced Concrete – Fracture Mechanics Methods Applied on Self-Compacting Concrete and Energetically Modified Binders", *Doctoral Thesis*, Department of Civil and Mining Engineering, Division of Structural Engineering, Luleå University of Technology, Sweden, 237 pp.

Guerrero, P., and Naaman, A.E., 2000. "Effect of Mortar Fineness and Adhesive Agents on Pullout Response of Steel Fibers", *ACI Material Journal*, Vol. 97, No. 1, January-February, pp: 12-20.

Hoang, L.C., 1997. "Shear Strengths of Non-Shear Reinforced Concrete Elements, Part 2 – T-Beams", *Report R No. 29,* Technical University of Denmark, Department of Structural Engineering and Materials, Lyngby, 35 pp.

Hughes, B.P., and Fattuhi, N.I., 1975. "Fiber Bond Strength in Cement and Concrete", *Magazine of Concrete Research*, Vol. 27, No. 92, pp: 161-166.

Imam, M., Vandewalle, L., and Mortelmans, F., 1994. "Shear Capacity of Steel Fiber High Strength Concrete Beams", *High-Performance Concrete,* SP-149, American Concrete Institute, Detroit, pp: 227-241.

Jimenez, R., 1977. "A Model Analysis of Shear Panels with Low Height to Length", *MSc Thesis*, Cornell University, Ithaca, New York, May.

Jindal, R.L., 1984. "Shear and Moment Capacities of Steel Fiber Reinforced Concrete Beams", *Fiber Reinforced Concrete,* SP-81, American Concrete Institute, Detroit, pp: 1-16.

Johansen, K.W., 1958. "Brudbetingelse for sten og beton (Failure Criteria for Rock and Concrete)", *Bygningsstatiske Meddelelser*, Vol. 29, No.2, pp: 25-44.

Kanda, T., and Li, V.C., 1998. "Interface Property and Apparent Strength of High Strength Hydrophilic Fiber in Cement Matrix", *Journal of Materials in Civil Engineering*, Vol. 10, No. 1, February, pp: 5-13.

Kaushik, S.K., Gupta, V.K., and Tarafdar, N.K., 1987. "Behaviour of Fiber Reinforced Concrete Beams in Shear", *Proceedings of the International Symposium on Fibre Reinforced Concrete,* Madras, India, December, pp: 1.133-1.149.

Kong, F.K., 1990. *Reinforced Concrete Deep Beams*, Blakie, London, 288 pp.

Kong, F.K., and Robbins, P.J., 1971. "Web Reinforcement Effects on Lightweight Concrete Deep Beams", *ACI Journal*, Vol. 68, No. 7, July, pp: 514-520.

Kong, F.K., and Sharp, G.R., 1973. "Shear Strength of Lightweight Reinforced Concrete Deep Beams with Web Openings", Proceeding of the Institution of Structural Engineers, UK, *The Structural Engineer*, Vol. 51, No.8, pp: 267-275.

Kong, F.K., and Sharp, G.R., 1977. "Structural Idealisation for Deep Beams with Web Openings", *Magazine of Concrete Research*, Vol. 29, No.99, pp: 81-91.

Kong, F.K., and Singh, A., 1972. "Diagonal Cracking and Ultimate Loads of Lightweight Concrete Deep Beams", *ACI Journal Proceedings*, Title No. 69-47, pp: 513-521.

Kong, F.K., Robbins, P.J., and Cole, D.F., 1970. "Web Reinforcement Effects on Deep Beams", *ACI Journal Proceedings*, Vol. 67, No. 12, Dec, pp: 1010-1017.

Kong, F.K., Robbins, P.J., and Sharp, G.R., 1975. "Design of Reinforced Concrete Deep Beams in Current Practice", *The Structural Engineer*, Vol. 53, No. 4, pp: 173-180.

Kong, F.K., Robbins, P.J., and Short, D.R., 1972. "Deep Beams with Inclined Web Reinforcement", *ACI Journal Proceedings*, Title No. 69-16, pp: 172-176.

Kong, F.K., Robbins, P.J., Singh, A., and Sharp, G.R., 1972."Shear Analysis and Design of Reinforced Concrete Deep Beams", *The Structural Engineer*, Vol. 50, No.10, pp: 405-409.

Kong, F.K., Sharp, G.R., Beaumont, C.J., and Kubik, L.A., 1978. "Structural Idealization for Deep Beams with Web Openings: Further Evidence", *Magazine of Concrete Research*, Vol. 30, No. 103, pp: 89-95.

Kotsovos, M.D., 1988a. "Compressive Force Path Concept: Basis for Reinforced Concrete Ultimate Limit State Design", *ACI Structural Journal*, Vol. 85, No. 1, Jan-Feb, pp: 68-75.

Kotsovos, M.D., 1988b. "Design of Reinforced Concrete Deep Beams", *The Structural Engineer*, Vol. 66, No, 2, Jan., pp: 28-32.

Kupfer, H.B., Gerstle, K.H., 1973. "Behaviour of Concrete under Biaxial Stresses", *Journal of the Engineering Mechanics Division*, Vol. 99, No. EM4, pp: 853-866.

Kützing, L., and Meister, M., 1998. "Some Aspects of the Shear Capacity of Steel Fibre Reinforced Concrete (SFRC) Beams", *Lacer*, No. 3, Leipzig, pp: 153-163.

Lachemi, M., Bastien, J., Adeline, R., Ballivy, G., and Aïtchin, P.C., 1998. "Monitoring of the World's First Reactive Powder Concrete Bridge", *5th International Conference on Short and Medium Span Bridges*, Calgary, Alberta, Canada, July, 10 pp.

LaFraugh, R.W., and Moustafa, S.E., 1975. "Experimental Investigation of the use of Steel Fibers for Shear Reinforcement", *Concrete Technology Association*, Tacoma, January, 53 pp.

Leonhardt, F., and Walther, R., 1966. "Wandartige Trager", Bulletin No. 178, Whihelm Ernst & Sohn, Berlin, 159 pp.

Li, Q., and Ansari, F., 2000. "High-Strength Concrete in Uniaxial Tension", *ACI Materials Journal*, Vol. 97, No. 1, January-February, pp: 49-57.

Li, V.C., 1992. "Postcracking Scaling Relations for Fibre Reinforced Cementitious Composites", *Journal of Materials in Civil Engineering*, ASCE, Vol. 4, No. 1, pp: 41-57.

Li, V.C., and Wu, H.C., 1992. "Conditions for Preudo Strain-Hardening in Fiber Reinforced Brittle Matrix Composites", *Micromechanical Modelling of Quasi-Brittle Materials Behavior*, Li, C. V., Ed., Appl. Mech. Rev., Vol., 46, No. 3, August, pp: 390-398.

Li, V.C., Ward, R., and Hamza, A.M., 1992. "Steel and Synthetic Fibers as Shear Reinforcement", *ACI Materials Journal,* Vol. 89, No. 5, September-October, pp: 499-508.

Li, Z., Li F., Chang, T.Y.P., and Mai, Y.W., 1998. "Uniaxial Tensile Behavior of Concrete Reinforced with Randomly Distributed Short Fibers", *ACI Materials Journals*, Vol. 15, No. 5, Sep-Oct, pp: 564-574.

Lim, T.Y., Paramasivam, P., and Lee, S.L., 1987a. "Shear and Moment Capacity of Reinforced Steel-Fiber-Concrete Beams", *Magazine of Concrete Research,* Vol. 39, No. 140, September, pp: 148-160.

Lim, T.Y., Paramasivam, P., and Lee, S.L., 1987b. "Analytical Model for Tensile Behavior of Steel-Fiber Concrete", *ACI Materials Journals*, July-Aug, pp: 286-298.

Liu, C.Y., Nilson, A.H., and Slate, F.O., 1972. "Biaxial Stress-Strain Relationship for Concrete", *Journal of the Structural Division*, ASCE, Vol. 98, No. St5, May, pp: 1025-1034.

Maage, M., 1977. "Interaction Between Steel Fibers and Cement Based Matrices", *Materials and Structures*, Research and Testing (RILEM, Paris), Vol. 10, No. 59, pp: 297-301.

Maage, M., 1978. "Fibre Bond and Friction in Cement and Concrete", *Testing and Test Methods of Fibre Cement Composites*, RILEM Symposium, Construction Press, Lanchester, pp: 329-336.

Maalej, M., Li., C.V., and Hashida, T., 1995. "Effect of Fiber Rupture on Tensile Properties of Short Fiber Composites", *Journal of Engineering Mechanics*, ASCE, Vol. 121, No. 8, August, pp: 903-913.

Mandel, J.A., Wei, S., and Said, S., 1987. "Studies of the Properties of the Fiber Matrix Interface in Steel Fiber Reinforced Mortar", *ACI Material Journal*, March-April, pp: 101-109.

Mansur, M.A., and Alwis, W.A.M., 1984. "Reinforced Fibre Concrete Deep Beams with Web Openings", *The International Journal of Cement Composites and Lightweight Concrete*, Vol. 6, No. 4, November, pp: 263-271.

Mansur, M.A., and Ong, K.C., 1991. "Behavior of Reinforced Fiber Concrete Deep Beams in Shear", *ACI Structural Journal*, Vol. 88, No. 1, Jan-Feb, pp: 98-105.

Mansur, M.A., Ong, K.C., and Paramasivam, P., 1986. "Shear Strength of Fibrous Concrete Beams without Stirrups", *Journal of Structural Engineering,* ACSE, Vol. 112, No. 9, September, pp: 2066-2079.

Manuel, R.F., Slight, B.W., and Suter, G.T., 1971. "Deep Beam Behavior Affected by Length and Shear Span Variations", *ACI Journal*, Vol. 68, No. 12, pp: 954-958.

Marti, P., 1978. "Plastic Analysis of Reinforced Concrete Shear Wall", *Bericht Nr. 37*, Institut fur Baustatik und Konstruktion, Zurich, Nov.

Marti, P., 1989. "Size Effect in Double-Punch Tests on Concrete Cylinders", *ACI Materials Journal,* 86-M58, pp: 597-601.

Marti, P., Pfyl, T., Sigrit, Viktor, and Ulaga, T., 1999. "Harmonized Test Procedure for Steel Fibre-Reinforced Concrete", *ACI Materials Journal*, Vol. 96, No. 6, Nov-Dec, pp: 676-685.

Matte, V., and Moranville, M., 1999. "Durability of Reactive Powder Concrete: Influence of Silica Fume on the Leaching Properties of very Low Water/Binder Pastes", *Cement and Concrete Composite*, Vol. 21, No. 1, pp: 1-9.

Mau, S.T., and Hsu, T.T.C, 1987. "Shear Strength Prediction for Deep Beams with Web Reinforcement", *ACI Journal*, Vol. 84, No. 6, pp: 513-523.

Mau, S.T., and Hsu, T.T.C., 1989. "Formula for the Shear Strength of Deep Beams", *ACI Structural Journal*, Vol. 86, No. 5, Sept, pp: 516-523.

Morton, J., and Groves, G.W., 1974. "The Cracking of Composites Consisting of Discontinuous Ductile Fibres in a Brittle Matrix-Effect of Fibre Orientation", *Journal of Materials Science*, Vol. 9, pp: 1436-1445.

Mueller, P., 1979. "Plastic Analysis of Torsion and Shear in Reinforced Concrete", Colloquim on Plasticity in Reinforced Concrete, *IABSE Reports of the Working Commissions*, Vol. 29, Copenhagen.

Muhidin, N.A., and Regan, P.E., 1977. "Chopped Steel Fibres as Shear Reinforcement in Concrete Beams", *Fibre Reinforced Materials*, Institution of Civil Engineers, London, pp: 149-163.

Murty, D.S.R., and Venkatacharyulu, T., 1987. "Fibre Reinforced Concrete Beams Subjected to Shear Force", *Proceedings of the International Symposium on Fibre Reinforced Concrete,* Madras, India, December, pp: 1.125-1.132.

Naaman, A.E., and Shah, S.P., 1976. "Pull-Out Mechanism in Steel Fiber-Reinforced Concrete", *Journal of the Structural Division*, Proceedings of ASCE, Vol. 102, No. ST8, August, pp: 1537-1548.

Naaman, A.E., Argon, A.S., and Moavenzadeh, F., 1973. "Fracture Model for Fibre Reinforced Cementitious Materials", *Cement and Concrete Research*, Vol. 3, No. 4, July, pp: 397-411.

Naaman, A.E., Namur, G., Alwan, J., and Najm, H.S., 1991a. "Fiber Pullout and Bond Slip I: Analytical Study", *Journal of Structural Engineer*ing, ASCE, Vol. 117, No. 9, September, pp: 2769-2790.

Naaman, A.E., Namur, G., Najm, H.S., and Alwan, J., 1989. "Bond Mechanisms in Fiber Reinforced Cement-Based Composites", *Report No. UMCE-89-9*, University of Michigan, August, 253 pp.

Namur, G.G., and Naaman, A.E., 1989. "A Bond Stress Model for Fiber Reinforced Concrete Based on Bond Stress Slip Relationship", *ACI Materials Journal*, Vol. 86, No. 1, pp: 45-57.

Namur, G.G., Naaman, A.E., and Clark, S.K., 1987. "Analytical Prediction of Pullout Behaviour of Steel Fibers in Cementitious Matrices", *Symposium Proceedings*, Materials Research Society, 114, pp: 217-224.

Narayanan, R., and Darwish, I.Y.S., 1987. "Use of Steel Fibers as Shear Reinforcement", *ACI Structural Journal,* Vol. 84, No. 3, May – June, pp: 216-227.

Narayanan, R., and Darwish, I.Y.S., 1988. "Fiber Concrete Deep Beams in Shear", *ACI Structural Journal,* Vol. 85, No. 2, March – April, pp: 141-149.

Nielsen, M.P., 1963. "Yield Condition for Reinforced Concrete Shells in the Membrane State", Non-Classical Shell Problems (ed. Olszak and Sawczuk), *Proc. IASS Symposium*, Warsaw, Amsterdam, pp: 1030-1040.

Nielsen, M.P., 1967. "Om forskydningsarmering i jernbetonbjælker- On Shear Reinforcement in Reinforced Concrete Beams", *Bygninsstatiske Meddelelser*, Vol. 38, No. 2, November, pp: 33-58.

Nielsen, M.P., Braestrup, M.W., Jensen, B.C., and Bach, F., 1978. "Concrete Plasticity, Beam Shear-Shear in Joints, Punching Shear", *Special Publication of the Danish Society for Structural Science and Engineering*, Technical University of Denmark, Lyngby, Copenhagen, 129 pp.

Noghabai, K., 2000. "Beams of Fibrous Concrete in Shear and Bending: Experiment and Model", *Journal of Structural Engineering*, Vol. 126, No. 2, pp: 243-251.

Orange, G., Acker, P., and Vernet, C., 1999. "A New Generation of UHP Concrete: Ductal Damage Resistance and Micromechanical Analysis", *Third International Workshop on High Performance Fiber Reinforced Cement Composites (HPFRCC3)*, Rilem Publications, Mainz, Germany, May 16-19, pp: 101-111.

Pakotiprapha, B., 1976. "A Study of Bamboo Pulp and Fibre Cement Paste Composite", *PhD. Engineering Dissertation*, Asian Institute of Technology, Bangkok.

Pakotiprapha, B., Pama, R.P., and Lee, S.L., 1974. "Mechanical Properties of Cement Mortar with Randomly Oriented Short Steel Wires", *Magazine of Concrete Research*, Vol. 26, No. 86, March, pp: 3-15.

Parimi, S.R., and Sridhar, Rao, J.K., 1973. "Fracture Toughness of Fibre Concrete", *International Symposium of Fiber Reinforced Concrete, ACI*, Publication No. SP-44, Oct, pp: 80-92.

Petersson, P.E., 1980. "Fracture Mechanical Calculations and Tests for Fibre-Reinforced Cementitious Materials", *Proceedings from Advances in Cement Matrix Composites*, Mat. Res. Soc., Annual Meeting, Boston, pp: 95-106.

Petersson, P.E., 1981. "Crack Growth and Development of Fracture Zones in Plain Concrete and Similar Materials", *Report TVBM-1006*, University of Lund, 174 pp.

Pinchin, D.J., and Tabor, D., 1978. "Interfacial Contact Pressure and Frictional Stress Transfer in Steel Fiber", *Proceeding, RILEM Symposium on Testing and Test Methods of Fibre Cement Composites*, Swamy, R.N., ed., The Construction Press, pp: 337-334.

Ramakrishnan,V., and Ananthanarayana, Y., 1968. "Ultimate Strength of Deep Beams in Shear", *ACI Journal Proceedings*, Vol. 65, No. 2, Feb, pp: 87-97.

Richard, P., 1996. "Reactive Powder Concrete: A New Ultra-High-Strength Cementitious Material", *4th International Symposium on Utilization of High Strength/High Performance Concrete*, Paris, Editors: F. de Larrard and R. Lacroix, Press de l'Ecole Naturale des Ponts et Chaussées, Vol. 3, pp: 1343-1349.

Richard, P., and Cheyrezy, M., 1995. "Composition of Reactive Powder Concretes", *Cement and Concrete Research*, Vol. 25, No. 7, pp: 1501-1511.

Richard, P., and Cheyrezy, M.H., 1994. "Reactive Powder Concretes with High Ductility and 200-800 MPa Compressive Strength", *ACI*, SP-144(24), San Francisco, CA, pp: 507-518.

Ricketts, D.R. and Macgregor, 1985. "Ultimate Behaviour of Continuous Deep Reinforced Concrete Beams", *Structural Engineering Report No. 126*, Dept. of Civil Engineering, University of Alberta, Edmonton, Canada, January.

Roberts, T.M., and Ho, N.L., 1982. "Shear Failure of Deep Fiber Reinforced Concrete Beams", *International Journal of Cement Composites and Lightweight Concrete* (Harlow), Vol. 4, No. 3, August, pp: 145-152.

Rogowsky, D.M, and MacGregor, J.G., 1983. "Shear Strength of Deep Reinforced Concrete Continuous Beams", *Structural Engineering Report No. 110*, Dept of Civil Engineering, University of Alberta, Edmonton, Canada, Nov.

Rogowsky, D.M., MacGregor, J.G., and Ong, S.Y., 1986. "Tests of Reinforced Concrete Beams", *ACI Journal Proceedings*, Title no. 83-55, July-August, pp: 614-623.

Romualdi, J.P., and Batson, G.B., 1963. "Behaviour of Reinforced Concrete Beams with Closely Spaced Reinforcement", *Journal of the American Concrete Institute*, Proceedings, Vol. 60, No. 6, June, pp: 775-789.

Romualdi, J.P., and Mandel, J.A., 1964. "Tensile Strength of Concrete Affected by Uniformly Distributed and Closely Spaced Short Length Wire Reinforcement", *Journal, American Concrete Institute Proc.*, Vol. 61, No. 6, June, pp: 657-671.

Romualdi, J.P., Ramey, M., and Sanday, S.C., 1968. "Prevention and Control of Cracking by use of Cracking in Concrete", Detroit, *ACI*, Publication SP-20, pp: 179-203.

Roux, N., Andrade, C., and Sanjuan, M.A., 1996. "Experimental Study of Durability of Reactive Powder Concretes", *Journal of Materials in Civil Engineering*, Vol. 8, No. 1, February, pp: 1-6.

Sandbye, P., 1965. "A Plastic Theory for Plain Concrete", *Bygningsstatiske Meddelelser*, Vol. 36, No.2, pp: 41-62.

Schueller, W., 1990. "The Vertical Building Structure", *New York: Van Nostrand Reinhold*, New York, 658 pp.

Selvam, V.K.M., and Natarajan, S., 1985. "Shear Strength of Continuous Deep Beams", *Indian Concrete Journal*, November, pp: 305-308.

Shaeffer, R.E., 1992. "Reinforced Concrete: Preliminary Design for Architects and Builders", *McGraw-Hill*, 196 pp.

Shah, S.P., and Rangan, B.V., 1971. "Fiber Reinforced Concrete Properties", *Journal of American Concrete Institute,* Proceedings, Vol. 68, No. 2, February, pp: 126-135.

Sharma, A.K., 1986. "Shear Strength of Steel Fiber Reinforced Concrete Beams", *ACI Journal Proceedings,* Vol. 83, No. 4, July – August, pp: 624-628.

Shin, S.W., Lee, K.S., Moon, J., and Ghosh, S.K., 1999. "Shear Strength of Reinforced High Strength Concrete Beams with Shear Span-to-Depth Ratios between 1.5 and 2.5", *ACI Structural Journal*, Vol. 96, No.4, July-Aug, pp: 549-556.

Shin, S.W., Oh, J., and Ghosh, S.K., 1994. "Shear Behavior of Laboratory-Sized High-Strength Concrete Beams Reinforced with Bars and Steel Fibers", *Fiber Reinforced Concrete Developments and Innovations,* SP-142, American Concrete Institute, Farmington Hills, pp: 181-200.

Singh, R., Ray, S.P., and Reddy, C.S., 1980. "Some Tests on Reinforced Concrete Deep Beams with and without Openings in the Web", *Indian Concrete Journal*, July, pp: 189-194.

Skempton, A.W., 1982. "John Smeaton, FRS", *American Society of Civil Engineering,* December, 291 pp.

Smith, K.N., and Vantsiotis, A.S., 1982. "Shear Strength of Deep Beams", *ACI Journal*, Vol. 79, No. 3, May-June, pp: 201-213.

Soroushian, P., and Bayasi, Z., 1991. "Fiber-Type Effects on the Performance of Steel Fiber Reinforced Concrete", *ACI Materials Journal*, Vol. 88, No. 2, March-April, pp: 129-145.

Subedi, N.K., Vardy, A.E., and Kubota, N., 1986. "Reinforced Concrete Deep Beams – Some Test Results", *Magazine of Concrete Research*, Vol. 38, No. 137, December, pp: 206-219.

Swamy, R.N., and Bahia, H.M., 1985. "The Effectiveness of Steel Fibers as Shear Reinforcement", *Concrete International,* Vol. 7, No. 3, March, pp: 35-40.

Swamy, R.N., Jones, R., and Chiam, A.T.P., 1993. "Influence of Steel Fibers on the Shear Resistance of Lightweight Concrete I-Beams", *ACI Structural Journal,* Vol. 90, No. 1, January-February, pp: 103-114.

Tan, K.H., and Mansur, M.A., 1982. "Partial Prestressing in Concrete Corbel and Deep Beams", *ACI Structural Journal*, Vol. 89, No. 3, pp: 251-262.

Tan, K.H., and Tong, K., 1999. "Shear Behaviour and Analysis of Partially Prestressed I-Girders, *Structural Engineer, The (United Kingdom),* Vol. 77, No. 23 & 24, pp: 28-34.

Tan, K.H., Kong, F.K., Teng, S., and Guan, L.W., 1995. "High Strength Concrete Deep Beams with Effective Span and Shear Span Variations", *ACI Journal, Proceedings*, Vol. 92, No. 4, July-Aug, pp: 395-405.

Tan, K.H., Lu, H.Y., and Teng, S., 1999. "Size Effect in Large Prestressed Concrete Deep Beams", *ACI Structural Journal*, Vol. 96, No. 6, Nov-Dec, pp: 937-946.

Tan, K.H., Murugappan, K., and Paramasivam, P., 1993. "Shear Behaviour of Steel Fiber Reinforced Concrete Beams", *ACI Structural Journal*, Vol. 89, No. 6, pp: 3-11.

Tasuji, M.E., Nilson, A.H., and Slate, F.O., 1976. "The Behaviour of Plain Concrete Subject to Biaxial Stress", *Report No. 360*, Dept. of Structural Engineering, Cornell University, Ithaca, New York, March.

Teng, S., Kong, F.K., and Poh, S.P., 1998a. "Shear Strength of Reinforced and Prestressed Concrete Deep Beams (Part I: Current Design Methods and a Proposed Equation)", *Proceedings of Institution of Civil Engineering, Structural and Buildings*, Vol. 128, No. 2, pp: 112-123.

Teng, S., Kong, F.K., and Poh, S.P., 1998b. "Shear Strength of Reinforced and Prestressed Concrete Deep Beams (Part II: The Supporting Evidence)", *Proceedings of Institution of Civil Engineering, Structural and Buildings*, Vol. 128, No. 2, pp: 124-143.

Thorenfeldt, E., Tomaszewicz, A., and Jensen, J.J., 1987. "Mechanical Properties of High Strength Concrete and Application in Design", *International Symposium on Utilization of High Strength Concrete*, Stavanger, Norway, June, pp: 149-159.

Timoshenko, S., 1941. *Strength of Materials*, MacMillan, London, U.K.

Torrenti, J.M., Matte, V., Maret, V., and Richet, C., 1996. "High Integrity Containers for Interim Storage of Nuclear Wastes using Reactive Powder Concrete", *4th International Symposium on Utilization of High Strength/High Performance Concrete*, Paris, Editors: F. de Larrard and R. Lacroix, Press de l'Ecole Naturale des Ponts et Chaussées, Vol. 3, pp: 1407-1413.

Toutlemonde, F., Sercombe, J., Torrenti, J.M., and Adeline, R., 1999. "Développement d'un Counteneur Pour L'entreposage de Déchets Nucléaires: Résistance au Choc", *Revue Française de Génie Civil*, Vol. 3, No. 7, pp: 729-756.

Uhlmann, H.L., 1952. "The Theory of Girder Walls with Special Reference to Reinforced Concrete Design", *The Structural Engineer*, No.8, London, England, Aug., pp: 172-181.

Vecchio, F.J., 1989." Nonlinear Finite Element Analysis of Reinforced Concrete Membranes", *ACI Structural Journal*, Vol. 86, No. 1, pp: 26-35.

Vecchio, F.J., and Collins, M.P., 1982. "The Response of Reinforced Concrete to In-Plain Shear and Normal Stresses", *Research Report*, Publication No. 82-03, Dept. of Civil Engineering, University of Toronto, 332 pp.

Vecchio, F.J., and Collins, M.P., 1986. "The Modified Compression Field Theory for Reinforced Concrete Elements Subjected to Shear", *ACI Journal*, Vol. 83, No. 2, March-April, pp: 219-231.

Visalvanich, K., and Naaman, A.E., 1983. "Fracture Model for Fibre Reinforced Concrete", *ACI Journal Proceedings*, Vol. 80, No. 2, pp: 128-138.

Wang, Y., 1989. "Mechanics of Fiber Reinforced Cementitious Composites", *PhD Thesis*, Department of Mechanical Engineering, Massachusetts Institute of Technology, Cambridge, USA, 306 pp.

Wang, Y., Li, C.V., and Backer, S., 1990a. "Tensile Properties of Synthetic Fiber Reinforced Mortar", *Cement and Concrete Composites*, Vol. 12, pp: 29-40.

Wang, Y., Li, C.V., and Backer, S., 1990b. "Experimental Determination of Tensile Behavior of Fiber Reinforced Concrete", *ACI Materials Journals*, Vol. 87, No. 5, Sep-Oct, pp: 461-468.

Williamson, G.R., and Knab, L.I., 1975. "Full-Scale Fiber Concrete Beam Tests", *Proceedings,* RILEM Symposium on Fiber Reinforced Cement Concrete, London, Construction Press, Lancaster, pp: 209-214.

Zanni, H., Cheyrezy, M., Maret, V., Philippot, S., and Nieto, P., 1996. "Investigation of Hydration and Pozzolanic Reaction in Reactive Powder Concrete (RPC) using ^{29}Si NMR", *Cement and Concrete Research,* Vol. 26, No. 1, pp: 93-100.

Zhang, J.P., 1994. "Strength of Cracked Concrete: Part 1 – Shear Strength of Conventional Reinforced Concrete Beams, Deep Beams, Corbels, and Prestressed Reinforced Concrete Beams without Shear Reinforcement", *Report No. 311*, Technical University of Denmark, Department of Structural Engineering, Lyngby, 106 pp.

APPENDIX A – RAW DATA FOR CONTROL SPECIMEN STRENGTH TESTS

Table A1 – Cylinder compressive strength of RPC on mixes 1 to 10 (in MPa).

Control Sample No.	Mix Design No.									
	1	2	3	4	5	6	7	8	9	10
1	156	145	126	180	160	143	188	172	165	161
2	156	140	128	172	163	145	182	185	167	163
3	157	156	135	164	157	139	186	179	165	166
4	164	148	133	171	159	131	175	171	160	157
5	165	145	145	150	170	130	180	176	162	158
6	167	151	133	169	150	142	177	171	157	160
7	-	-	-	-	150	133	-	-	-	-
8	-	-	-	-	140	136	-	-	-	-
9	-	-	-	-	154	137	-	-	-	-
10	-	-	-	-	153	-	-	-	-	-
11	-	-	-	-	156	-	-	-	-	-
Average	161	148	133	168	156	137	181	176	163	161
Std. Dev.	5.0	5.5	6.6	10.1	7.8	5.3	5.0	5.6	3.7	3.3

Table A2 – Cylinder compressive strength of RPC on mixes 11 to 19 (in MPa).

Control Sample No.	Mix Design No.								
	11	12	13	14	15	16	17	18	19
1	137	180	186	164	167	155	149	178	169
2	141	185	180	156	162	156	159	169	176
3	138	183	187	160	162	143	159	166	167
4	149	186	173	149	161	160	162	178	168
5	155	192	165	154	160	151	150	177	167
6	140	185	170	150	136	165	161	170	169
7	151	-	-	155	161	-	-	-	-
8	151	-	-	176	160	-	-	-	-
9	144	-	-	164	156	-	-	-	-
10	144	-	-	164	143	-	-	-	-
11	142	-	-	175	140	-	-	-	-
12	142	-	-	162	162	-	-	-	-
13	147	-	-	166	-	-	-	-	-
14	143	-	-	150	-	-	-	-	-
Average	145	185	177	160	156	155	157	173	169
Std. Dev.	5.3	4.0	8.9	8.6	10.2	7.6	5.7	5.3	5.6

Table A3 – Cube 70 mm compressive strength of RPC on mixes 1 to 10 (in MPa).

Control Sample No.	Mix Design No.									
	1	2	3	4	5	6	7	8	9	10
1	-	-	-	194	192	167	214	180	180	177
2	-	-	-	200	189	177	219	178	176	184
3	-	-	-	193	177	164	209	175	175	183
4	-	-	-	196	178	167	205	186	176	179
5	-	-	-	182	170	178	213	189	178	186
6	-	-	-	199	176	164	228	180	184	174
7	-	-	-	179	189	163	216	-	165	175
8	-	-	-	192	178	159	207	-	169	172
9	-	-	-	196	185	-	-	-	178	174
10	-	-	-	202	168	-	-	-	176	176
11	-	-	-	205	181	-	-	-	175	178
12	-	-	-	-	178	-	-	-	178	181
Average	-	-	-	194	180	167	214	181	176	178
Std. Dev.	-	-	-	7.9	7.5	6.8	7.3	5.0	4.9	4.4

Table A4 – Cube 70 mm compressive strength of RPC on mixes 11 to 19 (in MPa).

Control Sample No.	Mix Design No.								
	11	12	13	14	15	16	17	18	19
1	170	207	200	180	-	-	167	192	169
2	175	213	197	187	-	-	171	182	176
3	165	220	196	190	-	-	162	189	167
4	167	214	213	175	-	-	163	185	169
5	162	210	199	185	-	-	167	194	189
6	171	217	206	189	-	-	159	198	190
7	164	-	-	-	-	-	168	185	192
8	167	-	-	-	-	-	175	191	197
9	156	-	-	-	-	-	171	186	189
10	158	-	-	-	-	-	174	187	196
11	168	-	-	-	-	-	178	187	200
12	165	-	-	-	-	-	164	162	185
Average	166	214	202	184	-	-	168	187	185
Std. Dev.	5.33	4.7	6.5	5.8	-	-	5.7	8.9	11.7

Table A5 – Split cylinder tensile strength of RPC on mixes 1 to 10 (in MPa).

Control Sample No.	Mix Design No.									
	1	2	3	4	5	6	7	8	9	10
1	8.0	8.3	7.4	18.4	18.8	19.4	26.9	22.0	18.8	21.4
2	6.7	7.5	6.8	19.9	19.1	17.0	22.6	28.6	22.7	20
3	8.9	6.7	7.7	22.4	18.6	19.7	23.6	20.6	17.3	21.9
4	-	-	-	-	19.4	12.7	-	-	19.1	20.7
5	-	-	-	-	17.2	12.7	-	-	17.2	20.8
6	-	-	-	-	19.4	11.1	-	-	20.1	20.5
7	-	-	-	-	18.4	13.7	-	-	-	-
8	-	-	-	-	16.7	-	-	-	-	-
9	-	-	-	-	16.9	-	-	-	-	-
Average	7.9	7.5	7.3	20.2	18.3	15.2	24.4	23.7	19.2	20.9
Std. Dev.	1.1	0.8	0.5	2.0	1.1	3.5	2.3	4.3	2.0	0.7

Table A6 – Split cylinder tensile strength of RPC on mixes 11 to 19 (in MPa).

Control Sample No.	Mix Design No.								
	11	12	13	14	15	16	17	18	19
1	19.5	26.8	25.2	27.3	21.9	-	17.7	22.8	22.6
2	18.2	26.0	26.8	21.4	21.0	-	18.5	22.5	22.9
3	23.1	27.9	23.1	23.4	22.0	-	17.6	21.9	24
4	16.6	-	-	22.3	22.6	-	17.1	22.5	24.2
5	24.2	-	-	-	23.0	-	21	22.3	24.1
6	21.4	-	-	-	20.0	-	18.1	22.3	23.2
7	21.1	-	-	-	-	-	-	-	-
8	22.0	-	-	-	-	-	-	-	-
9	21.1	-	-	-	-	-	-	-	-
10	21.9	-	-	-	-	-	-	-	-
Average	20.9	26.9	25.0	23.6	21.8	-	18.3	22.4	23.5
Std. Dev.	2.4	1.0	1.9	2.6	1.1	-	1.4	0.3	0.7

Table A7 – Double punch tensile strength of RPC on mixes 1 to 10 (in MPa).

Control Sample No.	Mix Design No.									
	1	2	3	4	5	6	7	8	9	10
1	8.7	7.8	7.6	11.2	10.7	8.5	11.4	12.8	11.8	10.8
2	7.8	8.0	7.5	11.4	9.4	9.4	11.6	11.6	12.3	11.9
3	8.2	7.9	7.6	11.1	10.2	6.9	12.7	11.4	12.9	10.2
4	-	-	-	-	-	8.3	12.3	11.2	11.2	11.4
5	-	-	-	-	-	8.0	-	13.4	12.1	11.5
6	-	-	-	-	-	9.5	-	10.2	11.2	11.2
7	-	-	-	-	-	-	-	11.8	-	-
8	-	-	-	-	-	-	-	12.1	-	-
9	-	-	-	-	-	-	-	11.8	-	-
10	-	-	-	-	-	-	-	12.3	-	-
11	-	-	-	-	-	-	-	11.4	-	-
12	-	-	-	-	-	-	-	12.7	-	-
Average	8.2	7.9	7.6	11.2	10.1	8.4	12.0	11.9	11.9	11.2
Std. Dev.	0.5	0.1	0.1	0.2	0.7	1.0	0.6	0.8	0.7	0.6

Table A8 – Double punch tensile strength of RPC on mixes 11 to 19 (in MPa).

Control Sample No.	Mix Design No.								
	11	12	13	14	15	16	17	18	19
1	8.4	15.9	13.4	12.5	-	-	10.8	13.9	12.5
2	10.7	16.1	13.5	12.4	-	-	11.9	13.7	11.4
3	9.2	14.9	13.1	12.0	-	-	11.7	13.3	12.7
4	9.0	15.4	13.3	11.5	-	-	10.4	13.5	12.2
5	10.2	15.6	13.3	13.1	-	-	10.6	13.7	11.8
6	11.6	15.8	12.7	11.6	-	-	11.0	13.5	12.6
7	10.0	-	-	-	-	-	-	-	-
8	10.6	-	-	-	-	-	-	-	-
Average	10.0	15.6	13.2	12.2	-	-	11.1	13.6	12.2
Std. Dev.	1.0	0.4	0.3	0.6	-	-	0.6	0.2	0.5

APPENDIX B – RAW DATA FOR DEEP PANEL TESTS

Table B1– Panel 1: Raw data for DMs 1 to 5.

Panel 1	Strain (με)				
Load (kN)	**DM1**	**DM2**	**DM3**	**DM4**	**DM5**
0	0	0	0	0	0
100	13	-6	-13	-13	0
200	44	-38	-13	-13	0
300	69	-19	-19	-19	-13
400	95	0	-69	-25	-6
600	164	32	-6	-38	-32
800	151	44	76	-32	-25
1000	151	57	158	-13	-38
1200	151	-13	265	44	-32
1400	120	-32	328	151	-25
1600	113	57	422	372	57
1800	101	101	756	649	151
2000	107	139	1103	914	265
2200	101	139	1814	1537	599
2400	107	107	3736	2444	1254

Table B2 – Panel 2: Raw data for DMs 1 to 5.

Panel 2	Strain (με)				
Load (kN)	**DM1**	**DM2**	**DM3**	**DM4**	**DM5**
0	0	0	0	0	0
100	38	0	-6	-6	-19
200	95	13	-25	-101	-82
300	151	57	6	-25	-50
400	76	195	50	-6	-38
600	76	321	88	25	-6
800	57	372	95	-50	0
1000	50	347	69	0	0
1200	0	0	0	0	0
1400	38	0	-6	-6	-19

Table B3 – Panel 3: Raw data for DMs 1 to 9.

Panel 3	Strain (με)								
Load (kN)	DM1	DM2	DM3	DM4	DM5	DM6	DM7	DM8	DM9
0	0	0	0	0	0	0	0	0	0
100	13	-19	0	-6	25	0	25	-13	19
200	32	6	-13	-6	57	13	25	-6	38
300	82	6	0	-13	82	0	25	-6	63
400	76	32	-13	-6	101	25	-19	-19	95
500	195	32	-19	-32	120	57	25	-19	195
600	239	63	-13	-25	176	82	25	-13	233
700	290	126	13	-25	233	101	32	-19	315
800	334	176	32	-25	290	151	44	-6	359
900	523	296	82	-25	384	164	57	57	542
1000	617	340	76	-25	447	195	88	0	668
1100	819	498	151	-6	479	195	208	19	863
1200	1071	649	176	32	504	183	265	44	1090
1300	1594	1033	410	69	479	183	372	95	1638
1400	2022	1310	580	164	517	195	485	164	2079
1500	2804	1833	914	334	447	195	794	340	2904
1600	5891	4246	2709	1487	384	580	1802	1512	6067

Table B4 – Panel 3: Raw data for DMs 10 to 17.

Panel 3	Strain (με)							
Load (kN)	DM10	DM11	DM12	DM13	DM14	DM15	DM16	DM17
100	-32	6	0	-6	-25	-19	-6	-25
200	-6	0	6	-32	-63	-63	-44	-32
300	0	0	0	-57	-95	-95	-76	-101
400	-13	6	0	-88	-145	-126	-95	-113
500	32	0	19	-145	-170	-158	-139	-164
600	50	0	6	-183	-208	-189	-170	-208
700	107	13	-25	-252	-258	-221	-183	-239
800	132	25	-6	-258	-271	-252	-227	-271
900	252	63	-19	-302	-334	-271	-239	-309
1000	334	107	13	-353	-353	-334	-296	-347
1100	466	170	32	-397	-403	-353	-321	-403
1200	599	284	50	-447	-447	-397	-372	-441
1300	951	517	158	-523	-498	-428	-403	-504
1400	1216	680	233	-586	-542	-460	-441	-561
1500	1745	1052	422	-649	-592	-485	-466	-599
1600	4152	2514	1392	-775	-611	-523	-498	-725

Table B5 – Panel 4: Raw data for DMs 1 to 9.

Panel 4	**Strain (με)**								
Load (kN)	**DM1**	**DM2**	**DM3**	**DM4**	**DM5**	**DM6**	**DM7**	**DM8**	**DM9**
0	0	0	0	0	0	0	0	0	0
100	50	19	6	6	44	25	19	19	38
200	101	69	38	25	88	57	50	32	88
300	158	95	50	38	145	82	63	50	120
400	170	132	88	57	271	139	76	69	164
500	183	284	145	82	340	189	113	95	378
600	221	548	246	132	567	284	176	113	586
700	378	693	372	195	743	365	176	132	819
800	504	1254	693	365	844	416	202	139	1418
900	643	1915	1128	636	964	473	214	139	2142

Table B6 – Panel 4: Raw data for DMs 10 to 17.

Panel 4	**Strain (με)**							
Load (kN)	**DM10**	**DM11**	**DM12**	**DM13**	**DM14**	**DM15**	**DM16**	**DM17**
0	0	0	0	0	0	0	0	0
100	32	19	13	-63	-50	-32	-50	-63
200	63	44	13	-101	-126	-95	-126	-126
300	88	63	38	-126	-158	-176	-189	-158
400	120	88	63	-158	-221	-258	-277	-189
500	252	132	76	-189	-284	-334	-328	-239
600	403	227	120	-221	-334	-391	-391	-309
700	580	353	189	-252	-384	-473	-466	-347
800	1033	643	359	-309	-441	-517	-523	-410
900	1632	1071	630	-378	-504	-567	-586	-473

Table B7 – Panel 5: Raw data for DMs 1 to 9.

Panel 5	**Strain (με)**								
Load (kN)	**DM1**	**DM2**	**DM3**	**DM4**	**DM5**	**DM6***	**DM7**	**DM8***	**DM9***
0	0	0	0	0	0	-	0	-	-
100	38	50	19	0	0	-	13	-	-
200	63	82	19	-19	63	-	13	-	-
300	126	113	25	44	107	-	13	-	-
400	208	195	38	32	126	-	13	-	-
500	284	284	32	32	145	-	32	-	-
600	473	347	38	25	189	-	44	-	-
700	882	586	170	82	221	-	76	-	-
800	1512	995	378	145	221	-	88	-	-
900	2709	1373	586	221	221	-	95	-	-
1000	3182	2161	1040	441	189	-	107	-	-

* Note: no data – targets located out of gauge range.

Table B8– Panel 5: Raw data for DMs 10 to 17.

Panel 5	**Strain (με)**							
Load (kN)	**DM10**	**DM11**	**DM12**	**DM13**	**DM14**	**DM15**	**DM16**	**DM17**
0	0	0	0	0	0	0	0	0
100	32	32	63	-44	-63	-32	-32	-13
200	13	19	76	-82	-50	-95	-57	-44
300	25	25	76	-126	-95	-158	-113	-76
400	76	0	63	-164	-126	-189	-158	-107
500	76	-63	-32	-214	-202	-252	-252	-139
600	170	32	-63	-227	-239	-334	-347	-189
700	422	126	76	-252	-302	-378	-410	-233
800	800	334	189	-	-378	-441	-473	-296
900	1147	536	252	-	-441	-473	-504	-328
1000	1934	1008	410	-	-473	-536	-517	-359

Table B9 – Panel 6: Raw data for DM1s to 9.

Panel 6	Strain (με)								
Load (kN)	DM1	DM2	DM3	DM4	DM5	DM6	DM7	DM8	DM9
0	0	0	0	0	0	0	0	0	0
100	50	19	19	13	76	32	19	-25	2
200	82	19	0	-38	113	50	25	-25	12
300	132	25	-6	-107	126	57	6	-25	16
400	145	38	-13	-221	164	50	13	-38	20
500	315	113	32	-208	195	95	19	-32	120
600	428	164	50	-202	195	151	25	-44	220
700	851	334	63	-139	221	202	38	-25	500
800	1140	536	164	-57	252	315	107	0	900
900	1575	851	302	0	271	441	189	32	1400
1000	2142	1166	491	38	277	473	422	113	2000
1100	2873	1739	863	183	265	460	750	284	2890
1200	3749	2381	1254	422	252	504	1128	491	4000
1300	5424	3629	2129	592	403	725	1934	1008	5000
1400	7025	4857	2451	1222	410	1323	2577	1323	6700
1500	9261	7264	4775	2608	536	2489	3994	2318	8566

Table B10 – Panel 6: Raw data for DMs 10 to 17.

Panel 6	Strain (με)							
Load (kN)	DM10	DM11	DM12	DM13	DM14	DM15	DM16	DM17
0	0	0	0	0	0	0	0	0
100	0	-13	-6	-44	-13	-25	-44	-32
200	13	-25	-13	-88	-32	-44	-76	-107
300	6	-25	-13	-126	-95	-69	-139	-189
400	6	-38	-25	-139	-126	-139	-170	-221
500	82	0	-32	-170	-139	-221	-202	-252
600	183	13	-32	-176	-189	-233	-233	-252
700	353	63	-6	-214	-233	-328	-277	-284
800	529	113	6	-239	-284	-347	-296	-315
900	800	252	38	-258	-296	-391	-328	-347
1000	1178	485	82	-277	-315	-441	-359	-378
1100	1720	832	284	-328	-378	-441	-422	-441
1200	2344	1336	523	-391	-441	-504	-485	-504
1300	3541	2029	1065	-580	-473	-504	-517	-693
1400	4801	3257	1707	-706	-504	-536	-580	-788
1500	6313	5242	2936	-737	-567	-567	-611	-851

APPENDIX C – RAW DATA FOR CONTROL SPECIMEN STRENGTH TESTS FOR SHEAR BEAMS

Table C1 – Cylinder compressive strength (f_{cm}) of specimens SB1 to 7 (in MPa).

Control Specimens No.	Shear Beam No.						
	1	2	3	4	5	6	7
1	165	161	140	169	178	149	169
2	167	163	144	168	169	159	176
3	165	166	140	154	166	159	167
4	160	157	150	177	178	162	168
5	162	158	166	156	177	150	167
6	157	160	146	165	170	161	169
7*	151	155	158	161	162	161	165
Average	161	160	149	164	171	157	169
Std. Dev.	5.57	3.74	9.72	7.99	6.37	5.44	3.50
COV.	0.035	0.023	0.065	0.049	0.037	0.035	0.021

Specimens Sizes : 200 mm high and 100 mm by diameter
Loading Rate : 20 MPa/min for control specimens 1 to 6.
Circumferential Rate : 30 μm/min for specimen 7
Notes: * modulus of elasticity test

Table C2 – Cube compressive strength (f_{cu}) of specimens SB1 to 7 (in MPa).

Control Specimens No.	Shear Beam No.						
	1	2	3	4	5	6	7
1	180	177	170	192	192	167	169
2	176	184	175	189	182	171	176
3	175	183	165	177	189	162	167
4	176	179	167	178	185	163	169
5	178	186	162	170	194	167	189
6	184	174	171	176	198	159	190
7	165	175	164	189	185	168	192
8	169	172	167	178	191	175	197
9	178	174	156	185	186	171	189
10	176	176	158	168	187	174	196
Average	176	178	166	180	187	168	185
Std. Dev.	4.90	4.43	5.33	7.46	8.90	5.74	11.7
COV.	0.028	0.025	0.032	0.042	0.048	0.034	0.063

Specimens Sizes : 70 mm cube   Loading Rate : 20 MPa/min

Table C3 – Double punch tensile strength (f_{dp}) of specimens SB1 to 7 (in MPa).

Control Specimens No.	**Shear Beam No.**						
	1	**2**	**3**	**4**	**5**	**6**	**7**
1	11.8	10.8	10.2	10.2	13.9	10.8	12.5
2	12.3	11.9	10.2	11	13.7	11.9	11.4
3	12.9	10.2	9.4	9.8	13.3	11.7	12.7
4	11.2	11.4	11.1	10.2	13.5	10.4	12.2
5	12.1	11.5	11.6	10.6	13.7	10.6	11.8
6	11.2	11.2	11.2	10.2	13.5	11.0	12.6
Average	11.9	11.2	10.6	10.3	13.6	11.1	12.2
Std. Dev.	0.63	0.60	0.82	0.41	0.21	0.62	0.51
COV.	0.053	0.053	0.077	0.040	0.015	0.056	0.042
Specimens Sizes : 200 mm high and 100 mm by diameter Loading Rate : 1.0 MPa/min							

Table C4 – Split tensile strength (f_{sp}) of specimens SB1 to 7 (in MPa).

Control Specimens No.	**Shear Beam No.**						
	1	**2**	**3**	**4**	**5**	**6**	**7**
1	18.8	21.4	24.2	19.4	22.8	17.7	22.6
2	22.7	20	21.4	17.2	22.5	18.5	22.9
3	17.3	21.9	21.1	19.4	21.9	17.6	24
4	19.1	20.7	22.0	18.4	22.5	17.1	24.2
5	17.2	20.8	21.1	16.7	22.3	21	24.1
6	20.1	20.5	21.9	16.9	22.3	18.1	23.2
Average	19.2	20.9	21.9	18.0	22.4	18.3	23.5
Std. Dev.	2.04	0.67	1.17	1.24	0.30	1.40	0.70
COV.	0.011	0.032	0.053	0.069	0.014	0.076	0.030
Specimens Sizes : 200 mm high and 100 mm by diameter cylinder Loading Rate : 1.0 MPa/min							

Table C5 – Three point flexural strength (f_{cf}) and fracture energy (G_f) of specimens SB1 to 7 (in MPa and N/mm, respectively).

Shear Beam No.	f_{cf} (MPa)	$G_{f,CMOD}$ (N/mm)	$G_{f,mid}$ (N/mm)	$\frac{G_{f,CMOD}}{G_{f,mid}}$
1	29.75	27.73	27.64	1.00
2a	27.42	27.06	26.11	1.04
2b	25.31	23.19	22.20	1.04
3	23.24	21.43	20.49	1.05
4a	15.44	15.70	15.53	1.01
4b	14.19	13.03	12.72	1.02
5	26.25	15.60	15.25	1.02
6a	24.88	12.62	12.19	1.04
6b	25.52	12.10	12.45	0.97
7a	25.78	19.77	19.84	1.00
7b	21.77	17.30	17.25	1.00
Average				1.02
COV.				0.023

Specimens Sizes : 100 mm by 100 mm and 500 mm long prism
Notched Depth : 25 mm
CMOD Control Rate : 500 με/min
Specimen 2, 4 and 6 have two prisms and they denoted as specimen a and b.

APPENDIX D –DEMEC STRAINS FOR SHEAR BEAM STREGTH TESTS

Table D1 – SB1: Raw data on Demec strains (zero pre-strain).

SB 1	Strain (με)							
Load (kN)	0	100	200	300	400	500	650	850
DM 1	0	-6	0	-6	-6	13	13	25
DM 2	0	-19	-50	0	25	44	-19	63
DM 3	0	-82	-145	-63	-32	-19	-25	699
DM 4	0	-57	-69	-88	-101	-151	-139	384
DM 5	0	-25	-82	-107	-202	-126	-158	158
DM 6	0	-32	-38	-107	-145	-202	-208	0
DM 7	0	-88	-25	-57	-44	-63	-63	-95
DM 8	0	-50	-120	-158	-246	-315	-378	-397
DM 9	0	-95	-170	-221	-284	-365	-460	-491
DM 10	0	-63	-151	-195	-233	-321	-403	-435
DM 11	0	-69	-101	-145	-195	-239	-227	-246
DM 12	0	-32	-76	-120	-151	-164	-195	-183
DM 13	0	-32	-50	-95	-132	-189	-151	-132
DM 14	0	-32	-63	-76	-69	-95	-63	-63
DM 15	0	-25	-38	-25	-32	-38	-25	-6
DM 16	0	-6	-6	-13	-19	-32	-25	-13
DM 17	0	38	50	88	378	649	1071	2961
DM 18	0	13	13	88	309	491	592	781
DM 19	0	32	113	189	328	580	1071	1499
DM 20	0	44	95	126	378	630	1071	1940
DM 21	0	120	158	365	762	1090	1556	2356
DM 22	0	0	321	813	1317	1833	2734	4416
DM 23	0	95	302	536	895	1166	1777	2678
DM 24	0	88	202	491	863	1260	1852	2848
DM 25	0	82	176	428	794	1191	1783	2665
DM 26	0	82	151	504	876	1241	1808	2640
DM 27	0	693	756	1002	1355	1638	2237	2552
DM 28	0	82	139	258	680	1046	1594	2747
DM 29	0	6	95	158	252	617	1121	2583
DM 30	0	13	76	113	151	265	731	1600
DM 31	0	57	63	107	107	139	359	832

Table D1 – Continued.

SB 1	Strain (με)							
Load (kN)	0	100	200	300	400	500	650	850
DM 32	0	50	50	57	82	113	189	460
DM 33	0	-25	19	32	-19	-25	-63	-158
DM 34	0	-76	-107	-113	-265	-296	-378	-693
DM 35	0	88	95	107	737	989	1191	11460
DM 36	0	76	113	145	712	964	536	10805
DM 37	0	-38	-50	-82	-145	-208	-347	1972
DM 38	0	-25	-19	-63	-82	-132	-221	-838
DM 39	0	-13	-6	6	-19	-57	-164	-384
DM 40	0	0	25	258	655	1065	2010	3459
DM 41	0	0	6	-13	258	473	743	1134
DM 42	0	-6	-32	44	277	611	1040	4958
DM 43	0	-365	-410	-397	-428	-391	-397	-775
DM 44	0	-38	-13	-38	-44	-63	-113	-466
DM 45	0	-19	-6	-19	-38	-69	-113	-132
DM 46	0	25	-13	-13	-19	-69	-158	-334
DM 47	0	25	6	13	6	-13	88	50
DM 48	0	-44	13	25	13	19	6	-32
DM 49	0	353	403	416	365	347	315	662
DM 50	0	32	-57	57	473	901	1670	1764
DM 51	0	6	25	25	195	542	794	8228
DM 52	0	0	0	19	-50	-25	-32	139
DM 53	0	6	38	69	151	195	132	120
DM 54	0	32	44	44	50	82	82	284
DM 55	0	32	44	44	50	82	82	284
DM 56	0	57	252	901	1556	2350	3906	5903
DM 57	0	63	107	246	460	674	977	1304
DM 58	0	63	107	265	680	907	1336	1556
DM 59	0	57	139	265	504	838	1512	8285
DM 60	0	120	164	277	630	800	1556	16393
DM 61	0	120	145	145	183	315	498	15385
DM 62	0	25	25	50	88	139	466	781
DM 63	0	19	25	57	38	57	227	353
DM 64	0	113	151	164	183	176	176	189
DM 65	0	-88	-38	-63	63	76	95	76
DM 66	0	-32	-19	-25	-32	-44	-82	-95

Table D1 – Continued.

SB 1	Strain (με)							
Load (kN)	0	100	200	300	400	500	650	850
DM 67	0	-6	13	25	76	202	265	328
DM 68	0	6	-6	-6	0	-13	-151	-25
DM 69	0	88	120	202	851	1468	2678	2835
DM 70	0	82	113	139	120	189	347	57
DM 71	0	95	101	239	1695	2999	6224	19549
DM 72	0	25	19	25	50	113	554	13910
DM 73	0	44	113	176	334	788	2205	12726
DM 74	0	0	13	19	6	38	-13	-113
DM 75	0	63	95	504	819	1210	1355	1859
DM 76	0	0	13	19	25	13	0	-19
DM 77	0	19	57	82	158	221	378	284
DM 78	0	-32	-38	-101	-176	-290	-479	-195
DM 79	0	-25	176	958	2022	2923	5487	6187
DM 80	0	13	0	88	214	340	655	1588
DM 81	0	-132	-25	353	958	1569	3112	5664
DM 82	0	69	32	95	132	208	164	321
DM 83	0	-32	-38	-38	-32	-50	57	139
DM 84	0	19	50	195	510	876	1292	1355
DM 85	0	-32	-95	-113	-132	-164	-113	-25
DM 86	0	95	139	410	1065	2155	4265	14975
DM 87	0	-57	-183	-101	-32	120	756	9576
DM 88	0	44	120	271	958	1896	3912	4983
DM 89	0	-25	-69	-120	-195	-139	189	5563
DM 90	0	38	107	145	290	347	1972	2709
DM 91	0	-50	-88	-126	-158	-145	170	863
DM 92	0	69	113	164	233	548	1556	3037
DM 93	0	-44	-120	-126	-183	-239	-151	258
DM 94	0	82	95	151	202	315	819	1796
DM 95	0	-57	-126	-151	-221	-252	-347	-391
DM 96	0	50	0	63	113	158	353	662
DM 97	0	-63	6	25	-6	6	6	-6
DM 98	0	44	-19	13	13	13	57	95
DM 99	0	-44	-113	-164	-164	-221	-195	-195

Table D2 – SB2: Raw data on Demec strains (including prestrain).

SB 2	Strain (με)					
Load (kN)	0	300	450	600	750	900
DM 1	-162	-231	-194	-212	-212	-181
DM 2	-146	-222	-241	-222	-234	-222
DM 3	-142	-243	-268	-300	-325	-312
DM 4	-142	-262	-312	-325	-350	-388
DM 5	-142	-306	-388	-400	-451	-482
DM 6	-142	-344	-419	-495	-533	-608
DM 7	-143	-376	-445	-553	-660	-679
DM 8	-142	-337	-444	-520	-615	-646
DM 9	-142	-400	-489	-564	-633	-646
DM 10	-143	-420	-483	-628	-679	-754
DM 11	-142	-255	-331	-426	-470	-552
DM 12	-142	-287	-337	-381	-407	-463
DM 13	-142	-287	-337	-350	-337	-381
DM 14	-142	-218	-255	-262	-268	-255
DM 15	-146	-178	-209	-203	-171	-165
DM 16	-162	-162	-162	-162	-149	-137
DM 17	-492	-429	-410	-391	-353	-316
DM 18	-469	-406	-374	-324	-274	-204
DM 19	-465	-396	-333	-263	-181	115
DM 20	-464	-319	-269	-168	147	689
DM 21	-465	-282	-219	-55	587	1236
DM 22	-465	-244	-181	291	890	1583
DM 23	-465	-194	8	606	1381	2087
DM 24	-465	-55	215	682	1375	2030
DM 25	-465	-163	146	782	1463	2168
DM 26	-465	-200	159	839	1444	2194
DM 27	-465	-257	-181	524	1299	2087
DM 28	-465	-263	-188	26	795	1652
DM 29	-465	-333	-270	-188	26	518
DM 30	-465	-301	-263	-194	-49	266
DM 31	-468	-386	-355	-310	-235	-147
DM 32	-492	-505	-492	-460	-435	-379
DM 33	-147	168	181	200	181	168

Table D2 – Continued.

SB 2	**Strain (με)**					
Load (kN)	0	300	450	600	750	900
DM 34	-220	-214	-220	-233	-252	-283
DM 35	-240	-347	-353	-385	-429	151
DM 36	-242	-248	-267	-305	-368	-412
DM 37	-241	-285	-310	-329	-443	-537
DM 38	-240	-284	-316	-145	472	1272
DM 39	-241	-506	-512	-474	-525	2500
DM 40	-240	-221	-215	18	485	611
DM 41	-240	-240	-240	-82	516	1058
DM 42	-240	-316	-328	-215	-139	144
DM 43	-240	-240	-265	-227	-215	-7
DM 44	-242	-248	-280	-305	-299	-274
DM 45	-241	-342	-348	-361	-184	43
DM 46	-240	-297	-303	-335	-391	-467
DM 47	-241	-209	-228	-216	-285	-336
DM 48	-148	41	47	54	54	41
DM 49	-183	-126	-88	-57	-57	-114
DM 50	-317	-273	-254	-254	-216	-134
DM 51	-361	-317	-292	-229	-153	-90
DM 52	-369	-300	-287	-249	-67	311
DM 53	-368	-292	-261	-72	407	1144
DM 54	-368	-204	-166	-97	149	401
DM 55	-368	-299	-223	111	533	848
DM 56	-368	-229	-91	262	798	1333
DM 57	-368	-198	-59	344	785	1270
DM 58	-368	-242	-15	564	1491	2247
DM 59	-368	-198	-185	445	1818	2858
DM 60	-368	-261	-217	-129	-40	79
DM 61	-368	-255	-223	-286	-204	199
DM 62	-369	-287	-262	-243	-268	-199
DM 63	-361	-336	-317	-304	23	231
DM 64	-317	-235	-222	-191	-216	-128
DM 65	-183	-70	-44	-7	12	-7
DM 66	13	108	108	89	63	95

Table D2 – Continued.

SB 2	Strain (με)					
Load (kN)	0	300	450	600	750	900
DM 67	-75	20	57	108	120	127
DM 68	-81	-144	-257	-220	-276	-358
DM 69	-71	87	162	231	339	603
DM 70	-60	-142	-136	-173	-224	-230
DM 71	-51	-51	-51	-51	-51	503
DM 72	-45	-77	-140	-89	-51	150
DM 73	-43	127	190	423	1198	2792
DM 74	-42	-86	-130	-67	166	670
DM 75	-42	97	160	714	2604	6107
DM 76	-42	-80	-124	2	746	2239
DM 77	-42	116	179	796	2799	6479
DM 78	-42	-155	-218	-212	-149	267
DM 79	-42	90	166	456	1054	2113
DM 80	-42	-99	-137	-137	-92	-105
DM 81	-42	2	65	317	947	1231
DM 82	-41	-66	-85	-3	72	85
DM 83	-41	-79	-117	-73	-66	9
DM 84	-42	65	141	720	1533	2276
DM 85	-42	-99	-174	-181	-269	-332
DM 86	-42	122	103	651	1098	1665
DM 87	-42	-92	-155	-263	-401	-452
DM 88	-42	153	204	254	393	676
DM 89	-42	-105	-149	-200	-225	27
DM 90	-42	134	179	223	525	1634
DM 91	-42	-80	-130	-155	-105	-23
DM 92	-43	127	178	272	1123	2383
DM 93	-45	-70	-95	-133	188	635
DM 94	-51	88	170	239	1234	2431
DM 95	-60	-110	-148	-205	-224	-173
DM 96	-71	131	181	257	357	654
DM 97	-81	-138	-201	-251	-264	-339
DM 98	-75	335	366	398	435	429
DM 99	13	32	32	0	0	0

Table D3 – SB3: Raw data on Demec strains (including prestrain).

SB 3	Strain (με)							
Load (kN)	0	200	300	400	500	600	700	800
DM 1	-81	-87	-94	-100	-100	-94	-94	-100
DM 2	-73	-117	-105	-117	-105	-98	-130	-142
DM 3	-71	-166	-172	-216	-222	-216	-235	-247
DM 4	-71	-247	-247	-273	-317	-336	-348	-367
DM 5	-71	-279	-298	-310	-329	-373	-430	-487
DM 6	-71	-203	-260	-355	-418	-506	-581	-644
DM 7	-72	-217	-324	-387	-456	-538	-601	-620
DM 8	-71	-235	-310	-367	-411	-462	-512	-569
DM 9	-71	-260	-323	-386	-449	-518	-562	-619
DM 10	-72	-198	-280	-299	-343	-444	-482	-526
DM 11	-71	-229	-279	-329	-386	-443	-481	-512
DM 12	-71	-241	-247	-273	-310	-317	-329	-373
DM 13	-71	-96	-109	-121	-140	-166	-184	-191
DM 14	-71	-84	-96	-128	-109	-84	-109	-134
DM 15	-73	-92	-98	-117	-92	-86	-86	-111
DM 16	-81	-81	-81	-81	-81	-81	-75	-94
DM 17	-246	-214	-196	-177	-164	-126	-88	-38
DM 18	-234	-202	-184	-171	-95	-58	-45	56
DM 19	-232	-163	-125	-106	-37	70	360	493
DM 20	-232	-119	-68	-37	178	518	871	1091
DM 21	-232	-156	-68	26	430	757	1198	1387
DM 22	-232	-119	-56	278	738	1167	1576	1708
DM 23	-232	11	256	685	1126	1567	1989	2153
DM 24	-232	-18	234	694	1211	1652	2118	2471
DM 25	-232	-37	335	801	1293	1734	2156	2534
DM 26	-232	-49	524	1034	1557	2055	2565	2975
DM 27	-232	-112	215	663	1135	1652	2131	2439
DM 28	-232	-128	-15	389	817	1195	1661	1995
DM 29	-232	-172	-103	86	458	899	1296	1674
DM 30	-232	-188	-150	-43	247	663	1072	1595
DM 31	-234	-209	-184	-133	-108	100	365	1039
DM 32	-246	-246	-246	-227	-196	-151	-25	321
DM 33	-74	109	172	140	-17	140	109	77

Table D3 – Continued.

SB 3	Strain (με)							
Load (kN)	0	200	300	400	500	600	700	800
DM 34	-110	-154	-160	-167	-192	-179	-192	-255
DM 35	-120	-152	-158	-170	-152	-76	19	258
DM 36	-121	-153	-153	-153	-171	-197	-102	68
DM 37	-120	-180	-180	-161	-92	60	123	192
DM 38	-120	-183	-139	-101	25	245	403	529
DM 39	-120	-139	-76	101	296	523	699	875
DM 40	-120	-227	107	397	794	1310	1764	2621
DM 41	-120	1118	1181	1338	1458	1609	1899	2378
DM 42	-120	-1515	-1515	-1471	-1421	-1440	-1471	-835
DM 43	-120	-192	-192	-224	-281	-199	-142	-507
DM 44	-121	-156	-168	-61	52	52	-36	-452
DM 45	-120	-145	-158	-215	-246	-372	-341	-448
DM 46	-120	-120	-120	-120	-120	-120	-120	-120
DM 47	-120	-51	-32	-25	0	19	31	132
DM 48	-74	-49	-17	-24	8	52	58	430
DM 49	-92	-79	-60	-60	-48	15	141	292
DM 50	-158	-114	-95	-63	31	157	441	535
DM 51	-180	-123	-104	-85	104	330	626	904
DM 52	-184	-102	-71	68	307	604	793	1423
DM 53	-184	-96	-26	226	528	824	1139	1580
DM 54	-184	5	68	396	824	1114	1410	1826
DM 55	-184	-99	140	569	941	1344	1678	1810
DM 56	-184	50	378	712	1121	1550	2016	2747
DM 57	-184	-159	383	717	1234	1738	2368	3218
DM 58	-184	-178	-140	201	359	718	1153	970
DM 59	-184	-184	-184	-184	118	433	937	4321
DM 60	-184	-171	-152	-184	-108	100	112	150
DM 61	-184	-165	-146	18	-26	-14	-64	-77
DM 62	-184	-203	-178	-216	-77	18	87	49
DM 63	-180	-22	-123	-136	-148	-136	-148	-142
DM 64	-158	-114	-95	-63	31	157	441	315
DM 65	-92	-193	-205	-224	-300	-313	-344	-268
DM 66	6	-29	-98	-148	-186	-186	-211	-262

Table D3 – Continued.

SB 3	Strain (με)							
Load (kN)	0	200	300	400	500	600	700	800
DM 67	-37	10	73	117	231	483	911	1428
DM 68	-40	-90	-122	-153	-210	-229	-248	-311
DM 69	-35	41	148	192	368	576	1124	1710
DM 70	-30	-99	-106	-131	-143	-137	-137	-150
DM 71	-25	54	98	148	369	753	1377	1849
DM 72	-23	-118	-118	-118	-105	-86	-55	-181
DM 73	-21	74	86	212	515	1019	1592	2279
DM 74	-21	-141	-116	-147	-147	-141	-153	-298
DM 75	-21	-27	-21	-21	-21	231	722	1239
DM 76	-21	-141	-97	-134	-116	-179	-235	-557
DM 77	-21	-2	-2	86	326	458	622	1126
DM 78	-21	11	395	590	653	830	855	1050
DM 79	-21	-93	-125	-100	-49	-56	-37	285
DM 80	-21	521	565	578	546	641	767	1056
DM 81	-21	-109	-141	-134	-153	-78	36	552
DM 82	-21	-2	546	1157	1919	3047	3715	4250
DM 83	-21	-213	-295	-320	-371	-345	-320	96
DM 84	-21	11	55	496	836	1523	2373	7319
DM 85	-21	-138	-182	-156	-87	-43	-37	89
DM 86	-21	14	70	291	933	1822	3113	11858
DM 87	-21	-112	-119	-169	-182	-131	-68	-245
DM 88	-21	61	137	225	395	1019	1485	1346
DM 89	-21	-97	-141	-172	-185	-179	-172	-172
DM 90	-21	33	96	499	940	1337	1790	1696
DM 91	-21	-134	-147	-197	-116	-27	61	42
DM 92	-21	70	96	114	505	820	1072	927
DM 93	-23	-124	-155	-187	-212	-206	-218	-256
DM 94	-25	-19	-12	-6	57	76	139	227
DM 95	-30	-106	-106	-118	-125	-93	-93	-62
DM 96	-35	37	50	69	126	163	208	371
DM 97	-40	-65	-103	-128	-147	-179	-191	-273
DM 98	-37	42	35	117	218	325	502	716
DM 99	6	0	-19	-38	-44	-63	-70	-89

Table D4 – SB4: Raw data on Demec strains (including prestrain).

SB 4	Strain (με)						
Load (kN)	0	200	300	400	500	600	650
DM 1	-81	119	219	319	419	519	569
DM 2	-73	-29	-48	-48	-60	-60	-73
DM 3	-71	-96	-115	-128	-103	-109	-147
DM 4	-71	-134	-159	-184	-172	-178	-197
DM 5	-71	-147	-184	-222	-229	-254	-279
DM 6	-71	-191	-247	-310	-329	-373	-380
DM 7	-72	-198	-280	-374	-425	-482	-500
DM 8	-71	-285	-361	-474	-537	-644	-695
DM 9	-71	-203	-361	-462	-525	-575	-651
DM 10	-72	-204	-387	-500	-551	-639	-683
DM 11	-71	-247	-342	-430	-481	-569	-632
DM 12	-71	-197	-260	-317	-367	-418	-449
DM 13	-71	-172	-229	-266	-298	-329	-342
DM 14	-71	-153	-172	-197	-210	-229	-241
DM 15	-73	-105	-117	-130	-123	-199	-218
DM 16	-81	-113	-125	-119	-81	-81	-94
DM 17	-246	-246	-271	-240	-214	-214	-202
DM 18	-234	-215	-215	-190	-127	24	94
DM 19	-232	-163	-137	-87	20	310	430
DM 20	-232	-194	-175	-112	222	612	738
DM 21	-232	-150	-112	39	417	763	808
DM 22	-232	-112	-43	316	776	1091	1217
DM 23	-232	-182	26	486	902	1305	1488
DM 24	-232	-81	285	738	1148	1620	1746
DM 25	-232	-87	348	820	1261	1753	2068
DM 26	-232	-68	385	858	1381	1822	2137
DM 27	-232	-93	222	675	1167	1576	1860
DM 28	-232	-119	83	562	984	1406	1708
DM 29	-232	-131	-68	379	782	1148	1412
DM 30	-232	-144	-106	234	612	1041	1293
DM 31	-234	-177	-139	-39	251	585	787
DM 32	-246	-183	-151	-101	25	233	321
DM 33	-74	-49	-42	-11	14	84	191

Table D4 – Continued.

SB 4	Strain (με)						
Load (kN)	0	200	300	400	500	600	650
DM 34	-110	-123	-116	-135	-142	-198	-22
DM 35	-120	-139	-158	-177	-183	-215	-76
DM 36	-121	-146	-159	-171	-102	-184	-20
DM 37	-120	-152	-158	-164	-139	-51	327
DM 38	-120	-177	-177	-189	-586	359	768
DM 39	-120	-32	69	491	731	1090	1707
DM 40	-120	-152	-95	-82	233	542	699
DM 41	-120	-139	0	447	932	1342	2060
DM 42	-120	-152	-57	44	164	447	516
DM 43	-120	-133	-139	-13	453	983	5172
DM 44	-121	-171	-190	-159	-234	-285	30
DM 45	-120	-145	-170	-189	-227	-385	-448
DM 46	-120	-158	-133	-177	-215	-252	-284
DM 47	-120	-233	-252	-170	-126	-290	-347
DM 48	-74	-150	-137	-213	-150	-175	-213
DM 49	-92	-35	-4	-4	9	-4	-29
DM 50	-158	-145	-101	-95	-82	-139	-177
DM 51	-180	-142	-130	-130	15	91	9
DM 52	-184	-134	-121	-134	-96	219	496
DM 53	-184	-134	-89	-8	415	534	1618
DM 54	-184	-134	-108	257	748	1152	1486
DM 55	-184	-108	81	484	786	1240	1794
DM 56	-184	-121	151	529	1046	1480	1713
DM 57	-184	-89	125	377	742	1013	1353
DM 58	-184	-184	-184	19	214	731	1077
DM 59	-184	-134	55	421	862	1038	1315
DM 60	-184	-121	-33	238	333	459	534
DM 61	-184	-140	-127	270	912	1013	1435
DM 62	-184	-134	-127	43	270	1278	5461
DM 63	-180	-161	-142	-41	148	116	179
DM 64	-158	-126	37	-13	-26	12	157
DM 65	-92	-92	-92	-48	-10	-29	-54
DM 66	6	-13	-13	-63	-32	-32	-63

Table D4 – Continued.

SB 4	Strain (με)						
Load (kN)	0	200	300	400	500	600	650
DM 67	-37	-12	13	51	102	133	473
DM 68	-40	-59	-97	-141	-185	-185	-216
DM 69	-35	66	116	167	280	456	1124
DM 70	-30	-106	-156	-181	-194	-232	-288
DM 71	-25	76	126	189	693	1657	3434
DM 72	-23	-73	-111	-136	9	462	733
DM 73	-21	67	124	143	641	2165	4421
DM 74	-21	-65	-103	-147	-90	420	571
DM 75	-21	86	130	332	1107	3079	6273
DM 76	-21	-59	-90	-103	-122	578	1012
DM 77	-21	61	74	678	1913	3822	7035
DM 78	-21	-109	-122	-109	124	382	767
DM 79	-21	55	250	993	1699	3003	5082
DM 80	-21	-116	-128	-147	-172	-160	23
DM 81	-21	-2	111	288	729	1138	1422
DM 82	-21	-53	-21	-27	99	67	-27
DM 83	-21	-46	-53	11	80	118	168
DM 84	-21	-59	250	779	1523	2197	2449
DM 85	-21	-65	-65	29	187	332	407
DM 86	-21	250	445	1541	3192	3406	3967
DM 87	-21	-71	-84	55	263	540	918
DM 88	-21	42	231	1560	3828	7325	8522
DM 89	-21	-78	-90	250	1289	3072	13543
DM 90	-21	61	105	1371	3809	7690	9372
DM 91	-21	-71	-65	55	452	2027	10248
DM 92	-21	92	130	767	1869	4421	5693
DM 93	-23	-55	-99	-55	97	210	160
DM 94	-25	70	126	334	807	1374	2728
DM 95	-30	-62	-87	-118	-131	-68	-55
DM 96	-35	-22	66	230	293	513	2044
DM 97	-40	-103	-153	-153	-147	-198	-229
DM 98	-37	-18	1	20	121	58	1689
DM 99	6	-32	6	50	31	50	25

Table D5 – SB5: Raw data on Demec strains (including prestrain).

SB5	Strain (με)					
Load (kN)	0	200	300	450	600	800	860
DM 1	-81	-169	-138	-176	-188	-150	-144
DM 2	-73	-243	-205	-281	-306	-294	-212
DM 3	-71	-166	-191	-260	-279	-317	-241
DM 4	-71	-166	-203	-292	-323	-355	-292
DM 5	-71	-254	-317	-380	-455	-518	-443
DM 6	-71	-178	-266	-348	-430	-556	-537
DM 7	-72	-261	-400	-526	-608	-778	-765
DM 8	-71	-197	-310	-455	-493	-600	-481
DM 9	-71	-222	-336	-449	-474	-544	-367
DM 10	-72	-148	-242	-305	-400	-557	-494
DM 11	-71	-153	-310	-348	-424	-506	-525
DM 12	-71	-147	-247	-273	-336	-392	-361
DM 13	-71	-121	-184	-197	-247	-285	-247
DM 14	-71	-178	-178	-229	-229	-229	-178
DM 15	-73	-111	-123	-98	-130	-123	-35
DM 16	-81	-100	-113	-81	-81	-68	-49
DM 17	-246	-284	-233	-214	-183	-63	-7
DM 18	-234	-171	-121	-95	-39	182	472
DM 19	-232	-156	-106	-56	127	713	1324
DM 20	-232	-137	-62	-18	455	1154	1942
DM 21	-232	-119	-87	304	820	1614	2370
DM 22	-232	-68	20	493	1041	1847	2194
DM 23	-232	-137	-11	461	1028	1816	2194
DM 24	-232	-81	89	644	1337	2181	2313
DM 25	-232	-100	127	694	1324	2175	2345
DM 26	-232	-125	39	511	1148	1967	2086
DM 27	-232	-106	-18	392	997	1847	1942
DM 28	-232	-106	20	146	587	1280	1469
DM 29	-232	-137	-74	26	436	1186	1299
DM 30	-232	-150	-87	-74	184	700	858
DM 31	-234	-171	-127	-95	-45	283	396
DM 32	-246	-208	-158	-126	-95	38	69
DM 33	-74	-74	-36	-36	-42	-49	-87

Table D5 – Continued.

SB5	Strain (με)						
Load (kN)	0	200	300	450	600	800	860
DM 34	-110	-123	-142	-123	-179	-179	-293
DM 35	-120	-183	-170	-202	-227	-284	-422
DM 36	-121	-165	-159	-197	-197	-197	-197
DM 37	-120	-133	-139	-183	-227	-196	-485
DM 38	-120	-183	-189	-202	-177	-57	-372
DM 39	-120	-196	-227	-120	6	441	1096
DM 40	-120	-183	-202	-95	94	409	967
DM 41	-120	-170	-183	6	308	686	838
DM 42	-120	-196	-183	-107	0	258	308
DM 43	-120	-164	-177	-126	94	271	353
DM 44	-121	-153	-159	-146	-33	169	156
DM 45	-120	-145	-139	-158	-76	19	50
DM 46	-120	-139	-120	-145	-183	-88	69
DM 47	-120	-120	-107	-95	-76	-13	-32
DM 48	-74	-61	-42	-49	-42	-68	-55
DM 49	-92	-92	-92	-92	-92	-92	-92
DM 50	-158	-95	63	189	176	214	277
DM 51	-180	-85	9	15	15	91	299
DM 52	-184	-134	-83	-71	30	408	1196
DM 53	-184	-121	-96	-89	100	415	982
DM 54	-184	-108	-52	251	811	1675	6343
DM 55	-184	-115	-64	163	616	1196	1372
DM 56	-184	-96	25	504	894	1543	1669
DM 57	-184	-115	5	402	1051	1725	1882
DM 58	-184	-115	-14	397	825	1386	1417
DM 59	-184	-134	-77	163	509	1171	1234
DM 60	-184	-140	-96	188	553	1007	1070
DM 61	-184	-152	-102	-52	352	717	742
DM 62	-184	-146	-115	-83	24	377	465
DM 63	-180	-155	-130	-104	53	437	507
DM 64	-158	-145	-95	-95	-63	220	315
DM 65	-92	-54	-29	-16	34	21	40
DM 66	6	-183	-208	-322	-391	-656	-435

Table D5 – Continued.

SB5	Strain (με)						
Load (kN)	0	200	300	450	600	800	860
DM 67	-37	13	58	76	95	139	139
DM 68	-40	-248	-248	-355	-481	-607	-563
DM 69	-35	66	167	223	255	444	501
DM 70	-30	-112	-194	-276	-377	-660	-1088
DM 71	-25	133	290	347	403	895	1159
DM 72	-23	-237	-451	-527	-596	-836	-458
DM 73	-21	86	124	181	496	1913	1787
DM 74	-21	-134	-179	-248	-286	105	231
DM 75	-21	42	105	137	533	2266	2052
DM 76	-21	-103	-185	-242	-273	36	-8
DM 77	-21	42	86	407	1573	5403	15263
DM 78	-21	-134	-172	-229	-34	80	5441
DM 79	-21	17	29	319	1617	3476	7123
DM 80	-21	-153	-216	-279	-311	-216	571
DM 81	-21	-21	23	395	987	2159	3917
DM 82	-21	-160	-204	-254	-267	-317	-286
DM 83	-21	-116	-134	-191	-15	48	124
DM 84	-21	-8	-8	130	313	697	779
DM 85	-21	-128	-179	-242	-305	-399	-368
DM 86	-21	11	74	168	533	1478	1806
DM 87	-21	-134	-197	-216	-242	-273	-210
DM 88	-21	42	99	344	1100	2449	2852
DM 89	-21	-103	-147	-197	-286	-216	-97
DM 90	-21	42	92	155	830	2398	2638
DM 91	-21	-97	-141	-191	-210	80	174
DM 92	-21	4	105	200	735	2486	2783
DM 93	-23	-111	-143	-193	-168	153	261
DM 94	-25	25	88	151	473	1771	2130
DM 95	-30	-112	-150	-213	-238	-282	-162
DM 96	-35	60	97	154	261	822	998
DM 97	-40	-128	-179	-279	-292	-355	-305
DM 98	-37	7	26	45	83	83	114
DM 99	6	-51	-57	-82	-82	-76	-38

Table D6 – SB6: Raw data on Demec strains (including prestrain).

SB 6	Strain (με)				
Load (kN)	0	200	300	450	600
DM 1	-81	-106	-169	-138	-106
DM 2	-73	-130	-224	-161	-149
DM 3	-71	-115	-172	-159	-184
DM 4	-71	-159	-298	-235	-273
DM 5	-71	-222	-292	-348	-386
DM 6	-71	-273	-367	-462	-525
DM 7	-72	-293	-406	-519	-608
DM 8	-71	-247	-304	-418	-544
DM 9	-71	-241	-336	-405	-512
DM 10	-72	-280	-387	-488	-589
DM 11	-71	-247	-386	-474	-575
DM 12	-71	-191	-273	-348	-418
DM 13	-71	-159	-210	-235	-254
DM 14	-71	-172	-235	-210	-216
DM 15	-73	-117	-136	-105	-105
DM 16	-81	-94	-94	-75	-62
DM 17	-246	-183	-196	-133	-25
DM 18	-234	-196	-202	-121	150
DM 19	-232	-182	-182	228	889
DM 20	-232	133	165	820	1438
DM 21	-232	-100	133	845	1450
DM 22	-232	-68	480	1141	1834
DM 23	-232	77	713	1450	2143
DM 24	-232	272	789	1551	2307
DM 25	-232	133	556	1816	2383
DM 26	-232	-37	795	1614	2389
DM 27	-232	-87	442	1154	1853
DM 28	-232	-93	203	959	1683
DM 29	-232	-93	52	663	1343
DM 30	-232	-156	-144	757	1261
DM 31	-234	-228	-215	-95	163
DM 32	-246	-183	-164	-120	25
DM 33	-74	-87	-99	-24	-200

Table D6 – Continued.

SB 6	Strain (με)				
Load (kN)	0	200	300	450	600
DM 34	-110	-148	-179	-192	-261
DM 35	-120	-70	-95	-133	-259
DM 36	-121	-178	-197	-121	-121
DM 37	-120	-158	-158	-126	19
DM 38	-120	-196	-189	107	724
DM 39	-120	-152	-95	107	31
DM 40	-120	-101	208	661	1323
DM 41	-120	-126	101	605	920
DM 42	-120	-189	-44	12	579
DM 43	-120	-177	-164	-38	-196
DM 44	-121	-140	-247	-140	-272
DM 45	-120	-126	-183	126	353
DM 46	-120	-158	-183	-76	283
DM 47	-120	-158	-164	-240	-347
DM 48	-74	-74	-74	-87	-124
DM 49	-92	-29	-10	53	15
DM 50	-158	-76	-70	-51	-57
DM 51	-180	-180	-161	-193	173
DM 52	-184	-184	-178	629	1574
DM 53	-184	-178	-190	-1	698
DM 54	-184	-115	93	364	975
DM 55	-184	-45	289	887	1643
DM 56	-184	31	649	1405	2167
DM 57	-184	-165	37	396	522
DM 58	-184	107	661	1083	1669
DM 59	-184	-121	377	1183	1876
DM 60	-184	-102	181	622	1158
DM 61	-184	-152	-152	207	585
DM 62	-184	-146	-121	131	194
DM 63	-180	-193	-180	9	204
DM 64	-158	-126	-120	-70	478
DM 65	-92	-29	-10	15	3
DM 66	6	12	31	69	88

Table D6 – Continued.

SB 6	Strain (με)				
Load (kN)	0	200	300	450	600
DM 67	-37	297	322	366	417
DM 68	-40	-216	-292	-387	-418
DM 69	-35	60	53	179	286
DM 70	-30	-131	-143	-156	-181
DM 71	-25	101	151	303	1348
DM 72	-23	-67	-111	-124	191
DM 73	-21	111	155	1604	4742
DM 74	-21	-97	-116	105	1302
DM 75	-21	124	149	1397	4087
DM 76	-21	-84	-116	29	659
DM 77	-21	105	370	1516	3236
DM 78	-21	-78	-90	23	130
DM 79	-21	80	483	1478	2783
DM 80	-21	-90	-134	-153	-71
DM 81	-21	250	659	4282	5668
DM 82	-21	-122	-53	-90	-153
DM 83	-21	-40	-53	-103	-147
DM 84	-21	105	407	1025	1478
DM 85	-21	-90	-172	-286	-305
DM 86	-21	42	470	1378	2946
DM 87	-21	-40	-71	-153	-185
DM 88	-21	17	263	1019	2184
DM 89	-21	-8	-34	-84	-160
DM 90	-21	92	181	716	1466
DM 91	-21	-40	-71	-210	-298
DM 92	-21	29	92	1113	2348
DM 93	-23	-92	-118	-61	229
DM 94	-25	25	88	889	2766
DM 95	-30	-68	-99	-99	178
DM 96	-35	41	97	299	1483
DM 97	-40	-72	-103	-109	-172
DM 98	-37	32	64	121	127
DM 99	6	31	31	44	75

Table D7 – SB7: Raw data on Demec strains (including prestrain).

SB 7	Strain (με)					
Load (kN)	0	200	400	500	600	700	790
DM 1	-81	-87	-100	-94	-94	-81	-94
DM 2	-73	-111	-136	-136	-149	-155	-161
DM 3	-71	-128	-172	-184	-216	-210	-222
DM 4	-71	-134	-191	-216	-235	-247	-273
DM 5	-71	-134	-216	-254	-310	-329	-355
DM 6	-71	-159	-304	-342	-399	-462	-506
DM 7	-72	-217	-381	-456	-532	-576	-633
DM 8	-71	-184	-400	-500	-550	-600	-602
DM 9	-71	-153	-350	-460	-512	-570	-580
DM 10	-72	-167	-324	-400	-463	-519	-557
DM 11	-71	-128	-241	-298	-373	-424	-468
DM 12	-71	-121	-184	-229	-254	-285	-317
DM 13	-71	-121	-166	-178	-203	-191	-210
DM 14	-71	-96	-115	-121	-140	-134	-166
DM 15	-73	-98	-117	-123	-111	-86	-35
DM 16	-81	-68	-68	-62	-56	-24	7
DM 17	-246	-227	-214	-177	-164	-88	19
DM 18	-234	-184	-146	-108	-64	144	365
DM 19	-232	-169	-106	-43	146	398	650
DM 20	-232	-144	-49	140	543	852	1198
DM 21	-232	-125	45	455	770	1148	1463
DM 22	-232	-131	864	1230	1658	2042	2389
DM 23	-232	-56	965	1343	1797	2212	2616
DM 24	-232	-49	556	990	1425	1853	2257
DM 25	-232	-49	612	990	1400	1847	2294
DM 26	-232	-62	442	833	1261	1727	2143
DM 27	-232	-93	404	745	1141	1526	2005
DM 28	-232	20	493	808	1173	1570	2036
DM 29	-232	-150	398	467	795	1154	1753
DM 30	-232	-150	-5	367	688	997	1696
DM 31	-234	-202	-139	-13	314	648	869
DM 32	-246	-227	-139	-7	107	296	1279
DM 33	-74	-36	-36	-24	-24	-24	-36

Table D7 – Continued.

SB 7	Strain (με)						
Load (kN)	0	200	400	500	600	700	790
DM 34	-110	-104	-110	-135	-142	-167	-198
DM 35	-120	-145	-164	-158	-177	-126	-32
DM 36	-121	-146	-153	-140	-89	-96	-96
DM 37	-120	-202	-208	-208	-19	220	327
DM 38	-120	-133	-139	-88	-19	31	252
DM 39	-120	-152	-95	151	302	573	819
DM 40	-120	-158	25	138	327	441	523
DM 41	-120	-158	19	233	472	850	1178
DM 42	-120	-95	12	258	586	989	1518
DM 43	-120	-139	-114	-32	151	252	82
DM 44	-121	-159	-127	-108	-115	-108	-436
DM 45	-120	-152	-139	-107	-44	88	3011
DM 46	-120	-139	-145	-133	-164	-164	-920
DM 47	-120	-145	-164	-177	-233	-246	-555
DM 48	-74	-87	-80	-93	-87	-93	-232
DM 49	-92	3	40	59	53	72	91
DM 50	-158	-133	-114	-95	-120	-89	31
DM 51	-180	-130	-161	-123	-35	217	343
DM 52	-184	-77	-45	-33	112	364	667
DM 53	-184	-165	-102	-33	282	471	692
DM 54	-184	-146	-39	295	534	925	1114
DM 55	-184	-89	226	604	919	1177	1410
DM 56	-184	-115	283	586	888	1127	1373
DM 57	-184	-121	459	837	1234	1656	2097
DM 58	-184	-127	252	504	838	1197	1228
DM 59	-184	-102	282	736	1202	1530	1756
DM 60	-184	-96	100	352	711	1221	1914
DM 61	-184	-146	11	213	566	931	673
DM 62	-184	-152	-152	-108	-52	-140	-562
DM 63	-180	-111	3	66	299	444	4803
DM 64	-158	-158	-133	-95	-63	157	-568
DM 65	-92	-60	-29	-23	-23	-10	-180
DM 66	6	-120	-202	-328	-246	-347	-410

Table D7 – Continued.

SB 7	Strain (με)						
Load (kN)	0	200	400	500	600	700	790
DM 67	-37	7	39	39	51	58	76
DM 68	-40	-179	-317	-374	-424	-468	-531
DM 69	-35	72	135	167	217	324	627
DM 70	-30	-137	-238	-301	-383	-402	-402
DM 71	-25	57	114	240	511	1103	1865
DM 72	-23	-80	-187	-218	-237	-231	-130
DM 73	-21	36	105	206	678	1617	2783
DM 74	-21	-97	-179	-229	-191	86	477
DM 75	-21	17	80	187	1031	2216	3665
DM 76	-21	-122	-191	-229	-248	-153	250
DM 77	-21	36	130	540	1075	2083	3312
DM 78	-21	-128	-210	-223	-210	-46	124
DM 79	-21	23	218	773	1283	2127	2801
DM 80	-21	-122	-254	-267	-260	-235	-298
DM 81	-21	-2	118	275	477	666	792
DM 82	-21	-172	-147	-109	-84	-34	11
DM 83	-21	-122	-153	-109	-65	17	86
DM 84	-21	-59	92	269	578	930	1378
DM 85	-21	-109	-223	-242	-273	-298	-248
DM 86	-21	11	370	981	1957	3028	5328
DM 87	-21	-109	-235	-279	-210	17	830
DM 88	-21	-2	225	767	1838	3331	6424
DM 89	-21	-141	-317	-323	-122	244	1535
DM 90	-21	4	168	634	1611	2745	4698
DM 91	-21	-153	-305	-361	-330	-330	596
DM 92	-21	17	67	294	949	1604	6619
DM 93	-23	-124	-275	-338	-237	27	7367
DM 94	-25	-6	158	479	1166	2123	11013
DM 95	-30	-200	-358	-484	-559	-490	-685
DM 96	-35	-67	-67	47	198	658	469
DM 97	-40	-223	-424	-525	-613	-720	-758
DM 98	-37	-132	-182	-232	-245	-270	-132
DM 99	6	-152	-309	-378	-441	-511	-485

APPENDIX E –LVDT DATA FOR SHEAR BEAM TESTS

In this appendix, the raw experimental data of LVDTs 1 to 7 used in the experimental program are presented. The layout and numbering of the LVDTs are given in Figure E1.

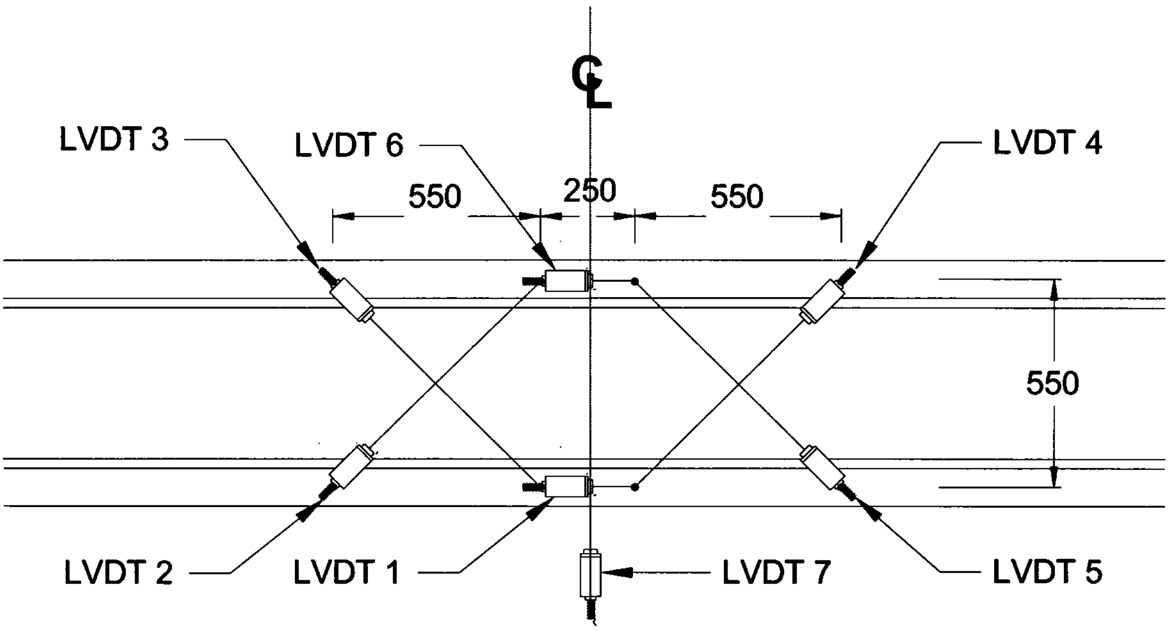

Figure E1 – Layout and numbering of LVDTs.

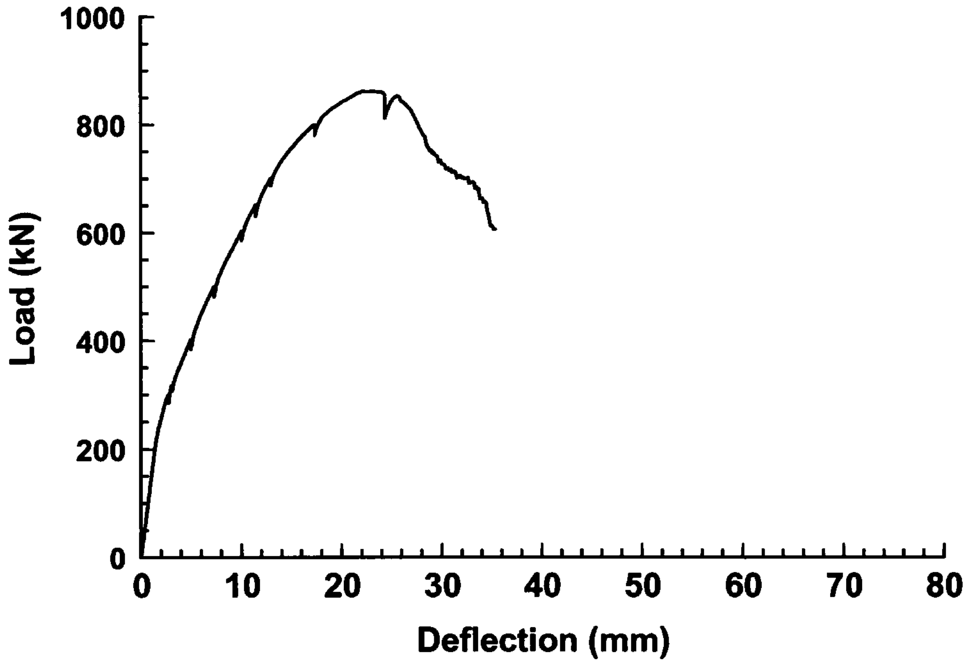

Figure E2 – SB1: load versus LVDT 7.

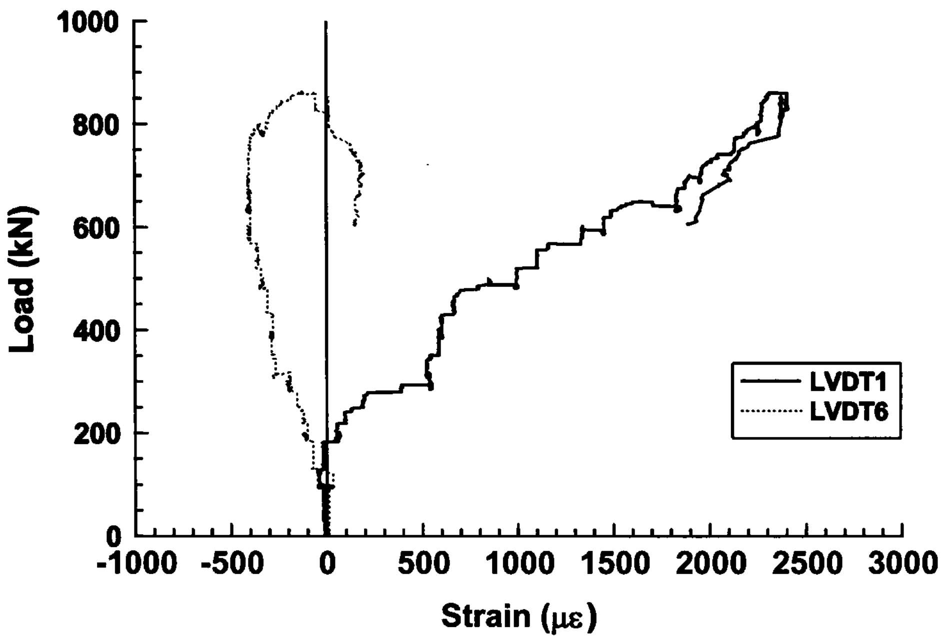

Figure E3 – SB1: load Versus LVDTs 1 and 6.

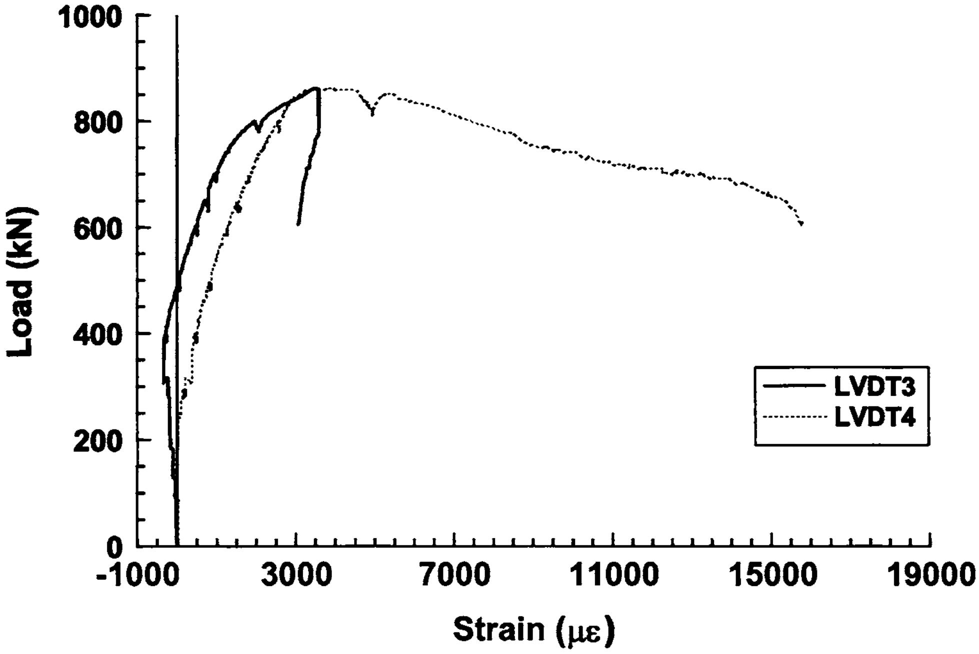

Figure E4 – SB1: load Versus LVDTs 3 and 4.

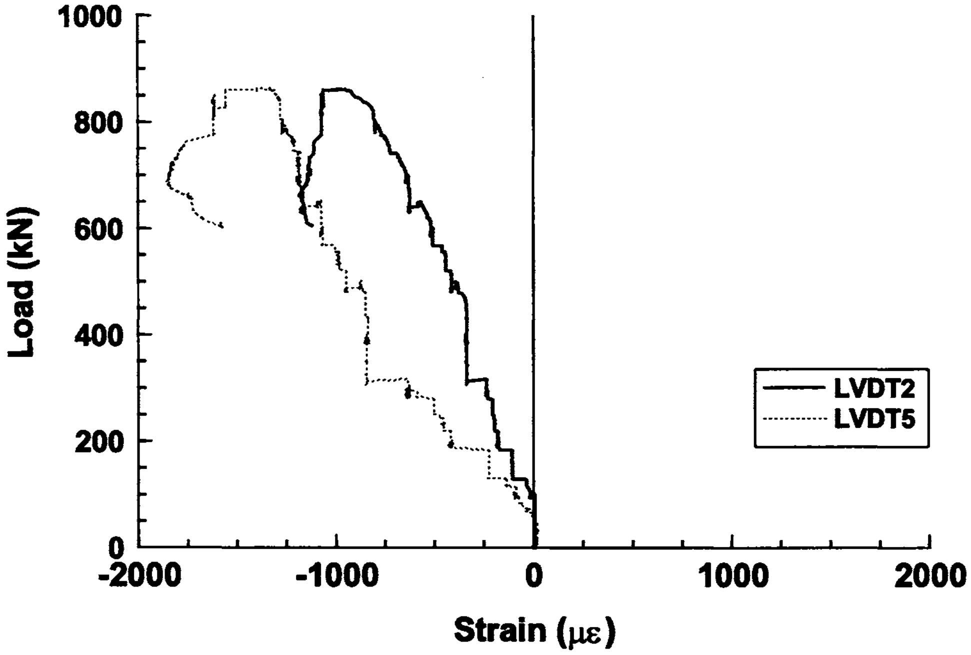

Figure E5 – SB1: load Versus LVDTs 2 and 5.

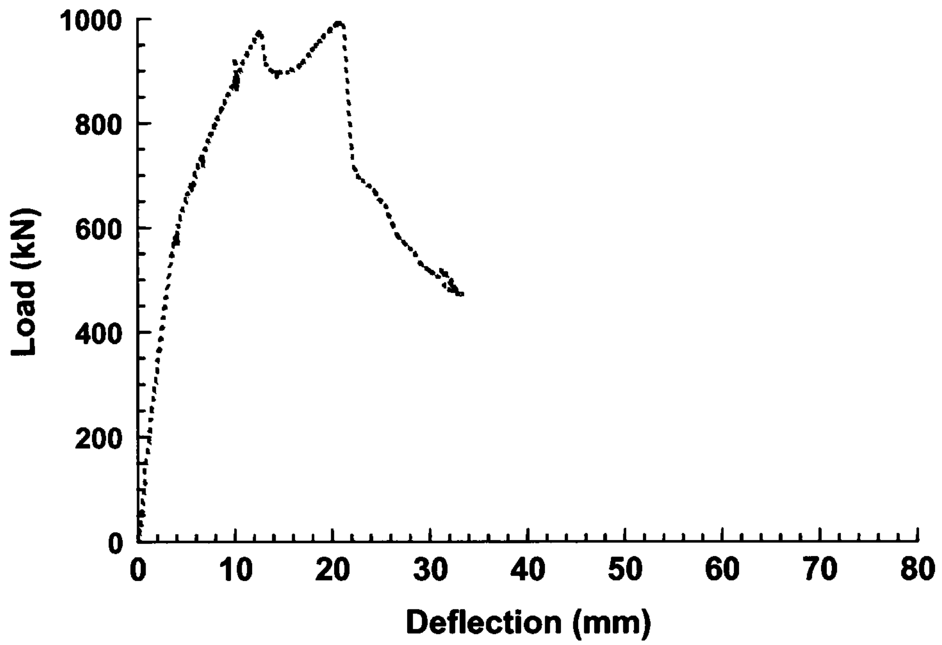

Figure E6 – SB2: load Versus LVDT 7.

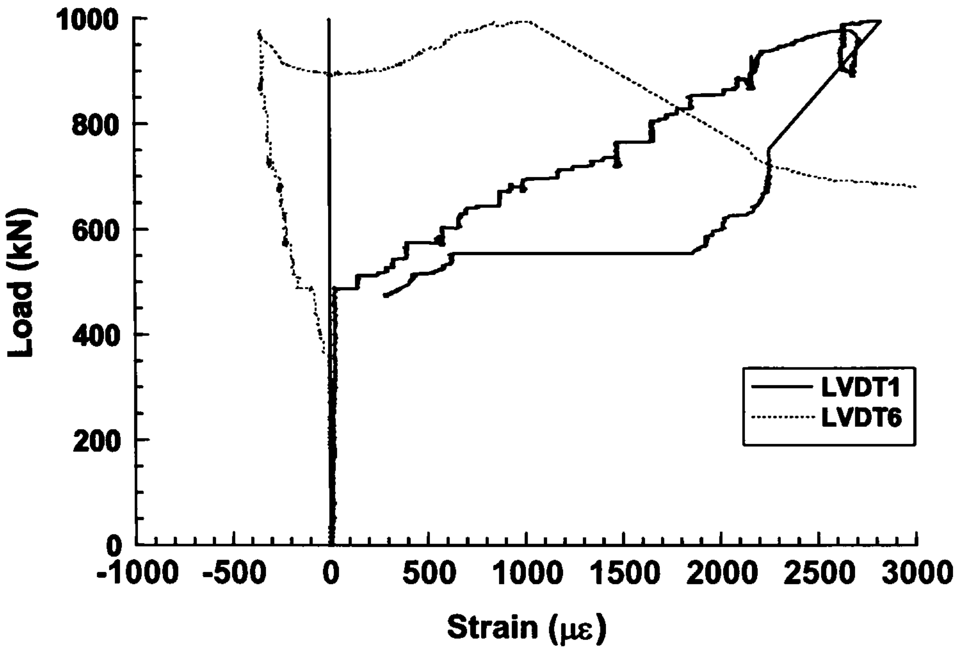

Figure E7 – SB2: load Versus LVDTs 1 and 6.

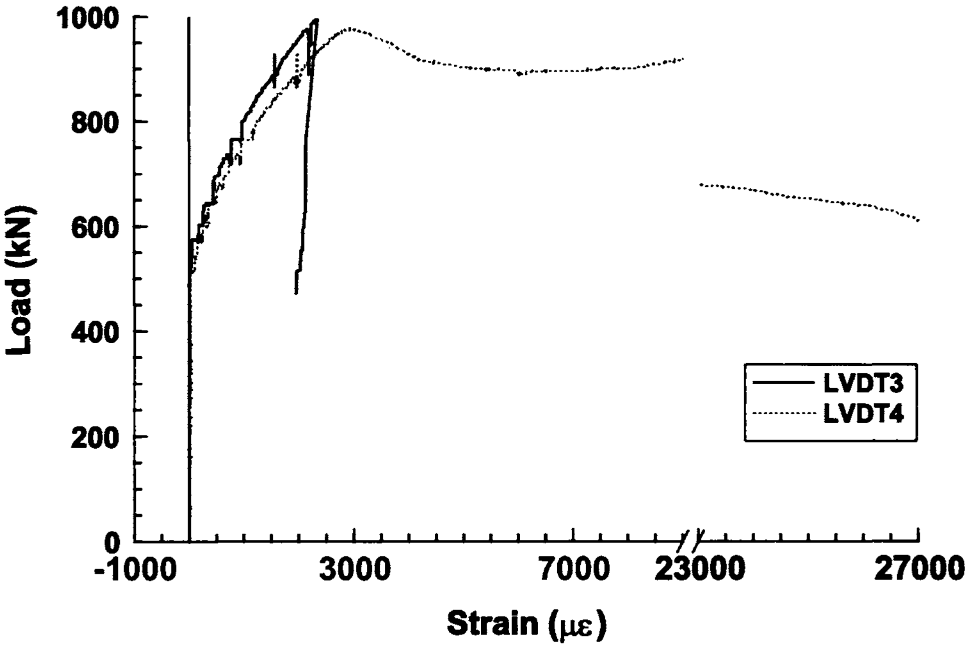

Figure E8 – SB2: load Versus LVDTs 3 and 4.

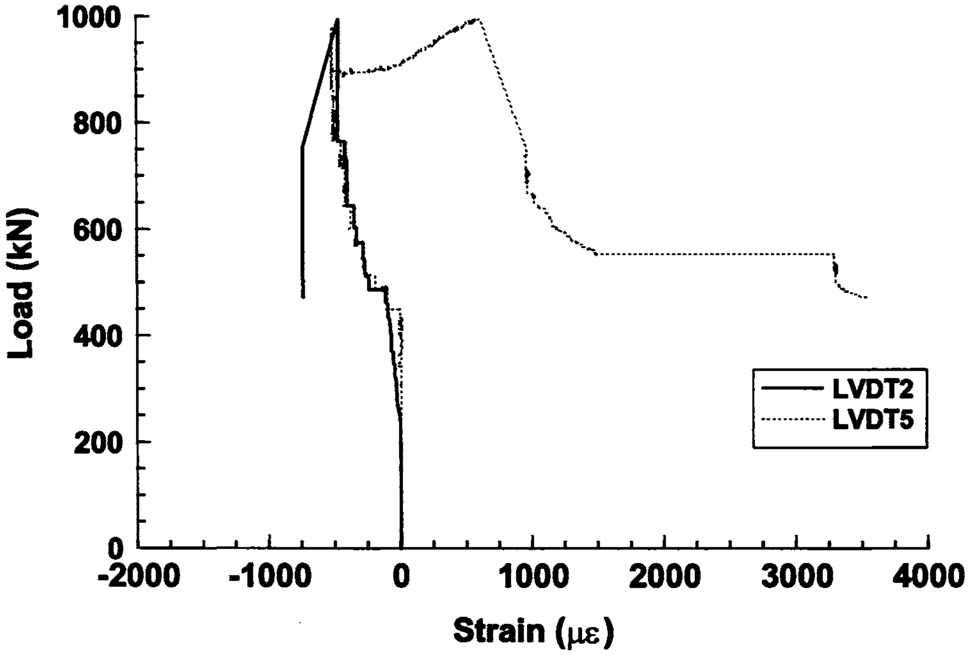

Figure E9 – SB2: load Versus LVDTs 2 and 5.

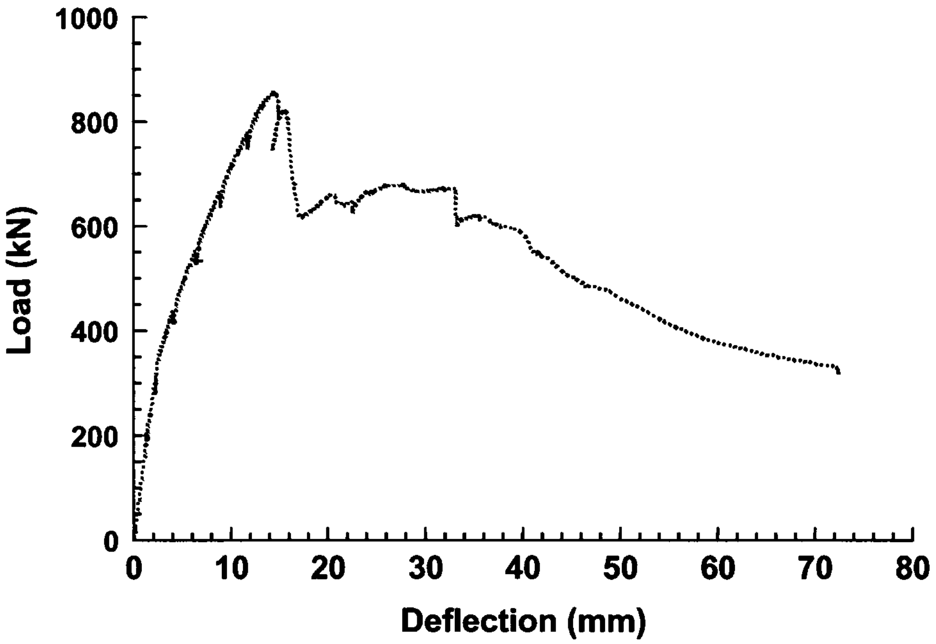

Figure E10 – SB3: load Versus LVDT 7.

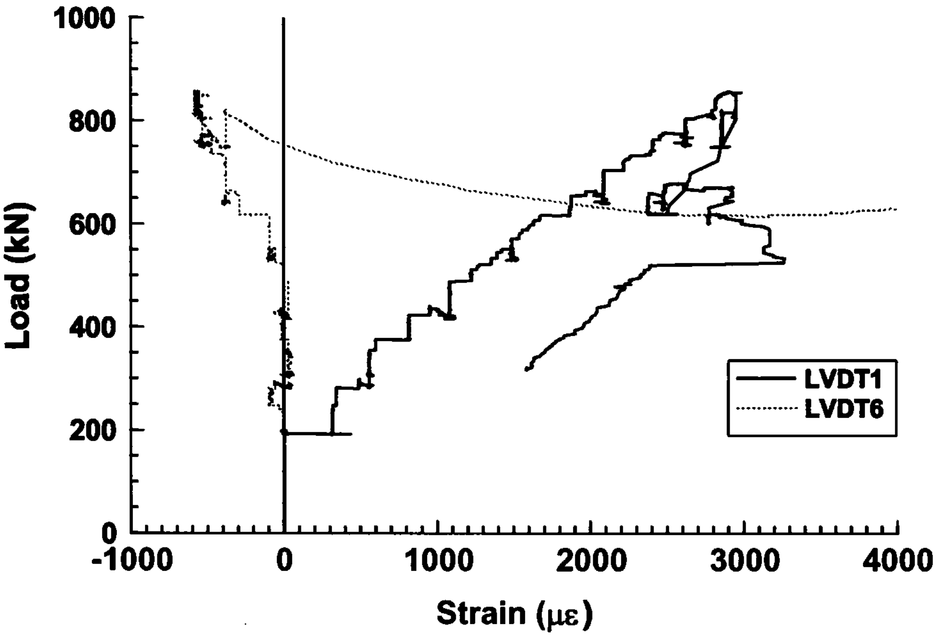

Figure E11 – SB3: load Versus LVDTs 1 and 6.

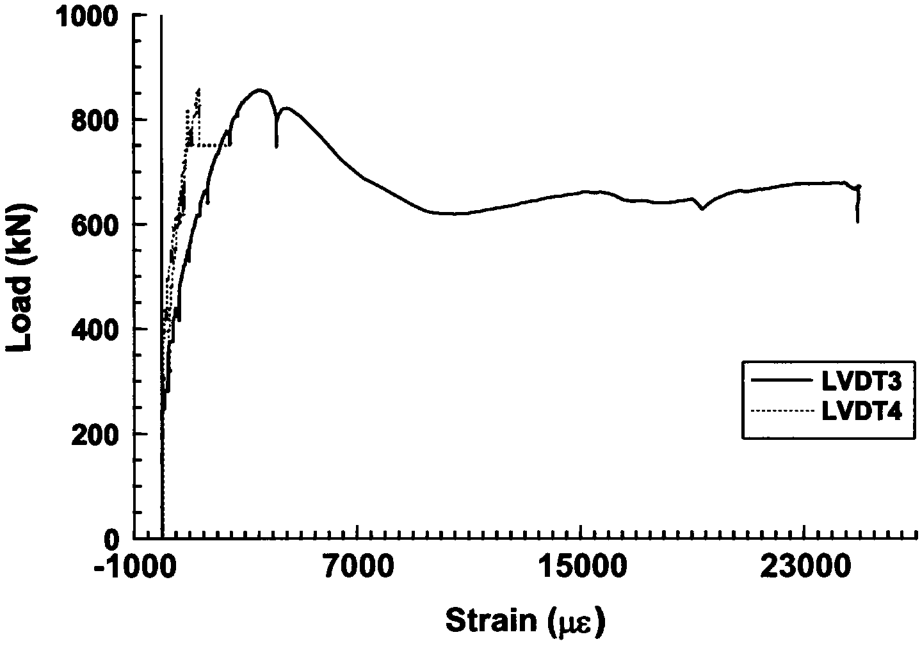

Figure E12 – SB3: load Versus LVDTs 3 and 4.

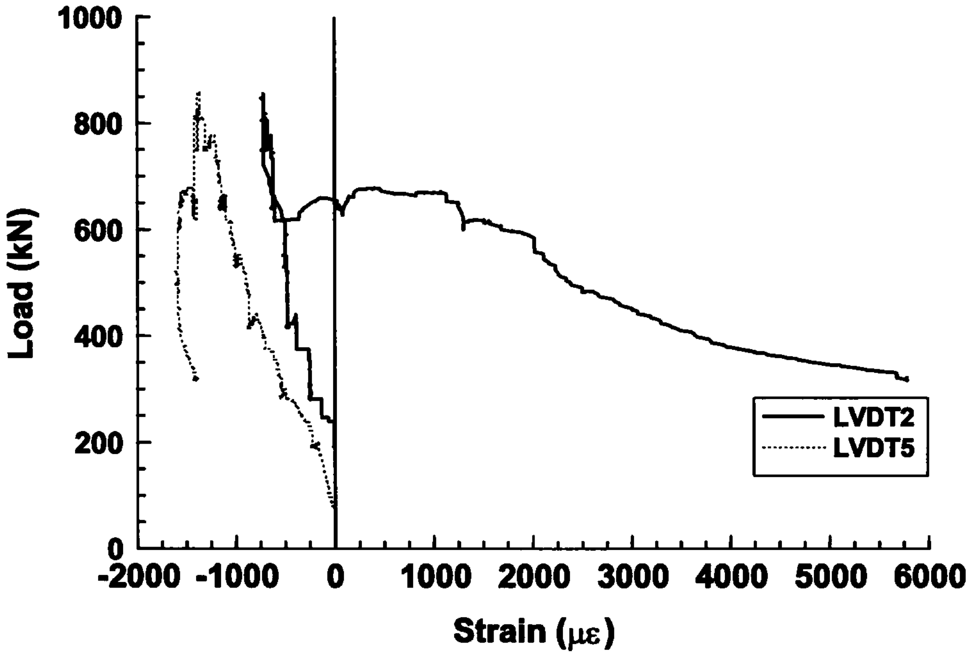

Figure E13 – SB3: load Versus LVDTs 2 and 5.

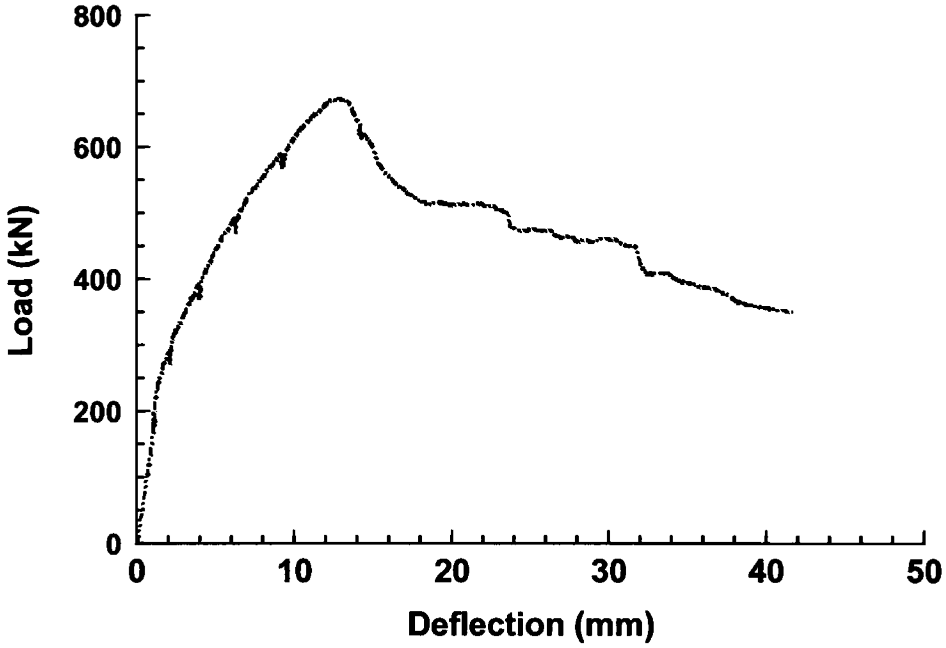

Figure E14 – SB4: load Versus LVDT 7.

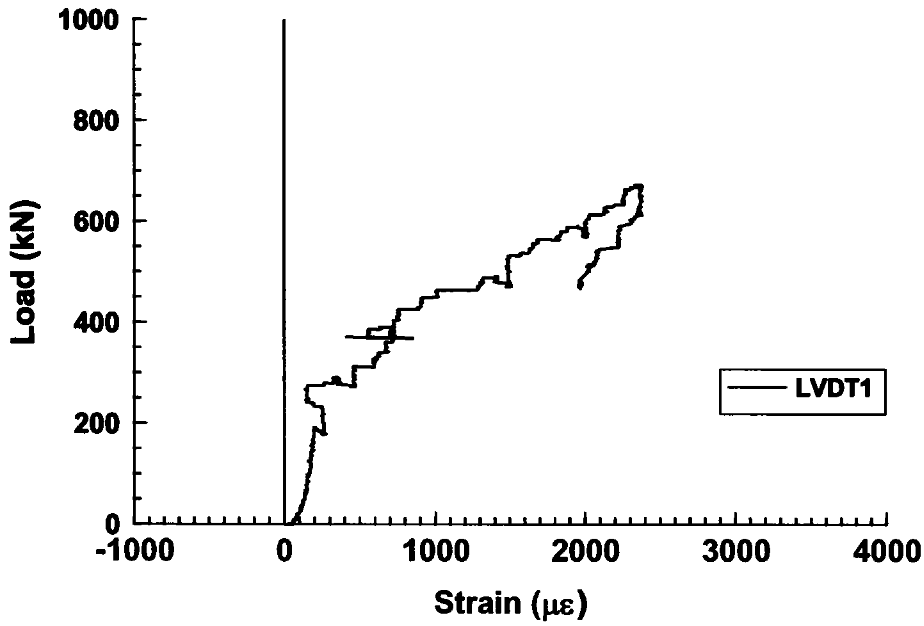

Figure E15– SB4: load Versus LVDTs 1 and 6.

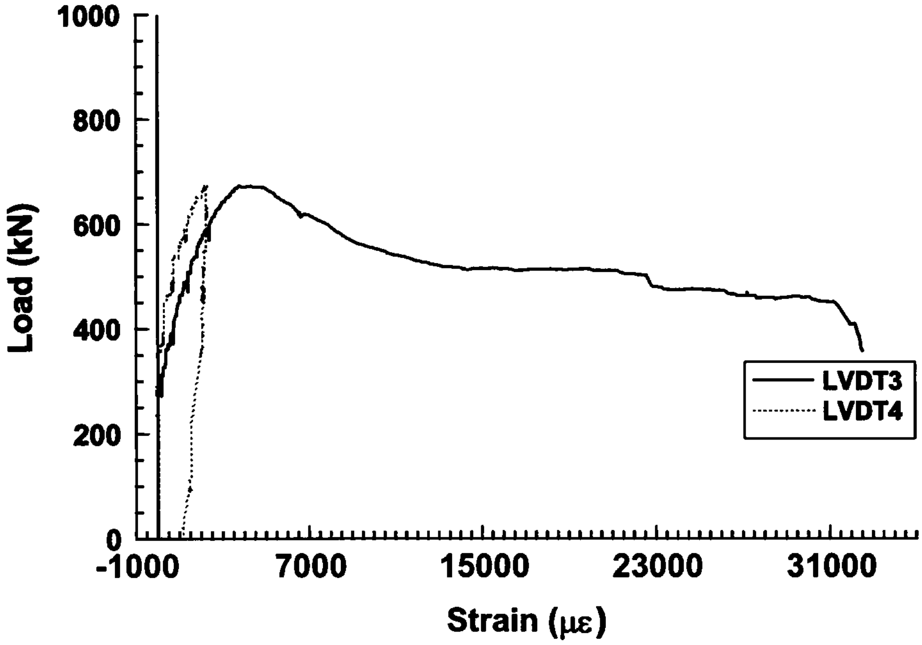

Figure E16 – SB4: load Versus LVDTs 3 and 4.

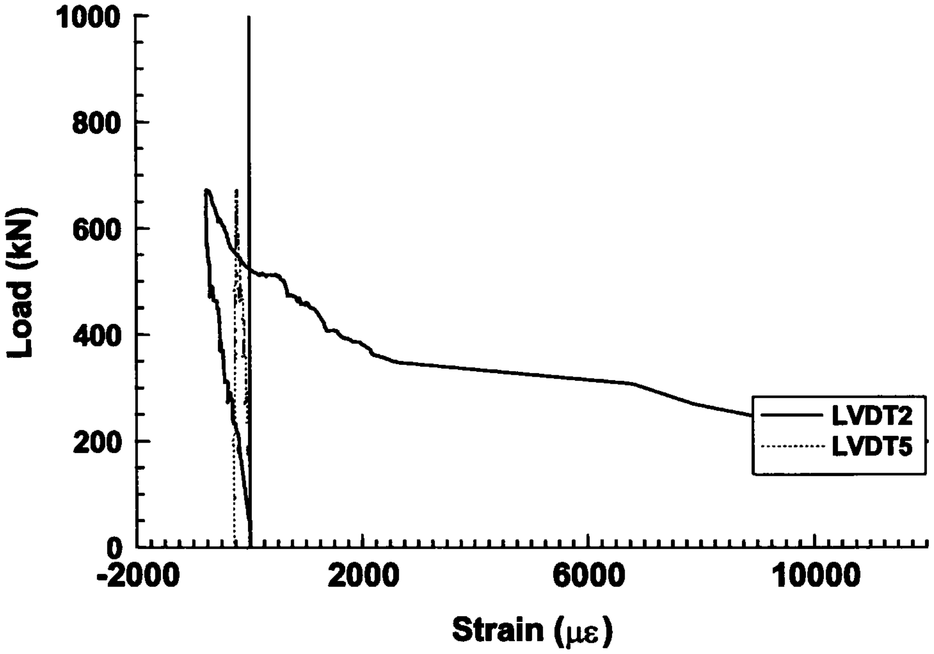

Figure E17 – SB4: load Versus LVDTs 2 and 5.

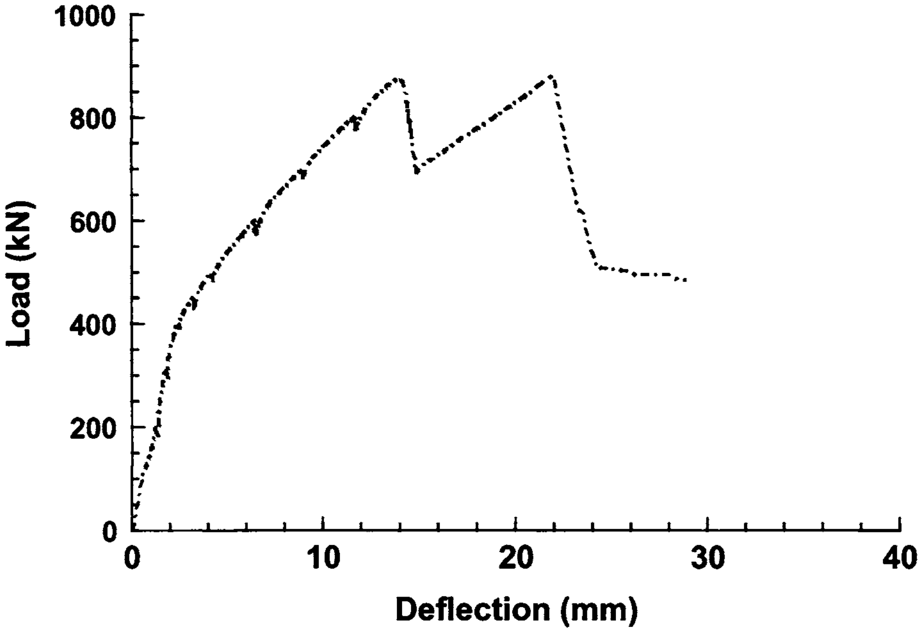

Figure E18 – SB5: load Versus LVDT 7.

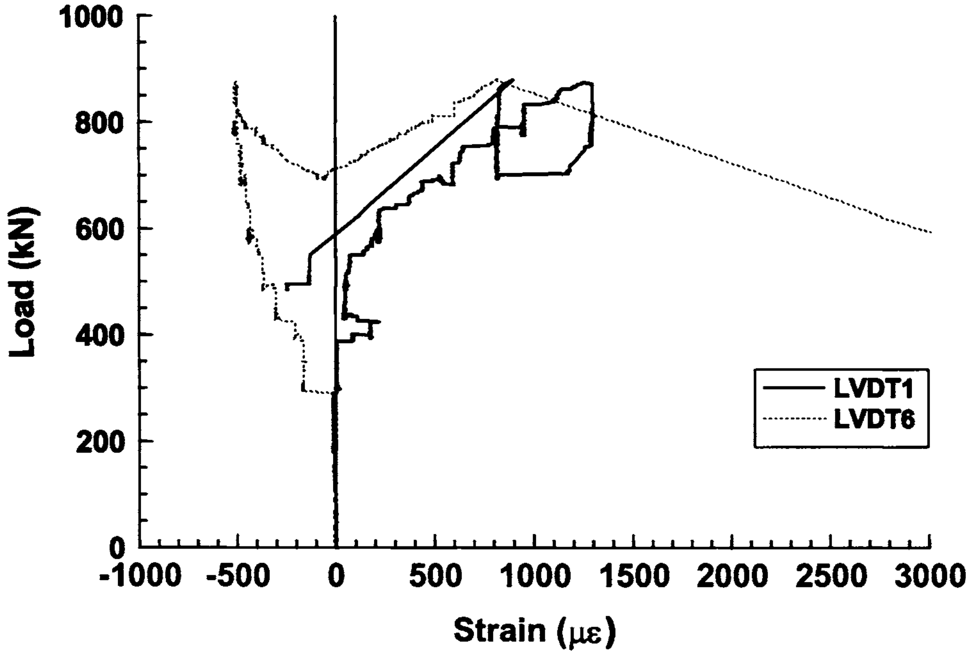

Figure E19 – SB5: load Versus LVDTs 1 and 6.

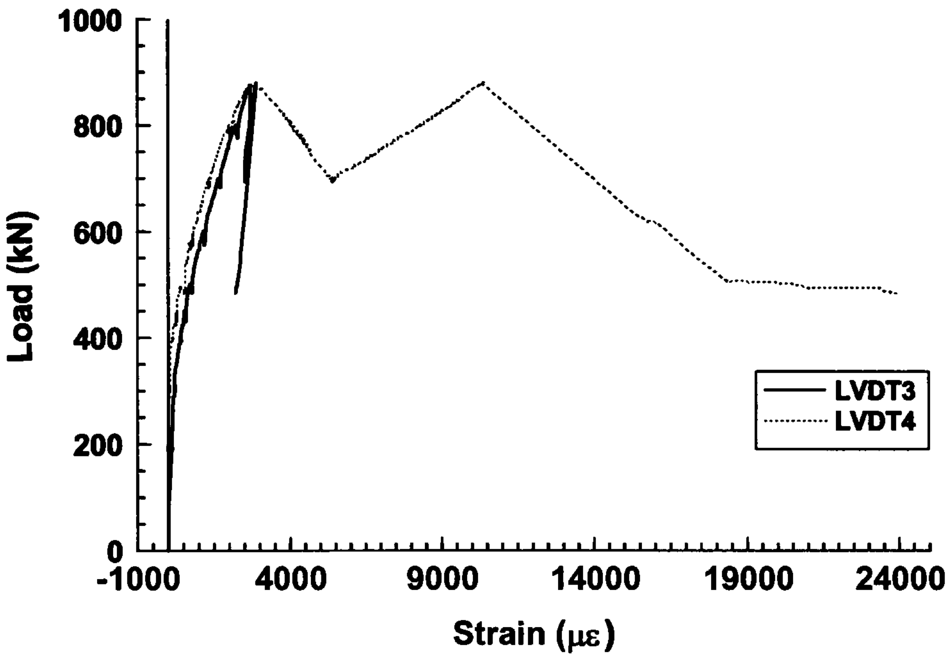

Figure E20 – SB5: load Versus LVDTs 3 and 4.

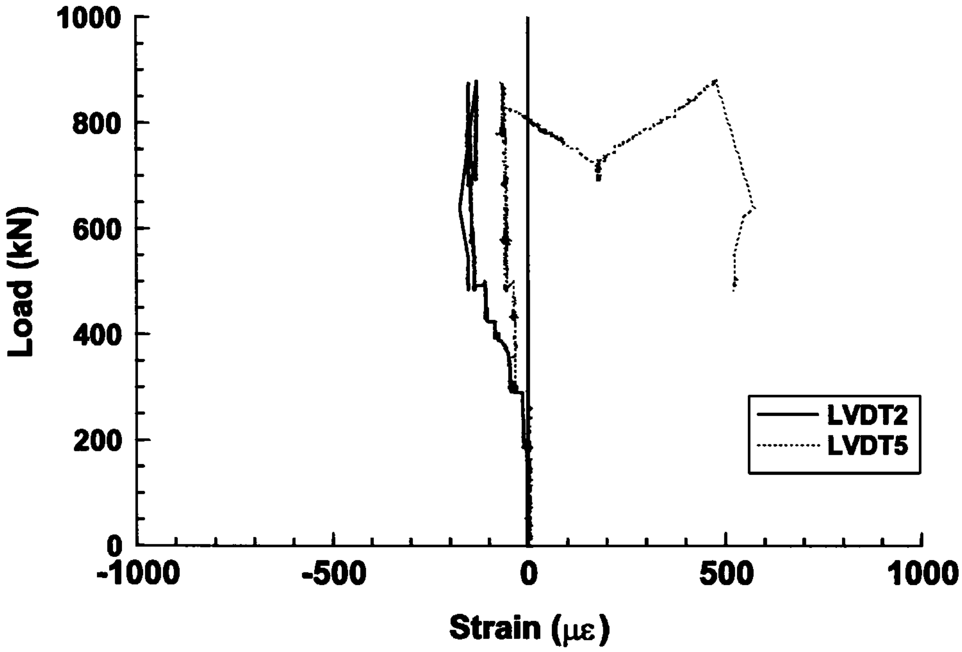

Figure E21– SB5: load Versus LVDTs 2 and 5.

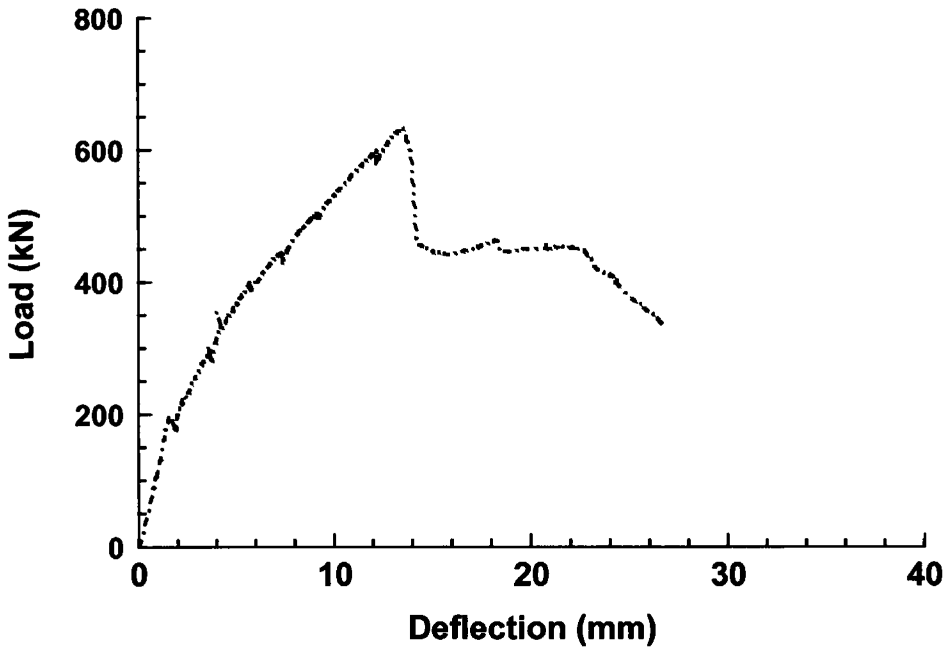

Figure E22 – SB6: load Versus LVDT 7.

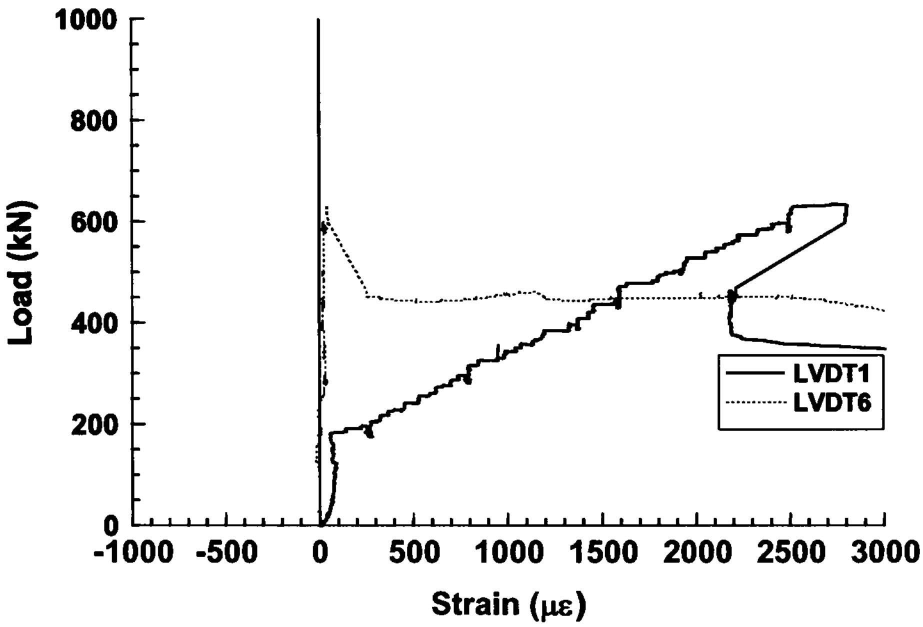

Figure E23 – SB6: load Versus LVDTs 1 and 6.

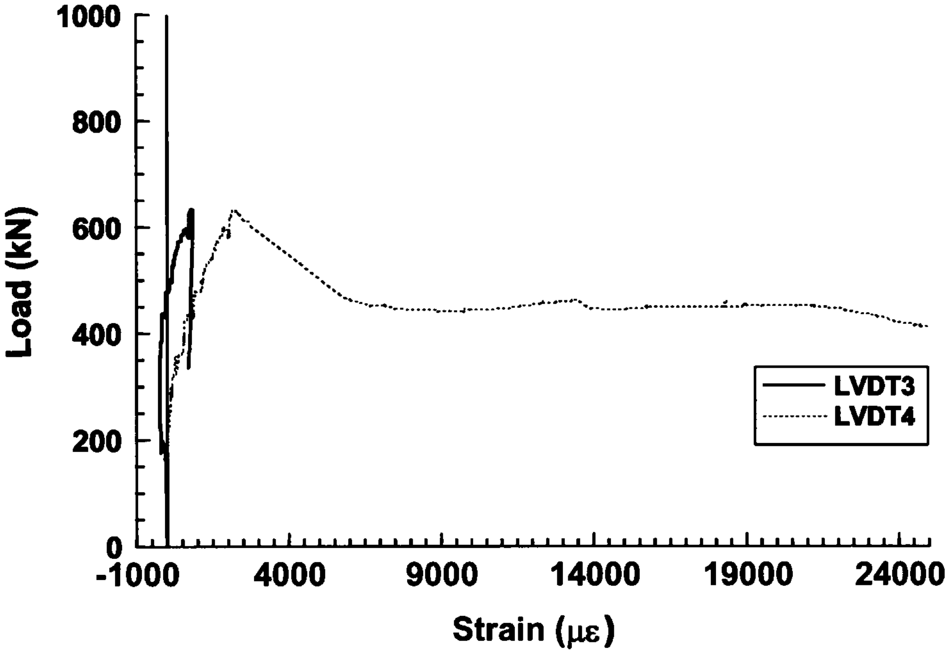

Figure E24 – SB6: load Versus LVDTs 3 and 4.

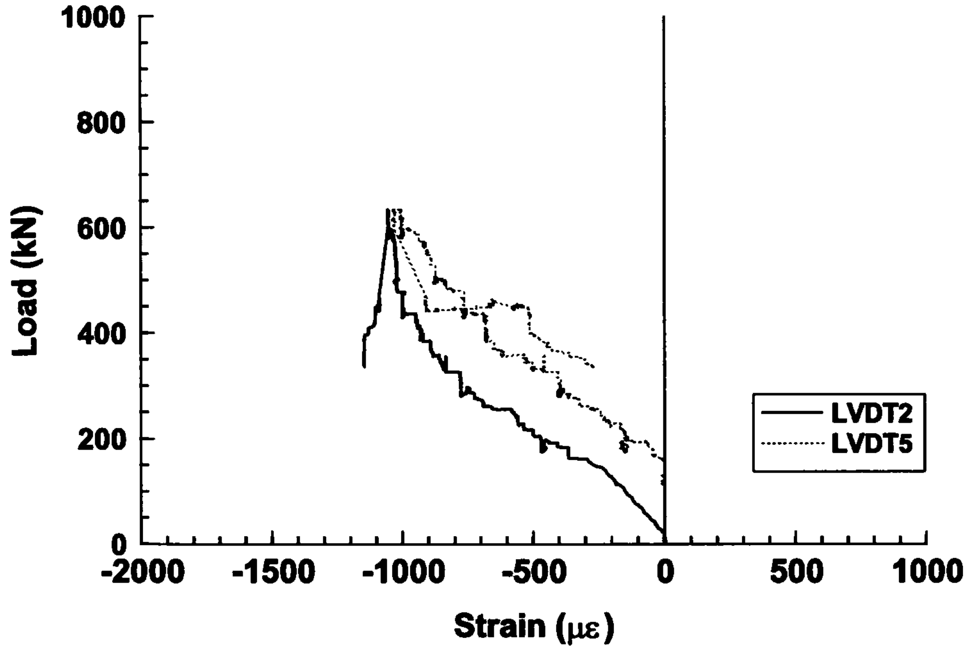

Figure E25 – SB6: load Versus LVDTs 2 and 5.

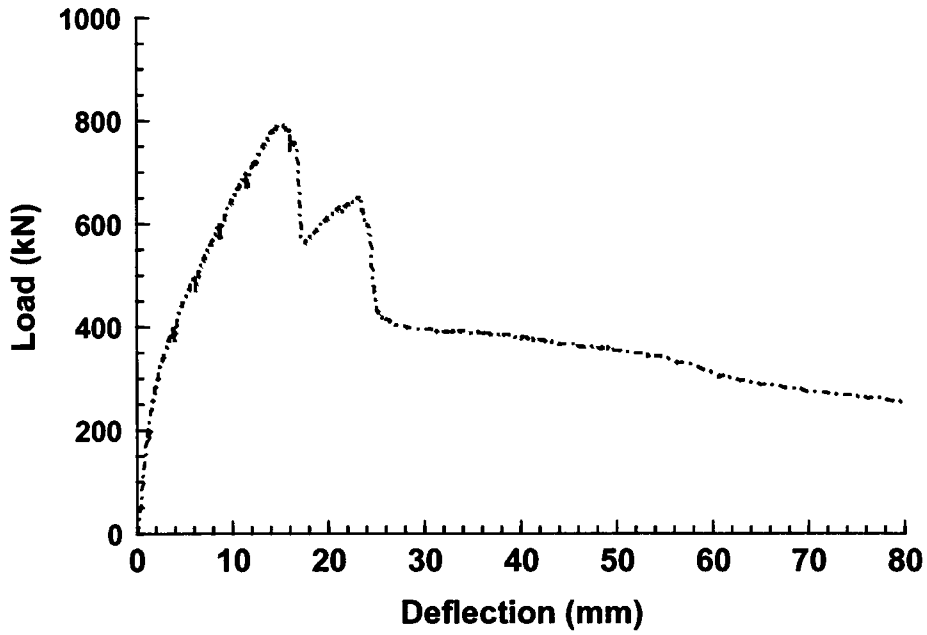

Figure E26 – SB7: load Versus LVDT 7.

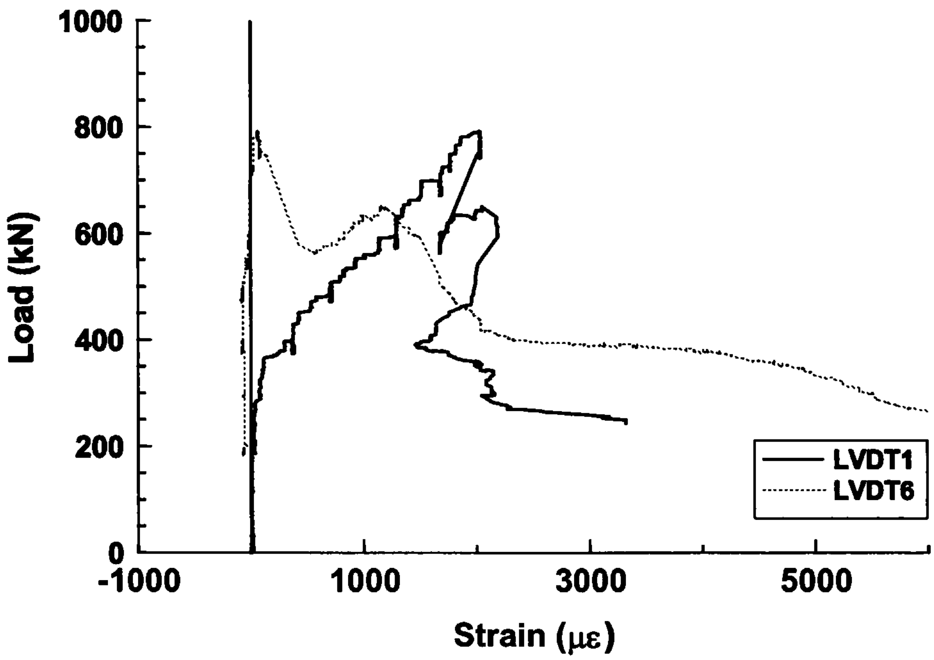

Figure E27 – SB7: load Versus LVDTs 1 and 6.

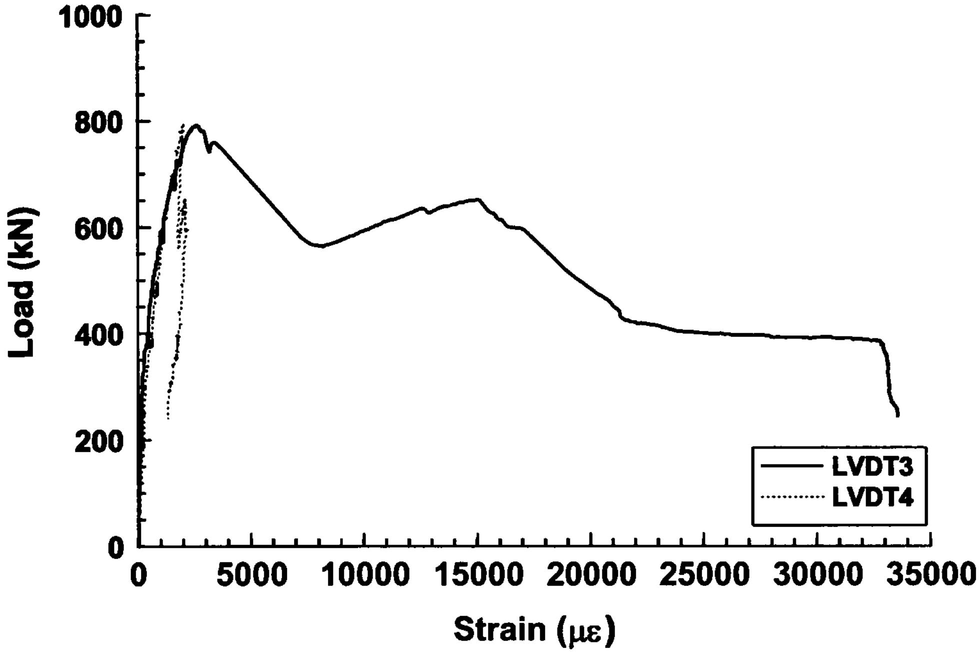

Figure E28 – SB7: load Versus LVDTs 3 and 4.

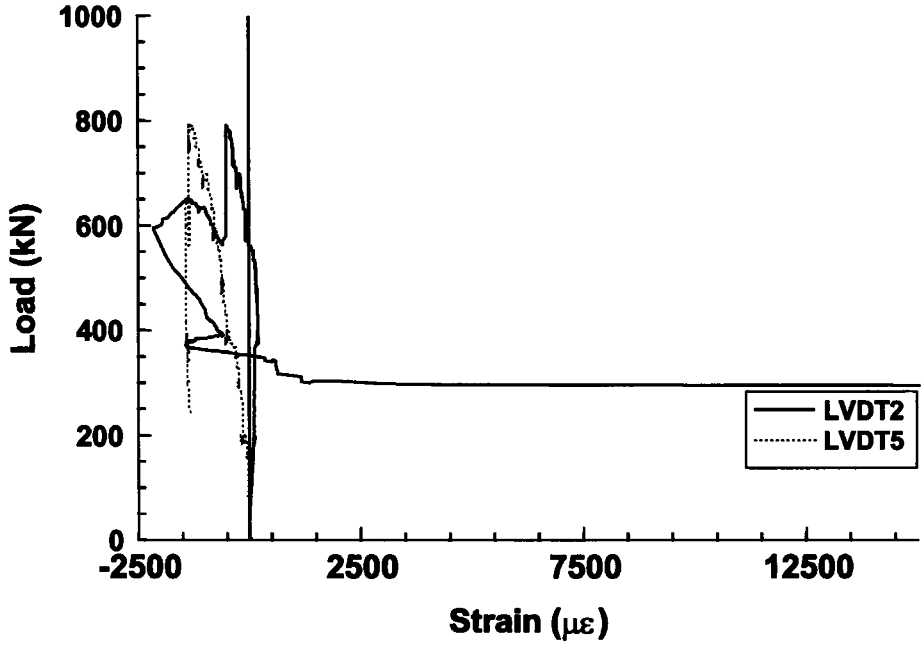

Figure E29 – SB7: load Versus LVDTs 2 and 5.

APPENDIX F – MATERIAL DATA FOR SPECIMENS USED IN VEM VERIFICATION

Table F1 – Comparison of VEM with straight steel FRC (Lim et al., 1987b).

	Lim et al. (1987)			
Fibre Properties - Steel				
Type	Steel	Steel	Steel	Steel
Configuration	S	S	S	S
l_f, mm	30	30	30	50
d_f, mm	0.565	0.565	0.565	0.565
E_f, GPa	210	210	210	210
σ_{fu}, MPa	345	345	345	345
ε_{fu}, με	1640	1640	1640	1640
Matrix Properties				
Type	NSC	NSC	NSC	NSC
E_m, GPa	21.9	21.9	21.9	21.9
f_{ct}, MPa	2.19	2.19	2.19	2.19
ε_{ct}, με	100	100	100	100
w/b ratio	0.5	0.5	0.5	0.5
s/c ratio	0	0	0	0
f_{cm}, MPa	-	-	-	-
Composite and Testing Properties				
Specimen Section, mm	70×100	70×100	70×100	70×100
Extension Rate, mm/min	0.25	0.25	0.25	0.25
Gauge length, mm	200	200	200	200
f_{cm}, MPa	-	-	-	-
ρ_f, %	0.5	1.0	1.5	1.0
Exp. $f_{ct,c}$, MPa	2.46	2.55	2.33	2.42
Exp. G_F, N/mm	-	-	-	-
τ_b, MPa	2.75	3.05	2.71	1.73
K_d	1	1	1	1
l_c, mm	35	32	36	56
Failure mode	P	P	P	P
α	0.15	0.15	0.15	0.15
d_f / α	3.77	3.77	3.77	3.77
Theo. $f_{ct,c}$, MPa	2.19	2.19	2.19	2.19
Theo. G_F, N/mm	-	-	-	-
$f_{ct,c}$ VEM / $f_{ct,c}$ Exp.	0.90	0.86	0.94	0.97
G_F VEM / G_F Exp.	-	-	-	-

S	straight fibre	EH	end-hooked fibre
NSC	normal strength concrete	#	determined from Table 2
P	pull through of fibres only	PF	pull though and fracture of fibres
*	mean of split cylinder tests	↑	taken as 0.8 of the cube strength

Table F2 – Comparison of VEM with end-hooked steel FRC (Lim et al., 1987b).

	Lim et al. (1987b)			
Fibre Properties - Steel				
Type	Steel	Steel	Steel	Steel
Configuration	EH	EH	EH	EH
l_f, mm	30	30	30	50
d_f, mm	0.5	0.5	0.5	0.5
E_f, GPa	200	200	200	200
σ_{fu}, MPa	1130	1130	1130	1130
ε_{fu}, $\mu\varepsilon$	5650	5650	5650	5650
Matrix Properties				
Type	NSC	NSC	NSC	NSC
E_m, GPa	25.3	25.3	25.3	25.3
f_{ct}, MPa	2.66	2.66	2.66	2.66
ε_{ct}, $\mu\varepsilon$	105	105	105	105
w/b ratio	0.5	0.5	0.5	0.5
s/c ratio	0	0	0	0
f_{cm}, MPa	-	-	-	-
Composite and Testing Properties				
Specimen Section, mm	70×100	70×100	70×100	70×100
Extension Rate, mm/min	0.25	0.25	0.25	0.25
Gauge length, mm	200	200	200	200
f_{cm}, MPa	-	-	-	-
ρ_f, %	0.5	1.0	1.5	1.0
Exp. $f_{ct,c}$, MPa	2.78	3.04	3.03	2.84
Exp. G_F, N/mm	-	-	-	-
τ_b, MPa	6.87	6.72	7.10	5.85
K_d	1	1	1	1
l_c., mm	41	42	40	48
Failure mode	P	P	P	PF
α	0.15	0.15	0.15	0.15
d_f / α	3.33	3.33	3.33	3.33
Theo. $f_{ct,c}$, MPa	2.66	2.66	2.66	2.66
Theo. G_F, N/mm	-	-	-	-
$f_{ct,c}$ VEM / $f_{ct,c}$ Exp.	0.96	0.95	0.88	0.94
G_F VEM / G_F Exp.	-	-	-	-

S	straight fibre	EH	end-hooked fibre
NSC	normal strength concrete	NSM	normal strength mortar
HSC	high strength concrete	#	determined from Table 2
P	pull through of fibres only	PF	pull though and fracture of fibres
†	assumed value	††	net dimension after notched
*	mean of split cylinder tests	↑	taken as 0.8 of the cube strength
‡	determined from $0.33\sqrt{f_{cm}}$		

Table F3 – Comparison of VEM with steel FRC (Petersson, 1980, Barragán et al., 2003 and Li et al., 1998).

	Petersson (1980)			Barragán et al. (2003)	Li et al. (1998)
Fibre Properties - Steel					
Type	Steel	Steel	Steel	Steel-Dramix	Steel
Configuration	S	S	S	EH	EH
l_f, mm	30	30	30	60	30
d_f, mm	0.3	0.3	0.3	0.75	0.5
E_f, GPa	-	-	-	-	200
σ_{fu}, MPa	1000†	1000†	1000†	1000	1000
ε_{fu}, $\mu\varepsilon$	-	-	-	-	-
Matrix Properties					
Type	NSM	NSM	NSM	NSC	NSC
E_m, GPa	-	-	-	-	-
f_{ct}, MPa	3	3	3	2.12‡	4.2
ε_{ct}, $\mu\varepsilon$	-	-	-	-	-
w/b ratio	0.6	0.6	0.6	0.57	0.4
s/c ratio	0	0	0	0	0.1
f_{cm}, MPa	-	-	-	41.1	52
Composite and Testing Properties					
Specimen Section, mm	20×30††	20×30††	20×30††	dia. 120††	100×20
Extension Rate, mm/min	0.02-2.0	0.02-2.0	0.02-2.0	0.005-0.5	0.004
Gauge length, mm	-	-	-	25	120
f_{cm}, MPa	-	-	-	-	-
ρ_f, %	0.25	0.5	1.0	0.45	6
Exp. $f_{ct,c}$, MPa	3.0	3.0	3.0	2.6	-
Exp. G_F, N/mm (partial)	1.69	4.10	7.10	1.84	9.04
w @ Exp G_F, mm	7	7	7	2	1
τ_b, MPa	3.0$^{\#}$	3.0$^{\#}$	3.0$^{\#}$	5.3$^{\#}$	10.5$^{\#}$
K_d	1	1	1	1	1
l_c., mm	41	42	40	71	23.8
Failure mode	P	P	P	P	PF
α	0.08	0.08	0.08	0.2	0.133
d_f / α	3.75	3.75	3.75	3.75	3.75
Theo. $f_{ct,c}$, MPa	3.0	3.0	3.0	2.12	-
Theo. G_F N/mm (partial)	1.55	3.05	6.06	1.64	8.90
$f_{ct,c}$ VEM / $f_{ct,c}$ Exp.	1.0	1.0	1.0	0.82	-
G_F VEM / G_F Exp.	0.92	0.74	0.85	0.89	0.99

S	straight fibre	EH	end-hooked fibre
NSC	normal strength concrete	#	determined from Table 2
P	pull through of fibres only	PF	pull though and fracture of fibres
†	assumed value	††	net dimension after notched
*	mean of split cylinder tests	‡	determined from $0.33\sqrt{f_{cm}}$

Table F4 – Comparison of VEM with steel FRC (Groth, 2000).

	Groth (2000)			
Fibre Properties - Steel				
Type	Steel	Steel	Steel	Steel
Configuration	S	S	S	S
l_f, mm	20	20	20	20
d_f, mm	0.13	0.13	0.13	0.13
E_f, GPa	200	200	200	200
σ_{fu}, MPa	1000	1000	1000	1000
ε_{fu}, $\mu\varepsilon$	-	-	-	-
Matrix Properties				
Type	NSM-OPC	NSM-S50	NSM-Q50	NSM-EMC500
E_m, GPa	-	-	-	-
f_{ct}, MPa	2.22‡	2.32‡	1.80‡	2.40‡
ε_{ct}, $\mu\varepsilon$	-	-	-	-
w/b ratio	0.5	0.5	0.5	0.5
s/c ratio	0	0	0	0.05
f_{cm}, MPa	45.3↑	49.4↑	28.8↑	52↑
Composite and Testing Properties				
Specimen Section, mm	dia. 90	dia. 90	dia. 90	dia. 90
Extension Rate, mm/min	-	-	-	-
Gauge length, mm	-	-	-	-
f_{cm}, MPa	44.1↑	-	-	-
ρ_f, %	0.7	0.7	0.7	0.7
Exp. $f_{ct,c}$, MPa	3.3	4.2	3.7	3.3
Exp. G_F, N/mm (partial)	1.82	1.61	1.39	1.78
w @ Exp G_F, mm	1.5	1.5	1.5	1.5
τ_b, MPa	2.22#	2.32#	1.8#	2.4#
K_d	1	1	1	1
l_c, mm	29	28	36	27
Failure mode	P	P	P	P
α	0.04	0.04	0.04	0.04
d_f / α	1	1	1	1
Theo. $f_{ct,c}$, MPa	2.96	3.58	3.49	2.80
Theo. G_F, N/mm (partial)	1.51	1.57	1.24	1.64
$f_{ct,c}$ VEM / $f_{ct,c}$ Exp.	0.90	0.85	0.94	0.85
G_F VEM / G_F Exp.	0.83	0.96	0.89	0.92

S	straight fibre	EH	end-hooked fibre
NSC	normal strength concrete	NSM	normal strength mortar
HSC	high strength concrete	#	determined from Table 2
P	pull through of fibres only	PF	pull though and fracture of fibres
†	assumed value	††	net dimension after notched
*	mean of split cylinder tests	↑	taken as 0.8 of the cube strength
‡	determined from $0.33\sqrt{f_{cm}}$		

Table F5 – Comparison of VEM with high-strength and high-modulus polyethylene FRC (Wang et al., 1990a, b).

	Wang et al. (1990a,b)		
Fibre Properties - Steel			
Type	Spectra 900	Spectra 900	Spectra 900
Configuration	S	S	S
l_f, mm	12.7	12.7	6.35
d_f, mm	0.038	0.038	0.038
E_f, GPa	120	120	120
σ_{fu}, MPa	2600	2600	2600
ε_{fu}, $\mu\varepsilon$	3500	3500	3500
Matrix Properties			
Type	NSM	NSM	HSC
E_m, GPa	-	-	-
f_{ct}, MPa	1.8*	1.8*	4.2
ε_{ct}, $\mu\varepsilon$	-	-	-
w/b ratio	0.5	0.5	0.22
s/c ratio	0	0	0.133
f_{cm}, MPa	-	-	-
Composite and Testing Properties			
Specimen Section, mm	50.8×50.8††	50.8×50.8††	50.8×50.8††
Extension Rate, mm/min	0.3-1.5	0.3-1.5	0.3-1.5
Gauge length, mm	12.7	12.7	12.7
f_{cm}, MPa	-	-	-
ρ_f, %	1	2	0.6
Exp. $f_{ct,c}$, MPa	2.39	2.70	4.21
Exp. G_F, N/mm (full curve)	5.98	5.62	0.85
τ_b, MPa	1.02	1.02	1.5
K_d	-	0.8	-
l_c, mm	48	48	33
Failure mode	P	P	P
α	0.10	0.10	0.10
d_f / α	0.76	0.76	0.76
Theo. $f_{ct,c}$, MPa	1.85	2.53	4.2
Theo. G_F, N/mm (full curve)	3.22	6.48	0.79
$f_{ct,c}$ VEM / $f_{ct,c}$ Exp.	0.77	0.94	1.0
G_F VEM / G_F Exp	0.54	1.15	0.93

S	straight fibre	EH	end-hooked fibre
NSC	normal strength concrete	NSM	normal strength mortar
HSC	high strength concrete	#	determined from Table 2
P	pull through of fibres only	PF	pull though and fracture of fibres
†	assumed value	††	net dimension after notched
*	mean of split cylinder tests	↑	taken as 0.8 of the cube strength

Table F5 – Comparison of VEM with high-strength and high-modulus polyethylene FRC (Wang et al., 1990a, b).

	Wang et al. (1990a,b)		
Fibre Properties - Steel			
Type	Spectra 900	Spectra 900	Spectra 900
Configuration	S	S	S
l_f, mm	12.7	12.7	6.35
d_f, mm	0.038	0.038	0.038
E_f, GPa	120	120	120
σ_{fu}, MPa	2600	2600	2600
ε_{fu}, με	3500	3500	3500
Matrix Properties			
Type	NSM	NSM	HSC
E_m, GPa	-	-	-
f_{ct}, MPa	1.8*	1.8*	4.2
ε_{ct}, με	-	-	-
w/b ratio	0.5	0.5	0.22
s/c ratio	0	0	0.133
f_{cm}, MPa	-	-	-
Composite and Testing Properties			
Specimen Section, mm	50.8×50.8††	50.8×50.8††	50.8×50.8††
Extension Rate, mm/min	0.3-1.5	0.3-1.5	0.3-1.5
Gauge length, mm	12.7	12.7	12.7
f_{cm}, MPa	-	-	-
ρ_f, %	1	2	0.6
Exp. $f_{ct,c}$, MPa	2.39	2.70	4.21
Exp. G_F, N/mm (full curve)	5.98	5.62	0.85
τ_b, MPa	1.02	1.02	1.5
K_d	-	0.8	-
l_c., mm	48	48	33
Failure mode	P	P	P
α	0.10	0.10	0.10
d_f / α	0.76	0.76	0.76
Theo. $f_{ct,c}$, MPa	1.85	2.53	4.2
Theo. G_F, N/mm (full curve)	3.22	6.48	0.79
$f_{ct,c}$ VEM / $f_{ct,c}$ Exp.	0.77	0.94	1.0
G_F VEM / G_F Exp	0.54	1.15	0.93

S	straight fibre	EH	end-hooked fibre
NSC	normal strength concrete	NSM	normal strength mortar
HSC	high strength concrete	#	determined from Table 2
P	pull through of fibres only	PF	pull though and fracture of fibres
†	assumed value	††	net dimension after notched
*	mean of split cylinder tests	↑	taken as 0.8 of the cube strength

Table F6 - Comparison of VEM with aramid FRC (Wang et al., 1990a, b).

	Wang et al. (1990a,b)			
Fibre Properties - Steel				
Type	Kevlar 49	Technora	Technora	Technora
Configuration	S	S	S	S
l_f, mm	6.35	6.35	6.35	6.35
d_f, mm	0.012	0.012	0.012	0.012
E_f, GPa	69.8	59.9	59.9	59.9
σ_{fu}, MPa	3310	3940	3940	3940
ε_{fu}, με	2500	4400	4400	4400
Matrix Properties				
Type	NSM	NSM	NSM	NSM
E_m, GPa	-	-	-	-
f_{ct}, MPa	1.8 *	1.8 *	1.8 *	1.8 *
ε_{ct}, με	-	-	-	-
w/b ratio	0.5	0.5	0.5	0.5
s/c ratio	0	0	0	0
f_{cm}, MPa	-	-	-	-
Composite and Testing Properties				
Specimen Section, mm	50.8×50.8††	50.8×50.8††	50.8×50.8††	50.8×50.8††
Extension Rate, mm/min	0.3-1.5	0.3-1.5	0.3-1.5	0.3-1.5
Gauge length, mm	12.7	12.7	12.7	12.7
f_{cm}, MPa	-	-	-	-
ρ_f, %	2	1	2	3
Exp. $f_{ct,c}$, MPa	3.96	3.31	3.11	3.65
Exp. G_F, N/mm (full curve)	1.31	1.42	1.28	1.87
τ_b, MPa	4.5	4.5	4.5	4.5
K_d	1	1	0.5	0.33
l_c, mm	4.4	5.3	5.3	5.3
Failure mode	PF	PF	PF	PF
α	0.02	0.02	0.02	0.02
β	20	20	20	20
d_f / α	0.6	0.6	0.6	0.6
Theo. $f_{ct,c}$, MPa	3.33	3.36	3.36	3.36
Theo. G_F, N/mm (full curve)	1.27	1.49	1.49	1.49
$f_{ct,c}$ VEM / $f_{ct,c}$ Exp.	0.84	1.02	1.08	0.92
G_F VEM / G_F Exp.	0.97	1.05	1.16	0.80

S	straight fibre	EH	end-hooked fibre
NSC	normal strength concrete	NSM	normal strength mortar
HSC	high strength concrete	#	determined from Table 2
P	pull through of fibres only	PF	pull though and fracture of fibres
†	assumed value	††	net dimension after notched
*	mean of split cylinder tests	↑	taken as 0.8 of the cube strength
‡	determined from $0.33\sqrt{f_{cm}}$		

Table F7 – Comparison of VEM with FR-RPC (Behloul, 1996 and Denarié et al., 2003).

	Noghabai, 2000		Behloul, 1996	Denarié et al., 2003
Fibre Properties – Steel				
Type	Steel	Steel	Steel	Steel
Configuration	SS	SS	SS	SS
l_f, mm	6	6	12	13
d_f, mm	0.15	0.15	0.2	0.15
E_f, GPa	200	200	200	200
σ_{fu}, MPa	2600	2600	2000†	-
ε_{fu}, με	-	-	-	-
Matrix Properties				
Type	HSC	HSC	RPC	RPC
E_m, GPa	36	27.2	-	-
f_{ct}, MPa	4.15	3.77	10	-
ε_{ct}, με	-	-	-	-
w/b ratio	0.33	0.29	0.18	0.14
s/c ratio	1.5	1.5	1.1	-
f_{cm}, MPa	114	99	-	-
Composite and Testing Properties				
Specimen Section, mm	dia. 55††	dia. 55††	50 × 50††	160 × 50††
Extension Rate, mm/min	-	-	-	-
Gauge length, mm	30	30	-	100
f_{cm}, MPa	129	109	200	171
ρ_f, %	1	1	2.6	2
Exp. $f_{ct,c}$, MPa	4.57	4.32	11	7.4
Exp. G_F, N/mm (full curve)	1.53	0.83	17.4	16.0
τ_b, MPa	5.0	4.5	10†	10†
K_d	-	-	-	-
l_c, mm	39	43	20	-
Failure mode	P	P	P	P
α	0.043	0.043	0.057	0.043
d_f / α	3.5	3.5	3.5	3.5
Theo. $f_{ct,c}$, MPa	4.15	3.77	10	7.25
Theo. G_F, N/mm (full curve)	1.17	1.06	15.1	18.0
$f_{ct,c}$ VEM / $f_{ct,c}$ Exp.	0.91	0.87	0.91	0.98
G_F VEM / G_F Exp	0.77	1.27	0.87	1.13

S	straight fibre	EH	end-hooked fibre
NSC	normal strength concrete	NSM	normal strength mortar
HSC	high strength concrete	#	determined from Table 2
P	pull through of fibres only	PF	pull though and fracture of fibres
†	assumed value	††	net dimension after notched
*	mean of split cylinder tests	↑	taken as 0.8 of the cube strength

Table F8 - Comparison of VEM with Kevlar 49 FRC (Maalej et al., 1995)

	Maalej et al. (1995)
Fibre Properties - Steel	
Type	Kevlar 49
Configuration	S
l_f, mm	12.7
d_f, mm	0.012
E_f, GPa	69.8
σ_{fu}, MPa	3310
ε_{fu}, $\mu\varepsilon$	2500
Matrix Properties	
Type	NSM
E_m, GPa	13
f_{ct}, MPa	4.0†
ε_{ct}, $\mu\varepsilon$	-
w/b ratio	0.25
s/c ratio	0.1
f_{cm}, MPa	-
Composite and Testing Properties	
Specimen Section, mm	50×13††
Extension Rate, mm/min	-
Gauge length, mm	10
f_{cm}, MPa	-
ρ_f, %	2.0
Exp. $f_{ct,c}$, MPa	4.2
Exp. G_F, N/mm (full curve)	1.70
τ_b, MPa	4.5
K_d	-
l_c., mm	4.4
Failure mode	PF
α	0.02
β	20
d_f / α	0.60
Theo. $f_{ct,c}$, MPa	4.27
Theo. G_F, N/mm (full curve)	1.26
$f_{ct,c}$ VEM / $f_{ct,c}$ Exp.	1.02
G_F VEM / G_F Exp.	0.74

S	straight fibre	EH	end-hooked fibre
NSC	normal strength concrete	NSM	normal strength mortar
HSC	high strength concrete	#	determined from Table 2
P	pull through of fibres only	PF	pull though and fracture of fibres
†	assumed value	††	net dimension after notched
*	mean of split cylinder tests	↑	taken as 0.8 of the cube strength
‡	determined from $0.33\sqrt{f_{cm}}$		

APPENDIX G – AXIAL STRENGTH OF DUCTILE FIBRES IN COMBINED BENDING AND TENSION

In one limit of behaviour we may take ductile fibres as being formed from a rigid-plastic material. For such a material the strain and stress distribution through the depth of the fibre, d_f, for a fibre in combined tension and bending are as shown in Figure G1.

Complicit with the assumption of rigid-plastic behaviour, for bending to occur in the fibre a tensile strain must exist (else the fibre is under a constant compressive stress with the centroid of the stress block aligned with the centroidal axis of the fibre). The case of fibre fracture with the condition of zero strain in the extreme tension fibre gives

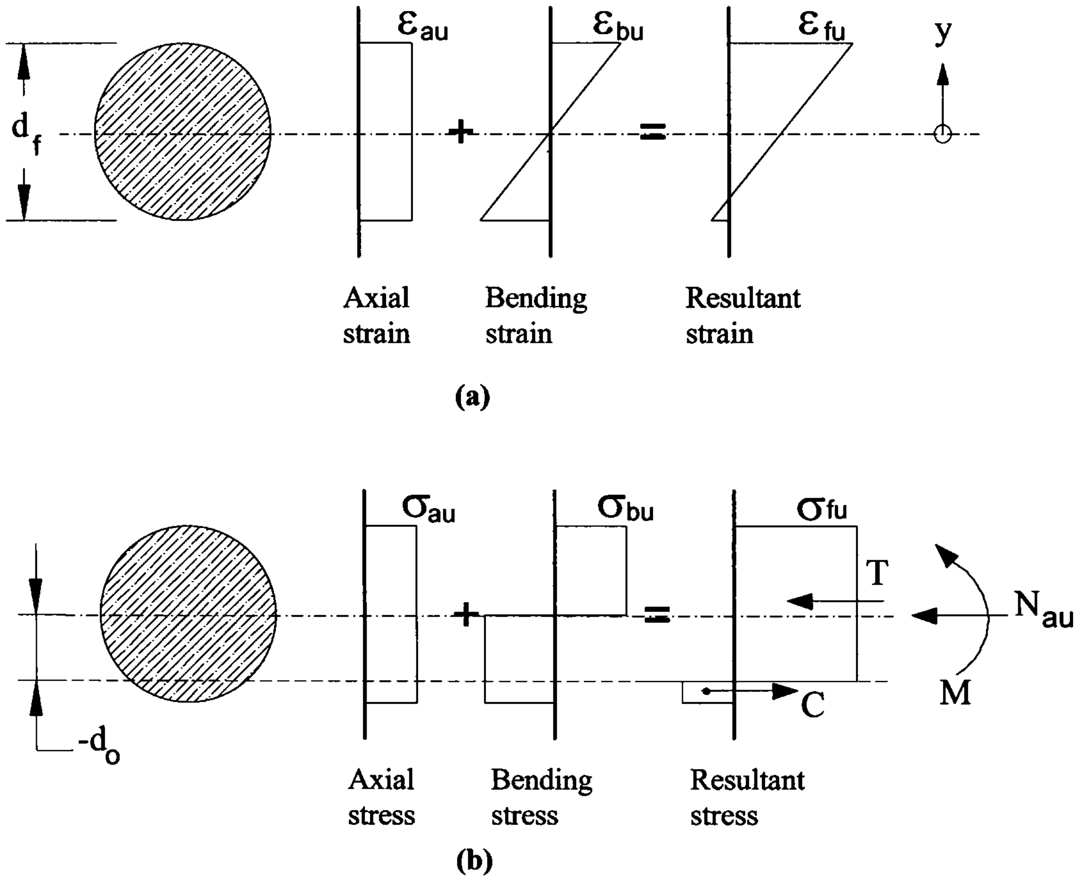

Figure G1 – Stress and strain diagram of ductile fibre in combined bending and tension.

$$\varepsilon_{au} + \varepsilon_{bu} = \varepsilon_{fu} \tag{G1}$$

$$\varepsilon_{au} - \varepsilon_{bu} = 0 \tag{G2}$$

Substituting of Eq. G2 into Eq. G1 and converting to stress we find that

$$\sigma_{au} = \sigma_{fu} \qquad \text{for} \qquad \varepsilon_{bu} \le \varepsilon_{fu}/2 \tag{G3}$$

For the case of $\varepsilon_{bu} > \varepsilon_{fu}/2$, the average axial stress on the gross cross section is

$$\sigma_{au} = \frac{N_{ua}}{A_f} \tag{G4}$$

where N_{ua} is the limiting axial force that can be applied to the fibre at the point of fracture and A_f is the cross sectional area of the fibre ($A_f = \pi d_f^2/4$).

Integrating the stress blocks over the depth of the fibre (refer Figure G1b) the tension and compression forces are found, that is

$$\begin{aligned} T &= \int_{-d_o}^{d_f/2} \sigma_{fu}\, dA \\ &= 2\sigma_{fu} \bullet \left[\int_{-d_o}^{d_f/2} \sqrt{\left(\frac{d_f}{2}\right)^2 - y^2}\; dy \right] \\ &= 2\sigma_{fu} \bullet \left[\frac{y}{2}\sqrt{\left(\frac{d_f}{2}\right)^2 - y^2} + \frac{d_f^2}{8}\sin^{-1}\left(\frac{2y}{d_f}\right) \right]_{-d_o}^{d_f/2} \\ &= \sigma_{fu} \bullet \left[\frac{d_f^2}{8}\pi + d_o\sqrt{\left(\frac{d_f}{2}\right)^2 - d_o^2} + \frac{d_f^2}{4}\sin^{-1}\left(\frac{2d_o}{d_f}\right) \right] \end{aligned} \tag{G5}$$

$$C = \int_{-d_f/2}^{-d_o} \sigma_{fu}\, dA$$

$$= 2\sigma_{fu} \bullet \left[\int_{-d_f/2}^{-d_o} \sqrt{\left(\frac{d_f}{2}\right)^2 - y^2}\; dy \right]$$

$$= 2\sigma_{fu} \bullet \left[\frac{y}{2}\sqrt{\left(\frac{d_f}{2}\right)^2 - y^2} + \frac{d_f^2}{8}\sin^{-1}\left(\frac{2d_o}{d_f}\right) \right]_{-d_f/2}^{-d_o} \tag{G6}$$

$$= \sigma_{fu} \bullet \left[\frac{\pi\, d_f^2}{8} - d_o\sqrt{\left(\frac{d_f}{2}\right)^2 - d_o^2} - \frac{d_f^2}{4}\sin^{-1}\left(\frac{2d_o}{d_f}\right) \right]$$

where d_o is the distance of the neutral axis from the plastic centroidal axis of the fibre and is given by

$$d_o = \frac{d_f}{2}\left(\frac{\varepsilon_{fu}}{\varepsilon_{bu}} - 1\right) \tag{G7}$$

By equilibrium of forces on the section, the axial force is

$$N_{ua} = T - C = \sigma_{fu} \bullet \left[2d_o\sqrt{\left(\frac{d_f}{2}\right)^2 - d_o^2} + \frac{d_f^2}{2}\sin^{-1}\left(\frac{2d_o}{d_f}\right) \right] \tag{G8}$$

and the average axial stress

$$\sigma_{ua} = \frac{\sigma_{fu} \bullet \left[2d_o\sqrt{\left(\frac{d_f}{2}\right)^2 - d_o^2} + \frac{d_f^2}{2}\sin^{-1}\left(\frac{2d_o}{d_f}\right) \right]}{\pi d_f^{\,2}/4}$$

$$= \frac{\sigma_{fu}}{\pi} \bullet \left[2\bar{d}\sqrt{1 - \left(\bar{d}\right)^2} + 2\sin^{-1}\left(\bar{d}\right) \right] \tag{G9}$$

where $\bar{d} = 2d_o / d_f$.

APPENDIX H – DETAILS OF PLASTIC MODEL CALCULATIONS

Table H1 – Shear strength calculations using plastic model on I-section.

	SB1	SB2	SB3	SB4	SB5	SB6	SB7
Sectional Properties							
A_{st} (mm^2)	1716	1716	1716	1716	1716	1716	1716
A_{sc} (mm^2)	858	858	858	858	858	858	858
ρ_w (%)	5.72	5.72	5.72	5.72	5.72	5.72	5.72
σ_p (MPa)	1750	1750	1750	1750	1750	1750	1750
d (mm)	600	600	600	600	600	600	600
h (mm)	650	650	650	650	650	650	650
b_w (mm)	50	50	50	50	50	50	50
a (mm)	2000	2000	2000	2000	2000	2000	2000
a/d	3.3	3.3	3.3	3.3	3.3	3.3	3.3
a/h	3.1	3.1	3.1	3.1	3.1	3.1	3.1
f_{cm}	161	160	149	164	171	157	169
ρ_f (%)	2.5	2.5	2.5	1.3	2.5	2.5	2.5
α_f	65	65	65	65	65 / 60	60	65 / 60
d_f (mm)	0.20	0.20	0.20	0.20	0.20 / 0.5	0.5	0.20 / 0.5
l_f (mm)	13	13	13	13	13 / 30	30	13 / 30
σ_f (MPa)- Type I	1800	1800	1800	1800	1800	-	1800
σ_f (MPa)- Type II	-	-	-	-	1200	1200	1200
P_1 (kN)	0.00	450	225	225	225	225	225
P_2 (kN)	0.00	900	450	450	450	450	450
d_1 (mm)	50	50	50	50	50	50	50
d_2 (mm)	600	600	600	600	600	600	600

Table H1 – Continued.

Calculation – Plastic theory							
υ_c	0.80	0.80	0.80	0.80	0.80	0.80	0.80
f_c^* (MPa)	129	128	119	131	137	126	135
υ_t	0.80	0.80	0.80	0.80	0.80	0.80	0.80
f_{tf} (MPa)	6.50	6.50	6.50	3.40	5.39	3.91	5.81
f_t^* (MPa)	5.20	5.20	5.20	2.72	4.31	3.13	4.65
t (mm)	114	114	114	114	114	114	114
t/h	0.18	0.18	0.18	0.18	0.18	0.18	0.18
b_f (mm)	400	400	400	400	400	400	400
b_{fef} (mm) - guess	400	400	400	400	400	400	400
a' (mm)	1894	1184	1418	1670	1594	1675	1552
A_c (mm^2)	94375	94375	94375	94375	94375	94375	94375
A_{cf} (mm^2)	45600	45600	45600	45600	45600	45600	45600
$A_{cf,ef}$ (mm^2)	45600	45600	45600	45600	45600	45600	45600
A_{cw} (mm^2)	26800	26800	26800	26800	26800	26800	26800
β_{ef}	1.7	1.7	1.7	1.7	1.7	1.7	1.7
e (mm)	277	277	277	277	277	277	277
e/h	0.43	0.43	0.43	0.43	0.43	0.43	0.43
υ_m	0.16	0.16	0.16	0.16	0.15	0.16	0.15
ξ	0.20	0.20	0.20	0.20	0.19	0.20	0.19
B	1.65	1.65	1.65	1.65	1.65	1.65	1.65
A	0.07	0.07	0.07	0.07	0.07	0.07	0.07
x/a'	0.59	0.59	0.59	0.59	0.59	0.59	0.59
a'/h	2.91	1.82	2.18	2.57	2.45	2.58	2.39
b_{fef} (mm)- Eq.14	1020	657	777	905	866	908	845
x (mm)	1121	700	838	988	943	990	919
x_w (mm)	924	578	691	815	778	817	757
x_f (mm)	970	607	727	855	816	858	795
$x \le a'$	TRUE	TRUE	TRUE	TRUE	TRUE	TRUE	TRUE
$a' \le a$	TRUE	TRUE	TRUE	TRUE	TRUE	TRUE	TRUE
$V_{u,theo}$ (kN)	338	430	336	312	340	299	345
$V_{cr,theo}$ (kN)	338	430	336	312	340	299	345
$\tau_{u,theo}$ (MPa)	10.39	13.23	10.34	9.60	10.45	9.19	10.62
$V_{u,\exp}$ (kN)	430	497	428	337	440	320	400
$\tau_{u,\exp}$ (MPa)	13.23	15.29	13.17	10.35	13.54	9.85	12.31
Theo/Exp	0.79	0.86	0.79	0.93	0.77	0.93	0.86

Table H2 – Shear strength calculations using plastic model on rectangular section.

	SB1	SB2	SB3	SB4	SB5	SB6	SB7
Sectional Properties							
A_{st} (mm^2)	1716	1716	1716	1716	1716	1716	1716
A_{sc} (mm^2)	858	858	858	858	858	858	858
ρ_w (%)	5.72	5.72	5.72	5.72	5.72	5.72	5.72
σ_p (MPa)	1750	1750	1750	1750	1750	1750	1750
d (mm)	600	600	600	600	600	600	600
h (mm)	650	650	650	650	650	650	650
b_w (mm)	50	50	50	50	50	50	50
a (mm)	2000	2000	2000	2000	2000	2000	2000
a/d	3.3	3.3	3.3	3.3	3.3	3.3	3.3
a/h	3.1	3.1	3.1	3.1	3.1	3.1	3.1
f_{cm} (MPa)	161	160	149	164	171	157	169
ρ_f (%)	2.5	2.5	2.5	1.3	2.5	2.5	2.5
α_f	65	65	65	65	65	65	65
d_f (mm)	0.20	0.20	0.20	0.20	0.20 / 0.5	0.5	0.20 / 0.5
l_f (mm)	13	13	13	13	13 / 30	30	13 / 30
σ_f (MPa)-Type I	1800	1800	1800	1800	1800	-	1800
σ_f (MPa)-Type II	-	-	-	-	1200	1200	1200
P_1 (kN)	0.00	450	225	225	225	225	225
P_2 (kN)	0.00	900	450	450	450	450	450
d_1 (mm)	50	50	50	50	50	50	50
d_2 (mm)	600	600	600	600	600	600	600

Table H2 – Continued.

Calculation – Plastic theory							
υ_c	0.80	0.80	0.80	0.80	0.80	0.80	0.80
f_c^* (MPa)	129	128	119	131	137	126	135
υ_t	0.80	0.80	0.80	0.80	0.80	0.80	0.80
f_{tf} (MPa)	6.50	6.50	6.50	3.40	5.39	3.91	5.81
f_t^* (MPa)	5.20	5.20	5.20	2.72	4.31	3.13	4.65
x (mm) – guess	2000	1449	1704	2000	1930	2000	1876
$x \leq a$	TRUE	TRUE	TRUE	TRUE	TRUE	TRUE	TRUE
$V_{u,theo}$ (kN)	332	445	357	338	364	323	370
$V_{cr,theo}$ (kN)	287	445	357	291	364	314	370
$\tau_{u,theo}$ (MPa)	10.20	13.70	10.98	10.39	11.21	9.95	11.38
$V_{u,\exp}$ (kN)	430	497	428	337	440	320	400
$\tau_{u,\exp}$ (MPa)	13.23	15.29	13.17	10.35	13.54	9.85	12.31
Theo/Exp	0.77	0.90	0.83	1.00	0.83	0.98	0.92